Structure and Bonding 161
Series Editor: D.M.P. Mingos

D. Michael P. Mingos *Editor*

Gold Clusters, Colloids and Nanoparticles I

Springer

161
Structure and Bonding

Aims and Scope

The series *Structure and Bonding* publishes critical reviews on topics of research concerned with chemical structure and bonding. The scope of the series spans the entire Periodic Table and addresses structure and bonding issues associated with all of the elements. It also focuses attention on new and developing areas of modern structural and theoretical chemistry such as nanostructures, molecular electronics, designed molecular solids, surfaces, metal clusters and supramolecular structures. Physical and spectroscopic techniques used to determine, examine and model structures fall within the purview of *Structure and Bonding* to the extent that the focus is on the scientific results obtained and not on specialist information concerning the techniques themselves. Issues associated with the development of bonding models and generalizations that illuminate the reactivity pathways and rates of chemical processes are also relevant

The individual volumes in the series are thematic. The goal of each volume is to give the reader, whether at a university or in industry, a comprehensive overview of an area where new insights are emerging that are of interest to a larger scientific audience. Thus each review within the volume critically surveys one aspect of that topic and places it within the context of the volume as a whole. The most significant developments of the last 5 to 10 years should be presented using selected examples to illustrate the principles discussed. A description of the physical basis of the experimental techniques that have been used to provide the primary data may also be appropriate, if it has not been covered in detail elsewhere. The coverage need not be exhaustive in data, but should rather be conceptual, concentrating on the new principles being developed that will allow the reader, who is not a specialist in the area covered, to understand the data presented. Discussion of possible future research directions in the area is welcomed.

Review articles for the individual volumes are invited by the volume editors.

In references *Structure and Bonding* is abbreviated *Struct Bond* and is cited as a journal.

More information about this series at
http://www.springer.com/series/430

D. Michael P. Mingos
Editor

Gold Clusters, Colloids and Nanoparticles I

With contributions by

J. Broda · W. Chen · A. Dass · A. Fielicke · R. Jin · V.R. Jupally · K. Konishi · C. Kumara · Y. Lu · D.M.P. Mingos · G. Schmid · U. Simon · A.P. Woodham · C. Zeng

Springer

Editor
D. Michael P. Mingos
Inorganic Chemistry Laboratory
University of Oxford
Oxford
United Kingdom

ISSN 0081-5993 ISSN 1616-8550 (electronic)
ISBN 978-3-319-07847-2 ISBN 978-3-319-07848-9 (eBook)
DOI 10.1007/978-3-319-07848-9
Springer Cham Heidelberg New York Dordrecht London

Library of Congress Control Number: 2014949194

Printed on acid-free paper

Springer is part of Springer Science+Business Media (www.springer.com)

Preface

Gold has a special place in the history of mankind – its chemical inertness and enduring physical qualities make it an ideal metal for the fabrication of high value coins and jewellery. They retain their bright appearance even after exposure to extreme conditions for tens or hundreds of years. Indeed as I write some intrepid gold hunters are seeking to bring up a billion dollars worth of gold bullion from the bottom of the Atlantic. It was originally mined during the Californian gold rush of the 1850s and lost at sea 150 miles East of the Carolinas in 1857 whilst being transported to New York. Colloidal gold has been known since ancient times and was used for making highly coloured glasses. Red and mauve glasses were particularly highly valued by the Romans. The realisation that colloids of the more noble metals could be studied and understood using scientific methods can be traced back to Michael Faraday's research at the Royal Institution in the 1850s. The term colloid was proposed in 1861 by Graham, by which time Faraday had established that gold, silver, copper, platinum, tin, iron, lead, zinc, palladium, aluminium, rhodium, iridium, mercury and arsenic shared the ability to form dilute clear solutions and thin films, which could be detected and studied by their ability to interact with light. This suggested that their dimensions were of the same order of magnitude as the wavelength of light.

In the mid-twentieth century the first examples of structurally characterised molecular cluster compounds of gold were reported by Malatesta and Mason and as a result of research in England and Holland the field was expanded and higher nuclearity examples of these metal–metal bonded compounds were established by crystallographic techniques. These highly coloured compounds were stabilised by tertiaryphosphine ligands, and their relevance to nano-chemistry and colloids was recognised at an early stage. In the twenty-first century the development of a very flexible synthetic route to cluster compounds of gold based on thiolato-ligands provided an important impetus to the field. This coincided with the recognition that gold which has previously been thought to be inferior to the platinum metals as a catalyst for the transformation of organic feedstocks was shown to be active as a homogenous and heterogeneous catalyst. These exciting developments have made

it timely to publish a pair of volumes of *Structure and Bonding* devoted to gold clusters, colloids and nano-particles.

The first volume opens with a historical overview of the area and provides not only a broad introduction to the area and defines more clearly the characteristics of gold clusters, colloids and nano-particle. It also addresses their characterisation and their chemical and physical properties. The potential applications of these species are also discussed. Professor Konishi provides a review of recent developments in "Phosphine-coordinated Pure-Gold Clusters: Diverse Geometrical Structures and their Unique Optical Properties". This area originated in the 1960s, and Professor Konishi has made notable contributions to this area in recent years. This is followed by three chapters by Professors Jin, Chen and Dass, and their co-authors which describe the synthesis of gold clusters based on organothiolato-ligands. An area which blossomed following the report of a widely applicable synthetic method by Brust, Schiffrin and their coworkers in 2006. Although the synthesis of these compounds is relatively straightforward the methods result in mixtures of cluster compounds and these chapters discuss the techniques which have been developed in order to produce mixtures which either contain fewer components or are amenable to modern separation techniques. The development of more sophisticated purification techniques has led to single crystals of many of these clusters which have been structurally characterised to atomic resolutions. These structures have revealed some novel architectures and also led to the important realisation that in these clusters the gold atoms have a dual role. They not only contribute to the central core, but also contribute novel gold-thiolato-ligands, which protect the surface of the cluster. Professor Schmid, who was an important contributor to the original development of the syntheses of high nuclearity gold clusters, has written with Professor Simon and Dr. Broda a chapter on the "Size and Ligand Specific Bioresponse of Gold Clusters and Nanoparticles". They emphasise new research which suggests that the high nuclearity gold phosphine clusters have important applications in the areas of biochemistry and medicine. These chapters generally deal with the synthesis of clusters prepared in water or organic solvents and the balance is restored by an important chapter by Professor Fielicke and Dr. Woodham which discusses the synthesis and properties of gold clusters in the gas phase.

The second volume starts with historically based account of the bonding in gold clusters. In the late twentieth century empirical molecular orbital calculations provided some important insights into the bonding in these clusters and led to the development of bonding models which were sufficiently robust to predict the structures of specific clusters and provide a broad framework for understanding the structures and reactions of molecular cluster compounds. The great increase in computer power since that time has made it possible to apply ab initio molecular orbital calculations to large gold clusters and the results have provided important insights into the bonding interactions which are responsible for their stabilities and structures. The importance of DFT calculations is emphasised in the chapter by Professors Johnston and Li on gold nano-alloys and clusters. The importance of gold clusters in catalysis is stressed in the chapter by Professor Freund and his co-authors titled "Model Catalysts Based on Au Clusters and Nano Particles".

The final chapter by Professor O'Hair and his co-authors underlines the importance of mass-spectrometry in the characterisation of gold clusters in their chapter titled "Gas Phase Formation, Structure and Reactivity of Gold Cluster Ions".

This is an exciting and rapidly developing area of nano-science and is attracting chemists, physicists and material scientists. The resulting interdisciplinary research continues to throw up many interesting structures and applications. I thank all the authors and the editorial staff at Springer for contributing to a volume which helps to define the field for those who are outside it and the stimulation to those in the field to make it one of the important areas of science in this century.

Oxford, UK Michael Mingos
May 2014

Contents

Struct Bond (2014) 161: 1–48
DOI: 10.1007/430_2013_138

Published online: 28 February 2014

Historical Introduction to Gold Colloids, Clusters and Nanoparticles

D. Michael P. Mingos

Abstract Colloidal gold is a suspension of sub-micrometre-sized particles of gold in a fluid either water or an organic solvent. Although the gold colloids cannot be viewed using optical microscopy, the sol has an intense colour (red for particles less than 100 nm or blue/purple for larger particles). The unique optical, electronic and molecular recognition properties of gold colloids have attracted substantial interest in recent years. The properties and applications of colloidal gold particles strongly depend upon their size and shape. For example, rod-like particles have both transverse and longitudinal absorption peaks, and the anisotropy of their shapes influences their self-assembly. Gold colloids and nanoparticles have found applications in electron microscopy, electronics, nanotechnology, materials science and medicine. The development of straightforward syntheses of gold colloids in organic solvents has had a major impact on the field and the development of etching and focusing techniques has led to the isolation of some monodispersed crystalline samples which have been characterised at the atomic level. Simultaneously the isolation of molecular cluster compounds of gold, initially stabilised by phosphine and more recently organothiolato ligands, has resulted in the characterisation at the atomic level of metal particles with 3–100s of atoms. These developments have provided interesting insights into the relationships between colloids and clusters. As the diameters of these species approach the nanoscale, interesting chemical, physical and catalytic properties have emerged.

Keywords Ascorbic acid · Catalysis · Citric acid · Clusters · Clusters · Colloids · Electron microscopy · Nanoparticles · Self-assembly

D.M.P. Mingos (✉)
Inorganic Chemistry Laboratory, Oxford University, South Parks Road, Oxford OX1 3QR, UK
e-mail: michael.mingos@seh.ox.ac.uk

Contents

Abbreviations

ANP	Gold nanoparticle
Ar	Aryl
ccp	Cubic close packed
ccs	Collision cross section
dppe	bis(diphenylphosphino)ethane
dppm	bis(diphenylphosphino)methane
dppp	bis(diphenylphosphino)propane
DFT	Density functional theory
DOSY	Diffusion-ordered spectroscopy
ESI-MS	Electrospray mass spectrometry
Et	Ethyl
EXAFS	Extended X-ray absorption fine structure
FABS	Fast atom bombardment mass spectrometry
FELIX	Free electron laser for infrared
GSH	Glutathione
hcp	Hexagonal close packed
HAADF	High-angle annular dark-field imaging
HOMO	Highest occupied molecular orbital
HRTEM	High-resolution transmission electron microscopy
i-Pr	Isopropyl
IM-MS	Combined ion mobility mass spectrometry
IMS	Ion mobility mass spectrometry
LDI-MS	Laser desorption/ionisation mass spectrometry
LUMO	Lowest unoccupied molecular orbital

MALDI	Matrix-assisted laser desorption and ionisation (mass spectrometry)
MBA	Mercapto-benzoic acid
Me	Methyl
Mes	Mesityl, 2,4,6-trimethylphenyl (not methanesulfonyl)
MS	Mass spectrometry
octyl	*n*-octyl
Pc	Phthalocyanine
Ph	Phenyl
Pr	Propyl
PAGE	Polyacrylamide gel electrophoresis
PPTT	Plasmonic photothermal therapy
ROS	Reactive oxygen species
SAXS	Small-angle X-ray scattering
SEC	Size-exclusion chromatography
SEM	Scanning electron microscopy
SERS	Surface-enhanced Raman spectroscopy
SP	Surface plasmon
SPR	Surface plasmon resonance
SR	Organothiolato ligands
t-Bu	*tert*-butyl
TEM	Transmission electron microscopy
TGA	Thermogravimetric analysis
Tio	Tiopronin
Tol	4-Methylphenyl
TOAB	Tetra(*n*-octyl)ammonium bromide
XRD	X-ray diffraction

1 Introduction

Colloidal gold has been known since ancient times and was used for producing highly coloured glasses, for example, red or mauve glasses were highly valued by the Romans. The alchemists believed that the discovery of a soluble form of gold would result in a potion called the "elixir of life", which if ingested would lead to eternal life. Hindu chemists also developed gold potions in ancient times. In the seventeenth century, the glass-colouring process was refined by Andreus Cassius and Johann Kunckel [1]. In 1842, John Herschel invented a primitive photographic process called Chrysotype (from the Greek word for gold) which used colloidal gold to record images on paper. The recognition that colloids of the more noble metals could be studied using scientific methods and may lead to interesting applications can be traced back to Michael Faraday's research at the Royal Institution in the 1850s. Peter Edwards and Sir John Muerig Thomas celebrated the 150th Anniversary of Faraday's Royal Society Bakerian Lecture on colloids with an excellent review in 2007 of his contributions and their implications [2–4]. Faraday

always emphasised that he was primarily an experimentalist and the lecture elegantly described his experiments on metal hydrosols, thin metal films, metal-island films and aerosols. The term colloid was proposed in 1861 by Graham [5], by which time Faraday had established that gold, silver, copper, platinum, tin, iron, lead, zinc, palladium, aluminium, rhodium, iridium, mercury and arsenic shared the ability to form dilute clear solutions and thin films, which could be detected and studied by their ability to interact with light. This suggested that their dimensions were of the same order of magnitude as the wavelength of light. Thus Faraday was the first to recognise that the colour was due to the minute size of the gold particles and he established that the particles of the metals in the colloids must be very small indeed because they could not be observed with the highest powered microscopes of the day. He noted their colours ranged from ruby, green, violet and blue. Gustav Mie was the first to provide a general theory for scattering and absorption of light by spherical metal particles [6]. Approximately a century later the shorter wavelengths generated in electron microscopes showed that Faraday's gold colloids had diameters from 3 to 30 nm.

The importance of gold colloids for colouring glasses and the possible medical applications of gold colloids were recognised at an early stage. The latter reinforced the alchemical view that a soluble form of gold could be an elixir of life and indeed was widely investigated as a possible treatment for rheumatoid arthritis. The ability to use electron microscopy to study the size and morphology of metal colloids has led to an important renaissance in the study of metal colloids and these studies have led to the investigation and exploitation of their properties.

The discussion above has highlighted the long and distinguished history of metal colloids. In the twentieth century the closely related areas of cluster chemistry and nanochemistry have developed and many research articles and proposals tend to merge all three areas under the portmanteau term "nanotechnology" or "nanoscience" and do not take care to clearly define the characteristics of each area and their borders [7–9]. Nanoscience is the study of phenomena and manipulation of materials at the atomic, molecular and macromolecular scales, where properties differ significantly from those at a larger scale. Nanotechnologies are the design, characterisation, production and application of structures, devices and systems by controlling shape and size at the nanometre scale. Implicit in this definition is the belief that "Novel properties that differentiate 'nanoparticles' from the 'bulk material' typically develop at a critical length scale of under 100 nm". The promise of "novel properties" has stimulated much research and emphasised the strongly held view that at the nanoscale, the physical and chemical properties of nanoparticles are different from those of the bulk material [10–24]. This view has emphasised the importance of the size of nanoparticles; however, it represents an oversimplification since clusters, colloids and nanoparticles differ from their parent bulk material in more subtle and interesting ways. Therefore it is important to try and define their similarities and differences while recognising that some materials lie in overlapping border regions. It is also important to establish for a specific chemical or physical property the dimension when the behaviour of the nanoparticle or colloid no longer mirrors that of the bulk and recognise that the transition may not be identical for each property.

Therefore, before discussing significant developments in these fields, it is perhaps useful to try and define more clearly the characteristic features of each sub-discipline. The IUPAC Gold Book [25] provides the following definitions:

Colloidal is a state of subdivision, implying that the molecules or polymolecular particles dispersed in a medium have at least in one direction a dimension roughly between 1 nm and 1 μm or that in a system discontinuities are found at distances of that order. The following are characteristic features [7–9, 11]:

1. Traditionally colloids had poorly defined compositions and >15% dispersion in size, but there have been improvements in synthetic methods which have improved their quality. The colloidal particle contains between 400 and 40,000 metal atoms and their agglomeration to bulk metal is prevented by the build-up of charges on their surface. These charges may arise from surface metal atoms in a different oxidation state, or ligands attached to the surface metal atoms. In the solution around the colloid charged particles are present in higher concentrations than the bulk of the solvent. The Stern layer shown in Fig. 1 is defined as those charged species which migrate with the colloid particle under the influence of an electric field. The presence of this charged layer means that the ionic strength of the solution may alter the dimensions and properties of the colloid.
2. Electron microscopy studies have established that colloids may be synthesised with ordered structures based on close-packed arrangements of metals even when the particle diameters are in the nanometre range. This ordering manifests itself either in single or twinned crystals and for smaller-sized particles structures with fivefold symmetry based on the icosahedrons and dodecahedron are commonly observed for silver and gold. These particles are described as multiply twinned [2, 3, 26, 27].
3. Electron microscopy is not able to resolve the lighter ligating atoms on the metal surface and consequently the colloids have an ill-defined quantity of surface anions such as O^{2-}, X^{-}, $OH^{-}$and solvent molecules such as H_2O or polar organic molecules.
4. Although the colloids of particular interest in this review are based on metals a wide range of inorganic and organic molecular species also form colloids.
5. They form optically clear solutions (*sols*) which have spectroscopic properties which may be related to the sizes of the particles (see below).
6. Reproducible syntheses have been developed which can lead to a wide range and specifically sized metal colloids and the dispersities of the colloid may be reduced by more controlled synthetic procedures. This reproducibility means that colloids with specified dimensions and dispersities are now commercially available [28].
7. Traditional colloids are not readily isolated as solids or re-dissolved, but recently made thiolato-based colloids have been made which do re-dissolve in organic solvents.
8. Traditionally produced colloids did not have reproducible catalytic properties, but improved synthetic methods and the availability of standard samples have increased the reliability of the results.

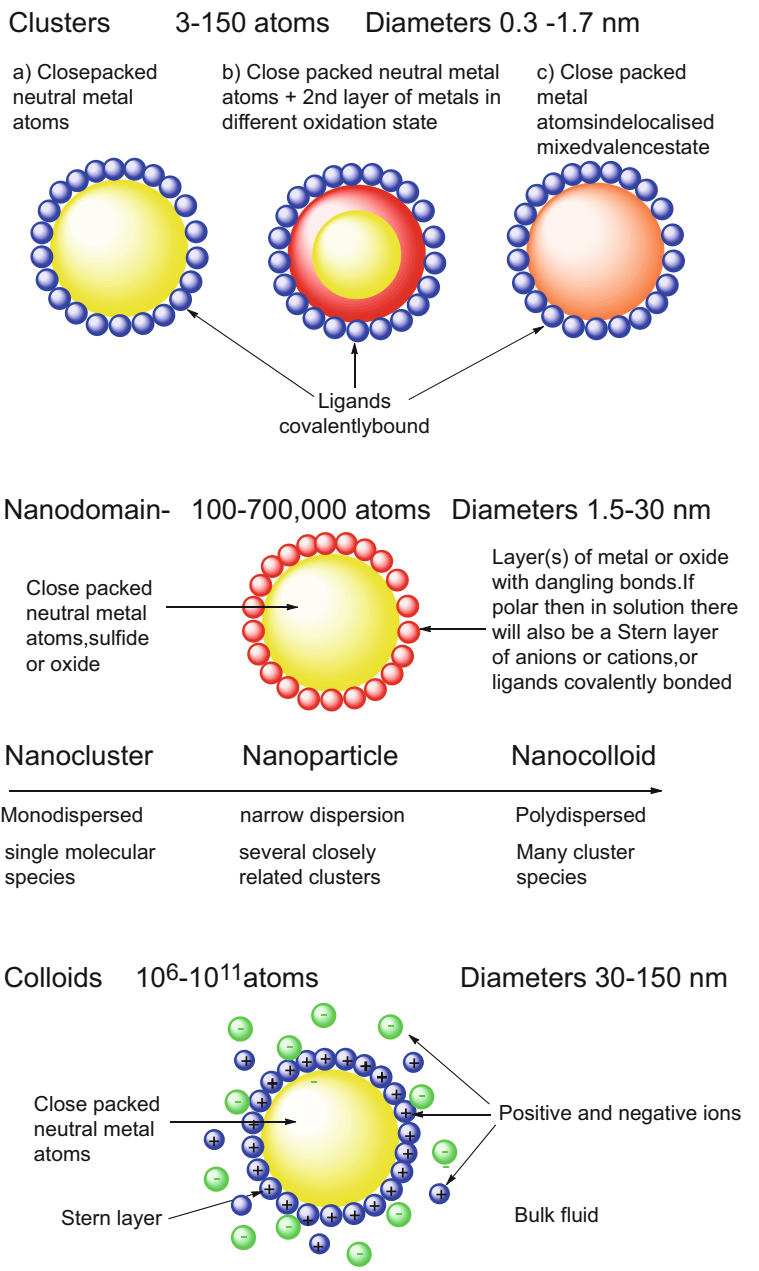

Fig. 1 Schematic illustrations of clusters and colloids and the nano-domain with nanoclusters, nanoparticles and nanocolloids (the particles are not drawn to scale). The gold atom has a metallic radius of 0.144 nm and a close-packed gold particle with a diameter of D nm has approximately $31D^3$ atoms

The interaction of gold colloids with light is strongly influenced by their environment, size and physical dimensions. The oscillating electric field of light interacts with the free electrons, causing a concerted oscillation of electron charge that is in resonance with the frequency of visible light. These resonant oscillations are known as surface plasmons. For small (~30 nm) monodispersed gold particles the surface plasmon resonance (SPR) results in an absorption of light in the blue–green portion of the spectrum (~450 nm) while red light (~700 nm) is reflected, giving the colloid solution a rich red colour. When the particle size is increased, the wavelength of the surface plasmon resonance shifts to longer wavelengths. Red light is then absorbed, and blue light is reflected, yielding sols with a pale blue or purple colour. As the particle size continues to increase toward the bulk limit, surface plasmon resonance wavelengths move into the IR portion of the spectrum and most visible wavelengths are reflected, giving the sols a clear or translucent colour. If NaCl is added to a gold colloid sol, the surface charge on the gold particles becomes neutral and they aggregate. The larger average size results in a colour change from red to blue. The degree of aggregation may be reduced by polymers, ligands and biological molecules with good donor atoms, e.g. N, P or S. This surface modification enables gold nanoparticles to be used extensively in the chemical, biological, engineering and medical applications discussed below [7–9, 11, 28].

The interpretation of SPR depends primarily on a paper published in 1908 by Mie [6], who solved Maxwell's equations for spherical particles with the appropriate boundary conditions. It attributes the surface plasmon resonance to the dipole oscillations of the free electrons in the conduction band which occupy energy levels directly below the Fermi level. The theory rationalises the following broad features of SPR: (1) its position around 520 nm, (2) its decrease when the colloid core size is reduced to 1.4–3.2 nm because of the onset of quantum size effects, (3) for particles with 1.1–1.9 nm diameters, sharper transitions which may be attributed to discrete "molecular transitions" are observed which is also suggestive of quantum size effects, (4) the decrease in intensity of SPR as the size of the colloid decreases is accompanied by a broadening of the bandwidth. The SPR maximum wavelength and bandwidth are greatly influenced by the size and shape of the colloid particle and the refractive index of the solvent. Not surprisingly the position of SPR also depends on the strength of interaction between ligands and the metal atoms. For example, sulphur ligands, which are particularly effective at bonding to surface gold atoms, cause a large perturbation. The charge on the metal core is another significant factor and an excess electronic charge results in shifts to higher frequencies and a deficiency to lower frequencies.

For non-spherical particles multiple plasmon bands may be observed if the asymmetry is significant. The positions and intensities of the bands depend on the size, shape and the local dielectric environment. Gold nanorods which have a high degree of asymmetry have attracted considerable attention in recent years and are discussed further in Sect. 4.4.

Cluster is defined as a number of metal centres grouped close together which can have direct metal–metal bonding interactions or interactions through a bridging ligand, but are not necessarily held together by these interactions. Molecular cluster

compounds of gold with phosphine ligands were extensively studied by the groups of Mingos [29–38] and Steggerda [39–42] between 1970 and 2000 and more recently thiolato ligands have been used to synthesise higher nuclearity clusters. These studies have established the following characteristic features:

1. They have very well defined chemical compositions and structures, which result from crystallographic and spectroscopic data.
2. They have a single composition with 2–150 metal atoms and therefore 0% size dispersion.
3. The central core and ligand sphere are defined with atomic precision.
4. Their syntheses generally are made in the solution phase and are well defined and reproducible. In labile systems the size and number of ligands may control the size of the cluster formed.
5. They form clear (and generally highly coloured) solutions and have well-defined spectroscopic properties which are attributed to molecular transitions which originate from occupied to empty delocalised molecular orbitals. The HOMO-LUMO gap generally becomes smaller with increasing cluster size.
6. Clusters are generally soluble in organic solvents, but the ligands may be functionalised to make the cluster compounds water soluble. The solid-solution equilibrium is generally reversible and therefore the compounds may be recrystallised.
7. They have reproducible catalytic properties – although not many show high catalytic activities.
8. Unlike colloids they do not have an ill-defined number of weakly held surface anions.
9. Neutral clusters have a central metallic core stabilised by neutral ligands, e.g. CO, PR_3, and anionic ligands, e.g. Cl^-, SR^-. Cationic clusters may be generally described as delocalised mixed valence compounds where the metals cannot be described by localised oxidation states, but there are some recent examples of larger clusters which have a central core and an outer layer of metal atoms with different formal oxidation states [43, 44]. Anionic clusters with carbonyl ligands are also well known for the later transition metals, but not for gold.

The structures and bonding properties of gold clusters are discussed in greater depth in a separate chapter in the accompanying volume and this chapter will concentrate on colloids and nanoparticles.

There is no accepted IUPAC definition of *nanoparticle*, but one given in the UK PAS71 (BSI Standards Publication 2 Nanoparticles-Vocabulary) is: A particle having one or more dimensions of the order of 100 nm or less. Nanoparticles have the following characteristics [7, 8, 10, 12–23]:

1. They have well-defined compositions and may include a wide range of inorganic classes of compounds, e.g. metals, oxides, sulphides, etc.
2. They have a relatively narrow size range, i.e. their dispersion is $<15\%$.

3. Their synthesis may be achieved by either solution or solid-state methods. Many nanomaterials are made directly as dry powders, and it is a common myth that these powders will stay in the same state when stored. In fact, they sometimes rapidly aggregate through a solid bridging mechanism in as little as a few seconds. The dangling bonds at the surface of the nanoparticle make them reactive. If the nanoparticles need to be kept separate, then they must be prepared and stored in a liquid medium designed to facilitate sufficient inter-particle repulsion forces to prevent aggregation.
4. If the nanoclusters are made in solution, then their properties depend on the ability of the ligands to co-ordinate to the surface of the particle. Strong chelating ligands lead to more clearly defined materials.
5. Some nanoparticles may be re-dissolved to give clear solutions in organic solvents and water.
6. They have reproducible electronic and catalytic properties, which depend closely on the sizes of the particles.

Nanoparticles may be synthesised either by attrition methods which involve the fragmentation of bulk solids (top-down) or by pyrolysis, inert gas condensation, solvothermal reactions and sol–gel fabrication (bottom-up) techniques. The attrition methods involve grinding bulk solids by ball mill, planetary ball mill or related size reducing techniques. These result in a broad distribution of particle sizes – 10–1,000 nm – and a variety of shapes. Applications include nano-composites and nano-grained bulk materials. Bottom-up methods may be executed in the gas and liquid phases. For metals this involves evaporation followed by gas-phase reactions. Nucleation/condensation at the substrate interface results in agglomeration and grain growth. Liquid-phase fabrication involves the initial reaction in the liquid phase followed once again by agglomeration and grain growth. The liquid-phase methods include hydrothermal and solvothermal methods, sol–gel methods and micro-emulsion syntheses in structured materials. Pyrolysis involves the evaporation of a volatile precursor and it is then forced through a hole or opening at high pressure and burned. Instead of evaporation a thermal plasma, which achieves temperatures of 10,000 K, can cause the evaporation of small (micrometre) particles, which on cooling form nanoparticles. The plasmas may be dc plasma jet, dc arc plasma and radio-frequency induction plasmas.

Nanoparticles may be classified according to their dimensionality, morphology, composition, uniformity and degree of aggregation. The definition of the dimensionality of colloids has caused some confusion and it is generally more common to define the dimensionality (nD) in terms of the number of pseudo-infinite axes. Therefore a nanosurface is 2D and a nanoparticle is 0D. 1D nanomaterials are one dimensional in the nanometre range. Their applications in electronics include circuitry in computer chips and anti-reflection coatings on lenses. 2D nanomaterials frequently have their nanostructures attached to a substrate or nanopore filters used for molecular separation. Asbestos fibres represent examples of 2D nanoparticles. The difference between nanorods and nanowires is subtle, since although the former are typically thicker and shorter than the latter there are regions where the characteristics overlap.

Although the similarities and differences which characterise colloids, clusters and nanoparticles have been emphasised in the discussion above, it is important to note that the fields have grown closer together in recent years as a result of dogged synthetic and purification techniques and great advances in structural and spectroscopic methodologies. Specifically colloids, clusters and nanoparticles are consistently produced by the reduction of gold(I) or gold(III) complexes in the presence of Lewis bases which are capable of bonding to the surface of the closely packed collection of gold atoms. Therefore a continuum of properties may be observed. Lewis bases which bond strongly to gold, e.g. tertiary phosphines and organothiolates, lead to a smaller range of cluster sizes and dispersities and therefore present greater opportunities for isolating pure compounds which can be structurally characterised by single-crystal X-ray techniques. These well-defined compounds provide effective test beds for testing theories which develop the underlying science responsible for the unusual catalytic, biological and electronic properties of gold clusters and colloids. Less strongly bound ligands encourage cluster growth-producing clusters with larger diameters, which have the advantage that they more closely resemble the parent metal, but this is accompanied by a greater uncertainty in defining the precise nature of the metal–ligand interactions. Some important features of clusters, nanoparticles and colloids are represented schematically in Fig. 1. This figure emphasises the important size differences which distinguish clusters, nanoclusters, nanoparticles and colloids, but it does not adequately represent the possible range of similar species which may exist in each category, i.e. their dispersities. Crystalline molecular clusters with 3–40 metal atoms studied since the 1960s are "atomically precise" since they are essentially free of impurities and have a well-defined formula established from analytical data and a structure determined by single-crystal X-ray techniques. In the solid and in solution they have a homogeneous distribution of identical molecules and may therefore be described as "monodispersed" and atomically precise [43]. Furthermore, in these molecular clusters, the exchange processes involving the ligands are sufficiently slow that it is reasonable to assume that the composition established for the solid is maintained in solution, although the small clusters may undergo intramolecular ligand and skeletal rearrangements on the NMR time scale. In recent years, larger clusters with 40–120 metal atoms have been formed initially as a mixture of similar clusters, i.e. a polydispersed mixture of clusters with differing numbers of metal atoms and ligands. As a result of either purification or chemical-focusing methods and some luck, a monodispersed sample may be obtained from these mixtures. It is reasonable to describe these species as nanoclusters as the diameter approaches nanodimensions [43]. Crystallisation of these pure compounds leads to an ambiguous characterisation of these species and the overall process mirrors that established for smaller clusters in earlier decades. Specifically, this monodispersed sample may be crystallised and its structure uniquely defined by single-crystal X-ray techniques and its atomic composition confirmed by mass spectrometry. There have been major advances in this area during the last decade, which have resulted in relatively monodispersed nanoclusters with 3–100 nm diameters, and these exciting developments are described in other chapters of this

volume. If these separation and purification techniques do not result in a chemically pure sample, then the resultant sample remains a mixture of cluster molecules. If these mixtures have many components, this leads to a Gaussian distribution of cluster sizes and compositions. The dispersity of the sample indicates the breadth of the distribution function. The dispersity depends primarily on the variation in the number of metal atoms which occur in the nanoparticles, but may also be influenced by the number of ligands attached to the metal surface. These polydispersed samples are no longer directly analogous to pure molecular clusters and begin to resemble classical colloidal species. Their dispersities are estimated on the basis of a statistical analysis of the sample dimensions using electron microscopy. In this review these alternative possibilities are defined as follows: *nanocluster* for analytically pure and monodispersed clusters and *nanoparticles* or *nanocolloids* for polydispersed samples containing several closely related cluster species.

As the average size of the particles increases and the stabilising ligands become more labile, then more facile equilibria involving the exchange of ligands and solvent on the surface of the metal particle become more important. Faraday's colloids belong to this category since they have wide distribution of dispersities and in solution complex equilibria involving the metal atoms, solvent and ligands. The complexity of colloids is represented pictorially at the bottom of Fig. 1. An important "holy grail" of nanochemistry is the preparation of atomically precise nanoclusters which are as well defined as the giant molecules found in molecular clusters. As Jin has noted, "the atomic precision" is a stricter and more accurate criterion than the conventional term "monodispersity" used for regular nanoparticles, and correspondingly, mass spectrometry is a more definitive characterisation technique than TEM and is indeed indispensible in nanocluster characterisation [43].

Recent X-ray crystallographic studies [44] have established that the long held view that clusters and nanoparticles of gold contain a close-packed central core of gold atoms, resembling that found in the bulk metal, surrounded by soft ligands bonded to the surface gold atoms is perhaps an oversimplification. In particular these studies have demonstrated that surface gold atoms may combine with organothiolato ligands (RS) to form mono-anionic metallo-thiolato ligands $[(RS)Au(SR)]^-$ and $[(RS)_3Au_2]^-$. These ligands are able to co-ordinate to core metal atoms using conventional RS–Au dative bonds, which may be supplemented by aurophilic gold–gold interactions [44, 45]. These metallo-thiolato ligands are represented schematically in Fig. 2. The cyclic $[Au_4(SR)_4]$ units shown in Fig. 2 are commonly observed in the fragmentation patterns observed in the mass spectra of gold thiolato-colloids [46, 47]. These observations suggest that those clusters and nanoparticles are actually mixed-valency compounds and indeed their characteristic colours may arise from mixed valence electronic transitions from the Fermi level of the core atoms to the empty valence orbitals on the gold(I) surface atoms.

Although the section above has tried to define more clearly the distinctions between clusters, colloids and nanoparticles, there are also grey areas in-between where the differences remain blurred. The original syntheses of gold cluster compounds stabilised by phosphine ligands originated in the late 1960s from Malatesta's group in Milan [48–51] and were extended primarily by Mingos

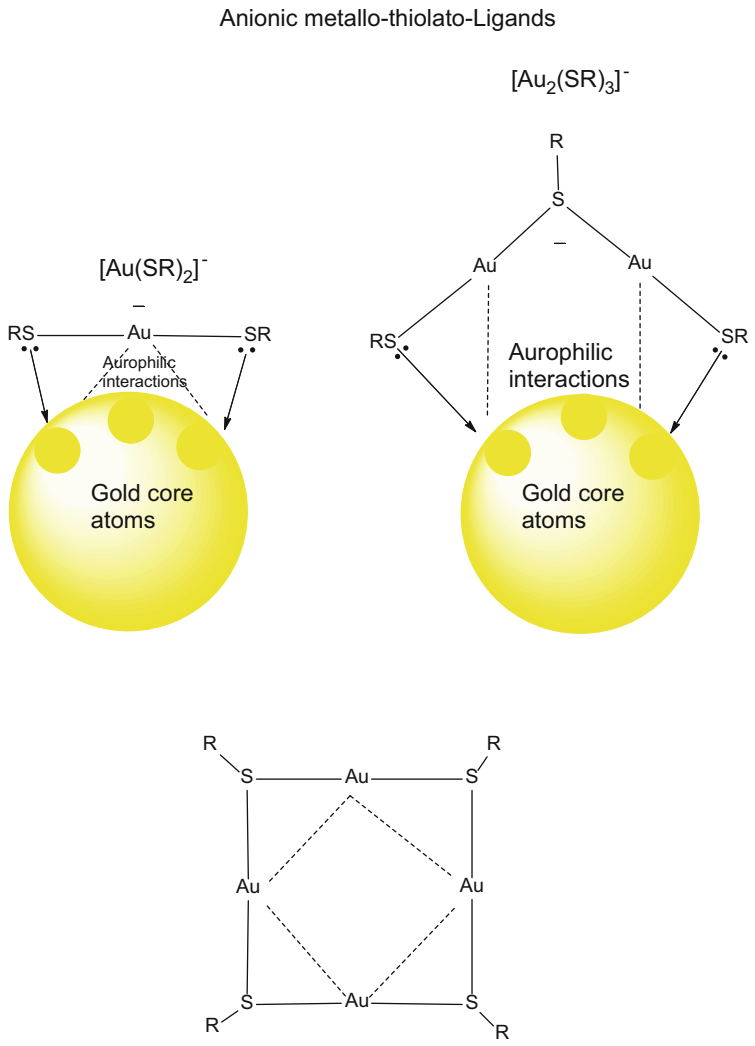

Fig. 2 In the mono-anionic gold-thiolato ligands (shown at the *top* of the figure) the primary bonding involves dative bonds from the sulphurs of the thioato ligands, but additional aurophilic interactions may occur between these metallo-thiolato ligands and the metal core. Although a formal negative charge is assigned to these ligands (mainly for electron counting purposes) the electroneutrality principle suggests that the charges on individual atoms are close to zero. The neutral metallo-thiolato-ring shown at the bottom may bind on the surfaces of gold particles is also possible and has been identified in theoretical calculations

[29–38] and Steggerda [39–42] in the 1970s and 1980s. The molecular cluster compounds had 8–13 gold atoms and their characterisation using single-crystal X-ray crystallographic techniques led to unambiguous chemical formulations. In 1981 Schmid et al. reported [7, 8, 52–54] that if diborane B_2H_6 was used rather than

$NaBH_4$ to reduce gold(I) triphenylphosphine complexes, then the resultant product was $[Au_{55}(PPh_3)_{12}Cl_6]$, which he formulated as a very stable closed-shell and close-packed cluster with 42 surface atoms [54]; 12 of which are stabilised by triphenylphosphine and six by chloro ligands. Au_{55} is the second of the series of so-called close-packed "full-shell clusters". In the absence of definitive crystallographically based structural data, it was proposed that it consists of a fragment of close-packed cuboctahedral structure similar to that found in bulk gold (see I and II). Full-shell close-packed clusters have $10n^2 + 2$ atoms in the nth shell and when $n = 2$ there are 42 atoms on the surface surrounding a core-centred cuboctahedron with 13 gold atoms. Schmid has argued that clusters having these close-packed arrangements are especially stable [54]. Despite many attempts over the last 30 years it has proved impossible to crystallise this material and confirm unambiguously its molecular structure. Careful analytical work has concluded that Schmid's material is probably heterogeneous and actually has particles with a size range of 1–3 nm with a maximum of 1.4 nm [55, 56]. Subsequently, Hutchinson et al. [57] developed a refined synthesis based on the reduction of $[AuCl_4]^-$ with $NaBH_4$ in aqueous solutions with tetra-octylammonium cations as phase-transfer agents to the toluene layer containing triphenylphosphine. They proposed an approximated composition of $[Au_{101}(PPh_3)_{21}Cl_5]$ for the 1.4 nm particles synthesised in this manner [57]. Therefore, although Schmid's material is probably not a unique Au_{55} cluster, its discovery encouraged a great deal of research [58] and the chapter by Broda et al. provides a detailed description of its widespread applications in the biological area [58]. To date the largest unambiguously characterised gold phosphine cluster compound is $[Au_{39}(PPh_3)_{14}Cl_6]$ which has a structure based on fused icosahedra [44, 59, 60].

Broda et al. [59] have argued that Au_{55} occupies an extraordinary position in the range between molecule and extended solid and this is demonstrated not only by its physical properties but also its bio-response. Physically it exhibits quantised charging effects associated with adding an extra electron to a small capacitance, which results in applications as a single electron switch at room temperature. The stability of this gold nanoparticle has indeed an important influence on bio-response, because of the interaction mechanisms between the nanoparticle and the relevant bio-systems. The interaction with any kind of biomolecule and the metal core can only happen if the original ligands are either completely or at least partially released or replaced during the chemical processes. $[Au_{55}(Ph_2PC_6H_4SO_3Na)_{12}Cl_6]$ is a water-soluble derivative of the original compound $[Au_{55}(PPh_3)_{12}Cl_6]$ and plays the dominant role in the work reported by Broda et al. Their review also compares larger and smaller nanoparticles and highlights the emerging field of applications for gold nanoparticles in diagnostics and therapy [58].

In vitro applications of gold nanoparticles utilise their size-dependent properties in their interactions with proteins and cells. Their effectiveness depends on the partial replacement of the ligand and therefore the kinetics of ligand replacement is an important consideration. Broda et al. have noted that 1.4 nm-sized Au_{55} nanoparticles with relatively weakly bound phosphine ligands are very cytotoxic [58]. This was shown in a series of tests with human cancer cell lines. They

proposed two reasons for the cytotoxicity: (1) the size of the 1.4 nm Au_{55} clusters fits perfectly to the height of the major grooves of DNA (1.3–1.5 nm) and thus may block transcription of DNA and (2) it induces the formation of reactive oxygen species (ROS) as a consequence of its electronic properties, leading to oxidative damage of adjacent biomolecules and subcellular units. Studies with smaller and larger gold phosphine-stabilised nanoparticles show a much less toxicity, supporting their contention that $[Au_{55}(Ph_2PC_6H_4SO_3Na)_{12}Cl_6]$ has a very special bio-response. Therefore, a contradiction remains – the specificity of the bio-response suggests a well-defined molecular species, but the more detailed analytical studies suggest that the material has the characteristics of a colloid with a narrow range of dispersities.

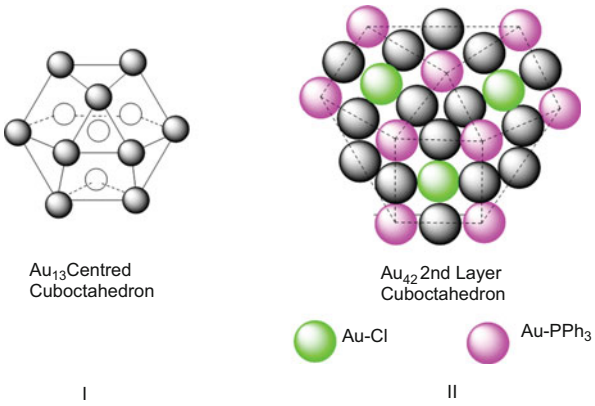

The study of gold colloids has similarly provided some new inroads and insights into molecular gold cluster chemistry and thereby blurred the distinction between the two disciplines. For example, the synthesis of gold colloids using the method developed by Brust et al. which is discussed more fully in the next section has also proved to be very versatile and useful for making thiolato-protected colloids which can be handled using the experimental techniques of modern inorganic and organic chemistry. These techniques have been used to refine the spread of species formed by focusing the syntheses. The dispersities of the colloids are reduced to such an extent that single molecular species may be isolated and crystallised. This has resulted in the single-crystal characterisation of $[Au_{25}(SR)_{18}]$, $[Au_{38}(SR)_{24}]$ and $[Au_{102}(SR)_{44}]$ for example and the development of the important "divide and protect concept" whereby the central gold cluster is stabilised by gold thiolato ligands in the manner illustrated in Fig. 2 [44, 61–66]. The successful crystallisation and structural elucidation of $[Au_{102}(p\text{-MBA})_{44}]$ by Kornberg and co-workers [63] was pivotal in redefining the nature of the gold–sulphur bonding in colloids and nanoclusters. It established that the SR group is not as previously thought a simple 2e Lewis base or a 4e bridging ligand bonded to the surface of the gold particle but plays a unique role in forming the novel oligomeric gold thiolato-motifs ($[Au(SR)_2]$ and $[Au_2(SR)_3]$ shown in Fig. 2) which are capable of protecting the central gold

fragments which are based either on icosahedra or cuboctahedra. These unambiguous crystallographic determinations have therefore not only extended greatly the range of molecular gold cluster compounds but also provided an important generalisation that gold colloids may actually be based on a mixed valency combination of a central core (Au(0)/Au(I)) and thiolato-Au(I) chelating ligands, which are described as "staple motifs".

The distinction between nanoparticles and clusters or colloids is a subtle one and one which is becoming more clearly defined as a result of the new developments which are articulated in these reviews. The view that nanoparticles constitute a new class of material, which have properties which are fundamentally different from those of discrete cluster molecules or the bulk metal, has gained ground in recent years. Nanoparticles with dimensions of the order of 1–20 nm fall between small molecular clusters with discrete energy levels and the bulk metal which has continuous energy states. Many properties of metal nanoparticles, e.g. ionisation energy, electron affinity, cohesive energy, absorption frequency electrical conductivity, melting points and chemical reactivity, should show a regular variation with cluster size according to classical physics theory, i.e. they should follow a relationship of $1/R$, where R is the radius of the metal particle; however, quantum size effects may result in important discontinuities when the particles have dimensions lie in the nano-range [2, 3]. These quantum size effects could have important implications for the chemical, catalytic, biological and electronic properties of these species.

2 Synthesis of Gold Colloids

2.1 Aqueous Solutions

Faraday produced colloids of gold using $H[AuCl_4]$ as the source of gold and phosphorus vapour as the reducing agent. They are stabilised in solution because the solvent molecules and negative charges associated with the reducing agent inhibit the aggregation of the gold particles to form larger samples of bulk gold which would precipitate from the solution. They are therefore kinetically stabilised relative to the bulk metal and require stabilising anions and solvents which do not readily re-oxidise the colloidal gold particles to gold(I). The preparation of gold sols may be classified according to whether they are prepared in aqueous or non-aqueous solvents and whether they are made by dispersion (physical) methods or reductive chemical condensation processes. $H[AuCl_4]$ is still the most widely used precursor for gold colloids in aqueous solutions, and the reducing agent and concentrations are varied in order to vary the size and size distribution of the resultant gold particles. Phosphorus initially preferred by Faraday [4] is still employed for preparing colloids with mean diameters of 3–12 nm. Specifically a gold sol with a mean diameter of 5 nm may be made from $H[AuCl_4]$ neutralised by

the addition of K_2CO_3 followed by the addition of white phosphorus in diethyl ether. The success of the procedure is indicated by the development of purple–brown colouration in the aqueous layer. Other reducing agents which are commonly used include sodium citrate and ascorbic acid. The sodium citrate recipe, which was developed by Turkevich (in the 1950s) [67, 68] and Frens (in the 1970s) [69, 70], is the most commonly cited method. The procedure is based on the addition of sodium citrate to a boiling aqueous solution of $H[AuCl_4]$ which initially gives a grey colour which changes to a lavender colour and with continued boiling becomes deep red. Gold colloids with mean diameters that range from 12 to 147 nm may be made by varying the concentration of sodium citrate. Smaller colloid diameters have been achieved with alternative reducing agents such as sodium thiocyanate and hydrolysed tetrakis(hydroxymethyl)phosphonium chloride. The kinetic stabilisation of gold colloids is so effective that some of Faraday's samples are still available for viewing at the Royal Institution in London. The synthetic procedure is sufficiently routine that several chemical suppliers sell gold colloid solutions with well-defined mean diameters (e.g. see [28]). This commercialisation has encouraged their widespread use in medical applications and catalysis. Recently, the molecular evolution of spherical gold nanoparticles in the Turkevich/Frens reaction has been investigated in more detail. Widespread networks of gold nanowires are formed initially as transient intermediates and they are responsible for the dark colour of the reaction solution before it takes up its characteristic ruby-red colour [71].

Larger particles are formed when less sodium citrate is added (possibly down to 0.05%, after which there simply would not be enough to reduce all the gold). The reduction in the amount of sodium citrate will reduce the amount of the citrate ions available for stabilising the particles, and this will cause the small particles to aggregate into bigger ones (until the total surface area of all particles becomes small enough to be covered by the existing citrate ions). It has been proposed that colloids produced by the citrate synthetic route are stabilised at their surface by a combination of citrate and chloride anions. Addition of stronger Lewis bases may result in the displacement of these anions and the disproportionation of the colloid to larger aggregates and in the limit insoluble bulk gold particles and gold(I) complexes of gold. For example the addition of pyridine to a gold sol causes the colloidal particles into strings or chains of gold particles. The chelate effect has been widely used in co-ordination chemistry to stabilise metal complexes and polymers and surfactant molecules have been used in a similar manner to form a protective sheath on the surface of colloidal particles. The protective sheath bonds more strongly to the surface gold atoms and thereby assists the solvation of gold colloids. In Victorian times gelatin and agar were commonly used, but currently organic synthetic polymers are used. At times the polymer may combine a co-ordination and reducing role. For example, poly(ethylenimine) reduces $H[AuCl_4]$ and adheres to the surface of the colloidal particles and thereby generates particles with very small average diameters [71].

In 2009 Perrault and Chan [72] developed a seed-based synthesis of gold sols using hydroquinone to reduce $H[AuCl_4]$. Gold nanoparticle acts as the seeds in much the same way that reduced silver particles seed silver halide particles in the

photographic process. Gold nanoparticles formed by hydroquinone reduction may catalyse reduction of ionic gold onto the surface of the colloidal particles and the presence of a stabiliser such as citrate results in controlled particle growth. Typically, the nanoparticle seeds are produced using the citrate method. The hydroquinone method complements that of Frens [69, 70] as it extends the range of monodispersed spherical particle sizes that can be produced. The Frens recipe is ideal for making colloids mean with diameters 12–20 nm and the hydroquinone recipe produces colloids from 30 to 250 nm.

2.2 *Non-aqueous Solutions*

Among the various solution phase-based syntheses, the Brust–Schiffrin [73–75] or closely related methods have been widely applied to the preparation of gold nanoclusters due to their simplicity and versatility. Mulvaney and Giersig first reported the stabilisation of gold colloidal particles by alkanethiols in 1993 [76], but the publication by Brust and Schiffrin in 1994 which reported the synthesis of gold colloids in non-aqueous solvents has had a major impact in the field [77]. The widespread adoption of this method arose because the synthetic procedure resulted in thermally and air-stable colloids with small dispersities and relatively controlled particle sizes (1.5–5.2 nm). Moreover the resultant colloids were readily isolated and could be re-dissolved in organic solvents. $H[AuCl_4]$ dissolved in water is still used as the gold source, and $NaBH_4$ the reducing agent (although it probably also functions as an anti-coagulant) and thiolato ligands, e.g. dodecanethiol, are dissolved in the toluene layer (see Fig. 3). Tetra(*n*-octyl)ammonium bromide (TOAB) acts as a phase-transfer agent across the water/toluene interface and the bromide ions act as supplementary stabilising ligands. The organic phase rapidly changes colour on addition of $NaBH_4$ from orange to deep brown. The resultant gold colloidal particles have mean diameters of 1–3 nm, with a maximum of 2.0–2.5 nm in the distribution function [77, 78]. TOAB does not bind to the gold colloid particles strongly, so the solution aggregates slowly over the course of 12–16 days. These alkanethiolato-stabilised gold nanoparticles may be precipitated and then re-dissolved. The phase-transfer agent may remain bonded to the purified nanoparticles and thereby increasing their solubilities. The synthesis of gold colloids protected by a monolayer of organothiolato ligands is readily reproducible. By carefully varying the stirring rate and reaction temperature for the initial formation of Au(I)SR oligomers Jin and co-workers [79] have successfully synthesised Au_{25} nanoclusters in high yield. Larger thiolato-/gold ratios give smaller average core sizes, and smaller particles may be obtained if the reducing agent is added quickly and the reaction is quenched. Transmission electron microscopy (TEM) studies have established that the metal particles have mainly cuboctahedral and icosahedral structures.

In the single-phase Brust–Schiffrin procedure [80] polar solvents, e.g. THF or methanol, replace the two-phase system. In recent years, various modified

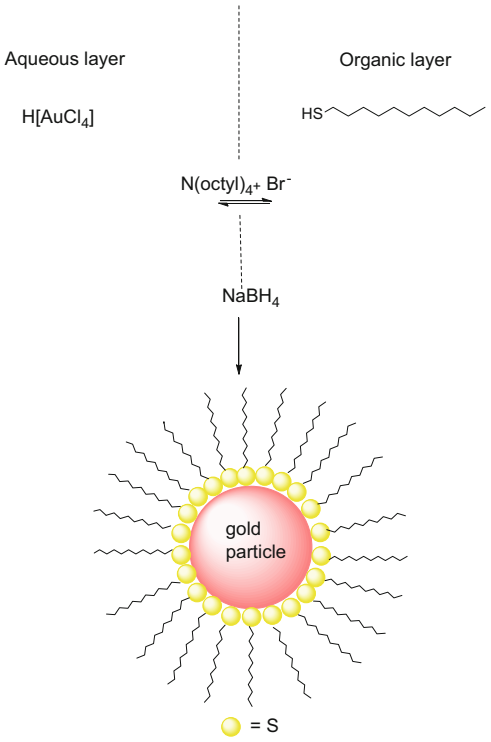

Fig. 3 Schematic illustration of the biphasic Brust–Schiffrin synthesis of gold colloids

Brust–Schiffrin methods have been developed for the synthesis of gold nanoclusters with different core sizes. Wu et al. [81] have introduced a facile, single-phase THF procedure that produced monodispersed Au_{25} nanoclusters via a "size-focusing" process.

One great advantage of the thiolato-colloids prepared in organic solvents is that it is possible to undergo substitution chemistry akin to that which has been developed for co-ordination compounds. Murray et al. [82, 83] have studied exchange of some of the alkane thiolato ligands by polyfunctionalised thiolato ligands (see Fig. 4) and this has led for example to a range of ferrocenyl-functionalised derivatives. Some basic inorganic reactions, e.g. oxidation and reduction, have also been studied. In these syntheses, different types of organic compounds have been used as capping ligands to protect gold nano-clusters, e.g. thiolate, phosphine, selenolate, carbonyl, alkyne, DNA and protein cages. In addition other sulphur-containing ligands, e.g. xanthanates, di- and tri-thiols, disulfides and polythioethers, have been utilised as stabilising ligands [82, 83].

Heating these colloidal sols near the boiling point of the solvent, i.e. at approximately 140°C for a few minutes followed by a longer period of heating at approximately 110°C, leads to smaller average particle sizes and smaller polydispersities. This procedure has also led to the formation of 2D and 3D superlattices, which have been investigated extensively by Klabunde et al. [84]. The availability of nano-sized

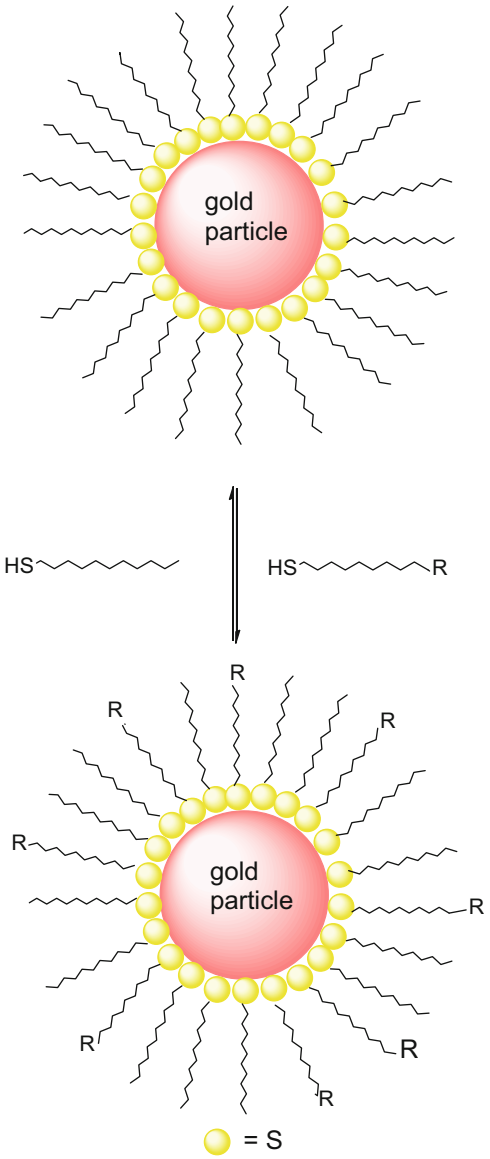

Fig. 4 Schematic illustration of ligand exchange reactions in organic solvents of gold thiolato colloids

conducting particles separated by an insulating monolayer sheath has also proved to be an ideal system for studying the size confinement of conduction electrons [2, 3].

The syntheses described above are flexible and convenient, but by the standards of molecular chemistry still produce a crude product which has a range of colloidal sizes and this limits the structural knowledge which can be derived by spectroscopic methods and definitive structural characterisation using crystallographic techniques. Therefore, in order to produce a monodispersed sample or a more

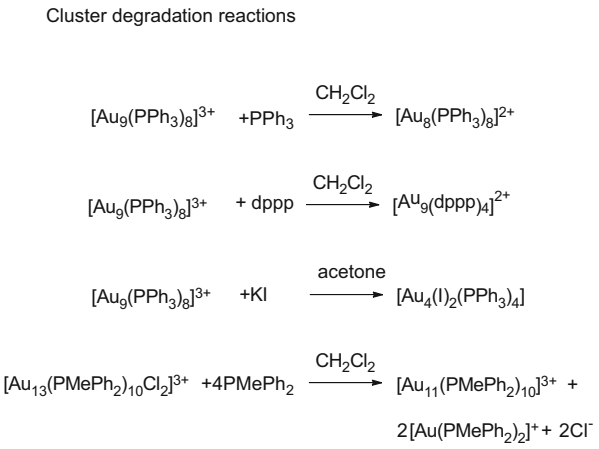

Fig. 5 Some examples of cluster degradation reactions for small molecular gold clusters

crystalline material, which may be characterised by single-crystal analysis, it is necessary to prepare monodispersed samples. This technical separation problem has not been completely solved so that purification procedures have become routine, but some significant progress has been made in recent years. Specifically, fractional crystallisation, solvent extraction, chromatography and electrophoresis techniques have been used to produce less polydispersed samples.

In the 1980s, it was shown largely as the result of the work done by the groups of Steggarda [39–42] and Mingos [29–38] on well-defined molecular clusters that their nuclearities could be reduced or increased by the addition of specific reagents. Figure 5 illustrates some typical degradation reactions of gold cluster cations which result in the loss of a few gold atoms. The degradation process is induced by the addition of phosphines or soft anionic ligands which shift the equilibrium by co-ordinating to the outgoing $AuPR_3^+$ cation. Figure 6 illustrates some typical aggregation reactions which are encouraged either by the addition of mononuclear gold(I) complexes or the replacement of phosphine by smaller (and harder) anionic ligands. In general these degradation and aggregation reactions are faster than those observed for metal carbonyl clusters of the platinum metals. In recent years these procedures have been elegantly extended by Konishi and others, who have shown that growth and etching processes may be used to convert $[Au_6(dppp)_4](NO_3]_2$ into $[Au_8(dppp)_4Cl_2]^{2+}$ and $[Au_8(dppp)_4](NO_3)_2$ [85, 86].

These principles have also been extended to reduce the dispersities of the initial colloid mixture produced by the Brust–Schiffrin reaction. These processes have been described as “etching” reactions and generally involve the treatment of the initial mixture with thiols – sometimes with heating. This corresponds to the use of phosphines and soft anionic ligands described above for molecular clusters. Whetten, Jin and co-workers utilised “etching” reactions to purify Au_{38} clusters to a sufficient extent that they could be characterised by single-crystal X-ray studies [87, 88]. Jin et al. [89] have recently reviewed size focusing in gold thiolate nanoparticles. They suggest that a successful size-focusing methodology depends

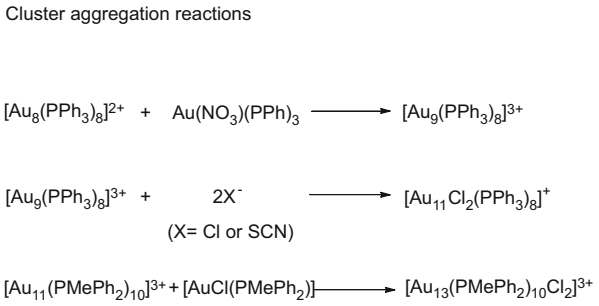

Fig. 6 Some cluster aggregation reactions of small molecular gold cluster cations

on having a suitable initial mixture of colloid particles and the "ageing" and "etching" processes have the effect of weeding out the less stable particles and thereby increasing the concentration of the more stable component. They have suggested that this procedure is adaptable to other $Au_n(SR)_m$ particles. Pradeep and his co-workers [90] have characterised some Au_{15} nanoclusters anchored to cyclodextrin via core "etching" reactions of larger clusters Au(SG) by treating them with a tripeptide based on *N*-γ-glutamyl-cysteinyl-glycine (GSH) and cyclodextrin in water at 70°C for 48 h. The GSH acts as the etching agent and cyclodextrin as the host cavity. Dass has used "etching" processes based on thiophenol in THF to convert mixtures containing primarily Au_{68} and Au_{102} clusters and required refluxing at 80°C with vigorous stirring. In this way $[Au_{36}(SPh)_{23}]$ was purified and characterised using MALDI-TOF mass spectrometric techniques [81, 91]. Jin's group [92, 93] has been particularly effective in using size-exclusion chromatography (SEC) for separations which have resulted in monodispersed $[Au_{40}(SR)_{24}]$ from $[Au_{38}(SR)_{24}]$ clusters and Zhu has separated $[Au_{18}(SePh)_{14}]$ from related clusters with 15, 19, 20 clusters using HPLC with an SEC column [94].

Tsukuda and Whetten have used gel electrophoresis (PAGE) to effectively develop the chemistry of gold colloids capped by GSH [95–101]. Recent developments in the field include the development of procedures which can be scaled up [102], and the development of catalytically active nanoparticles supported on polymers [103, 104], one-pot synthesis [79] and simplification by Dass [47, 105] who demonstrated that almost no fragmentation of Au nanoclusters was observed in the MALDI-TOF mass spectra of $Au_{25}(SCH_2CH_2Ph)_{18}$ clusters using *trans*-2-[3-(4-*tert*-butylphenyl)-2-methyl-2-propenyldidene] malononitrile (abbreviated as DCTB) as matrix with low laser pulse intensity (just above the threshold intensity). Since then, more gold nanoclusters with various compositions have also been characterised by the efficient MALDI-TOF MS technique.

Figure 7 indicates that pure Au_{25} nanoclusters [79] may be prepared by a two-step procedure from $H[AuCl_4]$ which is first reduced to Au(I) by thiols and subsequently reduced by $NaBH_4$ to metallic clusters. Low temperatures and slow stirring conditions are critical for the formation of the right type of Au(I):SR intermediate species, which lead to the formation of Au_{25} in high yield in the second reduction step. The high purity of Au_{25} nanoclusters achieved using this

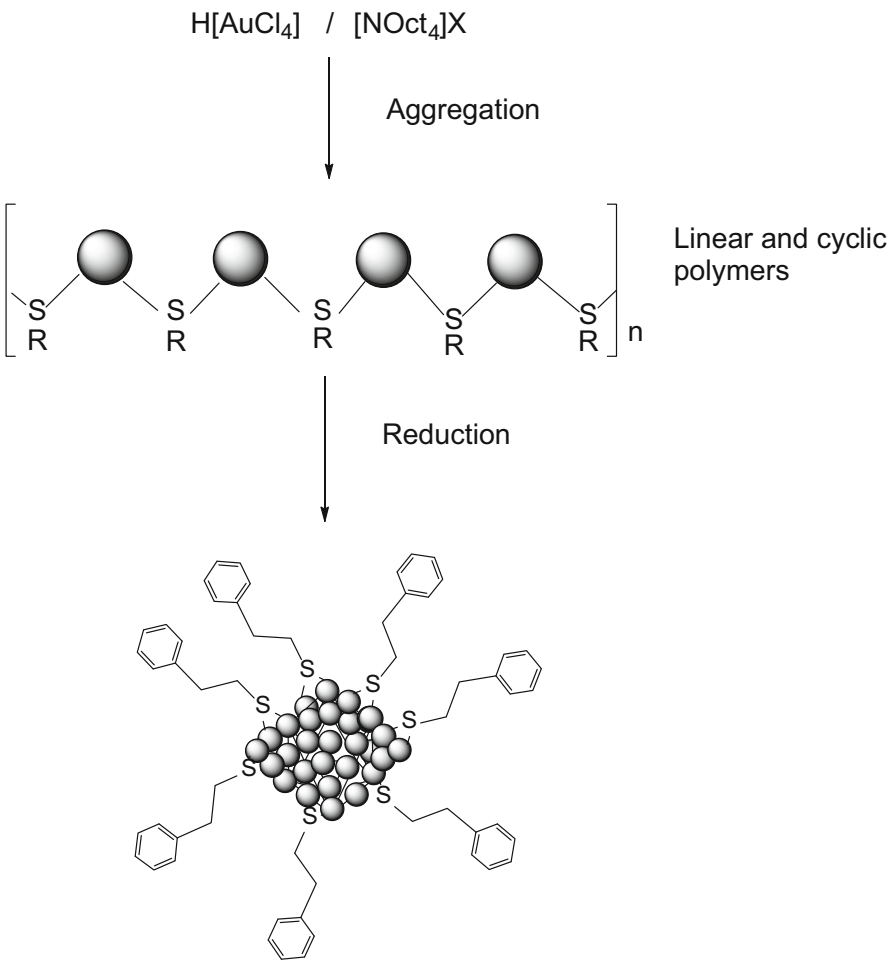

Fig. 7 Two-step procedure in the synthesis of an Au_{25} cluster developed by Jin et al. [89]

kinetically controlled synthesis has resulted in the isolation of good quality Au_{25} single crystals suitable for X-ray determination [106]. Based on the "kinetic control" principle in two-phase systems, a one-phase approach using THF as solvent has been developed for the preparation of highly monodispersed Au_{25} nanoclusters with different thiolato ligands through the so-called size-focusing process [81, 107]. The use of THF as solvent can significantly improve the purity and yield of Au_{25} nanoclusters. Au_{25} nanoclusters with a range of thiolato ligands, including those bearing functional groups, such as –OH, –COOH, have been successfully synthesised using this procedure. Dass and co-workers [47, 105] systematically investigated the size evolution process by using MALDI-TOF MS.

The usefulness of size-focusing in producing pure clusters, which can be crystallised, is illustrated by the example in Fig. 8. $AuCl_4^-$ is first mixed with

excess thiol and TOAB in methanol to form Au(I)-SR polymers. $NaBH_4$ aqueous solution is then added to produce polydispersed Au nano-clusters. After size-focusing processes, only two monodispersed components $Au_{144}(SR)_{60}$ (major product) and $Au_{25}(SR)_{18}$ (side product) are present in the product (see Fig. 8). By taking the advantage of large solubility difference in acetone, pure $Au_{144}(SR)_{60}$ can be separated with a yield of 10–20% [81, 106, 107]. By controlling the size range of the initial polydispersed clusters, pure $Au_{25}(SR)_{18}$ or $Au_{144}(SR)_{60}$ clusters without the need of the above isolation have also been achieved by Jin and co-workers.

Topochemical polymerisation of diynes attached to the surface of gold has been neatly used to encapsulate the gold particles. Gold nanoparticles (AuNPs) coated with the diacetylene henicosa-10,12-diyn-1-yl (DS9) disulfide were made by the direct synthesis in toluene solutions. The average size of the nano-hybrid metal core was finely adjusted by manipulation of the preparative conditions in the diameter range from 1.6 to 7.5 nm using transmission electron microscopy. The topochemical polymerisation of DS9 was carried out in colloidal suspensions using UV radiation. The results showed that in these assemblies the monomer undergoes an intra-particle polymerisation and that the dominant polydiacetylene phase present is ruled by the core size. The deposition of the photo-irradiated colloids onto different substrates was found to leave the polydiacetylene conjugation unaltered [108].

An important characteristic of thiol-stabilised gold colloids is that on evaporation of the organic solvent they spontaneously form highly ordered 2D and 3D thin-film arrays on suitable substrates. This makes it possible to tune the optical and electrical properties of the thin films by varying the sizes of the metal particles and the inter-particle spacings. The protecting groups and capping molecules on the surface of the metal particles are modified using standard organic chemistry procedures. Pelka [109] has shown that varying the chain length of the hydrocarbon of linking thiolato ligands on 4–5 nm gold nanoparticles self-assembled on glass has a dramatic effect on their dc conductivities. Measurements made down to 4.2 K show a strong relationship between the dc conductivity and the spacer length. Corbierre [110] has recently combined electron beam lithography and controlled nanoparticle nucleation and growth to create precisely patterned 1D arrays of gold particles. The inter-particle distances and the patterns of nanoparticles are precisely tuned by varying the electron beam parameters.

2.3 Metal Vapour Syntheses, Radiolysis and Sonolysis Techniques

Metal vapour synthesis techniques have been used to synthesise molecular gold clusters with 5–11 metal atoms and gold colloids. The former are favoured if the organic solutions contain strongly binding phosphine ligands, whereas the latter are favoured when these ligands are absent [111–113]. Gold colloid particles with

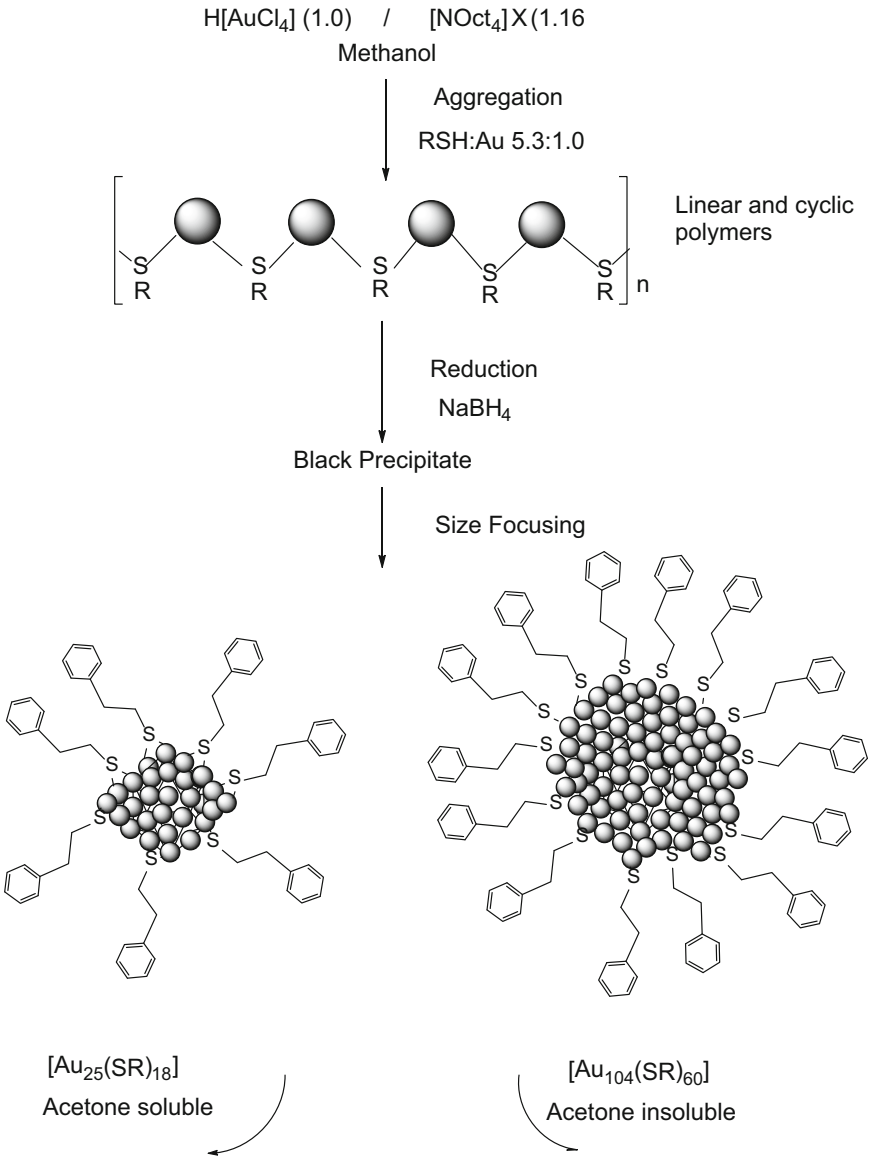

Fig. 8 The separation of Au_{25} and Au_{144} clusters based on solubility differences following size-focussing procedures

mean dimensions of 4–9 nm are formed when gold is evaporated into acetone solutions at 77 K followed by warming to room temperature. Other dispersing media which have been used include styrene, methacrylate monomer and fluorocarbons. The mean diameters of the colloids are also influenced by the rate of

evaporation of the metal and the pressure within the metal vapour apparatus [114, 115].

$H[AuCl_4]$ aqueous solutions may be reduced to colloids using radiolysis or pulsed laser techniques [116–118]. For examples, solvated electrons may be generated by pulsed radiolysis or by 353 nm laser pulses in either pure water or emulsions. The colloidal particles formed in this way generally have small mean diameters and low polydispersities. Sonication may also be used to produce colloids [119, 120]. Ultrasound treatment of an aqueous solution of $H[AuCl_4]$ in the presence of glucose leads to ribbons of gold with widths of 30–50 nm and length of several micrometres. The reducing agents (hydroxyl radicals and sugar pyrolysis radicals) are produced at the interfacial region between the collapsing cavities and the bulk water. When glucose is replaced by cyclodextrin spherical gold particles are obtained suggesting that glucose is essential in forming the ribbons.

2.4 Laser Ablation Techniques

Gold colloid particles may be produced by laser ablation of a gold metal plate in an aqueous solution of sodium dodecyl sulphate as a surfactant. The absorption spectra of the gold particles closely resemble those of gold particles prepared by more conventional chemical procedures. The size distribution of the particles was found to shift to a smaller mean diameter with an increase in surfactant concentration. This behaviour was explained in terms of the dynamic formation model. The particle abundance depends on the surfactant concentration and stable gold particles are formed as the surfactant concentration exceeds 10^{-5} M. The gold particles having mean diameters larger than 5 nm were pulverised into those with diameters of 1–5 nm using a 532-nm laser [121].

3 Characterisation of Colloids and Nanoparticles

The deep colours of gold sols are strongly affected by the environment, size and physical dimensions of the metal particles and so have played an important role in their characterisation. These relatively easy spectral measurements provide circumstantial evidence regarding the broad structural features and sizes of the colloidal particles. These spectral properties arise from surface plasmons, which have been discussed above, and are underpinned by Mie's theoretical model. Qualitatively the reactions of colloidal solutions with salts, ligands, polymers and biological materials may be monitored by following the spectral changes. The development of nanoscience into a predictable and reproducible discipline requires a more detailed understanding and control of the atomic structures of the metallic cores of colloids and nanoparticles and spectroscopic and analytical techniques which lead to the

identification and location of ligands and solvent molecules on the particle's surface [2, 3, 7–9, 11, 26, 27].

The analytical technique which is commonly used in the initial stages of characterisation is thermogravimetric analysis (TGA). The noble character of gold means that, under thermal decomposition conditions, clusters and colloids result in the formation of the pure metal and the loss of ligated and solvating species. This information when combined with conventional chemical analyses may give an initial indication of the composition of the colloidal or nanoparticle species which have been formed in the synthetic procedure. However, unless the specific number of metal atoms is defined experimentally, then the molecular composition remains ill-defined and "atomic precision" is not achieved [122, 123].

Traditional techniques for the characterisation of large metal nanoparticles, viz., scanning electron microscopy (SEM), low-resolution transmission electron microscopy (TEM) and powder X-ray diffraction (XRD), define the size, morphology and crystallinity of the particles, but do not provide the detailed information required for defining the precise atomic structures of metal nanoclusters with core size smaller than 2 nm. The imaging the atomic distribution of particles in real space has led to the identification of particles with fivefold symmetry based on icosahedra and dodecahedra and provided a clearer definition of the multiple twinning effects which occur as a result from the competition between maximising the number of nearest neighbours which may be achieved with structures with fivefold symmetry and the requirements of establishing a regular close-packed structure [2, 3, 26, 27] The size and atomic arrangement of the metal atoms in the metal nanoparticles with approximately 2.0 nm diameters may be directly observed using high-resolution transmission electron microscopy (HRTEM). The atomic arrangements in very small clusters (smaller than 1.0 nm) are not clearly defined by HRTEM and long electron beam irradiation times may lead to aggregation and the formation of larger nanoparticles [65, 66, 124–130]. Recently progress has been made in determining the structures of gold nanoclusters using HAADF-STEM techniques. Electron microscopy tomography requires a series of images for many different specimen orientations and is most effective for larger particles which are not modified greatly by the electron beam. Recently aberration-corrected scanning transmission electron microscopy coupled with image simulation has been used to study smaller clusters [130]. The rapid development of the technologies and physics of aberration-corrected electron microscopy (AC-TEM and AC-STEM) has resulted from improvements in physical toolkits for the conversion of single-shot images into 3D representations by combining them with image simulation techniques [130].

X-ray crystallographic techniques have been used traditionally to estimate the sizes of gold colloid particles [23], but in recent years the availability of single crystals of large clusters and improvements in the technology means that the technique has become more applicable to smaller crystals [59, 63, 88, 91–93, 100, 106, 131–136]. Low temperature techniques, narrower beams and synchrotron sources have all contributed to a situation where smaller and smaller crystals have become more amenable to X-ray structural techniques which provide unambiguous structural information on the metal cores and the mode of attachment of the ligands on their surface. This detailed structural information has proved invaluable for

providing background knowledge about the structures of colloids and nanoparticles which cannot be studied directly because they involve a range of sizes and compositions. Such studies have led to the realisation that a nanoparticle may not necessarily be defined just in terms of a metal core and surface ligand shell, but the surface may indeed have a metallo-ligand shell with metal-ligand oligomers acting as ligands to the central metal core as illustrated in Fig. 2. The crystal structures of several large gold clusters have been crystallographically determined in recent years: these include $[Au_{25}(SR)_{18}]^q$ ($q = -1,\ 0$), $[Au_{28}(SR)_{20}]$, $[Au_{36}(SR)_{24}]$, $[Au_{38}(SR)_{24}]$ and $[Au_{102}(SR)_{44}]$. These clusters have provided excellent models for the colloids produced in non-aqueous solvents in the presence of organothiolato ligands [122, 123]. These structural determinations have established that the metal core geometries do not necessarily adopt the face-centred cubic (fcc) packing arrangement observed in bulk gold and alternative structures based on polyhedra with fivefold symmetry are also observed. They have indicated that these large cluster species do not necessarily adopt "full-shell magic number" close-packed arrangements with 13, 55, 147, 309 and 561 metal atoms. Furthermore the structures have revealed that the surfaces of colloid particles may not necessarily involve simple metal-ligand bonds but metallo-thiolato fragments such as those illustrated in Fig. 3. These structures and the bonding models which have been developed to rationalise the structures are discussed in some detail in other chapters of this volume. The steric requirements of the ligands are also important in determining the nuclearities of the clusters and the geometries of the metal cores. These effects were recognised for phosphine clusters and a "cluster cone angle" was defined which was analogous to the Tolman cone angle for mononuclear co-ordination and organometallic compounds [137–139].

Mass spectrometry (MS) is another technique which has matured to the point that it is able to make a significant contribution to our knowledge of nanoparticles with hundreds of atoms and has deepened our understanding of the composition of larger and larger clusters and colloid and nanoparticles which have diameters less than 2 nm [140–144]. Mass spectrometry is capable of revealing information about gold nanoparticles (ANPs) which is otherwise difficult, if not impossible, to obtain using other techniques. The contributions of Whetten [142], Murray [143] and Tsukuda [144] have been particularly significant. Arnold and Reilly's time of flight experiments [145] and Dass' MALDI TOF experiments [46, 47, 105, 146, 147] using low laser pulse energies have also been informative. The capping motif based either on $[Au_4(SR)_4]$ rings or "linear staples" $[Au(SR)_2]^-$ and $[Au_2(SR)_3]^-$ illustrated in Fig. 2 were experimentally established by Kornberg and co-workers' 2007 crystal structure of $[Au_{102}(p\text{-MBA})_{44}]$, which revealed semi-ring "staple" capping surface moieties [75, 136]. Theoretical studies on $[Au(SR)_2]$ and $[Au_2(SR)_3]$ moieties and clusters derived from them have been completed by Häkkinen. In 2007, Cliffel and colleagues [140, 141] studied tiopronin (Tio)-protected AuNPs by electrospray (ESI)-MS and discovered a tetrameric $Au_4(Tio)_4$ ion and proposed an eight-membered ring structure as shown in Fig. 2. Electrospray ionisation mass spectrometry (ESI) and laser desorption ionisation mass spectrometry (LDI-MS) have been widely used as well as fast atom bombardment (FAB) techniques. In the first unfragmented MALDI

spectrum of $[Au_{25}(SCH_2CH_2Ph)_{18}]$, $[Au_{38}(SCH_2CH_2Ph)_{24}]$ and $[Au_{68}(SCH_2CH_2Ph)_{34}]$, a fragment corresponding to a loss of $[Au_4(SCH_2CH_2Ph)_4]$ appeared in positive mode, although the crystal structure of $[Au_{25}(SCH_2CH_2Ph)_{18}]^-$ did not show $[Au_4(SCH_2CH_2Ph)_4]$ as a prominent feature [148–150].

A complementary technique which has been used for the analysis of ligand-protected AuNPs in the gas phase is the ion mobility spectrometry (IMS). Separation selectivity in IMS reflects the ion size and more specifically ion surface area. In IMS ions are injected into a gas-filled drift tube where they experience numerous low-energy collisions with a background gas which separates ions based on the ion-neutral collision cross sections (CCS). Smaller ions elute faster than larger ions which experience more collisions. IMS has been used to measure the diameter of ligand-protected AuNPs. Following the report of Jarrold [151], Kappes and colleagues [152] published two reports in 2002 on positively charged gold clusters (<25 atoms). The ion CCS of each cluster provides convincing circumstantial evidence for assigning geometries. The ability to distinguish between various three-dimensional geometries illustrates the structural capabilities of IMS for small gold clusters. Building on this foundation, Harkness et al. [140] have reported the first application of combined ion mobility spectrometry–mass spectrometry (IMS-MS) to the analysis of ligand-protected AuNPs. By integrating mass and ion CCS separation, gold-thiolate ions can be isolated from nearly isobaric but larger organic ions (i.e. chemical noise). IM-MS is well suited for studying fragments generated from ligand-protected AuNPs, because of the signal-to-noise enhancement and structural characterisation capability. Their study of AuNPs protected by tiopronin or phenylethanethiolate by MALDI-IM-MS revealed significant features. In the negative ion mode, many of these fragments correlate to capping structural motifs proposed previously. In the positive ion mode, the fragment ions are nearly identical to the positive ions generated from the gold-thiolate AuNP precursor complexes. This suggests that energetic processes during laser desorption/ionisation induce a structural rearrangement in the capping gold-thiolate structure of the AuNP. This results in the generation of positively charged gold-thiolate complexes similar to the precursors of AuNP formation by reduction and negatively charged complexes which are more representative of the AuNP surface.

The structures of small gold clusters in the gas phase have also been established by a combination of mass spectrometry, vibrational spectroscopy and theoretical calculations. Bare gold metal clusters with one or two krypton ligands are formed by means of laser vaporisation from a gold rod in a continuous flow of helium and krypton (1.5% Kr in He) at 100 K. The molecular beam is overlapped with a pulsed FIR beam delivered by the Free Electron Laser for Infrared eXperiments (FELIX). The neutral complexes are analysed in a time-of-flight mass spectrometer. The subsequent heating of the complex results in the evaporation of a loosely bound krypton ligand and a depletion of the corresponding mass spectrometric signal. Recording the mass spectrometric signal while scanning the wavelength of FELIX leads to depletion spectra, from which absorption spectra are reconstructed. The geometries of the Au_x clusters were established by comparing the experimental spectrum to the calculated vibrational spectra for multiple isomers predicted by density functional theory (DFT) calculations. For Au_7 Fielicke et al. proposed a

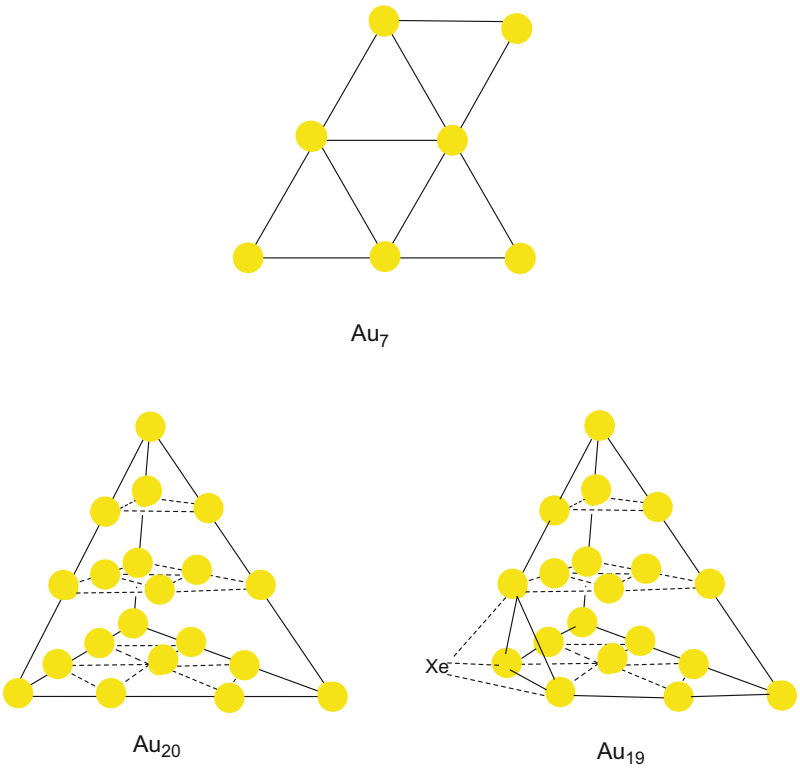

Fig. 9 Proposed structures of neutral Au_7, Au_{19} and Au_{20} clusters of gold on the basis of FELIX data. Krypton atoms interact weakly with the clusters through van der Waals' forces

planar edge capped triangle with C_s symmetry and Au_{19} and Au_{20} have close-packed structures based on a tetrahedron (see Fig. 9) [153]. These structures have been predicted as the global minima on the basis of DFT calculations. Recent developments in this field are discussed in the chapter authored by Fielicke and Woodham.

In the 1970s and 1980s, solution and solid-state NMR were used to study the structures of molecular gold cluster compounds with 4–13 metal atoms. The clusters whose structures had been unambiguously determined by single-crystal X-ray crystallographic determinations were used to define the strengths and limitations of the technique [111, 154–157]. NMR studies on small clusters with phosphine are structurally informative since their $^{31}P\{^1H\}$nuclei have the appropriate abundance and sensitivity to provide good high-resolution spectra. However, many of the larger clusters have stereochemically non-rigid skeletal geometries in solution (even at low temperatures) and consequently the structural information obtained was not as helpful as originally anticipated [111, 154–157]. $^{31}P\{^1H\}$NMR proved to be more helpful for studying clusters in the solid state, where their stereochemical rigidity provides more structural information [154]. Since the majority of stabilising ligands used in colloid and cluster syntheses are organically based, ^1H NMR is very useful for confirming the presence of these molecules on the

surface of colloids, but the technique does not provide direct information regarding the ratio of ligands to the number of metal atoms in the core and even the size of the cluster. ^{31}P NMR has recently been used to study triphenylphosphine (PPh_3)-capped 1.8 nm diameter gold nanoparticles in both solution and the solid state [158]. NMR has also been used as an analytical tool to estimate the size of thiol-stabilised gold nanoclusters in solution. For example, by using diffusion-ordered NMR spectroscopy (DOSY), Salorinne et al. [159] successfully estimated the size of Au_{25}, Au_{38} and Au_{144} nanoclusters by determining the diffusion coefficient and hydrodynamic radius from solution samples. The determined cluster sizes agree well with the diameters from the measurements of the corresponding single-crystal or theoretical structures reported previously. The technique has also been used to probe the chirality of gold nanoclusters [160].

Other spectroscopic techniques which were originally applied to small- to medium-sized clusters have subsequently been applied to gold clusters, colloids and nanoparticles. These include gold Mössbauer spectroscopy [161, 162], X-ray photoelectron spectroscopy [163, 164] and EXAFS [165]. For example, EXAFS has been used recently to study the cluster nucleation process when solutions of $H[AuCl_4]$ are reduced [166]. Initially dimeric $[Cl_3Au–AuCl_3]$ species are thought to form which agglomerate to $[Au_nCl_{(n+x)}]$ species which initially form 2 nm colloidal particles. Small-angle X-ray scattering (SAXS) and X-ray absorption near edge spectroscopy have also been utilised to study this problem [167]. The number of particles, their size distribution, and the yield of the reaction are determined in real time through the quantitative analysis of the SAXS data and thus the effect of the ligand on the nucleation and colloid growth rates may be analysed. When an alkanoic acid is used, a nucleation phase of 1 s is followed by a growth step whose rate is limited by the reaction of the monomers at the interface, but when an alkylamine is used the nucleation rate is increased by an order of magnitude. High-pressure techniques have also been used to study the pressure-induced skeletal isomerisation of gold cluster compounds in the solid state [168] and also to quantify the effect of pressure on the surface plasmon resonance of gold and silver colloids [169].

4 Applications of Gold Colloids and Nanoparticles

The properties of gold colloids and nanoparticles described above make them excellent scaffolds for the sensing of chemical and biologically active molecules. They possess unique optoelectronic properties and their high surface area-to-volume ratios lead to efficient detecting systems and their excellent bio-compatibilities limit the extent of untoward side effects. Furthermore their properties may be tuned by varying the sizes and shapes of the nanoparticles and changing the surrounding chemical environment. The recently published review by Saha et al. provides an excellent introduction to this important area [170].

A field that has grown rapidly over the past decades is the use of gold nanoparticles in biology and life sciences. These bio-applications may be classified into four areas: (1) labelling, (2) delivery, (3) heating and (4) sensing. For labelling the electron-dense nature of the heavy metal particles is exploited to improve the contrast of the transmission electron microscopy images. Their small size and the possibility of functionalising the particles, for instance, with antibodies (immunostaining), mean that they also provide extremely high spatial resolution and specificity in many labelling applications. Similarly, the particles' optical properties – strong absorption, scattering and especially plasmon resonance – make them ideal for a large variety of light-based techniques including combined applications such as photothermal or photo-acoustic imaging. In addition, gold nanoparticles can be radioactively labelled by neutron activation, which allows for very sensitive detection as an X-ray contrasting agent.

4.1 Colorimetric Analyses and Surface-Enhanced Raman Spectroscopy

The characteristic surface plasmon resonances (SPR) of gold colloids which depend on the size of the particle and its chemical environment have been discussed in some detail above. This property has been exploited to develop sensors to detect a wide range of chemicals and biomolecules. The light scattering cross section of 60 nm for gold nanoparticles is 4–5 orders of magnitude greater than that of commonly used fluorescence dyes such as fluorescein, and this property when combined with dynamic light scattering techniques which are sensitive to the size of gold particles may be used as a very sensitive technique for detecting low concentrations of DNA. The aggregation of the gold particles is related to the concentration of DNA [171]. Zare et al. have demonstrated that the colour changes associated with spherical particles of gold may be used to provide a simple colorimetric sensor for studying the conformational changes of the yeast iso-c-cytochrome c (Cyt c) protein [172]. A fuller discussion of the biological applications of gold nanoparticles and clusters is to be found in the chapter by Broda et al. [173]. Although the emphasis in recent years has been on the biological and medical applications, gold colloids and nanoparticles have also been used to detect inorganic metal ions and anions. For example, the applications of fluorescent gold nanoclusters as chemical sensors for the detection of inorganic molecules and ions (e.g. Hg^{2+}, CN^{-}) have been reviewed [174].

Surface-enhanced Raman spectroscopy (SERS) has shown that molecules bound to the surfaces of gold colloids have vibrational bands whose intensities are many orders of magnitude stronger than those observed for the unattached molecules. This enormous enhancement of sensitivity has been exploited to detect very low concentrations of organic molecules and biomolecules. Therefore this technique

has been used for the detection of proteins and pollutants. Two mechanisms have been proposed to account for this enhancement of the Raman active vibrations: chemical enhancement and electromagnetic field enhancement. Different signal strengths are observed on the same substrate with different chemicals suggesting a chemical origin. However, the bonding strength affects the number of molecules bound and in contact with the surface of the gold particle and the time spent in a given "hot spot". Thus, the chemical effect could arise simply from the time spent adjacent to a high electromagnetic field. The electromagnetic field enhancement mechanism attributes this effect to the local field strength generated by the surface plasmon oscillations. The situation is complicated because aggregates of nanoparticles appear to generate much larger enhancements and a fuller discussion is given in [175]. SERS signatures have also been measured from single living cells in the presence of gold nanoparticles. The spectra suggest chemical changes in the environment of the nanostructures, which vary with time. The observed increase in the SERS signal strength and parallel TEM studies indicates the formation of nano-aggregates providing optimum SERS enhancement for ultrasensitive probing inside the endosomal compartment. The medical and biotechnology applications of SERS nanosensors in cells are going to be important in the future [176].

4.2 Electron Microscopy

In transmission electron microscopy (TEM) the gold nanoparticles or colloids are dispersed on a relatively electron transparent substrate, e.g. thin carbon-coated micro-grid, and the large difference in electron densities provides a good contrast between the metal atoms and the organic ligands or polymers. High-resolution TEM (HRTEM) provides resolution to the Å level and thereby provides data on the packing of the metal atoms rather than the overall morphology of the metal particle. In scanning transmission electron microscopy (STEM) the electron beam is scanned across the sample providing extra resolution and when combined with high-angle annular dark field (HAADF) can distinguish different order patterns in alloyed nanoparticles as long as the metals have significantly different atomic numbers. In scanning electron microscopy (SEM) the image is due to the emission of secondary electrons which have been excited by the electron beam. Their resolution is lower than TEM, but SEM is better at imaging bulk samples and creating a better depth of view. This property leads to more reliable 3D images [177, 178].

In 1977 Horisberger and Rosset [179] demonstrated that gold colloidal particles had a suitable size to act as electron-dense markers for biological structures in transmission electron microscopy and scanning electron microscopy imaging. The gold colloids were prepared with gold granules labelled with a monolayer of specific macromolecules. The method they developed proved to be simple, rapid and seems to be general since gold granules have been labelled with polysaccharides and proteins. As homogeneous populations of gold granules having different

sizes can be prepared the method is also suitable for double marking experiments. This technique is illustrated by the localisation of polysaccharides and glycoproteins on yeast cell walls and erythrocyte membranes by transmission electron microscopy and on yeast cells and intact erythrocytes by scanning electron microscopy. Good spatial resolution of the marker was achieved in all cases. The method is also suitable for marking thin sections [179]. Broda et al. provide an excellent summary of recent developments in this field in their chapter [173].

4.3 Biochemical Applications

4.3.1 Diagnostics and Tumour Detection

As discussed above the optical properties of gold particles change upon binding to a wide range of biomolecules and thereby allowing the detection and quantification of analytes. The absorption spectra of gold nanoparticles change drastically when several particles come close to each other. This may be exploited for very sensitive DNA detection, even of a single-base mismatch. Gold nanoparticles are also used to detect biomarkers in the diagnosis of heart diseases, cancers and infectious agents. They are also common in lateral flow immunoassays [180]. New research into the unique properties of gold nanoparticles should lead to well-established, routinely used assays for a variety of biological applications. Another strategy for sensing makes use of fluorescence quenching. Fluorescent molecules that are excited and in close proximity to a gold particle can transfer their energy to the metal, resulting in a non-radiative relaxation of the fluorophore. In several different detection schemes, the analyte displaces the fluorescent molecules from the particle surface or changes their conformation, so that the optical emission of those reporter molecules is changed in the presence of the analyte. While many of the unique optical properties of gold nanoparticles have been exploited in recent applications, there is still plenty of room for new research. This should eventually lead to well-established, routinely used assays for a variety of biological applications in the near future.

4.3.2 Drug Carriers: Therapeutic Agent Delivery

Gold nanoparticles can serve as carriers for drug and gene delivery. Biologically active molecules adsorbed on the particle surfaces can be guided inside cells and released. DNA delivery, for instance, is the basis for gene therapy. Therapeutic agents can also be coated onto the surface of gold nanoparticles. The large surface area-to-volume ratio of gold nanoparticles enables their surface to be coated with hundreds of molecules (including therapeutics, targeting agents and anti-fouling polymers) [181].

4.3.3 Photothermal Agents

The light-absorbing properties of gold nanoparticles make them effective heat-mediating transmitters. The absorbed light energy is dissipated to surrounding molecules and thereby elevating the temperature of the surrounding area. This effect may be used to open polymer microcapsules for drug delivery purposes. Near-IR absorbing gold nanoparticles (including gold nanoshells and nanorods) rapidly produce heat when excited by light at wavelengths from 700 to 800 nm. This property has been used to kill targeted tumour cells (hyperthermia or photodynamic therapy). The emergence of gold nanoparticles in this application arises because of their unique photophysical properties which make them very suitable for cancer phototherapy. The plasmon surface resonance results in visible and near-infrared light absorption several orders of magnitude more intense than that of conventional phototherapy cancer agents. Huang et al. have recently reviewed plasmonic photothermal therapy (PPTT) in the treatment of malignant tumours [182]. In addition appropriately functionalised nanoparticles may be designed to bind specifically to certain cells and thereby target and destroy malignant cells. The potential cytotoxicity of the nanoparticles is a side effect which cannot be ignored [183]. Gold nanoparticles (2–4 nm) stabilised by a phthalocyanine (Pc) photosensitiser and a phase-transfer agent have been shown to form a three-component system to generate singlet oxygen with enhanced quantum yields compared to the free Pc. Additionally, the association of the transfer reagent promoted the solubility of the surface-bound hydrophobic sensitiser in polar solvents which would facilitate their systemic injection [184]. The results demonstrate a potentially useful vehicle for the delivery of photosensitiser agents in photodynamic therapy.

4.4 Nanoelectronics and Optics

Gold nanoparticles have been used in a wide range of applications in the electronics industry and particularly as conductors in printable inks and electronic chips. Nanoscale gold nanoparticles are being used to connect resistors, conductors and other elements to electronic chips. As the goal of producing even smaller electronic devices is achieved, nanoparticles become potentially more important components in chip design [185]. In addition to miniaturisation the distances between transistors and related switching elements on a chip get shorter and quantum effects become relevant. Today's nano-lithographic fabrication techniques allow scaling down to 50 nm or below [186]. This has already made a great impact on the performance of traditional semiconductor circuits, and it opens up new opportunities utilising quantum effects. Following the utilisation of charging effects, the so-called Coulomb effects, in metallic circuits which are based on tunnel junctions with submicron sizes, individual charge carriers become a realistic possibility [187]. Potential developments in this field, described as single electronics [187], have recently been

reviewed by Homberger and Simon [188]. It remains a major challenge to assemble nanoparticles into highly ordered and defect-free arrangements. Mirkin has obtained fascinating results using DNA to order the nanoparticles [189–191].

The discussion above has highlighted how their surface plasmon resonance leads to important applications, but has concentrated on spherical nanoparticles. The lower symmetries of nanorods leads to two or multiple plasmon bands whose position and intensity are intimately connected to their size, shape, degree of aggregation and local dielectric environment. Gold nanorods are especially intriguing as they offer strong plasmonic fields while exhibiting excellent tunability and biocompatibility. The absorption and scattering of light by gold and silver nanorods may be tuned throughout the visible and near-infrared portions of the electromagnetic spectrum [192–194]. Recently these studies have been extended to bimetallic core-shell nanorods based on gold. Johnston discusses the theoretical aspects of the nanorods and in particular their interfacial structures in his chapter [177].

The seed-mediated growth method is the most common route for synthesising high-quality gold nanorods and they may also be obtained from commercial suppliers. Typically citrate-capped gold nanospheres serve as seeds when added to an Au(I) growth solution which is obtained by the reduction of $HAuCl_4$ with ascorbic acid in the presence of cetyltrimethylammonium bromide (CTAB) surfactant and silver ions. Longer nanorods (up to an aspect ratio of 25) may be obtained in the absence of silver nitrate by use of a three-step addition procedure. Recent reviews on the synthesis of nanorod synthesis have emphasised spontaneous self-assembly, chemically driven assembly and polymer-based alignment [195]. Routine organic synthetic chemistry may be used to place molecules on the nanorod surface and polyelectrolyte layer-by-layer adsorption may be used to position them at desired distances, and possibly orientations. The nanorods may be surface modified to recognise biological materials, bacteria for example. Murphy and her co-workers [196–199] have used the elastic light scattering properties of gold nanorods as "nano-strain gauges" to measure the deformation of soft matrices by living cells. The inelastic light scattering (Raman) properties of gold nanorods is used to interrogate the local chemical environment of the nanorods. Irradiation into nanorod plasmon bands causes large temperature jumps in the local environment, which they have exploited as a way to kill multidrug-resistant bacteria.

4.5 Catalysis

Until recently it was generally thought that the catalytic chemistry of gold was far less important than that of the platinum group metals (PGM) which are adjacent in the periodic table. In the 1970s Bond [200] established that nano-crystalline gold particles were good catalysts for a limited class of reactions, e.g. the hydrogenation of dienes, but they were no more effective than palladium and platinum, which could be used for a wide range of reactions of interest to the heavy chemical and petrochemical industries. However, this prejudice was overcome in 1989 when

Haruta and his co-workers reported that gold nanoparticles supported on Co_3O_4, Fe_2O_3 or TiO_2 were highly active catalysts for CO and H_2 oxidation, NO reduction, the water–gas shift reaction, CO_2 reduction and the oxidation of methanol [201–203]. Hutchings also demonstrated that gold was an effective catalyst for the hydrochlorination of acetylene to vinyl chloride [204]. Subsequently the epoxidation of propylene was shown to be catalysed by gold nanoparticles. The report by Christensen and co-workers that gold nanoparticles suspended on the inert spinel $MgAl_2O_4$ catalyse the aqueous-phase oxidation of ethanol by air to acetic acid proved to be very significant [205]. The observation that the catalytic activities of gold nanoparticles are very dependent on the size of the particles has encouraged the view that quantum size effects may be responsible and has highlighted an important difference between gold and the platinum metals. Goodman and co-workers [206] have argued that the catalytic activity correlates with the electronic state of gold and Boyen et al. [207] have reported calculations on Au_{55} clusters (1.4 nm) which suggest that they are particularly effective in CO dissociation. Theoretical calculations by Lopez and Norskov [208] have suggested that small clusters of gold are capable of forming very strong bonds to adsorbates such as CO, H_2 and O_2 because the strengths of the Au–CO and Au–O bonds depend markedly on the metal co-ordination number. Specifically gold atoms on corners and steps appear to have d levels that are close to the Fermi level and result in strong metal-adsorbate interactions. From a chemical point of view the observation that crystalline gold does not dissociatively chemisorb CO or H_2, but gold nanoparticles participate in catalytic processes involving these substrates is significant. They show exceptional activities with O_2 and for example catalyse the production of H_2O_2 from H_2 and O_2 [209].

The preparation of the catalyst and the nature of the support are crucial for ensuring a high catalytic activity at lower than ambient temperatures. In particular Haruta has shown that large nano-crystals (>10 nm) of gold on TiO_2 supports are relatively inactive and he has developed alternative routes which ensure that only small crystallites (2–4 nm) are generated by controlling the pH of the gold solutions [210]. It is noteworthy that particles with diameters of 2–4 nm are two orders of magnitude more active than particles with diameters of 20–30 nm. The underlying causes of the high catalytic activities of gold nanoparticles are still the subject of active debate. Bond and Thompson [211] have proposed that the active sites involve gold atoms in a positive oxidation state at the interface with the support oxide surface, but they have not been able to establish the formal oxidation state of the gold atoms at these sites. Haruta [212] has argued that Au(0) atoms may be responsible for CO dissociation on the surface of the nanoparticles and dioxygen is activated at the interface where the gold atoms have a higher oxidation state. Detailed Mössbauer, high-resolution electron microscopy and X-ray absorption experiments by Hutchings have provided strong evidence that cationic gold is crucial to the high activity of gold. Currently the spectroscopic studies which have been made have not provided an unambiguous characterisation of the active sites. A detailed evaluation of these results has recently been provided by Hutchings and Edwards [213]. The chemical characteristics of the support are important for

stabilising cationic gold species [214] and surface hydroxyl groups appear to play an important role at the active site. The chapter contributed by Freud et al. reports the growth of Au on ultrathin films and thicker, more bulk-like substrates by physical vapour deposition. Their recent studies which have combined imaging and spectroscopic techniques has have resulted in a detailed picture of how clusters form from single Au atoms to clusters and further on to nanoparticles. Ultrathin MgO and alumina lead to electron transfer to the supported Au, whereas iron oxide leads to electron transfer from the Au to the support [215]. These important developments in catalysis using gold have encouraged the study of nanoalloys of gold with other metals. Recent theoretical developments in this field have been discussed by Johnston [216, 217].

Interestingly this renaissance has been matched by important developments in the use of gold complexes as homogeneous catalysts in the transformation of organic molecules. Recent literature compilations by Hashmi provide an excellent introduction to the recent developments in this field [218]. The emergence of this important area was initiated in 1986 by Ito and Hayashi's discovery of the asymmetric aldol reaction [219], and sustained by Teles' [220, 221] 1998 finding of highly active catalysts for the addition of heteronucleophiles to alkynes and the C–C-bond formation reactions developed by Hashmi et al. in 2000 [222–224]. The importance of these developments in the context of organic chemistry is summarised in [225].

4.6 Metal Insulator Transition

Frohlich and Kubo have argued that the electrical conductivity within a metal particle is expected to decrease rapidly when the diameter of the metal particle approaches the de Broglie wavelength of the conduction electrons. Chemically this corresponds to the localisation of electrons as valence electrons become highly confined and quantum effects predominate. This transition has attracted considerable theoretical interest, but experimental verification has been limited by the absence of reliable synthetic routes to monodispersed gold particles with well-defined dimensions. The Schriffen–Brust method for synthesising large gold clusters described above has provided a method for making well-defined large clusters which may be characterised by single-crystal X-ray techniques. They provide individual mesoscopic conductors well separated from each other by a sheath of insulating organic ligands and provide ideal systems for studying the size confinement of metallic conduction electrons. Using microwave absorption techniques, it has recently been shown that individual gold particles with diameters approximately 4 nm have electrical conductivities 10^7 smaller than that of bulk gold. Edwards and Thomas have suggested that this is a dramatic example of size-induced metal-insulator transition [2, 3] and have given a full account of the relevant experimental and theoretical work.

5 Summary

This chapter gives a historically based introduction to gold colloids and nanoparticles and hopefully has provided a suitable introduction to the other excellent contributions in this volume, which give a more contemporary and detailed account of recent important developments. Besides defining the differences between clusters, colloids and nanoparticles it has emphasised the important developments in synthesis and characterisation during the last decades and indicated how their unique physical and spectroscopic properties have led to important applications. The chapter has not dealt in great detail with the structures and electronic structures of molecular nanoclusters. The accompanying volume has a separate introductory chapter which provides a historical perspective into these bonding and structural aspects.

References

1. Landgraf G (1999) Gold in decoration of glass and ceramics. In: Schmidbaur H (ed) Gold: progress in chemistry, biochemistry and technology. Wiley, Chichester
2. Edwards PP, Thomas JM (2007) Gold in a metallic divided state – from Faraday to present day nanoscience. Angew Chem Int Ed 46:5480–5486
3. Edwards PP (1992) Probing the nature of divided metals. Mat Res Soc Symp Proc 272: 311–328
4. Faraday M (1857) Bakerian lecture – experimental relations of gold (and other metals) to light. Phil Trans R Soc Lond 147:145–181
5. Graham TH (1861) Phil Trans R Soc Lond 151:1183–1196
6. Mie G (1908) Ann Phys (Leipzig) 25:377–445
7. Schmid G (2005) Nanoparticles from theory to applications. Wiley-VCH, Weinheim
8. Schmid G (2008) Clusters and colloids – from theory to applications. Wiley-VCH, Weinheim
9. Curuso F (2008) Colloids and colloid assemblies – synthesis modification, organization and utilization of colloid particles. Wiley-VCH, Weinheim
10. Fendler JH (2008) Nanoparticles and nanostructured films – preparation, characterization and applications. Wiley-VCH, Weinheim
11. Halaciuga I (2008) Formation mechanisms of metal colloids. Clarkson University Press, USA
12. Feldheim DL, Foss CA Jr (2002) Metal nanoparticles – synthesis, characterization, applications. Marcel Dekker, New York
13. Johnston RL, Wilcoxon JP (2012) Metal nanoparticles and nanoalloys. Elsevier, Amsterdam
14. Rai M, Duran NE (2011) Metal nanoparticles in microbiology. Springer, Heidelberg
15. Jennings T, Strouse G (2007) Past, present and future of gold nanoparticles. Adv Exp Med Biol 620:34–47
16. Sau TK, Rogach AL (2012) Complex shaped metal nanoparticles, bottom-up syntheses and applications. Wiley-VCH, Weinheim
17. Mott DM (2008) Synthesis, characterization of nanoparticles. UMI, Ann Arbor
18. Chang H-T, Chau L-K (2012) From bioimaging to biosensors, noble metal nanoparticles in biodetection. Pan Stanford Publishing Pte Ltd, Singapore
19. Niedelberger M, Pinna N (2009) Metal oxide nanoparticles in organic solvents, synthesis, formation, assembly and engineering, materials and processes. Springer, Heidelberg

20. Klimov VI (2004) Semiconductor and metal nanocrystals – synthesis, electronic structures, optical properties and characterization. Marcel Dekker, New York
21. Rotello VM (2004) Nanoparticle building blocks for nanotechnology. Springer, Heidelberg
22. Astruc D (2008) Nanoparticles in catalysis. Wiley-VCH, Weinheim
23. Rao CNR, Thomas PJ, Kulkarni GU (2007) Nanoparticles – synthesis, preparation, and applications. Springer, Heidelberg
24. Mariscal MM, Oviedo OA, Leiva EPM (2013) Model clusters and nanoalloys – from models to applications. Springer, Heidelberg
25. McNaught AD, Wilkinson A (1997) Compendium of chemical terminology, the gold book, vol 2. Blackwell, Oxford
26. Duff DG, Baiker A, Edwards PP (1993) A new hydrosol of gold clusters. J Chem Soc Chem Commun 96–98
27. Duff DG, Curtis AC, Edwards PP, Jefferson DA, Johnson BFG, Kirkland AI, Logan DE (1987) The morphology and microstructure of colloidal silver and gold. Angew Chem Int Ed Engl 26:676–678
28. Aldrich Chemicals http://www.sigmaaldrich.com/materials-science/nanomaterials/gold-anoparticles.html
29. Mingos DMP (1996) Gold – a flexible friend in cluster chemistry. J Chem Soc Dalton Trans 561–566
30. Mingos DMP (1993) Recent developments in the cluster chemistry of gold. Chemistry of the Copper and Zinc Triads. Roy Soc Chem Spec Publ 131:189–197
31. Mingos DMP (1992) High-nuclearity clusters of the transition metals and a re-evaluation of the cluster surface analogy. J Cluster Sci 3:397–409
32. Mingos DMP, Watson MJ (1992) Heteronuclear gold cluster compounds. Adv Inorg Chem 39:327–399
33. Mingos DMP, Watson MJ (1991) TMC literature highlights – 27. Recent developments in the homo- and hetero-metallic cluster compounds of gold. Trans Met Chem 16:285–287
34. Mingos DMP (1984) Structure and bonding in cluster compounds of gold. Polyhedron 3:1289–1297
35. Hall KP, Mingos DMP (1984) Homo- and heteronuclear cluster compounds of gold. Prog Inorg Chem 32:237–325
36. Mingos DMP (1984) Gold cluster compounds. Are they metals in miniature? Gold Bull (Geneva) 17:5–12
37. Mingos DMP (1982) Some theoretical and structural aspects of gold cluster chemistry. Phil Trans Roy Soc (Lond) 308:75–83
38. Mingos DMP (1980) Theoretical and structural studies on organometallic cluster molecules. Pure Appl Chem 52:705–712
39. Steggerda JJ, Bour JJ, van der Velden JWA (1982) Preparation and properties of gold cluster compounds. Rec des Travaux Chimiques des Pays-Bas 101:164–170
40. Kanters RPF, Schlebos PPJ, Bour JJ, Wijnhoven J, van den Berg JE, Steggerda JJ (1990) Isonitrile-containing platinum–gold phosphine clusters. J Organomet Chem 388:233–242
41. van der Velden JWA, Bour JJ, Steggerda JJ, Beurskens PT, Roseboom M, Noordik JH (1982) Gold clusters preparation, X-ray analysis, gold-197 Mössbauer and $^{31}P\{^{1}H\}$ NMR spectroscopy. Inorg Chem 21:4321–4324
42. Kanters RPF, Steggerda JJ (1990) Recognition of torroidal and spherical geometries in metal clusters of gold. J Cluster Sci 1:229–239
43. Zeng C, Jin R (2014) Gold nanoclusters: size-controlled synthesis and crystal structures. Struct Bond (Ed Mingos DMP) (in press)
44. Häkkinen H (2012) Ligand protected gold nanoclusters as superatoms – insights from theory and computations. In: Johnston RL, Wilcoxon JP (eds) Metal nanoparticles and nanoalloys. Frontiers of nanoscience, Palmer RE (series editor), vol 3. Elsevier, Amsterdam, pp 129–154

45. Pyykkö P, Mendizabal F (1997) Theory of the d10–d10 closed-shell attraction. II. Long-distance behavior and non-additive effects in dimers and trimers of type [(X-Au-L)n] (n = 2, 3; X = Cl, I, H; L = PH3, PMe3, –N ≡ CH). Chem Eur J 3:1458–1465
46. Dass A (2009) Mass spectrometric identification of $Au_{68}(SR)_{34}$ molecular gold nanoclusters with 34-electron shell closing. J Am Chem Soc 131:11666–11667
47. Dass A, Holt K, Parker JF, Feldberg MRW (2008) Mass spectrometrically detected statistical aspects of ligand populations in mixed monolayer $Au_{25}L_{18}$ nanoparticles. J Phys Chem C 112:20276–20283
48. Malatesta L (1975) Cluster compounds of gold. Gold Bull 8:48–52
49. Naldini L, Cariaati F, Simonetta G, Malatesta L (1965) Gold tertiary phosphine derivatives with intermetallic bonds. J Chem Soc Chem Commun 212–213
50. Malatesta L, Naldini L, Simonetta G, Cariati F (1966) Triphenylposphine gold(0)-gold(I) compounds. Coord Chem Rev 1:255–262
51. McPartlin M, Mason R, Malatesta L (1969) Custer compounds of gold(0)–gold(I). J Chem Soc Chem Commun 334
52. Schmid G, Pfeil R, Boese R, Bandermann F, Meyer S, Galis GHM, van der Velden JWA (1981) $Au_{55}(PPh_3)_{12}Cl_6$ – a gold cluster of unusual size. Chem Ber 114:3634–42
53. Wallenberg LR, Bovin JO, Schmid G (1985) $Au_{55}(PPh_3)_{12}Cl_6$ – TEM study of a gold cluster of unusual size. Surf Sci 156:256–264
54. Schmid G (1985) Developments in transition metal cluster chemistry: the way to large clusters. Struct Bond 62:52–85
55. Häkkinen H (2012) Ligand protected gold nanoclusters as superatoms – insights from theory and computations. In: Johnston RL, Wilcoxon JP (eds) Metal nanoparticles and nanoalloys. Frontiers of nanoscience, Palmer RE (series editor), vol 3. Elsevier, Amsterdam, pp 121–122
56. Rapoport DH, Vogel W, Coelfen H, Schlogegel R (1997) Ligand stabilised clusters: reinvestigation of the structure of $Au_{55}(PPh_3)_{12}Cl_6$. J Phys Chem 101:4175–4183
57. Brown LO, Hutchinson JE (1997) Convenient preparation of stable narrow-dispersity gold nanocrystals by ligand exchange reactions. J Am Chem Soc 119:12384
58. Broda J, Schmid G, Simon U (2013) Size and ligand specific response of gold clusters and nanoparticles: challenges and perspectives. Struct Bond (Ed Mingos DMP)
59. Teo BK, Shi X, Zhang H (1992) Pure gold cluster of 1:9:9:1:9:1:9:1 layered structure: a novel 39 metal atom cluster $[Au_{39}Cl_6(PPh_3)_{14}]Cl_2$ with an interstitial gold in a hexagonal antiprismatic cage. J Am Chem Soc 114:2743–2745
60. Teo BK, Zhang H (1995) Polyicosahedracity: icosahedraon to icosahedrons of icosahedral growth pathway to bimetallic and trimetallic Au, Ag, M (M = Ni, Pd, Pt) supraclusters – synthetic strategies and stereochemical principles. Coord Chem Rev 143:611–636
61. Walter M, Akola J, Lopez-Acevedo O, Jadinsky PD, Calero G, Ackerson CJ, Whetten RL, Gronbeck H, Häkkinen H (2008) A unified view of ligand protected gold clusters as a super atom complexes. Proc Natl Acad Sci U S A 105:9157–9162
62. Häkkinen H, Barnett RN, Landman U (1999) Electronic structure of passivated $[Au_{38}(SCH_3)_{24}]$ nanocrystal. Phys Rev Lett 82:3264
63. Jadzinsky PD, Calero G, Ackerson CJ, Bushnell DA, Kornberg RD (2007) Structure of a thiol monolayer protected gold nanoparticle at 1.1A resolution. Science 318:430–433
64. Price R, Whetten RL (2007) Nano-golden order. Science 318:407–408
65. Häkkinen H (2008) Atomic and electronic structure of gold clusters: understanding flakes, cages and superatoms from simple concepts. Chem Soc Rev 37–59:1847–1859
66. Murray RW (2008) Nanoelectrochemistry: metal nanoparticles, nanoelectrodes, and nanopores. Chem Rev 108:2688–2720
67. Turkevich J, Stevenson PC, Hillier J (1951) A study of the nucleation and growth processes in the synthesis of colloidal gold. Discuss Faraday Soc 11:55–75
68. Kimling J, Maier M, Okenve B, Kotaidis V, Ballot H, Plech A (2006) Turkevich method for gold nanoparticle synthesis revisited. J Phys Chem B 110:15700–15707

69. Frens G (1972) Particle size and sol stability in metal colloids. Colloid Polym Sci 250: 736–741
70. Frens G (1973) Controlled nucleation for the regulation of the particle size in mono-disperse gold suspensions. Nature (London) Phys Sci 241:20–22
71. Pong BK et al (2007) New insights on the nanoparticle growth mechanism in the citrate reduction of gold(III) salt: formation of the Au nanowire intermediate and its nonlinear optical properties. J Phys Chem C 111:6281–6287
72. Perrault SD, Chan WCW (2009) Synthesis and surface modification of highly monodispersed, spherical gold nanoparticles of 50–200 nm. J Am Chem Soc 131:17042–17043
73. Brust M, Walker M, Bethell D, Schiffrin DJ, Whyman R (1994) Synthesis of thiol-derivatised gold nanoparticles in a two-phase liquid–liquid system. J Chem Soc Chem Commun 801–802
74. Kiely CJ, Fink J, Brust M, Walker M, Bethell D, Schiffrin DJ (1998) Synthesis of thiol-derivatised gold nanoparticles in a two-phase liquid–liquid system. Nature 396:444–446
75. Brust M, Kiely CJ (2002) Some recent advances in nanostructure preparation from gold and silver particles: a short topical review. Colloids Surf A 202:175–186
76. Giersig P, Mulvaney P (1993) Preparation of ordered colloid monolayers by electrophoretic deposition. Langmuir 9:3408–3413
77. Daniel M-C, Astruc D (2004) Gold nanoparticles assembly, supramolecular chemistry, quantum size related properties, applications towards biology, catalysis and nanotechnology. Chem Rev 104:293–346
78. Manna A, Chen P, Akiyama H, Wei T, Tamada K, Knoll W (2003) Optimised photoisomerization on gold nanoparticles capped by unsymmetrical azobenzene disulfides. Chem Mater 15:20–28
79. Zhu M, Lanni E, Garg N, Bier ME, Jin R (2008) Kinetically controlled, high-yield synthesis of Au_{25} clusters. J Am Chem Soc 130:1138–1139
80. Brust M, Fink J, Bethell D, Schiffrin DJ, Kiely C (1995) Synthesis and reactions of functionalised gold nanoparticles. J Chem Soc Chem Commun 1655–1656
81. Wu Z, Suhan J, Jin RC (2009) One-Pot synthesis of atomically monodisperse, thiol-functionalized Au_{25} nanoclusters. J Mater Chem 19:622–626
82. Templeton AC, Hostetler MJ, Kraft CT, Murray RW (1998) Reactivity of monolayer-protected gold cluster molecules steric effects. J Am Chem Soc 120:1906–1911
83. Hostetler MJ, Templeton AC, Murray RW (1999) Dynamics of place-exchange reactions on monolayer-protected gold cluster molecules. Langmuir 15:3782–3789
84. Lin XM, Jaeger HM, Sorensen CM, Klabunde KJ (2001) Formation of long-range-ordered nanocrystal superlattices on silicon nitride substrates. Phys Chem B 105:3353–3357
85. Kamei Y, Shichuba Y, Konishi K (2011) Generation of small clusters with unique geometries through cluster-cluster transformations; octanuclear clusters with edge-sharing gold tetrahedron motifs. Angew Chem Int Ed 50:7442–7445
86. Guo WW, Yuan JP, Wang EK (2012) Organo-soluble fluorescent Au_8 clusters generated from heterophase ligand-exchange etching of gold nanoparticles and their electroluminesence. J Chem Soc Chem Commun 48:3076–3078
87. Schaaff TG, Whetten RL (1999) Controlled etching of Au:SR cluster compounds. J Phys Chem B 103:9394–9396
88. Qian H, Eckenhoff WT, Zhu Y, Pintauer T, Jin R (2010) Total structure determination of thiolate-protected Au_{38} nanoparticles. J Am Chem Soc 132:8280–8281
89. Jin R, Qian HF, Wu Z, Zhu Y, Zhu M, Mohanty A, Gay N (2010) Size focusing: a methodology for synthesising atomically precise gold clusters. Nanotechnology 21:2903–2910
90. Pradeep T, Shibu ES (2011) Quantum clusters in cavities: trapped Au_{15} in cyclodextrins. Chem Mater 23:989–999
91. Nimmala PR, Dass A (2011) $Au_{36}(SPh)_{23}$ nanomolecules. J Am Chem Soc 133:9175–9177
92. Qian H, Zhu Y, Jin R (2009) Size-focusing synthesis, optical and electrochemical properties of monodispersed $Au_{38}(SC_2H_4Ph)_{24}$. Nanoclusters 3:3795–3803

93. Qian H, Jin R (2009) Controlling nanoparticles with atomic precision: the case of $Au_{104}(SCH_2CH_2Ph)_{60}$. Nano Lett 9:4083–4087
94. Xu Q, Wang SX, Liu Z, Xu GY, Meng SM, Zhu MZ (2013) Synthesis of selenato- protected $Au_{18}(SePh)_{14}$ nano-clusters. Nanoscale 5:1176–1182
95. Tsunoyama H, Negishi Y, Tsukuda T (2006) Chromatographic isolation of "missing" Au_{55} clusters protected by alkanethiolates. J Am Chem Soc 128:6036–6037
96. Negishi Y, Nobusada K, Tsukuda T (2005) Glutathione-protected gold clusters revisited: bridging the gap between gold(I)-thiolate complexes and thiolate-protected gold nanocrystals. J Am Chem Soc:5261–5270
97. Seo D, Park JC, Song H (2006) Polyhedral gold nanocrystals with Oh symmetry: from octahedra to cubes. J Am Chem Soc 128:14863–14870
98. Schaaff TG, Knight G, Shafigullin MN, Borkman RF, Whetten RL (1998) Isolation and selected properties of 10.4 kDa gold: glutathione cluster compound. J Phys Chem B 102: 10643–10646
99. Schaaff TG, Whetten RL (1999) Controlled etching of Au:SR cluster compounds. J Phys Chem 103:9394–9396
100. Whetten RL, Shafigullin MN, Khoury JT, Schaaff TG, Alvarez MM, Wilkinson A (1999) Crystal structures of molecular gold nanocrystal arrays. Acc Chem Res 32:397–406
101. Ingram RS, Hostetler MJ, Murray RW, Schaaff TG, Khoury J, Whetten RL, Bigioni TP, Guthrie DK, First PN (1997) 28 kDa alkanethiolate-protected Au clusters give analogous solution electrochemistry and STM Coulomb staircases. J Am Chem Soc 119:9279–9280
102. Shichubu Y, Negishi Y, Tsukada T, Teranishi T (2005) Large-scale synthesis of thiolated Au_{25} clusters via ligand exchange reactions of phosphine-stabilised Au_{11} clusters. J Am Chem Soc 127:13464–13465
103. Tsunoyama H, Sakurai H, Negishi Y, Tsukuda T (2005) Size-specific catalytic activity of polymer-stabilised gold nanoclusters for aerobic alcohol oxidation in water. J Am Chem Soc 127:9374–9375
104. Tsunoyama H, Sakurai H, Negishi Y, Tsukuda T (2007) Size-specific catalytic activity of polymer-stabilised gold nanoclusters for aerobic alcohol oxidation in water. J Am Chem Soc 129:11322
105. Dass A, Stevenson A, Dubay GB, Tracy JB, Murray RW (2008) MALDI-TOF nanoparticle mass spectrometry without fragmentation: $Au_{25}(SCH_2CH_2Ph)_{18}$ and mixed monolayer $Au_{25}(SCH_2CH_2Ph)_{18-x}(L)_x$. J Am Chem Soc 130:5940–5946
106. Zhu M, Aikens CM, Hollander FJ, Schatz GC, Jin R (2008) Correlating the crystal structure of a thiol-protected Au_{25} cluster and optical properties. J Am Chem Soc 130:5883–5885
107. Qian HF, Jin R (2011) Ambient synthesis of $Au_{104}(SR)_{60}$ nanoclusters in methanol. Chem Mater 23:2209–2217
108. Alloisio M, Demartini A, Cuniberti C, Muniz-Miranda M, Giorgetti E, Giusti A (2008) Photopolymerization of diacetylene-capped gold nanoparticles. Phys Chem Chem Phys 10: 2214–2220
109. Pelka JB, Brust M, Gierlowski P, Paszkowsicz W, Schell N (2006) Structure and conductivity of self-assembled films of gold nanoparticles. Appl Phys Lett 89:063110–063113
110. Corbierre MK, Bearens J, Beauvais J, Lennox RB (2006) Uniform one-dimensional arrays of tunable gold nanoparticles with tunable interparticle distances. Chem Mater 18:2628–2631
111. Vollenbroek FA, Bouten DCP, Trooster JP, van der Berg JP, Bour JJ (1978) Mössbauer investigation and novel synthesis of gold cluster compounds. Inorg Chem 17:1345–1347
112. van der Velden JWA, Bour JJ, Vollenbroek FA, Beurskens PT, Smits JMM (1979) Synthesis of a new pentanuclear gold cluster by metal evaporation. Preparation and X-ray structure determination of [tris{bis(diphenylphosphino)methane}][bis(diphenylphosphino)methanido] pentagold dinitrate. J Chem Soc Chem Commun 1162–1163
113. van der Velden JWA, Bour JJ, Beurskens PT, Dosman WP, Noordik JM, Kolenbrander M, Buskes JAKM (1984) Intermediates in the formation of gold clusters. Preparation and X-ray

analysis of $[Au_7(PPh_3)_7]^+$ and synthesis and characterization of $[Au_8(PPh_3)_6I]PF_6$. Inorg Chem 23:146–151
114. Lin ST, Franklin MT, Klabunde KJ (1986) Nonaqueous colloidal gold. Clustering of metal atoms in organic media – 12. Langmuir 2:259–260
115. Cardines-Trevino G, Klabunde KJ, Dale EB (1987) Living colloidal palladium in nonaqueous solvents. Formation, stability, and film-forming properties. Clustering of metal atoms in organic media – 14. Langmuir 3:986–992
116. Belloni J, Delecourt MO, Leclerc C (1982) Radiation-induced preparation of metal catalysts: iridium aggregates. New J Chem 6:507–518
117. Gachard E, Remita H, Khatouri J, Keita B, Nadjo L, Belloni J (1998) Radiation-induced and chemical formation of gold clusters. New J Chem 22:1257–1265
118. Treuger M, de Cointet C, Remita H, Khatouri J, Mostafavi M, Amblard J, Belloni J, de Keyzer R (1998) Dose effects on radiolytic synthesis of gold-silver bimetallic clusters in solution. J Phys Chem B 102:1310–1321
119. Zhang J, Du J, Man B, Liu Z, Jiang T, Zhang Z (2006) Sonochemical formation of single crystalline gold nanoclusters. Angew Chem Int Ed 118:1134–1137
120. Uppal J, Kafizas A, Ewing MB, Parkin IP (2010) The effect of initiation method on the size, monodispersity and shapes of gold nanoparticles formed by the Turkevich method. New J Chem 24:2006–2014
121. Mafuné F, Kohno J, Takeda Y, Kondow T, Sawabe H (2001) Formation of gold nanoparticles by laser ablation in aqueous solution of surfactant. J Phys Chem B 105:5114–5120; 9050–9056
122. Leff DV, Brandt L, Heath JR (1996) Synthesis and characterization of hydrophobic, organically-soluble gold nanocrystals functionalized with primary amines. Langmuir 12: 4723–4730
123. Shi W, Sahoo Y, Swihart MT (2004) Gold nanoparticles surface-terminated with bifunctional ligands. Colloids Surf A Physicochem Eng Asp 246:109–113
124. Li Z (2012) Scanning transmission electron microscopy studies of mono- and bi-metallic nanoclusters. In: Johnston RL, Wilcoxon JP (eds) Metal nanoparticles and alloys. Elsevier, Amsterdam, pp 213–245
125. Chen Y, Palmer RE, Wilcoxon JP (2006) Sintering of passivated gold nanoparticles under the electron beam. Langmuir 22:2851–2855
126. Wilcoxon JP, Provencio PP (2004) Heterogeneous growth of metal clusters from solutions of seed nanoparticles. J Am Chem Soc 126:6402–6408
127. Martin JE, Odinek J, Wilcoxon JP, Anderson RA, Provencio PP (2003) Sintering of alkanethiol-capped gold and platinum nanoclusters. J Phys Chem B 107:430
128. Horisberger M (1981) Colloidal gold: a cytochemical marker marker for light and fluorescent microscopy and for scanning electron microscopy. Scan Electron Microsc 2:9–31
129. Wang ZL (2000) Transmission electron microscopy of shape controlled nano-crystals and their assemblies. J Phys Chem B 104:1153–1175
130. Li ZY, Young NP, Di Vecc M, Palomba S, Palmer RE, Bleloch AL, Curley BC, Johnston RL, Jiang J, Yuan J (2008) Three dimensional atomic – scale structure of size selected gold nanoclusters. Nature 451:46–48; Li ZY 213–247 in Ref. [13]
131. Jiang D (2013) The expanding universe of thiolated gold nanoclusters and beyond. Nanoscale 5:7149–7160
132. Heaven MW, Dass A, White PS, Holt KM, Murray RW (2008) Crystal structure of the gold nanoparticle $[N(C_8H_{17})_4][Au_{25}(SCH_2CH_2Ph)_{18}]$. J Am Chem Soc 130:3754–3755
133. Qian H, Zhu M, Lanni E, Zhu Y, Bier ME, Jin R (2009) Conversion of polydisperse Au nanoparticles into monodisperse Au_{25} nanorods and nanospheres. J Phys Chem C 113: 17599–17603
134. Qian H, Zhu Y, Jin R (2009) Size-focusing synthesis, optical and electrochemical properties of monodisperse $Au_{38}(SC_2H_4Ph)_{24}$ nanoclusters. ACS Nano 3:3795–3803

135. Zeng C, Qian H, Li T, Li G, Rosi NL, Yoon B, Barnett RN, Whetten RL, Landman U, Jin R (2012) Total structure and electronic properties of the gold nanocrystal $Au_{36}(SR)_{24}$. Angew Chem Int Ed 51:13114–13118
136. Zeng C, Li T, Das A, Rosi NL, Jin R (2013) Chiral structure of thiolate-protected 28-gold-atom nanocluster determined by X-ray crystallography. J Am Chem Soc 135:10011–10013
137. Mingos DMP (1982) Steric effects in metal cluster chemistry. Inorg Chem 21:466–468
138. Vollenbroek FA (1979) Ph D Thesis University of Nijmegen
139. Krommenhoek PJ, Wang J, Hentz N, Johnston-Peck AC, Kozek KA, Kalyuzhny G, Tracy JB, Bulky A (2012) Cyclohexanethiolate ligands favor smaller gold nanoparticles with altered discrete sizes. ACS Nano 6:4903–4911
140. Harkness KM, Cliffel DE, McLean JA (2010) Characterization of thiolate-protected gold nanoparticles by mass spectrometry. Analyst 135:868–874
141. Harkness KM, Fenn LS, Cliffel DE, McLean JA (2010) Surface fragmentation of complexes from thiolate protected gold particles by mass spectrometry. Anal Chem 82:3061–3066
142. Whetten RL, Khoury JT, Alvarez MM, Marcos M, Murthy SM, Vezmar I, Wang ZL, Stephens PW, Cleveland CL, Luedtke WD, Landman U (1996) Nanocrystal gold molecules. Adv Mater 8:428–433
143. Tracy JB, Kalyuzhny G, Crowe MC, Balasubramanian R, Choi JP, Murray RW (2007) Poly (ethylene glycol) ligands for high-resolution nanoparticle mass spectrometry. J Am Chem Soc 129:6706–6707
144. Chaki NK, Negishi Y, Tsunoyama H, Shichibu Y, Tsukuda T (2008) Ubiquitous 8 and 29 kDa gold:alkanethiolate cluster compounds: mass-spectrometric determination of molecular formulas and structural implications. J Am Chem Soc 130:8608–8610
145. Arnold RJ, Reilly JP (1998) High-resolution time-of-flight mass spectra of alkanethiolate-coated gold nanocrystals. J Am Chem Soc 120:1528–1532
146. Dass A, Dubay George R, Fields-Zinna CA, Murray RW (2008) FAB mass spectrometry of $Au_{25}(SR)_{18}$ nanoparticles. Anal Chem (Washington, DC) 80:6845–6849
147. Dass A, Guo R, Tracy JB, Balasubramanian R, Douglas AD, Murray RW (2008) Gold nanoparticles with perfluorothiolate ligands. Langmuir 24:310–315
148. Tracy JB, Crowe MC, Parker JF, Hampe O, Fields-Zinna CA, Dass A, Murray RW (2007) Electrospray ionization mass spectrometry of uniform and mixed monolayer nanoparticles: $Au_{25}[S(CH_2)_2Ph]_{18}$ and $Au_{25}[S(CH_2)_2Ph]_{18-x}(SR)_x$. J Am Chem Soc 129:16209–16215
149. Qian H, Zhu M, Wu Z, Jin R (2012) Quantum sized gold nanoclusters with atomic precision. Acc Chem Res 45:1470–1479
150. Wu Z, Gayathri C, Gil RR, Jin R (2009) Probing the structure and charge state of glutathione-capped $Au_{25}(SG)_{18}$ clusters by NMR and mass spectrometry. J Am Chem Soc 131: 6535–6542
151. Shvartsburg A, Jarrold M (2000) Modeling Ion mobilities by scattering on electronic density isosurfaces-applied to silicon cluster anions. Chem Phys Lett 317:615–618
152. Weis P, Biersieller T, Volmer T, Kappes MM (2002) Au_9^+ rapid isomerizations at 140 K. J Chem Phys 117:9293–9297
153. Gruene P, Rayner DM, Redlich B, van der Meer AFG, Lyon JT, Meijer G, Fielicke A (2008) Structures of neutral Au_7 Au_{19}, and Au_{20} clusters in the gas phase. Science (Washington DC) 321:674–676
154. Clayden NJ, Dobson CM, Hall KP, Mingos DMP, Smith DJ (1985) Studies of gold cluster compounds using high-resolution phosphorus-31 solid-state nuclear magnetic resonance spectroscopy. Inorg Chem 25:1811–1814
155. Diesveld JW, Menger EM, Edzes HT, Veeman WS (1980) J Am Chem Soc 102:7935
156. van der Velden JWA, Bour JJ, Bosman WP, Noordik JH, Beurskens PT (1984) Electrochemical preparation of $[Au_9(PPh3)8]^+$. A comparative study of structures. Receuil (J R Neth Chem Soc) 103:13–16
157. van der Velden JWA, Bour JJ, Steggerda JJ, Beurskens PT, Roseboom M, Noordik JH (1983) Gold clusters. Tetrakis[1,3-bis(diphenylphosphino)propane]hexagold dinitrate: preparation,

X-ray analysis, and gold-197 Mössbauer and phosphorus-31{proton} NMR spectra. Inorg Chem 21:4321–4324
158. Sharma R, Holland GP, Solomon VC, Zimmermann H, Schiffenhaus S, Amin SA, Buttry DA, Yarger JL (2009) NMR characterization of ligand binding and exchange dynamics in triphenylphosphine-capped gold nanoparticles. J Phys Chem C 113:16387–16393
159. Salorinne K, Lahtinen T, Koivisto J, Kalenius E, Nissinen M, Pettersson M, Häkkinen H (2013) Non-destructive size determination of thiol-stabilised gold nanoclusters in solution by diffusion ordered NMR spectroscopy. Anal Chem 85:3489–3492
160. Qian H, Zhu M, Gayathri C, Gil RR, Jin R (2011) Chirality in gold nanoclusters probed by NMR spectroscopy. ACS Nano 5:8935–8942
161. Parish RV, Moore LS, Dens AJ, Mingos DMP, Sherman DJ (1988) Iron-57 and gold-197 Mössbauer spectro-scopic investigation of the bonding in two gold-iron cluster compounds. Inorg Chem 27:781–783
162. Parish RV, Moore LS, Dens AJ, Mingos DMP, Sherman DJ (1989) Gold-197 Mössbauer spectra and the bonding of some gold–gold and gold–platinum clusters. J Chem Soc Dalton Trans Inorg Chem 539–543
163. Battistoni C, Mattogno G, Mingos DMP (1984) Characterization of some gold cluster compounds by X-ray photoelectron spectroscopy. Inorg Chim Acta 33:107–113
164. Arfelli M, Battistoni C, Mattogno G, Mingos DMP (1989) X-ray photoelectron spectroscopic evidence for the electrophilic character of the AuL [gold-ligand] fragment in the cluster compound $(Pt_3Au(\mu^2\text{-}CO)_3\ L_4)PF_6$. J Elect Spectr Rel Phenomena 49:273–277
165. Chevrier DM, Chatt A, Sham TK, Zhang P (2013) A comparative EXAFS study of gold-thiolate nanoparticles and nanoclusters. J Phys Conf Ser 430:120–129
166. Yao T, Sun Z, Li Y, Pan Z, Wei H, Xie Y, Nomura M, Niwa Y, Yan W, Wu Z, Jiang Y, Liu Q, Wei S (2010) Insights into initial kinetic nucleation of gold nanocrystals. J Am Chem Soc 132:7696–7701
167. Abecassis B, Testard F, Spalla O, Barboux P (2007) Probing in situ the nucleation and growth of gold nanoparticles by small-angle X-ray scattering. Nano Lett 7:1723–1727
168. Coffer JL, Shapley JR, Drickamer HG (1990) Pressure-induced skeletal isomerization of octakis-(triphenylphosphine)nonagold(3+) hexafluorophosphate in the solid state. Inorg Chem 29:3000–3001
169. Coffer JL, Shapley JR, Drickamer HG (1990) The effect of pressure on the surface plasmon absorption spectrum of colloidal gold and silver particles. J Am Chem Soc 112:3736–3742
170. Saha K, Agasti SS, Kim C, Li X (2012) Gold sensors in chemical and biological systems. Chem Rev 112:2739–2779
171. Zhang Y, Fei W-W, Jia N-Q (2005) A facile method for the detection of DNA using gold nanoparticle probes coupled with dynamic light scattering. Nanoscale Lett 7:564–569
172. Chah S, Hammond MR, Zare PN (2005) Gold nanoparticles as a colorometric sensor for protein conformational changes. Chem Biol 12:323–328
173. Durgadas CV, Sharma CP, Sreenivasan K (2011) Fluorescent gold clusters as nanosensors for copper ions in live cells. Analyst 136:933–940
174. Ali ME, Hashim U, Mustafa S, Che-Man YB, Islam KH (2012) Development of swine-specific DNA markers for biosensor-based halal authentication. Genet Mol Res 11: 1762–1772
175. Eustis S, El-Sayed M (2006) Why gold nanoparticles are more precious than pretty gold: noble metal surface plasmon resonance and its enhancement of the radiative and non-radiative properties of nanocrystals of different shapes. Chem Soc Rev 35:209–217
176. Kneipp J, Kneipp H, McLaughlin M, Brown D, Kneipp K (2006) In vivo molecular probing of cellular compartments with gold nanoparticles and nanoaggregates. Nano Lett 6: 2225–2231
177. Johnston RL (2012) In: Johnston RL, Wilcoxon JP (eds) Metal nanoparticles and alloys. Elsevier, Amsterdam, pp 1–42

178. Kim Y, Johnson RC, Hupp JT (2001) Gold nanoparticle-based sensing of "spectroscopically silent" heavy metal ions. Nano Lett 1:165–167
179. Horisberger M, Rosset JJ (1977) Colloidal gold, a useful marker for transmission and scanning electron microscopy. J Histochem Cytochem 25:295–305
180. Peng G, Tisch U, Adams O, Hakim M, Shehada N, Broza YY, Bilan S, Abdah-Bortnyak R, Kuten A, Haick H (2009) Diagnosing lung cancer in exhaled breath using gold nanoparticles. Nat Nanotechnol 4:669–673
181. Brown SD, Nativo P, Smith J-A, Stirling D, Edwards PR, Venugopal B, Flint DJ, Plumb JA, Graham D, Wheate NJ (2010) Gold nanoparticles for the improved anticancer drug delivery of the active component of oxaliplatinum. J Am Chem Soc 132:4678–4684
182. Huang X, Jain PK, El-Sayed IH, El-Sayed MA (2008) Plasmonic photothermal therapy (PPTT) using gold particles. Lasers Med Sci 23:217–228
183. Stuchinskaya T, Moreno M, Cook MJ, Edwards DR, Russell DA (2011) Targeted photodynamic therapy of breast cancer cells using antibody-phthalocyanine-gold nanoparticle conjugates. Photochem Photobiol Sci 10:822–831
184. Hone DC, Walker PI, Evans-Gowing R, Fitzgerald S, Beeby A, Chambrier I, Cook MJ, Russell DA (2002) Generation of cytotoxic singlet oxygen via phthalocyanin, stabilised gold-nanoparticles: a potential delivery vehicle for photodynamic therapy. Langmuir 18: 2985–2987
185. Huang D, Liao F, Molesa S, Redinger D, Subramanian V (2003) Plastic-compatible Low resistance printable gold nanoparticle conductors for flexible electronics. J Electrochem Soc 150:G412–G417
186. Okazaki S, Moers J (2005) Lithography. In: Waser R (ed) Nanoelectronics and information technology, 2nd edn. Wiley-VCH, Weinheim, pp 221–247
187. Grabert H (1991) Single charge tunneling: a brief introduction. Z Phys B 85:319–325
188. Homberger M, Simon U (2010) On the application potential of gold nanoparticles in nanoelectronics and biomedicine. Phil Trans R Soc A 368:1405–1453
189. Mirkin CA (2000) Programming the assembly of two- and three-dimensional architectures with DNA and nanoscale inorganic building blocks. Inorg Chem 39:2258–2272
190. Mirkin CA, Letsinger RL, Mucic RC, Storhoff JJ (1996) A DNA-based method for rationally assembling nanoparticles into macroscopic materials. Nature 382:607–609
191. Macfarlane RJ, O'Brien MN, Petrosko SH, Mirkin CA (2013) Nucleic acid-modified nanostructures as programmable atom equivalents: forging a New "table of elements". Angew Chem Int Ed 52:5688–5698
192. Huang X, Neretina S, El-Sayed MA (2009) Gold nanorods: from synthesis and properties to biological and biomedical applications. Adv Mater 21:4880–4910
193. Lohse SE, Murphy CJ (2013) The quest for shape control: a history of gold nanorod synthesis. Chem Mater 25:1250–1261
194. Hou S, Hu X, Wen T, Wenqi L, Wu X (2013) Core-shell noble metal nanostructures templated by gold nanorods. Adv Mater 25:3857–3862
195. Alkilany AM, Thompson LB, Buolos SP, Sisco PN, Murphy CJ (2012) Gold nanorods: their potential for photothermal therapeutics and drug delivery, tempered by the complexity of their biological interactions. Adv Drug Deliv Rev 64:190–199
196. Murphy CJ, Gole AM, Stone JW, Sisco PN, Alkilany AM, Goldsmith EC, Baxter SC (2008) Gold nanoparticles in biology: beyond toxicity to cellular imaging. Acc Chem Res 41: 1721–1730
197. Murphy CJ, Gole AM, Hunyadi SE, Orendorff CJ (2008) One-dimensional colloidal gold and silver nanostructures. Inorg Chem 45:7544–7554
198. Jain PK, Rivest JB (2005) Cation exchange on the nanoscale: an emerging technique for new material synthesis, device fabrication, and chemical sensing. Chem Soc Rev 42:89–96
199. Huang X, Jain PK, El-Sayed IH, El-Sayed MA (2007) Gold nanoparticles: interesting optical properties and recent applications in cancer diagnostics and therapy. Nanomedicine 2: 681–693
200. Bond GC, Sermon PA (1973) Gold catalysts in olefin hydrogenation. Transmutation of catalytic properties. Gold Bull (Geneva) 6:102–105

201. Haruta M, Kobayashi T, Sano H, Yamada N (1987) Novel gold catalysts for the oxidation of carbon monoxide at a temperature far below 0°C. Chem Lett 16:405–406
202. Haruta M, Yamada N, Kobayashi T, Ijima S (1989) Gold catalysts prepared by co-precipitation for low-temperature oxidation of hydrogen and of carbon monoxide. J Catal 115:301–309
203. Haruta M (1997) Size- and support-dependency in the catalysis of gold. Catal Today 36:153–166
204. Hutchings GJ (1985) Vapor phase hydrochlorination of acetylene: correlation of catalytic activity of supported metal chloride catalysts. J Catal 96:292–295
205. Christensen CH, Jorgensen B, Rass-Hansen J, Egeblad K, Madsen R, Klitgaard SK, Hansen SM, Hansen MR, Andersen HC, Riisager A (2006) Formation of acetic acid by aqueous-phase oxidation of ethanol with air in the presence of a heterogeneous gold catalyst. Angew Chem Int Ed 45:4648–4651
206. Valden M, Lai X, Goodman DW (1998) Onset of catalytic activity of gold clusters on titania with the appearance of non-metallic properties. Science (Washington DC) 281:1647–1650
207. Boyen HG, Kaestle G, Weigl F, Koslowski B, Dietrich C, Ziemann P (2002) Oxidation-resistant gold-55 clusters. Science (Washington DC) 297:1533–1536
208. Lopez N, Novorsky JK, Catalytic CO (2002) Oxidation by a gold nanoparticle: a density functional study. J Am Chem Soc 124:11262–11263
209. Landon P, Collier PJ, Papworth AJ, Kiely CJ, Hutchings GJ (2002) Direct formation of hydrogen peroxide from H_2/O_2 using a gold catalyst. J Chem Soc Chem Commun 18: 2058–2059
210. Haruta M (1997) Novel catalysis of gold deposited on metal oxides. Catal Surv Jpn 1:61–73
211. Bond GC, Thompson DT (2000) Gold catalysed oxidation of carbon monoxide. Gold Bull 33:41–51
212. Sinha AK, Seelan S, Tsuboata S, Haruta M (2004) Vital Roe of moisture in the catalytic activity of supported gold nanoparticles. Angew Chem Int Ed 43:1546–1548
213. Hutchings GC, Edwards JK (2012) Application of gold nanoparticles in catalysis. In: Johnston RL, Wilcoxon JP (eds) Metal nanoparticles and alloys. Elsevier, Amsterdam, Holland, pp 249–293
214. Okazaki K, Ichikawa S, Maeda Y, Haruta M, Kohyama M (2005) Electronic structures of gold supported on TiO_2. Appl Catal A Gen 291:37–44; 45–54
215. Nilius N, Risse T, Shaikhutdinov S, Sterrer M, Freund H-J (2013) Metal catalysts based on gold clusters. Struct (Ed Mingos DMP)
216. Li Z, Johnston RL (2014) Nanoalloys of gold. Struct Bond (Ed Mingos DMP)
217. Ferrando R, Jellinek J, Johnston RL (2008) Nanoalloys: from theory to applications of alloy clusters and nanoparticles. Chem Rev 108:845–910
218. Hashmi ASK (2004) Homogeneous catalysis by gold. Gold Bull 37:51–65
219. Ito Y, Sawamura M, Hayashi T (1986) Catalytic asymmetric aldol reaction: reactions of aldehydes with isocyanates catalysed by a chiral ferrocenyl-phosphine gold(I) complex. J Am Chem Soc 108:6405–6406
220. Teles JH, Brode S, Chabanas M (1998) Cationic gold(I) complexes: highly efficient catalysts for the addition of alcohols to alkynes. Angew Chem 110:1475–1478
221. Teles JH, Brode S, Chabanas M (1998) Cationic gold(I) complexes: highly efficient catalysts for the addition of alcohols to alkynes. Angew Chem Int Ed 37:1415–1418
222. Hashmi ASK, Schwarz L, Choi J-H, Frost TM (2000) A new gold catalysed C–C bond formation. Angew Chem 112:2382–2385
223. Hashmi ASK, Schwarz L, Choi J-H, Frost TM (2000) A new gold catalysed C–C bond formation. Angew Chem Int Ed 39:2285–2288
224. Hashmi ASK, Frost TM, Bats JW (2000) Highly selective gold(I) catalysed arene synthesis. J Am Chem Soc 122:11553–11554
225. Dyker G (2000) An Eldorado for homogeneous catalysis. Angew Chem 39:4237–4239

Struct Bond (2014) 161: 49–86
DOI: 10.1007/430_2014_143

Published online: 26 March 2014

Phosphine-Coordinated Pure-Gold Clusters: Diverse Geometrical Structures and Unique Optical Properties/Responses

Katsuaki Konishi

Abstract Synthetic techniques, geometrical structures, and electronic absorption spectra of phosphine-coordinated pure-gold molecular clusters (PGCs) accumulated over 40 years are comprehensively collected especially for those with unambiguous X-ray crystal structures available. Inspection of the electronic absorption spectra from geometrical aspects reveals that their optical properties are highly dependent on the cluster geometries rather than the nuclearity. Recent examples of unusual clusters that show unique color/photoluminescence properties and their utilization for stimuli-responsive modules are also presented.

Keywords Absorption spectrum · Chromism · Gold cluster · Optical property · Phosphine · Photoluminescence · Stimuli-responsive materials

Contents

K. Konishi (✉)
Faculty of Environmental Earth Science and Graduate School of Environmental Science, Hokkaido University, North 10 West 5, Sapporo 060-0810, Japan
e-mail: konishi@ees.hokudai.ac.jp

Abbreviations

Ar	Aryl
AZS	Alizarinsulfonate
Bu	Butyl
DCM	Dichloromethane
dppb	Bis(diphenylphosphino)butane
dppe	Bis(diphenylphosphino)propane
dpph	Bis(diphenylphosphino)hexane
dppm	Bis(diphenylphosphino)methane
dppo	Bis(diphenylphosphino)octane
dpppe	Bis(diphenylphosphino)pentane
equiv	Equivalent(s)
Et	Ethyl
i-Pr	Isopropyl
Mes	Mesityl
PL	Photoluminescence
py	Pyridyl
t-Bu	*Tert*-butyl
Tol	Tolyl

1 Introduction

During the last several decades, the chemistry of ligand-protected noble metal nanoparticles/clusters has progressed rapidly. Fundamental aspects have been addressed and practical uses have been found in diverse research areas including medicine, electronics, and catalysis [1–6]. The most prominent property of conventional gold particles (diameter >2 nm) is localized surface plasmon bands, which have been widely exploited for biomedical applications [4, 7]. On the other hand, for very small clusters in the subnanometer size regime (d ~1 nm or less), such plasmon resonances disappear and discrete electronic transitions emerge which are characteristic molecular properties [8–12]. Thus, it is now well recognized that the subnano-sized clusters are virtually different from conventional colloidal particles/clusters in terms of electronic structures and properties [8]. Especially in recent years, much attention has been paid to their unique optical properties since the discovery of photoluminescence of some ultrasmall gold clusters in this size regime [13]. The reactivity and catalysis of the ultrasmall metal entities have also attracted great interest [5].

Structurally defined molecular metal clusters offer nice models to establish the structure–property relationship in the subnanometer regime. Molecular structures of numerous phosphine- and thiolate-ligated gold clusters, which form major families in cluster chemistry, have been determined. From a structural standpoint, thiolate-capped clusters, whose molecular structures were extensively elucidated just recently, are interesting but somewhat complicated because the metal cores are covered by multiple gold-thiolate staples [14–18]. On the other hand, phosphine-capped gold clusters (PGCs) have simple core-shell structures composed of the inorganic moiety (metal core) and surrounding organic ligands (shell) because of the neutral character of phosphine, thus they provide a useful platform to assess the nature of the inner gold core moieties and organic–inorganic interfaces. Further, PGCs have a long history of studies to provide a large structure library. Surveying of the Cambridge Structural Database (CSD) (2012) has identified approximately 300 crystal structures of gold-based cluster compounds.

The first example of PGC can be traced back to the pioneering work by Malatesta in 1966 [19], but the structure could not be accurately defined. Later, in 1970s and early 1980s, definitive X-ray structure determinations were achieved independently mainly by a Nijmegen group [20–33] and Mingos et al. [34–43] for various PGCs with nuclearity of 5–13 [44–49]. Most of these clusters exploited monodentate phosphines as the ligands, revealing the general trend of the geometrical preference in the formation of ultrasmall clusters under unconstrained conditions. Through these studies, fundamental structure and bonding of this class of compounds were comprehensively established and were also interpreted theoretically [50–52]. Thereafter, major interests in ligand-coordinated gold clusters moved to heterometallic, higher-nuclearity (e.g., Au_{39}, Au_{55}), and thiolate-capped families. However, the interests in ultrasmall molecular PGCs have recently revisited [8, 53–55] in relation to the advances of structural chemistry of thiolate-capped clusters. Further, the use of state-of-the-art analytical instruments together with the advanced computation technology has opened the door to unusual cluster species.

Asides from conventional clusters, there is another line of studies on "Au(I)" clusters which do not contain formally zero-valent gold atoms [56, 57]. Further, there are extensive studies on clusters whose skeletons are constituted primarily by gold but contain other metal elements [58, 59] or encapsulated main group element (e.g., C, N) [60]. This chapter does not cover them and focuses on homoleptic and heteroleptic phosphine-coordinated pure-gold cluster compounds with formally mixed-valence character (formal averaged oxidation number lies between 0 and 1). Thus the general formula can be described as $[Au_N(PR_3)_mX_s]^{z+}$ ($N > z$), in which tertiary phosphines (PR_3) serve as primary protecting ligands and additional ligands (X), such as halide and thiolate anions, sometimes coordinate with the surface metals as sub-ligands. This chapter first discusses the characterization and synthetic techniques of PGCs and then surveys the structural features and electronic absorptions/photoluminescence properties. Since the studies before 1990 established by the first generation have been already comprehensively summarized in literatures [25, 34, 35] and also in this book, emphases are placed on the recent advances in the clusters with unusual structures. In the last part of this chapter, the application of PGCs for stimuli-responsive chromic modules is also presented.

2 Characterization

Identification and characterization of PGCs have been achieved in terms of nuclearity (size), molecular formulae, and geometrical structures by various analytical techniques. Among them, single-crystal X-ray crystallography is still the most definitive technique to elucidate the geometrical structures, but it is limited to the clusters that give high-quality crystals suitable for the structure determination. Recently mass spectrometry coupled with soft-ionization techniques (e.g., electrospray ionization (ESI), matrix-assisted laser desorption ionization (MALDI)) are found to be powerful tools to obtain direct information about the molecular mass and formulae of cluster species. ESI-mass spectroscopy is especially useful since it can analyze solution samples, allowing the direct analyses of the reaction mixtures. However, one must note that the observed peak, especially before the purification procedure, may be a result of fragmentation/recombination in the gas phase, and the results sometimes strongly depend on the measurement conditions (e.g., voltage). Further, mass spectra give only molecular formula information so the geometrical structures must be deduced with the aid of other characterization methods. ^{1}H and ^{31}P NMR spectra are useful to investigate the dynamics of the coordinated ligands on the cluster surface, but are not suitable to obtain definitive molecular structures. TEM has been used to estimate the size and nuclearity of large clusters but the application for small clusters is limited because of the resolution limitation.

Electronic absorption (UV–visible) spectroscopy is classical but has been most conveniently utilized as a characterization tool. The spectral features of cluster species in the subnanometer-regime are unique to individual clusters and are sensitive to the structures/nuclearity of the cluster compounds, so it is possible to identify unknown species based on the spectral pattern of structurally identified authentic samples. Further, since the spectral profiles are closely correlated with the electronic structures, they are useful to understand the geometry- or nuclearity (size)-dependent profiles of PGCs. This aspect will be discussed in Sect. 5.

3 Synthesis

Generally, PGCs are synthesized in homogeneous solution either by the reduction of ionic gold sources (e.g., gold(I) phosphine complex, tetrachloroaurate) or by the post-synthetic methods involving the growth and/or etching of preformed PGCs. Other methods have also been known, but most of the synthetic procedures reported to date fall into these two categories. The representative examples were summarized in Schemes 1, 2, 3, 4, 5, 6, 7, 8, and 9 in terms of the reaction types.

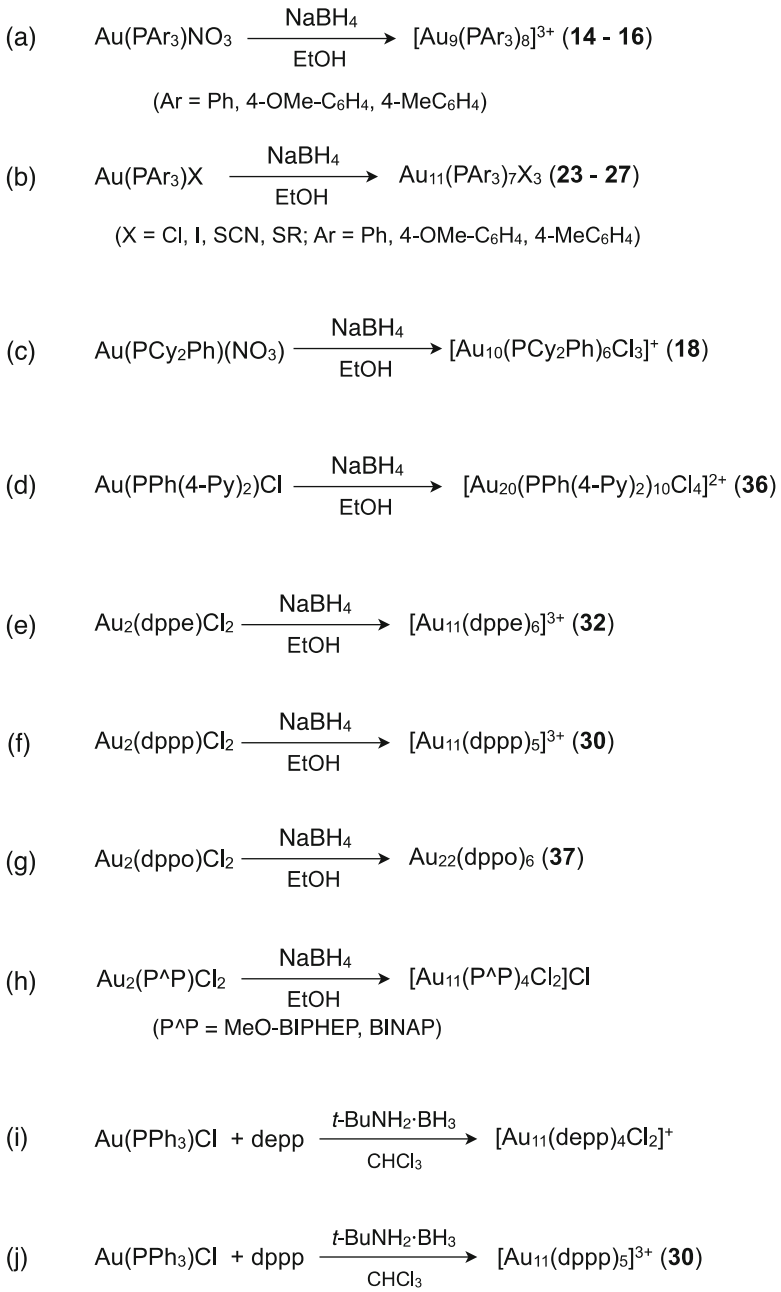

Scheme 1 Selected examples of PGC syntheses via hydride reduction of gold(I) phosphine complexes

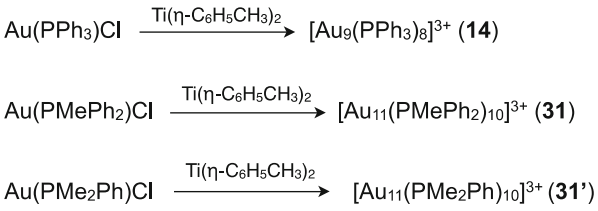

Scheme 2 Syntheses of Au_9 and Au_{11} clusters by the reduction with zero-valent titanium reagent

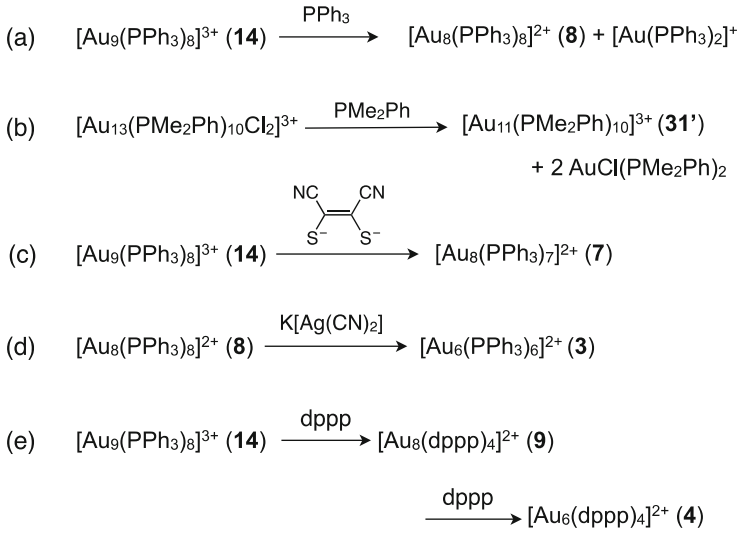

Scheme 3 Examples of PGC syntheses via etching reactions

3.1 Direct Syntheses from Gold Complex Ion or Bulk Gold

3.1.1 Borohydride or Borane Reduction of Gold(I) Phosphine Complex

The borohydride reduction of monophosphine gold(I) complex ($Au(PR_3)X$) in ethanol is the original recipe and has been most widely used as a conventional method, which generally yields Au_9 [27, 37, 38, 61, 62] or Au_{11} species [19, 44–48, 63–65]. $NaBH_4$ is commonly exploited as the reducing agent, because of the ease in handling. From gold(I) triarylphosphine complex ($Au(PAr_3)_3X$) with a strongly coordinating anion (X=Cl, I, SCN, S-4-py), neutral deca-coordinated undecagold clusters $Au_{11}(PAr_3)_7X_3$ (e.g., **23**–**27**, Table 1) are preferentially formed (Scheme 1a), whereas the formation of cationic octa-coordinated nonagold cluster $[Au_9(PAr_3)_8]^{3+}$ (e.g., **14**–**16**) is preferred when X is NO_3 with a weak coordinating character (Scheme 1a). The steric hindrance and the presence of additional coordination sites in the phosphine ligand affect the extent of the cluster growth processes.

(a) $[Au_8(PPh_3)_8]^{2+}$ (**8**) + $Au(NO_3)(PPh_3)$ ⟶ $[Au_9(PPh_3)_8]^{3+}$ (**14**)

(b) $[Au_{11}(PMe_2Ph)_{10}]^{3+}$ (**31'**) + 2 $AuCl(PMe_2Ph)_2$ ⟶ $[Au_{13}(PMe_2Ph)_{10}Cl_2]^{3+}$ (**33**)

(c) $[Au_6(dppp)_4]^{2+}$ (**4**) + 2 $AuCl(PPh_3)$ ⟶ $[Au_8(dppp)_4Cl_2]^{2+}$ (**11**)

(d) $[Au_9(PPh_3)_8]^{3+}$ (**14**) $\xrightarrow{[Au(C_6F_5)]^-}$ $Au_{10}(PPh_3)_3(C_6F_5)_4$ (**20**)

(e) $[Au_9(PPh_3)_8]^{3+}$ (**14**) $\xrightarrow{Cl^-}$ $[Au_{11}(PPh_3)_8Cl_2]^+$ (**29**)

(f) $[Au_9(PPh_3)_8]^{3+}$ (**14**) $\xrightarrow{4\text{-}pyS^-}$ $Au_{11}(PPh_3)_7(4\text{-}pyS)_3$ (**27**)

(g) $[Au_{11}(PMe_2Ph)_{10}]^{3+}$ (**31'**) $\xrightarrow{Cl^-}$ $[Au_{13}(PMe_2Ph)_{10}Cl_2]^{3+}$ (**33**)

(h) $[(Au(PMes)_3)_3O]^+$ $\xrightarrow{CO}$ $[Au_8(PMes_3)_6]^{2+}$ (**10**)

(i) $[Au_{11}(PPh_3)_8Cl_2]^+$ (**29**) $\xrightarrow{EtSH}$ $[Au_{25}(PPh_3)_{10}(SEt)_5]^{2+}$ (**39**)

Scheme 4 Examples of PGC syntheses via growth (aggregation) reactions

$[Au_9(PPh_3)_8]^{3+}$ (**14**) $\xrightarrow{dpph}$ $[Au_9(dpph)_4]^{3+}$ (**17**)

$Au_{11}(PAr_3)_7(SCN)_3$ $\xrightarrow{dppp}$ $[Au_{11}(dppp)_5]^{3+}$ (**30**)

Scheme 5 Examples of simple ligand-exchange reaction

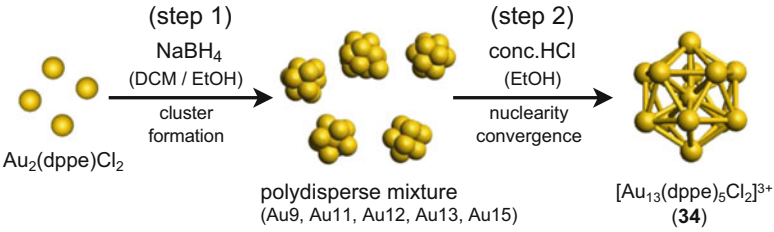

Scheme 6 Two-step synthesis of icosahedral Au_{13} cluster via HCl-promoted growth/etching

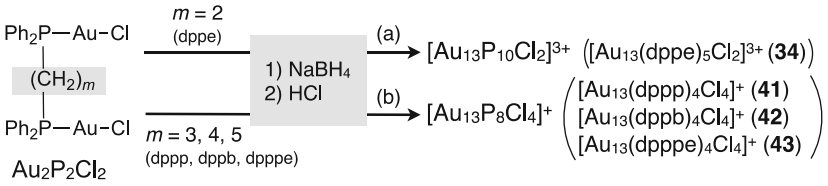

Scheme 7 Formation of two types of Au_{13} clusters

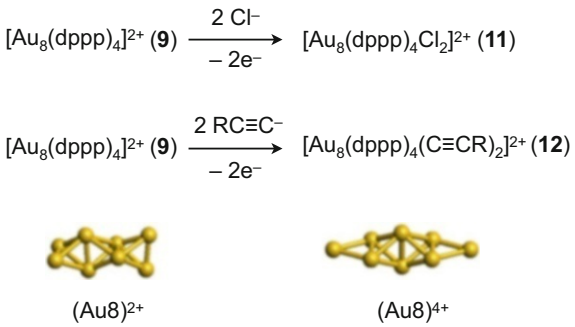

Scheme 8 Nucleophilic addition to $[Au_8(dppp)_4]^{2+}$ (**9**) accompanying the oxidative skeletal isomerization

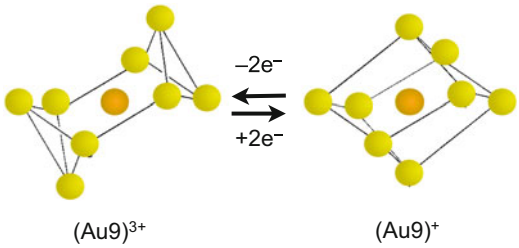

Scheme 9 Schematic illustration of the two-electron redox processes between $[Au_9(PPh_3)_8]^{3+}$ (**14**) and $[Au_9(PPh_3)_8]^{+}$

Reaction of $Au(PCy_2Ph)(NO_3)$ with $NaBH_4$ affords $[Au_{10}(PCy_2Ph)_6Cl_3]^+$ (**18**) (c) [39]. Recently, Wang et al. reported that the reduction of $AuCl(PPh(4\text{-}py)_2)$ with $NaBH_4$ yields a larger cluster with an ionic formula $[Au_{20}(PPh(4\text{-}py)_2)_{10}Cl_4]^{2+}$ (**36**), in which the pyridyl groups (py) additionally coordinate with the surface gold atoms (d) [66]. Diborane can be also utilized as the reducing agent. Reduction of $Au(PPh_3)Cl$ in benzene gives $Au_{55}(PPh_3)_{12}Cl_6$ [67], but its single-crystal structure is not available yet.

Diphosphines (P^P) have also been used as the ligands in the borohydride reduction of chlorogold(I) complex ions (Scheme 1e–j). Similarly to the reduction of monophosphine complex, this reaction system generally affords deca-

coordinated $Au_{11}L_{10}$-type (L=phosphine or Cl) clusters predominantly, but the ligand ratio (P:Cl) is different. For example, in the reduction of $Au(PPh_3)Cl$ with *t*-$BuNH_2{\cdot}BH_3$ in chloroform in the presence of C3-bridged diphosphine (dppp), the predominant formation of $Au_{11}P_{10}$-type cluster ($[Au_{11}(dppp)_5]^{3+}$, **30**) is detected in the mass spectra (j) [68]. We have also found that the simple $NaBH_4$ reduction of $Au_2(dppp)Cl_2$ in ethanol gives **30** as the main cluster product (f) [69]. On the other hand, the mass spectrometric analyses of the reduction system $Au(PPh_3)Cl$/*t*-$BuNH_2{\cdot}BH_3$ coupled with non-phenyl type C3-bridged diphosphine ligand ($Et_2P(CH_2)_3PEt_2$, depp) showed the preferential formation of $Au_{11}P_8Cl_2$-type cluster $[Au_{11}(depp)_4Cl_2]^+$ (i) together with $[Au_{12}(depp)_4Cl_3]^+$ and $[Au_{13}(depp)_4Cl_3]^+$ [70]. Such $Au_{11}P_8Cl_2$-type clusters are also obtained as the main cluster products in the $NaBH_4$ reduction of dinuclear chlorogold complexes of chiral diphosphines BINAP [71] and MeO-BIPHEP [72] in ethanol (h), which are identified by mass and absorption spectra but their single-crystal X-ray structures are not available.

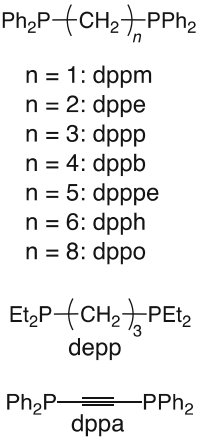

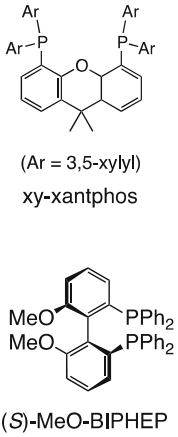

On the other hand, the use of particular diphosphines results in the formation of different cluster species due to the steric and chelating effects of diphosphines. For example, the above $Au(PPh_3)Cl/tBuNH_2{\cdot}BH_3$ system coupled with C5- (dpppe, $Ph_2P(CH_2)_5PPh_2$) or C6-bridged (dpph, $Ph_2P(CH_2)_6PPh_2$) diphosphine gives $[Au_8(P\text{^}P)_4]^{2+}$ and $[Au_{10}(P\text{^}P)_4]^{2+}$ as the main cluster products. Wang et al. have recently reported that the $NaBH_4$ reduction of chlorogold(I) complex of C8-bridged diphosphine (dppo) affords a larger cluster $Au_{22}(dppo)_6$ (**37**, Scheme 1g) [73]. We have also shown that the use of C2-bridged diphosphine (dppp) for the $NaBH_4$ reduction of chlorogold(I) complex in ethanol results in the formation of an Au_{11} species, which however accommodate a different number of coordinating phosphine ligands ($Au_{11}L_{12}$ type) (e) [74]. The ionic formula is $[Au_{11}(dppe)_6]^{3+}$ (**32**), which exhibits an unusual green color. In this reaction, the cluster products are strictly dependent on the reaction medium. When the same reaction is conducted in CH_2Cl_2 / EtOH (50/50 v/v), the ESI-mass spectrum gives multiple signals

assignable to $[Au_9(dppe)_5]^{3+}$, $[Au_{11}(dppe)_5]^{3+}$, $[Au_{12}(dppe)_5Cl]^{3+}$, $[Au_{13}(dppe)_5Cl_2]^{3+}$, and $[Au_{15}(dppe)_6ClH]^{3+}$ (Scheme 6, vide infra) [75]. On the other hand, the same reduction system from the C3-bridged complex ($Au_2(dppp)_2Cl_2$) in CH_2Cl_2/EtOH (50/50 v/v) affords ESI-mass signals assignable to higher nuclearity clusters $[Au_{38}(dppp)_9Cl_2]^{4+}$ and $[Au_{39}(dppp)Cl_3]^{4+}$ [76]. These results imply that the cluster growth processes are not only governed by the intrinsic stability of the gold core but also notably affected by the steric and cheating effects of multidentate ligands and reaction conditions.

3.1.2 Other Methods

Other reducing agents have also been utilized. The utilization of $Ti(\eta\text{-}C_6H_5CH_3)_2$ developed by Mingos et al. affords $[Au_9(PAr_3)_8]^{3+}$ (**14**, **16**) from $AuCl(PPh_3)$ (Scheme 2) [36]. The same reduction system from $Au(PMe_2Ph)Cl$ and $Au(PMePh_2)Cl$) results in the formation of deca-phosphine-coordinated Au_{11} cluster compounds having no Cl ligands on the cluster surface ($[Au_{11}(PMePh_2)_{10}]^{3+}$ (**31**) and $[Au_{11}(PMe_2Ph)_{10}]^{3+}$ (**31′**) [34, 42]. Recently, $[Au_6(xy\text{-}xantphos)_3]Cl$ (**5**·Cl) was isolated by recrystallization from the reaction mixture of Au(xy-xantphos)Cl and $PhMe_2SiH$ [77].

$HAuCl_4$ instead of gold phosphine complex is usable as the starting gold source. Upon reduction of $HAuCl_4$ by $NaBH_4$ in the presence of trioctylphosphine in aqueous THF, $[Au_{13}(POct_3)_8Cl_4]^+$ is obtained as a minor product [76]. $[Au_{39}(PPh_3)_{14}Cl_6]Cl_2$ (**40**·Cl), which is, to date, the largest PGC characterized by single-crystal X-ray diffraction, was synthesized by the reduction of $HAuCl_4$ by $NaBH_4$ [78]. Recently, $[Au_{24}(PPh_3)_{10}(SC_2H_4Ph)_5X_2]^+$ (**38**) was synthesized by Jin et al. through the $NaBH_4$ reduction of $HAuCl_4$ based on the Brust's two-phase method [79].

Several other gold sources have also been utilized. $[Au_7(PPh_3)_7]^+$ (**6**) can be prepared by the reaction of gold vapor with PPh_3 in toluene [31]. Azido complex $AuN_3(PPh_3)$ is also usable as a precursor, which affords $[Au_8(PPh_3)_8]^{2+}$ (**8**) upon photolysis in THF [80].

3.2 Post Synthesis

As noted in Sect. 3.1, Au_9 and Au_{11} clusters are frequently found as the primary products in the direct PGC synthesis from gold(I) precursors and thus appear to be relatively stable compounds. However, due to the flexible nature of the cluster skeletons and lability of Au–Au interactions, they can be easily converted into different cluster species via post-synthetic aggregation-mediated growth and degradation-mediated etching processes, thus acting as useful intermediates for a variety of PGC compounds.

3.2.1 Etching Reactions

Several etching (degradation) reactions of monophosphine-protected Au_9 and Au_{11} clusters upon treatment with free phosphines have been reported. $[Au_8(PPh_3)_8]^{2+}$ (**8**) can be obtained by the reaction of $[Au_9(PPh_3)_8]^{3+}$ (**14**) with free PPh_3, which accompanies the liberation of $Au(PPh_3)^+$ (Scheme 3a) [20, 49]. In a similar fashion, $[Au_{11}(PMe_2Ph)]^{3+}$ (**31′**) can be synthesized from $[Au_{13}(PMe_2Ph)_{10}Cl_2]^{3+}$ (**33**) in the presence of free PMe_2Ph (b) [34]. Reaction of $[Au_9(PPh_3)_8]^{3+}$ (**14**) with sodium maleonitriledithiolate ($MNTNa_2$:$Na_2S_2C_2(CN)_2$) affords hepta-coordinated Au_8 cluster ($[Au_8(PPh_3)_7]^{2+}$, **7**) (c) [41], which can also be obtained by the phosphine abstract reaction of **8** by $[RhCl(cyclooctene)_2]_2$ [30]. The reaction of $[Au_8(PPhR_2)_8](NO_3)_2$ (R=Ph, **8**·NO_3) in the presence of $K[Ag(CN)_2]$ affords edge-sharing bitetrahedral $[Au_6(PPhR_2)_8]^{2+}$ (R=Ph (**3**), 2-MeC_6H_4, Cy) (d) [40].

The etching reactions during the ligand exchange reaction with diphosphine have also been reported. The treatment of $[Au_9(PPh_3)_8](NO_3)_3$ (**14**·NO_3) with excess free dppp results in the formation of core+*exo* type $[Au_6(dppp)_4]^{2+}$ (**4**) (e) [26]. As an intermediate cluster species in this reaction, $[Au_8(dppp)_4]^{2+}$ (**9**) have been isolated and identified by mass spectrometry and single-crystal X-ray diffraction studies [81].

3.2.2 Growth Reactions

The addition reaction of mononuclear gold species to preformed cluster species results in the growth of the cluster nuclearity. The reaction of $[Au_8(PPh_3)_8]^{2+}$ (**8**) with $Au(NO_3)(PPh_3)$ leads to the formation of $[Au_9(PPh_3)_8](NO_3)_3$ (**14**·NO_3) (Scheme 4a) [21, 31]. Likewise, $[Au_{11}(PMe_2Ph)_{10}]^{3+}$ (**31′**) grows to $[Au_{13}Cl_2(PMe_2Ph)_{10}]^{3+}$ (**33**) by the addition of $AuCl(PMe_2Ph)$ (b) [34]. The treatment of $Au_6(dppp)(NO_3)_2$ (**4**·NO_3) with $Au(PPh_3)Cl$ results in the formation of $[Au_8(dppp)Cl_2]^{2+}$ (**11**) (c) [81]. An organometallic cluster $Au_{10}(PPh_3)_3(C_6F_5)_4$ (**20**) can be obtained by the reaction of $[Au_9(PPh_3)_8]^{3+}$ (**14**) with $(NBu_4)[Au(C_6F_5)]$ (d) [82].

The reactions with nucleophilic agents are known to induce aggregation reactions between several cluster molecules. This reaction is unpredictable, but sometimes useful for the syntheses of higher nuclearity clusters. In the presence of Cl^- with coordinating capability, $[Au_{11}(PMe_2Ph)_{10}]^{3+}$ and $[Au_9(PPh_3)_8]^{3+}$ (**14**) are converted into $[Au_{13}Cl_2(PMe_2Ph)_{10}]^{3+}$ (**33**) [36] and $[Au_{11}(PPh_3)_8Cl_2]^+$ (**29**) [21, 83], respectively (Scheme 4e and g). The reaction of $[Au_9(PPh_3)_8]^{3+}$ (**14**) with 4-pyridinethiol in alkaline methanol results in the formation of $Au_{11}(PPh_3)_7(4\text{-}pyS)_3$ (f) [84]. Shichibu et al. reported the synthesis of $[Au_{25}(PPh_3)_{10}(SEt)_5Cl_2]^{2+}$ (**39**) by the reaction of $[Au_{11}(PPh_3)_8Cl_2]Cl$ (**29**·Cl) and ethanethiol [85].

For other examples, the reduction of trinuclear oxonium salt $[Au(PMes)_3]_3O]^+$ by CO affords hexa-coordinated Au_8 cluster $[Au_8(PMes_3)_6]^{2+}$ (**10**) (Scheme 4h) [86]. The decomposition of trinuclear hydradizo complex $[(AuPPh_3)_3NNR_2]BF_4$ leads to

the formation of $[Au_6(PPh_3)_6]^{2+}$ (**3**) [87], which is isostructural to that obtained by the silver-mediated etching reaction of $[Au_8(PPh_3)_8]^{2+}$ (**8**).

3.2.3 Ligand Exchange Reactions

As noted above, the reaction of once generated clusters with free ligands often results in the nuclearity alteration through the etching and growth of the cluster cores, but simple exchange reactions with the retention of the cluster nuclearity and structure take place when appropriate free ligands are utilized. For example, $[Au_{11}(dppp)_5]^{3+}$ (**30**) is obtained by the reaction of $[Au_{11}(P(4\text{-}ClC_6H_4)_3)_7(SCN)_3]^{3+}$ with dppp (Scheme 5) [24]. Likewise, the reaction of dpph with $[Au_9(PPh_3)_8](NO_3)_3$ (**14**·NO_3) with four equiv of dpph affords $[Au_9(dpph)_4]^{3+}$ (**17**) quantitatively [88].

3.2.4 Growth/Etching During Crystallization Process

Due to the soft potential surface of gold clusters, crystallization process sometimes allows the formation of unexpected cluster species that is different from the original cluster in the mother liquors. For example, crystallization of $[Au_8(PPh_3)_7][S_2C_2(CN_2)_2]$ from CH_2Cl_2/MeCN results in the formation of the crystals of $Au_{10}(PCy_3)_7(MNT)$ (**19**) [41]. The formation of crystals containing Au_7 and Au_9 clusters has been reported when the polyoxometalate and fullerene salts of $[Au_8(PPh_3)_8]^{2+}$ are crystallized [61, 89]. Very recently, crystals of $Au_{14}(PPh_3)_8(NO_3)_4$ (**35**) have been isolated during the crystallization process in the $Au_9(PPh_3)_8(NO_3)_3$ (**14**·NO_3) synthesis by the $Au(PPh_3)NO_3/NaBH_4$ system [90].

3.2.5 Nuclearity Convergence Through Simultaneous Etching/Growth

We have recently found that HCl has a unique capability to promote the etching and growth of PGCs [75, 76]. Through the simultaneous etching/growth processes, a polydisperse mixture of several dppe-coordinated clusters, which was formed by the $NaBH_4$ reduction of $Au_2(dppe)Cl_2$ in CH_2Cl_2/EtOH, is exclusively converted into $[Au_{13}Cl_2(dppe)_5]^{3+}$ (**34**) upon treatment with aqueous HCl (12 M) in EtOH (Scheme 6). This method is practically useful, allowing gram-scale preparation of icosahedral Au_{13} cluster (total yield exceeds 70%). Other protonic acids such as acetic acid and sulfuric acid, and tetraethyl ammonium chloride also served as promoters but are much inferior to hydrochloric acid, indicating that the effective nuclearity convergence is a result of growth/etching under thermodynamic conditions by the cooperation of acidic proton and chloride anion. The chelation effect of the diphosphine ligands plays a critical role in keeping the cluster structure and also affects the composition of the coordinating ligands of the final cluster products. With monophosphine ligand, the intermediate cluster species does not survive

the strongly acidic condition, while the use of diphosphine ligands with a longer alkyl bridge (dppp, dppb, dpppe) results in the preferential formation of $[Au_{13}Cl_4(P\text{^}P)_4]^{3+}$ (**41**–**43**) (Scheme 7).

3.2.6 Redox Reactions

As mentioned in the above paragraphs, the addition of nucleophiles such as Cl- to monophosphine-coordinated clusters promotes the aggregation-induced growth of the cluster core. However, we recently found that the nucleophilic reaction towards $[Au_8(dppp)_4]^{2+}$ (**9**) proceeds with the retention of the nuclearity but accompanies two-electron autoxidation and rearrangement of the cluster skeleton[91]. For instance, the reactions with nucleophiles such as halide and acetylide anions afford $[Au_8(dppp)_4X_2]^{2+}$ (X=Cl (**11**), X=C≡CPh (**12**)), where the charge of the Au_8 skeleton is altered from 2+ to 4+ (Scheme 8). In this relation, electrochemical two-electron redox processes between $[Au_9(PPh_3)_8]^{3+}$ (**14**) and $[Au_9(PPh_3)_8]^{+}$, which accompany the skeletal rearrangement from toroidal to spherical, have also been reported (Scheme 9) [32, 92]. The large structural change may reflect the soft potential energy surface of this class of compounds.

3.2.7 Summary

A variety of PGCs can be synthesized in good yields when the appropriate reagents and pathways are used. However the cluster products are generally unpredictable and vary significantly with the subtle difference of synthetic parameters (methods, conditions, reagents, and so on).

4 Geometrical Structure

As noted in Sect. 2, single-crystal X-ray crystallography is the sole definitive method to elucidate the 3-dimensional structural features. PGCs with a nuclearity of 5, 6, 7, 8, 9, 10, 11, 13, 14, 20, 22, 24, 25, and 39 have been structurally identified. For selected examples, geometrical descriptions and Au–Au bond distances are summarized in the nuclearity order (Tables 1 and 2). Centered polyhedral geometries are generally favored because the center-to-peripheral interactions effectively enhance the stability of cluster skeleton. The majority of the clusters with $N \geq 8$ fall into this category. However, the use of sterically hindered ligands or chelating diphosphines sometimes allows the generation of exceptional structures that cannot be described only with polyhedra.

Table 1 Geometrical structures of crystallographically defined PGCs with nuclearity (N) of 5–13

	Counter anion	Geometry	Au–Au dist. (Å)	References
($N = 5$)				
$[Au_5(dppm)_3(Ph_2PCHPPh_2)]^{2+}$ (**1**)	NO_3	Tetrahedron + 1 *exo*	2.702–3.013	[48]
($N = 6$)				
$[Au_6(PPh_2C_6H_4)_4]^{2+}$ (**2**)	SbF_6	Octahedron	2.721–3.155	[93]
$[Au_6(PPh_3)_6]^{2+}$ (**3**)	NO_3	Edge-sharing bitetrahedron	2.652–2.839	[40]
$[Au_6(dppp)_4]^{2+}$ (**4**)	NO_3	Tetrahedron + 2 *exo*	2.630–2.923	[26]
$[Au_6(xy\text{-}xantphos)_3]^{+}$ (**5**)	Cl	Face-sharing tritetrahedron	2.653–3.104	[77]
($N = 7$)				
$[Au_7(PPh_3)_7]^{+}$ (**6**)	OH	Pentagonal bipyramid	2.582–3.007	[31, 94]
	C_{60}	Pentagonal bipyramid	2.561–3.092	[89]
($N = 8$)				
$[Au_8(PPh_3)_7]^{2+}$ (**7**)	NO_3	Capped centered chair[a]	2.629–2.942	[22]
$[Au_8(PPh_3)_8]^{2+}$ (**8**)	AZS	Capped centered chair[a]	2.689–2.938	[49]
	PF_6	Capped centered chair[a]	2.634–2.960	[20]
	$SiMo_{12}O_{40}$	Capped centered chair[a]	2.650–2.909	[95]
$[Au_8(dppp)_4]^{2+}$ (**9**)	NO_3	Edge-sharing tritetrahedron	2.616–2.752	[81]
$[Au_8(PMes_3)_6]^{2+}$ (**10**)	BF_4	Tetrahedron + 4 *exo*	2.616–2.752	[86]
$[Au_8(dppp)_4Cl_2]^{2+}$ (**11**)	PF_6	Edge-sharing bitetrahedron + 2 *exo*	2.607–2.896	[81]
$[Au_8(dppp)_4(C{\equiv}CPh)_2]^{2+}$ (**12**)	NO_3	Edge-sharing bitetrahedron + 2 *exo*	2.648–3.072	[91]
$[Au_8(dppa)_4Cl_2]^{2+}$ (**13**)	ClO_4	Edge-sharing bitetrahedron + 2 *exo*	2.619–3.052	[96]
($N = 9$)				
$[Au_9(PPh_3)_8]^{3+}$ (**14a**)	NO_3	Bicapped centered chair (butterfly)[a]	2.675–2.880	[62]
	$PW_{12}O_{40}$	Bicapped centered chair (butterfly)[a]	2.688–2.926	[61]
$[Au_9(PPh_3)_8]^{3+}$ (**14b**)	$PW_{12}O_{40}$	Centered crown	2.662–2.806	[61]
	$PMo_{12}O_{40}$	Centered crown	2.661–2.810	[95]
$[Au_9(P\{p\text{-}Tol\}_3)_8]^{3+}$ (**15**)	PF_6	Bicapped centered chair (butterfly)[a]	2.686–2.891	[27]
$[Au_9(P\{p\text{-}MeOC_6H_4\}_3)_8]^{3+}$ (**16a**)	BF_4	Centered crown	2.651–2.838	[37]
	NO_3	Centered crown	2.659–2.843	[38]

$[Au_9(P\{p\text{-}MeOC_6H_4\}_3)_8]^{3+}$ (**16b**)	NO_3	Bicapped centered chair (butterfly)[a]	2.689–2.899	[38]
$[Au_9(dpph)_4]^{3+}$ (**17**)	$PW_{12}O_{40}$	Centered crown	2.643–3.249	[88]
($N = 10$)				
$[Au_{10}(PPhCy_2)_6Cl_3]^{+}$ (**18**)	NO_3	Tricapped centered chair (toroidal)[a]	2.666–2.941	[39]
$Au_{10}(PPh_3)_7(MNT)_2$ (**19**)	–	Tricapped centered chair (toroidal)[a]	2.567–3.055	[41]
$Au_{10}(PPh_3)_5(C_6F_5)_4$ (**20**)	–	Tricapped centered chair (toroidal)[a]	2.639–2.964	[82]
$Au_{10}(PPh_3)_8Cl(NCO)$ (**21**)	–	Capped centered square antiprism (spherical)	2.635–3.174	[97]
$[Au_{10}(PPh_3)_8Cl]^{+}$ (**22**)	PF_6	Capped centered square antiprism (spherical)	2.637–3.151	[98]
($N = 11$)				
$Au_{11}(PPh_3)_7Cl_3$ (**23**)	–	Tetracapped centered chair[a]	2.608–2.968	[65]
$Au_{11}(PPh_3)_7I_3$ (**24**)	–	Tetracapped centered chair[a]	2.634–3.193	[45]
$Au_{11}(P\{p\text{-}FC_6H_4\}_3)_7I_3$ (**25**)	–	Tetracapped centered chair[a]	2.670–3.184	[47]
$Au_{11}(P\{m\text{-}CF_3C_6H_4\}_3)_7Cl_3$ (**26**)	–	Tetracapped centered chair[a]	2.663–3.126	[99]
$Au_{11}(PPh_3)_7(4\text{-}pyS)_3$ (**27**)	–	Tetracapped centered chair[a]	2.629–3.122	[84]
$[Au_{11}(PPh_3)_7(CN\mathit{i}Pr)_2I]^{2+}$ (**28**)	PF_6	Tetracapped centered chair[a]	2.670–3.127	[33]
$[Au_{11}(PPh_3)_8Cl_2]^{+}$ (**29**)	W_6O_{19}	Tetracapped centered chair[a]	2.625–3.185	[88]
$[Au_{11}(dppp)_5]^{3+}$ (**30**)	SCN	Tetracapped centered chair[a]	2.669–3.088	[29]
$[Au_{11}(PMePh_2)_{10}]^{3+}$ (**31**)	$C_2B_9H_{12}$	Capped centered square antiprism	2.646–3.048	[42]
$[Au_{11}(dppe)_6]^{3+}$ (**32**)	SbF_6	Butterfly Au_9 + 2 *exo*	2.608–3.216	[74]
($N = 13$)				
$[Au_{13}(PMe_2Ph)_{10}Cl_2]^{13+}$ (**33**)	PF_6	Icosahedron	2.715–2.955	[36]
$[Au_{13}(dppe)_5Cl_2]^{3+}$ (**34**)	SbF_6	Icosahedron	2.696–2.974	[75]

[a]Can also be described as a derivative or substructure of icosahedral Au_{13}

4.1 Centered Polyhedral Clusters

4.1.1 $N \leq 13$

Crystal structures of PGCs with $8 \leq N \leq 13$ were extensively studied before 1990, and the general preference centered polyhedral geometries have been almost established. The majority of these centered clusters have skeletal structures based on centered icosahedron, which can also be described as capped centered hexagonal chairs. Such icosahedron-based structures are found for a series Au_8L_7, Au_8L_7, Au_9L_8, $Au_{10}L_9$, and $Au_{11}L_{10}$ clusters, which finally complete with the icosahedral $Au_{13}L_{12}$-type clusters (Table 1). Representative examples are shown in the structures of **7** (Au_8L_7), **8** (Au_8L_7), **18** ($Au_{10}L_9$), **23** ($Au_{11}L_{10}$), **30** ($Au_{11}L_{10}$), and **34** ($Au_{13}L_{12}$) (Fig. 1). The exceptional structures that cannot be described based on icosahedron are also found in several cases. For example, Mingos et al. reported green and golden-brown crystals of $[Au_9(P(4\text{-}MeOC_6H_4)_3)_8](NO_3)_3$ (**16**·NO_3) and showed that the former has a bicapped chair D_{2h} geometry derived from icosahedron whereas the latter has a centered crown geometry [38]. The interconversion between the two forms seems easy since they share a common structure in solution. The crown geometries have also been found in the several polyoxometalate salts of Au_9P_8 clusters. Jansen et al. recently reported that the appropriate choice of recrystallization solvents allows the selective formation of either of the two skeletal geometries of **14**·$PW_{12}O_{40}$ (Fig. 2) [61].

As other examples of deviation from icosahedron-derived structures, capped centered square antiprism (approximately D_{4d} symmetry) geometries have been reported for $[Au_{11}(PMePh_2)_{10}]^{3+}$ (**31**) (Fig. 1) [42], which is obviously different from the icosahedron-based structures with approximately C_{3v} symmetry found in the conventional $Au_{11}(PAr_3)_{10}$ clusters for various combinations of phosphine, sub-ligands, and counter anion [28, 29, 33, 47, 65, 84, 88, 99] (Table 1 and **23** and **30** in Fig. 1). This geometry can also be viewed as a capped crown, which is also found for $Au_{10}L_9$ clusters (**22** in Fig. 1) [98].

As mentioned in previous papers and reviews [35, 42], the center-to-peripheral radial bond distances are shorter than the peripheral bond distances, indicating the crucial contribution of radial bonding to the stability of cluster skeleton. The overall shape of these clusters can be categorized into toroidal (ellipsoidal, 2D) and hemispherical/spherical (3D), which have been accounted for in terms of polyhedral electron counting and molecular orbital calculations [34, 51].

4.1.2 Higher-Nuclearity Clusters

Several examples of higher-nuclearity centered clusters have appeared recently and their structures are shown in Fig. 3. Simon et al. showed that the crystal structure of $[Au_{14}(PPh_3)_8(NO_3)_4]$ (**35**) exhibits a unique geometry, in which two face-sharing tetrahedron dimers are connected by four $AuNO_3$ units [90]. The distance between

Table 2 Geometrical structures of higher nuclearity PGCs with $N > 13$

Cluster formula	Counter anion	Description	Au–Au dist. (Å)	References
$Au_{14}(PPh_3)_8(NO_3)_4$ (**35**)	–	Trigonal bipyramid dimer linked by 4 $AuNO_3$	2.582–2.984	[90]
$[Au_{20}(PPh\{4\text{-}Py\}_2)_{10}Cl_4]^{2+}$ (**36**)	Cl	Edge-sharing icosahedral Au_{11} dimer	2.644–3.189	[66]
$Au_{22}(dppo)_6$ (**37**)	–	Icosahedral Au_{11} dimer	2.631–3.227	[73]
$[Au_{24}(PPh_3)_{10}(SC_2H_4Ph)_5X_2]^+$ (**38**)	Unknown	Incomplete icosahedral Au_{12} dimer	2.721–2.990	[79]
$[Au_{25}(PPh_3)_{10}(SEt)_5Cl_2]^{2+}$ (**39**)	SbF_6	Vertex-sharing icosahedral Au13 dimer	2.695–3.116	[85]
$[Au_{39}(PPh_3)_{14}Cl_6]^{2+}$ (**40**)	Cl	1:9:9:1:9:9:1 layered	2.690–3.112	[78]

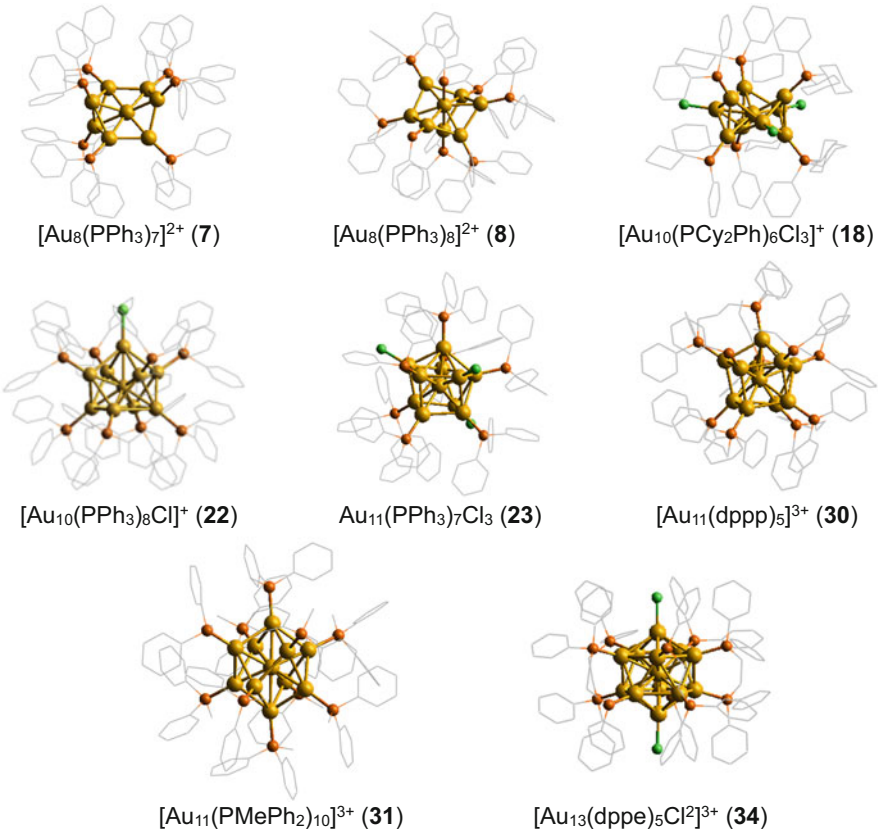

Fig. 1 Single-crystal X-ray structures of $[Au_8(PPh_3)_7]^{2+}$ (**7**), $[Au_8(PPh_3)_8]^{2+}$ (**8**), $[Au_{10}(PPhCy_2)_6Cl_3]^+$ (**18**), $[Au_{10}(PPh_3)_8Cl]^+$ (**22**), $Au_{11}(PPh_3)_7Cl_3$ (**23**), $[Au_{11}(dppp)_5]^{3+}$ (**30**), $[Au_{11}(PMePh_2)_{10}]^{3+}$ (**31**) and $[Au_{13}(dppe)_5Cl_2]^{3+}$ (**34**). For counter ions (see Table 1). For **7**, **8**, **18**, **23**, **30**, and **34**, the gold core units can be described as capped chairs (icosahedron derivatives), whereas those of **22** and **31** can be described as D_{4d} bicapped crowns

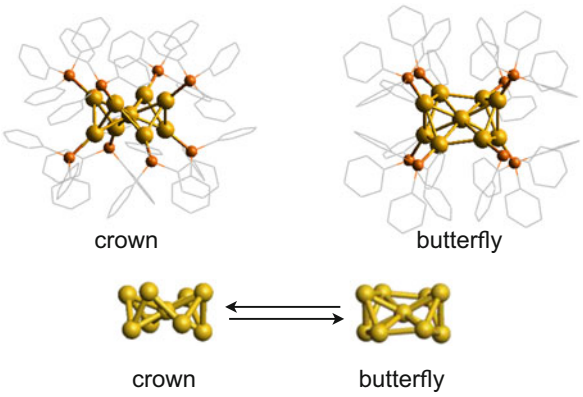

Fig. 2 Single-crystal X-ray structures of two isomeric structures of the cluster moieties of $[Au_9(PPh_3)_8](PW_{12}O_{40})$ (**14**·$PW_{12}O_{40}$)

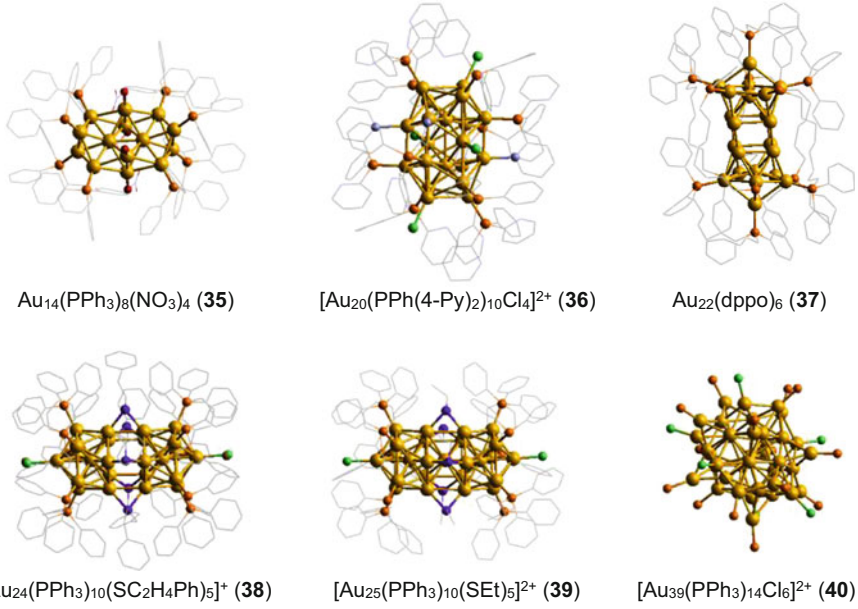

Fig. 3 Single-crystal X-ray structures of Au_{14} (**35**) Au_{20} (**36**), Au_{22} (**37**), Au_{24} (**38**), Au_{25} (**40**) and Au_{39} (**41**) clusters. Counter anion: Cl (**36**), SbF_6 (**40**), Cl (**41**)

two nearest neighbor nitrated gold atoms are very short (2.58 Å). The icosahedral Au_{13} and quasi-icosahedral Au_{11} can serve as the building units of prolate-shaped higher nuclearity clusters when additional attractive forces or steric effects are applied. Q. M. Wang et al. recently reported the structure of $[Au_{20}(PPy_2Ph)_{10}Cl_4]^{2+}$ (**36**), which can be viewed as an edge-sharing dimer of icosahedron-based Au_{11} cluster [66]. The additional coordination of pyridyl groups to the cluster surface

appears to assist the holding of the cluster skeleton. Wang et al. reported that $Au_{22}(dppo)_6$ (**37**), although its charge is ambiguous, has a structure composed of two quasi-icosahedral Au_{11} units fused via four short Au–Au bridges [73]. There are also examples of the utilization of thiolate as bridging ligands. Shichibu et al. demonstrated that the structure of $[Au_{25}(PPh_3)_{10}(SC_2H_5)Cl_2]^{2+}$ (**39**) cluster can be defined as two Au_{13} cluster units joined through five thiolate bridges by vertex sharing [85]. An analogous thiolate-bridged PGC composed of two incomplete icosahedral Au_{12} units, in which one vertex atom of Au_{13} icosahedron is missing, has been recently reported by Jin et al. for $[Au_{24}(PPh_3)_{10}(SC_2H_4Ph)_5X_2]^+$ (X=Br or Cl, **38**) [79]. The Au–Au bond distances in these icosahedron-based clusters (**36**–**39**) are similar to those of smaller centered clusters, being in the range 2.63–3.23 Å (Table 2). Short distances less than 2.7 Å are observed for the center-peripheral radial bonds.

On the other hand, the structures of $[Au_{39}(PPh_3)_{14}Cl_6]Cl_2$ **40**·Cl) is exceptional, being defined as a 1:9:9:1:9:9:1 layered hcp/hcp′, which is virtually different from the icosahedron-based structure.

4.2 Non-centered Polyhedral Clusters

Lower nuclearity clusters favor condensed polyhedra rather than centered geometries (Fig. 4). For hexanuclear clusters ($N = 6$), the simplest geometry is octahedron. Bellon et al. reported an octahedral structure for $[Au_6\{P(p\text{-}Tol)_3\}_6]^{3+}$ [48], but later it is identified to be a carbon-centered octahedron [100]. Very recently Echavarren et al. reported organometallic Au_6 clusters protected by ortho-aurated PPh_3 ligands $[Au_6(PPh_2C_6H_4)_4](SbF_6)_2$ (**2**·SbF_6), though their gold atoms are formally monovalent, adopt an octahedron [93]. In this structure, the octahedron is severely distorted, where some edges are short in the range 2.72–2.75 Å but the other bonds are longer than 3.10 Å. Au_6 cluster can also adopt tetrahedron-based geometries. Mingos et al. reported an edge-sharing bitetrahedral structure of $[Au_6(PPh_3)_6]^{2+}$ (**3**) [40], where the shared (2.652 Å) and terminal (2.662 and 2.669 Å) edges are significantly shorter than the other eight edges (2.762–2.839 Å) (Table 3). We have recently shown that an edge-sharing Au_4 tetrahedron trimer ($[Au_8(dppp)_4]^{2+}$, **9**), which is an extended version of **3**, has a similar structural feature [81]. The bond distances of two shared and terminal edges are 2.623 and 2.607 Å, respectively, which are again shorter than the distances of the remaining connecting bonds (2.824–2.896 Å) (Table 3). A face-sharing tritetrahedral structure has been reported for $[Au_6(xy\text{-}xantphos)_3]Cl$ (**5**), where the edge shared by three Au_4 tetrahedra shows a short distance (2.653 Å) [77]. Thus, in the structures based on Au_4 tetrahedron, the short distances are found for the shared and terminal edges.

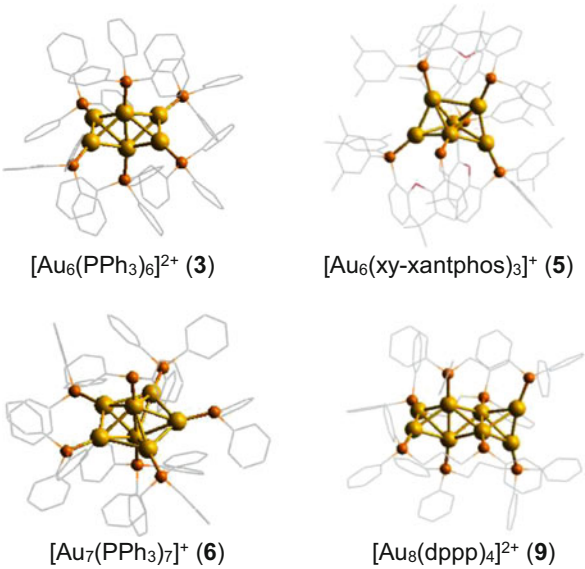

Fig. 4 Single-crystal X-ray structures of non-centered polyhedral Au_6, Au_7, and Au_8 clusters. Counter anion: NO_3 (**1**, **2**, **9**), Cl (**5**), C_{60} (**6**)

Table 3 Au–Au bond distances (Å) of Au_4 tetrahedron-based clusters

	Polyhedral core				
	Distance range (mean)	Shared edge	Terminal edge	*exo*-to-core	References
Tetrahedral					
$[Au_5(dppm)_3(Ph_2PCHPPh_2)](NO_3)_2$ (**1**·NO_3)	2.702–3.006 (2.828)			3.013	[23]
$[Au_6(dppp)_4](NO_3)_2$ (**4**·NO_3)	2.630–2.923 (2.825)	–	2.630[a]	2.798	[26]
$[Au_8(PMes_3)_6](BF_4)_2$ (**10** BF_4)	2.697–2.711 (2.707)	–	–	2.616, 2.623	[86]
Bitetrahedral					
$[Au_6(PPh_3)_6](NO_3)_2$ (**3** NO_3)	2.652–2.839 (2.759)	2.652	2.662, 2.669[b]	–	[40]
$[Au_8(dppp)_4Cl_2](PF_6)_2$ (**11**·PF_6)	2.648–2.872 (2.775)	2.648	2.650, 2.658[a]	2.970–3.072	[81]
$[Au_8(dppp)_4(C{\equiv}CPh)_2](NO_3)_2$ (**12**·NO_3)	2.628–2.865 (2.786)	2.628	2.666[a]	2.932, 3.019	[91]
$[Au_8(dppa)_4Cl_2]Cl_2$ (**13**·Cl)	2.619–2.814 (2.728)	2.619	2.621[a]	2.974–3.052	[96]
Tri-tetrahedral					
$[Au_8(dppp)_4](NO_3)_2$ (**9** NO_3)	2.607–2.896 (2.790)	2.630	2.607[b]	–	[81]
$[Au_6(xy\text{-}xantphos)_3]Cl$ (**5**·Cl)	2.653–3.105 (2.779)	2.653[c]		–	[77]

[a]*Exo*-bridged edges
[b]Edges not containing gold atoms shared by two or more Au_4 tetrahedra
[c]The edge shared by three Au_4 tetrahedra

In contrast to the diverse geometries of hexanuclear clusters, pentagonal bipyramid is the only one geometry known for Au_7 clusters (**6**). The distances between the two vertexes are extremely short in the range 2.561–2.581 Å.

4.3 Exo-*attached Polyhedral Clusters (core*+exo *Type)*

As described in the previous sections, assembling of gold atoms intrinsically favors to form polyhedral skeletons. However, some clusters adopt unusual geometries with extra gold atoms located outside the polyhedral core ("core+*exo*" type), especially when coupled with bidentate phosphine ligand. The first example reported by van der Verden et al. in 1979 is $[Au_5(dppm)_3(dppm\text{-}H)]^{2+}$ (**1**), which has a tetrahedral Au_4 core and an additional gold atom outside the tetrahedron [23]. The second example is "blue" Au_6 cluster ($[Au_6(dppp)_4]^{2+}$, **4**) reported by van der Verden et al. in 1982 [26]. The single-crystal structure shows this cluster contains a tetrahedral Au_4 core and two gold atoms bridged at opposite edges of the tetrahedron, thus being described as an Au_4+2Au type structure. Each of the gold atoms forming the central tetrahedron is coordinated by a single phosphine ligand, while the gold atoms at the *exo* positions accommodate two phosphine ligands. The core-to-*exo* distances (distances of *exo* gold atom from bonded gold atoms in the polyhedral core) are 2.798 Å, which fall in the typical distance range of PGCs (Table 3). For a long time, these have been supposed to be unusual cases, but we have recently reported higher-nuclearity clusters with similar structural features (**11**, **12**, **32** in Fig. 5).

$[Au_8(dppp)_4Cl_2]^{2+}$ (**11**) has an edge-sharing bi-tetrahedral Au_6 core with two *exo* gold atoms bridged on the terminal edges of the bitetrahedron, thus being viewed as an extended version of **4**. The two chloride ligands, each of which is bonded to one of the terminal gold atoms, are forced to be oriented in *trans* configuration because of the chelation restriction by the dppp ligands. The bitetrahedral Au_6 core shows distances of the shared edge of 2.648 Å and the bridged terminal edges of 2.666 Å, which are nearly identical to those of $[Au_6(PPh_3)_6]^{2+}$ (**3**) (2.652 and 2.666 Å) and are evidently shorter than the other Au–Au bonds (2.779–2.872 Å) (Table 3) [40]. On the other hand, the core-to-*exo* distances are in the range 2.970–3.072 Å, which are markedly longer than Au–Au distance in the bitetrahedral core (2.648–2.872 Å). Other Au_6+2Au type clusters (**12** and **13**) were reported recently [91, 96], which show almost similar structural parameters (Table 4).

We have also recently synthesized a new dodeca-coordinated Au_{11} cluster $[Au_{11}(dppe)_6]^{3+}$ (**32**) ($Au_{11}P_{12}$ type) [74]. Unlike conventional deca-coordinated $Au_{11}L_{10}$ clusters with polyhedral-only geometries (**23** – **31**), **32** has a core+*exo* type geometrical feature. Its polyhedral core is a butterfly-shaped Au_9, which resembles the Au_9 core of **14a**, **15**, and **16a**. The *exo* atoms form triangles by sharing an edge of the Au_9 core. Each of the *exo* gold atoms is bonded to the two phosphine ligands, whereas the eight peripheral gold atoms of the Au_9 core accommodate single

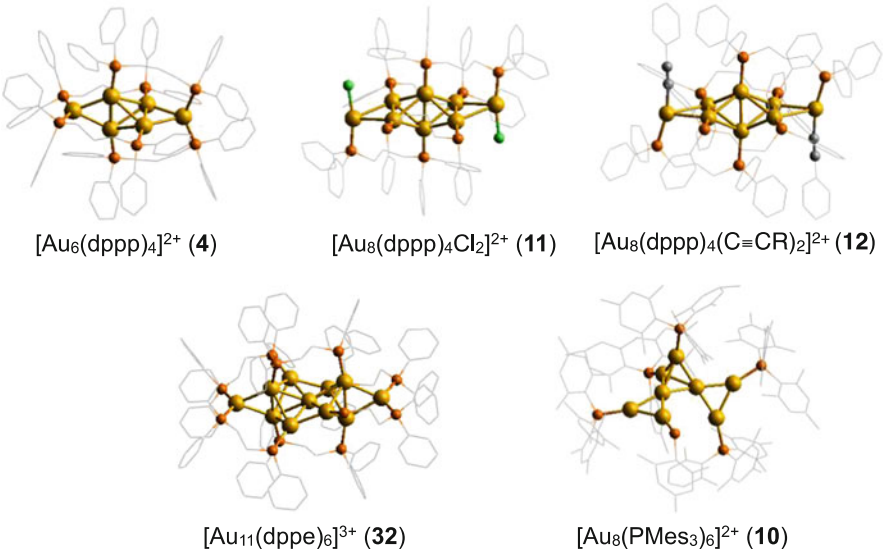

Fig. 5 Single-crystal X-ray structures of clusters having a polyhedral core with *exo*-attached gold atoms. Counter anion: NO_3 (**4**, **12**), PF_6 (**11**), BF_4 (**10**), SbF_6 (**32**)

Table 4 Au–Au bond distances (Å) of butterfly-shaped Au_9 unit of $[Au_9(PPh_3)_8]^{3+}$ (**14a**) and that of Au_9+2Au type Au_{11} cluster $(Au_{11}(dppe)_6)^{3+}$, **32**)

	Mean dist. of Au_9 unit	Radial	Peripheral	*exo*-to-core	References
$[Au_9(PPh_3)_8](NO_3)_3$ (**14a**·NO_3)	2.777	2.675–2.708 (2.691)	2.762–2.880 (2.834)	–	[62]
$[Au_{11}(dppe)_6](SbF_6)_3$ (**32**·SbF_6)	2.814	2.666–2.824 (2.745)	2.629–2.971 (2.860)	2.777, 2.824	[74]

phosphine ligands. The Au_9 core unit is apparently similar to previously known examples of butterfly-shaped clusters, although it has a slightly wider range of Au–Au bond distances (2.629–2.971 Å) than $[Au_9(PPh_3)_8]^{3+}$ (2.675–2.880 Å) (Table 4) [62]. Significantly, the *exo*-bridged edges are very short (2.629 Å) compared with the shortest peripheral–peripheral bonds of the non-*exo* type clusters (i.e., 2.762 Å for **14a**·NO_3). This may reflect some distortion caused by the bridging of the *exo* gold atoms. The core-to-*exo* distances were 2.777 and 2.824 Å, which lie in the range of the bond distances in the central butterfly unit.

These core+*exo* type clusters exhibit impressive colors that are different from conventional centered polyhedral clusters. This aspect will be mentioned in the next section. Among the three core+*exo* type clusters (Au_6, Au_8, Au_{11}), Au_8 clusters (**11**–**13**) are different in the context that they have additional anionic ligands (sub-ligands). The long *exo*-to-core distance in **11**–**13** can be attributed to the

electron-withdrawing character of the anionic ligands attached to the *exo* gold atoms, which may weaken the Au–Au interaction between the *exo* Au atoms and the central Au_6 unit [101]. This is noteworthy in comparison with the short Au-AuCl distances in Au_{13} clusters [34].

As a different core+*exo* type geometry, Sharp et al. reported Au_8 cluster coordinated by sterically hindered monophosphines ($[Au_8(PMes_3)_6]^{2+}$ (**10**) [86]. This cluster has a tetrahedral core with edge distances of 2.697–2.711 Å, where two triangles are attached to the adjacent tetrahedral vertexes. The *exo*-to-core distances (2.616 and 2.623 Å) are slightly shorter than the tetrahedron edges.

5 Optical Properties

5.1 Electronic Absorption Spectra

Generally PGCs are highly colored, so UV–visible electronic absorption spectra have been widely utilized for characterization. Unlike well-known red colors of large gold colloids (sizes of ~2 nm or above) offered by localized surface plasmon, the colors of ultrasmall gold clusters including PGCs essentially originate from the discrete electronic transitions, which is supported theoretically [102]. Therefore, the absorption spectra are useful not only for characterization but also to obtain insights into the electronic structures of cluster compounds. On the other hand, in the nano-size regime, it is well accepted that the lowest optical transition energy of metal atom assemblies increases as the size is reduced, which is known as quantum-size effects. In this relation, studies on the relationship between the nuclearity and the absorption spectra would provide useful knowledge about the intermediate between nano-objects and molecules.

5.1.1 Centered Polyhedral Clusters

Solution absorption spectra of Au_8P_8 (**8**·BF_4), Au_9P_8 (**14**·NO_3), $Au_{11}P_8Cl_2$ (**29**·Cl) $Au_{11}P_{10}$ (**30**·NO_3), $Au_{13}P_{10}Cl_2$ (**34**·Cl), and $Au_{13}P_{10}Cl_2$ (**41**·Cl) clusters, which adopt centered polyhedral geometries, are shown in Fig. 6a. The spectra except **8**·BF_4 were measured in our laboratory for crystallographically characterized or equivalently pure samples. The spectrum of **8**·BF_4 is from the literature [34]. The spectral data together with those in literatures are summarized in Table 5. As a common feature, these centered polyhedral clusters exhibit tail-and-humps spectral characteristics, in which relatively weak visible absorption bands are overlapped with the main band in the UV region tailing to the red. For example, Au_9P_8 cluster (**14**) shows the lowest energy visible band at ~450 nm and more intense UV band at ~315 nm. Au_{11} clusters ($[Au_{11}P_8Cl_2]^+$ (**29**) and $[Au_{11}P_{10}]^{3+}$ (**41**)) show sets of a visible band at ~420 nm and more intense UV bands at ~300 nm. The spectral

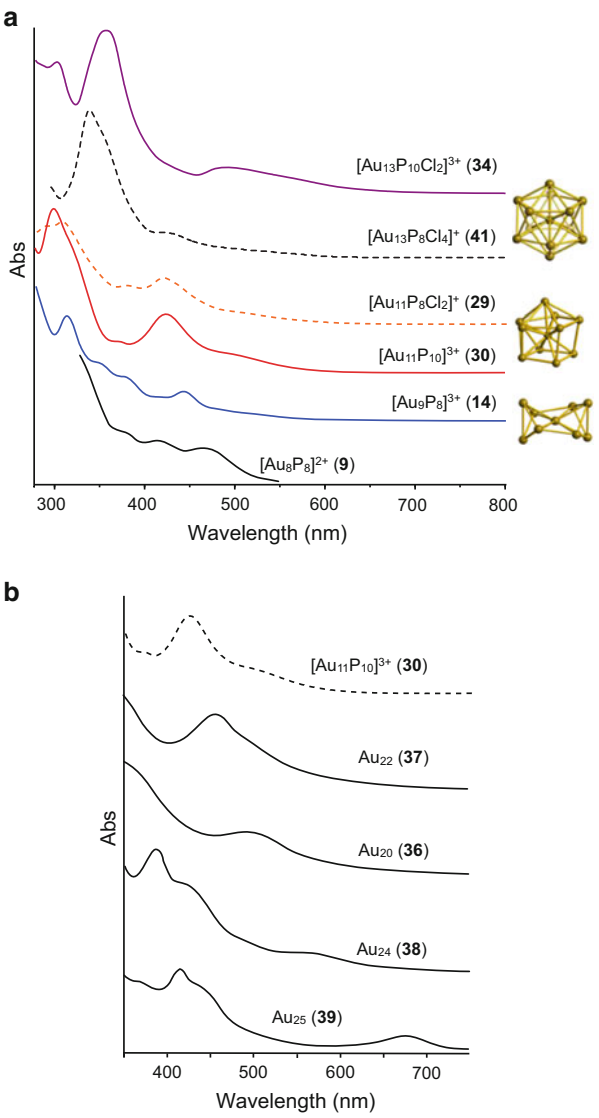

Fig. 6 Absorption spectra of selected centered clusters at ambient temperature. For solvents and counter ions (see Table 5)

patterns of the other $[Au_{11}P_{10}]^{3+}$ clusters (**31** and **31′**) and neutral $Au_{11}P_7Cl_3$ cluster (**29′**) are essentially similar (Table 5) [65, 71], so they seem to be unaffected by the associated surface ligands, cluster charge, and counter anions.

For Au_{13} clusters, Mingos et al. have reported that $[Au_{13}(PMe_2Ph)_{10}Cl_2]^{3+}$ (**33**, $Au_{13}P_{10}Cl_2$ type) and $[Au_{13}(PMePh_2)_{10}Cl_4]$ (**33′**, $Au_{13}P_8Cl_4$ type) clusters give almost identical spectra in DCM with intense UV band at ~340 and a smaller hump (shoulder) at ~430 nm. From this observation, they concluded that the spectra is solely dependent on the nuclearity but is far less so on the surrounding ligands

Table 5 Electronic absorption and photoluminescence spectral data of crystallographically characterized centered PGCs and related clusters[a]

N	Cluster formula	Solvent	Abs bands (nm)[b]	ε (M^{-1} cm^{-1})	PL λ_{em} (nm) [c]	References
8	$[Au_8(PPh_3)_8](BF_4)_2$ (**8**·BF_4)	MeOH	460 412 370	nd	–	[34]
9	$[Au_9(PPh_3)_8](NO_3)_2$ (**14**·NO_3)	MeOH	443 375 352 314	1.6×10^4 (443 nm)	NP	[34]
9	$[Au_9(P\{p\text{-}MeOC_6H_4\}_3)_8]$ $(BF_4)_3$ (**16**·BF_4)	DCM	456 379 342 316	1.6×10^4 (456 nm)	nd	[34]
11	$[Au_{11}(PPh_3)_8Cl_2]Cl$ (**29**·Cl)[e]	MeOH	~500 (sh) 421 380 308	4.0×10^4 (421 nm)	NP	[69]
11	$[Au_{11}(dppp)_5](NO_3)_3$ (**30**·NO_3)	DCM	~500 (sh) 425 370 301	nd	NP	[69]
11	$[Au_{11}(PMePh_2)_{10}](BPh_4)_3$ (**31**·BPh_4)[e]	DCM	422 374, 298	2.2×10^4 (422 nm)	nd	[34]
11	$[Au_{11}(PMePh_2)_{10}](CB)_3$ (**31**·CB)[d]	DCM	425 378 302	3.8×10^4 (425 nm)	nd	[42]
11	$[Au_{11}(PMe_2Ph)_{10}](BPh_4)_3$ (**31′**·BPh_4)[e]	DCM	412, 368, 293	3.0×10^4 (412 nm)	nd	[34]
13	$[Au_{13}(PMe_2Ph)_{10}Cl_2](PF_6)_3$ (**33**·PF_6)	DCM	428 338	1.0×10^5 (338 nm)	nd	[34]
13	$[Au_{13}(PMePh_2)_8Cl_4](CB)$[e] (**33′**·CB)	DCM	425 (sh) 341	1.2×10^5 (341 nm)	nd	[43]
13	$[Au_{13}(dppe)_5Cl_2]Cl_3$ (**34**·Cl)	MeCN	493 359 304	9.3×10^4 (359 nm)	766	[75]
13	$[Au_{13}(dppp)_4Cl_4]Cl$ (**41**·Cl)[e]	MeCN	430 340	nd	~780	[76]
20	$[Au_{20}(PPh\{4\text{-}Py\}_2)_{10}Cl_4]Cl_2$ (**36**·Cl)	DCM	493 344(sh)	nd	nd	[66]
22	$Au_{22}(dppo)_6$ (**37**)	DCM	456	nd	~700	[73]
24	$[Au_{24}(PPh_3)_{10}(SC_2H_4Ph)_5X_2]^+$ (**38**)	DCM	560 383	nd	~818[f]	[79]
25	$[Au_{25}(PPh_3)_{10}(SEt)_5Cl_2]^{2+}$ (**39**)	DCM	670, 415	nd	~1000	[85]

[a]*NP* no photoluminescence, *nd* no data given
[b]Shown for the bands at >290 nm
[c]Excitation at lowest-energy absorption band
[d]CB: $C_2B_9H_{12}$
[e]Not identified by single-crystal X-ray diffraction but the purity was checked by mass spectral and/or elemental analyses
[f]$\lambda_{ex} = 500$ nm

(P:Cl ratio). We observed similar spectral patterns for $[Au_{13}(dppp)_4Cl_4]^+$ (**41**, $Au_{13}P_8Cl_4$ type) in MeCN (Fig. 6a) and in DCM [76]. On the other hand, the spectrum of $[Au_{13}(dppe)_5Cl_2]^{3+}$ (**34**, $Au_{13}P_{10}Cl_2$ type) in MeCN is markedly different, showing a main band at ~360 nm together with a broad weaker band at ~500 nm (Fig. 6a) [75]. Therefore, for the diphosphine-coordinated series, the absorption profiles are critically dependent on the number of Cl ligand ratio, suggesting the involvement of the ligand-mediated transitions in the observed electronic absorptions.

The spectra of higher-nuclearity centered clusters (**36**–**39**) taken from the literatures [66, 73, 79, 85] are summarized in Fig. 6b. They all exhibit tail-and-humps profiles. There seems no relationship between the nuclearity and the positions of the lowest-energy visible bands, and the transitions are interpreted in individual cases. For **36** and **37**, whose structures can be viewed as the dimers of the icosahedron-based Au_{11} clusters, the visible bands are observed at lower energies than that of the parent cluster. For **39**, the exceptionally low-energy band (680 nm) is noteworthy, which suggests the effective electronic interaction between two Au_{13} cluster units via vertex sharing.

5.1.2 Non-centered and Core+*exo* Clusters

Figure 7 shows the solution absorption spectra of edge-sharing bitetrahedral Au_6P_6 cluster (**3**·NO_3), tritetrahedral Au_8P_6 cluster (**9**·NO_3), and [core+*exo*]-type Au_6P_8 (**4**·NO_3) $Au_8P_8Cl_2$ (**11**·Cl), and $Au_{11}P_{12}$ (**32**·SbF_6) clusters, together with the spectra of centered toroidal Au_9P_8 (**14**·NO_3) and spherical $Au_{11}P_{10}$ (**30**·NO_3) clusters for comparison. Except the spectrum of **6**, which is taken from the literature [34], all spectra were measured in our laboratory and the sample purity was checked by ESI-MS and NMR. The spectral data are summarized in Table 6. Similarly to the above-mentioned cases of centered polyhedral core-only clusters, the spectrum of the bitetrahedral cluster (**3**) can be described as the combination of intense UV bands and relatively weak visible bands. However, the visible bands at 452 and 476 nm are considerably separated from the UV bands. A similar trend was observed for the edge-sharing trimer of the tetrahedral Au_4 motif (**9**). The spectrum showed a band at 520 nm together with a smaller shoulder band at ~590 nm, which are completely separated from the UV band at 308 nm. At the present stage, these transitions are not assigned, but seem to be a common feature of edge-sharing tetrahedral clusters. The low energies of the visible absorptions of the trimer (**9**) when compared with the dimer (**3**) can be attributed to the simple mixing of MOs of the tetrahedral-based units (bitetrahedron and tetrahedron).

[Core+*exo*]-type clusters having edge-sharing gold triangle moieties exhibit more distinctive spectral features. For example, Au_4+2Au type Au_6P_8 (**4**), Au_6+2Au type $Au_8P_8Cl_2$ (**11**), and Au_9+2Au type $Au_{11}P_{12}$ (**32**) all showed single visible bands at 587, 508, and 663 nm, respectively, which are fairly separated from the short-wavelength bands spreading into the UV regions. These spectra are much different in pattern from the tail-and-humps feature of centered only-polyhedral

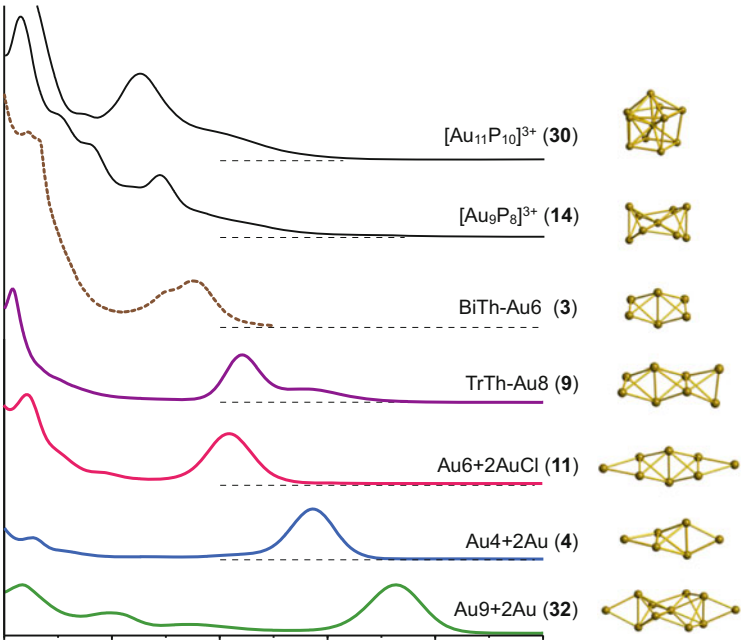

Fig. 7 Solution absorption spectra of selected non-centered and core+*exo* clusters at ambient temperature. For conditions and counter ions (see Table 5)

clusters such as toroidal Au_9P_8 cluster (**14**) and spherical $Au_{11}P_8$ cluster (**30**). Therefore, the "isolated" absorption bands are likely a common feature of [core +*exo*] type clusters. The attachment of extra gold atoms to the polyhedral core may allow the generation of new electronic structures that are associated with the characteristic visible absorptions. Actually the absorption bands of **32** did not coincide with any bands of $[Au_9(PPh_3)_8]^{3+}$ (**14**), which has a toroidal core and thus can be a model of the central substructure of **32**. It should also be noted that the lowest transition energy increased in the order Au_{11} (**32**, 1.87 eV) < Au_6 (**4**, 2.11 eV) < Au_8 (**11**, 2.44 eV), not matching the order of nuclearity. Furthermore, noticeable differences in the spectral profiles are found between the isomeric structures of Au_6 (**3** vs **4**), Au_8 (**8** vs **9** vs **11**), and Au_{11} (**30** vs **32**). Therefore, the optical properties of these clusters depend more strongly on geometric structure than on nuclearity.

Table 6 summarizes the spectra data of the tetrahedron-based and core+*exo* type clusters. For the core+*exo* series, the ε values of the all-phosphine type clusters (**3** and **32**) are noticeably larger than those of **8** and **9** with anionic ligands, which may be correlated with the long core-to-*exo* distances (Tables 3 and 4). Density functional theory (DFT) studies on corresponding non-phenyl models of **3**, **8**, and **30** show that they have similar electronic structures with discrete HOMO and LUMO bands, which are predominantly constituted by Au(6sp) orbitals (sp bands) and are appreciably separated from the closest orbitals. The theoretical

Table 6 Electronic absorption spectral data of non-centered and core+*exo* type PGCs[a, b]

N	Cluster formula	Structure type	Abs bands (nm)	ε (M^{-1} cm^{-1})	PL λ_{em} (nm)[d]	References
6	$[Au_6(PPh_3)_6](NO_3)_2$ (**3**·NO_3)	Bitetrahedral	476 452 330 319	nd	nd	[34]
8	$[Au_8(dppp)_4](NO_3)_2$ (**9**·NO_3)	Tritetrahedral	590 (sh) 520 308	3.0×10^4 (520 nm)	NL	[81]
6	$[Au_6(dppp)_4](NO_3)_2$ (**4**·NO_3)	Au_4+2Au	587 432 326 [c]	8.9×10^4 (587 nm)	nd[e]	[101]
8	$[Au_8(dppp)_4Cl_2](Cl)_2$ (**11**·Cl)	Au_6+2Au	508 390 322	2.7×10^4 (508 nm)	597	[81]
8	$[Au_8(dppp)_4(C{\equiv}CPh)_2](NO_3)_2$ (**12**·NO_3)	Au_6+2Au	509 393 325	3.9×10^4 (509 nm)	577	[91]
11	$[Au_{11}(dppe)_6](SbF_6)_3$ (**32**·SbF_6)	Au_9+2Au	663 471 390 316	8.9×10^4 (663 nm)	nd[e]	[74]

[a]*NL* non-luminescent, *nd* no data given

[b]In DCM at room temperature unless otherwise noted. Almost identical spectra were obtained in MeCN and MeOH

[c]In MeOH

[d]Excited at the lowest-energy absorption band

[e]Essentially PL active (Fig. 9b)

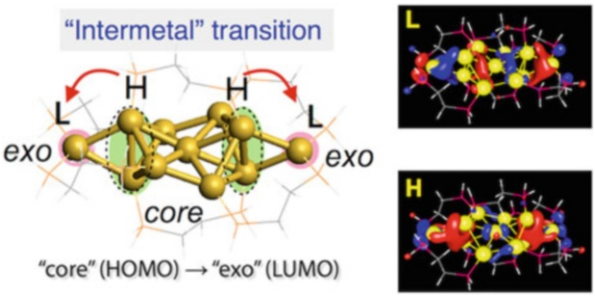

Fig. 8 Schematic illustration of HOMO and LUMO of $[Au_{11}(dppe)_6]^{3+}$ (**32**)

spectra generated by time-dependent DFT (TD-DFT) calculations reproduce well the experimental spectra, leading to the assignment of the characteristic visible bands to intermetal HOMO–LUMO transitions. Orbital distribution analyses demonstrate the HOMO and LUMO are both found in proximity to the terminal Au_3 triangles containing the *exo* gold atom, and the HOMO→LUMO transition occurs in the core→*exo* direction (Fig. 8).

5.1.3 Summary

Electronic absorption properties of PGCs are strictly dependent not only on the nuclearity but also on the geometrical structures of the cluster units. Centered polyhedral-only clusters generally show tail-and-humps spectra, while tetrahedron-based and [core+*exo*]-type clusters give isolated absorption bands in the visible region. Except some exceptions, the spectral profiles are essentially defined by the nuclearity/geometry of the gold cluster units, and the modification of the surface ligands cause little effects on the spectral pattern. The transition energies (band positions) show no clear correlation with the order of nuclearity and vary significantly with the individual arrangements of gold atoms, indicating the strong "molecular" characters of this class of cluster compounds.

5.2 Photoluminescence

In recent years there has been intense interest in the luminescence properties of ultrasmall noble metal clusters due to their potential utility as quantum dots [13]. However, the origin of the luminescence has not been elucidated yet because of the lack of the geometrical information. Ligand-coordinated ultrasmall gold clusters including PGCs are potentially photoluminescent due to the small size, but there have been very limited studies. We found that $[Au_9(PPh_3)_8]^{3+}$ (**14**) and $[Au_{11}L_{10}]^{3+}$ clusters (**29**, **29′** and **30**) are virtually PL inactive. In contrast, $Au_{13}P_{10}Cl_2$ cluster **34** is appreciably photoluminescent, giving a PL band in the near IR region (766 nm) when excited at 500 nm, with a moderately high quantum

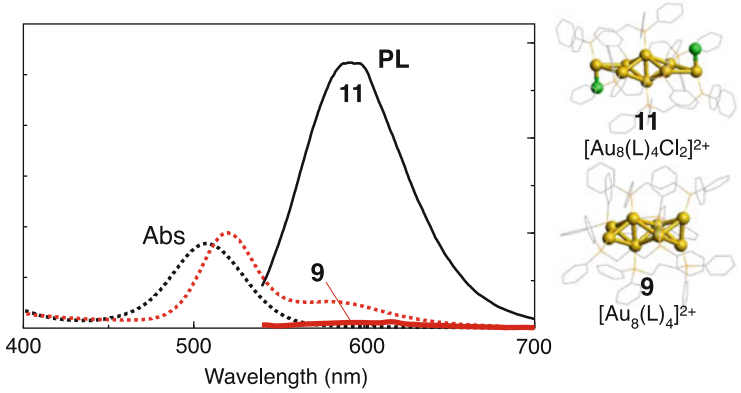

Fig. 9 Absorption (*dotted lines*) and PL (*solid lines*) spectra of two isomeric forms of Au_8 clusters: **9**·NO_3 (*red*) and **11**·Cl (*black*) in MeOH at 25°C

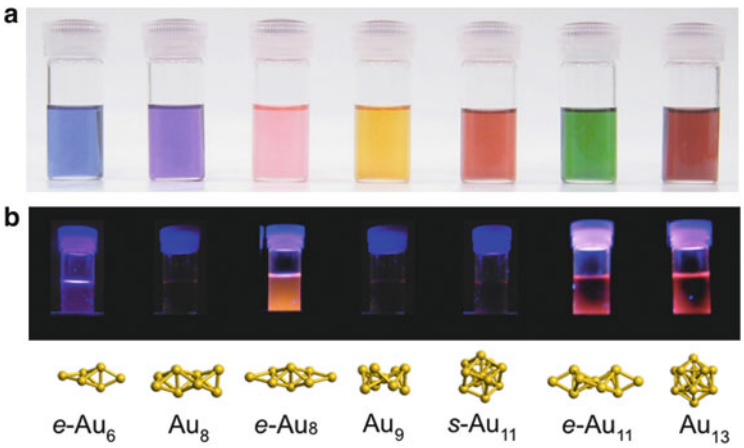

Fig. 10 Pictures of solution samples of PGCs (**a**) under room light and (**b**) under irradiation of a 365-nm handy UV lamp. (*Left* to *right*) $[Au_6(dppp)_4](NO_3)_2$ (**4**·NO_3); $[Au_8(dppp)_4](NO_3)_2$ (**9**·NO_3); $[Au_8(dppp)_4Cl_2](Cl)_2$ (**11**·Cl); $[Au_9(PPh_3)_8](NO_3)_2$ (**14**·NO_3); $[Au_{11}(PPh_3)_8Cl_2]Cl$ (**29**·Cl); $[Au_{11}(dppe)_6](SbF_6)_3$ (**32**·SbF_6); $[Au_{13}(dppe)_5Cl_2]Cl_3$ (**34**·Cl)

yield (0.076) [75]. On the other hand, the $Au_{13}P_8Cl_4$ cluster **41** shows a PL band at a similar wavelength but the quantum efficiency is considerably small (0.008), indicating that the local environment (ligand) in proximity to the gold core notably affects the radiative path that contributes the PL emission.

We have also found that [core+*exo*]-type Au_6, Au_8, and Au_{11} clusters are essentially PL active (Fig. 10b). For example, $[Au_8(dppp)_4Cl_2]^{2+}$ (**11**) shows an evident photoluminescence band at 597 nm upon excitation at 509 nm (Fig. 9, black solid line). The excitation spectrum monitored at 600 nm almost coincided with the absorption spectrum. Similarly to the abovementioned Au_{13} clusters, the PL profiles

of the core+*exo* type Au_8 clusters appear to be notably affected by the sub-ligand (e.g., Cl in **11**). $[Au_8(dppp)_4(C{\equiv}CPh)_2](NO_3)_2$ (**12**·NO_3), which has two acetylide units in place of chloride ligands, shows a similar PL band at a noticeably higher energy (577 nm). On the other hand, $[Au_8(dppp)_4](NO_3)_2$ (**9**·NO_3) having a tetrahedron trimer motif, which is isomeric to that of **11** and **12**, was almost PL inactive (red solid line), again indicating that the optical properties of PGCs are strictly dependent on their geometries.

5.3 Gold Clusters as Stimuli-Responsive Chromic Modules

As expected from the visible absorption profiles mentioned above, PGCs exhibit a wide variety of colors ranging over the whole visible region. Figure 10 shows the pictures of the solution samples of representative clusters under room light and UV-light, which reveal that their colors and PL activities are highly dependent on the number (nuclearity) and arrangement (geometry) of the gold atoms. Especially, the colors of the core+*exo* type clusters are impressive; their blue, pink, and green colors are unusual for gold clusters, which are markedly different from the plasmon-like reddish colors of conventional centered clusters such as Au_9, Au_{11}, and Au_{13}. This is surprising in the sense that the components of the clusters are virtually same and the optical property is simply governed by the arrangement of the gold atoms. The subtle difference in the arrangement leads to the great color differences.

In this context, one of the prominent features of gold clusters is their soft potential energy surfaces. This potentially allows the reversible interconversion among several particular geometries, through which the optical properties of the clusters would be altered. This idea can be supported by the earlier work by Mingos et al., who provide an example of the color and reflectance spectral difference between the butterfly and crown isomers of Au_9 cluster in the solid state [38]. Thus, if the cluster geometry can be tuned by external stimuli, one would see the optical responses in color change or PL on–off. Therefore, these gold clusters have a unique potential to serve as stimuli-responsive chromism modules and may be applied to chemical sensors.

As an example, we have recently shown a redox-induced chromism system based on the isomerization of the Au_8 units between **9** and **11** (Fig. 11) [81]. Thus, the formal charges of the Au_8 units of **9** and **11** were 2+ and 4+, respectively, which can be reversibly converted into each other via two-electron redox processes. As noted in the previous sections, the reduced form (**9**) is violet in color and PL inactive, whereas the oxidized form (**11**) is pink in color and PL active. As shown in Fig. 10, it is possible to switch the optical properties reversibly (color and PL) through chemical reduction/oxidation. The use of electrochemical processes would also be feasible, so the present cluster system has the potential for redox-based functions such as electrochromism.

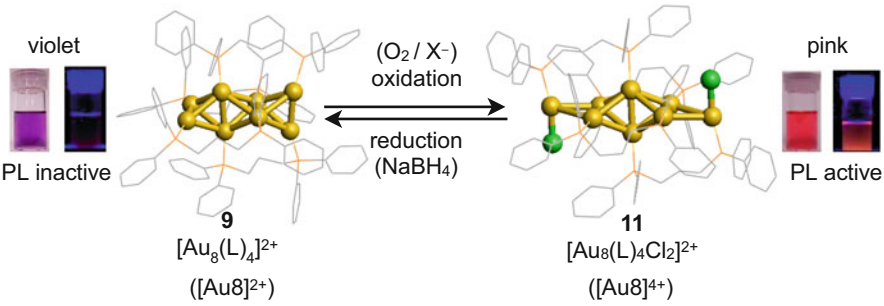

Fig. 11 Redox-mediated chromism between **9** and **11** associated with the isomerization of the Au_8 cluster framework

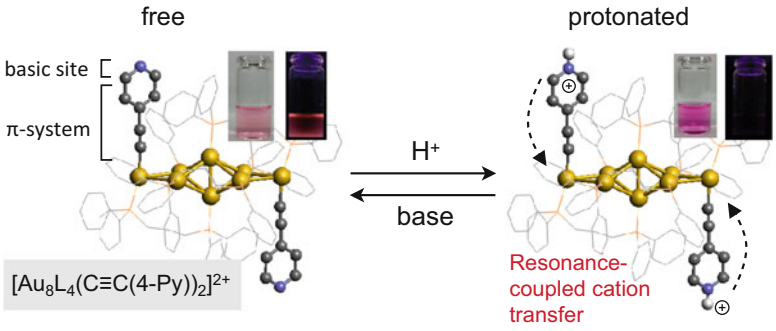

Fig. 12 Protonation-induced chromism of 4-pyridylethynyl-appended Au_8 cluster

Based on the general trend of the optical properties mentioned above, it is obvious that the nuclearity and geometries are primary factors to govern the optical properties of molecular gold clusters. In addition, the alteration of nearby or external environments or physical stimuli could affect the optical properties, but such aspects have not been explored. We have recently found that the electronic perturbation coupled with π-conjugated system actually affects the optical properties of the cluster units [91]. As shown in Fig. 12, the [core+*exo*]-type Au_8 clusters bearing two pyridylethynyl ligands on the *exo* gold atoms ($[Au_8(dppp)_4(C{\equiv}CPy)_2]^{2+}$) exhibit reversible visible absorption and photoluminescence responses to protonation/deprotonation events of the terminal pyridyl moieties. It is demonstrated that the chromism behaviors are highly dependent on the relative position of the pyridine nitrogen atom. Therefore the formation of extended charged resonance structures upon pyridine protonation causes significant perturbation effects on the electronic properties of the Au_8 unit. This is an example in which organic π-conjugated system and inorganic gold cluster are electronically combined, providing an implication for the design of cluster-based stimuli-responsive chromic modules.

6 Concluding Remarks

In the present chapter, the syntheses, X-ray structures (geometries), and optical properties of phosphine-coordinated molecular gold clusters (PGCs) have been summarized. The inspection of the optical properties in the context of the geometrical structures reveals a strong molecular character of PGCs. In addition to the conventional clusters discovered more than 30 years ago, several new families with unique geometrical and optical features have now been identified, thereby expanding the scope of this class of compounds. Among them, unusual optical properties of a series of [core+exo]-type clusters are quite interesting, which demonstrates that the attachment of only one or two gold atoms to polyhedral cores dramatically changes the electronic structures of total metal entities. This principle would be applicable to the colloidal system, which will benefit the rational design of functional colloids. It has been demonstrated that the use of bidentate ligands occasionally allows the generation of unusual cluster species, but it is still at a phenomenological level. The computer-aided design of multidentate phosphines would promote the emergence of unique PGCs. Finally, as shown in the last topic, the electronic structures (optical properties) of PGCs can be altered not only by the geometrical parameters but also by the electronic perturbation by the external stimuli. The combination with appropriate organic units as well as the design/discovery of novel skeletons would lead to the evolution of PGCs to functional materials.

Acknowledgments The author is grateful to Professor Michael Mingos for reading the drafts of this chapter and providing useful comments, and to Dr. Yutaro Kamei for his help in preparing graphics and also checking the structural and spectral data.

References

1. Daniel M-C, Astruc D (2004) Gold nanoparticles: assembly, supramolecular chemistry, quantum-size-related properties, and applications toward biology, catalysis, and nanotechnology. Chem Rev 104(1):293–346
2. Fernandez EJ, Monge M (2008) Gold nanomaterials. In: Laguna A (ed) Modern supra molecular gold chemistry: gold-metal interactions and applications. WILEY-VCH, Weinheim, pp 131–179. doi:10.1002/9783527623778.ch3
3. Sardar R, Funston A, Mulvaney P, Murray R (2009) Gold nanoparticles: past, present, and future. Langmuir 25(24):13840–13851
4. Giljohann D, Seferos D, Daniel W, Massich M, Patel P, Mirkin C (2010) Gold nanoparticles for biology and medicine. Angew Chem Int Ed 49(19):3280–3294
5. Takei T, Akita T, Nakamura I, Fujitani T, Okumura M, Okazaki K, Huang J, Ishida T, Haruta M (2012) Heterogeneous catalysis by gold. Adv Catal 55:1–126
6. Hutchings GJ, Edwards JK (2012) Application of gold nanoparticles in catalysis. Metal nanoparticles and nanoalloys. In: Johnstone RL, Wilcoxon JP (eds) Frontiers of nanoscience, vol 3. Elsevier, Oxford, pp 249–293

7. Wilson R (2008) The use of gold nanoparticles in diagnostics and detection. Chem Soc Rev 37(9):2028–2045
8. Bai C, Liu M (2013) From chemistry to nanoscience: not just a matter of size. Angew Chem Int Ed 52(10):2678–2683
9. Lu Y, Chen W (2012) Sub-nanometre sized metal clusters: from synthetic challenges to the unique property discoveries. Chem Soc Rev 41(9):3594–3623
10. Tsukuda T (2012) Toward an atomic-level understanding of size-specific properties of protected and stabilized gold clusters. Bull Chem Soc Jpn 85(2):151–168
11. Jin R (2010) Quantum sized, thiolate-protected gold nanoclusters. Nanoscale 2(3):343–362
12. Häkkinen H (2012) The gold-sulfur interface at the nanoscale. Nat Chem 4(6):443–455
13. Zheng J, Nicovich P, Dickson R (2007) Highly fluorescent noble-metal quantum dots. Ann Rev Phys Chem 58:409–431
14. Jadzinsky P, Calero G, Ackerson C, Bushnell D, Kornberg R (2007) Structure of a thiol monolayer-protected gold nanoparticle at 1.1 A resolution. Science 318(5849):430–433
15. Heaven MW, Dass A, White PS, Holt KM, Murray RW (2008) Crystal structure of the gold nanoparticle $[N(C_8H_{17})_4][Au_{25}(SCH_2CH_2Ph)_{18}]$. J Am Chem Soc 130(12):3754–3755
16. Zhu M, Eckenhoff WT, Pintauer T, Jin R (2008) Conversion of anionic $[Au_{25}(SCH_2CH_2Ph)_{18}]^-$ Cluster to charge neutral cluster via air oxidation. J Phys Chem C 112(37):14221–14224
17. Zhu M, Aikens C, Hollander F, Schatz G, Jin R (2008) Correlating the crystal structure of a thiol-protected Au_{25} cluster and optical properties. J Am Chem Soc 130(18):5883–5885
18. Qian H, Eckenhoff W, Zhu Y, Pintauer T, Jin R (2010) Total structure determination of thiolate-protected Au_{38} nanoparticles. J Am Chem Soc 132(24):8280–8281
19. Naldini L, Cariati F, Simonetta G, Malatesta L (1966) Gold? Tertiary phosphine derivatives with intermetallic bonds. Chem Commun 18:647
20. Vollenbroek FA, Bosman WP, Bour JJ, Noordik JH, Beurskens PT (1979) Reactions of gold? phosphine cluster compounds. Preparation and X-ray structure determination of octakis (triphenylphosphine)octa-gold bis(hexafluorophosphate). J Chem Soc Chem Commun (9):387–388
21. Vollenbroek FA, Bour JJ, van der Veden JWA (1980) Gold-phosphine cluster compounds: The reactions of $[Au_9L_8]^{3+}$ (L=PPh_3) with L, SCN− and Cl− to $[Au_8L_8]^{2+}$ $(Au_{11}L_8(SCN)_2]^+$ and $[Au_{11}L_8Cl_2]^+$. Recl Trav Chim Pays Bas 99(4):137–141
22. van der Velden JWA, Bour JJ, Bosman WP, Noordik JH (1981) Synthesis and X-ray crystal structure determination of the cationic gold cluster compound $[Au_8(PPh_3)_7](NO_3)_2$. J Chem Soc Chem Commun 23:1218–1219
23. van der Velden JWA, Vollenbroek FA, Bour JJ, Beurskens PT, Smits JMM, Bosnian WP (1981) Gold clusters containing bidentate phosphine ligands. Preparation and X-Ray structure investigation of $[Au_5(dppmH)_3(dppm)](NO_3)_2$ and $[Au_{13}(dppmH)_6](NO_3)$n. Recl Trav Chim Pays Bas 100(4):148–152
24. Vollenbroek FA, van der Velden JWA, Bour JJ, Trooster JM (1981) Mössbauer investigation of gold cluster compounds. Recl Trav Chim Pays-Bas 100(10):375–377
25. Steggerda JJ, Bour JJ, Velden JWAvd (1982) Preparation and properties of gold cluster compounds. Recl Trav Chim Pays Bas 101:164–170
26. Van der Velden JWA, Bour JJ, Steggerda JJ, Beurskens PT, Roseboom M, Noordik JH (1982) Gold clusters. Tetrakis[1,3-bis(diphenylphosphino)propane]hexagold dinitrate: preparation, X-ray analysis, and gold-197 Moessbauer and phosphorus-31{proton} NMR spectra. Inorg Chem 21(12):4321–4324
27. Smits JMM, Beurskens PT, Bour JJ, Vollenbroek FA (1983) X-ray analysis of octakis(tri-*p*-tolylphosphine) enneagoldtris(hexafluorophosphate), $[Au_9\{P(p\text{-}MeC_6H_4)_3\}_8](PF_6)_3$: a redetermination. J Cryst Spect Res 13(5):365–372
28. Smits JMM, Beurskens PT, Velden JWA, Bour JJ (1983) Partial X-ray analysis of triiodoheptakis (triphenylphosphine)undecagold, $Au_{11}C_{126}H_{105}I_3P_7$. J Cryst Spect Res 13(5): 373–379

29. Smits JMM, Bour JJ, Vollenbroek FA, Beurskens PT (1983) Preparation and X-ray structure determination of [pentakis{1,3-bis(diphenylphosphino)propane}] undecagoldtris(thiocyanate), $[Au_{11}\{PPh_2C_3H_6PPh_2\}_5](SCN)_3$. J Cryst Spect Res 13(5):355–363
30. Van der Velden JWA, Bour JJ, Bosman WP, Noordik JH (1983) Reactions of cationic gold clusters with Lewis bases. Preparation and X-ray structure investigation of $[Au_8(PPh_3)_7](NO_3)_2.2CH_2Cl_2$ and $Au_6(PPh_3)_4[Co(CO)_4]_2$. Inorg Chem 22(13):1913–1918
31. Van der Velden JWA, Beurskens PT, Bour JJ, Bosman WP, Noordik JH, Kolenbrander M, Buskes JAKM (1984) Intermediates in the formation of gold clusters. Preparation and X-ray analysis of $[Au_7(PPh_3)_7]^+$ and synthesis and characterization of $[Au_8(PPh_3)_6I]PF_6$. Inorg Chem 23(2):146–151
32. van der Velden JWA, Bour JJ, Bosman WP, Noordik JH, Beurskens PT (1984) The electrochemical preparation of $[Au_9(PPh_3)_8]^+$. A comparative study of the structures and properties of $[Au_9(PPh_3)_8]^+$ and $[Au_9(PPh_3)_8]^{3+}$. Recl Trav Chim Pays Bas 103(1):13–16
33. Bos W, Kanters RPF, Van Halen CJ, Bosman WP, Behm H, Smits JMM, Beurskens PT, Bour JJ, Pignolet LH (1986) Gold clusters: synthesis and characterization of $[Au_8(PPh_3)_7(CNR)]^{2+}$, $[Au_9(PPh_3)_6(CNR_2]^{3+}$ and $[Au_{11}(PPH_3)_7(CNR)_2I]^{2+}$ and their reactivity towards amines. The crystal structure of $[Au_{11}(PPh_3)_7(CN\text{-}i\text{-}Pr)_2I](PF_6)_2$. J Organomet Chem 307(3):385–398
34. Hall KP, Mingos DMP (1984) Homo-and heteronuclear cluster compounds of gold. Prog Inorg Chem 32:237–325
35. Mingos DMP (1984) Gold cluster compounds. Gold Bull 17(1):5–12
36. Briant CE, Theobald BRC, White JW, Bell LK, Mingos DMP, Welch AJ (1981) Synthesis and X-ray structural characterization of the centred icosahedral gold cluster compound $[Au_{13}(PMe_2Ph)_{10}Cl_2](PF_6)_3$; the realization of a theoretical prediction. J Chem Soc Chem Commun 5:201
37. Hall KP, Theoblad BRC, Gilmour DI, Mingos DMP, Welch AJ (1982) Synthesis and structural characterization of $[Au_9\{P(p\text{-}C_6H_4OMe)_3\}_8](BF_4)_3$; a cluster with a centred crown of gold atoms. J Chem Soc Chem Commun 10:528–530
38. Briant CE, Hall KP, Mingos DMP (1984) Structural characterisation of two crystalline modifications of $[Au_9\{P(C_6H_4OMe\text{-}p)_3\}_8](NO_3)_3$: the first example of skeletal isomerism in metal cluster chemistry. J Chem Soc Chem Commun 5:290–292
39. Briant CE, Hall KP, Wheeler AC, Mingos DMP (1984) Structural characterisation of $[Au_{10}Cl_3(PCy_2Ph)_6](NO_3)$(Cy=cyclohexyl) and the development of a structural principle for high nuclearity gold clusters. J Chem Soc Chem Commun 4:248–250
40. Briant CE, Hall KP, Mingos DMP, Wheeler AC (1986) Synthesis and structural characterisation of hexakis(triphenyl phosphine)hexagold(2+) nitrate, $[Au_6(PPh_3)_6][NO_3]_2$, and related clusters with edgesharing bitetrahedral geometries. J Chem Soc Dalton Trans 3: 687–692
41. Cheetham GMT, Harding MM, Haggitt JL, Mingos DMP, Powell HR (1993) Synthesis and microcrystal structure determination of $[Au_{10}(PPh_3)_7\{S_2C_2(CN)_2\}_2]$ with monochromatic synchrotron radiation. J Chem Soc Chem Commun 12:1000–1001
42. Copley RCB, Mingos DMP (1996) The novel structure of the $[Au_{11}(PMePh_2)_{10}]^{3+}$ cation: crystal structures of $[Au_{11}(PMePh_2)_{10}][C_2B_9H_{12}]_3{\cdot}4thf$ and $[Au_{11}(PMePh_2)_{10}][C_2B_9H_{12}]_3$(thf = tetrahydrofuran). J Chem Soc Dalton Trans 4:479–489
43. Copley RCB, Mingos DMP (1996) Synthesis and characterization of the centred icosahedral cluster series $[Au_9MIB_4Cl_4(PMePh_2)_8][C_2B_9H_{12}]$, where MIB=Au, Ag or Cu. J Chem Soc Dalton Trans 4:491
44. Cariati F, Naldini L, Simonetta G, Malatesta L (1967) Clusters of gold compounds with 1,2Bis(diphenylphosphino)ethane. Inorg Chim Acta 1:315–318
45. Albano VG, Bellon PL, Manasser M, Sansoni M (1970) Intermetallic pattern in metal-atom clusters – structural studies on $Au_{11}X_3(PR_3)_7$ Species. J Chem Soc D Chem Commun (18):1210–1211
46. Cariati F, Naldini L (1971) Trianionoeptakis(triarylphosphine)undecagold cluster compounds. Inorg Chim Acta 5:172–174

47. Bellon P, Manassero M, Sansoni M (1972) Crystal and molecular structure of tri-iodoheptakis (tri-*p*-fluorophenylphosphine)undecagold. J Chem Soc Dalton Trans 14:1481–1487
48. Bellon P, Manassero M, Sansoni M (1973) An octahedral gold cluster: crystal and molecular structure of hexakis[tris-(*p*-tolyl)phosphine]-octahedro-hexagold bis(tetraphenylborate). J Chem Soc Dalton Trans 22:2423–2427
49. Manassero M, Naldini L, Sansoni M (1979) A new class of gold cluster compounds. Synthesis and X-ray structure of the octakis(triphenylphosphinegold) dializarinsulphonate, $[Au_8(PPh_3)_8](aliz)_2$. J Chem Soc Chem Commun (9):385–386
50. Mingos DMP (1983) Polyhedral skeletal electron pair approach. A generalised principle for condensed polyhedra. J Chem Soc Chem Commun (12):706
51. Mingos DMP, Slee T, Zhenyang L (1990) Bonding models for ligated and bare clusters. Chem Rev 90(2):383–402
52. Wales DJ (2005) Electronic structure of clusters. Encyclopedia Inorg Chem. doi:10.1002/9781119951438.eibc0066
53. Schwerdtfeger P (2003) Gold goes nano–from small clusters to low-dimensional assemblies. Angew Chem Int Ed 42(17):1892–1895
54. Schmid G (2008) Ionically cross-linked gold clusters and gold nanoparticles. Angew Chem Int Ed 47(19):3496–3498
55. Schmid G (2008) The relevance of shape and size of Au_{55} clusters. Chem Soc Rev 37(9): 1909–1930
56. Yam V, Cheng E (2008) Highlights on the recent advances in gold chemistry–a photophysical perspective. Chem Soc Rev 37(9):1806–1813
57. Koshevoy I, Chang Y-C, Karttunen A, Selivanov S, Jänis J, Haukka M, Pakkanen T, Tunik S, Chou P-T (2012) Intensely luminescent homoleptic alkynyl decanuclear gold(I) clusters and their cationic octanuclear phosphine derivatives. Inorg Chem 51(13):7392–7403
58. Mingos DMP, Watson MJ (1992) Heteronuclear gold cluster compounds. Adv Inorg Chem 39:327–399
59. Teo BK, Zhang H (1995) Polyicosahedricity: icosahedron to icosahedron of icosahedra growth pathway for bimetallic (Au–Ag) and trimetallic (Au–Ag–M; M=Pt, Pd, Ni) supraclusters; synthetic strategies, site preference, and stereochemical principles. Coord Chem Rev 143:611–636
60. Schmidbaur H, Schier A (2012) Aurophilic interactions as a subject of current research: an up-date. Chem Soc Rev 41(1):370–412
61. Schulz-Dobrick M, Jansen M (2006) Supramolecular intercluster compounds consisting of gold clusters and Keggin anions. Eur J Inorg Chem 2006(22):4498–4502
62. Wen F, Englert U, Gutrath B, Simon U (2008) Crystal structure, electrochemical and optical properties of $[Au_9(PPh_3)_8](NO_3)_3$. Eur J Inorg Chem 2008(1):106–111
63. Cariati F, Naldini L, Simonetta G, Malatesta L (1967) Ethyldiphenylphosphine-gold derivatives with intermetallic bonds. Inorg Chim Acta 1:24–26
64. Bartlett PA, Bauer B, Singer SJ (1978) Synthesis of water-soluble undecagold cluster compounds of potential importance in electron microscopic and other studies of biological systems. J Am Chem Soc 100(16):5085–5089
65. Gutrath BS, Englert U, Wang Y, Simon U (2013) A missing link in undecagold cluster chemistry: single-crystal X-ray analysis of $[Au_{11}(PPh_3)_7Cl_3]$. Eur J Inorg Chem 2013(12): 2002–2006
66. Wan X-K, Lin Z-W, Wang Q-M (2012) Au_{20} nanocluster protected by hemilabile phosphines. J Am Chem Soc 134(36):14750–14752
67. Schmid G, Pfeil R, Boese R, Bandermann F, Meyer S, Calis GHM, van der Velden JWA (1981) $Au_{55}[P(C_6H_5)_3]12CI_6$ – ein Goldcluster ungewöhnlicher Größe. Chem Ber 114(11): 3634–3642
68. Bertino M, Sun Z-M, Zhang R, Wang L-S (2006) Facile syntheses of monodisperse ultrasmall Au clusters. J Phys Chem B 110(43):21416–21418
69. Kamei Y, Shichibu Y, Konishi K. unpublished results

70. Golightly JS, Gao L, Castleman AW, Bergeron DE, Hudgens JW, Magyar RJ, Gonzalez CA (2007) Impact of swapping ethyl for phenyl groups on diphosphine-protected undecagold. J Phys Chem C 111
71. Yanagimoto Y, Negishi Y, Fujihara H, Tsukuda T (2006) Chiroptical activity of BINAP-stabilized undecagold clusters. J Phys Chem B 110(24):11611–11614
72. Andreiadis E, Vitale M, Mézailles N, Le Goff X, Le Floch P, Toullec P, Michelet V (2010) Chiral undecagold clusters: synthesis, characterization and investigation in catalysis. Dalton Trans 39(44):10608–10616
73. Chen J, Zhang QF, Bonaccorso TA, Williard PG, Wang LS (2014) Controlling gold nanoclusters by diphospine ligands. J Am Chem Soc 136(1):92–95
74. Shichibu Y, Kamei Y, Konishi K (2012) Unique [core+two] structure and optical property of a dodeca-ligated undecagold cluster: critical contribution of the exo gold atoms to the electronic structure. Chem Commun 48(61):7559–7561
75. Shichibu Y, Konishi K (2010) HCl-induced nuclearity convergence in diphosphine-protected ultrasmall gold clusters: a novel synthetic route to "magic-number" Au_{13} clusters. Small 6(11):1216–1220
76. Shichibu Y, Suzuki K, Konishi K (2012) Facile synthesis and optical properties of magic-number Au_{13} clusters. Nanoscale 4(14):4125–4129
77. Ito H, Saito T, Miyahara T, Zhong C, Sawamura M (2009) Gold(I) hydride intermediate in catalysis: dehydrogenative alcohol silylation catalyzed by gold(I) complex. Organometallics 28(16):4829–4840
78. Teo BK, Shi X, Zhang H (1992) Pure gold cluster of 1:9:9:1:9:9:1 layered structure: a novel 39-metal-atom cluster $[(Ph_3P)_{14}Au_{39}Cl_6]Cl_2$ with an interstitial gold atom in a hexagonal antiprismatic cage. J Am Chem Soc 114(7):2743–2745
79. Das A, Li T, Nobusada K, Zeng Q, Rosi N, Jin R (2012) Total structure and optical properties of a phosphine/thiolate-protected Au_{24} nanocluster. J Am Chem Soc 134(50):20286–20289
80. Strähle J (1995) Synthesis of cluster compounds by photolysis of azido complexes. J Organomet Chem 488(1–2):15–24
81. Kamei Y, Shichibu Y, Konishi K (2011) Generation of small gold clusters with unique geometries through cluster-to-cluster transformations: octanuclear clusters with edge-sharing gold tetrahedron motifs. Angew Chem Int Ed Engl 50(32):7442–7445
82. Laguna A, Laguna M, Gimeno MC, Jones PG (1992) Synthesis and X-ray characterization of the neutral organometallic gold cluster $[Au_{10}(C_6F_5)_4(PPh_3)_5]$. Organometallics 11(8): 2759–2760
83. Vollenbroek FA, Bour JJ, Trooster JM, van der Velden JWA (1978) Reactions of gold? Phosphine cluster compounds. J Chem Soc Chem Commun 21:907
84. Nunokawa K, Onaka S, Ito M, Horibe M, Yonezawa T, Nishihara H, Ozeki T, Chiba H, Watase S, Nakamoto M (2006) Synthesis, single crystal X-ray analysis, and TEM for a single-sized Au_{11} cluster stabilized by SR ligands: the interface between molecules and particles. J Organomet Chem 691(4):638–642
85. Shichibu Y, Negishi Y, Watanabe T, Chaki NK, Kawaguchi H, Tsukuda T (2007) Biicosahedral Gold Clusters $[Au_{25}(PPh_3)_{10}(SC_nH_{2n+1})_5Cl_2]^{2+}$ ($n = 2$–18): a Stepping stone to cluster-assembled materials. J Phys Chem C 111(22):7845–7847
86. Yang Y, Sharp PR (1994) New gold clusters $[Au_8L_6](BF_4)_2$ and $[(AuL)_4](BF_4)_2$ (L=P (mesityl)$_3$). J Am Chem Soc 116(15):6983–6984
87. Ramamoorthy V, Wu Z, Yi Y, Sharp PR (1992) Preparation and decomposition of gold (I) hydrazido complexes: gold cluster formation. J Am Chem Soc 114(4):1526–1527
88. Schulz-Dobrick M, Jansen M (2007) Characterization of gold clusters by crystallization with polyoxometalates: the intercluster compounds $[Au_9(dpph)4][Mo_8O_{26}]$, $[Au_9(dpph)_4][PW_{12}O_{40}]$ and $[Au_{11}(PPh_3)_8Cl_2]_2[W_6O_{19}]$. Z Anorg Allg Chem 633(13–14):2326–2331
89. Schulz-Dobrick M, Jansen M (2008) Intercluster compounds consisting of gold clusters and fullerides: $[Au_7(PPh_3)_7]C_{60} \times THF$ and $[Au_8(PPh_3)_8](C_{60})_2$. Angew Chem Int Ed Engl 47 (12):2256–2259

90. Gutrath B, Oppel I, Presly O, Beljakov I, Meded V, Wenzel W, Simon U (2013) $[Au_{14}(PPh_3)_8(NO_3)_4]$: an example of a new class of $Au(NO_3)$-ligated superatom complexes. Angew Chem Int Ed 52(12):3529–3532
91. Kobayashi N, Kamei Y, Shichibu Y, Konishi K (2013) Protonation-induced chromism of pyridylethynyl-appended [core+*exo*]-type Au clusters. Resonance-coupled electronic perturbation through pi-conjugated group. J Am Chem Soc 135(43):16078–16081
92. Van der Linden JGM, Paulissen MLH, Schmitz JEJ (1983) Electrochemical reduction of the gold cluster $Au_9(PPh_3)_8^{3+}$. Evidence for an ErErCr mechanism. Formation of the paramagnetic gold cluster $Au_9(PPh_3)_8^{2+}$. J Am Chem Soc 105(7):1903–1907
93. Smirnova ES, Echavarren AM (2013) A hexanuclear gold cluster supported by three-center-two-electron bonds and aurophilic interactions. Angew Chem Int Ed Engl 52(34):9023–9026
94. Marsh RE (1984) Crystal structure of $Au_7(PPh_3)^{7+}$: corrigendum. Inorg Chem 23(22):3682–3682
95. Schulz-Dobrick M, Jansen M (2008) Synthesis and characterization of intercluster compounds consisting of various gold clusters and differently charged keggin anions. Z Anorg Allg Chem 634(15):2880–2884
96. Bhargava S, Kitadai K, Masashi T, Drumm DW, Russo SP, Yam VW, Lee TK, Wagler J, Mirzadeh N (2012) Synthesis and structures of cyclic gold complexes containing diphosphine ligands and luminescent properties of the high nuclearity species. Dalton Trans 41(16): 4789–4798
97. Pethe J, Strahle J (1999) Synthese und Kristallstruktur von $[Au(AuNCO)(AuPPh_3)_8]$ Cl. Z Naturforsh B 54(3):381–384
98. Pethe J, Maichle-Mössmer C, Strähle J (1998) Synthese und Struktur von $K[Au(AuCl)(AuPPh_3)_8)](PF_6)_2$. Z Anorg Allg Chem 624(7):1207–1210
99. Nunokawa K, Onaka S, Yamaguchi T, Ito T, Watase S, Nakamoto M (2003) Synthesis and characterization of the Au_{11} cluster with sterically demanding phosphine ligands by single crystal X-ray diffraction and XPS spectroscopy. Bull Chem Soc Jpn 76(8):1601–1602
100. Scherbaum F, Grohmann A, Huber B, Krüger C, Schmidbaur H (1988) "Aurophilicity" as a consequence of relativistic effects: the hexakis(triphenylphosphaneaurio)methane dication $[(Ph_3PAu)_6C]^{2\oplus}$. Angew Chem Int Ed Engl 27(11):1544–1546
101. Shichibu Y, Konishi K (2013) Electronic properties of [core+*exo*]-type gold clusters: factors affecting the unique optical transitions. Inorg Chem 52(11):6570–6575
102. Jaw HRC, Mason WR (1991) Magnetic circular dichroism spectra for the octakis(triphenylphosphino)nonagold(3+) ion. Inorg Chem 30(2):275–278

Struct Bond (2014) 161: 87–116
DOI: 10.1007/430_2014_146

Published online: 15 April 2014

Gold Nanoclusters: Size-Controlled Synthesis and Crystal Structures

Chenjie Zeng and Rongchao Jin

Abstract One of the major goals in nanoparticle research is to investigate their unique properties not seen in bulk materials or small molecules. In this chapter, we focus on a new class of gold nanoparticles (often called nanoclusters) that possess atomic precision (as opposed to conventional nanoparticles with a size distribution). The synthetic methods for obtaining atomically precise thiolate-protected gold nanocluters are first discussed, followed by the anatomy of the X-ray crystal structures of gold nanoclusters.

Keywords Atomic precision · Crystal structure · Gold · Nanocluster · Size-focusing · Thiol

Contents

C. Zeng and R. Jin (✉)
Department of Chemistry, Carnegie Mellon University, 4400 Fifth Ave, Pittsburgh, PA 15213, USA
e-mail: rongchao@andrew.cmu.edu

1 Introduction

One of the major goals in nanoparticle research is to investigate their unique properties not seen in bulk materials or small molecules. By tailoring the size or shape of nanoparticles, their physical and chemical properties exhibit significant changes compared to bulk materials [1]. In terms of size control, there have been major advances in the last decade, and a wide range of monodisperse nanoparticles (e.g., 3–100 nm diameter) are now accessible.

Monodispersity is the most important criterion in terms of the quality of nanoparticles and is typically assessed by transmission electron microscopy (TEM) (Fig. 1a, b). The ultimate control over nanoparticles is to obtain atomically precise particles [2]. While such atomic monodispersity has not been realized for regular sized nanoparticles (e.g., >3 nm diameter), ultrasmall nanoparticles (1–3 nm, equivalent to a few tens to hundreds of atoms) are now possible to achieve atomic precision, for example, 25-gold-atom nanoparticles (1 nm metal core diameter (Fig. 1c). The atomic monodispersity of nanoparticles is assessed by mass spectrometry (Fig. 1d). These ultrasmall nanoparticles are often called nanoclusters to distinguish from regular nanoparticles.

The term "monodispersity" used in nanochemistry is not as precise as the term "purity" in molecular chemistry. A pure compound should be free of impurities and also with a definite chemical formula. For molecularly pure nanoclusters, all the particles should have the same molecular weight and the same formula, i.e. "atomic precision." It has long been a major dream for nanochemists to prepare atomically precise nanoparticles. Such nanoparticles will be absolutely monodisperse and uniform at the atomic scale and thus can be treated as giant molecules. When all the nanoparticles in a sample are atomically monodisperse, mass spectrometry analysis will show a single molecular weight (Fig. 1d). Hence, the atomic precision is a stricter and more accurate criterion than the conventional term "monodispersity" used for regular nanoparticles, and correspondingly, mass spectrometry is a more accurate characterization tool than TEM and is indeed indispensible in nanocluster characterization.

To make atomically precise nanoclusters is of paramount importance for understanding the fundamental science of nanoclusters [3]. For molecularly pure nanoclusters, many well-established characterization tools in the traditional molecular chemistry can be applied and provide in-depth characterization. For example, one can employ mass spectrometry (e.g., electrospray ionization mass spectrometry, ESI-MS, and matrix-assisted laser desorption ionization mass spectrometry, MALDI-MS) to unambiguously determine the molecular weight of nanoclusters [3–6], single-crystal X-ray crystallography to determine the total structure of nanoclusters [7–13], nuclear magnetic resonance (NMR) spectroscopy to probe organic ligand environment and metal core chirality [14, 15], and so forth. These molecular characterization tools lead to fundamental understanding of the physical and chemical properties of atomically precise nanoclusters.

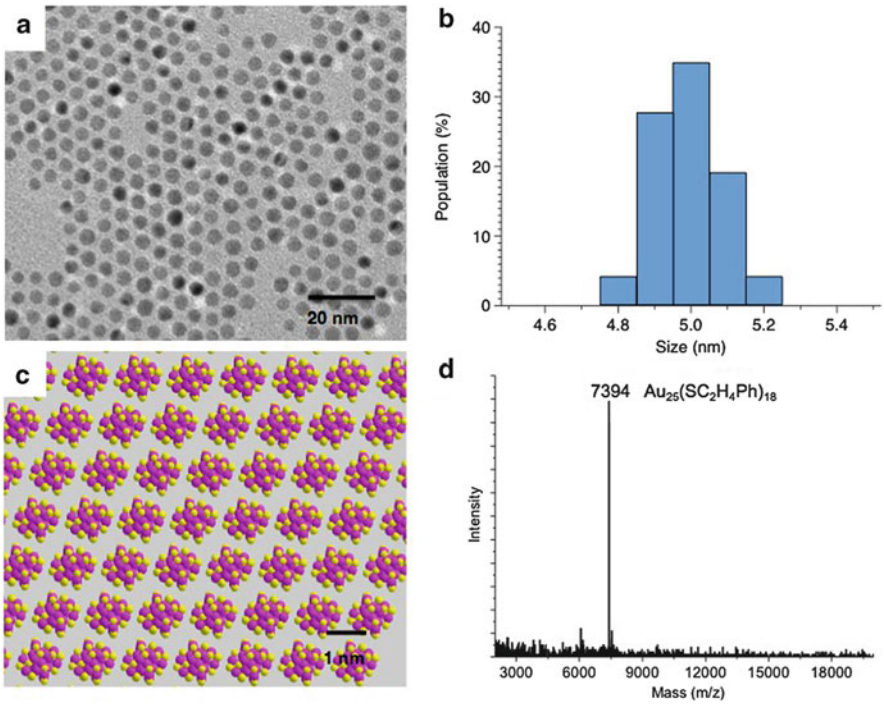

Fig. 1 (**a**) Monodisperse nanoparticles imaged by TEM; (**b**) histogram of size distribution (5 ± 0.3 nm diameter); (**c**) atomically precise $Au_{25}(SC_2H_4Ph)_{18}$ nanoclusters (1 nm metal core diameter, $-C_2H_4Ph$ groups are omitted, magenta = Au, yellow = S); (**d**) mass spectrometry characterization of $Au_{25}(SC_2H_4Ph)_{18}$ nanoclusters

2 Ligand-Protected Gold Nanoclusters

In solution phase, nanoclusters must be protected by ligands or stabilizers; otherwise, unprotected nanoclusters would immediately aggregate, forming a precipitate and losing the integrity of individual nanoclusters. For nanochemists, a major task is to find appropriate ligands for stabilizing nanoclusters and more importantly enabling controlled synthesis.

The early research on gold nanoclusters involved phosphine as ligand. The gold-phosphine chemistry was developed as a derivative of the coordination chemistry, which started in the 1960s. As a spin-off of the research of gold:phosphine complex compounds, an eleven-gold-atom cluster, $Au_{11}(PPh_3)_7(SCN)_3$, was reported in 1969 [16]. The Au_{11} structure exhibits an incomplete icosahedral framework. Mingos and coworkers predicted 13-atom-centered icosahedral cluster and successfully synthesized $[Au_{13}(PR_3)_{10}Cl_2]^{3+}$ and determined the structure in 1981 [17]. Schmid et al. reported $Au_{55}(PR_3)_{12}Cl_6$, although the structure has not been attained to date [18]. Teo et al. reported $[Au_{39}(PR_3)_{14}Cl_6]^{2+}$ and bimetal nanoclusters such as $[Au_{13}Ag_{12}(PR_3)_{10}Br_8]^{+}$, $[Au_{18}Ag_{19}(PR_3)_{12}Br_{11}]^{2+}$, and

$[Au_{18}Ag_{20}(PR_3)_{14}Cl_{12}]^{2+}$ [19–22]. Dahl and coworkers synthesized and characterized a series of phosphine-carbonyl Pd_n nanoclusters [23–26].

In recent development of gold-phosphine nanoclusters, Shichibu et al. reported diphosphine-protected Au_{13} icosahedral clusters [27]. Pettibone et al. carried out detailed work on the synthesis and growth mechanism of small gold-phosphine clusters [28]. Wan et al. reported the structure of $[Au_{20}(PPhpy_2)_{10}Cl_4]^{2+}$ cluster (where $Phpy_2$ = pyridyl phosphine), in which the core consists of two edge-shared Au_{11} units [29]. With phosphine/thiolate ligands, a biicosahedral $[Au_{25}(PPh_3)_{10}(SR)_5Cl_2]^{2+}$ cluster (SR = thiolate) has been obtained [30, 31]. Recently, Das et al. report a $[Au_{24}(PPh_3)_{10}(SC_2H_4Ph)_5X_2]^{+}$ nanocluster (where X = Cl/Br) [32]. Zheng and coworkers recently reported $Au_{13}Cu_x$ (x = 2, 4, 8) nanoclusters protected by mixed phosphine and thiolate ligands [33].

Thiol was extensively used in the synthesis of gold(I)-thiolate complexes in early research, and later thiol was used to prepare gold nanoparticles. In this chapter, we focus on the thiolate-protected *nanoclusters*, while the research on conventional gold-thiolate *nanoparticles* is not discussed herein.

3 Thiolate-Protected Gold Nanoclusters

The protecting molecules are very important for the stability of nanoclusters. Generally speaking, the protecting molecules provide barriers such as electrostatic and steric repulsions between particles to prevent them from aggregation into precipitate. Different types of protecting molecules impart different stability to nanoclusters. For conventional gold nanoparticles, simple ions (e.g., citrate), polymers, surfactants, as well as ligands have been used for stabilization (Fig. 2). Among these reagents, ligands – especially thiolate – render highly stable gold nanoparticles and nanoclusters, and thus are of wide interest. The high stability of thiolate-protected gold nanoparticles originates from the strong covalent bonding between thiolate and gold – the ligand is thus hard to dissociate from the nanoparticle surface. The carbon tails of the thiolate ligands provide further steric repulsion between nanoparticles, hence preventing aggregation.

The study of thiolate-protected gold nanoclusters experienced several stages, i.e. from polydispersed nanoclusters to monodispersed ones and finally to atomically precise nanoclusters [2, 34–37]. In early years, separation was done on the polydisperse nanoclusters in order to obtain relatively monodisperse ones [4, 35]. In recent years, the research progress has evolved to large-scale, controlled synthesis [37–43].

Whetten's group found that the thiolate-protected gold nanoclusters had the trend to form a series of *discrete* sizes [35]. The mixture of clusters was separated by solvent fractionation, and each fraction was characterized by laser desorption ionization mass spectrometry (LDI-MS). Distinct species with molecular weight of $5k$, $8k$, $14k$, $22k$, $29k$, etc., where k = 1,000 Da were identified; of note, these mass values correspond to the mass of Au_xS_y [36, 44–47]. Those species were quite

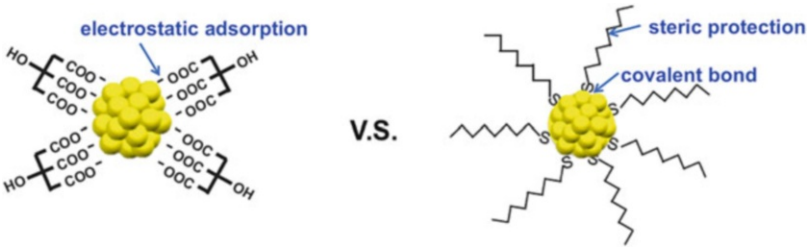

Fig. 2 Stability of traditional gold colloids (e.g., citrate-protected) and of thiolate-protected gold nanoparticles

monodispersed, but not atomically precise. No exact formula was assigned to those species due to fragmentation resulted by LDI-MS. For formula assignment, *intact* molecular ions (and hence accurate molecular weight) must be obtained first. Nevertheless, those early works on discrete gold nanocluster species provide valuable information and stimulation for later work for atomically precise nanoclusters.

With the improvement in the characterization techniques, especially the mass spectrometry, the accurate formula weights of gold nanoclusters were later obtained [4–6]. Combined with the improvement in the separation techniques, a series of "magic sizes" with well-defined chemical compositions were achieved, such as $Au_{25}(SR)_{18}$ and $Au_{38}(SR)_{24}$ (here SR represents thiolates generally) [4, 5, 48]. There are many other atomically precise species that were later obtained from separation [49–54]. However, it remained to devise synthetic methods for large-scale, controlled synthesis.

In recent years, great progress has been made in controlled synthesis of gold nanoclusters [37–43]. A systematic "size-focusing" methodology has been developed for attaining atomically precise nanoclusters with size control, based on earlier works that under harsh chemical and/or thermal conditions the initially polydispersed clusters could be size narrowed [37, 48, 55]. This methodology has led to direct syntheses of a series of atomically precise gold nanoclusters, including $Au_{25}(SR)_{18}$, $Au_{38}(SR)_{24}$, $Au_{144}(SR)_{60}$ and the largest ever $Au_{333}(SR)_{79}$ [38–41]. The development of the synthetic strategy greatly advanced the fundamental research on the optical and electronic properties of gold nanoclusters [9] as well as the applications of nanoclusters [56–59]. Below we shall give a detailed discussion on the size-focusing methodology for synthesizing atomically precise gold nanoclusters.

4 Size-Controlled Synthesis of Gold Nanoclusters with Atomic Precision

The chemistry for synthesizing gold-thiolate nanoclusters involves the reduction of a gold salt precursor by a reducing agent in the presence of thiol. The balance between growth and surface passivation controls the size of nanoclusters. Three chemicals are typically required in the synthesis of gold nanoclusters: the gold

precursor (e.g., $HAuCl_4$), protecting thiol ligand (e.g., HSR), and reducing agent (e.g., $NaBH_4$). However, to obtain atomically precise gold nanoclusters of molecular purity [3, 14, 15] is by no means easy. In nanochemistry, controlling the precise size and shape of nanoclusters is very difficult, for that during the reaction many factors can affect the size distribution of gold nanoclusters. For the static factors, examples are the concentration of gold precursor, the type of solvent used as reaction medium, the type and concentration of thiol, and the type and concentration of reducing agent, etc. For the dynamic factors, there are the reaction temperature, the stirring speed, the mixing of gold salt and ligand, the addition speed of the reductant, the reducing and aging time, etc. Tuning each of the above factors may result in different nanocluster products. Overall, for the synthesis of gold nanoclusters, the chemistry (i.e., reactions, mainly reduction of gold salt) is relatively simple, while the control over the subsequent growth of Au(0) atoms into well-defined nanoclusters can be quite complicated and requires significant efforts.

4.1 Size-Focusing Methodology

Among the synthetic methods for atomically precise gold nanoclusters, the recently established size-focusing methodology has been demonstrated to be quite universal [37]. There are two primary steps for a 'size-focusing' synthesis (Fig. 3). In step 1, polydispersed gold nanoclusters with a controlled size range are obtained through tuning the reaction conditions (i.e., the static and dynamic factors). In step 2, these initially polydispersed gold nanoclusters are focused into single-size product by aging/etching under a harsh environment.

The foundation of "size focusing" is based on the inherent stability difference of different-sized nanoclusters. Those stable sizes are sometimes called "magic sizes." When a harsh environment is applied to the mixture of nanoclusters, only the most robust species can survive size focusing, while the other species are either decomposed or converted to the most stable size [60]. The *'survival of the most robust'* principle somewhat resembles nature's law '*survival of the fittest*' [37].

With respect to the stability of magic-size nanoclusters, there are generally arguments invoking the geometric and electronic factors. For the geometric factor, certain geometric core arrangements (e.g., icosahedron) as well as the arrangement of surface thiolate ligands impart particular stability to the overall nanocluster structure. While for the electronic factor, those gold nanoclusters with the number of Au 6s free electrons satisfying electron-shell closing (i.e., $1S^21P^61D^{10}2S^2\ldots$) are regarded to be stable. This electron-shell picture resembles the electronic structure of atoms (i.e., $1s^22s^2p^6\ldots$). Some gold nanoclusters may be viewed as superatoms, such as anionic $[Au_{25}(SR)_{18}]^-$ [61], in which the number of Au 6s free electrons is counted as follows: 25 (the number of gold atoms) − 18 (the number of thiolate, each consumes 1e) + 1 (the anionic charge state) = 8e (consistent with $1S^21P^6$). But many exceptions exist, such as $[Au_{38}(SR)_{24}]^0$ (formal electron count: 14e, deviated from the closest 18e for $1S^21P^61D^{10}$). More discussions are in the Sect. 6.

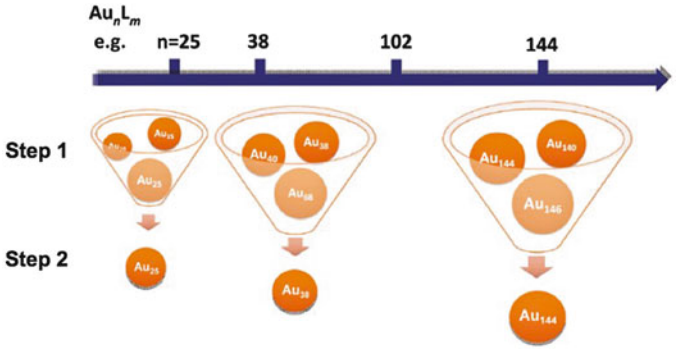

Fig. 3 Size-focusing methdology for the synthesis of atomically preciese gold nanoclusters. First step: control over size range; second step: size "focusing" into single-size product. By shifting the initial size range, different-sized nanoclusters are obtained. Adapted with permission from [37]

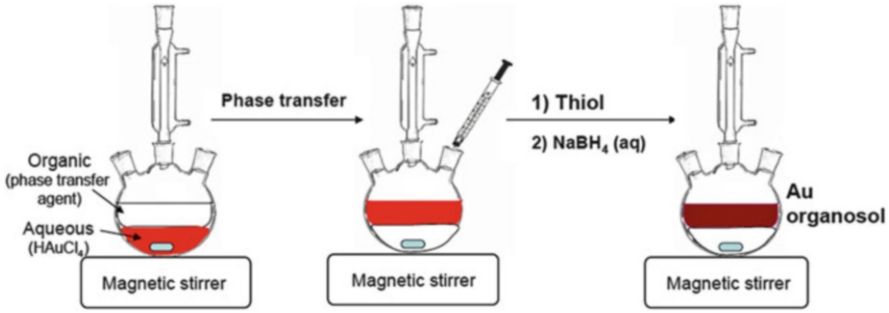

Fig. 4 Two-phase synthesis method of gold nanoclusters

A key to select one particular size of gold nanoclusters in the size-focusing methodology is to control the distribution of the starting nanoclusters in a proper size range (Fig. 3). If the size range of the starting nanoclusters is too wide, several stable species may be resulted after size focusing, which necessitates difficult post-synthetic separation. Control over the initial size distribution can be achieved through adjusting the reaction parameters such as gold to thiol ratio, solvent, ligand's bulkiness, and growth kinetics.

In the two-phase synthesis of thiolate-protected gold nanoclusters, four reagents are needed: the gold salt ($HAuCl_4$), phase transfer agent ((n-$C_8H_{17})_4NBr$, denoted as TOAB), protecting ligand (thiol), and reducing agent ($NaBH_4$). In a typical synthesis (Fig. 4), gold salt and phase transfer agent are first dissolved in water and toluene, respectively. Under the help of phase transfer agent TOA^+, the gold salt $[AuCl_4]^-$ is transferred from the aqueous phase to the toluene phase. Then thiol is added. The thiol reduces Au(III) into Au(I) to form colorless Au(I)-SR complexes or polymers. Then the reducing agent is added to reduce the Au(I) complex/polymer into gold nanoclusters protected by thiolate. The as-obtained gold nanoclusters are polydispersed, and they should be further subjected to size focusing in the presence of excess thiol and often at high temperature.

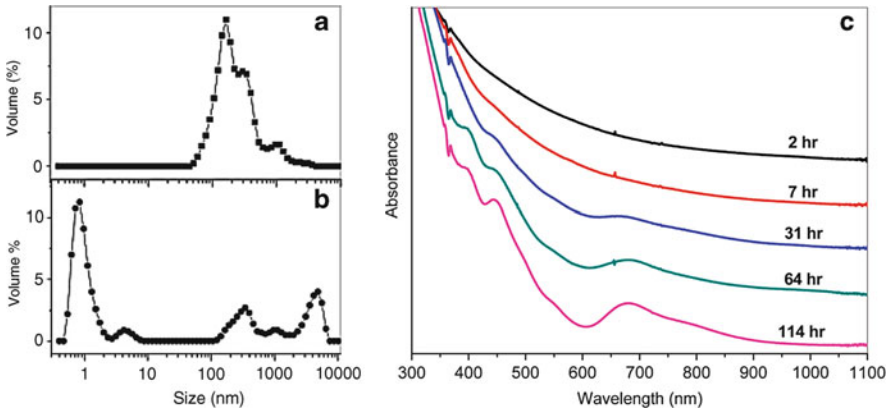

Fig. 5 Size-focusing synthesis of $Au_{25}(SC_2H_4Ph)_{18}$ nanoclusters. (**a**) and (**b**) Dynamic light scattering (DLS) characterization of Au(I)-SR intermediate in the form of aggregates (prepared with and without kinetic control, respectively); (**c**) evolution of the optical spectrum of the crude product with aging time in the presence of excess thiol. Adapted with permission from [38, 62]

Below we illustrate how to tune the initial size range by adjusting the reaction conditions to finally obtain pure gold nanoclusters with well-defined compositions, e.g. $Au_{25}(SC_2H_4Ph)_{18}$, $Au_{38}(SC_2H_4Ph)_{24}$, $Au_{144}(SC_2H_4Ph)_{60}$, and $Au_{333}(SC_2H_4Ph)_{79}$.

4.1.1 The Case of $Au_{25}(SR)_{18}$

Among the reported well-defined $Au_n(SR)_m$ nanoclusters capped by thiolates (*n* and *m* refer to the numbers of gold atoms and thiolate ligands, respectively), the 25-atom $Au_{25}(SR)_{18}$ nanocluster is perhaps the most extensively studied one [3], probably due to its ubiquitous nature in various syntheses. The reported, high yielding synthetic methods include size-conversion [42], two-phase and one-phase methods [38, 62].

In the two-phase synthesis, the size control was performed through kinetic control of the size of the initially formed Au(I)-SR complexes (or polymers). It was found that when mixing gold salt and PhC_2H_4SH thiol under conditions of *0°C and slow stirring*, the subsequent reduction Au(I)-SR (here R = C_2H_4Ph) by $NaBH_4$ and aging resulted in very pure $Au_{25}(SC_2H_4Ph)_{18}$ with high yield [38]. The preliminary study for the high yielding synthesis of $Au_{25}(SC_2H_4Ph)_{18}$ indicated that, under the low temperature and slow stirring conditions, the Au(I)-SR complex grew into aggregates with a unimodal distribution of size about 100–300 nm (Fig. 5a), while without kinetic control the Au(I)-SR complex aggregated randomly (Fig. 5b). The size range of the Au(I)-SR aggregates was found to be quite important for the exclusive formation of $Au_{25}(SC_2H_4Ph)_{18}$ nanoclusters via size focusing, evidenced by the appearance of distinct optical absorption peaks in the crude product's spectrum characteristic of $Au_{25}(SR)_{18}$ nanoclusters [38].

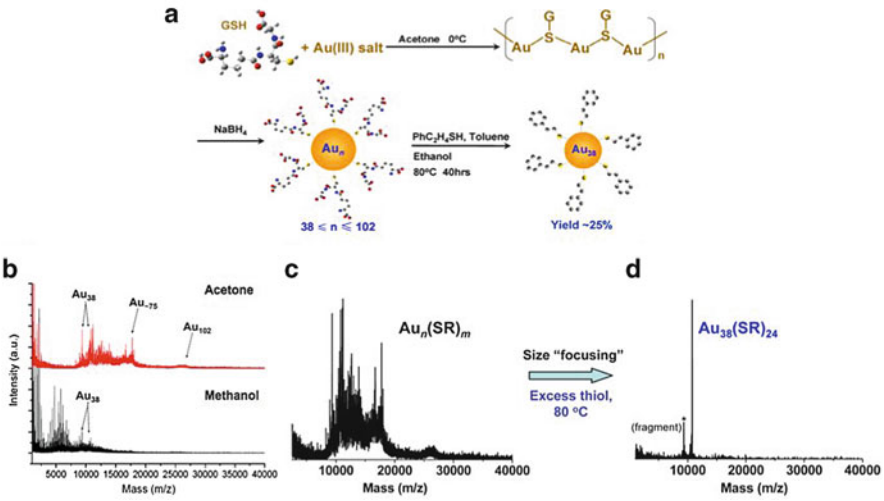

Fig. 6 (**a**) Scheme of the size-focusing synthesis of $Au_{38}(SR)_{24}$ nanoclusters; (**b**) the effect of solvent on the size range of the initial crude gold nanoclusters; (**c**, **d**) illustrate size focusing of polydispersed nanoclusters into pure $Au_{38}(SR)_{24}$. Adapted with permission from [39]

This was indeed the first high yielding synthesis of $Au_{25}(SR)_{18}$ nanoclusters (yield: 40–50%, Au atom basis). Recent work by Liu et al. further demonstrated the importance of controlling Au(I)-SR for the product size [63].

For the one-phase synthesis of $Au_{25}(SC_2H_4Ph)_{18}$, THF was used as the solvent to dissolve reactants $HAuCl_4$, PhC_2H_4SH, and TOABr. After reduction by $NaBH_4$ and spontaneous size focusing in the presence of excess thiol, pure $Au_{25}(SC_2H_4Ph)_{18}$ was obtained [62]. Figure 5c shows the evolution of the absorption spectrum of the product, in which the initial featureless UV-vis spectrum gradually evolved into the well-defined spectrum of $Au_{25}(SC_2H_4Ph)_{18}$. The solvent was found to play an important role in controlling the size distribution of the initial gold nanoclusters [62, 63]. In the THF system, the initially formed gold nanoclusters had a size range smaller than $Au_{\sim 100}$ [64], and further aging led to size focusing of the polydispersed product into single-sized $Au_{25}(SC_2H_4Ph)_{18}$. Different thiolate-ligand-protected $Au_{25}(SR)_{18}$ nanoclusters were also attained following the size-focusing method, where R = C_nH_{2n+1}, G (glutathione), and so on [62].

4.1.2 The Case of $Au_{38}(SR)_{24}$

Another well-known gold nanocluster is the 38-gold-atom cluster protected by 24 thiolate ligands, i.e. $Au_{38}(SR)_{24}$. In the synthesis, the size range of the initial gold nanoclusters was controlled by the solvent (acetone was used) [39]. The initial gold clusters were made by a water-soluble thiol (glutathione). Gold salt was first mixed with glutathione in acetone (Fig. 6a), giving a turbid yellow solution since

glutathione cannot dissolve in acetone. The adding of $NaBH_4$ resulted in the immediate precipitation of gold nanoclusters as glutathione-protected gold nanoclusters cannot dissolve in acetone. The precipitation prevented further growth of the initially formed gold nanoclusters; hence, the size range of glutathione-capped $Au_n(SR)_m$ clusters was controlled in ~38 < n < ~100 (Fig. 6c). The solvent played an important role in this case: if the solvent acetone was replaced by methanol (Fig. 6b), then the initial size range was smaller, probably due to the higher reduction ability of $NaBH_4$ in methanol [6].

The precipitate was collected and redissolved in H_2O. Excess phenylethanethiol (in toluene) was added, forming an organic layer on the top of the H_2O layer, followed by heating to 80°C. The ligand exchange process transferred the gold nanoclusters from the aqueous phase to the toluene phase in which the size focusing occurred. Due to the narrow distribution of the initial gold clusters, $Au_{38}(SR)_{24}$ was obtained as the final, pure product since $Au_{38}(SR)_{24}$ is the most stable species within this range (Fig. 6d). The yield of $Au_{38}(SR)_{24}$ was ~25 % (Au atom basis). Later work by Qian et al. further found the importance of the thermal condition [65]; using the same polydisperse $Au_n(SR)_m$ nanoclusters size focusing at room temperature led to $Au_{25}(SR)_{18}$, while thermal size focusing gave rise to $Au_{38}(SR)_{24}$. Different thiols have been used to make $Au_{38}(SR)_{24}$ nanoclusters [66].

4.1.3 The Case of $Au_{144}(SR)_{60}$

$Au_{144}(SR)_{60}$ constitutes the dominant component in the previously reported polydisperse 29 kDa species which had been studied for a long time [47]. The previous 29 kDa clusters were obtained through solvent fractionation [47] or HPLC separation [47, 48], by which the yield was low, albeit Tsukuda and coworkers obtained pure $Au_{144}(SR)_{59}$ (R = $C_{12}H_{25}$) [48]. Of note, the one-ligand difference (c.f. $Au_{144}(SR)_{60}$) is probably due to the oxidation treatment [48] prior to ESI-MS analysis.

The size-focusing method was applied to the synthesis of $Au_{144}(SR)_{60}$ nanoclusters [40]. This time, the initial size distribution was controlled through tuning the golt salt to thiol ratio (Au/SR). By adjusting the $HAuCl_4$ to PhC_2H_4SH ratio to 1:3, the size range was controlled around 29 kDa, together with some $Au_{25}(SC_2H_4Ph)_{18}$ clusters (Fig. 7a, black profile of mass spectrum). In the size-focusing step, the crude polydispersed clusters were incubated in large amounts of thiol at 80°C, and after 24 h of size focusing pure $Au_{144}(SC_2H_4Ph)_{60}$ was obtained; of note, the initially present $Au_{25}(SC_2H_4Ph)_{18}$ clusters were thermally decomposed during the harsh size-focusing process [40]. The polydispersed clusters show a decay-like UV-vis spectrum (Fig. 7b, black); after size focusing, step-like bands were observed at 510 and 700 nm (Fig. 7b, red). Note that the MALDI-MS spectrum showed a broad peak for pure $Au_{144}(SC_2H_4Ph)_{60}$, this was due to the inevitable fragmentation for large-sized gold nanoclusters in MALDI-MS analysis. In contrast, ESI-MS characterization gave rise to intact cluster ions; thus, the precise formula weight was measured and the $Au_{144}(SC_2H_4Ph)_{60}$ formula was determined (Fig. 7c–e). Au_{144} clusters with different –SR have been reported [67].

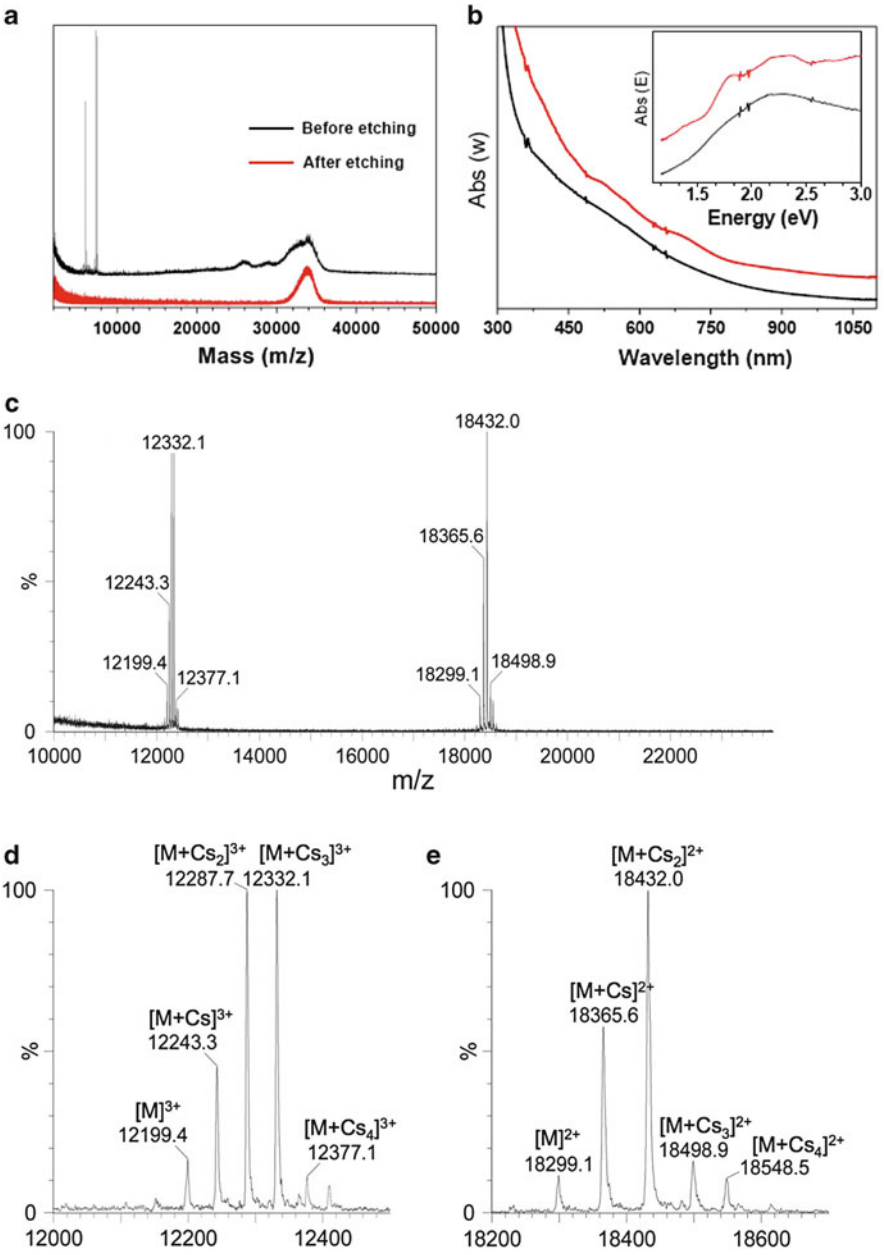

Fig. 7 Size-focusing synthesis of $Au_{144}(SC_2H_4Ph)_{60}$ nanoclusters. (**a**) MALDI of initial and final products of the size-focusing step, (**b**) UV-vis spectra of the initial and final products, (**c**) ESI-MS spectrum, and (**d**) and (**e**) zoom-in peaks (CsOAc was mixed with the clusters to form positively charged adducts for ESI detection). Adapted with permission from [40]

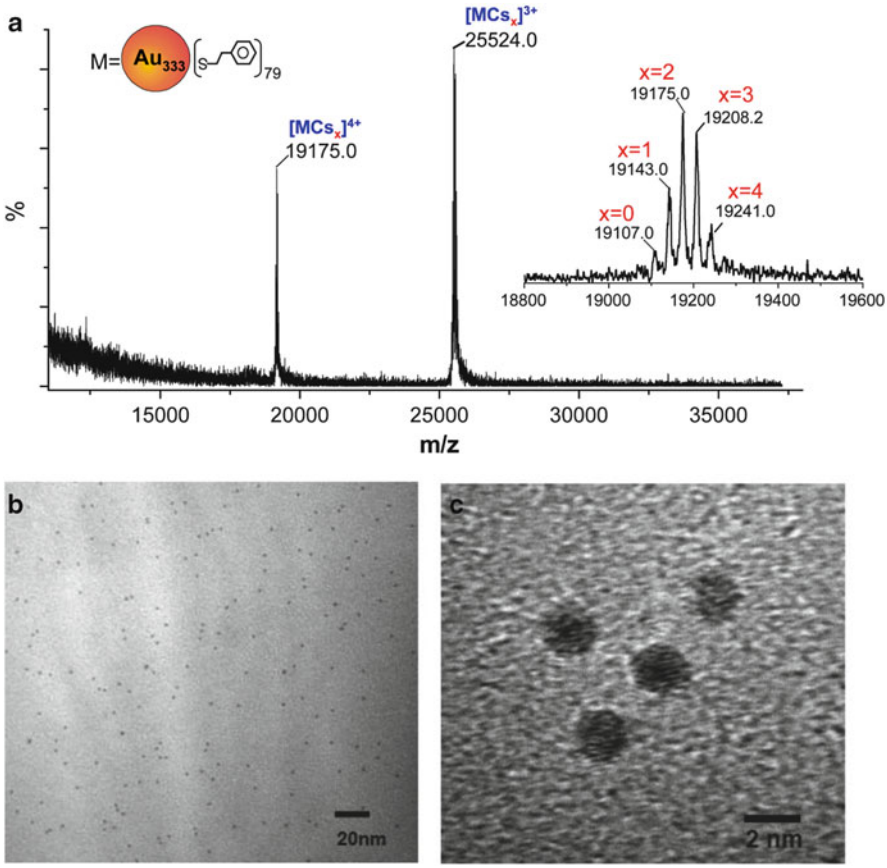

Fig. 8 (**a**) ESI-MS and (**b**) HR-TEM of the $Au_{333}(SC_2H_4Ph)_{79}$ nanoclusters. The *inset* of (**a**) shows the ($M + Cs_x$) adducts. Adapted with permission from [41]

4.1.4 The Case of $Au_{333}(SR)_{79}$

The size-focusing method was extended to the largest ever $Au_{333}(SR)_{79}$ nanocluster [41]. The synthetic protocol of this 2.2 nm atomically precise nanocluster is similar to the case of $Au_{144}(SR)_{60}$. Both cluster precursors were made through the two-phase method, with a major difference in the $HAuCl_4$ to PhC_2H_4SH ratio (i.e., 1:2 in the case of $Au_{333}(SR)_{79}$, instead of 1:3 in $Au_{144}(SR)_{60}$). Figure 8 shows a comparison of ESI-MS and TEM characterization of $Au_{333}(SR)_{79}$ nanoclusters. This giant nanocluster approaches the current detection limit of ESI-MS. New methods should be developed in future work to cope with giant nanoclusters of larger size.

4.2 Other Methods for Atomically Precise Gold Nanoclusters

Besides the ubiquitous $Au_{25}(SR)_{18}$, $Au_{38}(SR)_{24}$, $Au_{144}(SR)_{60}$, and $Au_{333}(SR)_{79}$ nanoclusters, there are increasingly more formulas of atomically precise gold nanoclusters discovered in other works, for example, $Au_{15}(SR)_{13}$, $Au_{18}(SR)_{14}$, $Au_{19}(SR)_{13}$, $Au_{20}(SR)_{16}$, $Au_{24}(SR)_{20}$, $Au_{28}(SR)_{20}$, $Au_{36}(SR)_{24}$, $Au_{40}(SR)_{24}$, $Au_{55}(SR)_{31}$, $Au_{67}(SR)_{35}$, $Au_{102}(SR)_{44}$, $Au_{130}(SR)_{50}$, and $Au_{187}(SR)_{68}$, etc. [4, 11, 12, 49–54, 68–72]. These gold nanoclusters were obtained by different methods.

4.2.1 Post-synthetic Size Separation

The $Au_{15}(SR)_{13}$, $Au_{18}(SR)_{14}$, $Au_{40}(SR)_{24}$, $Au_{55}(SR)_{31}$, $Au_{67}(SR)_{35}$, $Au_{130}(SR)_{50}$, and $Au_{187}(SR)_{68}$ were obtained through post-synthetic size separation step from a mixture of clusters [4, 49–54]. The separation methods such as HPLC, solvent fractionation, and polyacrylamide gel electrophoresis (PAGE) were successfully applied to the separation of gold nanoclusters. The separation is mainly based on the difference in solubility, size, charge state, and other factors among the nanoclusters.

4.2.2 Kinetic Control

Some nanoclusters were obtained through kinetic control, such as $Au_{19}(SR)_{13}$, $Au_{20}(SR)_{16}$, and $Au_{24}(SR)_{20}$ [60, 68, 69]. These clusters were all made by two-phase protocols, with the main difference in the reduction step. For the synthesis of $Au_{19}(SR)_{13}$, a weak-reducing agent borane-tert-butylamine $(CH_3)_3NH_2$-BH_3 (instead of $NaBH_4$) was used to reduce the Au(I)-SR complex, and it was found that the weak-reducing agent plays a key role in obtaining $Au_{19}(SR)_{13}$ [60]. If $NaBH_4$ was used, $Au_{25}(SR)_{18}$ would be the final product; hence, the rate of reduction from Au(I) to Au(0) is important for controlling the final cluster size. Controlling the reduction rate also gave rise to $Au_{20}(SR)_{16}$ [68]. In this case, small amount of $NaBH_4$ (1 equivalent per $HAuCl_4$) was drop-wise added over a 30-min period to reduce the Au(I)SR complex, instead of 10 equivalent of $NaBH_4$ poured into the reaction mixture all at once to synthesize $Au_{25}(SR)_{18}$. For the $Au_{24}(SR)_{20}$, the protocol was the same with $Au_{20}(SR)_{16}$, with the only difference in controlling the reduction process of Au(III) to Au(I) by thiol: for $Au_{20}(SR)_{16}$, the Au(III) to Au(I) reduction was kept stationary, while for the $Au_{24}(SR)_{20}$, the reduction process was kept at a slow stirring speed [69]. The glutathione-protected $Au_{15}(SR)_{13}$ and $Au_{18}(SR)_{14}$ were separated in early work [4] but recently have been individually synthesized through kinetic control [72, 73]. All these examples demonstrate the importance of kinetic control (including the reduction speed, the Au(I)-SR complex form, the type of reducing agent, the amount of reducing agent and adding speed, as well as pH if aqueous solution) in obtaining different-sized gold nanoclusters.

4.2.3 Size Conversion

Very recently, a new ligand-exchange-induced "size-conversion" method has been discovered [11, 12], which may become another universal synthetic methodology for atomically precise nanoclusters other than the size-focusing methodology. The size-conversion method allows one to expand the potpourri or size library of gold nanoclusters. It was found that the structure of the thiolate ligands plays an important role in controlling the size and structure of gold nanoclusters. For example, $Au_{28}(SPh\text{-}t\text{-}Bu)_{20}$ nanoclusters were obtained through ligand exchange of $Au_{25}(SC_2H_4Ph)_{18}$ with the 4-*tert*-butylbenzenethiol (HSPh-*t*-Bu), and similarly $Au_{36}(SPh\text{-}t\text{-}Bu)_{24}$ were obtained through ligand exchange of $Au_{38}(SC_2H_4Ph)_{24}$ [11, 12]. This size-conversion methodology is very effective, with yields larger than 90% in both cases. Mechanistic studies on the $Au_{38}(SC_2H_4Ph)_{24}$ to $Au_{36}(SPh\text{-}t\text{-}Bu)_{24}$ conversion show that the size and structure conversion process was triggered by the geometric bulkiness of –SPh-*t*-Bu thiolate [74]. Based on this size-conversion strategy, a series of *new* sizes of nanoclusters may be obtained in future work using well-defined nanoclusters as the starting materials (as opposed to gold salt as the starting material in direct synthesis).

5 Structures of Gold Nanoclusters

The great progress made in obtaining large amounts of atomically precise gold nanoclusters has led to successful crystallization and structure determination of some of the nanoclusters discussed above. The atomic structures of gold nanoclusters reveal how the gold atoms are assembled in a specific-size metal core and how the surface is protected by ligands. The recent progress in crystallization of gold nanoclusters starts to uncover the mystery and the beauty of nanoclusters [7–12]. Through single-crystal X-ray diffraction, the position of each gold atom in a gold nanocluster can be unambiguously pinned down. The gold atoms of a nanocluster indeed assemble into a variety of highly ordered geometric structures with various symmetries. One would be quite amazed that nature could find so many simple yet elegant ways to assembly atoms into highly stable, versatile structures. It is the versatility of structures of gold nanoclusters that makes the nanocluster research particularly appealing.

Besides the core structure in a ligand-protected gold nanocluster, the surface structure is also of major importance for understanding what determines the stability of the nanocluster. On the surface of the symmetric metal core, nature finds unique ways to arrange the surface ligands for each metal core structure in order to protect the core well. Owing to the specific chemistry between organic ligand and gold, nanoclusters with different types of ligands may have different bonding rules, as different types of organic ligands have different metal–ligand coordination modes, which are reflected in the surface structure of metal nanoclusters. For example,

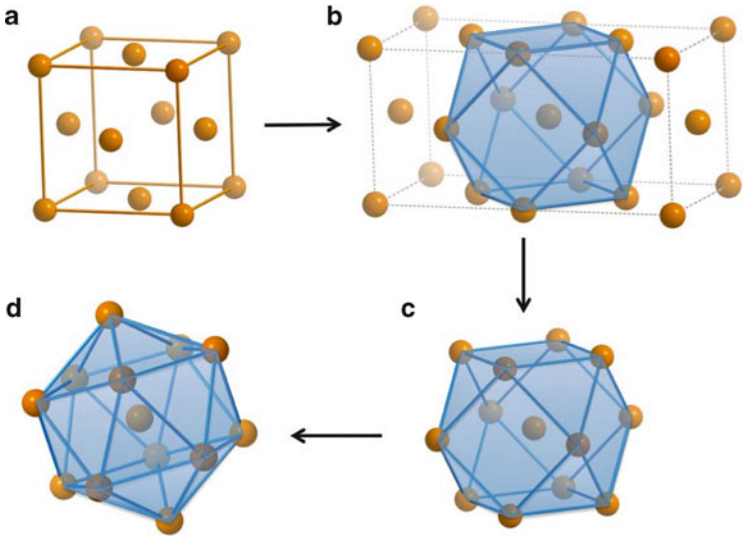

Fig. 9 (**a**) FCC unit cell; (**b** to **c**) construction of cuboctahedron from FCC; (**d**) icosahedron transformed from cuboctahedron by corrugating the middle 6-atom (Au_6) hexagon into a chair-like configuration

phosphine ligands tend to simply adsorb on the surface gold atoms via a one-on-one fashion (terminal bonding) [16–29], while thiolate ligands often form a chain-like structure by incorporating some gold atoms [7–13, 75–81]. The so far revealed surface structure modes [7–13] of gold nanoclusters provide valuable information on how the larger nanoclusters should be stabilized by the thiolate ligand and what factors determine their stability.

The reported structures of thiolate-protected gold nanoclusters can be categorized into FCC and non-FCC types (where FCC: face-centered cubic) [7–13]. Bulk gold adopts an FCC structure (Fig. 9a), and its unit cell comprises 8 vertices and 6 face centers. The 14-atom FCC unit cell is an empty structure (i.e., non-centered), from which a cuboctahedron consisting of 13 atoms can be readily constructed (Fig. 9b). The cuboctahedron is faceted by 6 squares and 8 triangles, and the center atom is coordinated to 12 first-shell atoms. Transformation of the 13-atom cuboctahedron gives rise to a 13-atom icosahedral structure (Fig. 9c, d) [82], which preserves the 12 coordination but the surface becomes exclusively triangular facets (Fig. 9d). Overall, the cuboctahedron is a fragment of FCC, but the icosahedron is not, as the presence of fivefold rotation axis in the icosahedron breaks the cubic symmetry.

Below we first discuss the non-FCC-type structures with increasing size, including $Au_{25}(SC_2H_4Ph)_{18}$, $Au_{38}(SC_2H_4Ph)_{24}$, and $Au_{102}(SPh\text{-}COOH)_{44}$ [7–10]. Examples of FCC structures include $Au_{28}(S\text{-}Ph\text{-}t\text{-}Bu)_{20}$ and $Au_{36}(S\text{-}Ph\text{-}t\text{-}Bu)_{24}$ [11, 12].

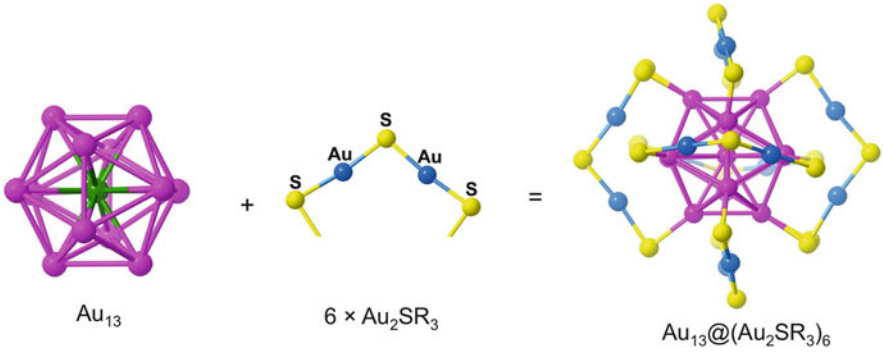

Fig. 10 Total structure of $Au_{25}(SC_2H_4Ph)_{18}$. The carbon tails ($-SC_2H_4Ph$) are omitted for clarity

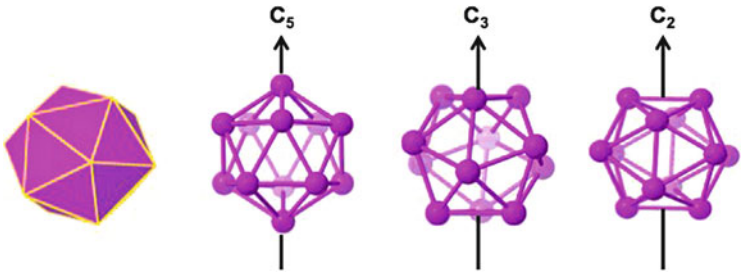

Fig. 11 Symmetry of an icosahedron (the center is removed for clarity)

5.1 Non-FCC Structures of Gold Nanoclusters

5.1.1 The Case of $Au_{25}(SC_2H_4Ph)_{18}$

The $Au_{25}(SC_2H_4Ph)_{18}$ nanocluster possesses a quasi-spherical structure and may be viewed as a kernel-shell structure [8, 9]. A unique feature in thiolate-protected gold nanoclusters is that not all the gold atoms are in the kernel; instead, some gold atoms are incorporated into the ligand shell to protect the kernel. For other organic ligands in the protected gold nanoclusters such as phosphine, simple adsorption bonding mode is seen, and the gold atoms in the formula are all located in the kernel.

There are 13 gold atoms in the kernel of $Au_{25}(SC_2H_4Ph)_{18}$; these 13 gold atoms assemble into a highly symmetric icosahedron, with one gold atom in the center and 12 gold atoms on the 12 vertices of the icosahedron (Fig. 10). The central gold atom forms 12 radial bonds with the outside 12 gold atoms, hence the coordinate number of the central atom is 12, identical with that of bulk gold.

Among the polyhedrons, the icosahedron has the highest symmetry (Fig. 11). It possesses 12 vertices, 30 edges, and 20 equal-lateral triangular faces. It can be viewed as 20 radially packed tetrahedrons sharing a common vertex and three facets

with neighboring tetrahedrons. Six five-fold (C_5) rotation axes can be readily identified on each opposite pair of *vertices*, and fifteen two-fold (C_2) axes on each opposite pair of *edges*, and ten three-fold (C_3) axes on each opposite pair of *faces*. Accordingly, one can have three views of an icosahedron based on its C_2, C_3, or C_5 axis (Fig. 11). If viewed with respect to a C_2 axis, a 2-2-4-2-2 five layers of atoms can be identified (the central atom not considered). Similarly, when viewing from a C_3 axis, there are four layers of atoms 3-3-3-3, and from C_5, there are also four layers of atoms but with a 1-5-5-1 configuration.

The icosahedral Au_{13} kernel is protected by six "V-shaped" –SR-Au-SR-Au-SR–chains or oligomers (Fig. 10). This oligomeric structure is often called a staple motif, because it has two sulfur ends binding two surface gold atoms of the kernel in a way resembling a staple. Based on the number of gold atoms in the chain, there are monomeric staples, dimeric staples, and so on. For example, the six V-shaped staples in $Au_{25}(SR)_{18}$ are called dimeric staples since there are two gold atoms incorporated in the chain. In regard to the distribution of the six dimeric staples on the icosahedron, if one views from the three mutually perpendicular C_2 axes of the icosahedron (Fig. 10), two dimeric staples are seen on the top and the bottom, another two on the front and the back, and two more on the left and the right. Since six staple motifs have 12 sulfur ends, all the 12 surface gold atoms of the Au_{13} icosahedron are protected by the –SR groups. In terms of symmetry, the Au_{13} kernel has the highest I_h symmetry, but the $Au_{25}S_{18}$ skeleton reduces its symmetry to D_{2h}. Following the above anatomy, the $Au_{25}(SC_2H_4Ph)_{18}$ structure may be represented as $Au_{13}@[Au_2(SR)_3]_6$ to illustrate the kernel and the exterior shell.

It should be stressed that the staple gold atoms also interact with the gold atoms of the Au_{13} kernel via face capping, with one shorter Au–Au contact (3.02–3.12 Å) and two longer ones (3.18–3.27 Å) to the other two Au atoms on the face it is capping.

The $Au_{25}(SR)_{18}$ nanocluster can have different, stable charge states (e.g., $q = -1$, 0, +1, etc.) [13, 83–88]. The initially reported $Au_{25}(SR)_{18}$ nanocluster was negatively charged, with a positive counterion $[N(n\text{-}C_8H_{17})_4]^+$ in the unit cell. The negatively charged Au_{25} can be oxidized to neutral $[Au_{25}(SR)_{18}]^0$, and the $Au_{25}S_{18}$ framework is preserved in the neutral $[Au_{25}(SR)_{18}]^0$, with the only difference in that the $[Au_{25}(SR)_{18}]^0$ framework is less distorted than the negatively charged $[Au_{25}(SR)_{18}]^-$ [13]. The $[Au_{25}(SR)_{18}]^0$ is paramagnetic [89], while the $[Au_{25}(SR)_{18}]^-$ and $[Au_{25}(SR)_{18}]^+$ are diamagnetic [84].

5.1.2 The Case of $Au_{38}(SC_2H_4Ph)_{24}$

The $Au_{38}(SC_2H_4Ph)_{24}$ nanocluster possesses an Au_{23} kernel which is composed of two icosahedrons (building blocks) via face-sharing (Fig. 12a) [10]. If we start with one icosahedron (with two opposite triangular faces on the top and the bottom, i.e. the C_3 orientation, see Fig. 11 above), next, place the second icosahedron on the

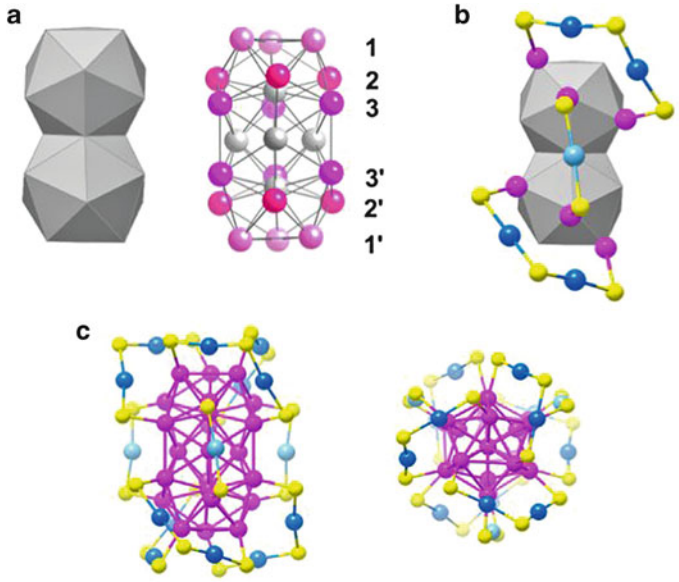

Fig. 12 Total structure of $Au_{38}(SC_2H_4Ph)_{24}$. The carbon tails ($-SC_2H_2Ph$) are omitted for clarity. (**a**) Au_{23} biicosahedral kernel. (**b**) Position of dimeric staples [$Au_2(SR)_3$] and monomeric staple [$Au(SR)_2$]. (**c**) *Side view* and *top view* of the $Au_{38}(SR)_{24}$ total structure. Color labels: *yellow* = sulfur, *other colors* = gold

top of the first one via sharing a triangular face, we obtain a rod-like biicosahedron structure (Fig. 12a). When counting the number of atoms, there are $13 + 13 - 3 = 23$ in this face-sharing biicosahedral structure; of note, face-sharing consumes 3 atoms. This Au_{23} kernel has a D_{3h} symmetry. Among the 23 atoms, 2 atoms are in the icosahedral centers, 3 atoms are used for face-sharing; hence, only 18 atoms are exposed and need protection by thiolate groups.

The 18 surface gold atoms on the biicosahedral kernel are protected by 9 staple motifs, with 3 of them being monomeric staples (–SR-Au-SR–), and the remaining 6 motifs being dimeric staples (–SR-Au-SR-Au-SR–). If viewed from the C_3 axis of the biicosahedral kernel, the 18 surface atoms can be divided into 6 layers (1–3 and mirror imaged 1′–3′, Fig. 12a). Three dimeric staples are located on the top icosahedron, with one end of each dimeric staple pinning down to the atom on layer 1, while the other end pining down on layer 3 (Fig. 12b). The rotary arrangement of the three dimeric staples along the C_3 axis resembles the tri-blades of a fan or propeller [10] (Fig. 12c). The remaining three dimeric staples are located on the bottom icosahedron with the same rotation direction. The three monomeric staples are located on the waist of the biicosahedral kernel, connecting the atoms on the layer 2 and 2′ together, reinforcing the connection between the two icosahedra. The protecting staples reduce the D_{3h} symmetry of the Au_{23} biicosahedral kernel to the D_3 symmetry of the overall $Au_{38}S_{24}$. Similar to the

anatomy of $Au_{25}(SR)_{18}$, the formula of $Au_{38}(SR)_{24}$ may be written as $Au_{23}@[Au(SR)_2]_3[Au_2(SR)_3]_6$, which indicates that Au_{38} nanocluster has a 23-gold-atom kernel protected by three monomeric staples and six dimeric staples.

The $Au_{38}(SR)_{24}$ structure is chiral, as reflected from the rotating arrangement of the dimeric staples. The unit cell of $Au_{38}(SR)_{24}$ nanoclusters indeed contains a pair of enantiomers. The dimeric staples can be arranged in a left-handed or right-handed way, forming two enantiomers of the Au_{38} nanocluster.

5.1.3 The Case of $Au_{102}(SPh\text{-}COOH)_{44}$

$Au_{102}(SR)_{44}$ was the first reported structure of thiolate-protected gold nanoclusters [7]. Its formula may be written as $Au_{79}@[Au(SR)_2]_{19}[Au_2(SR)_3]_2$. The Au_{102} nanocluster possesses a 79-gold-atom kernel. To understand the Au_{79} kernel, we first briefly discuss Marks' decahedron and rhombicosidodecahedron – which are important noncrystalline shapes.

The Marks' decahedron was discovered in early research on the multi-twinned nanoparticles. L. D. Marks found that a special form of decahedron is one of the common low-energy (i.e., stable) shapes for small nanoparticles [90, 91]. A decahedron can be viewed as five tetrahedrons assembled together by sharing a common edge (as the central axis), with each tetrahedron sharing two facets with neighboring tetrahedrons, hence forming a fivefold twinned structure (Fig. 13a). The remaining two facets of each tetrahedron are exposed, composing the total 10 triangular {111} surfaces of the decahedron. By truncating through the five horizontal edges of a decahedron, one obtains an Ino decahedron with additional five {100} facets (Fig. 13b). A Marks' decahedron is a derivative of Ino's decahedron. Marks found that when introducing a reentrant {111} surface at each of the five vertical edges of Ino's decahedron, a more stable decahedron structure can be obtained (Fig. 13c). A Marks' decahedron is denoted by (m, n, p), with m indicating the number of atoms on the equatorial edges, n the number of atoms on the vertical edge, and p the number of atoms on the reentrant edge (Fig. 13d) [44].

The central portion of the Au_{79} kernel of $Au_{102}(SR)_{44}$ is actually a 49-atom Marks' decahedron of (2,1,2). The 49 atoms can be counted as $4 \times 1 + 3 \times 5 + 2 \times 10 + 1 \times 10 = 49$, indicating that there are four atoms at the central axis, 3 atoms at the first pentagon column, 2 atoms on the second, and 1 atom on the third (Fig. 13e).

The Au_{49} Marks' decahedron has *ten* extended {111} facets. In order to reduce the exposed surface area, nature chooses to cover each {111} facet with *three* more atoms (Fig. 14a), giving rise to Au_{79}. The three additional atoms adopt close packing onto the Au_9 triangular {111} facets; hence, there are additional 15 gold atoms on the top of the Au_{49} decahedron and another 15 on the bottom (Fig. 14b), composing an Au_{79} kernel (Fig. 14c). The 15 atoms actually connect together to

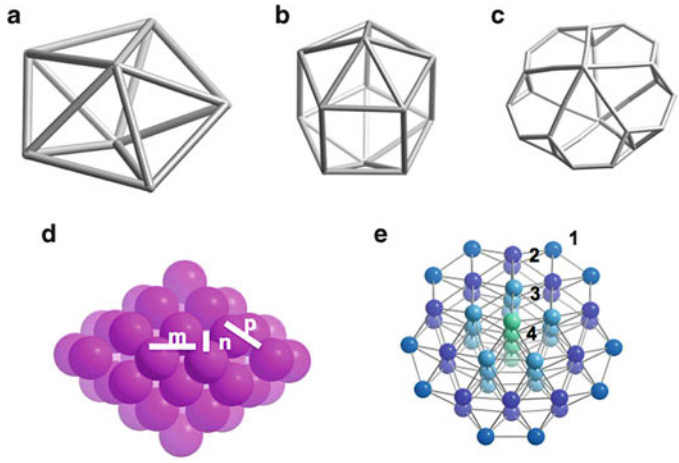

Fig. 13 (**a**–**c**) From decahedron to Ino's decahedron to Marks' decahedron; (**d**) *side view* of a 49-atom Marks' decahedron with (m, n, p) = (2, 1, 2); (**e**) C_5-axis tilted view of a 49-atom Marks' decahedron with numbers indicating the number of atoms in a column

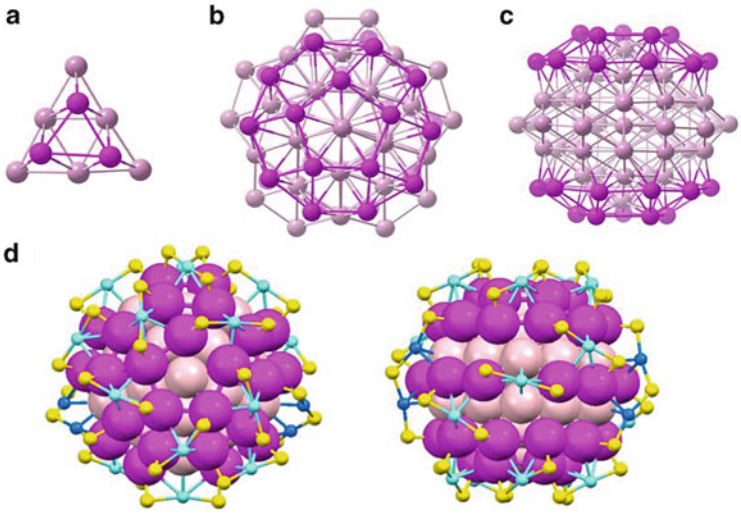

Fig. 14 Total structure of Au_{102}(SPh-*p*-COOH)$_{44}$. The carbon tails (–Ph-*p*-COOH) are omitted for clarity: (**a**–**c**) construction of Au_{79} kernel from Au_{49} Marks' decahedron by face capping; (**b**) *top view* and *side view* of $Au_{102}(SR)_{44}$. Color labels: *yellow* = sulfur, *other colors* = gold

form an umbrella-like structure to cover the top or bottom of the Marks' decahedron (Fig. 14b). It has a pentagon as the central part of the cap (Fig. 14b), five triangles and five squares which surround the pentagon. The two 15-atom caps are actually part of a rhombicosidodecahedron [92].

The addition of the two cap structures to the Marks' Au_{49} decahedron makes the kernel more vertex-exposing, instead of face-exposing. By doing so, the kernel provides more footholds for the thiolate staples to anchor on the surface. Together with the 10 atoms on the equator of the Marks' decahedron, there are 40 atoms total exposed on the surface. Each monomeric staple (–SR-Au-SR–) binds to a square of the rhombicosidodecahedron cap (Fig. 14d). Hence, there are 5 monomeric staples on the top of the 79-atom kernel and another 5 on the bottom. The other 9 monomeric staples together with 2 dimeric staples are distributed on the waist of the kernel. Of note, $Au_{102}(SR)_{24}$ is chiral due to the rotary arrangement of the staples.

5.2 FCC Structures

The prevalence of icosahedral structures in nanoclusters led researchers to conclude that FCC structures would not exist in gold-thiolate nanoclusters. However, recent work by Zeng et al. has successfully attained two FCC-structured nanoclusters, including Au_{28}(SPh-*t*-Bu)$_{20}$ and Au_{36}(SPh-*t*-Bu)$_{24}$ [11, 12]. This breaks the earlier thought that non-FCC icosahedral structures would be more stable than FCC-related cuboctahedral structures [44].

5.2.1 The Case of Au_{28}(SPh-*t*-Bu)$_{20}$

The Au_{28}(SPh-*t*-Bu)$_{20}$ nanocluster was converted from $[Au_{25}(SC_2H_4Ph)_{18}]^-TOA^+$ (where TOA = $^+N(n\text{-}C_8H_{17})_4$) by reaction with excess 4-*tert*-butylbenzenethiol (HSPh-*t*-Bu, TBBT) at 80°C [12]. Interestingly, the structure of $Au_{28}(SR)_{24}$ is significantly different from that of $Au_{25}(SR)_{18}$. The $Au_{28}(SR)_{20}$ nanocluster possesses a cuboctahedron-based kernel, while the kernel of $Au_{25}(SR)_{18}$ is an icosahedron.

$Au_{28}(SR)_{20}$ has a rod-like Au_{20} kernel, which is composed of two interpenetrating cuboctahedra (Fig. 15a, c) [12]. The two cuboctahedra share six gold atoms; hence, the number of gold atoms in the kernel is 13 + 13 − 6 = 20. This Au_{20} kernel can be viewed as a fragment of the bulk FCC structure. It exhibits layer-by-layer atomic planes; Fig. 15b indicates {111} planes marked as **a**-**b**-**c**. Besides, the Au_{20} kernel is enclosed by well-defined crystal planes: four isosceles-trapezoid-shaped {111} facets on the front and back (Fig. 15d, blue shadowed) and two rectangular-shaped {100} faces on the top and bottom (Fig. 15d, yellow shadowed). The Au_{20} kernel adopts quasi-D_{2h} symmetry.

The thiolate-protecting modes in the $Au_{28}(SR)_{20}$ structure comprise two types. First, four dimeric staples protecting the four {111} facets on the front and back sides of the Au_{20} rod, arranged in a rotating fashion (Fig. 16a). Besides, eight simple bridging thiolates can be identified, each residing on an edge of a square (i.e. {100} facet), as shown in Fig. 16b. The bridging thiolate mode was first identified in the FCC-based Au_{36}(SPh-*t*-Bu)$_{24}$ (vide infra) [11], and seems to be unique in the FCC

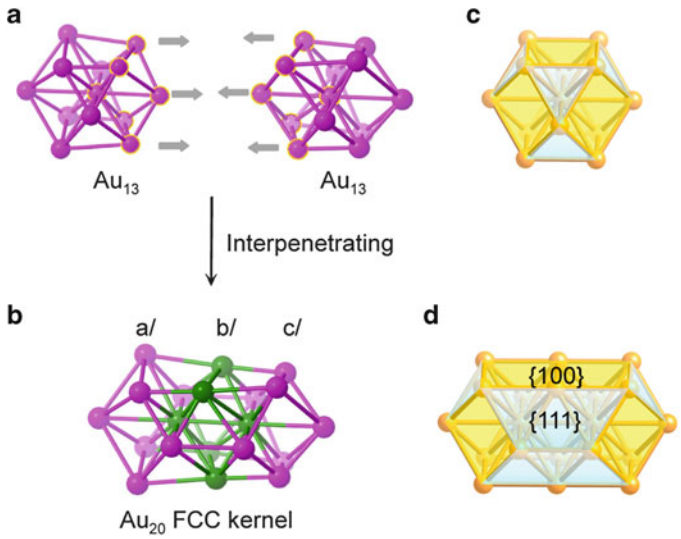

Fig. 15 (**a**, **b**) The Au_{20} kernel structure in $Au_{28}(SPh\text{-}t\text{-}Bu)_{20}$; (**c**, **d**) models of cuboctahedron and interpenetrated bicuboctahedron [12]

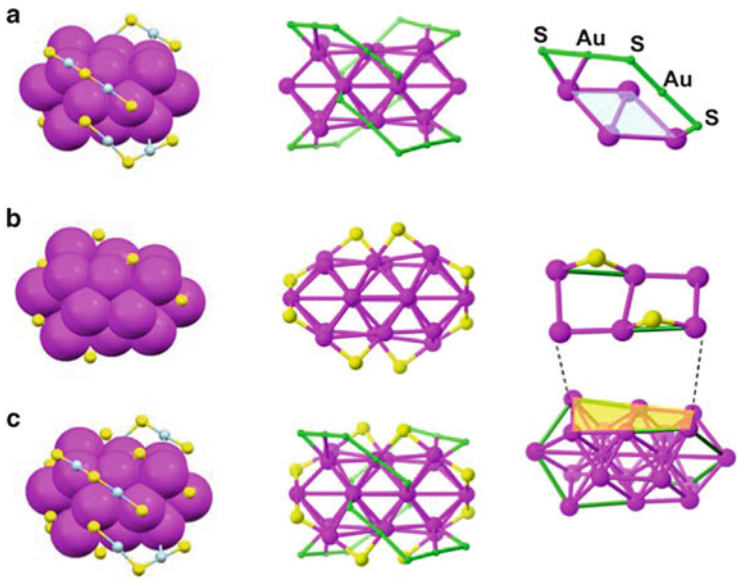

Fig. 16 Thiolate-binding modes in $Au_{28}(SPh\text{-}t\text{-}Bu)_{20}$: (**a**) dimeric staples (total: four); (**b**) bridging thiolates (total: eight); (**c**) overall $Au_{28}S_{20}$ framework. (Color labels: *magenta* = Au atoms in the kernel, *blue* = Au in dimeric staples, *yellow* = sulfur, the four dimeric staples are highlighted in *green* in panels **a** and **c**)

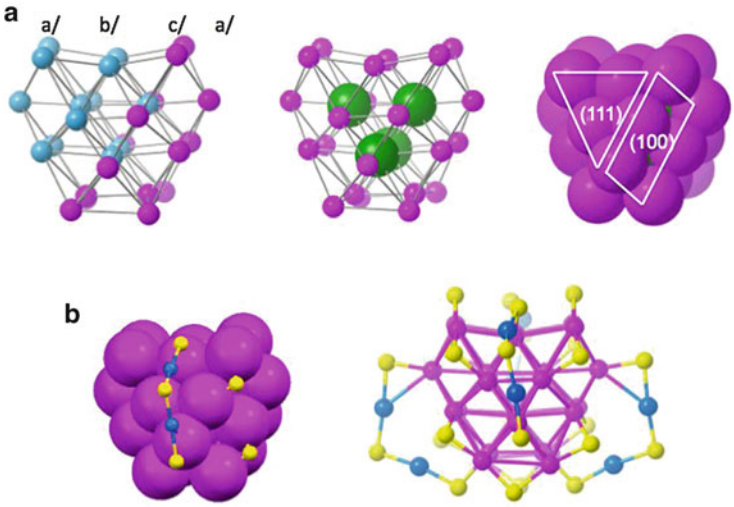

Fig. 17 Total structure of $Au_{36}(SPh\text{-}t\text{-}Bu)_{24}$. The carbon tails (–Ph-*t*-Bu) are omitted for clarity. (**a**) The view of kernel structure based on polyhedron fusion and shell-by-shell mode, respectively. (**b**) Surface thiolate-protecting modes and the total structure of $Au_{36}(SR)_{24}$ [11]. Color labels: *yellow* = sulfur, all the *other colors* are gold atoms

structure. The overall structure of $Au_{28}(SR)_{20}$ has a quasi-D_2 symmetry (Fig. 16c). The formula of $Au_{28}(SR)_{20}$ may be represented as $Au_{20}[Au_2(SR)_3]_4(SR)_8$. Note that the structure of $Au_{28}(SR)_{20}$ is also chiral as the case in $Au_{38}(SR)_{24}$ and $Au_{102}(SR)_{44}$, due to the rotation arrangement of the dimeric staples and bridging thiolates. A pair of enantiomers exists in the unit cell of the $Au_{28}(SR)_{24}$ single crystals.

5.2.2 The Case of $Au_{36}(SPh\text{-}t\text{-}Bu)_{24}$

The $Au_{36}(SPh\text{-}t\text{-}Bu)_{24}$ nanocluster was converted from $Au_{38}(C_2H_4Ph)_{24}$ by reaction with excess HSPh-*t*-Bu at 80°C [11]. It has a 28-gold-atom kernel. Unlike the icosahedron-based kernel in the $Au_{38}(SR)_{24}$ nanocluster, the 28-gold-atom kernel in Au_{36} is based on cuboctahedral building blocks and thus can be viewed as a fragment of the FCC structure. From the view of polyhedron fusion, the Au_{28} kernel is composed of four interpenetrating cuboctahedra, with two cuboctahedra on the top, the other two on the bottom (Fig. 17a). The four center atoms of the four cuboctahedra assemble into a tetrahedron. The other way to appreciate the kernel is to view it as a two-shelled structure. In the center of Au_{28} kernel, four gold atoms pack into an Au_4 tetrahedron. Onto each facet of the Au_4 tetrahedron, a six-atom Au_6 triangle is close-packed. Hence, there are 24 gold atoms on the second shell, forming a vertex/edge-truncated tetrahedron. Since this Au_{28} kernel has an FCC structure, one can identify **a-b-c-a** cubic-close-packing layers (Fig. 17a). The Au_{28} gold kernel exposes four {111} and six {100} facets. The four {111} facets

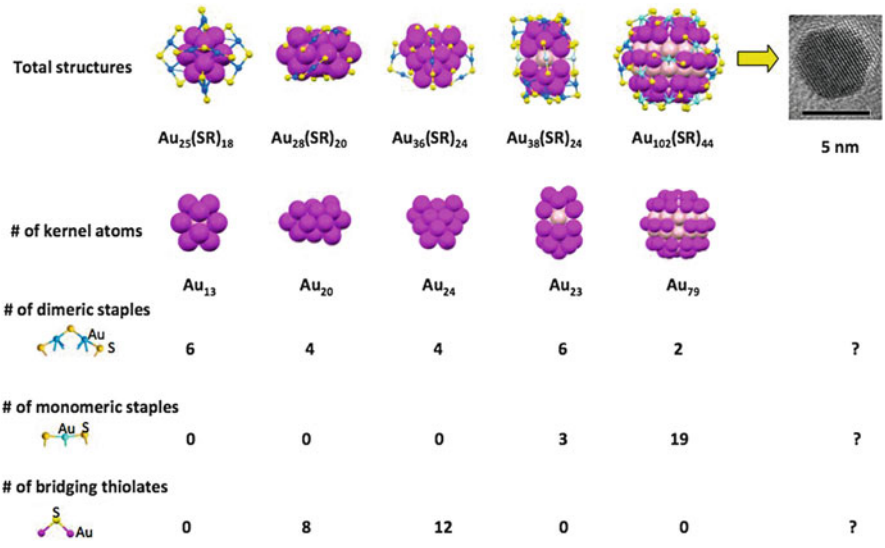

Fig. 18 Structural evolution of $Au_n(SR)_m$ nanoclusters

constitute the four faces of the truncated tetrahedral Au_{28} kernel, and six {100} facets on the six edges of the tetrahedron.

The Au_{28} kernel is protected by four dimeric staples (–SR-Au-SR-Au-SR–) and twelve bridging thiolates (–SR–). Each of the four dimeric staples protects one {111} facet (Fig. 17b). On each {100} facet (comprising two squares), two bridging thiolates can be identified (Fig. 17b). The $Au_{36}S_{24}$ framework has an overall D_{2h} symmetry and is *achiral*. With the above analysis, the formula of $Au_{36}(SR)_{24}$ may be represented as $Au_{28}[Au_2(SR)_3]_4(SR)_{12}$ to illustrate the partition of gold atoms in the kernel and surface of the cluster.

6 Summary

The above discussed nanocluster structures are summarized in Fig. 18, in which one can see the evolution or general trend of structural features with increasing size. Particularly interesting questions are: what structures in terms of kernel and staple motifs would be adopted in smaller nanoclusters ($n < 25$)? What structures would the intermediate-size ($38 < n < 102$) and larger nanoclusters ($n > 102$) exhibit? Future work is expected to reveal more structures and systematic structural rules may be formulated.

Other than the structures of nanoclusters, the electronic and optical properties of such nanoclusters remain to pursue in future work. For example, $Au_n(SR)_m$ nanoclusters are found to be fluorescent but the quantum yields are quite low (up to a few percent). What factors govern the photoluminescence properties? Is it possible to largely enhance the luminescence?

The biggest question in the field is what factors determine the stability of gold nanoclusters. As briefly discussed above, the geometric and electronic effects are two important aspects. Significant research is still needed to elucidate the stability mechanism. The electron-shell closing is not sufficient. For example, even for the well known $[Au_{25}(SR)_{18}]^-$, which has a formal electron count of 8e and thus satisfies electron-shell closing (i.e., $1S^21P^6$), and one expects that the cluster would hold the 8e tight and exhibit the least reactivity (like the Ne atom of $2s^22p^6$), but we found that $[Au_{25}(SR)_{18}]^-$ readily reacts with O_2 and loses one electron, forming $[Au_{25}(SR)_{18}]^0$ with an open electron-shell ($1S^21P^5$, i.e. radical) [13, 89]. We feel that the geometric factor is more important than the electronic factor in deciding the structural stability. Future work will shed more light on this and other major scientific questions of metal nanoclusters.

Acknowledgments We acknowledge financial support from the Air Force Office of Scientific Research under AFOSR Award No. FA9550-11-1-9999 (FA9550-11-1-0147) and the Camille Dreyfus Teacher-Scholar Awards Program.

References

1. Jin R, Cao Y, Mirkin CA, Kelly KL, Schatz GC, Zheng JG (2001) Photoinduced conversion of silver nanospheres to nanoprisms. Science 294:1901–1903
2. Jin R (2010) Quantum sized thiolate-protected gold nanoclusters. Nanoscale 2:343–362
3. Qian H, Zhu M, Wu Z, Jin R (2012) Quantum sized gold nanoclusters with atomic precision. Acc Chem Res 45:1470
4. Negishi Y, Nobusada K, Tsukuda T (2005) Glutathione-protected gold clusters revisited: bridging the gap between gold(I)-thiolate complexes and thiolate-protected gold nanocrystals. J Am Chem Soc 127:5261–5270
5. Tracy JB, Crowe MC, Parker JF, Hampe O, Fields-Zinna CA, Dass A, Murray RW (2007) Electrospray ionization mass spectrometry of uniform and mixed monolayer nanoparticles: $Au_{25}[S(CH_2)_2Ph]_{18}$ and $Au_{25}[S(CH_2)_2Ph]_{18-x}(SR)_x$. J Am Chem Soc 129:16209–16215
6. Qian H, Zhu M, Andersen UN, Jin R (2009) Facile, large-scale synthesis of dodecanethiol-stabilized Au_{38} clusters. J Phys Chem A 113:4281–4284
7. Jadzinsky PD, Calero G, Ackerson CJ, Bushnell DA, Kornberg RD (2007) Structure of a thiol monolayer-protected gold nanoparticle at 1.1Å resolution. Science 318:430–433
8. Heaven MW, Dass A, White PS, Holt KM, Murray RW (2008) Crystal structure of the gold nanoparticle $[N(C_8H_{17})_4][Au_{25}(SCH_2CH_2Ph)_{18}]$. J Am Chem Soc 130:3754–3755
9. Zhu M, Aikens CM, Hollander FJ, Schatz GC, Jin R (2008) Correlating the crystal structure of a thiol-protected Au_{25} cluster and optical properties. J Am Chem Soc 130:5883–5885
10. Qian H, Eckenhoff WT, Zhu Y, Pintauer T, Jin R (2010) Total structure determination of thiolate-protected Au_{38} nanoparticles. J Am Chem Soc 132:8280–8281
11. Zeng C, Qian H, Li T, Li G, Rosi NL, Yoon B, Barnett RN, Whetten RL, Landman U, Jin R (2012) Total structure and electronic properties of the gold nanocrystal $Au_{36}(SR)_{24}$. Angew Chem Int Ed 51:13114–13118
12. Zeng C, Li T, Das A, Rosi NL, Jin R (2013) Chiral structure of thiolate-protected 28-Gold-atom nanocluster determined by X-ray crystallography. J Am Chem Soc 135:10011–10013
13. Zhu M, Eckenhoff WT, Pintauer T, Jin R (2008) Conversion of anionic $[Au_{25}(SCH_2CH_2Ph)_{18}]^-$ cluster to charge neutral cluster via air oxidation. J Phys Chem C 112:14221–14224

14. Wu Z, Gayathri C, Gil RR, Jin R (2009) Probing the structure and charge state of glutathione-capped $Au_{25}(SG)_{18}$ clusters by NMR and mass spectrometry. J Am Chem Soc 131:6535–6542
15. Qian H, Zhu M, Gayathri C, Gil RR, Jin R (2011) Chirality in gold nanoclusters probed by NMR spectroscopy. ACS Nano 5:8935–8942
16. McPartlin M, Mason R, Malatesta L (1969) Novel cluster complexes of gold(0)-gold(I). J Chem Soc D 334–334
17. Briant CE, Theobald BRC, White JW, Bell LK, Mingos DMP, Welch AJ (1981) Synthesis and X-ray structural characterization of the centred icosahedral gold cluster compound $[Au_{13}(PMe_2Ph)_{10}Cl_2](PF_6)_3$; the realization of a theoretical prediction. J Chem Soc Chem Commun 201–202
18. Schmid G, Pfeil R, Boese R, Bandermann F, Meyer S, Calis GHM, Vandervelden WA (1981) $Au_{55}[P(C_6H_5)_3]_{12}Cl_6$ − a gold cluster of an exceptional size. Chem Ber 114:3634–3642
19. Teo BK, Shi XB, Zhang H (1992) Pure gold cluster of 1:9:9:1:9:9:1 layered structure: a novel 39-metal-atom cluster $[(Ph_3P)_{14}Au_{39}Cl_6]Cl_2$ with an interstitial gold atom in a hexagonal antiprismatic cage. J Am Chem Soc 114:2743–2745
20. Teo BK, Shi X, Zhang H (1991) Cluster of clusters. structure of a novel gold-silver cluster $[(Ph_3P)_{10}Au_{13}Ag_{12}Br_8](SbF_6)$ containing an exact staggered-eclipsed-staggered metal configuration. Evidence of icosahedral units as building blocks. J Am Chem Soc 113: 4329–4331
21. Boon KT, Hong MC, Hong Z, Huang DB (1987) Cluster of clusters: structure of the 37-atom cluster $[(p\text{-}Tol_3P)_{12}Au_{18}Ag_{19}Br_{11}]^{2+}$ and a novel series of supraclusters based on vertex-sharing icosahedra. Angew Chem Int Ed 26:897–900
22. Teo BK, Shi X, Zhang H (1993) Clusters of clusters. 25. Synthesis and structure of a new [gold-silver]-38-metal-atom cluster $[(Ph_3P)_{14}Au_{18}Ag_{20}Cl_{12}]Cl_2$ and its implications with regard to intracavity chemistry on metal cluster surfaces. Inorg Chem 32:3987–3988
23. Tran NT, Powell DR, Dahl LF (2000) Nanosized $Pd_{145}(CO)_x(PEt_3)_{30}$ containing a capped three-shell 145-atom metal-core geometry of pseudo icosahedral symmetry. Angew Chem Int Ed 39:4121–4125
24. Tran NT, Dahl LF (2003) Nanosized $[Pd_{69}(CO)_{36}(PEt_3)_{18}]$: metal-core geometry containing a linear assembly of three face-sharing centered Pd_{33} icosahedra inside of a hexagonal-shaped Pd_{30} tube. Angew Chem Int Ed 42:3533–3537
25. Mednikov EG, Ivanov SA, Slovokhotova IV, Dahl LF (2005) Nanosized $[Pd_{52}(CO)_{36}(PEt_3)_{14}]$ and $[Pd_{66}(CO)_{45}(PEt_3)_{16}]$ clusters based on a hypothetical Pd_{38} vertex-truncated ν_3 octahedron. Angew Chem Int Ed 44:6848–6854
26. Mednikov EG, Dahl LF (2008) Nanosized $Pd_{37}(CO)_{28}\{P(p\text{-}Tolyl)_3\}_{12}$ containing geometrically unprecedented central 23-atom interpenetrating tri-icosahedral palladium kernel of double icosahedral units: its postulated metal-core evolution and resulting stereochemical implications. J Am Chem Soc 130:14813–14821
27. Shichibu Y, Konishi K (2010) HCl-induced nuclearity convergence in diphosphine-protected ultrasmall gold clusters: a novel synthetic route to "Magic-Number" Au_{13} clusters. Small 6:1216–1220
28. Pettibone JM, Hudgens JW (2011) Gold cluster formation with phosphine ligands: etching as a size-selective synthetic pathway for small clusters? ACS Nano 5:2989–3002
29. Wan X-K, Lin Z-W, Wang Q-M (2012) Au_{20} nanocluster protected by hemilabile phosphines. J Am Chem Soc 134:14750–14752
30. Shichibu Y, Negishi Y, Watanabe T, Chaki NK, Kawaguchi H, Tsukuda T (2007) Biicosahedral gold clusters $[Au_{25}(PPh_3)_{10}(SC_nH_{2n+1})_5Cl_2]^{2+}$ (n = 2-18): a stepping stone to cluster-assembled materials. J Phys Chem C 111:7845–7847
31. Qian H, Eckenhoff WT, Bier ME, Pintauer T, Jin R (2011) Crystal structures of Au_2 complex and Au_{25} nanocluster and mechanistic insight into the conversion of polydisperse nanoparticles into monodisperse Au_{25} nanoclusters. Inorg Chem 50:10735–10739
32. Das A, Li T, Nobusada K, Zeng Q, Rosi NL, Jin R (2012) Total structure and optical properties of a phosphine/thiolate-protected Au_{24} nanocluster. J Am Chem Soc 134:20286–20289

33. Yang H, Wang Y, Lei J, Shi L, Wu X, Mäkinen V, Lin S, Tang Z, He J, Häkkinen H, Zheng L, Zheng N (2013) Ligand-stabilized $Au_{13}Cu_x$ (x = 2, 4, 8) bimetallic nanoclusters: ligand engineering to control the exposure of metal sites. J Am Chem Soc 135:9568–9571
34. Brust M, Walker M, Bethell D, Schiffrin DJ, Whyman R (1994) Synthesis of thiol-derivatized gold nanoparticles in a two-phase liquid-liquid system. J Chem Soc Chem Commun 7:801–802
35. Whetten RL, Khoury JT, Alvarez MM, Murthy S, Vezmar I, Wang ZL, Stephens PW, Cleveland CL, Luedtke WD, Landman U (1996) Nanocrystal Gold Molecules. Adv Mater 8: 428–433
36. Alvarez MM, Khoury JT, Schaaff TG, Shafigullin MN, Vezmar I, Whetten RL (1997) Optical absorption spectra of nanocrystal gold molecules. J Phys Chem B 101:3706–3712
37. Jin R, Qian H, Wu Z, Zhu Y, Zhu M, Mohanty A, Garg N (2010) Size focusing: a methodology for synthesizing atomically precise gold nanoclusters. J Phys Chem Lett 1:2903–2910
38. Zhu M, Lanni E, Garg N, Bier ME, Jin R (2008) Kinetically controlled, high-yield synthesis of Au_{25} clusters. J Am Chem Soc 130:1138–1139
39. Qian H, Zhu Y, Jin R (2009) Size-focusing synthesis, optical and electrochemical properties of monodisperse $Au_{38}(SC_2H_4Ph)_{24}$ nanoclusters. ACS Nano 3:3795–3803
40. Qian H, Jin R (2009) Controlling nanoparticles with atomic precision: the case of $Au_{144}(SCH_2CH_2Ph)_{60}$. Nano Lett 9:4083–4087
41. Qian H, Zhu Y, Jin R (2012) Atomically precise gold nanocrystal molecules with surface plasmon resonance. Proc Natl Acad Sci U S A 109:696–700
42. Shichibu Y, Negishi Y, Tsukuda T, Teranishi T (2005) Large-scale synthesis of thiolated Au_{25} clusters via ligand exchange reactions of phosphine-stabilized Au_{11} clusters. J Am Chem Soc 127:13464–13465
43. Nimmala PR, Dass A (2011) $Au_{36}(SPh)_{23}$ nanomolecules. J Am Chem Soc 133:9175–9177
44. Cleveland CL, Landman U, Schaaff TG, Shafigullin MN, Stephens PW, Whetten RL (1997) Structural evolution of smaller gold nanocrystals: the truncated decahedral motif. Phys Rev Lett 79:1873–1876
45. Schaaff TG, Shafigullin MN, Khoury JT, Vezmar I, Whetten RL, Cullen WG, First PN, Gutierrez-Wing C, Ascensio J, Jose-Yacaman MJ (1997) Isolation of smaller nanocrystal au molecules: robust quantum effects in optical spectra. J Phys Chem B 101:7885–7891
46. Schaaff TG, Knight G, Shafigullin MN, Borkman RF, Whetten RL (1998) Isolation and selected properties of a 10.4 kDa gold: glutathione cluster compound. J Phys Chem B 102: 10643–10646
47. Schaaff TG, Shafigullin MN, Khoury JT, Vezmar I, Whetten RL (2001) Properties of a ubiquitous 29 kDa Au: SR cluster compound. J Phys Chem B 105:8785–8796
48. Chaki NK, Negishi Y, Tsunoyama H, Shichibu Y, Tsukuda T (2008) Ubiquitous 8 and 29 kDa Gold:Alkanethiolate cluster compounds: mass-spectrometric determination of molecular formulas and structural implications. J Am Chem Soc 130:8608–8610
49. Tsunoyama H, Negishi Y, Tsukuda T (2006) Chromatographic isolation of "Missing" Au_{55} clusters protected by alkanethiolates. J Am Chem Soc 128:6036–6037
50. Qian H, Zhu Y, Jin R (2010) Isolation of ubiquitous $Au_{40}(SR)_{24}$ clusters from the 8 kDa gold clusters. J Am Chem Soc 132:4583–4585
51. Knoppe S, Boudon J, Dolamic I, Dass A, Burgi T (2011) Size exclusion chromatography for semipreparative scale separation of $Au_{38}(SR)_{24}$ and $Au_{40}(SR)_{24}$ and larger clusters. Anal Chem 83:5056–5061
52. Qian H, Jin R (2011) Synthesis and electrospray mass spectrometry determination of thiolate-protected $Au_{55}(SR)_{31}$ nanoclusters. Chem Comm 47:11462–11464
53. Negishi Y, Sakamoto C, Ohyama T, Tsukuda T (2012) Synthesis and the origin of the stability of thiolate-protected Au_{130} and Au_{187} clusters. J Phys Chem Lett 3:1624–1628
54. Nimmala PR, Yoon B, Whetten RL, Landman U, Dass A (2013) $Au_{67}(SR)_{35}$ nanomolecules: characteristic size-specific optical, electrochemical, structural properties and first-principles theoretical analysis. J Phys Chem A 117:504–517

55. Schaaff TG, Whetten RL (1999) Controlled etching of Au:SR cluster compounds. J Phys Chem B 103:9394–9396
56. Sakai N, Tatsuma T (2010) Photovoltaic properties of glutathione-protected gold clusters adsorbed on TiO_2 electrodes. Adv Mater 22:3185–3188
57. Sexton JZ, Ackerson CJ (2010) Determination of rigidity of protein bound Au_{144} clusters by electron cryomicroscopy. J Phys Chem C 114:16037–16042
58. Wu Z, Wang M, Yang J, Zheng X, Cai W, Meng G, Qian H, Wang H, Jin R (2012) Well-defined nanoclusters as fluorescent nanosensors: a case study on $Au_{25}(SG)_{18}$. Small 8:2028–2035
59. Li G, Jin R (2013) Atomically precise gold nanoclusters as new model catalysts. Acc Chem Res 46:1749–1758
60. Wu Z, MacDonald M, Chen J, Zhang P, Jin R (2011) Kinetic control and thermodynamic selection in the synthesis of atomically precise gold nanoclusters. J Am Chem Soc 133: 9670–9673
61. Akola J, Walter M, Whetten RL, Häkkinen H, Grönbeck H (2008) On the structure of thiolate-protected Au_{25}. J Am Chem Soc 130:3756–3757
62. Wu Z, Suhan J, Jin R (2009) One-pot synthesis of atomically monodisperse, thiol-functionalized Au_{25} nanoclusters. J Mater Chem 19:622–626
63. Liu C, Li G, Pang G, Jin R (2013) Toward understanding the growth mechanism of $Au_n(SR)_m$ nanoclusters: effect of solvent on cluster size. RSC Adv 3:9778–9784
64. Dharmaratne AC, Krick T, Dass A (2009) Nanocluster size evolution studied by mass spectrometry in room temperature $Au_{25}(SR)_{18}$ synthesis. J Am Chem Soc 131:13604–13605
65. Qian H, Liu C, Jin R (2012) Controlled growth of molecularly pure $Au_{25}(SR)_{18}$ and $Au_{38}(SR)_{24}$ nanoclusters from the same polydispersed crude product. Sci China Chem 55: 2359–2365
66. Stellwagen D, Weber A, Bovenkamp GL, Jin R, Bitter JH, Kumar CSSR (2012) Ligand control in thiol stabilized Au_{38} clusters. RSC Adv 2:2276–2283
67. Qian H, Jin R (2011) Ambient synthesis of $Au_{144}(SR)_{60}$ nanoclusters in methanol. Chem Mater 23:2209–2217
68. Zhu M, Qian H, Jin R (2009) Thiolate-protected Au_{20} clusters with a large energy gap of 2.1 eV. J Am Chem Soc 131:7220–7221
69. Zhu M, Qian H, Jin R (2010) Thiolate-protected $Au_{24}(SC_2H_4Ph)_{20}$ nanoclusters: superatoms or not? J Phys Chem Lett 1:1003–1007
70. Levi-Kalisman Y, Jadzinsky PD, Kalisman N, Tsunoyama H, Tsukuda T, Bushnell DA, Kornberg RD (2011) Synthesis and characterization of Au_{102}(p-MBA)$_{44}$ nanoparticles. J Am Chem Soc 133:2976–2983
71. Xu Q, Wang S, Liu Z, Xu G, Meng X, Zhu M (2013) Synthesis of selenolate-protected $Au_{18}(SeC_6H_5)_{14}$ nanoclusters. Nanoscale 5:1176–1182
72. Yu Y, Chen X, Yao Q, Yu Y, Yan N, Xie J (2013) Scalable and precise synthesis of thiolated $Au_{10–12}$, Au_{15}, Au_{18}, and Au_{25} nanoclusters via pH controlled CO reduction. Chem Mater 25: 946–952
73. Ghosh A, Udayabhaskararao T, Pradeep T (1997–2002) One-step route to luminescent $Au_{18}SG_{14}$ in the condensed phase and its closed shell molecular ions in the gas phase. J Phys Chem Lett 2012:3
74. Zeng C, Liu C, Pei Y, Jin R (2013) Thiol ligand-induced transformation of $Au_{38}(SC_2H_4Ph)_{24}$ to Au_{36}(SPh-*t*-Bu)$_{24}$. ACS Nano 7:6138–6145
75. Whetten RL, Price RC (2007) Nano-golden order. Science 318:407–408
76. Jiang D, Tiago ML, Luo W, Dai S (2008) The "Staple" Motif: a key to stability of thiolate-protected gold nanoclusters. J Am Chem Soc 130:2777–2779
77. Pei Y, Gao Y, Zeng XC (2008) Structural prediction of thiolate-protected Au_{38}: a face-fused bi-icosahedral Au core. J Am Chem Soc 130:7830–7832
78. Lopez-Acevedo O, Tsunoyama H, Tsukuda T, Häkkinen H, Aikens CM (2010) Chirality and electronic structure of the thiolate-protected Au_{38} nanocluster. J Am Chem Soc 132: 8210–8218

79. Jiang D-E, Overbury SH, Dai S (2013) Structure of $Au_{15}(SR)_{13}$ and its implication for the origin of the nucleus in thiolated gold nanoclusters. J Am Chem Soc 135:8786–8789
80. Pei Y, Gao Y, Shao N, Zeng XC (2009) Thiolate-protected $Au_{20}(SR)_{16}$ cluster: prolate Au_8 core with new $[Au_3(SR)_4]$ staple Motif. J Am Chem Soc 131:13619–13621
81. Iwasa T, Nobusada K (2007) Theoretical investigation of optimized structures of thiolated gold cluster $[Au_{25}(SCH_3)_{18}]^+$. J Phys Chem C 111:45–49
82. Jin R, Zhu Y, Qian H (2011) Quantum-sized gold nanoclusters: bridging the gap between organometallics and nanocrystals. Chem Eur J 17:6584–6593
83. Venzo A, Antonello S, Gascón JA, Guryanov I, Leapman RD, Perera NV, Sousa A, Zamuner M, Zanella A, Maran F (2011) Effect of the charge state (z = −1, 0, +1) on the nuclear magnetic resonance of monodisperse $Au_{25}[S(CH_2)_2Ph]_{18}^z$ clusters. Anal Chem 83: 6355–6362
84. Liu Z, Zhu M, Meng X, Xu G, Jin R (2011) Electron transfer between $[Au_{25}(SC_2H_4Ph)_{18}]^-TOA^+$ and oxoammonium cations. J Phys Chem Lett 2:2104–2109
85. Negishi Y, Chaki NK, Shichibu Y, Whetten RL, Tsukuda T (2007) Origin of magic stability of thiolated gold clusters: a case study on $Au_{25}(SC_6H_{13})_{18}$. J Am Chem Soc 129:11322–11323
86. Parker JF, Choi J-P, Wang W, Murray RW (2008) Electron self-exchange dynamics of the nanoparticle couple $[Au_{25}(SC_2Ph)_{18}]^{0/1-}$ by nuclear magnetic resonance line-broadening. J Phys Chem C 112:13976–13981
87. Kwak K, Lee D (2012) Electrochemical characterization of water-soluble Au_{25} nanoclusters enabled by phase-transfer reaction. J Phys Chem Lett 3:2476–2481
88. Swanick KN, Hesari M, Workentin MS, Ding Z (2012) Interrogating near-infrared electrogenerated chemiluminescence of $Au_{25}(SC_2H_4Ph)_{18}^+$ clusters. J Am Chem Soc 134: 15205–15208
89. Zhu M, Aikens CM, Hendrich MP, Gupta R, Qian H, Schatz GC, Jin R (2009) Reversible switching of magnetism in thiolate-protected Au_{25} superatoms. J Am Chem Soc 131: 2490–2492
90. Marks L (1983) Modified Wulff constructions for twinned particles. J Cryst Growth 61: 556–566
91. Marks L (1984) Surface structure and energetics of multiply twinned particles. Philos Mag A 49:81–93
92. Mednikov EG, Dahl LF (2008) Crystallographically proven nanometer-sized gold thiolate cluster $Au_{102}(SR)_{44}$: its unexpected molecular anatomy and resulting stereochemical and bonding consequences. Small 4:534–537

Struct Bond (2014) 161: 117–154
DOI: 10.1007/430_2013_126

Published online: 9 August 2014

Progress in the Synthesis and Characterization of Gold Nanoclusters

Yizhong Lu and Wei Chen

Abstract Quantum-sized, thiolate-protected gold nanoclusters (NCs) with atomic precision have attracted substantial research attention over the past decades due to their interesting optical, electronic properties and unusually high catalytic activities. However, despite the remarkable success has been made in the synthesis and characterization of gold nanoclusters, most synthetic approaches suffer from the production of a mixture of different cluster sizes and often a quite low yield of specific sized clusters. Therefore, the products have to be separated on the basis of various complicated processes. The difficulty in isolating and purifying nanoclusters has become a major obstacle to the practical applications of metal nanocluster materials. On the other hand, intensive studies have shown that the optical, electronic, and catalytic properties of gold nanoclusters are strongly dependent on the core size, composition, and structure. Thus, it is highly desirable to develop facile protocols that permit the synthesis, isolation, purification, and characterization of monodispersed, atomically precise gold nanoclusters with control over size in order to fully understand their size-dependent properties. This chapter describes the recent progress in the synthesis, characterization, and study of monodispersed gold nanoclusters.

Keywords Characterization · Gold · Nanoclusters · Nanoparticles · Synthesis

Y. Lu
State Key Laboratory of Electroanalytical Chemistry, Changchun Institute of Applied Chemistry, Chinese Academy of Sciences, Changchun 130022, Jilin, China

University of Chinese Academy of Sciences, Beijing 100039, China

W. Chen (✉)
State Key Laboratory of Electroanalytical Chemistry, Changchun Institute of Applied Chemistry, Chinese Academy of Sciences, Changchun 130022, Jilin, China
e-mail: weichen@ciac.jl.cn

Contents

1 Introduction

Transition metal cluster compounds have been investigated for a long time. From the early 1960s, the electronic structures and models of clusters have been intensively studied by Mingos et al. [1–6]. Gold nanoparticles (NPs, <100 nm), including gold nanocrystals and nanoclusters (NCs), have aroused significant scientific research interest in nanoscience and nanotechnology in recent years due to their unique optical, electrical, and catalytic properties, and their potential applications in the fabrication of optical devices, catalytic conversion, and biological labeling [7–11]. Gold nanoclusters have a distinct number of gold atoms (several to tens) and a number of protecting ligands. They are of fundamental importance for investigating the evolution of the atom-packing structure and physicochemical properties from the metallic state to the atomic scale. Because of their ultrasmall size comparable to the level of Fermi wavelength of electrons and the resulting quantum confinement effect, gold nanoclusters with core size smaller than 2 nm exhibit discrete, molecular-like electronic structure and unique properties, such as size-dependent fluorescence and unexpected catalytic properties, which are very different from those of the bulk metals and large nanoparticles [12–16]. Up to now,

various unique and efficient synthetic methods have been developed to prepare gold NCs with different core sizes. In general, two entirely independent methods, gas phase and solution phase syntheses, have been established to obtain monodispersed gold nanoclusters. In comparison with the unstable metal clusters obtained from gas phase, the nanoclusters synthesized from solution phase have relatively higher stability due to the surface passivation by protecting ligands. On the other hand, through chemical reactions in the solution phase, the core size and the composition of metal NCs can be easily manipulated by tuning the reaction conditions, such as the reaction temperature, relative strengths of reducing agents, the ratio of metal precursors to protecting ligands, and the choice of protecting ligands with different functional groups. Based on these considerations, modern syntheses of metal clusters have been mostly achieved in solution phase through chemical processes.

Among the various solution phase-based syntheses, the Brust–Schiffrin or modified methods have been widely applied to the preparation of gold nanoclusters due to their simplicity and versatility. In the syntheses, different types of organic compounds have been used as capping ligands to protect gold nanoclusters, such as thiolate, phosphine, selenolate, carbonyl, alkyne, DNA, protein cages, and so on. Generally, there are two most widely employed variants: the original Brust–Schiffrin method characterized with two-phase system in water and an organic solvent (toluene) and a modified one-phase system. In the two-phase method, gold salts (usually $HAuCl_4$) dissolved in water were first transferred to the toluene phase by phase-transferring reagents, such as tetraoctylammonium bromide (TOABr). Subsequently, organic protecting ligands were added to form Au(I)SR intermediates, followed by addition of $NaBH_4$ to produce gold nanoclusters. Briefly, the two-phase Brust–Schiffrin synthesis includes two processes: phase transfer of metal precursors and the reduction of metal ions. The two-step reaction mechanism can be summarized as follows [17]:

$$AuC1_4^- \,(\text{aq}) + N(C_8H_{17})_4^+ \,(\text{toluene}) \;\rightarrow\; N(C_8H_{17})_4^+ AuC1_4^- \,(\text{toluene}) \quad (1)$$

$$\begin{aligned} &m\text{AuCl}_4^- \,(\text{toluene}) + n\ C_{12}H_{25}SH \,(\text{toluene}) + 3m\ e^- \\ &\quad\rightarrow\ 4m\ Cl^- \,(\text{aq}) + (Au_m)\,(C_{12}H_{25}SH)_n \,(\text{toluene}) \end{aligned} \quad (2)$$

where BH_4^- is the reducing agent and m and n are the mole numbers of the metal precursor and the protecting ligand, respectively. In the one-phase Brust–Schiffrin method [18], polar solvents, such as THF and methanol, are usually used for preparing gold nanoclusters. In recent years, various modified Brust–Schiffrin methods have been developed for the synthesis of gold nanoclusters with different core sizes. For instance, by tuning the stirring rate for the formation of Au(I)SR intermediates and changing the reaction temperature, Jin and coworkers[19] have successfully synthesized Au_{25} nanoclusters in high yield. In another report, Wu et al. [20] introduced a facile, single-phase THF procedure that produced monodispersed Au_{25} nanoclusters via a "size focusing" process.

Except for the atom-precise synthesis of gold nanoclusters, their unique optical and chemical properties make them potentially useful in a wide variety of

application fields. Recently, several reports have demonstrated the application of fluorescent gold nanoclusters in chemical sensors for the detection of chemicals and ions (e.g., Hg^{2+}, CN^{-}) [21, 22]. Due to the high fraction of surface atoms and much low coordination numbers, the catalytic applications of nanoclusters have attracted increasing attention in recent years. Moreover, the clusters with different core sizes can provide ideal models for atomic-level understanding of structure–reactivity relationships.

It should be noted that despite the tremendous progress achieved on the solution phase synthesis and characterization of the thiolate-protected gold nanoclusters, several scientific and technological challenges of metal nanocluster still remain [14, 16]. One of the challenges is further to develop and improve the synthetic chemistry for effectively synthesizing atomically precise gold nanoclusters with high purity and yield. Because the physical and chemical properties of metal clusters are strongly dependent on their core size, how to obtain clusters with a specific size is important to study their size-dependent properties, especially the catalytic and optical properties. At present, the synthesized crude products are usually separated by several complex techniques to get monodispersed clusters, such as fractional crystallization, chromatography, solvent extraction, and electrophoresis. The difficulty in isolating and purifying has become a major obstacle to the practical applications of gold nanocluster materials. Second, the crystal structure determination of clusters remains the critical issue. Up to now, only a few of crystal structures of gold nanoclusters have been determined by X-ray techniques [23–25]. On the other hand, bimetallic clusters have received considerable research interest in recent years. Compared to the monometallic clusters, the doping of foreign atoms into gold NCs can significantly change the structure and thus the electronic and optical properties. For example, the Pt-doped $Pt_1Au_{24}(SR)_{18}$ nanoclusters exhibited higher stability and enhanced catalytic activity for styrene oxidation compared to the original $Au_{25}(SR)_{18}$ clusters [26]. Since alloy nanoclusters have more complicated structures and more varied properties than those of monometallic clusters, more synthetic and structural studies need to be performed on such novel nanoclusters to study the composition-dependent properties.

In the present chapter, we highlight the recent progress in the synthesis, isolation, and characterization of Au nanoclusters with distinct number of gold atoms protected by specific number of surface ligands. Since the characterization methods for metal nanoclusters have been reported in the previous review [16], here we just give a brief summary of the methods used for size discrimination, composition analysis, and structure determination.

2 Characterization Methods

The size, composition, and structure are the three essential aspects of gold nanoclusters. The rapid development of ultrasmall gold nanoclusters in recent years can be partly attributed to the well-developed analytical techniques such as

high-resolution transmission electron microscopy (HRTEM), nuclear magnetic resonance (NMR) [27, 28], mass spectrometry (MS) [29], electrochemistry [30], and more accurate theoretical calculations [31–33].

2.1 Size Determination

Intensive studies showed that the optical, electronic, and catalytic properties of metal nanoclusters are strongly dependent on the core size of metal nanoclusters. For instance, for the coinage metal nanoparticles with core diameters $d > \sim 2$ nm, obvious surface plasmon resonance (SPR) can be observed in the UV–Vis absorption spectra. This optical feature, however, is damped out for smaller-sized clusters. Instead, single band or multiband UV–Vis absorptions are observed for the sub-nanometer-sized metal clusters [16, 34, 35]. On the other hand, quantized capacitance charging has been observed for monolayer-protected Au nanoclusters (Au MPCs) with the diameters of ~ 1.5 nm $< d < \sim 2.5$ nm in both scanning tunneling microscope (STM) and electrochemical measurements, and this has been attributed to single electron charging of MPC with a very small capacitance. With even smaller metal core sizes ($d < \sim 1.5$ nm), the Au MPCs show HOMO–LUMO energy gap and exhibit molecular-like rather than metallic behaviors [13, 36]. Besides, with Au nanoclusters as catalysts, much work has been done to explore the size effect on the catalytic activity. Chen et al. [37] prepared a series of Au nanoclusters with 11 to 140 gold atoms in their cores (0.8–1.7 nm in diameter) and carried out detailed electrochemical studies in alkaline media to evaluate the size effect on the electrocatalytic activity for the oxygen reduction reaction. The results showed that the electrocatalytic activity for O_2 reduction increases with the core size decreasing and the Au_{11} clusters exhibit the highest catalytic activities. All these studies show that the core size has significant effect on the properties of gold nanoclusters. Therefore, size determination is of critical importance for the in-depth understanding the size-dependent properties of nanoclusters. TEM is a very powerful technique in the size and surface structure characterizations of nanomaterials. For metal nanoclusters with core size smaller than 2 nm, especially for sub-nanometer clusters ($d \leq 1$ nm), traditional techniques for the size characterization of large metal nanoparticles, including scanning electron microscopy (SEM), low-resolution transmission electron microscopy (TEM), and powder X-ray diffraction (XRD), will not be very reliable to get the size information precisely. Along with the rapid development of electronic technology, the resolution of HRTEM has been improved to less than 1.0 nm. The size and atom arrangement in the metal clusters can be directly observed by HRTEM measurement. However, ultra-tiny clusters smaller than 1.0 nm may be barely observable in HRTEM, and upon long electron beam irradiation, they can aggregate to large nanoparticle [38]. Mass spectrometry is another effective technique to analyze the exact core size of nanoclusters [39, 40]. Meanwhile, NMR has also been used as an analytical tool to estimate the size of thiol-stabilized gold

nanoclusters in solution. For example, by using diffusion-ordered NMR spectroscopy (DOSY), Salorinne et al. [41] successfully estimated the size of Au_{25}, Au_{38}, and Au_{144} nanoclusters by determining the diffusion coefficient and hydrodynamic radius from solution samples. The measured cluster sizes agree well with the average diameters of the corresponding single crystal or theoretical structures reported previously.

2.2 Composition Characterization

Since Whetten et al. [29] used innovative laser desorption ionization mass spectrometry (LDI-MS) to analyze the gold clusters, various types of MS techniques have become the most powerful tools to determine the composition of metal clusters. Recent studies on high-resolution mass spectrometry from Murray [42, 43] and Tsukuda [44] groups have unraveled the molecular formulas of some gold nanoclusters. Arnold and Reilly [45] analyzed the composition of gold nanoclusters by using high-resolution TOF mass spectrometry. The matrix-assisted laser desorption ionization mass spectrometry (MALDI-MS) of Au_{25} clusters showed the presence of only 25 Au atom species and no any 24 or 26 or other adjacent core sizes [43]. Recently, Dass et al. [39, 43] demonstrated that almost no fragmentation of Au nanoclusters was observed in the MALDI-TOF mass spectra of $Au_{25}(SCH_2CH_2Ph)_{18}$ clusters using *trans*-2-[3-(4-*tert*-butylphenyl)-2-methyl-2-propenylidene] malononitrile (abbreviated as DCTB) as matrix with low laser pulse intensity (just above the threshold intensity). Since then, more gold nanoclusters with various compositions have also been characterized by the efficient MALDI-TOF MS technique.

Size-exclusion chromatography (SEC) has been used recently for the separation of clusters with different compositions and preliminary characterization of the cluster purity. For instance, Jin's group used SEC to isolate $Au_{40}(SR)_{24}$ from $Au_{38}(SR)_{24}$ nanoclusters [46] as well as Pd-doped 25-atom $Pd_1Au_{24}(SR)_{18}$ nanoclusters from homogold $Au_{25}(SR)_{18}$ [47] and $Pt_1Au_{24}(SR)_{18}$ nanoclusters from $Au_{25}(SR)_{18}$ [48].

2.3 Structure Characterization

Structure of gold nanoclusters plays a decisive role in determining their unique properties. A precise knowledge of the cluster atomic structure is important to fully understand the physical and chemical properties of gold nanoclusters. Based upon crystal structures, the relationship between the structure and the electronic, optical, and catalytic properties as well as the size-dependent evolution can be ultimately understood. Although the accurate compositions of various gold nanoclusters have been analyzed by MS, the core structure (arrangement of gold atoms) and surface

structure (Au-ligands bonding modes) of Au NCs are still not very clear except for a few of clusters. At present, X-ray crystallography is the most reliable approach used for the determination of the structure of metal clusters. In order to study the crystal structures, stable and high-quality single crystals have to be synthesized. The crystal structure of several gold clusters has been crystallographically determined so far, including $[Au_{25}(SR)_{18}]^q$ ($q = -1, 0$) [23, 24], $[Au_{38}(SR)_{24}]$ [49], and $[Au_{102}(SR)_{44}]$ [25]. The studies showed that they did not show the face-centered cubic (fcc) packing of the bulk metal and their cores exhibited unique molecule-like atomic structures. For instance, Au_{25} has a centered icosahedral Au_{13} core capped by an exterior shell composed of the remaining 12 Au atoms in the form of six –RS–Au–RS–Au–RS– motifs. It should be noted that the crystal structures may be fine tuned by changing the chemical environments, which is important for manipulating the properties of gold nanoclusters.

3 Syntheses of Atomic Precise Au Nanoclusters with Different Compositions

3.1 Au_5 Nanoclusters

Tan and coworkers [50] successfully prepared water-soluble fluorescent Au_5 nanoclusters through a robust photoreduction of $HAuCl_4$ in the presence of poly (methacrylic acid) functionalized with pentaerythritol tetrakis 3-mercaptopropionate (PTMP–PMAA). Under irradiation with an ultraviolet light source (8 W, wavelength = 365 nm), the initial clear solutions gradually changed from yellow to orange, accompanied by the evolution of emission peaks. The morphology and size of Au_5 nanoclusters were characterized using a TEM, which shows the Au nanoclusters with a diameter of 0.6 ± 0.4 nm. MALDI-TOF MS displayed that Au_5 nanoclusters are the dominant Au-containing components in the colloidal solution.

3.2 Au_8 Nanoclusters

Zheng et al. [51] synthesized water-soluble, monodispersed, blue-emitting Au_8 nanoclusters encapsulated in biocompatible poly(amidoamine) PAMAM dendrimer. Gold ions were first sequestered into internal core of dendrimers, where the tertiary amines could form coordination bonds with the $AuCl_4^-$ ions. Upon addition of $NaBH_4$, gold atoms aggregate within the dendrimers to form small nanoclusters and protected by the external shell of dendrimer which can prevent cluster aggregation into large nanoparticles. From the electrospray ionization (ESI) mass spectrometry measurements, Au_8 was found to be the dominant Au-containing component in the fluorescent solutions. Interestingly, the

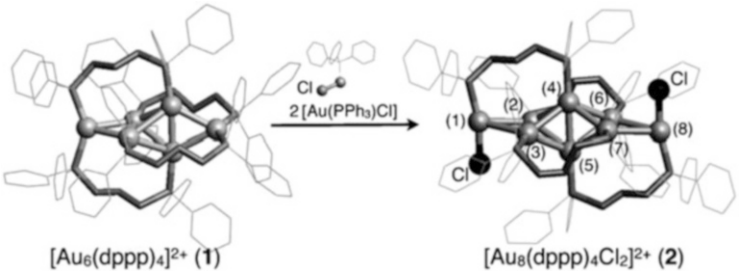

Fig. 1 X-ray crystal structures of the cationic moieties of the Au_6 and Au_8 clusters and the growth from Au_6 to Au_8 through the reaction with [$Au(PPh_3)Cl$]. Gold: *gray* spheres. Reprinted from [52] with permission by Wiley-VCH

as-synthesized Au_8 nanoclusters show strong size-dependent emission, with a quantum yield of ~41% in aqueous solution, which makes them novel fluorophores due to the more than 100-fold enhancement in quantum yield.

Konishi and coworkers [52] reported the synthesis of two novel cluster cations $[Au_8(dppp)_4Cl_2]^{2+}$ and $[Au_8(dppp)_4]^{2+}$ (dppp = 1,3-bis(diphenylphosphino) propane) through a growth/etching process (as shown in Fig. 1). The synthesis starts from well-defined Au_6 nanoclusters ($[Au_6(dppp)_4]I(NO_3)_2$), whose core contains a tetrahedral Au_4 unit plus two gold atoms bridged at opposite edges of the tetrahedron. After the Au_6 nanoclusters were mixed with [$Au(PPh_3)Cl$] in methanol/chloroform at room temperature, a gradual color change of the solution from intense blue to optic pink was observed, indicating the formation of a new nanocluster. The reaction process was monitored by UV–Vis absorption spectroscopy. With the reaction time increasing, the characteristic absorption of Au_6 nanoclusters decreased, while a new band at 510 nm appeared and gradually grew up. From the ESI-MS of the product, a set of signals at approximately m/z 1,648 appeared, which was unambiguously assigned to the divalent $[Au_8(dppp)_4Cl_2]^{2+}$ cluster cation. After crystallization from dichloromethane/ether, only a sole cluster species ($m/z = 1613$), assigned to $[Au_8(dppp)_4]^{2+}$, was isolated. X-ray crystallographic analysis revealed that the core of such cluster adopts edge-shared tri-tetrahedral geometry and thus has a prolate shape, which is clearly different from that of the $[Au_8(dppp)_4Cl_2]^{2+}$. Interestingly, the authors found that $[Au_8(dppp)_4]^{2+}$ could be instantly oxidized to $[Au_8(dppp)_4Cl_2]^{2+}$ under aerobic conditions upon addition of tetraethylammonium chloride (Cl^- and air). In the reverse reaction, $[Au_8(dppp)_4Cl_2]^{2+}$ may be reduced to $[Au_8(dppp)_4]^{2+}$ using $NaBH_4$. This work emphasizes that the electronic properties of Au nanoclusters depend on not only the Au number in the core but also the core geometry and oxidation states. Moreover, this study also displayed the preparation of novel small nanoclusters with unique geometries through post-synthetic methods utilizing growth/etching processes.

Inspired by the etching route for the synthesis of fluorescent gold nanoclusters, Guo et al. [53] demonstrated a unique heterophase ligand-exchange-induced etching process to synthesize water-soluble fluorescent Au_8 nanoclusters. In the

synthesis, dodecylamine (DDA)-capped gold nanoparticles (~3.7 nm) were first synthesized through a modified Brust–Schiffrin method, and toluene solution of gold nanoparticles was then mixed with phosphate buffer (pH) aqueous solution containing thiol ligands (2-(dimethylamino) ethanethiol, DMAET) to form two-phase mixture. After 3 days of stirring, the characteristic purple of gold nanoparticles disappeared completely and both the toluene and water phases became transparent. MALDI-TOF mass spectrometry showed an intense peak at *m*/*z* 2,256.4, which can be assigned to the Au_8 nanocluster with a formula of $[Au_8C_{36}H_{82}N_5S_3]^+$.

3.3 Au_{10} Nanoclusters

Recently, through an ultra-facile one-step reaction, Yang et al. [54] successfully synthesized water-soluble, monodispersed, and bluish-green-emitting Au_{10} nanoclusters. Briefly, an aqueous solution of $HAuCl_4$ was mixed with an aqueous solution of histidine at room temperature. After incubated for 2 h, monodispersed Au_{10} nanocluster was formed. In this preparation protocol, the histidine serves as both reducing agent and protecting ligand. From the UV–Vis spectrum, the characteristic SPR peak of gold nanoparticles was not observed; instead, the absorption rises sharply below 300 nm with a band edge of 450 nm, indicating the molecular-like properties of formed gold clusters [55]. From the ESI mass spectrometry of the as-synthesized Au nanoclusters, the major peak at $m/z = 1{,}760$ was assigned to the $[Au_{10}His_{10}]^{2-}$, while the major peaks at *m*/*z* 1,139 and 1,449 were assigned to the $[Au_{10}His_2]^{2-}$ and $[Au_{10}His_6]^{2-}$, respectively. The MS results clearly suggested that the cluster is composed of 10 gold atoms. X-ray photoelectron spectroscopy (XPS) result further indicated that the products are exclusively gold clusters consisting of Au^0 atoms rather than bulk gold or gold thiolates. With the proposed method, Au_{10} nanoclusters can be produced at a relatively wide pH range from 2 to 12 and the fluorescence intensity of clusters changed with the pH and the concentration ratio of histidine to Au^{3+} ions. Yu et al. [56] studied the temperature-dependent fluorescence of the histidine-protected Au_{10} nanoclusters and it was found that with temperature increasing, the fluorescence intensity decreased due to the thermal activation of nonradiative trapping, the energy band gap exhibited a small blue shift due to the lattice torsional fluctuation, and the fluorescence bandwidth showed a broadening because of the electron–electron interactions.

3.4 Au_{11} Nanoclusters

In earlier studies, the Au_{11} nanoclusters were always synthesized by using phosphine or amino-substituted triarylphosphine as protecting ligands [5, 57]. For example, Bartlett et al. [5] have reported the synthesis of Au_{11} nanoclusters ($d = 0.8$ nm)

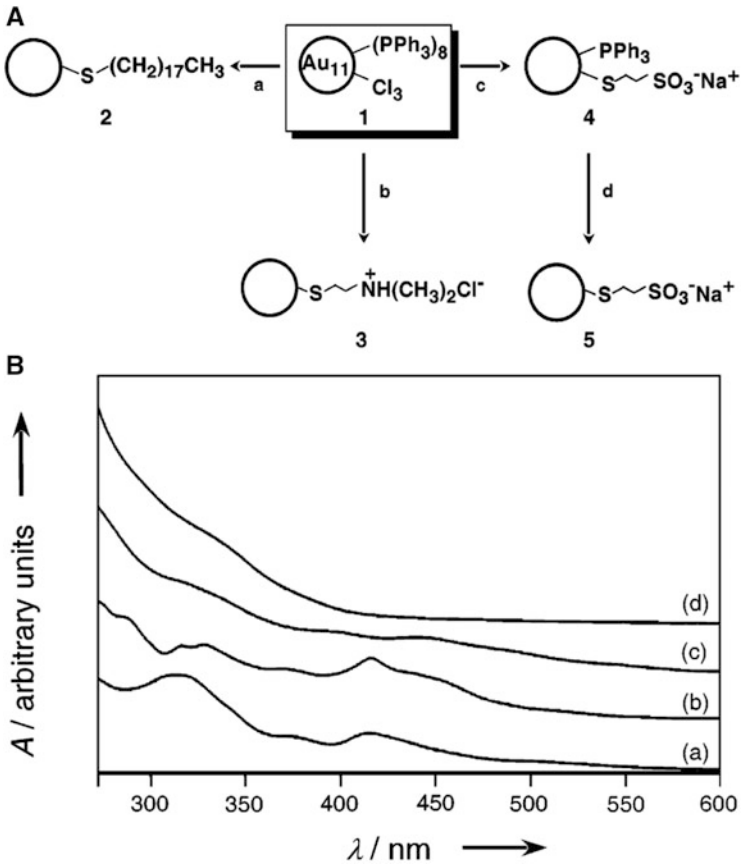

Fig. 2 (**A**) Schematic diagram of synthesis of gold nanoclusters from the $Au_{11}(PPh_3)_8Cl_3$ cluster precursor **1**. Synthesis conditions: (*a*) Ligand exchange of **1** in $CHCl_3$ at 55°C with excess octadecanethiol produces the thiol-stabilized particle **2**; (*b*) Interfacial ($CHCl_3/H_2O$) ligand exchange of **1** at 55°C with (*N*,*N*-dimethylamino)ethanethiol hydrochloride produces the cationic thiol-stabilized particle **3** in a single step; (*c*) Interfacial ($CHCl_3/H_2O$) ligand exchange of **1** at 55°C with sodium 2-mercaptoethanesulfonate (MESA) produces the anionic particle **4**, which contains a mixed ligand shell; (*d*) Treatment of **4** with excess MESA in 1:1 THF/H_2O yields particle **5** containing only MESA in the ligand shell. (**B**) UV–Vis spectra of the gold precursor and the formed nanoclusters through ligand exchange process as described in **A**. (*a*) precursor cluster **1**; (*b*) cluster **2**; (*c*) cluster **3**; (*d*) cluster **5**. Reprinted from [58] with permission by the American Chemical Society

protected by 4, 4, 4-phosphinidynetri(benzenemethanamine). However, these clusters are normally not stable and are prone to oxidative decomposition when exposed to ambient conditions. In order to overcome such problem, Hutchison and coworkers [58] synthesized stable Au_{11} nanoclusters protected by alkanethiols through an exchange-reaction process. As shown in Fig. 2A, such ligand exchange strategy could be applied to the preparation of different thiol-stabilized Au

nanoclusters from a single, easily prepared precursor, $Au_{11}(PPh_3)_8Cl_3$. By controlled ligand exchange, organic-soluble nanoclusters can be produced through the reaction with octadecanethiol (ODT), while water-soluble ones can be obtained by ligand exchange with *N*,*N*-dimethylaminoethanethiol (DMAT) or mercaptoethanesulfonic acid (MESA). From the UV–Vis absorption spectra shown in Fig. 2B, the obtained nanoclusters showed similar absorption features but with more fine structures and broadened absorption peaks compared to the $Au_{11}(PPh_3)_8Cl_3$ precursor. The TEM characterizations showed that all of the thiol-protected Au_{11} nanoclusters displayed the same core size as the initial $Au_{11}(PPh_3)_8Cl_3$ clusters (~0.8 nm). More importantly, after ligand exchange, the nanoclusters exhibited remarkably enhanced thermal stability compared with the precursor clusters. With a slightly different procedure from that described by Bartlett et al., Yang and Chen [59] successfully synthesized stable and monodispersed $Au_{11}C_{l3}(PPh_3)_7$ nanoclusters upon reduction of the precursor chloro(triphenylphosphine)gold (I) ($AuPPh_3Cl$) by $NaBH_4$ in ethanol. It was also found that in contrast to the $Au_{11}C_{l3}(PPh_3)_7$ clusters with no fluorescence, photoluminescence at 840 nm was observed after the ligand exchange with alkanethiols. This study strongly suggests that the surface functionalization can dramatically change the electronic energy structure of metal clusters.

3.5 Au_{13} Nanoclusters

Recently, M_{13}-type clusters have attracted special attention as they can take the smallest geometrically stable shell-closed structure ("magic number") [52]. As for Au_{13} nanoclusters, the previous structure study on single crystal has shown that they have icosahedral core geometry [2] which has been proposed to be the subunit in the structures of larger gold clusters such as Au_{25} and Au_{38} [23, 24, 49]. Although the Au_{13} nanoclusters have been expected to be thermodynamically stable due to the closed shell geometry, the synthesis of monodispersed clusters is still a great challenge. In the earlier syntheses, nonconventional reducing agents were used in the preparation of Au_{13} nanoclusters [2, 60]. Fortunately, by using the unique capability of HCl to induce the nuclearity convergence in polydispersed Au clusters, Konishi and coworkers [61, 62] successfully synthesized highly pure Au_{13} nanoclusters protected by C2-bridged diphosphine ligand (Ph_2P-$(CH_2)_2$-PPh_2, dppe). As shown in the Scheme 1, a polydispersed mixture of ultrasmall gold nanoclusters (Au_N; $9 \leq N \leq 15$) was first synthesized by reducing $Au_2(dppe)Cl_2$ (dppe: 1,2-bis(diphenylphosphino) ethane) with $NaBH_4$ in dichloromethane/ethanol (96:4 v/v). In the second step, aqueous hydrochloric acid was added into the polydispersed sample dissolved in ethanol. From the ESI-MS spectra shown in Fig. 3A, after the polydispersed clusters were treated with HCl for 3 h, the product showed a very simple MS spectrum that was mostly dominated by a set of signals at $m/z \approx 1{,}541$, which could be assigned to $[Au_{13}(dppe)_5Cl_2]^{3+}$. Accordingly, with treatment time increasing, two new absorption bands centered at 360 and 490 nm

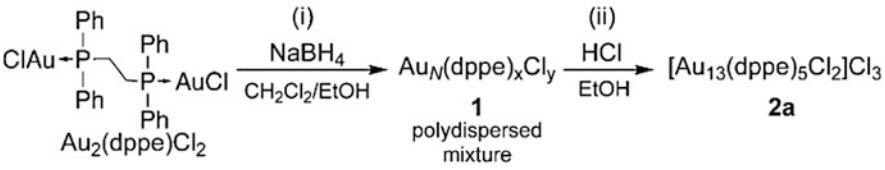

Scheme 1 Two-step synthetic route to Au_{13} clusters. Reprinted from [61] with permission by Wiley-VCH

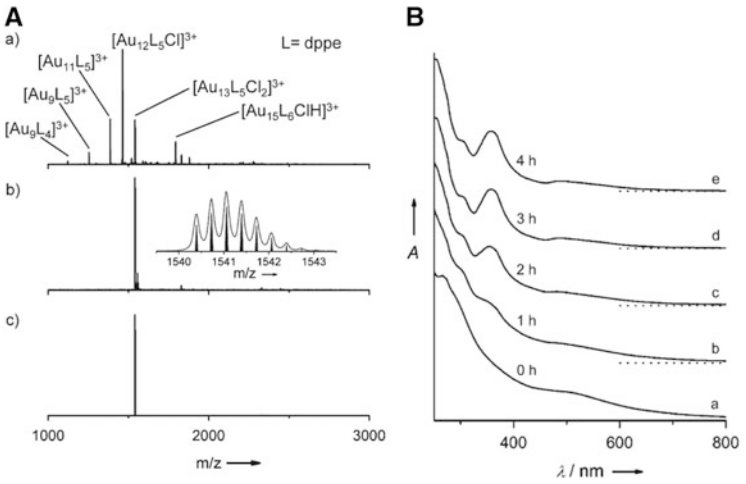

Fig. 3 (**A**) Positive-ion ESI-MS spectra of (*a*) polydispersed mixture of gold clusters, (*b*) after treatment with HCl for 3 h, and (*c*) the clusters after purification. The insets show a comparison of the experimental data with the calculated isotope pattern of $[Au_{13}(dppe)_5Cl_2]^{3+}$. (**B**) Dependence of UV–Vis absorption spectra of polydispersed mixture of gold clusters on time after the addition of aqueous HCl in ethanol at room temperature. Reprinted from [61] with permission by Wiley-VCH

gradually appeared and increased (Fig. 3B), accompanying with the solution color change from brown to red. Obviously, this synthetic method is quite simple and could produce exclusively $[Au_{13}(dppe)_5Cl_2]^{3+}$ as the single nanocluster species, which allow the large-scale preparation of highly monodispersed, atomic precise Au_{13} nanoclusters.

Earlier studies have shown that the possible structures of Au_{13} clusters are either geometrically shell-closed cuboctahedron or icosahedrons, but the latter structure is the one that has generally been found in crystal structures [2, 63]. Recently, Li et al. [64] found that as revealed by in-depth analysis of X-ray and UV–Vis absorption, an icosahedral-to-cuboctahedral structural transformation of Au_{13} nanoclusters could be achieved by a so-called "hexane-driven" method. For icosahedral Au_{13} clusters protected by a mixture of dodecanethiol and triphenylphosphine ligands, the solvent exchange of ethanol by hexane could lead to the

quick selective desorption of the thiolate layers from the cluster surface. The surviving Au cores underwent then a much slower energy minimization process via structural rearrangement and were finally stabilized in the cuboctahedral structure and protected by triphenylphosphine in hexane environment. Interestingly, the authors found that accompanied with the change of atomic structure, the character of the electronic structure transits from semiconductor to metal-like, indicating the strong structure–property relationship.

3.6 Au_{15} Nanoclusters

Recently, Pradeep and coworkers [65, 66] demonstrated a high-yield synthesis of Au_{15} nanoclusters anchored to cyclodextrin (CD) cavities via the core etching of larger clusters. In a typical synthesis, Au nanoparticles protected by –SG ligands were first synthesized. The synthesized Au nanoparticles were dissolved in water containing excess amount of GSH and cyclodextrin and then heated at 70°C for 48 h. Finally, brown powders with intense red emission in the solid state were obtained after centrifugation and freeze-dry treatment. Here, the excess GSH was used as etchant and cyclodextrin acted as host cavities which trapped the as-synthesized Au clusters and protected them from further core reduction [67]. Well-defined optical absorption spectrum in aqueous solution with absorption peaks at 318, 458, and 580 nm, which resembles the molecule-like absorption of $Au_{15}SG_{13}$ reported previously [68]. The characteristic UV–Vis spectrum together with ESI-MS confirms that the formed species are Au_{15} nanoclusters. ^{1}H NMR of the as-prepared Au nanoclusters showed the presence of both –SG protection and CD in the cluster products.

3.7 Au_{18} Nanoclusters

Gold nanoclusters capped by glutathione and other similar ligands have been synthesized and size-separated by Tsukuda's group [68, 69]. In the work, a series of fractions were separated from the original clusters by polyacrylamide gel electrophoresis (PAGE), and the chemical compositions of the nine smallest compositions were assigned to $Au_{10}(SG)_{10}$, $Au_{15}(SG)_{14}$, $Au_{18}(SG)_{14}$, $Au_{22}(SG)_{16}$, $Au_{22}(SG)_{17}$, $Au_{25}(SG)_{1}8$, $Au_{29}(SG)_{20}$, $Au_{33}(SG)_{22}$, and $Au_{39}(SG)_{24}$, respectively, by ESI-MS with high mass resolution and accurate mass calibration. Interestingly, the most abundant compound with enhanced stability was found to be the $Au_{18}(SG)_{14}$ nanoclusters, although it also has been shown that the $Au_{25}(SG)_{18}$ nanoclusters exhibited the highest stability against core etching [70]. Recently, Dass and coworkers [71] synthesized a mixture of thiolated gold nanoclusters with the most abundant cluster component of $Au_{18}(SR)_{14}$. In their synthesis, the usually needed tetraoctylammonium bromide surfactant was eliminated by dissolving the

Au(III) salt in a small volume of ethanol and subsequent addition of CH_2Cl_2. Phenylethanethiol as protecting ligand was added and stirred in an ice bath. Finally, the reductant $NaBH_4$ dissolved in ice cold water was added and allowed to continue for 24 h. The MALDI-TOF mass spectrum of the prepared nanoclusters showed two envelopes of peaks in the *m*/*z* ranges of 4,500–6,500 and 7,500–9,500, of which the most abundant nanoclusters could be assigned to $Au_{18}(SR)_{14}$. Discrete features with a peak at 800 nm and steplike features around 480 and 400 nm in the UV–Vis spectrum suggested the presence of small clusters. With first-principle calculations, the most stable structure of $Au_{18}(SR)_{14}$ nanoclusters with lowest energy was also systematically studied by Tlahuice and Garzon [72]. It was found that the structure of the $Au_{18}(SR)_{14}$ nanocluster consists of a prolate Au_8 core covered with two dimer (SR–Au–SR–Au–SR) and two trimer (SR–Au–SR–Au–SR–Au–SR) motifs.

The sizes and properties of metal nanoclusters are greatly affected by the synthetic conditions, such as the selected protecting ligands, solvent, and the metal/ligand ratio. Related studies showed that the reduction capability of the reducing agent also has a tremendous effect on the properties of cluster product because the core size of nanoclusters is generally determined by the relative rates of nucleation and the following crystal growth. A mild and selective reducing agent can slow down the nucleation and the growth of the nuclei, resulting in relatively small nanoclusters. Ghosh et al. [73] recently reported a one-step route for the synthesis of highly luminescent and water-soluble $Au_{18}(SG)_{14}$ nanoclusters through a slow reduction process. In the study, by using the weak reducing agent, $NaBH_3CN$, nearly pure $Au_{18}(SG)_{14}$ clusters were formed. The formula, $Au_{18}(SG)_{14,}$ and the purity were confirmed based on ESI and MALDI mass spectrometry. The $Au_{18}(SG)_{14}$ nanoclusters exhibited distinct absorption bands centered at 590 nm, a broad band at 515 nm, and another in the UV region at 290 nm. The UV–Vis absorption features match well with the recent results from first-principle calculations [72]. Moreover, the polyacrylamide gel electrophoresis (PAGE) of the as-synthesized nanoclusters showed principally one band, again indicating the formation of clusters with a single size.

In most syntheses of gold nanoclusters, thiolates are used as effective protecting ligands. Sulfur and selenium exhibit similar properties because they belong to the same group in the Periodic Table. Moreover, since the atomic radius and electronegativity of Se are closer to Au than S atom, the Au–Se bond should be more covalent than that of Au–S. For these reasons, there has been increasing interest in selenolate-protected gold nanoclusters. Zhu and coworkers [74] developed a strategy for the synthesis of $Au_{18}(SePh)_{14}$ nanoclusters. The synthesis was achieved through a ligand exchange process between $Au_{25}(SCH_2CH_2Ph)_{18}$ nanoclusters and PhSeH. The $Au_{18}(SePh)_{14}$ nanoclusters were separated from the mixed products including other cluster components, such as $Au_{15}(SePh)_{13}$, $Au_{19}(SePh)_{15}$, and $Au_{20}(SePh)_{16}$, by using HPLC equipped with a size-exclusion chromatography (SEC) column. From the chromatogram shown in Fig. 4a, the two species collected at different retention time correspond to $Au_{20}(SePh)_{16}$ and $Au_{19}(SePh)_{15}$ (31.711 min) and $Au_{18}(SePh)_{14}$ (33.149 min), respectively. The obtained Au_{18} and Au_{20} exhibited different absorption features (Fig. 4b). The compositions and

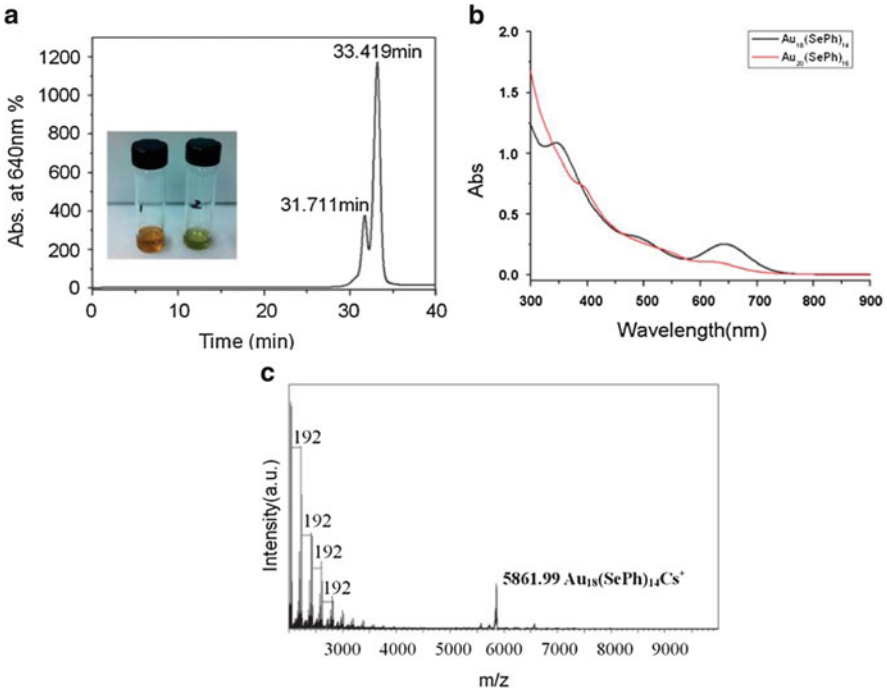

Fig. 4 (**a**) HPLC chromatogram of a mixture of stable Au–SePh clusters with the UV–Vis signal monitored at 640 nm. (**b**) Comparison of the UV–Vis spectra of the $Au_{18}(SePH)_{14}$ and $Au_{20}(SePH)_{16}$ clusters. (**c**) Positive-ion ESI-TOF mass spectra of $Au_{18}(SePh)_{14}$. The ion spacing of 192 is one CsOAc, and the prominent peak of 5861.99 corresponds to $Au_{18}(SePh)_{14}Cs^{+}$. Reprinted from [74] with permission by the Royal Society of Chemistry

the surface ligands were confirmed by ESI mass spectrometry (Fig. 4c), ^{1}H and ^{13}C NMR. According to the thermogravimetric analysis (TGA) result, the metal-to-organic ratio was found to be ~61:39, agreeing well with the theoretical value of $Au_{18}(SePh)_{14}$. Moreover, it was found that $Au_{18}(SePh)_{14}$ or $Au_{25}(SePh)_{18}$ nanoclusters can be produced simply in the same reaction system by controlling the concentrations of the reactants. For example, high concentrations of reactants gave rise to $Au_{25}(SePh)_{18}$ nanoclusters, while $Au_{18}(SePh)_{14}$ nanoclusters were obtained at low concentrations of reactants.

3.8 Au_{19} Nanoclusters

As mentioned above, by using a mild and selective reducing agent, atomically precise nanoclusters can be selectively produced. The successful cluster synthesis demonstrates that reductant with different reduction potential plays important roles in the synthesis of metal nanoclusters with desired core size. Recently,

Wu et al. [75] reported a one-pot process for the synthesis of 19 gold atom-contained nanoclusters ($Au_{19}(SC_2H_4Ph)_{13}$) by the combination of both kinetic control and thermodynamic selection principles. In a typical synthesis, Au (I) aggregates were first formed by adding phenylethylthiol into a cold solution of $HAuCl_4 \cdot 3H_2O$ (0°C) under constant stirring. In the next step, a freshly prepared toluene solution of borane–*tert*-butylamine complex was added drop by drop. In this reported method, the key point is that the usually used reducing agent $NaBH_4$ was replaced with a weaker one (borane–*tert*-butylamine complex). Under the preparation conditions, the initially formed nanocluster mixture underwent size convergence into a monodispersed 19-atom nanocluster after a prolonged aging process (~60 h). The purity of the as-prepared clusters was characterized by the SEC (Fig. 5a), from which all of the spectra are superimposable, indicating the high purity of the product. From the ESI-MS shown in Fig. 5b, a dominant peak at *m*/*z* 5,659.3 could be assigned to the $Au_{19}(SC_2H_4Ph)_{13}Cs^+$. In addition, LDI-MS analysis showed a core with a mass of 3–4 kDa, which is consistent with this formula. This work clearly demonstrates the importance of both kinetic control and thermodynamic selection in the synthesis of monodispersed metal nanoclusters and provides idea for the synthesis of atomically precise nanoclusters.

3.9 Au_{20} Nanoclusters

Since the synthesis of $Au_{55}(PPh_3)_{12}Cl_6$ by Schmid et al. [76], many efforts have been devoted to the syntheses and applications of phosphine-stabilized gold nanoclusters. Compared to the thiol-capped Au nanoclusters, the syntheses of phosphine-stabilized clusters need more tough reaction conditions, such as anaerobic atmosphere and diborane gas reducing agent. Hutchison and coworkers [77] developed a safer, more convenient, and more versatile process for the synthesis of phosphine-capped gold nanoclusters, which is analogous to those originally reported by Schmid. Based on the synthesis strategy, Zhang et al. [78] synthesized PPh_3-protected Au_{20} nanoclusters ($Au_{20}(PPh_3)_8$). In the synthesis, $AuCl(PPh_3)$ and tetraoctylammonium bromide (TOABr) were dissolved in a toluene/water mixture. $NaBH_4$ dissolved in water was then added dropwise under vigorous stirring. Gold nanoclusters were collected in dichloromethane after stirring the solution overnight. The HRTEM measurements showed that the majority of the nanoclusters have diameters of less than 1 nm and the cluster composition was determined to be $Au_{20}(PPh_3)_8^{2+}$ by the accurate mass measurement of its doubly charged cation.

Recently, Wang and coworkers [79] successfully synthesized phosphine-protected Au_{20} nanoclusters with novel structure through the $NaBH_4$ reduction of $Au(PPhpy_2)Cl$ ($PPhpy_2$ = bis(2-pyridyl)-phenylphosphine). With pyridyl phosphine as protecting ligand, the stability of the formed gold nanoclusters can be improved because the P and N donors in the pyridyl phosphine could bridge two

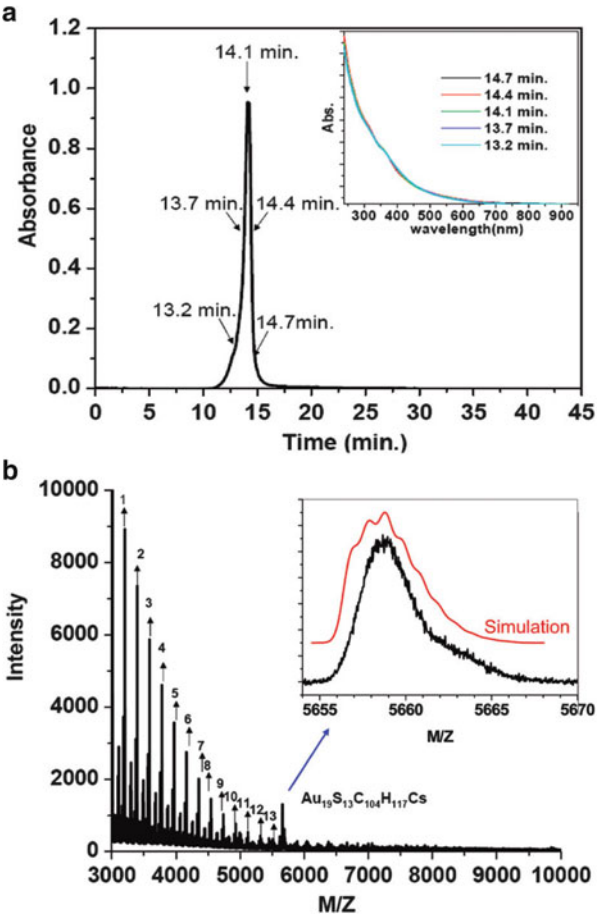

Fig. 5 (**a**) Size-exclusion chromatogram of the synthesized nanoclusters [monitored at $\lambda = 330$ nm using CH_2Cl_2 (0.5 mL/min) as the eluent]. *Inset*: online-recorded UV–Vis spectra corresponding to different retention times. (**b**) ESI-MS of $Au_{19}(SC_2H_4Ph)_{13}$ nanoclusters. Inset: isotope pattern of the peak at *m*/*z* 5,659 (assigned to the Au_{19} nanocluster-Cs^+ adduct) and a simulated pattern for $[Au_{19}(SC_8H_9)_{13}Cs]^+$. Peaks 1–13 correspond to $(CsOAc)_nCs^+$ ($n = 16$–28). Reprinted from [75] with permission by the American Chemical Society

metal centers. In a simple process, a freshly prepared ethanol solution of $NaBH_4$ was added dropwise to an ethanol suspension containing $Au(PPhpy_2)Cl$, under vigorous stirring. Its composition was determined to be $[Au_{20}(PPhpy_2)_{10}Cl_4]Cl_2$. From the mass spectrum shown in Fig. 6a, the intense peak at *m*/*z* 1,662.985 corresponding to the $[Au_{20}(PPhpy_2)_{10}Cl_2]^{4+}$ can be clearly observed, and its isotopic pattern agrees well with that from the simulation. The single-crystal X-ray structural analysis revealed that the Au_{20} skeleton could be viewed as the fusion of two Au_{11} incomplete icosahedra via sharing two vertices.

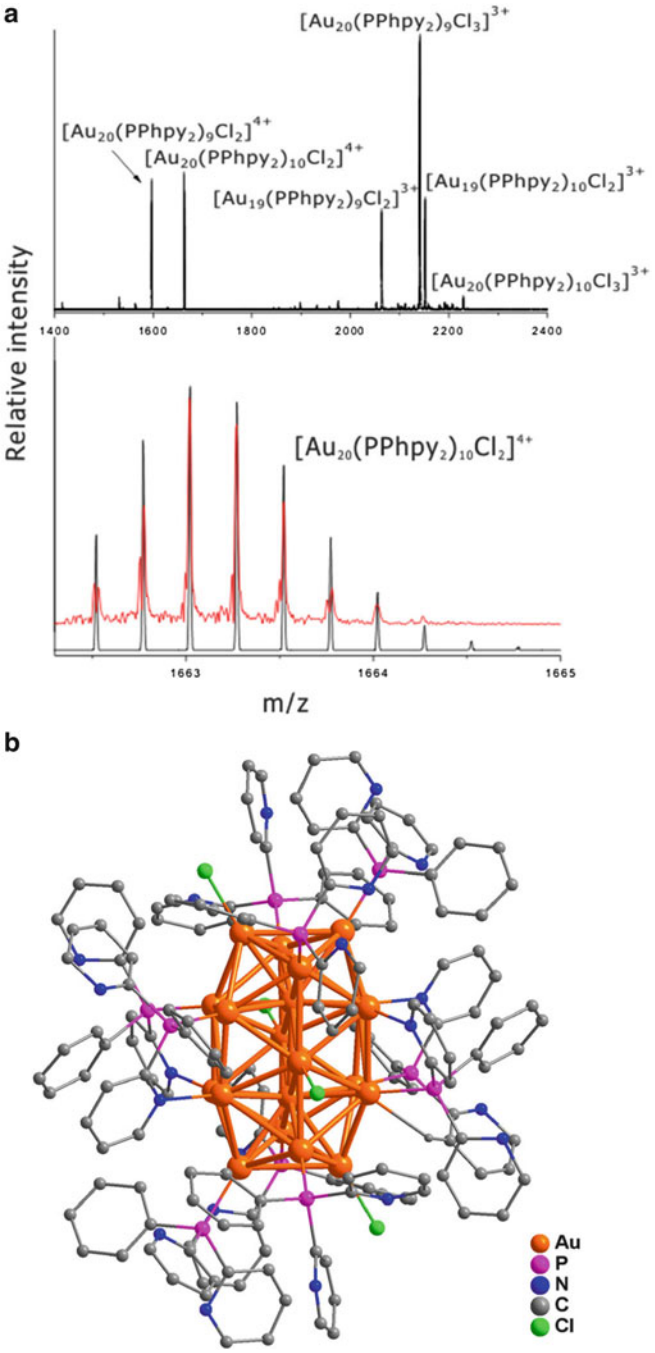

Fig. 6 (**a**) Mass spectrum of the Au_{20} clusters and the measured (*red trace*) and simulated (*black trace*) isotopic patterns. (**b**) The structure of the dicationic $[Au_{20}(PPhpy_2)_{10}Cl_4]^{2+}$ cluster. Reprinted from [79] with permission by the American Chemical Society

Although phosphine-stabilized gold nanoclusters have been studied extensively, the lower stability compared to thiol-capped clusters further inhibited their practical applications. Zhu et al. [80] reported a kinetically controlled approach for synthesizing thiolate-capped Au_{20} nanoclusters. In a typical experiment, $HAuCl_4{\cdot}3H_2O$ was phase transformed from an aqueous solution into toluene phase in the presence of TOABr. After the toluene phase was cooled to 0°C, phenylethylthiol was added to the solution at a low stirring rate (~50 rpm). After the formation of the $[Au^{(I)}SR]_x$ aggregates, $NaBH_4$ (1 equiv. of gold) solution was slowly added over a 30-min period to reduce the $[Au^{(I)}SR]_x$ aggregates. Here, the amount of $NaBH_4$ (~1 equiv.) and slow reduction of $[Au^{(I)}SR]_x$ aggregates were found to be critical for the formation of $Au_{20}(SR)_{16}$ clusters. Only one peak eluting at ~16.05 min in SEC analysis indicated the high purity of the as-synthesized Au nanoclusters. The composition of $Au_{20}(SCH_2CH_2Ph)_{16}$ can be determined from the ESI-MS-TOF analysis, which is in agreement with the simulated isotopic patterns. More interestingly, the Au_{20} nanoclusters were found to be particularly stable against excess thiol etching. Lately, Zeng and coworkers [81] performed a calculation on this Au_{20} nanoclusters and predicted that it has a prolate Au_8 core and four level-3 extended staple motifs –RS–Au–RS–Au–RS–Au–RS–.

3.10 Au_{24} Nanoclusters

Das et al. [82] reported the synthesis and total structural determination of Au_{24} nanocluster protected by mixed ligands of phosphines and thiolates. The precursor used in the synthesis is $HAuCl_4{\cdot}3H_2O$ rather than the commonly used $Au(PPh_3)Cl$ salt. In a typical synthesis, $HAuCl_4{\cdot}3H_2O$ was first phase transferred from water to toluene in the presence of TOABr. Upon the addition of PPh_3, Au(III) was reduced to Au(I), followed by further reduction by $NaBH_4$. After 16 h, the reddish-brown product was extracted by dichloromethane. Phenylethylthiol was then added to this solution and then reacted at 313 K for ~4 h. $[Au_{24}(PPh_3)_{10}(SCH_2CH_2Ph)_5X_2]^+$ (counterion (X) = halide ions) was obtained after the reaction continued for another 24 h with adding excess PPh_3 into the solution. In the process, the addition of excess PPh_3 is critical for producing Au_{24} nanoclusters. By comparing the UV–Vis absorption spectra displayed in Fig. 7, the Au_{24} clusters exhibited much different optical properties from that of Au_{25} clusters although there is only one-atom difference between the Au_{24} and Au_{25} clusters. The computed absorption spectrum of $[Au_{24}(PPh_3)_{10}(SCH_2CH_2Ph)_5X_2]^+$ from DFT calculation (Fig. 7c) agrees well with the experimental one. The absorption peaks of Au_{24} at 560 nm and Au_{25} clusters at 670 nm are from the HOMO–LUMO transition (LUMO + 2 molecular orbital is shown in Fig. 7d). From the single-crystal X-ray crystallographic analysis, the Au_{24} core consists of two incomplete icosahedral Au_{12} units joined together in an eclipsed fashion through five thiolate linkages.

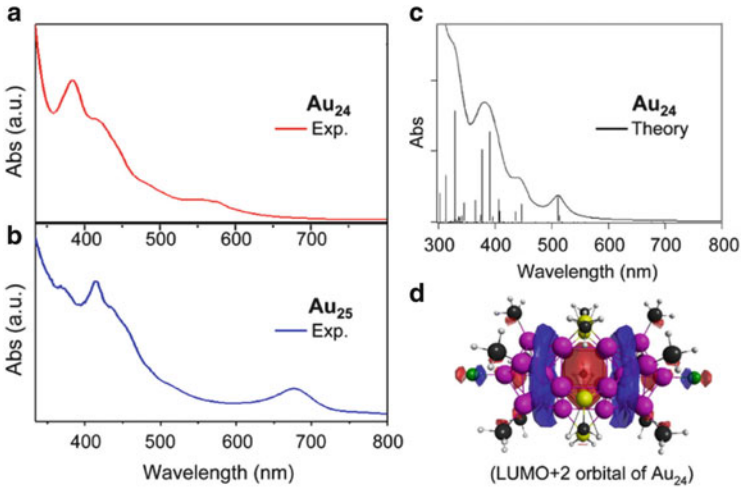

Fig. 7 (**a**) Experimental optical spectrum of $[Au_{24}(PPh_3)_{10}(SC_2H_4Ph)_5X_2]^+$ (in dichloromethane), (**b**) experimental optical spectrum of $[Au_{25}(PPh_3)_{10}(SC_2H_4Ph)_5X_2]^{2+}$ (in dichloromethane), (**c**) DFT-simulated optical spectrum of $[Au_{24}(PH_3)_{10}(SCH_3)_5X_2]^+$ model cluster, and (**d**) the LUMO + 2 molecular orbital of $[Au_{24}(PH_3)_{10}(SCH_3)_5X_2]^+$. Reprinted from [82] with permission by the American Chemical Society

3.11 Au_{25} Nanoclusters

Among the reported $Au_n(SR)_m$ nanoclusters, $Au_{25}(SR)_{18}$ has been most extensively studied due to their unique structure, high stability, and promising applications [83]. Recent single-crystal X-ray crystallography analyses and theoretical studies revealed that the structure of $Au_{25}(SR)_{18}$ nanoclusters can be viewed as an Au_{13} icosahedral core encapsulated by an incomplete shell consisting of the exterior 12 gold atoms in the form of six –RS–Au–RS–Au–RS– motifs [23, 24, 31]. The fully protected structure of the Au_{25} nanoclusters makes a significant contribution to the extraordinary stability against core etching and redox reactions. In the research field of metal nanoclusters, various studies have been focused on the synthesis and properties of Au_{25} nanoclusters. Au_{25} nanoclusters in appreciable yield were first synthesized in 1998 by Whetten and coworkers [27] by using the ubiquitous tripeptide glutathione, *N*-γ-glutamyl-cysteinyl-glycine (GSH), as the capping ligand. The synthesis includes the reduction of $HAuCl_4$ precursor with GSH in methanol/water by a rapid addition of aqueous $NaBH_4$, and the fractionation of the polydispersed product with gel electrophoresis. Since then, a number of research groups have made great efforts to develop synthetic routes to improve the yield and purity of Au_{25} nanoclusters [19, 20, 68, 71, 84–87]. The first successful synthesis of atomically precise Au_{25} nanoclusters with high yield was achieved by Shichibu and coworkers [87] via ligand exchange reaction of phosphine-stabilized Au_{11} nanoclusters. In a typical synthesis, $Au_{11}(PPh_3)_8$ nanoclusters were first prepared by the reduction of $AuCl(PPh_3)$ in ethanol by

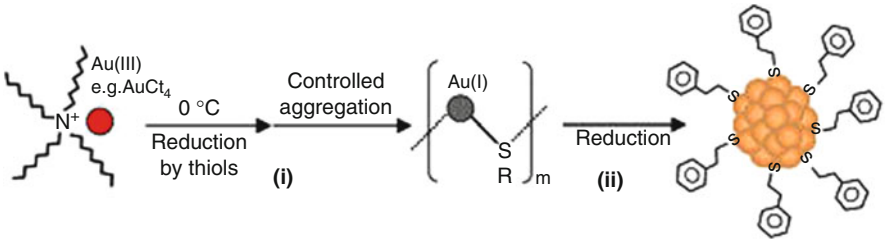

Scheme 2 Schematic representation of kinetically controlled and high-yield synthesis of Au_{25} nanoclusters. Reprinted from [19] with permission by the American Chemical Society

$NaBH_4$, then an aqueous solution of GSH was added under vigorous stirring. During this process, the phosphine-protected Au_{11} nanoclusters underwent aggregation and dissociation in reaction with GSH and finally produced $Au_{25}(SG)_{18}$ nanoclusters in high yield. Another successful high-yield synthesis of atomically precise Au_{25} nanoclusters was made by Tatsuya and coworkers [44] where a crude sample of Au:SC_n ($n = 6$, 10, 12) was first prepared using the modified Brust method and then extracted from the dried samples using pure acetone. In recent years, this method has been widely used for preparing highly monodispersed Au_{25} nanoclusters for various applications due to its simplicity and versatility [88, 89].

To further improve the yield and purity of Au_{25} nanoclusters, Zhu et al. developed a facile and kinetic-controlled method for high-yield synthesis of atomically precise Au_{25} nanoclusters [19]. As shown in the Scheme 2, two steps were involved in the synthesis. Au(III) was firstly reduced to Au(I) by thiols, and Au (I) was further reduced to metallic clusters by $NaBH_4$. The authors found that the preparation conditions with low temperature and slow stirring are critical for the formation of Au(I):SR intermediate species, which leads to the exclusive formation of Au_{25} in high yield in the second reduction step. The high purity of Au_{25} nanoclusters achieved with this kinetically controlled synthesis can also generate high-quality Au_{25} single crystals for X-ray structural determination [23]. Based on the kinetic control principle in two-phase method, a one-phase approach using THF as solvent was developed for the preparation of highly monodispersed Au_{25} nanoclusters with different thiol ligands through the so-called "size focusing" process [20]. Without any purification, the crude Au nanoclusters exhibited the three characteristic absorption bands at 685, 445, and 400 nm (Fig. 8). Moreover, the MALDI-TOF MS showed a single peak centered at 7,394 *m*/*z* corresponding the $Au_{25}(SR)_{18}$. This report provides a facile one-phase synthesis of Au_{25} nanoclusters in high yield. Here, the use of THF as solvent can significantly improve the purity and yield of Au_{25} nanoclusters. Based on this method, Au_{25} nanoclusters with different types of thiol ligands, in particular, those bearing functional groups such as –OH, –COOH, and atom transfer radical polymerization initiator –OC(O)C$(CH_3)_2$Br, have been successfully synthesized. Dass and coworkers [86] simplified the procedure, realizing the synthesis successfully at room temperature without restriction of low stirring conditions and systematically investigate the size

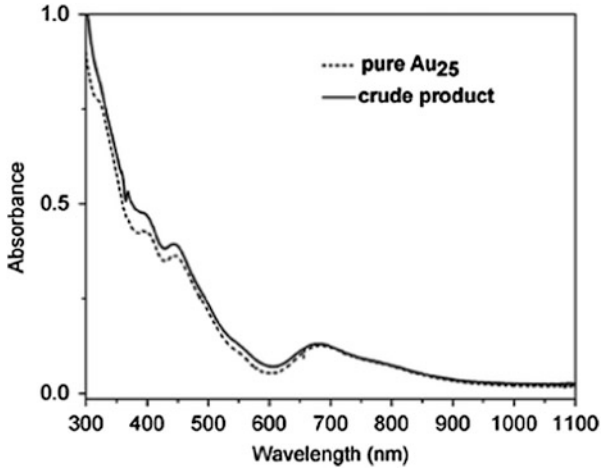

Fig. 8 UV–Vis absorption spectra of the as-prepared $Au_{25}(SCH_2CH_2Ph)_{18}$ crude product and the standard spectrum of pure Au_{25} nanoclusters (single crystal re-dissolved in solvent). Reprinted from [20] with permission by the Royal Society of Chemistry

evolution process by using MALDI-TOF MS. The MS results showed that the reaction in THF involves formation of a mixture of Au_{25}, Au_{38}, $Au_{\sim 44}$, Au_{68}, and Au_{102} at earlier reaction stage, followed by gradual size evolution to highly monodispersed Au_{25} nanoclusters as the final nanocluster product. In both methods, TOABr, the phase transfer reagent in the typical two-phase Brust method, was not used. Recently, Parker et al. [90] found that the addition of the surfactant salt of TOABr in the one-phase synthetic procedure enabled production of reduced Au_{25} nanoclusters having a fully occupied HOMO molecular energy level (Au_{25}^{-}), while the previous method produced oxidized state nanoclusters $\left(Au_{25}^{0}\right)$. These two nanoclusters with different charge states could be easily judged by examination of the detailed features of their UV–Vis absorption. By comparing the spectra shown in Fig. 9, the distinct difference is the relative intensity of the absorption peaks at 399 and 446 nm. For the oxidized nanoclusters, the 399 nm peak is more pronounced, while the 446 nm peak becomes prominent when the nanoclusters are in the reduced state. The authors also investigated the influence of H^+, Br^-, and O_2 on the synthesis of Au_{25} nanoclusters. The results indicated that acidity was somehow involved in the formation of Au_{25}, while Br^- played the role of avoiding nanoclusters oxidation and O_2 could help for re-forming larger-sized Au nanoclusters to smaller Au_{25} nanoclusters.

Recently, other new methods have been developed to synthesize atomic monodispersed Au_{25} nanoclusters. For instance, Xie's group [40] has established an efficient CO-directed synthesis and protection–deprotection method for the synthesis of monodispersed Au_{25} nanoclusters. In the synthesis, a gaseous reducing agent, CO, was used as a mild reducing agent to realize a slow and size-controlled growth of $Au_{25}(SR)_{18}$ nanoclusters. The preparation could be easily scaled up for

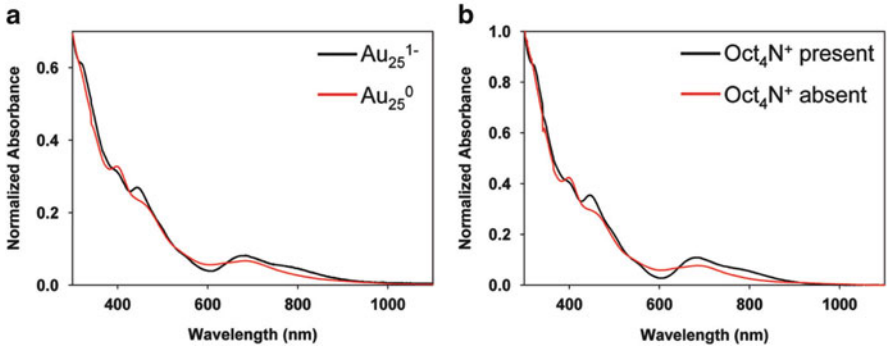

Fig. 9 (**a**) UV–Vis spectra of $Au_{25}(SC_2H_4Ph)_{18}$ in the reduced (*black curve*) form, isolated by extraction into acetonitrile (in which the oxidized form is insoluble) and of the oxidized (*red curve*) form prepared by chemical oxidation using Ce^{IV}. (**b**) Synthetic clusters obtained in single-phase THF synthesis in the presence (*black curve*) and absence (*red curve*) of $Oct_4N^+Br^-$. Reprinted from [90] with permission by the American Chemical Society

large-scale production of atomically precise Au nanoclusters protected by thiol ligands. In another report, Xie and coworkers [91] reported a fast synthetic strategy of thiolated Au_{25} nanoclusters via protection–deprotection method. Three steps were involved in the synthesis. In the first step, Au(I)SR complexes with a protecting layer of cetyltrimethyl ammonium bromide (CTAB) were prepared. The CTAB-protected Cys–Au^I complexes were then reduced by $NaBH_4$ to Cys-protected Au nanoclusters, followed by the transfer of clusters from the aqueous to organic phase. During this step, the protecting CTAB layer could provide a good steric hindrance and thus control the formation rate of thiolated Au nanoclusters, resulting in the formation of atomically precise Au_{25} nanoclusters inside the protecting layer. Finally, the protecting CTAB layer was removed from the surface of Au nanoclusters to bring back the water-soluble Cys–Au_{25} nanoclusters. This method provides a facile and highly efficient process for the production of high-purity Au_{25} nanoclusters within only 10 min.

3.12 Au_{36} Nanoclusters

In the synthesis of metal nanoclusters, the structure and property of selected protecting ligand can determine the size, surface properties (e.g., solubility, fluorescence, electronic structure, and chiral signature), and the application of the resulting clusters. Recently, Dass and coworkers [92] reported the synthesis of an aromatic thiol group-capped Au_{36} nanoclusters. The $Au_{36}(SPh)_{23}$ clusters were produced through a two-stage process. A mixture containing Au_{68} and Au_{102} as major species was first prepared according to a modified one-phase method established previously [20]. An etching process was conducted in the second

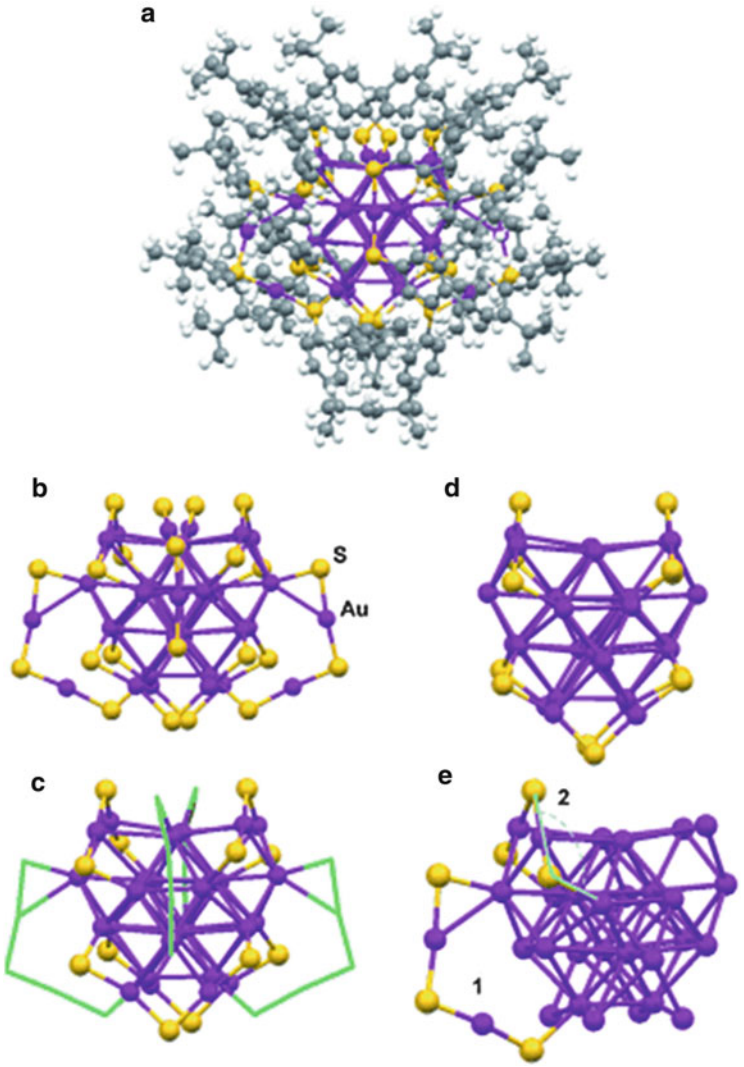

Fig. 10 Total structure of $[Au_{36}(SPh\text{-}tBu)_{24}]^0$. (**a**) The entire particle (Ph-*t*Bu = gray atoms), (**b**) the $Au_{36}S_{24}$ framework, (**c**) the four dimeric staples shown in green, (**d**) the $Au_{28}S_{12}$framework, (**e**) comparison of the ostensible dimeric staple (labeled **2**) and the standard dimeric staple (labeled **1**). Reprinted from [93] with permission by Wiley-VCH

stage where a mixture of the purified product in THF and thiophenol (HSPh) was refluxed at 80°C under vigorous stirring. The MALDI-TOF spectrum of the Au nanoclusters clearly indicated the monodispersed $Au_{36}(SPh)_{23}$ composition. Similar to other gold nanoclusters, the prepared $Au_{36}(SPh)_{23}$ also showed distinct electronic features in the UV–Vis region. This is the first report of 36-atom-sized gold nanoclusters fully capped by aromatic thiols. Unfortunately, the structure of the nanocluster was not determined in the report.

Recently, Jin's group [93] synthesized another Au_{36} nanocluster with 24 thiol ligands and reported the face-centered cubic (FCC)-type core structure of $Au_{36}(SR)_{24}$(SR: 4-*tert*-butylbenzenethiolate (SPh-*t*Bu)). In this synthesis, pure $Au_{38}(SCH_2CH_2Ph)_{24}$ obtained by a size-focusing method was used as precursor [94]. In spite of the high thermal and redox stability of $Au_{38}(SCH_2CH_2Ph)_{24}$ nanoclusters, new clusters could been obtained when reacting with HSPh-*t*Bu at appropriate conditions. From both ESI-MS and TGA analyses, the formula of the nanocluster was determined to be $Au_{36}(SR)_{24}$, which is different from the previously reported composition of $Au_{36}(SPh)_{23}$ [92]. X-ray crystallography was also used to analyze the crystal structure of $Au_{36}(SPh\text{-}tBu)_{24}$ rhombic single crystal. The total structure of the as-synthesized $Au_{36}(SPh\text{-}tBu)_{24}$ nanoclusters is shown in Fig. 10. The Au_{36} nanocluster displays an unusual FCC-type core structure consisting of an Au_{28} kernel with a truncated FCC tetrahedron exposing (111) and (100) facets. More interestingly, different from the previously reported Au clusters, a new type of thiolate-binding mode was discovered, that is, 12 of the 24 ligands bind to the underlying Au atoms in a simple bridging mode, with the remaining 12 thiolates forming the known dimeric staple motifs.

3.13 Au_{38} Nanoclusters

While tremendous work has been done on the atomically precise Au_{25} nanoclusters, thiolate ligands passivated gold nanoclusters with other specific number of gold atoms have also been pursued over the past years. Through controlled etching process, Schaaff et al. [95] first reported the synthesis of Au_{38} nanoclusters by heating larger Au:SR clusters (~Au_{75}, 1.1 nm in diameter) in neat dodecanethiol solution under inert atmosphere. Subsequently, Chaki et al. [44] successfully isolated the alkanethiolate-protected Au_{38} nanoclusters and determined the composition of $Au_{38}(SC_nH_{2n+1})_{24}$ by ESI-MS analysis. Different from the commonly used two-phase synthesis, unique etching process was used for the preparation of Au_{38} nanoclusters. In 2008, Toikkanen et al. [96] reported a facile synthesis strategy to obtain monodispersed hexanethiolate-protected $Au_{38}(SC_6)_{22}$ nanoclusters based on the highly thermodynamic stability of Au_{38} in excess thiol. Firstly, hexanethiolate-capped gold nanoclusters were synthesized according to the Brust–Schiffrin two-phase method. After phases separated and precipitated by acetonitrile (ACN). The dichloroethane (DCE) solution of nanoclusters was then exposed to excess hexanethiol under stirring for different times. Finally, Au_{38} nanoclusters fully passivated by the thiol monolayer were formed as the only product. It was found that the Au_{38} nanoclusters behave like molecules with a wide energy gap between HOMO and LUMO and undergo quantized charging at room temperature in electrochemical experiments. Cyclic voltammetry and scanning electrochemical microscopy measurements demonstrated that the Au_{38} nanoclusters could be reversibly oxidized to charge states $z = +1$ or +2; however, reduction to $z = -1$ leads to desorption of the protecting thiolate monolayer.

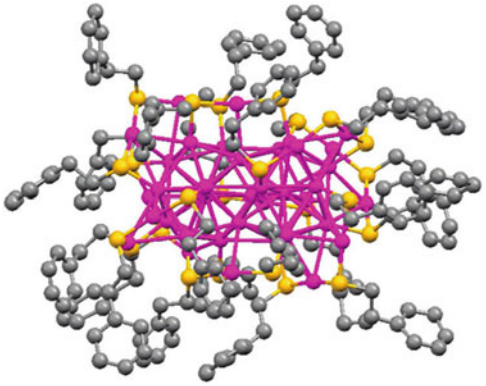

Fig. 11 Total structure of the left-handed $Au_{38}(SC_2H_4Ph)_{18}$ nanocluster (L-isomer, color labels: *magenta*, Au; *yellow*, S; *gray*: C, H atoms are omitted). Reprinted from [49] with permission by the American Chemical Society

Despite the successes in the synthesis of atomic monodispersed Au_{38} nanoclusters, the products are often in low yield and small quantities. In this context, recently, Qian et al. [97] reported a facile, large-scale synthesis of truly monodispersed $Au_{38}(SC_{12}H_{25})_{24}$ nanoclusters in high purity and yield of ~10%. The synthesis was realized through a two-phase ligand exchange process with glutathione-capped Au_n clusters as the starting material. The aqueous Au:SG clusters were then subject to ligand exchange using neat 1-dodecanethiol in a two-phase system. The authors found that the pre-synthesized gold cluster can be etched with the presence of neat dodecanethiols and secondary growth of clusters subsequently occurred, and eventually exclusively monodispersed Au_{38} nanoclusters were produced. The SEC confirmed the purity of the as-synthesized Au_{38} nanoclusters. To further improve the product yield, the authors developed a size-focusing method for synthesizing $Au_{38}(SCH_2CH_2Ph)_{24}$ nanoclusters in a yield of 25% [94]. The synthesis mainly includes two steps. Polydispersed Au_n nanoclusters stabilized by SG were first synthesized by reducing Au(I)–SG in acetone. The core size-mixed Au_n nanoclusters subsequently react with excess phenylethylthiol, during which $Au_{38}(SC_2H_4Ph)_{24}$ clusters were gradually converted from larger clusters in the thiol-etching-induced growth process. These studies demonstrated that size-focusing process is an effective route to synthesize stable $Au_n(SR)_m$ nanoclusters. Qian et al. [49] then determined the crystal structure of the $Au_{38}(SC_2H_4Ph)_{24}$ cluster by X-ray crystallography. It was found that the Au_{38} nanocluster has crystal structure with a triclinic space group $P\bar{1}$. The total structure of the left-handed $Au_{38}(SC_2H_4Ph)_{24}$ nanocluster shown in Fig. 11 can be viewed as a core–shell structure with face-fused biicosahedral Au_{23} core capped by other 15-atom shell or a Au_{23} core plus three monomeric staples (RS–Au–SR) and six dimeric staples (RS–Au–S(R)–Au–SR). This result is in good agreement with the structure previously reported by Pei et al. in DFT calculations [98].

3.14 Au_{40} Nanoclusters

During the etching synthesis of $Au_{38}(SC_2H_4Ph)_{24}$ nanoclusters, the $Au_{40}(SC_2H_4Ph)_{24}$ clusters are always produced simultaneously in good yield [94, 97]. Recently, Qian et al. [46] isolated and identified the $Au_{40}(SC_2H_4Ph)_{24}$ species by size-exclusion chromatography. Overall, three steps are needed to synthesize and isolate the $Au_{40}(SC_2H_4Ph)_{24}$ nanoclusters. In the first step, size-mixed $Au_n(SG)_m$ clusters ($38 \leq n \leq 102$) were prepared by reducing an Au(I)–SG polymer with $NaBH_4$ in an acetone solution. Subsequently, a thermal thiol etching process with excess PhC_2H_4SH was applied to obtain $Au_{40}(SC_2H_4Ph)_{24}$ and $Au_{38}(SC_2H_4Ph)_{24}$ size-mixed nanoclusters. During the etching process, the original polydispersed $Au_n(SG)_m$ clusters ($38 \leq n \leq 102$) could be gradually converted to $Au_{40}(SC_2H_4Ph)_{24}$ and $Au_{38}(SC_2H_4Ph)_{24}$ nanoclusters over 18 h due to the super stability of Au_{40} and Au_{38}. Finally, $Au_{40}(SC_2H_4Ph)_{24}$ was isolated by size-exclusion chromatography (SEC). Figure 12 shows a typical size-exclusion chromatogram of the product after 18-h etching, and two peaks (14.0 and 14.4 min) were obtained. The online-recorded UV–Vis spectra ranging from 12.5 to 14.0 min and 14.4 to 15.6 min are almost superimposable, respectively, indicating the high purity of the eluted clusters. MALDI-MS analyses confirmed that cluster eluted from 12.5 to 14.0 min is $Au_{40}(SC_2H_4Ph)_{24}$, while the cluster eluted from 14.4 to 15.6 min is $Au_{38}(SC_2H_4Ph)_{24}$. By replacing PHC_2H_4SH with other types of thiols (e.g., $C_6H_{13}SH$, $C_5H_{11}SH$), $Au_{40}(SC_6H_{13})_{24}$ and $Au_{40}(SC_5H_{13})_{24}$ nanoclusters were also obtained after different thermal thiol-etching time. These results further confirmed the molecular formula of $Au_{40}(SR)_{24}$ and demonstrated the high stability of Au_{40}.

Recently, the total structure of the isolated Au_{40} nanoclusters was predicted and analyzed by Hakkinen and coworkers [99]. By combing structural information extracted from ligand exchange reactions, circular dichroism and TEM measurements, the structure of $Au_{40}(SR)_{24}$ was analyzed in detail via DFT computations. A novel geometrical motif was proposed where a dimer of two icosahedral Au_{13} cores is protected by six RS–Au–SR and four RS–Au–SR–Au–SR oligomeric units, analogously to the "Divide and Protect" motif of known clusters of $Au_{25}(SR)_{18}$, $Au_{38}(SR)_{24}$, and $Au_{102}(SR)_{44}$.

3.15 Au_{55} Nanoclusters

From above, Au:SR clusters with different compositions could be isolated by various techniques, such as fractional crystallization, chromatography, and electrophoresis. However, the Au_{55}:SC_x clusters were not easily obtained by the typical Brust–Schiffrin method. By the ligand exchange reaction of $Au_{55}(PPh_3)_{12}Cl_6$ clusters with hexanethiol, Murray and coworkers [100] observed a small amount of 10 kDa clusters (most likely, Au_{55}) in Au:SC_6 clusters. In 2006, Tsunoyama

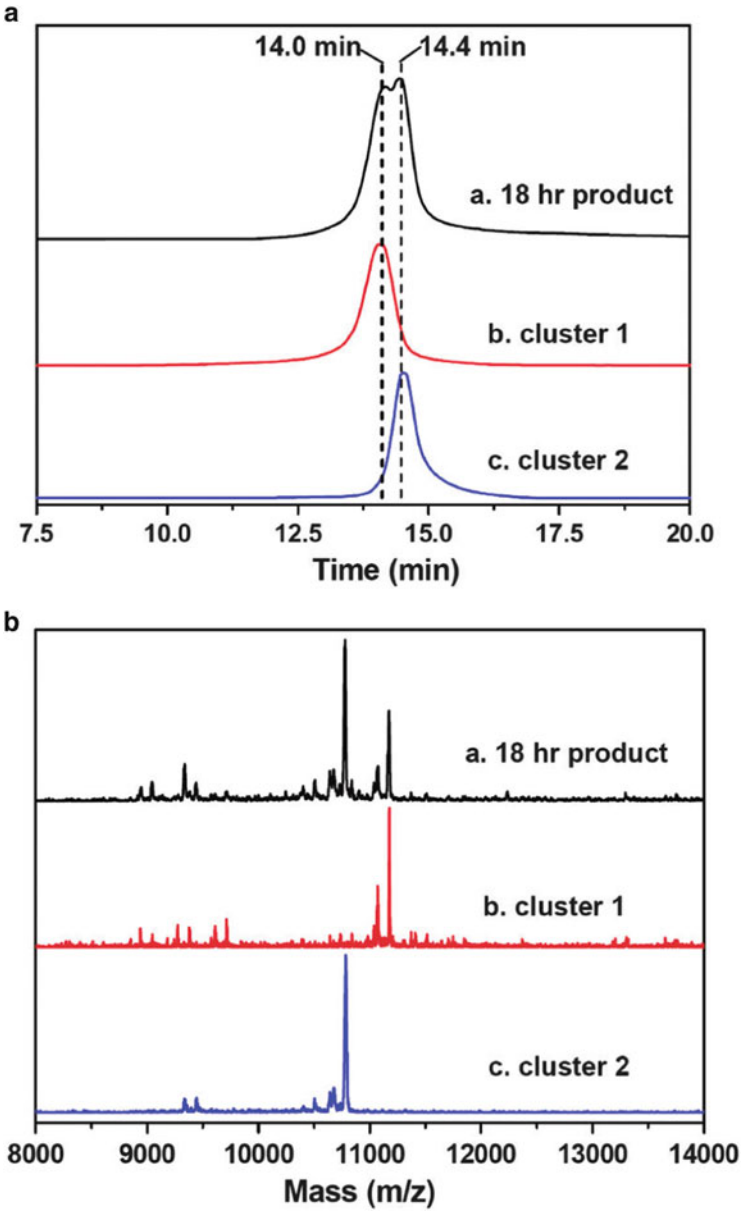

Fig. 12 (**a**) SEC chromatograms of clusters (monitored by diode array detector at 750 nm wavelength). (**b**) MALDI mass spectra of the crude product and isolated clusters (**1** and **2**). Reprinted from [46] with permission by the American Chemical Society

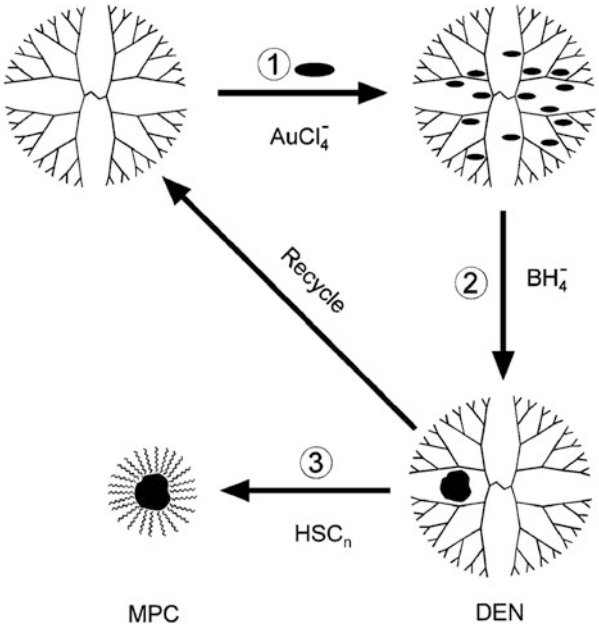

Scheme 3 Schematic illustration of the synthesis of gold clusters templated with dendrimers. Reprinted from [103] with permission by the American Chemical Society

et al. [101] for the first time demonstrated the synthesis of Au_{55}:SC_x clusters ($x = 12, 18$) by high-resolution chromatographic fractionation of Au:SC_x clusters prepared by thiolation of PVP-stabilized Au clusters and subsequent incubation in neat C_xSH. In this method, Au:PVP clusters were initially prepared by chemical reduction and the toluene solution of C_xSH was added into the hydrosol of Au:PVP cluster under vigorous stirring to generate Au:SC_x clusters. The prepared Au:SC_x clusters were then incubated at 80°C for 24 h in neat C_xSH liquid. Subsequently, the resulting clusters were successfully fractionated by recycling gel permeation chromatography (GPC) into Au_{38}:SC_x and Au_{55}:SC_x compositions.

Another facile synthesis of Au_{55} nanoclusters was achieved by using dendrimer (usually poly(amidoamine), PAMAM) as template [102, 103]. As shown in the Scheme 3, the synthesis follows the three-step process. Firstly, metal ions are extracted from solution into the dendrimer interior by taking advantage of the complexation reaction with the internal tertiary amines. Secondly, the metal ions are reduced by BH_4^-, and the resultant atoms subsequently aggregate to form zero-valent nanoclusters within the dendrimer templates. By controlling the ratio of $AuCl_4^-$ to dendrimer, Au_{55} nanoclusters could be obtained. Moreover, when the dendrimer-encapsuled clusters are treated with a toluene solution of an *n*-alkanethiol, *n*-alkanethiol could presumably self-assemble onto the cluster surface and the resulting thiolate-capped clusters can be extracted from the dendrimers to toluene phase [103].

3.16 Au_{67} Nanoclusters

By using a variety of mass spectrometric techniques, the formulas of a series of gold clusters with core sizes of 5, 8, 14, 22, and 29 kDa have been determined to be $Au_{25}(SR)_{18}$ [19], $Au_{38}(SR)_{24}$ [44], $Au_{102}(SR)_{44}$ [25], and $Au_{144}(SR)_{60}$ [104, 105], respectively. However, the unambiguous composition identification of the cluster with 14 kDa core mass has been largely impeded mainly due to the difficulty in obtaining a high yield of the 14 kDa nanoclusters in the synthetic process. By using single-phase method, Dass synthesized gold nanocluster enriched in 14 kDa mass [106]. It was found that Au_{68} nanoclusters in high yield could be specifically obtained when the growth rate is effectively lowered at certain levels of aggregation. With MDLDI MS employing threshold laser fluence and DCTB as matrix, the composition of the product was determined to be $Au_{68}(SR)_{34}$ on the basis of the detection of the parent molecular ion. However, due to lack of methods to produce pure Au_{68} nanoclusters in sufficient quantity and thus the incomplete characterizations, the obtained Au_{68} nanoclusters may be just an intermediate product [86]. Recently, Dass and coworkers [107] not only synthesized and isolated the pure species in high yield but also determined its composition of $Au_{67}(SR)_{35}$ on the basis of high-resolution ESI-MS on two different thiolate groups, i.e., 2-phenylethanethiol and *n*-hexanethiol. In their work, a cluster mixture with 14 and 22 kDa compounds were synthesized in THF. In the second stage, through mild thermochemical treatment of the polydispersed mixture in the presence of excess thiol, samples characterized by distinct peaks at 14 and 22 kDa were obtained. Finally, by using a THF–methanol mixture in appropriate ratios, pure Au_{67} nanoclusters were obtained in high yield. The optical absorption characterization of the purified Au_{67} compounds was carried out with UV–Vis measurement. As shown in Fig. 13, different from the spectra of Au_{38} and larger (~Au_{300}) clusters, the obtained Au_{67} shows a nearly monotonically rising absorption. The spectrum is in substantial agreement with that reported by Alvarez et al. [108]. Moreover, the $Au_{67}(SR)_{35}$ nanocluster was structurally considered to be the smallest one to adopt the complete truncated-decahedral motif for its core with a surface structure bearing greater similarity to the larger nanoparticles.

3.17 Au_{102} Nanoclusters

The first structure of Au_{102}(*p*-MBA)$_{44}$ (*p*-MBA = *para*-mercaptobenzoic acid) cluster was reported by Jadzinsky et al. in 2007 [25]. Based on the gold atomic packing in the cluster core and the Au–S bonding on the surface, a chiral crystal structure was proposed with the central gold atoms packed in a Marks decahedron and surrounded by additional layers of gold atoms in unanticipated geometries. Ackerson et al. [109] investigated effects of some synthetic conditions (e.g., ratios

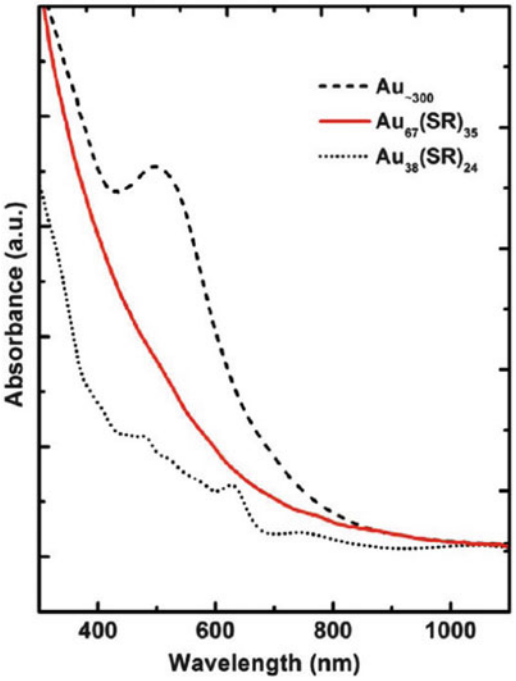

Fig. 13 UV–Vis absorption spectra of $Au_{67}(SR)_{35}$ (*red*), $Au_{38}(SR)_{24}$ (*dotted*), and a larger ~Au_{300}, 76.3 kDa (*dashed*) nanoclusters in toluene. Reprinted from [107] with permission by the American Chemical Society

of thiolate to gold, $NaBH_4$ to gold, and water to methanol), especially 36 water-soluble organothiolates on the formation of gold nanoclusters. However, the yields of the Au_{102} nanoclusters synthesized from the reported methods are very low. To obtain pure Au_{102} nanoclusters in high purity, Kornberg and coworkers [110] developed an improved strategy for synthesizing $Au_{102}(p\text{-MBA})_{44}$ nanoclusters in abundant, essentially pure form. In the synthesis, two steps were used. First, *p*-MBA and $HAuCl_4$ (3:1 ratio of *p*-MBA: gold) were dissolved in water and 47% methanol, followed by the reduction of $NaBH_4$ at room temperature. After a series of careful fractional precipitation with methanol, highly monodispersed, atomically precise $Au_{102}(p\text{-MBA})_{44}$ cluster was finally obtained. From the ESI-MS of the isolated nanoclusters shown in Fig. 14a, it can be seen that a series of peaks with mass-to-charge ratios corresponding to partially deprotonated states of $Au_{102}(p\text{-MBA})_{44}$ can be observed. The breadth of the peaks could suggest slight contamination by clusters of different compositions. The MALDI-TOF mass gave a broad peak centered at 22 kDa (Fig. 14b), consisting with 102 gold atoms and 44 sulfur atoms. These mass characterizations indicated the successful synthesis of highly monodispersed Au_{102} nanoclusters with high yield and purity. In recent years, the mechanism of the ligand exchange reaction of $Au_{102}(p\text{-MBA})_{44}$ was also

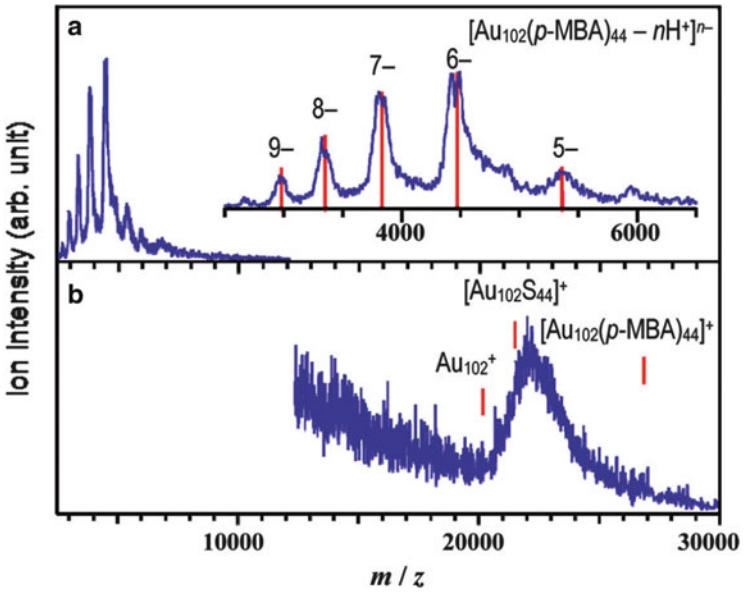

Fig. 14 ESI (**a**) and MALDI-TOF (**b**) mass spectra of the gold clusters. The *red bars* in panel **a** indicate the calculated peak positions for $[Au_{102}(p\text{-MBA})_{44} - nH^+]^{n-}$. Reprinted from [110] with permission by the American Chemical Society

investigated [111, 112]. Heinecke et al. [112] experimentally and theoretically studied the structure of a partially exchanged $Au_{102}(p\text{-MBA})_{40}(p\text{-BBT})_4$ (*p*-BBT: *para*-bromobenzene thiol) clusters. It was found that 2 of the 22 symmetry-unique *p*-MBA ligands are the most kinetically favorable exchange sites for partially exchange to *p*-BBT under the initial fast kinetics for 5 min. Another study indicated that the partial exchange of the *p*-MBA ligand does not affect the metal core of the clusters [111].

3.18 Au_{144} Nanoclusters

In the studies on the prepared gold nanoclusters, it has been found that the 5, 8, and 29 kDa Au clusters can survive the etching by free thiols, whereas the others are degraded by core etching, which indicates that the three clusters are thermodynamically and chemically stable [44, 95]. Of the three kinds of clusters, the core composition of the biggest 29 kDa clusters has been determined to be Au_{144} by ESI-MS analysis [44, 105]. Due to the relatively easy synthesis and high stability, the controlled preparation, electrochemical and optical properties of Au_{144} have been particularly well studied among the gold clusters [13, 44, 104, 113]. Because

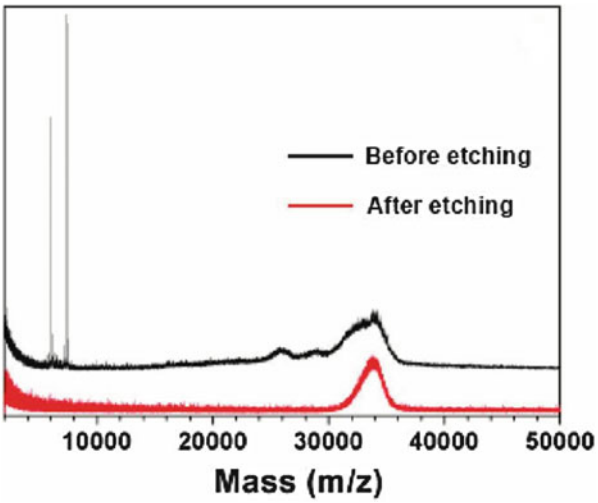

Fig. 15 MALDI mass spectra of Au nanoparticles before (*black profile*) and after thiol etching (*red profile*). DCTB was used as a matrix. Reprinted from [105] with permission by the American Chemical Society

of its high stability and widespread appearance, much effort has been devoted to the high-yield synthesis of Au_{144} nanoclusters.

Jin and coworkers [105] reported a facile, two-step synthetic method for preparing monodispersed $Au_{144}(SCH_2CH_2Ph)_{60}$ nanoclusters in a high yield of 20–30%. In the first step, polydispersed Au nanoparticles capped by $–SCH_2CH_2Ph$ were prepared via a modified Brust–Schiffrin method. Subsequently, the polydispersed Au nanoparticles dissolved in toluene were then etched by excess $PhCH_2CH_2SH$ at 80°C for ~24 h. With this procedure, an intriguing size "focusing" process occurred and only $Au_{144}(SCH_2CH_2Ph)_{60}$ was obtained finally. By comparing the MALDI-MS of the samples before and after etching process (Fig. 15), only one species centered at ~34 kDa was observed as the final product (after etching) and the other species presented in the original polydispersed particles disappeared. The MS characterization clearly indicates that the size "focusing" process can decompose the other unstable clusters and produce the highly pure Au_{144} composites. After etching, the UV–Vis absorption was also changed from featureless profile to prominent absorption bands at ~510 and ~700 nm. However, the elevated etching temperature and the high concentration of thiol limit the wide application of this method. In 2011, Jin's group [114] proposed another facile, one-pot method for preparing $Au_{144}(SR)_{60}$ nanoclusters under ambient conditions. The synthetic process is schematically illustrated in Scheme 4. Briefly, $AuCl_4^-$ was first mixed with excess thiol and TOABr in methanol to form Au(I)–SR polymers. $NaBH_4$ aqueous solution was then added to produce polydispersed Au nanoclusters. After size-focusing process, only two monodispersed components $Au_{144}(SR)_{60}$ (major product) and $Au_{25}(SR)_{18}$ (side product) are present in the product. By taking the

Scheme 4 Synthetic procedure for the synthesis of monodispersed $Au_{144}(SR)_{60}$ clusters in methanol. Reprinted from [114] with permission by the American Chemical Society

advantage of large solubility difference in acetone, pure $Au_{144}(SR)_{60}$ can be separated at a yield of 10–20%. Importantly, this method could be applied to the syntheses with different thiolate ligands, such as PhC_2H_4SH and various $C_nH_{2n+1}SH$ (where $n = 4$–8).

4 Concluding Remarks

In this chapter, we have shown the progress which has been made in recent years in the study of atomically precise gold nanoclusters. Their synthesis, structural characterization, optical properties, and core size determinations have been described above. It can be seen that in recent years, various synthetic strategies have been developed for the synthesis of monodispersed gold nanoclusters with high purity and high yield. Except for the normally stable clusters (such as Au_{144} and Au_{25}), other clusters with a wide range of gold atoms have also been successfully prepared by chemical processes. The crystal structures of several gold nanoclusters have been investigated experimentally and theoretically. It is exciting that in recent years, much attention has been paid to the study of Au-based bimetallic nanoclusters, which have more promising applications compared to the monometallic clusters. However, despite the great progress made recently for the gold nanoclusters, several challenges still remain. Firstly, more efficient high-yield synthetic approaches are expected to be developed to prepare metal clusters with atomically controlled core composition. Also complicated treatment processes in the currently reported methods need to be overcome. Secondly, most crystal structures of gold nanoclusters are not clear at present. The determination of cluster structure based on single crystals is of vital importance in understanding the relationship of structure–properties of gold nanoclusters. Thus far, only a few crystal structures of gold nanoclusters have been unambiguously determinate by X-ray crystallography, including Au_{13} [64], $Au_{25}(SR)_{18}$ [23], $Au_{36}(SR)_{24}$ [93],

$Au_{38}(SR)_{24}$ [49], and $Au_{102}(SR)_{44}$ [25] nanoclusters. The experimental and theoretical works have revealed a size-dependent general trend that starts from icosahedral atomic arrangements at smaller sizes to decahedral structures at larger ones [93]. Thirdly, although many properties of gold nanoclusters have been discovered, the exploration of their practical applications is still in its infancy. Due to the unique properties, it can be anticipated that further research on gold nanoclusters will stimulate broad scientific and technological interests in the near future.

Acknowledgments This work was supported by the National Natural Science Foundation of China (Nos. 21275136, 21043013) and the Natural Science Foundation of Jilin province, China (No. 201215090).

References

1. Mingos DMP, Slee T, Lin ZY (1990) Chem Rev 90:383
2. Briant CE, Theobald BRC, White JW, Bell LK, Mingos DMP (1981) J Chem Soc Chem Comm 201
3. Hall KP, Theobald BRC, Gilmour DI, Michael D, Mingos P, Welch AJ (1982) J Chem Soc Chem Comm 528
4. Vandervelden JWA, Bour JJ, Bosman WP, Noordik JH (1981) J Chem Soc Chem Comm 1218
5. Bartlett PA, Bauer B, Singer SJ (1978) J Am Chem Soc 100:5085
6. Bellon P, Sansoni M, Manasser M (1972) J Chem Soc Dalton 1481
7. Haruta M, Yamada N, Kobayashi T, Iijima S (1989) J Catal 115:301
8. Valden M, Lai X, Goodman DW (1998) Science 281:1647
9. Fan HY, Yang K, Boye DM et al (2004) Science 304:567
10. Wang CS, Li JY, Amatore C, Chen Y, Jiang H, Wang XM (2011) Angew Chem Int Edit 50:11644
11. Rosi NL, Giljohann DA, Thaxton CS, Lytton-Jean AKR, Han MS, Mirkin CA (2006) Science 312:1027
12. Zheng J, Dickson RM (2002) J Am Chem Soc 124:13982
13. Chen SW, Ingram RS, Hostetler MJ et al (1998) Science 280:2098
14. Qian HF, Zhu MZ, Wu ZK, Jin RC (2012) Accounts Chem Res 45:1470
15. Jin RC (2010) Nanoscale 2:343
16. Lu YZ, Chen W (2012) Chem Soc Rev 41:3594
17. Brust M, Walker M, Bethell D, Schiffrin DJ, Whyman R (1994) J Chem Soc Chem Comm 801
18. Brust M, Fink J, Bethell D, Schiffrin DJ, Kiely C (1995) J Chem Soc Chem Comm 1655
19. Zhu M, Lanni E, Garg N, Bier ME, Jin R (2008) J Am Chem Soc 130:1138
20. Wu Z, Suhan J, Jin RC (2009) J Mater Chem 19:622
21. Huang CC, Yang Z, Lee KH, Chang HT (2007) Angew Chem Int Edit 46:6824
22. Liu YL, Ai KL, Cheng XL, Huo LH, Lu LH (2010) Adv Funct Mater 20:951
23. Zhu M, Aikens CM, Hollander FJ, Schatz GC, Jin R (2008) J Am Chem Soc 130:5883
24. Heaven MW, Dass A, White PS, Holt KM, Murray RW (2008) J Am Chem Soc 130:3754
25. Jadzinsky PD, Calero G, Ackerson CJ, Bushnell DA, Kornberg RD (2007) Science 318:430
26. Qian HF, Jiang DE, Li G et al (2012) J Am Chem Soc 134:16159
27. Schaaff TG, Knight G, Shafigullin MN, Borkman RF, Whetten RL (1998) J Phys Chem B 102:10643
28. Wu ZW, Gayathri C, Gil RR, Jin RC (2009) J Am Chem Soc 131:6535

29. Whetten RL, Khoury JT, Alvarez MM et al (1996) Adv Mater 8:428
30. Murray RW (2008) Chem Rev 108:2688
31. Akola J, Walter M, Whetten RL, Hakkinen H, Gronbeck H (2008) J Am Chem Soc 130:3756
32. Jiang DE, Tiago ML, Luo WD, Dai S (2008) J Am Chem Soc 130:2777
33. Jiang DE, Luo W, Tiago ML, Dai S (2008) J Phys Chem C 112:13905
34. Lu YZ, Chen W (2012) J Power Sources 197:107
35. Wei WT, Lu YZ, Chen W, Chen SW (2011) J Am Chem Soc 133:2060
36. Ingram RS, Hostetler MJ, Murray RW et al (1997) J Am Chem Soc 119:9279
37. Chen W, Chen SW (2009) Angew Chem Int Edit 48:4386
38. Rao TUB, Pradeep T (2010) Angew Chem Int Edit 49:3925
39. Dass A, Holt K, Parker JF, Feldberg SW, Murray RW (2008) J Phys Chem C 112:20276
40. Yu Y, Luo ZT, Yu Y, Lee JY, Xie JP (2012) Acs Nano 6:7920
41. Salorinne K, Lahtinen T, Koivisto J et al (2013) Anal Chem 85:3489
42. Tracy JB, Kalyuzhny G, Crowe MC, Balasubramanian R, Choi JP, Murray RW (2007) J Am Chem Soc 129:6706
43. Dass A, Stevenson A, Dubay GR, Tracy JB, Murray RW (2008) J Am Chem Soc 130:5940
44. Chaki NK, Negishi Y, Tsunoyama H, Shichibu Y, Tsukuda T (2008) J Am Chem Soc 130:8608
45. Arnold RJ, Reilly JP (1998) J Am Chem Soc 120:1528
46. Qian HF, Zhu Y, Jin RC (2010) J Am Chem Soc 132:4583
47. Qian HF, Ellen B, Zhu Y, Jin RC (2011) Acta Phys Chim Sin 27:513
48. Zhu Y, Qian HF, Drake BA, Jin RC (2010) Angew Chem Int Edit 49:1295
49. Qian HF, Eckenhoff WT, Zhu Y, Pintauer T, Jin RC (2010) J Am Chem Soc 132:8280
50. Zhang H, Huang X, Li L et al (2012) Chem Commun 48:567
51. Zheng J, Petty JT, Dickson RM (2003) J Am Chem Soc 125:7780
52. Kamei Y, Shichibu Y, Konishi K (2011) Angew Chem Int Edit 50:7442
53. Guo WW, Yuan JP, Wang EK (2012) Chem Commun 48:3076
54. Yang X, Shi MM, Zhou RJ, Chen XQ, Chen HZ (2011) Nanoscale 3:2596
55. Xie JP, Zheng YG, Ying JY (2009) J Am Chem Soc 131:888
56. Yu P, Wen XM, Toh YR, Tang J (2012) J Phys Chem C 116:6567
57. Hainfeld JF (1987) Science 236:450
58. Woehrle GH, Warner MG, Hutchison JE (2002) J Phys Chem B 106:9979
59. Yang YY, Chen SW (2003) Nano Lett 3:75
60. Copley RCB, Mingos DMP (1996) J Chem Soc Dalton 491
61. Shichibu Y, Konishi K (2010) Small 6:1216
62. Shichibu Y, Suzuki K, Konishi K (2012) Nanoscale 4:4125
63. Laupp M, Strahle J (1994) Angew Chem Int Edn English 33:207
64. Li YY, Cheng H, Yao T et al (2012) J Am Chem Soc 134:17997
65. Shibu ES, Pradeep T (2011) Chem Mater 23:989
66. George A, Shibu ES, Maliyekkal SM, Bootharaju MS, Pradeep T (2012) Acs Appl Mater Inter 4:639
67. Shibu ES, Muhammed MAH, Tsukuda T, Pradeep T (2008) J Phys Chem C 112:12168
68. Negishi Y, Nobusada K, Tsukuda T (2005) J Am Chem Soc 127:5261
69. Negishi Y, Takasugi Y, Sato S, Yao H, Kimura K, Tsukuda T (2006) J Phys Chem B 110:12218
70. Shichibu Y, Negishi Y, Tsunoyama H, Kanehara M, Teranishi T, Tsukuda T (2007) Small 3:835
71. Reilly SA, Krick T, Dass A (2010) J Phys Chem C 114:741
72. Tlahuice A, Garzon IL (2012) Phys Chem Chem Phys 14:3737
73. Ghosh A, Udayabhaskararao T, Pradeep T (2012) J Phys Chem Lett 3:1997
74. Xu Q, Wang SX, Liu Z, Xu GY, Meng XM, Zhu MZ (2013) Nanoscale 5:1176
75. Wu ZK, MacDonald MA, Chen J, Zhang P, Jin RC (2011) J Am Chem Soc 133:9670
76. Schmid G, Pfeil R, Boese R et al (1981) Chem Ber Recl 114:3634

77. Weare WW, Reed SM, Warner MG, Hutchison JE (2000) J Am Chem Soc 122:12890
78. Zhang HF, Stender M, Zhang R, Wang CM, Li J, Wang LS (2004) J Phys Chem B 108:12259
79. Wan XK, Lin ZW, Wang QM (2012) J Am Chem Soc 134:14750
80. Zhu MZ, Qian HF, Jin RC (2009) J Am Chem Soc 131:7220
81. Pei Y, Gao Y, Shao N, Zeng XC (2009) J Am Chem Soc 131:13619
82. Das A, Li T, Nobusada K, Zeng Q, Rosi NL, Jin RC (2012) J Am Chem Soc 134:20286
83. Parker JF, Fields-Zinna CA, Murray RW (2010) Accounts Chem Res 43: 1289
84. Donkers RL, Lee D, Murray RW (2004) Langmuir 20:1945
85. Negishi Y, Takasugi Y, Sato S, Yao H, Kimura K, Tsukuda T (2004) J Am Chem Soc 126:6518
86. Dharmaratne AC, Krick T, Dass A (2009) J Am Chem Soc 131:13604
87. Shichibu Y, Negishi Y, Tsukuda T, Teranishi T (2005) J Am Chem Soc 127:13464
88. Xie SH, Tsunoyama H, Kurashige W, Negishi Y, Tsukuda T (2012) Acs Catal 2:1519
89. Negishi Y, Chaki NK, Y Shichibu, RL Whetten, T Tsukuda (2007) J Am Chem Soc 129:11322
90. Parker JF, Weaver JEF, McCallum F, Fields-Zinna CA, Murray RW (2010) Langmuir 26:13650
91. Yuan X, Yu Y, Yao QF, Zhang QB, Xie JP (2012) J Phys Chem Lett 3:2310
92. Nimmala PR, Dass A (2011) J Am Chem Soc 133:9175
93. Zeng CJ, Qian HF, Li T et al (2012) Angew Chem Int Edit 51:13114
94. Qian HF, Zhu Y, Jin RC (2009) Acs Nano 3:3795
95. Schaaff TG, Whetten RL (1999) J Phys Chem B 103:9394
96. Toikkanen O, Ruiz V, Ronholm G, Kalkkinen N, Liljeroth P, Quinn BM (2008) J Am Chem Soc 130:11049
97. Qian HF, Zhu MZ, Andersen UN, Jin RC (2009) J Phys Chem A 113:4281
98. Pei Y, Gao Y, Zeng XC (2008) J Am Chem Soc 130:7830
99. Malola S, Lehtovaara L, Knoppe S et al (2012) J Am Chem Soc 134:19560
100. Balasubramanian R, Guo R, Mills AJ, Murray RW (2005) J Am Chem Soc 127:8126
101. Tsunoyama H, Negishi Y, Tsukuda T (2006) J Am Chem Soc 128:6036
102. Crooks RM, Zhao MQ, Sun L, Chechik V, Yeung LK (2001) Accounts Chem Res 34:181
103. Garcia-Martinez JC, Crooks RM (2004) J Am Chem Soc 126:16170
104. Hicks JF, Miles DT, Murray RW (2002) J Am Chem Soc 124:13322
105. Qian HF, Jin RC (2009) Nano Lett 9:4083
106. Dass A (2009) J Am Chem Soc 131:11666
107. Nimmala PR, Yoon B, Whetten RL, Landman U, Dass A (2013) J Phys Chem A 117:504
108. Alvarez MM, Khoury JT, Schaaff TG, Shafigullin MN, Vezmar I, Whetten RL (1997) J Phys Chem B 101:3706
109. Ackerson CJ, Jadzinsky PD, Kornberg RD (2005) J Am Chem Soc 127:6550
110. Levi-Kalisman Y, Jadzinsky PD, Kalisman N et al (2011) J Am Chem Soc 133:2976
111. Hulkko E, Lopez-Acevedo O, Koivisto J et al (2011) J Am Chem Soc 133:3752
112. Heinecke CL, Ni TW, Malola S et al (2012) J Am Chem Soc 134:13316
113. Schaaff TG, Shafigullin MN, Khoury JT et al (1997) J Phys Chem B 101:7885
114. Qian HF, Jin RC (2011) Chem Mater 23:2209

Struct Bond (2014) 161: 155–188
DOI: 10.1007/430_2014_142

Published online: 10 April 2014

Gold Thiolate Nanomolecules: Synthesis, Mass Spectrometry, and Characterization

Chanaka Kumara, Vijay Reddy Jupally, and Amala Dass

Abstract This chapter summarizes the synthetic routes used for the following HS-CH_2-CH_2-Ph protected gold nanoclusters: $Au_{25}(SR)_{18}$, $Au_{38}(SR)_{24}$, $Au_{40}(SR)_{24}$, $Au_{67}(SR)_{35}$, $Au_{103–105}(SR)_{45–46}$, $Au_{130}(SR)_{50}$, and $Au_{144}(SR)_{60}$. The synthetic routes are based on either (a) direct synthetic route or (b) a core-size conversion route. The synthetic routes leading to the most stable clusters are discussed and the characterizational techniques used to study the products are described.

Keywords Clusters · Electrospray · Gold · MALDI · Nanoclusters · Nanomolecules · Nanoparticle mass spectrometry · Thiolated

Contents

C. Kumara, V.R. Jupally, and A. Dass (✉)
Department of Chemistry and Biochemistry, University of Mississippi, Oxford, MS 38677, USA
e-mail: amal@olemiss.edu

1 Introduction

Gold-thiolate nanomolecules are ultra-small (<2-nm) gold nanoparticles with a fixed composition, containing a precise number of gold atoms and thiolate ligands. These highly stable nanomolecules have a unique molecular formula and can be characterized by conventional analytical and spectroscopic techniques. They can be isolated in dried form and re-dispersed in solvents and are stable in air for several years. A typical example includes $Au_{25}(SCH_2CH_2Ph)_{18}^{-}$. The molecular weight of 7,394 Da was independently verified using electrospray ionization mass spectrometry (ESI-MS) and matrix-assisted laser desorption ionization mass spectrometry (MALDI-MS). Ligand variations were also used to determine its composition. This composition was also verified by X-ray crystallography and its structure was found to contain a central Au atom, surrounded by 12 atoms on the vertices of an icosahedron, protected by 6 [−SR-Au-SR-Au-SR−] units. The UV-visible spectrum displays a distinct step-like fine features, reminiscent of molecular behavior. Its redox properties were studied by cyclic voltammetry and displays molecule-like behavior, with a large electrochemical gap between oxidation and reduction waves [1]. The renewed interest in these thiolated gold nanomolecules, which are a form of thiolated gold clusters is twofold: (a) *molecular definition* – Contrary to naked metal clusters generated in gas phase, the solution phase synthesis of thiolate-protected gold nanomolecules yield exclusively one core-sized molecule. For example, the $Au_{25}(SR)_{18}$ synthesis yields exclusively $Au_{25}(SR)_{18}$ and there is no formation of Au_{23}, Au_{24}, Au_{26}, Au_{27} species; (b) *Stability* – Unlike phosphine and other ligated gold clusters, the thiolate-protected gold nanomolecules are ultra-stable. That is, the Au–S bond is strong and therefore the number of ligands is fixed, as opposed to the dynamic nature of ligands in the many Au-phosphine clusters and other ligated systems. Moreover, the thiolated nanomolecules are stable in air/oxygen, moisture, and high temperatures (up to 80°C) and can be dried and re-dispersed in solvents.

2 Overview of Various Thiolated Gold Nanomolecules

Typical examples of chemically well-defined gold nanomolecules protected by HS-CH_2-CH_2-Ph ligand include $Au_{25}(SR)_{18}$, $Au_{38}(SR)_{24}$, $Au_{40}(SR)_{24}$, $Au_{67}(SR)_{35}$, $Au_{103–105}(SR)_{45–46}$, $Au_{130}(SR)_{50}$, $Au_{144}(SR)_{60}$, and the 76.3 kDa $Au_{\sim 320}$ species.

2.1 Ultra-Stable Nanomolecules

Some core sizes are easily synthesized, with minimal purification procedures and are highly stable in air, moisture, and in some cases, even under thermal treatment in the presence of excess thiol. This includes $Au_{25}(SR)_{18}$, $Au_{38}(SR)_{24}$, and $Au_{144}(SR)_{60}$. These are also some of the earliest reported nanomolecules in the late 1990s and are therefore well studied. More recently, $Au_{40}(SR)_{24}$ and $Au_{130}(SR)_{50}$ have been synthesized and shown to have very high stabilities. In the nanomolecules discussed in this chapter, the R group is either $–CH_2CH_2Ph$ or $–C_6H_{13}$.

2.2 Meta-stable Nanomolecules

Other core sizes are stable under most conditions such as air, moisture, oxygen, but are unstable on high temperature treatment in the presence of excess thiol. Due to the lower stability, we term these as "*meta-stable*" nanomolecules. Meta-stable nanomolecules require extensive purification protocols to obtain monodispersed final products which are analytically pure. These include $Au_{67}(SR)_{35}$ and $Au_{103–105}(SR)_{45–46}$.

3 Synthetic Routes: Direct Synthesis vs. Core-Size Conversion

The synthesis of gold nanomolecules by reduction of Au(I) thiolate complexes by borohydride typically yields a mixture of clusters with various sizes. Depending on the stability, the syntheses of various nanomolecules require different synthetic protocols to obtain a monodispersed product in significant quantities. Broadly, the synthetic strategies are categorized as either direct synthetic route or core-size conversion route.

1. *Direct Synthesis:* The borohydride reduction of Au(I) thiolate is typically the first step in the nanomolecule synthesis, and this reaction is referred to here as *direct synthesis*. Based on the stability and the distribution of the various core sizes, various strategies such as a thermochemical treatment in excess thiol, purification, and separation steps may have to be employed. $Au_{25}(SR)_{18}$, $Au_{67}(SR)_{35}$, $Au_{103–105}(SR)_{45–46}$, $Au_{144}(SR)_{60}$, and the 76.3 kDa nanomolecules are produced by direct synthesis.
2. *Core-Size Conversion Synthesis:* $Au_{38}(SR)_{24}$, $Au_{40}(SR)_{24}$, and $Au_{130}(SR)_{50}$ are produced through core-size conversion syntheses. Here, larger core-sized and polydispersed nanoclusters are converted to smaller, single-sized nanomolecules.

3.1 Techniques Used to Study the Synthesis Reaction

The tools used during the syntheses reactions in our laboratory include mass spectrometry, size exclusion chromatography (SEC), and solvent fractionation purification procedures.

We routinely use mass spectrometry to study the synthesis reaction, product identification and to monitor the progress of the reaction [2]. We use MALDI-MS in nanomolecules synthesis, as thin layer chromatography (TLC) is used in small molecule organic synthesis. That is, MALDI-MS analysis of (a) aliquots of nanomolecule synthesis mixture as a function of time [2] and (b) fractions of SEC column and solvent fractionation steps is performed routinely [3, 4].

3.2 Historical Introduction to the Synthesis of Nanomolecules

The two-phase Brust–Schiffrin synthesis is the most common method used to prepare thiolated gold nanoparticles [5]. The foundation for thiolated gold nanomolecules, including the synthesis, mass spectrometry, purification, and X-ray diffraction methods was laid by Whetten and Murray's research groups. The idea of molecular definition – 'gold nanocrystal molecules,' [6] use of mass spectrometry for nanoparticle analysis [6], solvent fractionation, etching – thermochemical excess thiol treatment [7], was pioneered by Whetten. The idea of 'monolayer protected clusters' with a specific molecular formulae, the widespread use of HS-CH_2-CH_2-Ph ligand, all things pertaining to $Au_{25}(SCH_2CH_2Ph)_{18}^-$ though initially mis-assigned as $Au_{38}(SR)_{24}$ [1], organic solvent nanoparticle ESI mass spectrometry [8], DCTB matrix-based MALDI [9], synthesis/electrochemistry of $Au_{144}(SR)_{60}$ – initially assigned as 'Au_{140}', nanoparticle electrochemistry [10–12], crystal structure of $Au_{25}(SCH_2CH_2Ph)_{18}$ [13], first alloy nanomolecule $Au_{24}Pd_1(SCH_2CH_2Ph)_{18}$ [14] were pioneered by Murray. These studies were reported between 1996 and 2008. Nearly every recent study is built on these original reports. Many of these newer reports are modified versions of the original procedures that poorly cite these early reports [15].

4 Direct Synthesis

In this section, the syntheses of $Au_{25}(SR)_{18}$, $Au_{67}(SR)_{35}$, $Au_{103–105}(SR)_{45–46}$, and $Au_{144}(SR)_{60}$ nanomolecules by direct synthesis are presented. The syntheses are grouped into two sections: (a) the synthesis of ultra-stable $Au_{25}(SR)_{18}$, $Au_{144}(SR)_{60}$, and their analogous gold–silver alloy nanomolecules; (b) the synthesis of meta-stable $Au_{67}(SR)_{35}$ and $Au_{103–105}(SR)_{45–46}$.

4.1 *Ultra-Stable Nanomolecules: $Au_{25}(SR)_{18}$, $Au_{144}(SR)_{60}$, and Its Au–Ag alloys*

The syntheses of $Au_{25}(SR)_{18}$ and $Au_{144}(SR)_{60}$ have been studied in detail by Murray's group [1]. Several variations of these synthetic methods have been reported recently. Here, we mainly focus on more recent developments on these systems, where Ag atoms are doped into the 25- and 144-atom nanomolecules.

Gold nanoparticles are very stable compared to other metal nanoparticles and used in numerous applications including optoelectronics [16, 17], solar cells [18], biochemistry [17, 19], and catalysis [20, 21]. However, metallic silver is much cheaper than gold. Also, silver has interesting optical properties which can be used in plasmonic applications [22]. Antifungal and antibacterial properties of silver nanoparticles facilitate its application in water purification and both in vivo and in vitro applications [23]. However, instability and low resistance to oxidation prevent the practical applications of silver nanoparticles to some extent. The beneficial properties of gold and silver can be combined into one alloy unit in the form of ultra-small alloy nanomolecules.

In 2010 Negishi [24] reported the synthesis of $Au_{25-x}Ag_x(SR)_{18}$, where x is the number of silver atoms, determining the silver atom incorporation qualitatively and quantitatively using MALDI-MS. Further, they observed the continuous modulation of electronic structure upon silver incorporation. Silver has approximately the same atomic volume as gold [25]. This facilitates the incorporation of silver atoms into ultra-small gold nanomolecules. Inspired by Negishi's report, we further compressed the properties of both gold and silver into single stable unit in the form of ultra-small alloy to investigate the behavior of nanomolecules such as $Au_{38}(SR)_{24}$ and quantized double layer charging nanomolecules like $Au_{144}(SR)_{60}$. These bimetallic nanoparticles (alloys) exhibit novel optical and electrical properties compared to their monometallic counterparts. Furthermore, alloying can be used to tune the properties of nanoparticles. Thus, the beneficial properties of both the metals were combined to produce alloy nanomolecules that are superior in performance than the nanomolecules of individual metals.

4.1.1 $Au_{25}(SR)_{18}$ and $Au_{25-x}Ag_x(SCH_2CH_2Ph)_{18}$ Alloy Nanomolecules

Among the various $Au_n(SR)_m$ molecules, $Au_{25}(SR)_{18}$ is the most studied, due to its interesting optical [26] and electrochemical [27] properties and high stability. Murray's group pioneered the synthesis of $Au_{25}(SR)_{18}$ nanomolecules. Initially, this nanocluster was wrongly identified as $Au_{38}(SR)_{24}$. The synthesis was performed according to modified Brust method in THF. From the crude product obtained, using acetonitrile, $Au_{25}(SR)_{18}$ can be extracted from the mixture. The molecular formula was assigned as $Au_{25}(SR)_{18}$ by Tracy et al. using high-resolution ESI-MS [28]. The anionic nature of the nanomolecule was also identified during the ESI-MS experiments of Tracy et al.

After the Murray's group report on the synthesis of $Au_{25}(SR)_{18}$ nanomolecules several other synthetic protocols were reported to increase the final yield of the nanomolecules. Wu et al. reported a one-phase THF method [29]. In this method, gold salt and thiol are added to THF, without any water, as both the gold salt and ligand are nicely soluble in THF. Then the reducing agent $NaBH_4$ is added to the reaction mixture and the reaction is monitored by UV–vis spectroscopy [29].

We have used MALDI-TOF mass spectrometry to monitor the size evolution of $Au_{25}(SR)_{18}$ in one-phase THF method. In this report, the aliquots from the reaction were collected at different time intervals and analyzed by MALDI-TOF mass spectrometry. While Jin's work showed that $Au_{25}(SR)_{18}$ is formed in the reaction with time, this work nicely shows several gold nanoclusters that are formed in the synthesis and how the proportion of various nanomolecules evolves with time to yield $Au_{25}(SR)_{18}$. Figure 1 (left) shows the MALDI-TOF mass spectra of the samples collected at different time intervals.

Murray's group recently published another protocol to synthesize anionic $Au_{25}(SR)_{18}$ in high yield using phenylethanethiol ligand [30]. In this modified protocol, tetraoctylammoniumbromide (TOABr) is added to the THF along with the gold salt. Addition of TOABr aids the formation of anionic $Au_{25}(SR)_{18}$ in high yields (~50% yield) and stability (see Figure 1 right). Murray has recently summarized all the published work on $Au_{25}(SR)_{18}$ in the form of a review article [1].

Besides the synthesis and characterizations, atomic structures of $Au_{25}(SR)_{18}$ nanomolecule were reported independently by both Murray and Jin research groups [13, 31]. In the $Au_{25}(SR)_{18}$ family, several alloys have been reported by different research groups including $Au_{25-x}Ag_x(SR)_{18}^-$ [24], $Au_{24}Pd(SR)_{18}$ [32], $Au_{25-x}Cu_x(SR)_{18}$ [33], and $Au_{24}Pt(SR)_{18}$ [34]. Interestingly, Ag atom doping results in maximum heteroatom incorporation, i.e. up to 12 silver atoms.

The fundamental question arising from $Au_{25-x}Ag_x(SR)_{18}$ alloy nanomolecules is: Where are the silver atoms incorporated in the atomic structure? This question can be addressed in two different ways. **1**. *Computational/theoretical studies*. Lin and Mingos provided general rules for understanding the geometric preferences of alloy clusters in the 1980s and more recently DFT calculations have been used to interpret these preferences in thiolate clusters [35]. For example, Walter et al. [36] and Guidez et al. [37] have shown that the surface of the icosahedral core is energetically preferred for silver. Others [38] have also predicted the same. Jiang and coworkers theroretically predicted the doping of the icosahedral gold core of $MAu_{24}(SR)_{18}$, with several heteroatoms [35]. The synthesis and structural characterization of icosahedral $[Au_9M^{IB}{}_4Cl_4(PMePh_2)_8][C_2B_9H_{12}]$ alloy and its substitutional preferences were discussed [39, 40]. **2**. *Experimental determination using single crystal X-ray analysis*. Here, X-ray crystallography analysis was used to determine the location of silver doping.

$Au_{25-x}Ag_x(SCH_2CH_2Ph)_{18}^-$ alloy nanomolecules were synthesized using the direct synthesis methodology reported by Negishi [24]. Several batches of Au:Ag atomic combinations were synthesized using different Au:Ag incoming molar ratios. Crystallization of alloy nanomolecules were set up using vapor diffusion method. Crystals were obtained in dried form in the batch of Au:Ag 1:0.25

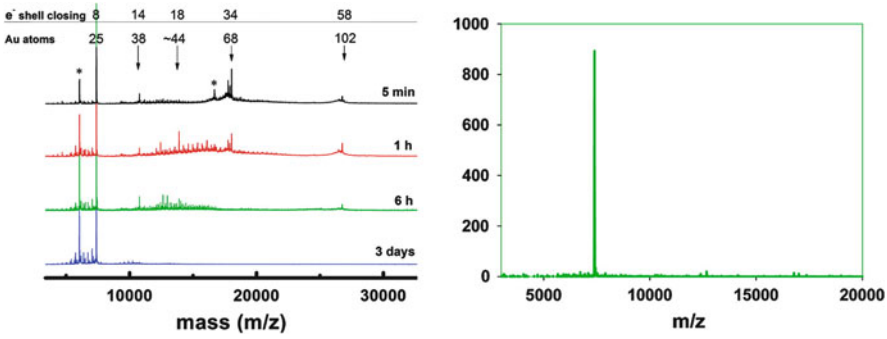

Fig. 1 $Au_{25}(SR)_{18}$ synthesis in THF. *Left*: MALDI-TOF mass spectra of the as-prepared nanoclusters using DCTB matrix and operating at threshold laser fluence. Nanocluster synthesis conditions: gold/phenylethanethiol molar ratio 1:6; room temperature; fast stirring (500 rpm); reaction solvent, THF. Samples were purified and analyzed at 5 min, 1 h, 6 h, and 3 days. Initially the nanocluster mixture contains Au_{25}, Au_{38}, Au_{44}, Au_{68}, and Au_{102}, which over time converges to Au_{25}. Peaks marked by asterisk are fragments. Reprinted with permission from [2]. Copyright 2009 American Chemical Society. *Right*: MALDI-MS of $[Oct_4N^+][Au_{25}(S(CH_2)_2Ph)_{18}^-]$ as synthesized in THF by the present procedure. The matrix used is *trans*-2-[3-(4-*tert*-butylphenyl)-2-methyl-2-propenylidene]malonotrile (DCTB). The spectrum shows a non-fragmented, monodisperse product. Reprinted with permission from [2, 30]. Copyright 2010 American Chemical Society

incoming molar ratio synthesis. This batch of crystals was used for X-ray crystallographic analysis.

Figure 2 shows the crystal structure of $Au_{25-x}Ag_x(SCH_2CH_2Ph)_{18}^-$, which crystallizes in the triclinic space group $P\bar{1}$. There are three different distinct locations where the silver atom can be doped into the $Au_{25}(SR)_{18}$ structure: (1) the one central atom of the icosahedral core, (2) the twelve atoms in the vertices of the icosahedral core, and (3) the twelve Au atoms forming the six dimeric staple [−SR-Au-SR-Au-SR−] motifs.

Single crystal X-ray structure indicates that the central atom is exclusively Au, as predicted by theory before [37]. The twelve atoms at the vertices of the icosahedral Au_{12-x} Ag_x cage show dual occupancy. The overall composition from XRD crystal structure consists of 6.70 Ag and 5.30 Au atoms. The partial occupancy of Ag and Au atoms was independently verified using mass spectrometry (see later section). The compositional disorder of Au and Ag atoms yields fractional occupancies. Figure 2a (inset table) shows the following percentages of Ag atoms: atoms Ag_2/Au_2 share the same site with the Ag_2 atom being present 59% of the time, Ag_3/Au_3 – 45%, Ag_4/Au_4 – 61%, Ag_5/Au_5 – 58%, Ag_6/Au_6 – 53%, and Ag_{10}/Au_{10} – 56%. Therefore, the cage composition can be formulated as $Au_{5.3}Ag_{6.7}$. The atoms in the staple groups contain exclusively gold.

It is interesting to note that the greatest (4 and 4′ site) and least Ag (3 and 3′ site) occupancy sites are located on the same plane. Partially occupied counter ions and solvent molecules were observed in crystal structure. There is clear evidence for the

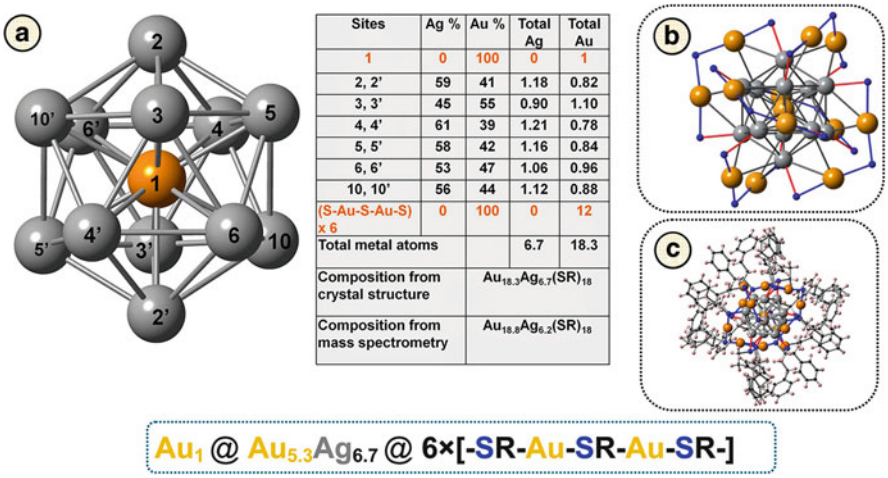

Sites	Ag %	Au %	Total Ag	Total Au
1	0	100	0	1
2, 2'	59	41	1.18	0.82
3, 3'	45	55	0.90	1.10
4, 4'	61	39	1.21	0.78
5, 5'	58	42	1.16	0.84
6, 6'	53	47	1.06	0.96
10, 10'	56	44	1.12	0.88
(S-Au-S-Au-S) x 6	0	100	0	12
Total metal atoms			6.7	18.3
Composition from crystal structure	$Au_{18.3}Ag_{6.7}(SR)_{18}$			
Composition from mass spectrometry	$Au_{18.8}Ag_{6.2}(SR)_{18}$			

Fig. 2 X-ray crystal structure of $Au_{25-x}Ag_x(SCH_2CH_2Ph)_{18}$ anion. The X-ray crystallography-based composition is $Au_{18.3}Ag_{6.7}(SCH_2CH_2Ph)_{18}^-$. This can be written as $Au_1@Au_{5.3}Ag_{6.7}@6\times[-SR\text{-}Au\text{-}SR\text{-}Au\text{-}SR\text{-}]$. (**a**) The 13-atom icosahedral alloy core geometry, showing a central Au atom (*yellow*) with 100% Au occupancy surrounded by 12 atoms that show partial occupancy of Au or Ag atoms, as shown in the inset table (**b**) $Au_{25}S_{18}$ framework showing the six [−SR-Au-SR-Au-SR−] dimeric units, where the dimeric units exclusively contain Au atoms, with 100% Au occupancy. (**c**) Total structure of $Au_{25-x}Ag_x(SCH_2CH_2Ph)_{18}^-$. *Blue lines* indicate Au–S bonds; *red lines* indicate possible Ag–S or Au–S bonds; color of atoms – *yellow* is Au, gray is Ag or Au, *blue* is S. (Table) The *inset* table in (**a**) shows that the 12 atoms at the icosahedral vertices are partially occupied by Ag or Au. The X-ray crystallographic structure is an *average* structure; that is, the X-ray composition $Au_{18.3}Ag_{6.7}(SCH_2CH_2Ph)_{18}^-$ is the average value obtained from diffraction of many $Au_{25-x}Ag_x(SR)_{18}$ molecules in the crystal. The Ag atoms were found distributed among the twelve icosahedral vertex atoms, with slight preference for sites 2, 2′, 4, 4′, 5, 5′, 10, and 10′ when compared with 3, 3′, 6, and 6′. For any individual $Au_{25-x}Ag_x(SR)_{18}$ molecule in the crystal, however, the composition is likely to be $Au_{21}Ag_4(SR)_{18}$, $Au_{20}Ag_5(SR)_{18}$, $Au_{19}Ag_6(SR)_{18}$, $Au_{18}Ag_7(SR)_{18}$, and $Au_{17}Ag_8(SR)_{18}$ with probabilities of 3.3%, 19.4%, 42.3%, 28.8%, and 6.6%, respectively, as shown by ESI-MS spectra in Fig. 3. The composition obtained independently by ESI-MS is $Au_{18.8}Ag_{6.2}(SCH_2CH_2Ph)_{18}$, in reasonable agreement with X-ray crystallographic composition. Reprinted with permission from [41]. Copyright 2014 American Chemical Society

presence of tetra-octyl ammonium counter ion, but it was not modeled in this work. Solvent loss or disordered solvent channel that increases the mosaicity of the crystals may have masked the identification of exact location of the counter ions.

When compared with reported monometallic $Au_{25}(SC_2H_4Ph)_{18}^-$ crystal structures [13, 31] major structural alterations were not observed upon silver incorporation. The silver atoms were simply doped into the twelve vertices of the icosahedral core. As the Ag incorporation increased, bond elongations were observed from central Au atom to icosahedral surface atoms.

Figure 3 shows the ESI mass spectra obtained from the THF solution of crystals used for X-ray diffraction. Individual peaks in ESI-MS show the presence of five species, $Au_{17}Ag_8(SR)_{18}$, $Au_{18}Ag_7(SR)_{18}$, $Au_{19}Ag_6(SR)_{18}$, $Au_{20}Ag_5(SR)_{18}$, and

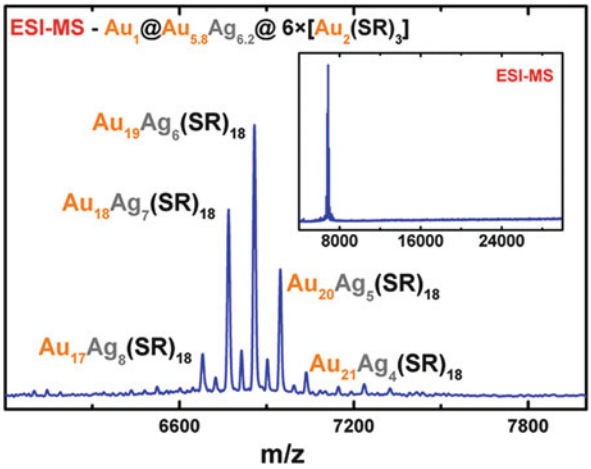

Fig. 3 ESI-MS of the $Au_{25-x}Ag_x(SCH_2CH_2Ph)_{18}^-$ crystals. Inset shows the spectrum from 4,000 to 35,000 Da mass range. Reprinted with permission from [41]. Copyright 2014 American Chemical Society

Table 1 Determination of silver composition by mass spectrometry

Nanomolecules	Ag percent as total[a]	Contribution of silver from each species
$Au_{21}Ag_4(SR)_{18}$	3.3	0.13
$Au_{20}Ag_5(SR)_{18}$	19.4	0.97
$Au_{19}Ag_6(SR)_{18}$	42.3	2.54
$Au_{18}Ag_7(SR)_{18}$	28.8	2.02
$Au_{17}Ag_8(SR)_{18}$	6.1	0.48
Total number of Ag derived from mass spectrometry		6.2

[a]Taken from mass spectrometry data
Reprinted with permission from [41]. Copyright 2014 American Chemical Society

$Au_{21}Ag_4(SR)_{18}$ nanomolecules. The relative percentages of each of these species were calculated from the peak height of the mass spectrum peaks. Then, using these percentage values, the average composition was calculated and found to be $Au_{18.8}Ag_{6.2}(SR)_{18}$. These calculations are summarized in Table 1.

X-ray crystallography also yields the average structure and average composition which is independently derived as 6.70 silver atoms, with the composition $Au_{18.3}Ag_{6.7}(SCH_2CH_2Ph)_{18}$. So mass spectrometry and X-ray crystallography independently determined the silver content as 6.2 and 6.7 atoms, respectively. This is a reasonable agreement, and the differences may be due to the mass spectrometric peak heights, which are correlated with the ionization efficiencies and slightly differ from what is present in the solution phase.

Detailed analysis on heteroatom doping location and related chemical and physical properties through the crystal structure information will facilitate the design of new and efficient catalysts based on $Au_{25}(SR)_{18}$ alloy nanomolecules.

4.1.2 $Au_{144}(SR)_{60}$ and $Au_{144-x}Ag_x(SCH_2CH_2Ph)_{18}$ Alloy Nanomolecules

The two-phase Brust–Schiffrin method [5] published in 1994 offers a way to synthesize stable thiol-protected gold nanoparticles. Using comprehensive analytical tools such as high-resolution transmission electron microscopy, NMR, small-angle X-ray scattering, and thermo gravimetric analysis, Murray and coworkers were able to determine the approximate cluster size, number of gold atoms, and core diameter of certain gold nanoparticles. Different sizes of nanoparticles were observed ranging from 1.5 to 5.2 nm, containing 100–4,800 Au atoms [42]. They observed nanoparticles with 140 gold atoms as one of the major products in the experiment conducted at 0°C, twofold excess thiol and rapid $NaBH_4$ (reduction agent) addition. Since then, the synthesis of Au_{140} (later corrected as Au_{144}) was established with optimized experimental conditions and interesting optical, monolayer, and electrochemical properties were revealed [10–12]. Later Whetten and coworkers identify Au_{140} as gold nanoclusters with 29 kDa core mass based on laser desorption ionization mass spectrometry and other supporting evidence [43]. Tsukuda and coworkers using electrospray mass spectrometry reported that this 29 kDa cluster contains 144 gold atoms and 59 ligands, namely $Au_{144}(SR)_{59}$ [44]. However DFT calculations suggested that the composition is $Au_{144}(SR)_{60}$ [45]. Later in 2009, Murray [8] and Jin [46] achieved high-resolution ESI MS data for the 29 kDa nanoclusters and assigned the composition to be $Au_{144}(SR)_{60}$, as shown in Fig. 4. Today, the synthesis of $Au_{144}(SR)_{60}$ is well established and research is in progress toward applications in drug delivery and catalysis.

In this section, we introduce the Ag alloy of the 144-Au atom species, namely the $Au_{144-x}Ag_x(SR)_{60}$. The synthesis of the $Au_{144-x}Ag_x(SR)_{60}$[47] also follows the direct synthesis protocol. However, it involves three steps. The first step involves the direct synthesis of $Au_{144-x}Ag_x(SR)_{60}$ crude product that contains polydisperse Au–Ag clusters. The second step is the etching of the crude product with excess thiol to remove meta-stable alloy nanomolecules to obtain $Au_{144-x}Ag_x(SR)_{60}$ in significant quantities. In this case, we used thermochemical treatment as further purification method. Final step is the isolation of highly monodisperse $Au_{144-x}Ag_x(SR)_{60}$ nanomolecules using solvent fractionation.

Figure 5 shows the negative mode ESI mass spectra of the nanomolecules focused on the 3- (triply charged) ions. The bottom curve (black) shows the ESI-MS of monometallic $Au_{144}(SR)_{60}$. Introduction of silver precursor in different molar ratio in the initial synthesis indicates the formation of $Au_{144-x}Ag_x(SR)_{60}$ alloys with different x values(silver atoms). However, interestingly the total number of metal atoms remains constant at 144. The envelope of peaks observed in the mass spectra is due to the different number of Ag atoms incorporated. The mass difference between the consecutive peaks in the mass spectra agrees with the mass difference between gold and silver (Au = 196.97 Da, Ag = 107.87 Da, m = 89.1 Da). Experiments at higher silver ratios (e.g., Au:Ag, 1:1) do not produce stable $Au_{144-x}Ag_x(SR)_{60}$ alloys and decompose upon etching. Synthesized products using 1:0.25 and 1:0.66 incoming Au:Ag mole ratio show additional

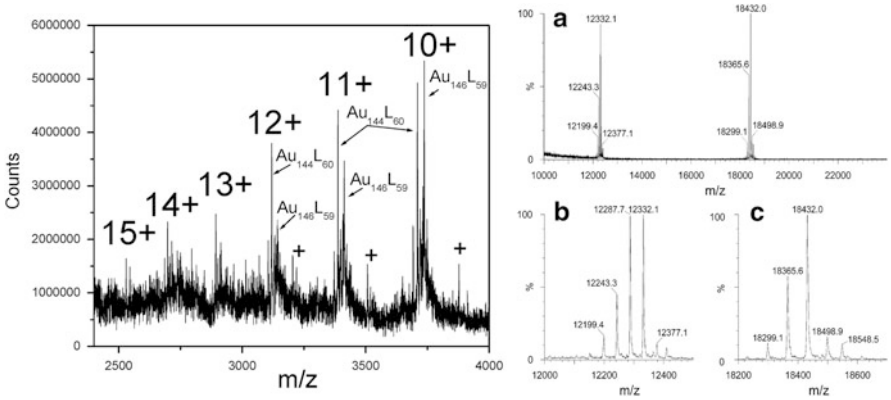

Fig. 4 *Left*: ESI-QQQ positive-mode spectrum of 1.6 nm diameter hexanethiolate-protected nanoparticle sample exchanged with $[HSC_{11}H_{22}(CH_2CH_3)_3N^+][Cl^-]$ ($STEA^+$, or T). Six charge states are detected, from 10^+ to 15^+, each including both $Au_{144}L_{60}$ and $Au_{146}L_{59}$. The charge z is due to the number of T ligands ($STEA^+$). Run in 70:30 MeCN:MeOH (optima grade), with no added electrolyte. Reprinted with permission from [2, 8]. Copyright 2009 American Chemical Society. *Right*: (**a**) ESI mass spectra of $Au_{144}(SCH_2CH_2Ph)_{60}$ nanoparticles. (**b**) Zoomed-in spectrum of the 3^+ ion set. (**c**) Zoomed-in spectrum of the 2+ ion set. In both sets, adducts of $Au_{144}(SCH_2CH_2Ph)_{60}$ with various numbers of Cs^+ were detected in addition to the plain particle. Reprinted with permission from [8, 46]. Copyright 2009 American Chemical Society

nanomolecules in minor quantities, which agree with the $Au_{145-x}Ag_x(SR)_{59}$ alloy composition. An average of 53 silver atom incorporations were found in 1:0.75 Au: Ag incoming molar ratio and maximum of 60 silver incorporations were found. Optical spectrum of the $Au_{144}(SR)_{60}$ is featureless since it lies close to the molecule to bulk transition point. Incorporation of ~30 silver atoms results in the broad features at 420 and 550 nm in the UV–visible spectrum. However broad features at 420 nm were well developed when ~52 silver atoms are incorporated. Optical features developed upon silver atom incorporation in the case of 144-metal atom nanomolecule.

Based on the proposed 3-shell structure of $Au_{144}(SR)_{60}$, Dass et al. [47] hypothesized that the Ag atoms are selectively incorporated into the 60-atom shell, making Au_{12}, Au_{42}, $\mathbf{Ag_{60}}$ shells with 30 –SR–Au–SR– dimeric motifs. Later, Häkkinen group theoretically predicted the incorporation of silver atoms into 60-atom shell to be the minimum energy isomer [48]. Experimentally determined single crystal X-ray analysis will confirm the total structure and silver atom doping positions in $Au_{144}(SR)_{60}$.

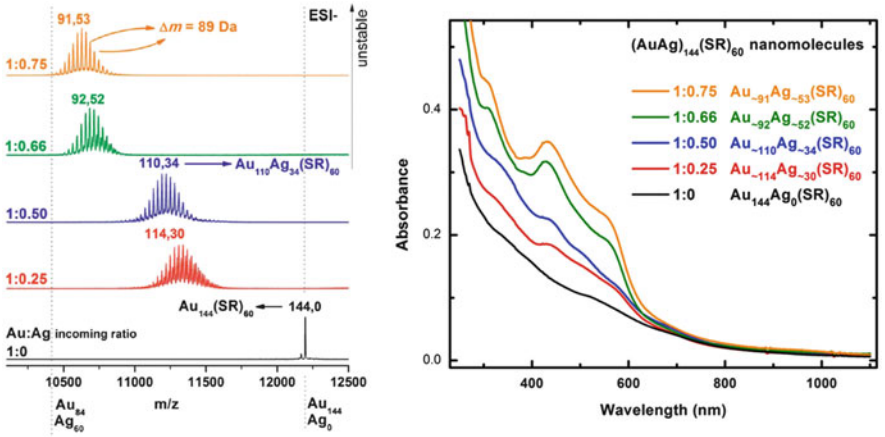

Fig. 5 *Left*: Electrospray ionization (ESI) mass spectrometry data (3-ions) of $Au_{144-x}Ag_x(SR)_{60}$ nanomolecules for Au:Ag precursor ratios of 1:0 (*black*), 1:0.25 (*red*), 1:0.50 (*blue*), 1:0.66 (*olive*), and 1:0.75 (*orange*) in the starting material. Samples were infused as 50:50 toluene:CH_3CN solution in negative mode. The mass difference between the peaks in nanoalloys corresponds to the Au (196.97 Da) and Ag (107.87 Da) mass difference, $\Delta m = 89$ Da. The average number of Au and Ag atoms is denoted above each distribution of peaks. *Right*: UV–vis spectra of $Au_{144-x}Ag_x(SR)_{60}$ nanomolecules in CH_2Cl_2 for Au:Ag precursor ratios of 1:0 (*black*), 1:0.25 (*red*), 1:0.50 (*blue*), 1:0.66 (*olive*), and 1:0.75(*orange*) in the starting material. Reproduced from [47] with permission from The Royal Society of Chemistry

4.2 Meta-Stable Nanomolecules: $Au_{67}(SR)_{35}$ and $Au_{103–105}(SR)_{45–46}$

4.2.1 $Au_{67}(SR)_{35}$ Nanomolecules

Direct synthesis of nanoparticles using Brust–Schiffrin method frequently yields crude products with $Au_{25}(SR)_{18}$ and $Au_{144}(SR)_{60}$ in significant quantities that can be detected using MALDI and ESI-MS. However, MALDI mass spectra of above direct synthesis product also show broad peaks at 18 and 26 kDa mass range (14 and 22 kDa as noted by core size). Using a nanoparticle synthesis using the single-phase THF method under controlled experimental conditions, the composition of this 14 kDa cluster was proposed as $Au_{68}(SR)_{34}$ using MALDI-MS [49]. More recently, these authors developed a new strategy to synthesize and isolate these 14 kDa nanomaterials in large scale using different thiols which facilitate further analytical studies [4]. This nanomolecule is more reactive and therefore is only meta-stable and subject to decomposition or conversion to other nanomolecules upon further etching, which will be discussed in detail in later sections.

Synthesis and isolation of $Au_{67}(SCH_2CH_2Ph)_{35}$ involves three steps. The first step is a synthesis of polydisperse product, rich in both 14 and 22 kDa compounds using one-phase tetrahydrofuran (THF) method. The second step is mild thermo-chemical treatment of the above polydisperse mixture to obtain distinct peaks at

18 and 26 kDa with a good baseline separation. Good baseline indicates the absence of any other meta-stable species between these two sizes. The final and key step involves multiple separation steps toward isolation of 14 kDa by removing the 26 kDa and any other species present in the sample. In this step, size-dependent solubility properties were applied for the thiolated gold nanoclusters. Toluene/acetone solvent mixtures in certain proportions were used to precipitate 22 kDa while leaving 14 kDa in the solution phase. Then, the THF/methanol mixture was used to precipitate 14 kDa and leaves smaller compounds like Au_{25} and Au_{38} in the solution. Figure 6 shows the detailed MALDI-MS data acquired for these separation steps for the isolation of 14 kDa.

Figure 7a shows the MALDI and ESI-MS spectrum (dark blue curve) of the 14 kDa nanomolecules prepared using 2-phenylethanethiol. ESI–MS shows multiply charged 2+ and 3+ ions of the parent molecule. Since these multiply charged ions are lower in mass-to-charge ratio compared to singly charged species, these peaks have better resolution and high accuracy. The deconvolution of 3+ and 2+ peaks indicates that the singly charged parent ion mass is at 17,999 Da. This is good match with the value 17,999.5 Da, calculated from the molecular formula of the $Au_{67}(SCH_2CH_2Ph)_{35}$ compound using isotopic masses and natural abundances. MALDI and ESI (red curve) mass spectra of the *n*-hexanethiolate protected nanomolecule are shown in Fig. 7b. It also shows a 2- peak at 8,650.5 Da/z and the deconvolution of this peak yields a 1- parent ion at 17,301 Da which is in agreement with the theoretical mass of $Au_{67}(SC_6H_{13})_{35}$ parent ion.

High-resolution ESI-MS analysis (see Fig. 7d) of the isolated 14 kDa nanomolecules synthesized using two different ligands (i.e., $-SCH_2CH_2Ph$ and $-SC_6H_{13}$) shows that the composition is $Au_{67}(SR)_{35}$. This is further confirmed by obtaining identical molecular ion peaks in both positive and negative ion modes (Fig. 7c). The optical spectra of these clusters exhibit featureless and monotonously rising absorbance curve. However this meta-stable $Au_{67}(SR)_{35}$ shows 0.74 V electrochemical gaps. Based on the compositional assignment and XRD diffraction a structural model for this nanomolecule was proposed.

4.2.2 $Au_{103–105}(SR)_{45–46}$ Clusters

The recent breakthrough in thiol-protected gold nanoparticles includes the crystal structure of the water soluble $Au_{102}(SR)_{44}$ [50] where 'SR' is the paramercaptobenzoic acid which is known as 22 kDa by its core size. We also observed the 22 kDa nanoclusters in our organic solvent-mediated synthesis using phenylethanethiol. High-resolution mass spectrometry data shows the existence of $Au_{103}(SR)_{45}$, $Au_{104}(SR)_{45}$, $Au_{104}(SR)_{46}$ and $Au_{105}(SR)_{46}$ as shown in Fig. 8 [51]. To rule out any adduct formation, alkali metal salts (of Na, K, and Rb) were intentionally added to promote the ionization. In this case both parent molecular ions and corresponding adducts were observed further confirming the presence of four individual species (see Fig. 8).

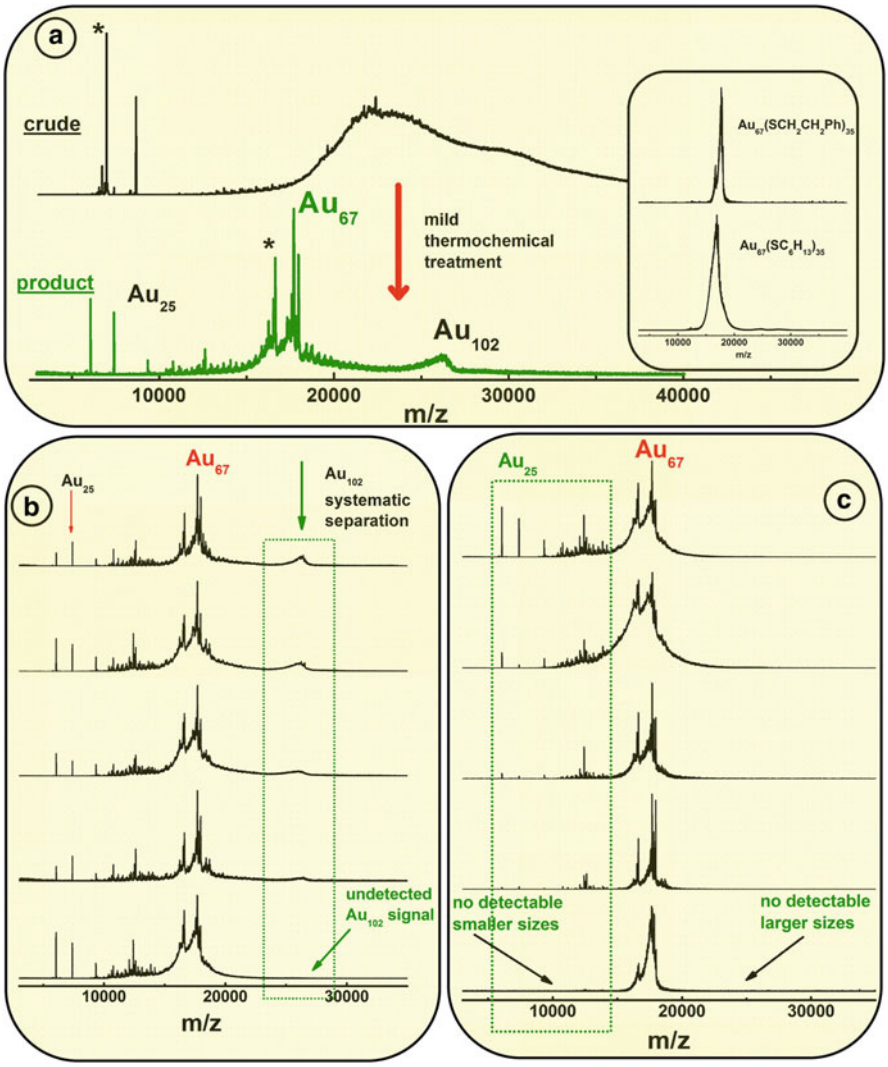

Fig. 6 (**a**) Typical reaction where the initial crude product (control – *top* MALDI-MS spectrum) was subjected to mild thermochemical treatment to obtain a product (*bottom* MALDI-MS spectrum) where Au_{67} is a major product and other sizes are diminished in signal. Peaks with asterisk denote fragments. (**b**) $Au_{67}(SR)_{35}$ purification separating larger clusters: MALDI spectra showing the systematic separation (top to bottom) of Au_{102} clusters from a mixture of Au_{25}, Au_{67}, and Au_{102}. The final product (*bottom*) is further used to separate the clusters lower in mass than $Au_{67}(SR)_{35}$. (**c**) $Au_{67}(SR)_{35}$ purification separating smaller clusters: Continuation of the separation process to remove sizes smaller than $Au_{67}(SR)_{35}$. Inset to part a: MALDI spectra of the pure $Au_{67}(SR)_{35}$ with two different ligands, phenylethanethiol (*top*) and hexanethiol (*bottom*) taken at very high laser fluence. At high laser fluence, even minor amounts of impurities or other core-size clusters will show higher signal intensity. Reprinted with permission from [4]. Copyright 2013 American Chemical Society

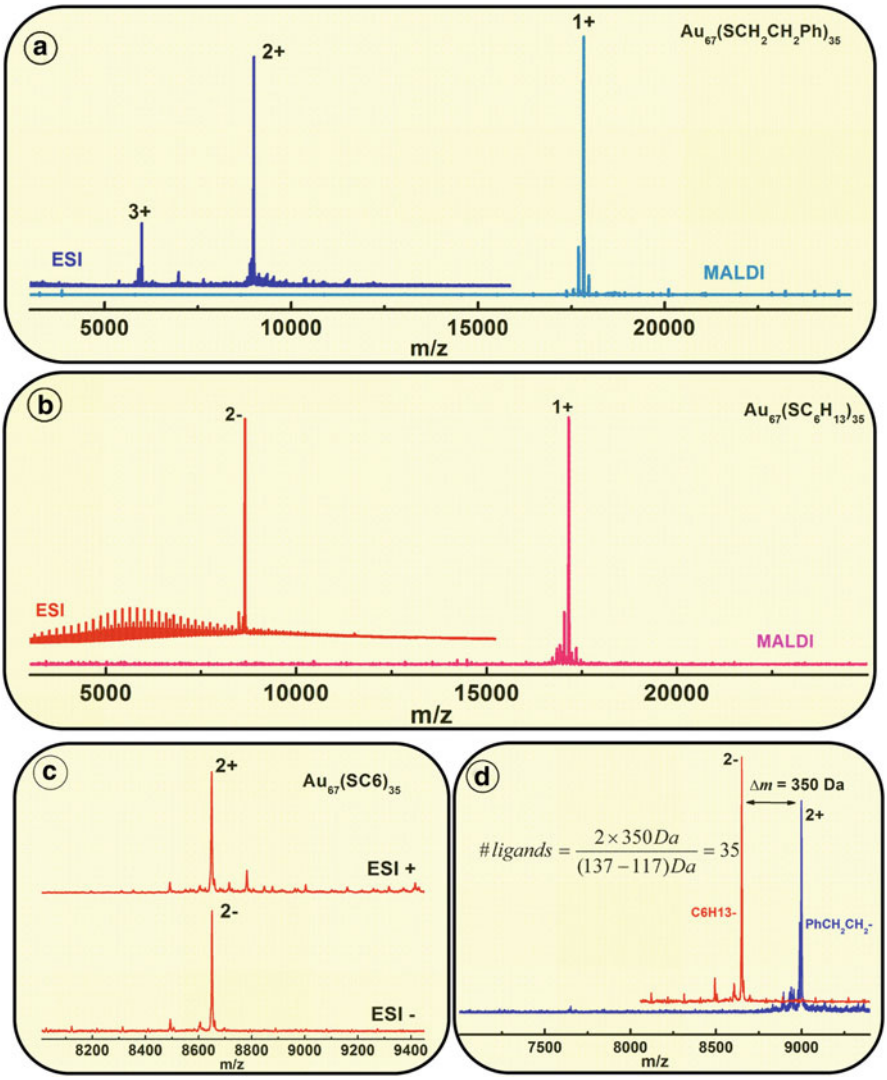

Fig. 7 (**a**) Positive mode MALDI-TOF mass spectra (MS) (in *light blue*) and ESI-MS (*dark blue*) of $Au_{67}(SCH_2CH_2Ph)_{35}$ nanomolecules. (**b**) Positive mode MALDI-TOF-MS (in *light red*) and the negative mode ESI-MS of $Au_{67}(SC_6H_{13})_{35}$. (**c**) Positive mode (*top*) and negative mode (*bottom*) ESI mass spectra of $Au_{67}(SC_6H_{13})_{35}$. (**d**) ESI mass spectra of $Au_{67}(SR)_{35}$ nanomolecules protected by phenylethanethiolate (*blue*) and *n*-hexanethiolate (ligands) showing a mass difference of 350 Da used to calculate the number of ligands in the Au_{67} to be 35. Reprinted with permission from [4]. Copyright 2013 American Chemical Society

Interestingly, $Au_{102}(SCH_2CH_2Ph)_{44}$ was not observed with phenylethanethiol and hexanethiol ligands. This could be due to the nature of the thiol group. For example, *p*-mercaptobenzoic acid is aromatic and hydrophilic, when compared

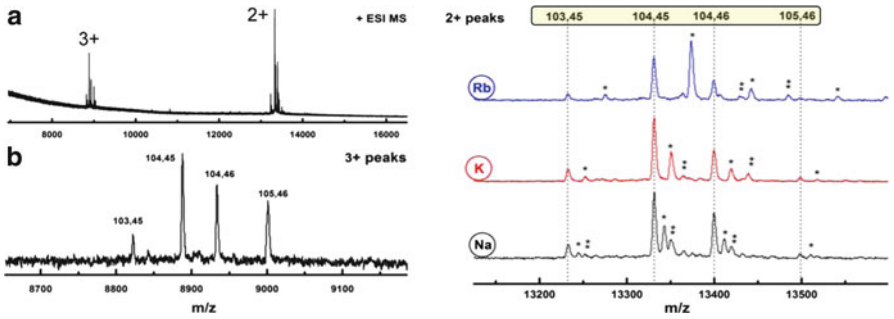

Fig. 8 *Left*: ESI mass spectra of the 22 kDa nanoclusters in 50:50 toluene:CH_3CN mixture with addition of metal acetates. (**a**) ESI spectra in the full mass range with KOAc and (**b**) expansion of 3+ molecular ion peaks showing the presence of $Au_{103}(SR)_{45}$, $Au_{104}(SR)_{45}$, $Au_{104}(SR)_{46}$, $Au_{105}(SR)_{46}$. *Right*: expansion of 2+ molecular ion peaks using rubidium(Rb), potassium(K), and sodium(Na) acetate salts, respectively, confirming the presence of the same set of peaks as in 3+ region. The peaks marked by one and two *asterisks* represent nanoclusters with one and two cationic adducts, respectively, the mass difference corresponding to the cations. Notably $Au_{102}(SR)_{44}$ is not detected. Reproduced from [51] with permission from The Royal Society of Chemistry

with $–SCH_2CH_2Ph$. Previously we showed that using −SPh in the synthesis leads to the formation of the 36-atom species instead of Au_{38} [52]. This clearly shows that using an aromatic ligand alters the core size in some cases when compared with $–SCH_2CH_2Ph$ or $–SC_6H_{13}$ ligands.

5 Synthesis Through Core-Size Conversion

In this section, the synthesis of $Au_{38}(SR)_{24}$, $Au_{40}(SR)_{24}$, and $Au_{130}(SR)_{50}$ through core-size conversion synthesis is discussed. Firstly, in Sect. 5.1, the core-size conversion syntheses of Au_{38} and Au_{40} are discussed. This involves the use of nanoclusters smaller than 120 metal atoms [53]. Secondly, in Sect. 5.2, core-size conversion synthesis of Au_{130} nanomolecules using nanoclusters larger than 200 metal atoms is discussed [54].

The two-phase Brust–Schiffrin synthesis is typically used to synthesize organo thiolated gold nanoclusters [5]. The product obtained from this synthesis is a polydispersed mixture of gold nanoclusters with several sizes present in the reaction mixture [2]. After the report on Brust–Schiffrin synthesis, several other synthetic protocols with increased yields and different synthetic approaches have been reported in the literature for several sizes of gold nanomolecules [2, 46, 52, 55–57]. To narrow down the size distribution of the polydisperse products obtained after synthesis, the products are etched with excess ligand at elevated temperatures.

Etching of thiolated gold nanoclusters was first introduced by Whetten and coworkers [7]. The etching procedures for phosphine-protected clusters were well

established before. The concept of etching was first used in self-assembled monolayers [58]. Murray's group and Tsukuda's group employed etching reactions to synthesize highly stable gold nanomolecules [44, 59]. More recently, many research groups have used etching as a synthetic route for making several stable nanomolecules [47, 60, 61].

When a mixture of gold nanoclusters is etched in the presence of excess thiol, gold nanoclusters can follow two possible routes. The first route is the conversion of unstable gold nanoclusters to Au-SR polymers [7]. The Au-SR aggregates formed in these reactions are not soluble in any solvent systems and are found as insoluble material in the reaction flasks. The formation of Au-SR aggregates was proved in the seminal work by Whetten and coworkers [7]. The second route is the conversion of gold nanoclusters to stable smaller sizes. This process of conversion of larger gold nanoclusters to smaller sizes is called as *core-size conversion*. During the core-size conversion reactions, the larger gold nanoclusters in the crude product for etching are not stable during etching and breakdown to smaller sizes. The smaller sizes formed are highly stable and accumulate in large quantities in these core-size conversion reactions.

5.1 Core-Size Conversion Synthesis of $Au_{38}(SR)_{24}$ and $Au_{40}(SR)_{24}$

Along with the two-phase Brust–Schiffrin method, one-phase THF method is also widely used for the synthesis of gold nanoclusters. Murray and coworkers have reported a one-phase THF/TOABr method for the synthesis of $Au_{25}(SR)_{18}$ gold nanomolecules in 2004 [55]. In 2008, similar one-phase method in THF for the synthesis of Au_{25} in high yield was reported by Jin and coworkers [29]. Recently, Dass's group studied the synthesis of Au_{25} by one-phase THF method by MALDI-TOF mass spectrometry to understand the nanoparticle size evolution during synthesis [2]. In the one-phase THF method, there are several species observed between Au_{25} and Au_{144}, namely Au_{67}, $Au_{103–105}$, and a series of clusters smaller than Au_{67}. Au_{102} was isolated and crystallized with *p*-mercaptobenzoic acid [50]. However, $Au_{102}(SR)_{44}$ is not observed with phenylethanethiol and hexanethiol. Instead, $Au_{103}(SR)_{45}$, $Au_{104}(SR)_{45}$, $Au_{104}(SR)_{46}$, and $Au_{105}(SR)_{46}$ were observed with phenylethanethiol and hexanethiol ligands. These clusters together are referred to as $Au_{103–105}(SR)_{45–46}$ for simplicity throughout this chapter [62].

When the crude products obtained from one-phase THF reaction were etched in excess ligand (phenylethanethiol or hexanethiol) at higher temperatures, Au_{38} and Au_{40} were observed in MALDI-MS data of the aliquots collected from the etching reactions. However, the following questions could not be answered from these etching reactions. Are these clusters formed during the synthesis and survive the etching process or larger clusters convert to Au_{38} and Au_{40}? If these nanomolecules

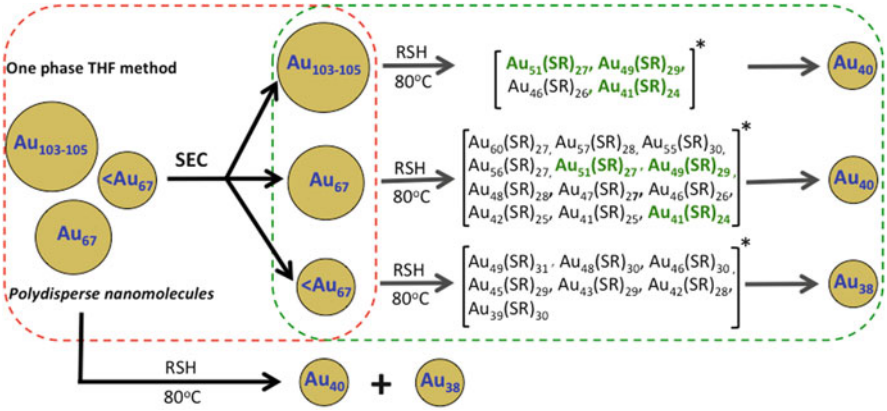

Scheme 1 Core-size conversion in clusters smaller than Au_{144}. One-phase THF synthesis typically yields a mixture of $Au_{103–105}$, Au_{67}, and clusters smaller than Au_{67} and Au_{25}. When this mixture is etched as such, a mixture of Au_{38} and Au_{40} by core-size conversion. From the same crude product, $Au_{103–105}$, Au_{67}, and clusters smaller than Au_{67} were separated by SEC (shown in the *green dotted box* in the scheme). Upon etching, $Au_{103–105}$ and Au_{67} core-converts to Au_{40} and clusters smaller than Au_{67} core-convert to pure Au_{38} (shown in the *red dotted box* in the scheme). Each of these core-size conversion reactions proceeds via several intermediate species identified by MALDI-TOF mass spectrometry. Based on the MALDI-TOF data we speculate that the core-size conversion reactions proceed via these intermediate species. Note that the core conversion is a gradual downsizing phenomenon. Gold atoms and ligands are systematically lost from the larger clusters and smaller sizes are formed

are formed by core-size conversion, which larger clusters convert to Au_{38} and which of them convert to Au_{40}? To answer these questions the etching reactions need to be studied in a systematic manner. For this purpose, the crude product from one-phase THF method was separated into several fractions and etched separately with excess thiol. The several fractions separated contain gold nanoclusters of different size regimes. From the crude product obtained from the one-phase THF method, $Au_{103–105}$ clusters, Au_{67}, and clusters smaller than Au_{67} (labeled $<Au_{67}$ in the Scheme 1) were separated and etched.

5.1.1 Core-Size Conversion of Au_{67} and Au_{102} to $Au_{40}(SR)_{24}$

Size exclusion chromatography (SEC) is one of the techniques used for separation of gold nanomolecules of several sizes [63]. The separation is based on the retention time of several gold nanomolecules on the size exclusion column. Pure $Au_{103–105}$ and Au_{67} fractions were obtained from the crude product of one-phase THF synthesis, using SEC. Figure 9 shows the MALDI-MS of the aliquots collected from the etching reaction at different time intervals. This MS result clearly shows that Au_{67}, up on etching, core converts to $Au_{40}(SR)_{24}$. The core-size conversion reactions were monitored as a function of time with the aid of MALDI-MS. In this time-monitored

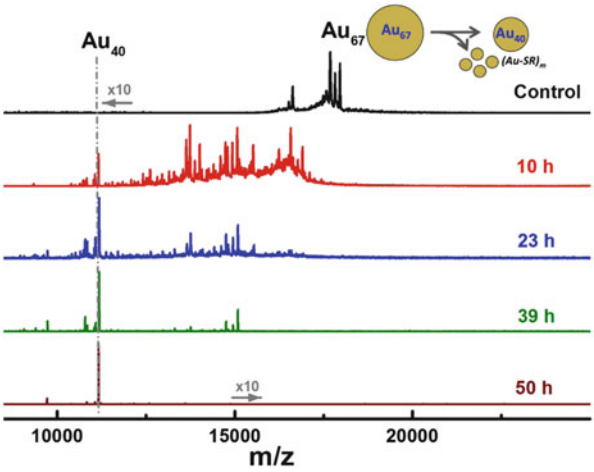

Fig. 9 Positive MALDI mass spectra of the samples collected from etching of pure Au_{67} in the presence of excess thiol. After 50 h, $Au_{40}(SR)_{24}$ is the only product in the reaction mixture. Please note that no $Au_{40}(SR)_{24}$ is present in the initial sample. This indicates that $Au_{40}(SR)_{24}$ is exclusively formed via a core-size conversion process from Au_{67}. For a discussion on the intermediates observed in the core conversion reactions, refer to later sections. The scheme depicts the conversion of Au_{67} to Au_{40}, with a possible loss of $(Au\text{-}SR)_m$ by-products

reaction, the 10 h sample shows several meta-stable species in the 13–17 kDa mass region. However, most of the Au_{67} has disappeared from the reaction mixture and peaks corresponding to $Au_{40}(SR)_{24}$ were observed in the MALDI mass spectrum. In the samples examined at 23 and 39 h, the amount of meta-stable clusters has decreased and no peaks corresponding to Au_{67} were observed. With the progress of the core size conversion reaction, $Au_{40}(SR)_{24}$ is the only species observed in the reaction mixture. $Au_{38}(SR)_{24}$ could not be observed in the final product. These results prove that $Au_{40}(SR)_{24}$ is formed by core-size conversion of $Au_{67}(SR)_{35}$.

To study the etching and core-size conversion reactions, the $Au_{103–105}$ fraction obtained from the crude product after SEC was reacted with excess thiol separately. Upon etching, this fraction has core-converted to $Au_{40}(SR)_{24}$. Figure 10 shows the progress of this etching reaction monitored by MALDI mass spectrometry. In the MALDI mass spectrum of 3 h sample, there were some meta-stable clusters observed around ~14 kDa mass range. With time, all the $Au_{103–105}$ clusters in the reaction mixture disappeared and only the meta-stable species were observed in the reaction mixture. In the 8 h sample, $Au_{40}(SR)_{24}$ was observed along with some other meta-stable clusters. After 11 h, $Au_{40}(SR)_{24}$ was the only product in the reaction mixture, suggesting that $Au_{103–105}$ has core-converted to $Au_{40}(SR)_{24}$. Some insoluble residue was also observed in these etching reactions. These are presumably Au-SR aggregates, as discussed in an earlier report by Whetten and coworkers [7]. This suggests that 100% of the metal atoms and ligands present in the $Au_{103–105}$ sample do not convert to Au_{40}. This is also the case with other core-size conversion reactions. Some of the starting material forms Au-SR by-products. So far,

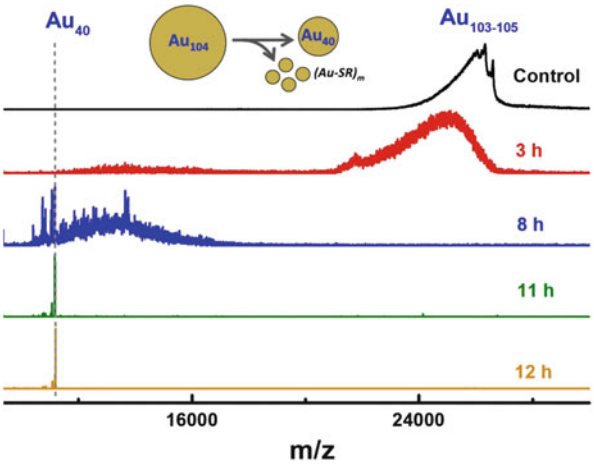

Fig. 10 Positive MALDI mass spectra of the samples collected from etching of pure $Au_{103–105}$ in the presence of excess thiol. After 22 h, $Au_{40}(SR)_{24}$ is the only product in the reaction mixture. Please note that no $Au_{40}(SR)_{24}$ is present in the initial sample. This indicates that $Au_{40}(SR)_{24}$ is exclusively formed via a core-size conversion process. For a discussion on the intermediates observed in the core conversion reactions, refer to later sections. The scheme depicts the conversion of $Au_{103–105}$ to Au_{40}

the etching reactions performed has shown that Au_{38} and Au_{40} gold nanomolecules are formed from the core conversion of larger gold nanoclusters.

For the synthesis of Au_{40} without any Au_{38}, pure $Au_{103–105}$ and Au_{67} samples can be etched in excess thiol. When a mixture of Au_{67} and Au_{104} was etched in excess thiol, this mixture core-converted to Au_{40}, adding confidence to the results obtained for the core conversion of pure Au_{67} and $Au_{103–105}$ fractions. The progress of this reaction is shown in Fig. 11. This core conversion reaction can be used to synthesize $Au_{40}(SR)_{24}$, where Au_{40} is the exclusive product without any Au_{38} present in the reaction mixture. This proves that core-size conversion reactions can also be used as synthetic routes for making highly stable monodisperse gold nanomolecules.

5.1.2 Synthesis of Au_{38} by Core-Size Conversion Reactions

Clusters smaller than Au_{67} were separated from the crude product of one-phase THF synthesis using size exclusion chromatography (labeled as $<Au_{67}$ in Scheme 1). Figure 12 shows the MALDI mass spectra of the aliquots collected from this etching reaction. $Au_{25}(SCH_2CH_2Ph)_{18}$ is also present in the starting material used for etching. Though Au_{25} is kinetically inert in the synthesis reactions and observed in the one-phase THF reactions even after 3 days, Au_{25} has lower thermochemical stability. In 1.5 and 2.5 h samples, Au_{38} is abundant with relatively

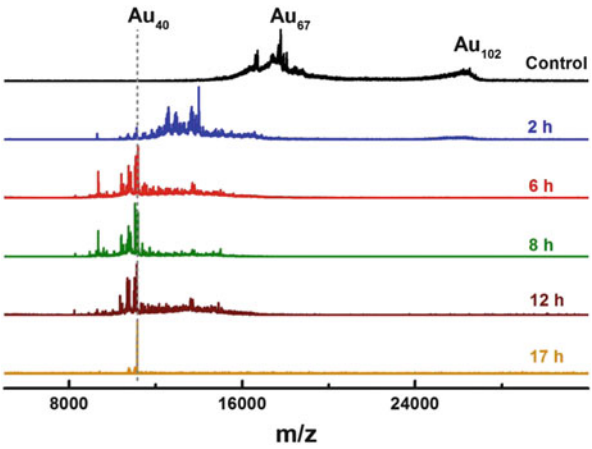

Fig. 11 MALDI mass spectra of the samples collected from the etching of a mixture of Au_{67} and $Au_{103–105}$. Upon etching $Au_{103–105}$ and Au_{67} core-convert to pure Au_{40}

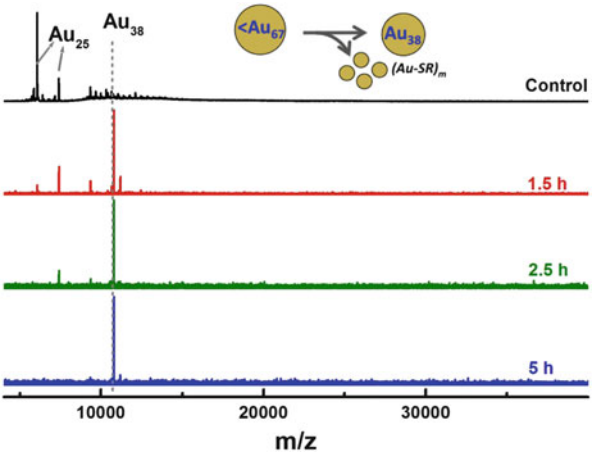

Fig. 12 Positive MALDI mass spectra of the samples collected from etching of clusters smaller than Au_{67} in the presence of excess thiol. After 5 h, $Au_{38}(SR)_{24}$ is the only product in the reaction mixture. Please note that no $Au_{38}(SR)_{24}$ is present in the initial sample. This indicates that $Au_{38}(SR)_{24}$ is exclusively formed via a core-size conversion process. For a discussion on the intermediates observed in the core conversion reactions, refer to later sections. The cartoon is a schematic way of depicting the conversion of clusters smaller than Au_{67} to Au_{38}

smaller amount of Au_{25} present in the samples. This is indicative of the low thermal stability of Au_{25}. As the etching reaction proceeds, Au_{38} is the only species observed in the mass spectrum suggesting that all the Au_{25} has decomposed. These etching reactions show that clusters smaller than Au_{67} core convert to Au_{38} exclusively, without any interference from Au_{40}.

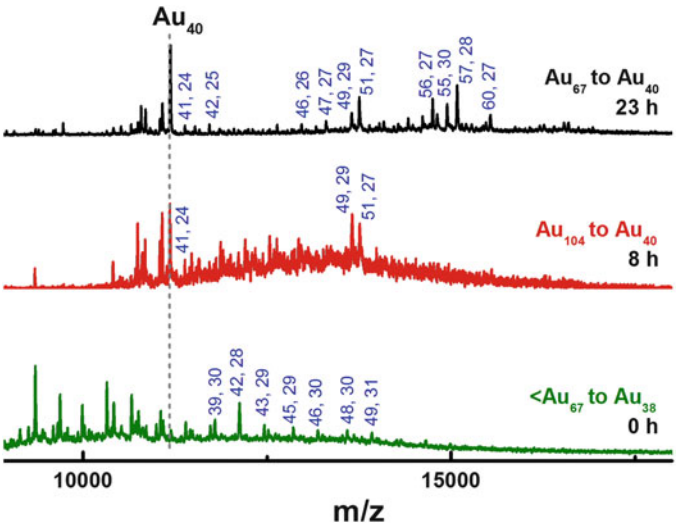

Fig. 13 Positive MALDI mass spectra of the meta-stable species observed in the core-size conversion reactions of Au_{67}, $Au_{103–105}$, and $<Au_{67}$ clusters

5.1.3 MS Data-Based Mechanism of Core-Size Conversion

Au_{38} and Au_{40} were observed in the core-size conversion reactions for a long time now, but the mechanism of formation of these nanomolecules is not completely understood. For the formation of smaller gold nanomolecules by core conversion, the larger nanoclusters need to break down and decrease in size. During the etching reactions, there are several meta-stable species observed in the MALDI-MS data of the samples. These peaks are well resolved in the MALDI-MS data acquired for the samples collected at different time intervals from the etching reactions.

To understand the mechanism in the formation of Au_{38} and Au_{40} during core-size conversion reactions, the transient species observed in the etching samples were studied in detail. Figure 13 shows the assignment of the meta-stable species observed during these reactions.

In the etching of Au_{67} (black curve in Fig. 13), the composition of the meta-stable species is indicated on top of each peak. Of the several species observed, $Au_{57}(SR)_{28}$, $Au_{55}(SR)_{30}$, $Au_{56}(SR)_{27}$, and $Au_{51}(SR)_{27}$ are the most dominant peaks in the mass spectra. Other species include $Au_{60}(SR)_{27}$, $Au_{49}(SR)_{29}$, $Au_{47}(SR)_{27}$, $Au_{46}(SR)_{26}$, and $Au_{41}(SR)_{24}$. Looking at the composition of these meta-stable species, it is reasonable to assume that there is a systematic loss of gold atoms and ligands to form $Au_{40}(SR)_{24}$ in the etching of Au_{67}.

$Au_{103–105}$ fraction, when etched, converts to Au_{40} through core-size conversion process. As the final product in both of the reactions is Au_{40}, it is highly likely that these reactions proceed via the same or closely related intermediate species. For both Au_{67} and $Au_{103–105}$ etching, $Au_{51}(SR)_{27}$, $Au_{49}(SR)_{29}$, and $Au_{41}(SR)_{24}$ were

observed. This suggests that these are intermediate species for the formation of $Au_{40}(SR)_{24}$.

The fraction $<Au_{67}$ obtained after SEC of the crude product shows peaks in the same mass region, as the meta-stable species observed in core-size conversion of Au_{67} and $Au_{103–105}$. In that case, the etching of this material should result in the formation of $Au_{40}(SR)_{24}$. But when the fraction $<Au_{67}$ is etched, $Au_{38}(SR)_{24}$ is formed. To solve this puzzle, the peaks observed in the MALDI mass spectrometry data (red curve in Fig. 13) of $<Au_{67}$ fraction were also assigned. The species observed in the $<Au_{67}$ fraction were different than the meta-stable intermediates observed in Au_{67} and $Au_{103–105}$ etching reactions. This proves that the size distribution of the crude product used affects the yield of Au_{38} or Au_{40} obtained in the core-size conversion reactions. To obtain higher yield of Au_{38}, it is important to have the clusters that convert to Au_{38} in greater abundance. The core-size conversion reactions proposed in this section can also be used for the exclusive synthesis of Au_{40} gold nanomolecules.

5.2 *Core-Size Conversion Synthesis of $Au_{38-x}Ag_x(SR)_{24}$ Alloys*

$Au_{38}(SR)_{24}$ crystallizes in the triclinic space group, P*i*, and the unit cell consists of a pair of enantiomers [64]. Later, Burgi and coworkers were able to isolate the enantiomers of $Au_{38}(SR)_{24}$ using chiral high-performance liquid chromatography [65]. $Au_{38}(SR)_{24}$ consists of six long staples (–SR–Au–SR–Au–SR–) and three short staples (SR–Au–SR), with a total of 15 gold atoms. The remaining 23 gold atoms are present as face-fused bi-icosahedral core. $Au_{38}(SR)_{24}$ has been extensively studied because of its interesting optical, electrochemical, chiral, and luminescence properties coupled with its high chemical stability [66–68].

The 38-metal atom Au–Ag alloy or $Au_{38-x}Ag_x(SR)_{24}$ synthesis also involves three steps. [69] Generally, the first step is the synthesis of polydispersed crude alloy nanomolecules mixture. The second step involves the core-size conversion step (thermochemical treatment to promote the core conversion of meta-stable nanoclusters to form $Au_{38-x}Ag_x(SR)_{24}$) and the final step is the isolation of $Au_{38-x}Ag_x(SR)_{24}$ in pure form using solvent fractionation. In this case, precursor Au:Ag ratio during the synthesis was varied from 1:0 to 1:0.30.

MALDI-TOF mass spectrometry was used for $Au_{38-x}Ag_x(SR)_{24}$ characterization, as the instrument had sufficient resolution to distinguish the Au and Ag mass difference in the ~11 kDa mass region. The bottom black spectrum in Fig. 14(left) shows the MALDI spectrum of $Au_{38}(SR)_{24}$. Introducing silver precursor in the starting material leads to the formation of atomically precise $Au_{38-x}Ag_x(SR)_{24}$ alloy nanomolecules.

In $Au_{38-x}Ag_x(SR)_{24}$, the mass difference between the peaks corresponds to the mass difference between gold and silver atoms. As the incoming silver mole ratio

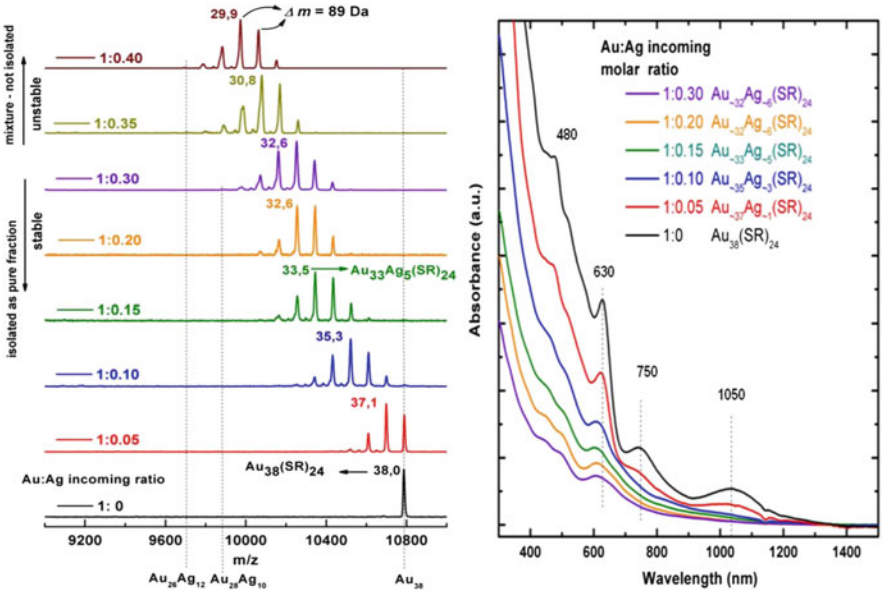

Fig. 14 *Left:* MALDI-TOF mass spectra (positive mode) of $Au_{38-x}Ag_x(SR)_{24}$ nanomolecules for Au:Ag precursor ratios of 1:0 (*black*), 1:0.05 (*red*), 1:0.10 (*blue*), 1:0.15 (*olive*), 1:0.20 (*orange*), 1:0.30 (*purple*), 1:0.35 (*dark yellow*), and 1:0.40 (*brown*) in the starting material. The mass difference between the peaks in nanoalloys corresponds to the Au (196.97 Da) and Ag (107.87 Da) mass difference, $\Delta m = 89.10$ Da. The number of Au and Ag atoms of most dominant peak is denoted above each distribution of peaks. *Right*: UV–visible spectra of $Au_{38-x}Ag_x(SR)_{24}$ nanomolecules in toluene with Au:Ag precursor ratios of 1:0 (*black*), 1:0.05 (*red*), 1:0.10 (*blue*), 1:0.15 (*olive*), 1:0.20 (*orange*), and 1:0.30 (*purple*) in the starting material. Reproduced from [69] with permission from The Royal Society of Chemistry

was increased in the initial synthesis, the number of silver atoms incorporated also increased and started to plateau at 1:0.20 Au:Ag mole ratio. The average and maximum number of silver atoms in 1:0.30 mole ratios remain at ~6 and 10, respectively. Increasing the Au:Ag incoming mole ratio to 1:0.35 and 1:0.40 still forms $Au_{38-x}Ag_x(SR)_{24}$, observed at early stages of etching, but decomposes with time indicating the instability towards further silver incorporations.

Figure 14 (right) shows the modulation of optical properties of $Au_{38}(SR)_{24}$ upon silver atom incorporation. $Au_{38}(SR)_{24}$ nanomolecules have distinct bands at 1,050, 750, 630, and 480 nm. Silver incorporation into $Au_{38}(SR)_{24}$ leads to blue shift in UV–visible spectrum. The band at 1,050 nm present in $Au_{38}(SR)_{24}$ diminishes with minimum silver incorporation (in 1:0.05, Au:Ag incoming molar ratio) and gradually disappears with increasing number of Ag atoms. This disappearance implies that the transitions at 1,050 and 675 nm are originating from pure $Au_{38}(SR)_{24}$ and thus silver may not facilitate the low energy transitions in $Au_{23-x}Ag_x$ core. Furthermore, the electronic transitions occurring at 480 and 630 nm seems to be broaden upon silver incorporation. In conclusion, the optical features of $Au_{38}(SR)_{24}$

diminish upon silver atom incorporation. This is in contrast to the observation in $Au_{144-x}Ag_x(SR)_{60}$ nanomolecules, where optical features emerged upon Ag incorporation.

5.3 *Core-Size Conversion Synthesis of $Au_{130}(SR)_{50}$ and Its Alloys*

In the previous section the core-size conversion reactions in nanoclusters smaller than 120 metal atoms were summarized. The size conversion reactions of clusters larger than 200 metal atoms are considered in this section. These gold nanoclusters are synthesized using two-phase Brust–Schiffrin method. The synthesis does not exclusively yield clusters larger than 200 metal atoms. To obtain clusters larger than 200 metal atoms, solvent fractionation was used. Once the clusters larger than 200 metal atoms were obtained they were etched in the presence of excess thiol at 85°C.

The etching reactions were monitored by collecting aliquots from the reaction mixture at different time intervals. Figure 15 shows the progress of etching reaction monitored by MALDI-TOF mass spectrometry. The crude mixture immediately after the synthesis (at 0 h) contains clusters larger than 40 kDa (200 metal atoms) with no peaks in the ~30 kDa mass range. With time, a new core-sized nanomolecule, $Au_{130}(SCH_2CH_2Ph)_{50}$ is formed, which is not present in initial product used for etching. Mass spectrometry data of the aliquots from the reaction mixture shows the accumulation of $Au_{130}(SCH_2CH_2Ph)_{50}$ with time in the reaction mixture. This mass spectrometric evidence proves that larger clusters (>40 kDa) are core-converting to form $Au_{130}(SCH_2CH_2Ph)_{50}$. When the crude products from the synthesis were etched prior to the separation of clusters larger than 40 kDa, a mixture of Au_{130}, Au_{137}, and Au_{144} is obtained. This suggests the greater stability of Au_{144} and Au_{137} nanomolecules during etching reactions. These nanomolecules can survive the etching process and remain stable in the reaction mixture.

The sample collected at 12 h shows several meta-stable clusters present in the reaction mixture. The meta-stable clusters were found at 43.6, 89.2, 113.3, and 140.7 kDa corresponding to ~220, 450, 570, and 710-atom species. In the 36 h sample, the MALDI spectrum is dominated by a peak at ~32 kDa (130-atom nanomolecules). The reaction was stopped after 48 h and processed. The time frame of the core-size conversion reactions is dependent on the crude product used for etching and varies for different batches. 76.3 kDa nanomolecule (~320-atoms) is also observed in these reactions [60, 70]. From the final product obtained after etching, 32 kDa species was isolated using size exclusion chromatography (SEC) and analyzed by ESI-MS to check the purity. ESI-MS data confirms that the nanomolecule formed is $Au_{130}(SR)_{50}$. This core-size conversion from >40 kDa clusters to $Au_{130}(SR)_{50}$ was repeated in different ligand systems. The

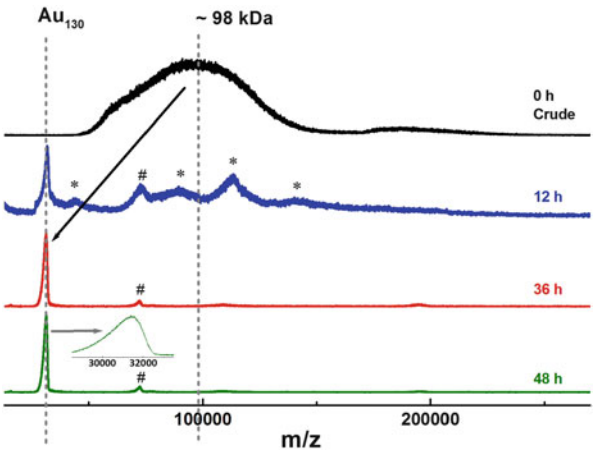

Fig. 15 MALDI mass spectra of the samples collected at several time intervals from etching of larger (>40 kDa) clusters. Note that (*1*) $Au_{130}(SR)_{50}$ is absent initially. $Au_{130}(SR)_{50}$ is formed by the core-size conversion of larger (> ~200 atom) nanoclusters, (*2*) $Au_{144}(SR)_{60}$ is not present in starting material or in the final product. So $Au_{144}(SR)_{60}$ is not a product of core-size conversion in this study. The absence of $Au_{144}(SR)_{60}$ in the final product, enables the preparative scale SEC separation and isolation of pure $Au_{130}(SR)_{50}$. Asterisk indicates meta-stable clusters. Peak labeled # in 12, 36, and 48 h samples corresponds to 76.3 kDa nanomolecule [60], which is stable throughout the etching process

formation of $Au_{130}(SR)_{50}$ was observed with different ligands like dodecanethiol and hexanethiol.

The molecular weight of $Au_{130}(SCH_2CH_2Ph)_{50}$ is 32,467 Da. Electrospray ionization mass spectrometry (ESI-MS) generally yields multiply charged peaks in the mass spectra. These multiply charged peaks appear at a lower mass than the molecular ions and are better resolved, thereby allowing the assignment of composition of nanomolecules. In Fig. 16, positive mode ESI-MS spectrum of the 3+ region of $Au_{130}(SCH_2CH_2Ph)_{50}$ nanomolecules is shown, at 10,822 m/z (32,467/3). Figure 16 shows all the different $Au_{130-x}(Metal)_x(SR)_{50}$ nanomolecules prepared by core-size conversion reactions, where R=$-CH_2CH_2Ph$, $-C_6H_{13}$, $-C_{12}H_{25}$ and Metal=Pd and Au. Using the mass difference between the peaks corresponding to $Au_{130}(SR)_{50}$ with different ligands, the number of ligands in the nanomolecule was confirmed to be 50. In both hexanethiol and dodecanethiol ligands, the number of ligands was 50, which adds confidence to the assigned formula. This also proves that the same core-size conversion is valid in all three ligand systems. Compositional isomers, in short "*Composomers*," of this 130-metal atom nanomolecule were prepared by the same core-size conversion reactions. Composomers have the same number of total metal atoms and ligands, while the number of individual type of metal atoms varies [71]. $Au_{110}Ag_{20}(SR)_{50}$ and $Au_{115}Ag_{15}(SR)_{50}$ are examples for 130-metal atom composomers. Here, the total number of metal atoms is 130. But the numbers of gold and silver atoms vary. Alloys of several nanomolecules are evident in the literature [25, 33, 34, 47, 69, 72].

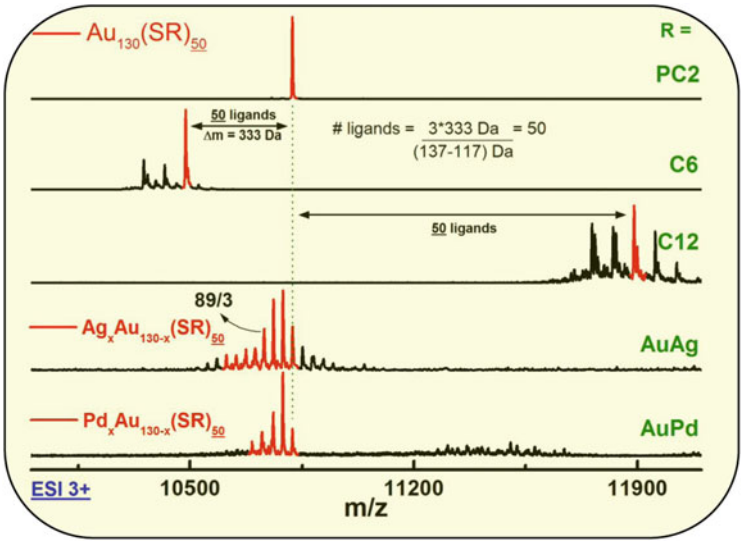

Fig. 16 Positive mode ESI-MS mass spectra showing 3+ region of $Au_{130}(SR)_{50}$ with several ligands phenylethanethiol (PC2), hexanethiol (C6), dodecanethiol (C12), $Au_{130-x}Ag_x(SR)_{50}$ and $Au_{130-x}Pd_x(SR)_{50}$. The purpose of this figure is to show that (**a**) the core-size conversion works with various ligands and alloy systems, (**b**) the 130-atom core has special stability associated with its structure

5.3.1 Core-Size Conversion in Au–Ag Alloy Nanoclusters

Core-size conversion process is also repeated with the alloy systems. Alloy gold nanomolecules like $Au_{144-x}Ag_x(SR)_{60}$ and $Au_{38-x}Ag_x(SR)_{24}$ have been reported previously [47, 69]. Using a mixture of gold ($HAuCl_4$) and silver ($AgNO_3$) salts, the crude product for alloy nanoclusters was synthesized. From this crude product, clusters larger than 40 kDa were isolated using SEC and etched in the presence of excess thiol at higher temperatures. During these etching reactions, $Au_{130-x}Ag_x(SR)_{50}$ was observed in the reaction mixtures. Figure 17 shows the positive mode ESI-MS of $Au_{130-x}Ag_x(SR)_{50}$ formed by two different Au:Ag precursor ratios. When 1:0.1 Au:Ag ratio was used in the synthesis of crude product, $Au_{130}(SCH_2CH_2Ph)_{50}$ was the major peak in ESI-MS of purified product, with about a maximum of three silver atom incorporations. When the precursor Au:Ag ratio was increased to 1:0.15, the number of silver atoms incorporated has increased with $Au_{125}Ag_5(SCH_2CH_2Ph)_{50}$ being the most intense peak in the ESI-MS spectra of the isolated product. But the maximum number of silver atom incorporations was increased to 20. With Au:Ag ratio of 1:0.1, the ESI-MS of the isolated product shows some peaks to the left of $Au_{130}(SR)_{50}$. These were assigned to nanomolecules comprising of 131 metal atoms. When the Au:Ag precursor ratio was further increased, there was no $Au_{130-x}Ag_x(SR)_{50}$ observed in the reaction

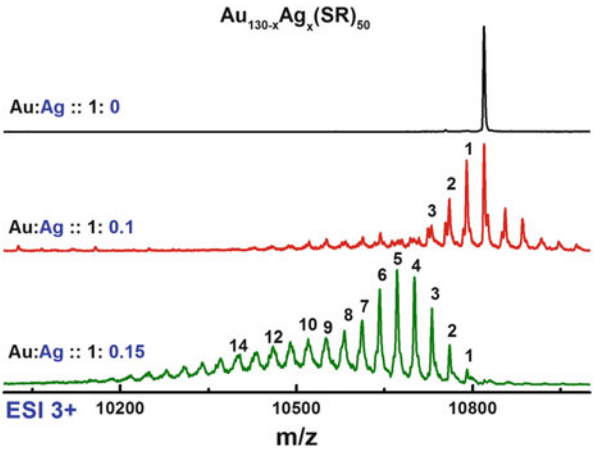

Fig. 17 Positive mode ESI MS of 3+ peaks for two different Au:Ag precursor ratios. Upon increasing the Au:Ag ratio to 1:0.15, $Au_{125}Ag_5(SCH_2CH_2Ph)_{50}$ is the major peak observed

mixtures. This could be because of the instability of the 130 metal atom clusters induced by higher silver incorporation. The silver incorporation in the 130 metal-atom nanomolecule suggests the high stability of the nanomolecule formed by the core-size conversion reaction. It has been reported in the literature that the doping of gold nanomolecules with palladium, platinum, and silver increases the stability and catalytic activity. $Au_{130}(SR)_{50}$ has also been reported by Negishi's group, who isolated the cluster on a small scale using analytical HPLC column [61].

5.3.2 MS Data-Based Core-Size Conversion and Proposed Mechanism

In Scheme 2, the starting material represents the polydispersed clusters larger than 40 kDa that are used for etching. This is same as the 0 h sample in Fig. 15. Mass spectrometric analysis of the samples collected from the etching reaction of larger clusters (>40 kDa) shows the accumulation of $Au_{130}(SR)_{50}$ in the reaction mixture over time. This mass spectrometric data provides clear evidence that $Au_{130}(SR)_{50}$ is formed by the core conversion of the larger clusters (>40 kDa). Due to the high stability of 76.3 kDa nanomolecule, it is observed during the etching reactions. Au-SR aggregates are the expected by-products of etching. However, the by-products in the etching of alloy clusters might be different, which need further detailed study.

For the formation of $Au_{130}(SR)_{50}$ by core-size conversion, the larger nanoclusters initially present in the reaction mixture should breakdown in size. One possible route one can imagine is the systematic removal of metal atoms and ligands from the surface of the larger clusters. This process continues until the $Au_{130}(SR)_{50}$ is formed in the reaction and does not proceed any further due to high stability of this 130-metal atom nanomolecule. However not all the larger clusters in the initial crude product undergo this process. Highly stable species like 76.3 kDa nanomolecule stays unaltered throughout the etching reaction. Only the meta-stable

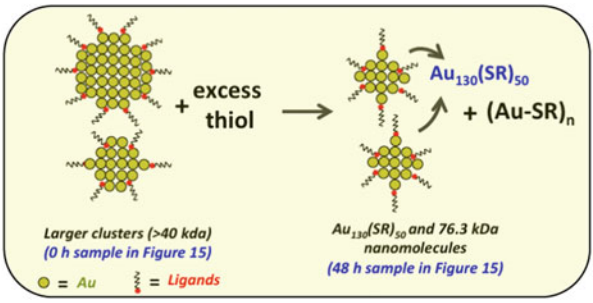

Scheme 2 Core-size conversion of larger nanoclusters to form $Au_{130}(SR)_{50}$. Breakdown-reaggregation approach where the metal atoms and ligands recombine with nanomolecules to form monodisperse nanomolecules

species or nanoclusters with low thermochemical stability undergo this core conversion process. After the surface metal atoms and ligands are removed from the larger clusters, remaining ligands and gold atoms might undergo some kind of rearrangement to increase the overall structural and geometrical stability to form $Au_{130}(SR)_{50}$.. However, based on the core-size conversion experiments conducted so far, this is only a proposed mechanism.

From the systematic etching reactions, the core-size conversion reactions in gold nanoclusters have been carefully studied. Au_{67} and $Au_{103–105}$ core-convert to $Au_{40}(SR)_{24}$ exclusively without any $Au_{38}(SR)_{24}$ upon etching. When clusters smaller than Au_{67} are etched with excess thiol, $Au_{38}(SR)_{24}$ is exclusively formed. In the case of larger gold nanoclusters, when clusters larger than 200 metal atoms are etched with excess thiol $Au_{130}(SR)_{50}$ is formed. The core-size conversion reactions in gold nanoclusters larger than 200 metal atoms have been investigated with three different ligand and two different alloy systems. There could also be similar core-size conversion in clusters larger than 1,000 or 2,000 metal atoms and this aspect still needs to be explored. The mechanism of these core-size conversion reactions is not completely understood and needs further experimental investigation.

6 Summary

We have reviewed various synthetic methods employed to prepare ultra-small gold nanomolecules protected by phenylethanethiol, HS-CH_2CH_2Ph. The synthesis of $Au_{25}(SR)_{18}$, $Au_{38}(SR)_{24}$, $Au_{40}(SR)_{24}$, $Au_{67}(SR)_{35}$, $Au_{103–105}(SR)_{45–46}$, $Au_{130}(SR)_{50}$, and $Au_{144}(SR)_{60}$ has been described. The stability of the nanomolecules is the key factor that dictates the synthetic protocol. Ultra-stable nanomolecules such as $Au_{25}(SR)_{18}$ and $Au_{144}(SR)_{60}$ can be easily prepared as these can withstand harsh processing and post-synthetic treatment. Meta-stable nanomolecules such as $Au_{67}(SR)_{35}$, and $Au_{103–105}(SR)_{45–46}$ can be prepared, but harsh post-synthetic treatment should be avoided and extensive chromatographic and/or solvent fractionation procedures need to be employed. $Au_{38}(SR)_{24}$, $Au_{40}(SR)_{24}$, and $Au_{130}(SR)_{50}$ are prepared through a core-size conversion

synthesis, where larger core-sized polydisperse clusters are converted to single-sized nanomolecules. Mass spectrometry, SEC separation, and solvent fractionation procedures are important in studying the reactions and facilitating the development of new synthetic protocols.

References

1. Parker JF, Fields-Zinna CA, Murray RW (2010) The story of a monodisperse gold nanoparticle: $Au_{25}L_{18}$. Acc Chem Res 43(9):1289–1296
2. Dharmaratne AC, Krick T, Dass A (2009) Nanocluster size evolution studied by mass spectrometry in room temperature $Au_{25}(SR)_{18}$ synthesis. J Am Chem Soc 131 (38):13604–13605
3. Knoppe S, Boudon J, Dolamic I, Dass A, Bürgi T (2011) Size exclusion chromatography for semipreparative scale separation of $Au_{38}(SR)_{24}$ and $Au_{40}(SR)_{24}$ and larger clusters. Anal Chem 83(13):5056–5061
4. Nimmala PR, Yoon B, Whetten RL, Landman U, Dass A (2013) $Au_{67}(SR)_{35}$ nanomolecules: characteristic size-specific optical, electrochemical, structural properties and first-principles theoretical analysis. J Phys Chem A 117(2):504–517
5. Brust M, Walker M, Bethell D, Schiffrin DJ, Whyman R (1994) Synthesis of thiol-derivatised gold nanoparticles in a two-phase Liquid–Liquid system. J Chem Soc Chem Commun 7:801–802
6. Whetten RL, Khoury JT, Alvarez MM, Murthy S, Vezmar I, Wang ZL, Stephens PW, Cleveland CL, Luedtke WD, Landman U (1996) Nanocrystal gold molecules. Adv Mater 8 (5):428–433
7. Schaaff TG, Whetten RL (1999) Controlled etching of Au:SR cluster compounds. J Phys Chem B 103(44):9394–9396
8. Fields-Zinna CA, Sardar R, Beasley CA, Murray RW (2009) Electrospray ionization mass spectrometry of intrinsically cationized nanoparticles, $[Au_{144/146}(SC_{11}H_{22}N(CH_2CH_3)_3^+)_x(S(CH_2)_5CH_3)_y]^{x+}$. J Am Chem Soc 131(44):16266–16271
9. Dass A, Stevenson A, Dubay GR, Tracy JB, Murray RW (2008) Nanoparticle MALDI-TOF mass spectrometry without fragmentation: $Au_{25}(SCH_2CH_2Ph)_{18}$ and mixed monolayer $Au_{25}(SCH_2CH_2Ph)_{18-x}(L)_x$. J Am Chem Soc 130(18):5940–5946
10. Wang G, Guo R, Kalyuzhny G, Choi J-P, Murray RW (2006) NIR luminescence intensities increase linearly with proportion of polar thiolate ligands in protecting monolayers of Au_{38} and Au_{140} quantum dots. J Phys Chem B 110(41):20282–20289
11. Guo R, Georganopoulou D, Feldberg SW, Donkers R, Murray RW (2005) Supporting electrolyte and solvent effects on single-electron double layer capacitance charging of hexanethiolate-coated Au_{140} nanoparticles. Anal Chem 77(8):2662–2669
12. Choi J-P, Murray RW (2006) Electron self-exchange between $Au_{140}^{+/0}$ nanoparticles is faster than that between $Au_{38}^{+/0}$ in solid-state, mixed-valent films. J Am Chem Soc 128 (32):10496–10502
13. Heaven MW, Dass A, White PS, Holt KM, Murray RW (2008) Crystal structure of the gold nanoparticle $[N(C_8H_{17})_4][Au_{25}(SCH_2CH_2Ph)_{18}]$. J Am Chem Soc 130(12):3754–3755
14. Fields-Zinna CA, Crowe MC, Dass A, Weaver JEF, Murray RW (2009) Mass spectrometry of small bimetal monolayer-protected clusters. Langmuir 25(13):7704–7710
15. Ecclesiastes 1:9
16. Seker F, Malenfant PRL, Larsen M, Alizadeh A, Conway K, Kulkarni AM, Goddard G, Garaas R (2005) On-demand control of optoelectronic coupling in gold nanoparticle arrays. Adv Mater 17(16):1941–1945. doi:10.1002/adma.200400734

17. Jain PK, Huang X, El-Sayed IH, El-Sayed MA (2008) Noble metals on the nanoscale: optical and photothermal properties and some applications in imaging, sensing, biology, and medicine. Acc Chem Res 41(12):1578–1586
18. Dingwen Z, Milton W, Alexandre GB, Jie S, Xiaodong L, Sumei H (2013) Enhanced performance of dye-sensitized solar cells using gold nanoparticles modified fluorine tin oxide electrodes. J Phys D: Appl Phys 46(2):024005
19. Khlebtsov NG, Dykman LA (2010) Optical properties and biomedical applications of plasmonic nanoparticles. J Quant Spectrosc Radiat Transfer 111(1):1–35
20. Turner M, Golovko VB, Vaughan OPH, Abdulkin P, Berenguer-Murcia A, Tikhov MS, Johnson BFG, Lambert RM (2008) Selective oxidation with dioxygen by gold nanoparticle catalysts derived from 55-atom clusters. Nature 454(7207):981–983
21. Zhou X, Xu W, Liu G, Panda D, Chen P (2009) Size-dependent catalytic activity and dynamics of gold nanoparticles at the single-molecule level. J Am Chem Soc 132(1):138–146
22. Rycenga M, Cobley CM, Zeng J, Li W, Moran CH, Zhang Q, Qin D, Xia Y (2011) Controlling the synthesis and assembly of silver nanostructures for plasmonic applications. Chem Rev 111 (6):3669–3712
23. Wei Z, Zhou Z, Yang M, Lin C, Zhao Z, Huang D, Chen Z, Gao J (2011) Multifunctional Ag@Fe_2O_3 yolk-shell nanoparticles for simultaneous capture, kill, and removal of pathogen. J Mater Chem 21(41):16344–16348
24. Negishi Y, Iwai T, Ide M (2010) Continuous modulation of electronic structure of stable thiolate-protected Au_{25} cluster by Ag doping. Chem Commun 46(26):4713–4715
25. Ferrando R, Jellinek J, Johnston RL (2008) Nanoalloys: from theory to applications of alloy clusters and nanoparticles. Chem Rev 108(3):845–910
26. Devadas MS, Bairu S, Qian H, Sinn E, Jin R, Ramakrishna G (2011) Temperature-dependent optical absorption properties of monolayer-protected Au_{25} and Au_{38} clusters. J Phys Chem Lett 2(21):2752–2758
27. García-Raya D, Madueño R, Blázquez M, Pineda T (2009) Electrochemistry of molecule-like Au_{25} nanoclusters protected by hexanethiolate. J Phys Chem C 113(20):8756–8761
28. Tracy JB, Crowe MC, Parker JF, Hampe O, Fields-Zinna CA, Dass A, Murray RW (2007) Electrospray ionization mass spectrometry of uniform and mixed monolayer nanoparticles: $Au_{25}[S(CH_2)2Ph]_{18}$ and $Au_{25}[S(CH_2)2Ph]_{18}$-x(SR)x. J Am Chem Soc 129(51):16209–16215
29. Wu Z, Suhan J, Jin R (2009) One-pot synthesis of atomically monodisperse, thiol-functionalized Au_{25} nanoclusters. J Mater Chem 19(5):622–626
30. Parker JF, Weaver JEF, McCallum F, Fields-Zinna CA, Murray RW (2010) Synthesis of monodisperse [Oct_4N+][$Au_{25}(SR)_{18}^-$] nanoparticles, with some mechanistic observations. Langmuir 26(16):13650–13654
31. Zhu M, Aikens CM, Hollander FJ, Schatz GC, Jin R (2008) Correlating the crystal structure of A thiol-protected Au_{25} cluster and optical properties. J Am Chem Soc 130(18):5883–5885. doi:10.1021/ja801173r
32. Negishi Y, Kurashige W, Niihori Y, Iwasa T, Nobusada K (2010) Isolation, structure, and stability of a dodecanethiolate-protected Pd_1Au_{24} cluster. Phys Chem Chem Phys 12 (23):6219–6225
33. Negishi Y, Munakata K, Ohgake W, Nobusada K (2012) Effect of copper doping on electronic structure, geometric structure, and stability of thiolate-protected Au_{25} nanoclusters. J Phys Chem Lett 3(16):2209–2214
34. Qian H, D-e J, Li G, Gayathri C, Das A, Gil RR, Jin R (2012) Monoplatinum doping of gold nanoclusters and catalytic application. J Am Chem Soc 134(39):16159–16162
35. D-e J, Dai S (2009) From superatomic $Au_{25}(SR)_{18}^-$ to superatomic M@$Au_{24}(SR)_{18}^q$ core−shell clusters. Inorg Chem 48(7):2720–2722
36. Walter M, Moseler M (2009) Ligand-protected gold alloy clusters: doping the superatom. J Phys Chem C 113(36):15834–15837

37. Guidez EB, Mäkinen V, Häkkinen H, Aikens CM (2012) Effects of silver doping on the geometric and electronic structure and optical absorption spectra of the $Au_{25-n}Ag_n(SH)_{18}^-$ ($n = 1, 2, 4, 6, 8, 10, 12$) bimetallic nanoclusters. J Phys Chem C 116(38):20617–20624
38. Kauffman DR, Alfonso D, Matranga C, Qian H, Jin R (2013) A quantum alloy: the ligand-protected $Au_{25-x}Ag_x(SR)_{18}$ cluster. J Phys Chem C 117(15):7914–7923
39. Copley RCB, Mingos DMP (1996) Synthesis and characterization of the centred icosahedral cluster series $[Au_9MIB_4C_{14}(PMePh_2)_8][C_2B_9H_{12}]$, where MIB=Au, Ag or Cu. J Chem Soc Dalton Trans 4:491–500
40. Mingos DMP, Zhenyang L (1989) Site preference effects in heterometallic clusters. Comments Inorg Chem 9(2):95–122. doi:10.1080/02603598908035805
41. Kumara C, Aikens CM, Dass A (2014) X-ray crystal structure and theoretical analysis of $Au_{25-x}Ag_x(SCH_2CH_2Ph)_{18-}$ Alloy. The J Phys Chem Lett 461–466. doi:10.1021/jz402441d
42. Hostetler MJ, Wingate JE, Zhong C-J, Harris JE, Vachet RW, Clark MR, Londono JD, Green SJ, Stokes JJ, Wignall GD, Glish GL, Porter MD, Evans ND, Murray RW (1998) Alkanethiolate gold cluster molecules with core diameters from 1.5 to 5.2 nm: core and monolayer properties as a function of core size. Langmuir 14(1):17–30
43. Schaaff TG, Shafigullin MN, Khoury JT, Vezmar I, Whetten RL (2001) Properties of a ubiquitous 29 kDa Au:SR cluster compound. J Phys Chem B 105(37):8785–8796
44. Chaki NK, Negishi Y, Tsunoyama H, Shichibu Y, Tsukuda T (2008) Ubiquitous 8 and 29 kDa gold:alkanethiolate cluster compounds: mass-spectrometric determination of molecular formulas and structural implications. J Am Chem Soc 130(27):8608–8610
45. Lopez-Acevedo O, Akola J, Whetten RL, Grönbeck H, Häkkinen H (2009) Structure and bonding in the ubiquitous icosahedral metallic gold cluster $Au_{144}(SR)_{60}$. J Phys Chem C 113 (13):5035–5038
46. Qian H, Jin R (2009) Controlling nanoparticles with atomic precision: the case of $Au_{144}(SCH_2CH_2Ph)_{60}$. Nano Lett 9(12):4083–4087
47. Kumara C, Dass A (2011) $(AuAg)_{144}(SR)_{60}$ alloy nanomolecules. Nanoscale 3(8):3064–3067
48. Malola S, Häkkinen H (2011) Electronic structure and bonding of icosahedral core–shell gold–silver nanoalloy clusters $Au_{144-x}Ag_x(SR)_{60}$. J Phys Chem Lett 2(18):2316–2321
49. Dass A (2009) Mass spectrometric identification of $Au_{68}(SR)_{34}$ molecular gold nanoclusters with 34-electron shell closing. J Am Chem Soc 131(33):11666–11667
50. Jadzinsky PD, Calero G, Ackerson CJ, Bushnell DA, Kornberg RD (2007) Structure of a thiol monolayer-protected gold nanoparticle at 1.1 Å resolution. Science 318(5849):430–433
51. Dass A, Nimmala PR, Jupally VR, Kothalawala N (2013) $Au_{103}(SR)_{45}$, $Au_{104}(SR)_{45}$, $Au_{104}(SR)_{46}$ and $Au_{105}(SR)_{46}$ nanoclusters. Nanoscale 5(24):12082–12085
52. Nimmala PR, Dass A (2011) $Au_{36}(SPh)_{23}$ nanomolecules. J Am Chem Soc 133(24):9175–9177
53. Nimmala PR, Jupally VR, Dass A (2014) Core size conversion: route for exclusive synthesis of Au38 or Au40 nanomolecules. Langmuir 30:2490–2497
54. Jupally VR, Dass A (2013) Synthesis of $Au_{130}(SR)_{50}$ and $Au_{130-x}Ag_x(SR)_{50}$ nanomolecules through core size conversion of larger metal clusters. Submitted for publication
55. Donkers RL, Lee D, Murray RW (2004) Synthesis and isolation of the molecule-like cluster $Au_{38}(PhCH_2CH_2S)_{24}$. Langmuir 20(5):1945–1952. doi:10.1021/la035706w
56. Qian H, Zhu M, Andersen UN, Jin R (2009) Facile, large-scale synthesis of dodecanethiol-stabilized Au_{38} clusters. J Phys Chem A 113(16):4281–4284
57. Meng X, Liu Z, Zhu M, Jin R (2012) Controlled reduction for size selective synthesis of thiolate-protected gold nanoclusters Aun ($n = 20, 24, 39, 40$). Nanoscale Res Lett 7:277
58. Edinger K, Goelzhaeuser A, Demota K, Woell C, Grunze M (1993) Formation of self-assembled monolayers of *n*-alkanethiols on gold: a scanning tunneling microscopy study on the modification of substrate morphology. Langmuir 9(1):4–8
59. Ingram RS, Hostetler MJ, Murray RW, Schaaff TG, Khoury JT, Whetten RL, Bigioni TP, Guthrie DK, First PN (1997) 28 kDa Alkanethiolate-protected au clusters give analogous solution electrochemistry and STM Coulomb staircases. J Am Chem Soc 119(39):9279–9280

60. Dass A (2011) Faradaurate nanomolecules: a superstable plasmonic 76.3 kDa cluster. J Am Chem Soc 133(48):19259–19261
61. Negishi Y, Sakamoto C, Ohyama T, Tsukuda T (2012) Synthesis and the origin of the stability of thiolate-protected Au_{130} and Au_{187} clusters. J Phys Chem Lett 3(12):1624–1628
62. Dass A, Nimmala PR, Jupally VR, Kothalawala N (2013) $Au_{103}(SR)_{45}$, $Au_{104}(SR)_{45}$, $Au_{104}(SR)_{46}$ and $Au_{105}(SR)46$ nanoclusters. Nanoscale 5:12082–12085
63. Knoppe S, Boudon J, Dolamic I, Dass A, Burgi T (2011) Size exclusion chromatography for semipreparative scale separation of $Au_{38}(SR)_{24}$ and $Au_{40}(SR)_{24}$ and larger clusters. Anal Chem 83(13):5056–5061
64. Qian H, Eckenhoff WT, Zhu Y, Pintauer T, Jin R (2010) Total structure determination of thiolate-protected Au_{38} nanoparticles. J Am Chem Soc 132(24):8280–8281
65. Dolamic I, Knoppe S, Dass A, Bürgi T (2012) First enantioseparation and circular dichroism spectra of Au38 clusters protected by achiral ligands. Nat Commun 3:798
66. Lopez-Acevedo O, Tsunoyama H, Tsukuda T, Häkkinen H, Aikens CM (2010) Chirality and electronic structure of the thiolate-protected Au_{38} nanocluster. J Am Chem Soc 132 (23):8210–8218
67. Toikkanen O, Carlsson S, Dass A, Rönnholm G, Kalkkinen N, Quinn BM (2009) Solvent-dependent stability of monolayer-protected Au_{38} clusters. J Phys Chem Lett 1(1):32–37
68. Knoppe S, Dharmaratne AC, Schreiner E, Dass A, Bürgi T (2010) Ligand exchange reactions on Au_{38} and Au_{40} clusters: a combined circular dichroism and mass spectrometry study. J Am Chem Soc 132(47):16783–16789
69. Kumara C, Dass A (2012) AuAg alloy nanomolecules with 38 metal atoms. Nanoscale 4 (14):4084–4086
70. Qian H, Zhu Y, Jin R (2012) Atomically precise gold nanocrystal molecules with surface plasmon resonance. Proc Natl Acad Sci 109(3):696–700
71. Lordeiro RA, Guimarães FF, Belchior JC, Johnston RL (2003) Determination of main structural compositions of nanoalloy clusters of Cu_xAu_y ($x + y \leq 30$) using a genetic algorithm approach. Int J Quantum Chem 95(2):112–125. doi:10.1002/qua.10660
72. Negishi Y, Igarashi K, Munakata K, Ohgake W, Nobusada K (2012) Palladium doping of magic gold cluster $Au_{38}(SC_2H_4Ph)_{24}$: formation of $Pd_2Au_{36}(SC_2H_4Ph)_{24}$ with higher stability than $Au_{38}(SC_2H_4Ph)_{24}$. Chem Commun (Cambridge, UK) 48(5):660–662

Struct Bond (2014) 161: 189–242
DOI: 10.1007/430_2013_127

Published online: 13 September 2014

Size- and Ligand-Specific Bioresponse of Gold Clusters and Nanoparticles: Challenges and Perspectives

Janine Broda, Günter Schmid, and Ulrich Simon

Abstract This review gives an introduction to the chemical and physical properties of gold clusters and nanoparticles (NPs) and reflects the present understanding how such particles interact with biological systems in vitro and in vivo. It will acquaint the reader with the basic principles of interaction from a chemical point of view and illustrates perspectives that arise for the application of gold nanoparticles (AuNPs) in biological environments.

Keywords Diagnostics · Gold nanoparticle · Ligand · Nanotoxicity · Size effect · Therapy

Contents

J. Broda and U. Simon (✉)
Institute of Inorganic Chemistry, RWTH Aachen University, 52074 Aachen, Germany
e-mail: Janine.Broda@ac.rwth-aachen.de; Ulrich.Simon@ac.rwth-aachen.de

G. Schmid
Institute of Inorganic Chemistry, University Duisburg-Essen, 45127 Essen, Germany
e-mail: Guenter.Schmid@uni-due.de

1 Introduction

The focus of this review article is the discussion of our present understanding of the interaction of gold nanoparticles (AuNPs) with biological materials in vitro and in vivo, called "bioresponse," as well as the illustration of perspectives that arise for the application of AuNPs in biological environments. The often applied definition of "nanoparticle" – namely to consist of species smaller than 100 nm – is, at least from a scientific viewpoint, too simple. The name nanoparticle should be linked with a characteristic change of properties as is, for instance, the case if AuNPs become smaller than approx. 100 nm when their dispersions in sols or liquids spontaneously become violet or red colored due to the surface plasmon resonance (SPR). Two more precise definitions of nanoscience are therefore cited in Sect. 2.

A prerequisite to understand bioresponse processes is a fundamental knowledge of the influence of size, shape, and surface constitution of the particles. As will be discussed in detail in Sect. 2, the size of a particle is the most important factor influencing predominantly its electronic structure. A gold particle, small enough to restrict the mean free path of the electrons, behaves significantly different from bulk gold. This effect is called "size quantization," saying that such species no longer follow classical physical laws but instead they obey quantum mechanical rules, traditionally used to describe the electronic nature of atoms and molecules. Metal NPs in general and AuNPs in particular have to become very small to reach that state, usually smaller than 2 nm. A prominent example is the Au_{55} cluster (the expression cluster is generally used for NPs with an exact chemical formula, see also Sect. 2) with a diameter of 1.4 nm. It exhibits size quantization properties even at room temperature, whereas larger particles reach this state only at very low temperatures and smaller clusters exhibit discrete electronic states of molecular orbitals. Examples are $[Au_{39}(PPh_3)_{14}Cl_6]Cl_2$ [1], $[Au_{14}(PPh_3)_8(NO_3)_4]$ [2], $[Au_{13}(PR_3)_{10}Cl_2]^{3+}$ [3], or $Au_{11}(PR_3)_7X_3$ [4–6] (X = halogen, thiolate).

The extraordinary position of Au_{55} in the transition range between molecule and extended solid has frequently been demonstrated by its physical properties. Among others, it exhibits quantized charging effects associated with adding an extra electron to a small capacitance, which give rise to applications as a single electron switch at room temperature. Apart from its electronic properties, Au_{55}, usually represented in a ligand-protected version, namely $Au_{55}(PPh_3)_{12}Cl_6$, has a second extraordinary feature: its stability. As will also be discussed in more detail, Au_{55}

is the second of the series of the so-called "full-shell clusters." It consists of a hexagonal close-packed structure like bulk gold and has a cuboctahedral shape. Full-shell clusters follow the composition $10\,n^2 + 2$ for the number of atoms in the nth shell. Particles following this rule are especially stable, as has been demonstrated in a variety of ways. The stability of AuNPs has indeed an important influence on bioresponse, because of the interaction mechanisms between NP and the relevant biosystems. As ligand-free AuNPs cannot be used because of their instability, only ligand-protected species are used. The interaction with any kind of biomolecule and the metal core can only happen, if the original ligands are either completely or at least partially released or replaced during the chemical processes. This means that the protecting ligand shell must have a special nature. If ligand molecules are not sufficiently labile to be removed from the particle's surface, the interaction between the particle and the biological environment only occurs via the protecting skin and not by the metal itself. Phosphine ligands in combination with gold usually fulfill these conditions. $Au_{55}(Ph_2PC_6H_4SO_3Na)_{12}Cl_6$, a water-soluble derivative of the original compound $Au_{55}(PPh_3)_{12}Cl_6$, therefore plays the dominant role in this article. Larger and smaller particles are introduced for comparisons as well as to highlight the emerging field of applications for AuNPs in diagnostics and therapy.

Size, stability, and electronic properties indeed determine bioresponse: Sect. 3 illustrates in vitro applications by discussing the interaction of AuNPs with proteins and cells. While these applications utilize the size-dependent properties of AuNPs as an analytical probe, the molecular mechanisms occur in the ligand shell of the molecules. In contrast 1.4 nm-sized Au_{55} with its weak-binding phosphine ligands turned out to be very cytotoxic. This is demonstrated in series of tests with human cancer cell lines. Two reasons for the cytotoxicity have been proposed: (1) the size of the 1.4 nm Au_{55} clusters fits perfectly to the height of the major grooves of DNA (1.3–1.5 nm) and thus may block transcription of DNA and (2) it induces the formation of reactive oxygen species (ROS) as a consequence of its electronic properties, leading to oxidative damage of neighbored biomolecules and subcellular units. Comparisons with smaller and larger AuNPs, decorated with the same ligand molecules like Au_{55}, clearly show a much less or even no toxicity, supporting the assumption that Au_{55} has a very special bioresponse.

Properties of AuNPs in vivo are introduced in Sect. 4. These experiments inform about distribution in a living body (exemplified by means of rat data), of course depending on the kind of administration. Again, size dependency plays the dominant role. Among a series of AuNPs from 1.4 up to 200 nm, only the 1.4 nm Au_{55} species distribute in all relevant organs, whereas larger particles are accumulated up to 97% in the liver. A further aspect of interest is the role of surface charge in relation to biodistribution experiments with positively and negatively charged 2.8 nm Au particles show little differences. Positively charged species are somewhat less assembled in the liver than negatively charged particles. Furthermore, a new model system for in vivo analyses, i.e., the zebrafish, is introduced with its potential to analyze the properties of AuNPs in whole animal tests.

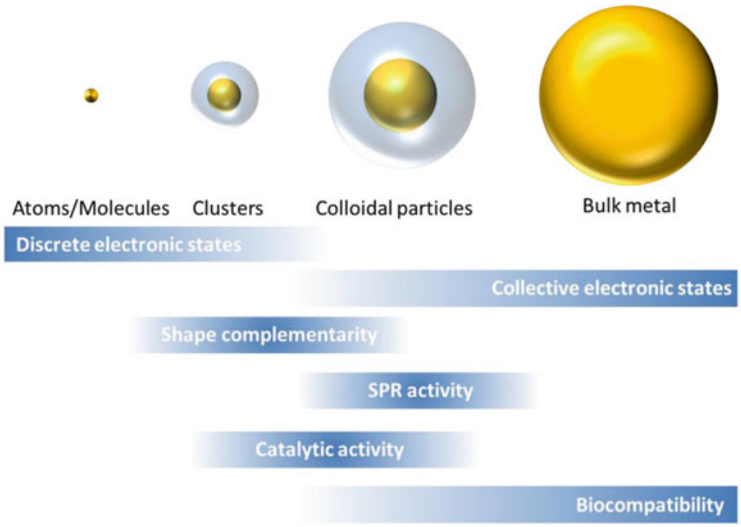

Fig. 1 Schematic presentation of the size-dependent properties of gold, spanning the size range from individual atoms via ligand-stabilized clusters and colloidal particles up to macroscopic bulk metal. The shaded areas indicate size ranges, where specific properties and features of gold occur. Atoms, molecules, and molecular clusters exhibit an electronic structure with discrete electronic states, while colloidal particles as well as bulk gold exhibit collective electronic states. In the size range of clusters and colloids, biological effects may occur due to complementarity in shape to biomolecules and cellular subunits. In this size range the surface plasmon resonance (SPR) dominates the optical properties and most of the size-dependent catalytic properties of gold nanoparticles occur. The biocompatibility increases with sizes above the typical cluster size. The marked areas are not drawn to scale

The final section of this article (Sect. 5) deals with perspectives and challenges of the above findings especially in medicine. Diagnostic and therapeutic aspects as well as drug delivery systems are already partially realized or can be prognosticated (Fig. 1).

2 Size-Dependent Properties of Metal Nanoparticles

The physical and chemical properties of defined materials, for instance elements or chemical compounds in the solid state, depend on size and shape of the particles under consideration. The size dependency of the properties usually becomes obvious in the nanometer regime. Nanotechnology is based on such effects which can have very different appearance. Whereas the bright color of bulk gold is based on relativistic effects [7–9], the red, purple, and blue color of gold nanoparticles (AuNPs) in the size regime of ca. 15 and 50 nm is based on the so-called surface

plasmon resonance (SPR). It is quantitatively described by the Mie theory [10]. The reason for the SPR is to be seen in a size- and shape-dependent collective electron oscillation by interaction with visible light. SPR for copper, silver, and gold is in the visible region and superimposes the relativistic effect, covering the typical color of bulk metals. For other metals it appears in the UV region and is therefore not observable with the naked eye.

Numerous other size effects such as changes of melting points, characteristic magnetic properties, and electronic behavior or the kind of interaction with other species are known and play dominant roles in what we call "nanotechnology." One definition of nanotechnology, considering these different effects, is the following [11]:

> Nanotechnology comprises the emerging application of Nanoscience. Nanoscience deals with functional systems either based on the use of subunits with specific size-dependent properties or of individual or combined functionalized subunits.

The so-called scaling effects, i.e., continuous changes of properties during downsizing a material, are excluded because nano-effects appear only below distinct sizes, resulting in properties which characteristically differ from the macroscopic counterparts. Another similar definition, given by the Royal Society and the Royal Academy of Engineering, also considers the use of molecules and macromolecular systems [12]:

> Nanoscience is the study of phenomena and manipulation of materials at atomic, molecular and macromolecular scales, where properties differ significantly from those at a larger scale. Nanotechnologies are the design, characterization, production and application of structures, devices and systems by controlling shape and size at the nanometre scale.

These definitions include the development of molecular motors and machines, molecular switches, single-electron memories, and, especially considered in this review article, the interaction of metal nanoparticles with biological systems. Why are size-dependent physical and chemical properties decisive for interactions with biosystems and responsible for bioresponse? These connections shall be briefly discussed in this section.

A single metal atom is not a metal in a classical sense. A huge number of atoms are necessary to reach the metallic state, for instance electric conductivity or metallic luster. Corresponding questions arise for other solid elements, for instance silicon. A single Si atom is not a semiconductor. The basic question therefore arises, namely how many atoms are necessary to reach the metallic state and what happens on the way to this state? In spite of various theoretical calculations, numerous experimental results during the last two to three decades have given us some fundamental answers.

The electronic situation in an atom or molecule is best described by following quantum mechanical rules (size quantization). Bulk systems consisting of an infinite number of atoms can widely be described by the laws of classical physics for bulk materials, based on the statistics of infinite numbers of electrons. Figure 2 illustrates the stepwise transition from a three-dimensional (3D) piece of metal (a) via a two-dimensional quantum well (2D) (b), a quantum wire (1D) (c), and

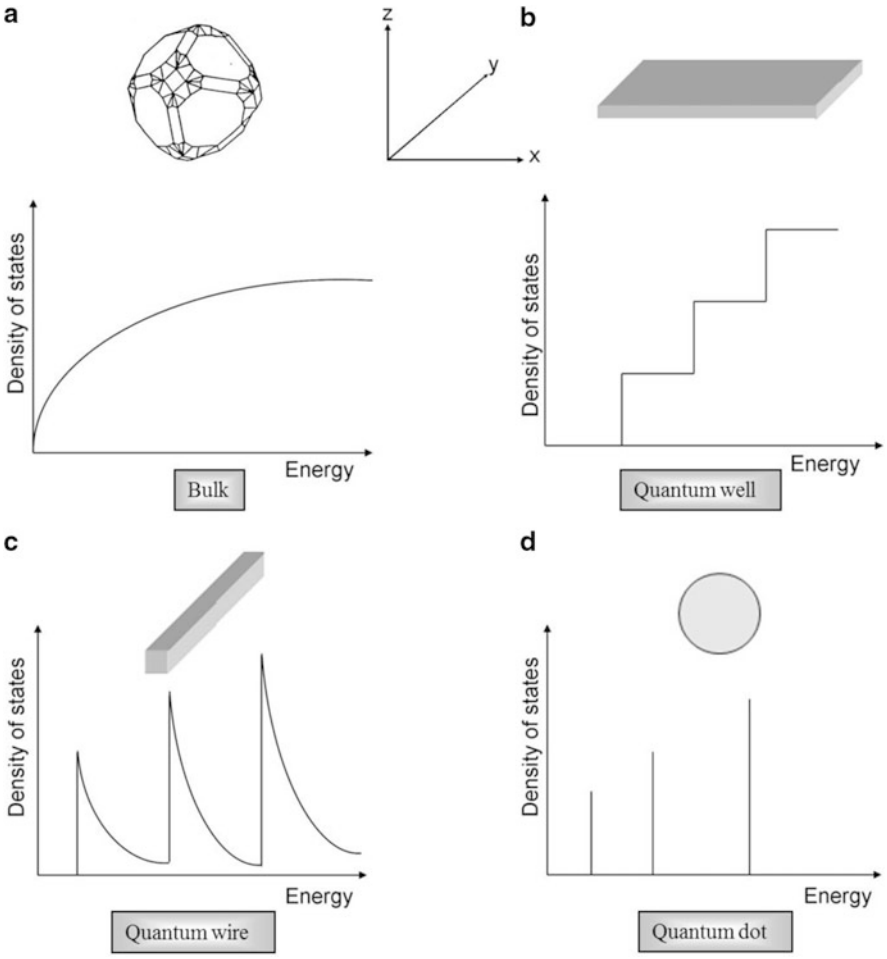

Fig. 2 Transition from a three-dimensional (3D) particle to a 0D quantum dot, correlating with the continuous discretion of the energy states

finally a quantum dot (0D) (d), considering the relation between the density of states and the energy.

On the way from a 3D system to a 2D quantum well, the relation between density of states and energy develops steps, spikes on the way to a 1D quantum wire and, finally, when small enough (0D), discrete energy levels characterize the relationship like in an atom or molecule. The development of a 0D quantum dot can formally also be considered by downsizing a metal particle as is indicated in Fig. 3.

The continuous energy band of s- and d-electrons in the bulk state (a) splits off when the particle is small enough (b, large cluster/nanoparticle) and forms

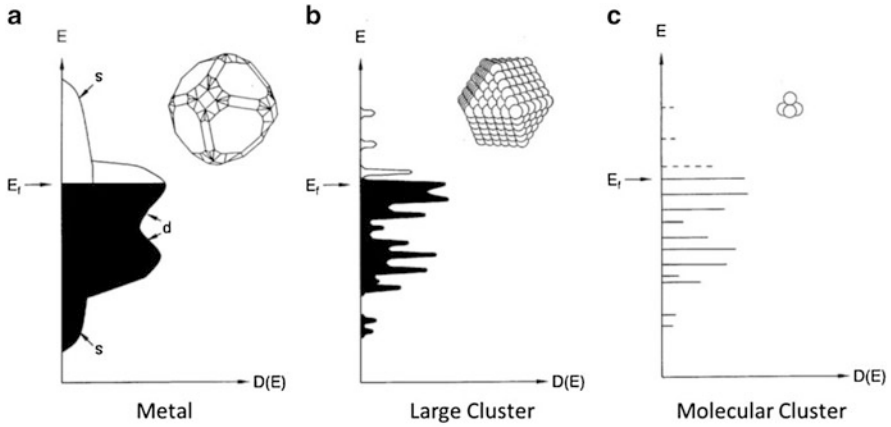

Fig. 3 Sketch of the transition from a metallic bulk state (**a**) via a large cluster (**b**) to a small molecule (**c**) indicating the changes of the electronic situations

sharp energy levels when a molecular cluster[1] is reached (c). What are the experimental results?

The most relevant physical method for investigating individual metal clusters and nanoparticles electronically is to determine the current (I) voltage (U) characteristic using a scanning tunneling microscopy (STM) tip to contact an individual particle on a conductive surface via the obligatory ligand shell. With this technique, single-electron transitions (SET) between tip, particle, and substrate can be observed, if some conditions are fulfilled. The nonconducting protecting ligand shell plays an important role, since neither the STM tip nor the conductive substrate touches the particle itself. SET can only be observed if the electrostatic energy $E_C = e^2/2C$ (C = capacity) is very large compared to the thermal energy $E_T = k_B T$ (k_B = Boltzmann's constant). Since $C = \varepsilon\varepsilon_0 A/d$ (ε = dielectric constant, ε_0 = electric field constant, d = distance of electrodes from metal core, A = surface area), the thickness of the ligand shell is important for the value of C. At very low temperatures single-electron transitions can be observed using rather large nanoparticles. For instance, the I–U characteristic of a 15 nm Pd particle, protected by a shell of $H_2NC_6H_4SO_3Na$ molecules and investigated at 295 K, clearly shows bulk properties, i.e., a linear I–U relationship following Ohm's law. However, at 4.2 K a so-called Coulomb blockade (CB) occurs, indicated by an interruption of conductivity between −55 and +55 mV by a single electron [13]. Figure 4 shows the I–U characteristics at both temperatures.

[1] The difference between the expression "cluster" and "nanoparticle" is not sharp. In the following we will use "cluster" for particles of a discrete number of atoms, whereas "nanoparticle" is used for less exactly defined species, allowing a certain size distribution.

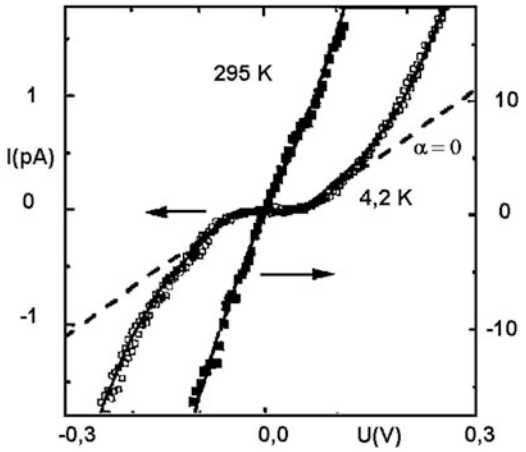

Fig. 4 Current (I)–voltage (U) characteristic of a ligand-protected 15 nm Pd particle at 295 K and 4.2 K. Ohm behavior is observed at 295 K, whereas a Coulomb blockade is existent at 4.2 K. Figure reprinted with kind permission from [13]

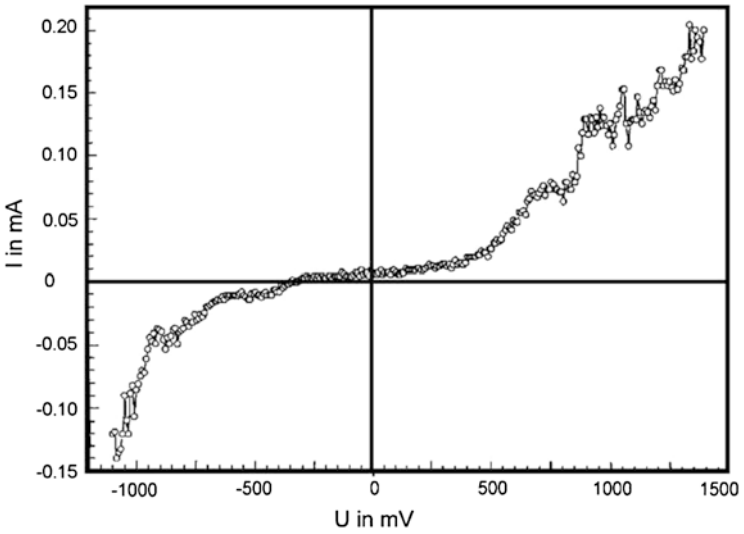

Fig. 5 I–U characteristic of Au_{55} $(PPh_3)_{12}Cl_6$ at 295 K exhibiting a well-expressed Coulomb blockade between −500 and +500 mV. Figure reprinted with kind permission from [15]

Of course, the existence of nanoparticles showing a Coulomb blockade already at room temperature is of high interest for future applications, for instance, as single electron switches. Indeed, such a particle (cluster) has been found with $Au_{55}(PPh_3)_{12}Cl_6$ [14]. The diameter of the Au_{55} core is only 1.4 nm. The I–U characteristic of an individual cluster clearly exhibits Coulomb blockade at 295 K between −500 and +500 mV as can be seen in Fig. 5 [15].

The Au_{55} cluster has another special property: it belongs to the so-called very stable full-shell clusters, species having an icosahedral or a hexagonal close-packed cuboctahedral shape, consisting of a distinct number of atoms per shell around 1 central atom, namely $10n^2 + 2$ atoms (n = number of shell). The smallest full-shell Au cluster with $n = 1$ consists of 1 + 12 atoms, well known since 1981 with icosahedrally structured Au_{13} cores [3, 16]. Numerous full-shell clusters of other metals have become known in the meantime, for instance the four- and five-shell clusters Pt_{309} [17] and Pd_{561} [18]. Whereas the ligand-protected Au_{13} cluster has still typical molecular properties, the Au_{55} species is just at the borderline between molecule and bulk and is therefore often called as "metal in the embryonic state."

The answer to the aforementioned question, why electronic and structural properties of clusters or nanoparticles are of relevance with respect to bioresponse, is not very surprising. First of all, the stability of metal particles in a biological medium is of high importance because less stable species would decompose, forming smaller or larger species with different properties. So, a stability guaranteeing structure and size is a condition for reliable results. The electronic structure is responsible for the chemical activity of a particle and so influences fundamentally the interactions with other materials. Some examples of these two factors are given.

Au_{55} and various smaller and larger gold nanoparticles and even bulk gold surfaces have been investigated with respect to their activity against oxygen in an oxygen plasma by means of X-ray photoelectron spectroscopy (XPS) [19]. Except Au_{55}, all other species became partially or quantitatively oxidized! Why not Au_{55}? This is because of its structure. Oxidation of the cuboctahedral structure would afford too much energy so that oxidation, even under the exceptional conditions in an oxygen plasma, does not happen.

The special stability of the Au_{55} nucleus becomes additionally visible when again AuNPs, smaller and larger than Au_{55}, are contacted with indium vapor. Bulk gold forms an alloy of the composition $AuIn_2$. All other NPs react easily with In vapor, but again not Au_{55}. It remains unreacted [19].

Theoretical [20] and experimental results [21] show that very small AuNPs are most active in oxygenation catalysis. Especially particles below ~3.5 nm are the most active species, indicating that electronic properties play a decisive role in chemical processes. $Au_{55}(PPh_3)_{12}Cl_6$ with a core diameter of 1.4 nm, supported on inert materials, turned out to be the most active catalyst for the selective oxidation of styrene by dioxygen [21]. In this case, particles larger than ~2 nm are completely inactive. This finding is of high importance considering the cell toxicity of Au_{55} species due to oxidative stress (reactive oxygen species, ROS) [22]. Though larger AuNPs also cause oxidative stress, the 1.4 nm cluster is the most active particle. Oxidative stress is caused by activation of dioxygen when touching the metal surface however, without oxidation of Au atoms. Details will be given in Sect. 3.

Another result indicating the special role of Au_{55} clusters shall briefly be mentioned. It is the relaxation behavior of excited electrons, compared with two other particle sizes [23]. If 0.7 nm (Au_{13}), 1.4 nm (Au_{55}), and 15 nm AuNPs are

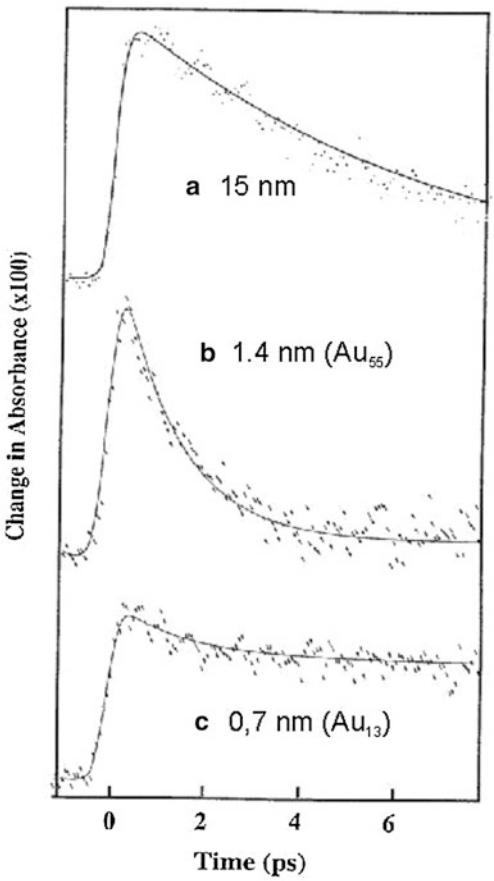

Fig. 6 Relaxation behavior of excited electrons in three differently sized AuNPs. Figure reprinted with kind permission from [23]

treated by femtosecond laser pulses, the corresponding relaxation times are size dependent. They are very different between Au_{55} and the other two species. The relaxation time is dependent on the electron–phonon coupling and the electron surface collision. In larger particles it is dominated by the weakening of the electron–phonon coupling, resulting in a slowdown of the relaxation. On the way from 15 to 1.4 nm, electron surface collision increases and consequently the relaxation time decreases. On the other side, the 0.7 nm Au_{13} cluster behaves molecular-like due to the fixed electrons between the Au atoms. Its relaxation is very slow. These results impressively demonstrate Au_{55} clusters to behave like species just one step before molecular and one step behind metallic state. These correlations can be followed from Fig. 6.

Up to here, we have discussed the influence of size, structure, and electronic properties on the relevance concerning bioresponse. However, there is another, very important factor: the protecting ligand shell. As already mentioned above, the use

of bare metal clusters and nanoparticles is not possible. Prevention of coalescence affords a "skin" of appropriate molecules on the particles' surface. The chemical nature of protecting molecules determines not only the solubility in different solvents, but it is decisively responsible for the initial contact between the particle and, in our case, a biosystem. For instance, $Au_{55}(PPh_3)_{12}Cl_6$ is only soluble in polar organic solvents and can therefore not be used for experiments in living systems. Therefore, a derivative with hydrophilic phosphine ligands is used, namely $PPh_2C_6H_4SO_3Na$ (monosulfonated triphenylphosphine, TPPMS) [24]. The "skin" determines what first happens. This fact can be used for surface recognition or specific targeting [25]. The specific nature of the metal particle becomes only effective if all or at least part of the ligand molecules are removed. Phosphines, coordinated to Au atoms, indeed fulfill this condition as has been shown by ^{31}P NMR studies [26] and as can be followed from the different results with respect to bioresponse, as will be demonstrated later. The cell toxicity of $Au_{55}(PPh_2C_6H_4SO_3Na)_{12}Cl_6$, discussed in more detail in Sect. 3, can clearly be traced back to the Au nucleus itself, since the phosphine ligands have been found to be nontoxic. If the easily removable phosphines are substituted by stronger coordinating thiols, the toxicity of the Au_{55} clusters is suppressed, since contacts between the clusters and the corresponding cell components happen only via the nontoxic end-groups of the thiols (e.g., glutathione, GSH) [22]. Living cells contain numerous different potential "ligands" that can substitute part or all of the original phosphines and then are directly in contact with the active Au_{55} cluster core. Unfortunately, these important relations between ligand-protected metal nanoparticles and any other system under investigation are often not sufficiently considered in the literature [27–29].

3 In Vitro Applications: Interaction with Proteins and Cells

AuNPs in general have attracted considerable interest for applications in vitro and in vivo. Since for most applications the particles' size is in the range of 10–20 nm and stabilizing ligands are thiols, they are typically considered nontoxic, and together with the relatively low amounts, which are applied for different purposes either in vitro or in vivo, it seems to be unlikely that AuNPs cause environmental pollution or health risk due to unintended exposure. Nevertheless, ultrasmall AuNPs can interact with cells and can induce cell death via different pathways, which is related to the size but also to the surface functionalization, as described above. The next two sections will shed light on the state of knowledge about the properties and applications of different classes of nontoxic AuNPs in vitro by means of selected examples. In these examples the AuNPs serve as a scaffold for the binding of (bio)molecules in in vitro applications so that the properties are determined by the binding molecules and by the particle itself. However, the

nanoscale features of the AuNPs, e.g., self-fluorescence or SPR, are utilized as probes to study the interaction with biomolecules. These two chapters will be followed by a chapter on in vitro studies on cytotoxic AuNPs, in particular of the 1.4 nm AuNPs, where the gold core itself is biologically active.

3.1 Interaction with Proteins: The Corona Effect

The functionality and bioactivity of AuNPs in biological fluids and in particular in cells are critically dependent on the dispersion state. While in well-dispersed AuNPs the properties of the individual particles are retained, aggregating nanoparticles will progressively approach the properties of micron-sized or even bulk material. For any kind of application, it is vital to control the interaction between the AuNPs and the biomolecules in their respective environment, which can cause aggregation and severe change in the surface properties of the nano-objects and, hence, affect their (hydrodynamic) particle size, surface charge, uptake mechanism, intracellular trajectory, and even the toxicity profile.

The most prominent protein which has been studied in its interaction with NPs of different sizes and composition is serum albumin, which is the most abundant globulin in serum. Due to its negative gross charge, it electrostatically binds to positively charged AuNPs, e.g., particles carrying a terminal amine group, and can overcompensate the particle charge turning it from positive to negative. This binding is associated with an increase of the hydrodynamic radius and enhances reabsorption of the AuNPs in tubules via the neonatal Fc receptor–albumin binding.

The nanoparticle protein-binding kinetics has been analyzed by means of several methods, which probe either fluorescence quenching or fluorescence enhancement of the AuNPs [30, 31]. It was shown that the fluorescence from tryptophan, tyrosine, and phenylalanine residues in proteins was quenched upon binding to the AuNP, which indicates a conformation change of the protein. This allowed analysis of the binding kinetics and the analysis of size effects. It turned out that ultrasmall AuNPs exhibit different binding affinities compared to larger ones. For sub-2 nm AuNPs even the strong self-fluorescence emission at 684 nm could be utilized to analyze the interaction with human serum albumin (HSA) protein, apo-transferrin, lysozyme, and apolipoprotein E4. A signal enhancement was observed upon protein adsorption with increasing concentration of the protein (cf. Fig. 7). Since these four proteins do not exhibit any fluorescence in this spectral range, it is assumed that binding of the proteins slows down the fluorescence decay rate and by this enhances the fluorescence signal intensity of the AuNPs by reducing the polarity of the local environment.

This is one example how the formation of a “protein corona” surrounding an AuNP can be analyzed, and it might be assumed that this process will occur either on the surface of the protecting ligand shell of the particles or directly on the particle surface, when weak-binding ligands, such as TPPMS, are replaced by

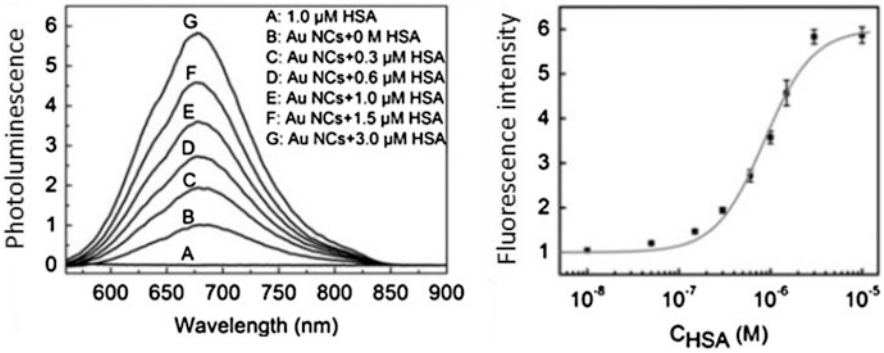

Fig. 7 *Left*: Photoluminescence spectra of HSA (curve *A*) and sub-2 nm AuNPs in the presence of different concentrations of HSA (curves *B–G*), taken with excitation at 550 nm. *Right*: Fluorescence intensity of these AuNPs, plotted as a function of the HSA concentration in the solution. The gray line fits to the data points using the adapted Hill equation. Figure adapted from [30]

stronger binding or multivalently coordinating molecules. Nevertheless, the mechanistic details of this interplay between AuNPs and proteins are still rather unexplored. A very recent review by Treuel and Nienhaus gives a comprehensive overview about the state of knowledge and the challenges in this particular field of nanoparticle research [32].

3.2 *Biofunctionalized Particles: Examples for In Vitro Applications*

A very robust form of functionalized AuNPs for application in vivo has been introduced by Mirkin and his group [33–48]. A very recent research perspective gives an excellent overview about the features and perspectives arising from this technology and shall briefly be summarized [49]. They introduced and intensively studied the assembly induced shift of the surface plasmon resonance (SPR) for the detection and sensing of nucleic acids. In this process AuNPs are functionalized with oligonucleotides via terminal thiol groups. These AuNPs, also described as spherical nucleic acids, possess designed recognition properties encoded by the nucleic acid sequence of the respective oligonucleotide ligands. Based on bases sequence complementarity of the oligonucleotides, either direct particle–particle hybridization or assembly via linker strands becomes possible. Hence, in a solution mixture of two kinds of AuNPs with noncomplementary base sequence, addition of a target DNA that is complementary to both sequences of surface-bound DNA (linker strand) will induce AuNP aggregation due to the binding to both kinds of AuNP via DNA hybridization (Fig. 8).

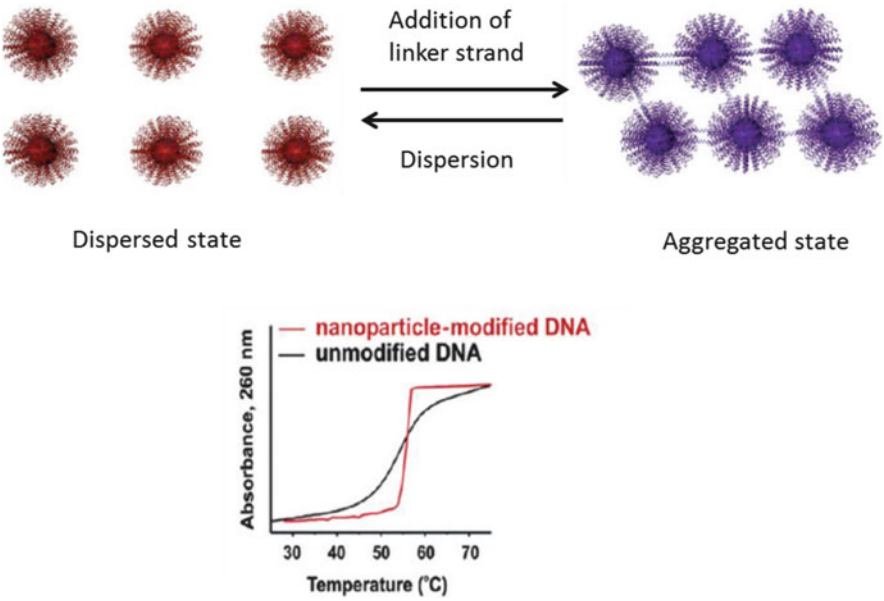

Fig. 8 *Top*: Schematic illustration of the aggregation and dispersion of DNA−AuNP conjugates. The corresponding SPR shift is indicated by the color of the AuNPs. The solution of dispersed particles appears red, whereas aggregated particles turn the samples purple. Aggregation can be induced via linker strands (as shown here) or by metal ions or any molecule that the oligonucleotide shell has been programmed to recognize and bind. *Bottom*: Compared to duplexes of free-strand DNA, which dissociates over a broad temperature range, the melting transitions of oligonucleotide functionalized AuNPs are sharp and occur over a very narrow temperature range due to the cooperative binding of the nucleic acids in the ligand shells. Figure adapted from [49]

Aggregation, i.e., polymeric macroscopic assembly of the AuNPs, can quite easily be followed by means of a SPR red shift, which causes a change of the solution color from red to blue. Since the aggregation results from DNA linkages, these DNA–NP conjugates can be disassembled through dehybridization of the duplexes via heating or by lowering the solution salt concentration. As it is well known from "free" DNA duplexes, melting dehybridization occurs when the temperature is raised above the melting point (T_m), whereas T_m is predictable by base sequence design. In contrast to "free" DNA duplexes, which exhibit melting transitions over a broad temperature range (~20°C), the melting transition in DNA–NP conjugates occurs over a very narrow temperature range (~2–8°C) and at a temperature higher than the T_m of the particle-free DNA duplex. This reflects cooperative binding in a highly predictable manner, where a single oligonucleotide base-pair mismatch can influence the melting behavior of the aggregate. It was immediately recognized that these striking features could be utilized for high-selectivity detection platforms, which include the quantitative measurement of enzymes, DNA-binding molecules, or bioactive metal ions [50–53].

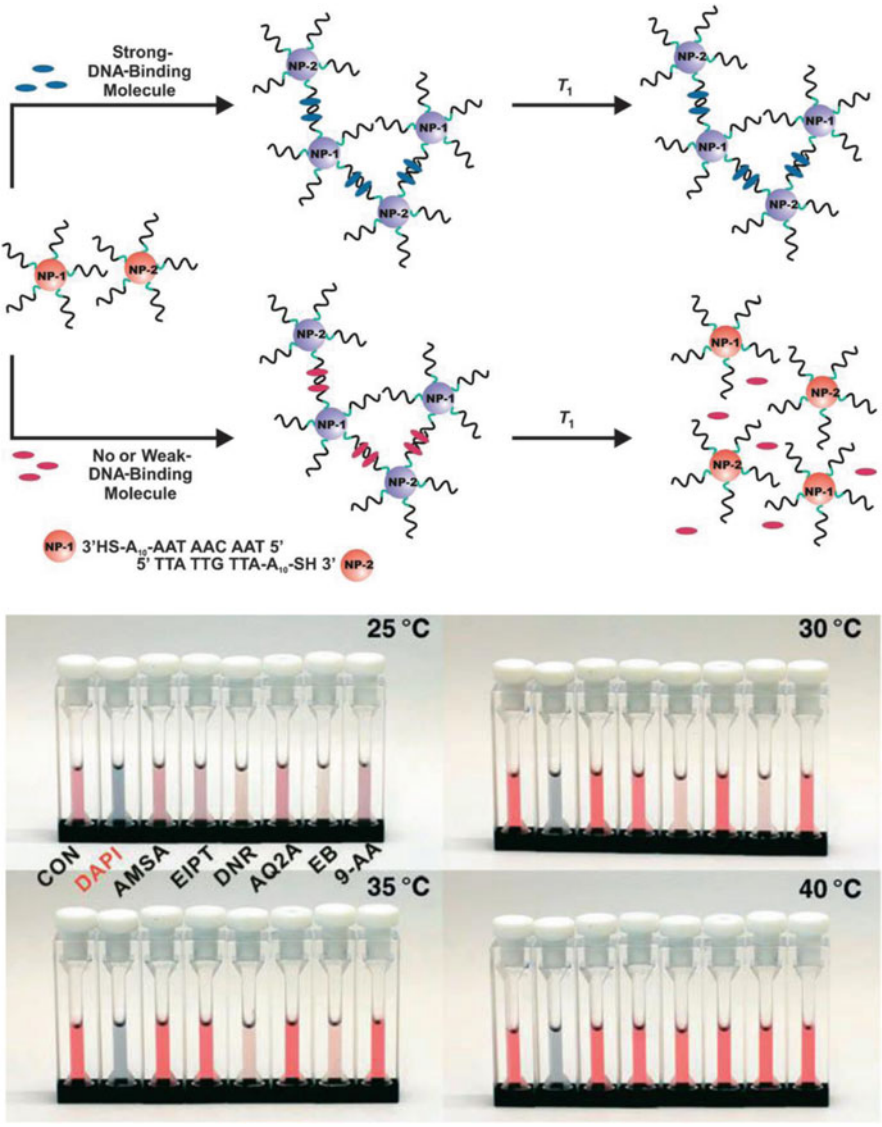

Fig. 9 *Top*: Schematic representation of the structural and color change of nanoparticle/DNA-binding molecule assemblies at a specific temperature (T1). *Bottom*: The color change of the nanoassembly (NP-1 and NP-2, each 1.5 nM) in the absence (CON) and presence of DNA-binding molecule (5 μM)-specific temperatures. Figure reprinted with kind permission from [52]

Figure 9 illustrates a colorimetric screening of DNA-binding molecules with AuNPs functionalized with oligonucleotides [52]. It was developed to determine the binding affinities between potential DNA-binding molecules and duplex DNA in AuNP–DNA networks. The colorimetric readout does not require additional instrumentation, since it relies of the color change via plasmon coupling upon

particle aggregation. When the networks are formed in the presence of duplex DNA-binding molecules, such as DAPI (4′,6-diamidino-2-phenylindole) or EB (ethidium bromide), the resulting duplexes connecting the AuNPs become more stable due to the DNA-binding interactions (p–p stacking, electrostatic, or hydrogen bonding). This increases the melting temperature so that the presence of different DNA-binding molecules can be read out from the temperature-dependent color change.

Based on this fundamental properties of DNA-functionalized AuNPs, Mirkin and others have developed more sophisticated techniques, including chip-based scanometric assays, which have been commercialized partially for highly sensitive molecular diagnostic technologies including clinical disease states, such as Alzheimer's disease or prostate cancer [49]. Furthermore, the unique set of properties is useful for intracellular applications. This includes the high affinity for complementary DNA and RNA [54], the pronounced stability against nuclease degradation [55], and no observed toxicity [56], which allows application as gene regulation agents [57].

Interestingly, despite their large negative charge due to the polyanionic DNA, the AuNP–DNA were found to easily enter cells. It was demonstrated recently that uptake of these particles in tumor cells (HeLa) is mediated by scavenger receptors. Blocking of these receptors with well-known ligands, polyinosinic acid (PolyI) and Fucoidan, has led to inhibition of particle uptake to a high degree, demonstrating competitive binding of AuNP–DNA and the inhibitors to the receptors. The extent of uptake increases with increasing number of DNA ligands per AuNP and is supported by positively charged scavenger proteins. The presence of serum proteins reduced particle uptake as the adsorption of these proteins on the AuNP–DNA is suspected to compete with receptor binding [58]. This suggests that the interactions between AuNP–DNA and scavenger receptors via the scavenger proteins are a charge-mediated process. These unique features hold great promise for applications in gene regulation therapies as well as in diagnostics, since it was shown that also other inorganic particles, in particular iron oxide particles [59] as well as the so-called "coreless spherical nucleic acids," i.e., cross-linked nucleic acids, which are oriented in the same way as in the case of AuNP–DNA but do not carry an inorganic core [57], exhibit the same uptake properties.

Recently, DNA-functionalized AuNPs have been used as a platform to study the interaction of even weaker-binding molecules in a similar colorimetric approach. Witten el al. introduced glyconanoparticles with thermally addressable DNA ligands, i.e., they bound glycomodified oligonucleotides to complementary functionalized DNA–AuNP to form glyco-DNA–gold nanoparticles (AuNP–DNA-glyco) [60]. These particles provide a multivalent presentation of DNA-glyco ligands that assemble as a result of the binding of carbohydrate-binding proteins, the so-called lectins, which carry a carbohydrate recognition domain (CRD). These carbohydrate–protein interactions play an important role in processes such as cell–cell or cell–matrix interactions and are exploited for the design of glyconanoparticles, e.g., for vaccine development or in vivo imaging [61]. In the example given, the coupling of AuNP–DNA with *N*-acetyl-d-glucosamine (GlcNAc)-modified

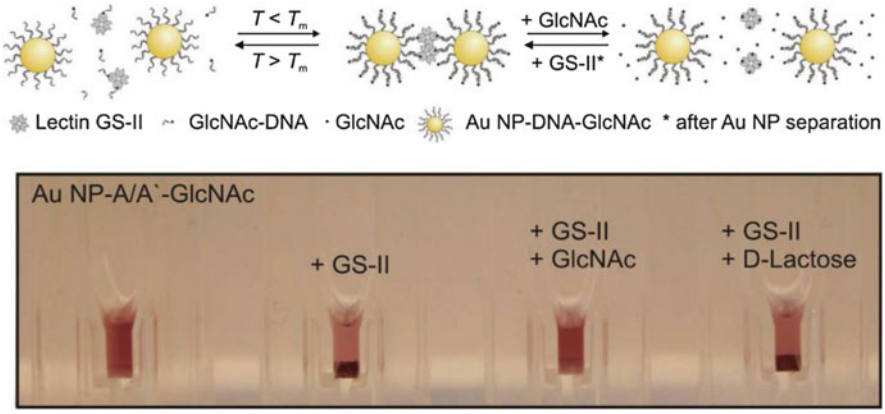

Fig. 10 *Top*: Schematic illustration of the reversible GS-II- and GlcNAc-DNA-mediated assembly of AuNP–DNA. Lectin–DNA–AuNP networks are dissociated by external stimuli: temperature-induced DNA melting or competition with free GlcNAc. After competition with free GlcNAc, the particles are separated by centrifugation enabling reassembly by the new addition of GS-II. Note that the scheme is not drawn to scale. ssDNA refers to single-stranded DNA. *Bottom*: GS-II-mediated assembly of AuNP–DNA-GlcNAc and subsequent competition with GlcNAc or D-lactose. Photographs of the samples: AuNP–DNA-GlcNAc, AuNP–DNA-GlcNAc 2 days after the addition of GS-II, AuNP–DNA-GlcNAc 2 days after addition of GS-II, and subsequent addition of GlcNAc or D-lactose (from left to right). Figure reprinted with kind permission from ref. [60]

single-stranded DNA (DNA-GlcNAc) to form DNA-GlcNAc-functionalized AuNPs (AuNP–DNA-GlcNAc) is demonstrated. The particles assemble in the presence of the tetrameric lectin GS-II with four CRDs with affinity for GlcNAc [62]. Assemblies built up by the GS-II AuNP–DNA-glyco interaction were shown to be equipped with two reversible binding modes that enable the reversible dissociation by two independent external stimuli: temperature-induced DNA duplex melting and displacement of the DNA-glyco ligands from the CRDs of the lectin by competition with free sugar [60] (Fig. 10).

3.3 Interaction with Cells

3.3.1 Cyto- and Genotoxicity

Numerous reports about toxicity and nontoxicity of metal nanoparticles can be found in literature [29, 63–80]. Most of the reports are dominated by results concerning AuNPs. Silver, known for its antibacterial function for more than 100 years, also plays an important role. However, gold absolutely dominates the scene. Silver (15–25 nm), gold (5–6 nm), and silver–gold alloy nanoparticles (10–12 nm), protected either by poly(vinylpyrrolidone) (PVP) or

tris(3-sulfonatophenyl)phosphine (TPPTS), have recently been tested toward human mesenchymal stem cells (hMSC). As expected, AgNPs showed a significant influence on the cell viability in contrast to the AuNPs with only a small effect. Surprisingly, the alloy particles, though containing silver, had no significant influence on the viability of the cells [81]. Most of the numerous reports on bioresponse of AuNPs are characterized by a disadvantage: the conditions of the various studies all differ so that comparisons are difficult to be drawn. First of all, the experiments differ not only by the particles' size and shape but, even more important, by their protecting ligand shell. As has already been discussed in Sect. 2, variations of the particles' skin may change toxicity into nontoxicity or vice versa. Another problem to compare literature data is the use of different cell lines, doses, time of observation, etc. If the metal-specific toxicity is of interest, contact between cell components and metal surface atoms is a condition, but not between ligand molecules and the corresponding biomolecules. Nontoxicity of cystein- and citrate-capped 4 nm AuNPs, glucose-covered 12 nm Au particles, or citrate-, biotin-, and cetylammonium bromide (CTAB)-modified 18 nm particles in human K562 Leukemia cells has been observed [82, 83], whereas toxicity of poly (ethyleneglycol) (PEG)-coated 13 nm AuNPs causes acute inflammation and apoptosis in the liver [27]. A review article with many details describes results of in vitro and in vivo toxicity studies up to 2010 [29].

As already mentioned in Sect. 2, reliable results regarding size dependency can only be gained if identically coated AuNPs are used and which, most importantly, quantitatively or at least partially lose their ligand shell in contact with cell species to allow direct contact between the gold surface and the relevant biomolecules. Phosphines, coordinated to the surface of AuNPs, fulfill this condition.

$Au_{55}(PPh_2C_6H_4SO_3Na)_{12}Cl_6$ has exclusively been applied to study toxicity in a series of human cancer cell lines. Preceding experiments with this cluster compound and B-DNA showed that phosphine molecules are substituted by DNA sections comprising the major grooves. The reason for this result is to be seen in the size conditions: the diameter of the Au_{55} nucleus is 1.4 nm and the height of the major grooves is 1.3–1.5 nm. As molecular calculations of that system showed, there are strong chemical interactions between the Au_{55} core and the DNA, supported by the polydentate character of the major grooves [84]. At least so many ligands are removed from the original cluster that Au_{55} fits into the groove to allow interactions with relevant DNA components. The coverage of B-DNA with Au_{55} clusters has already been supposed by a preliminary experiment, namely when B-DNA in aqueous solution was contacted with the coated clusters and investigated by atomic force microscopy (AFM) [85]. Cross sections show the correct difference in height between unloaded and cluster-containing DNA sections. The observed 1.8 nm sections correspond with the sum of the DNA plus about half of the cluster, possibly still having some ligand molecules outside. Figure 11 shows the AFM image and the cross section indicating the difference between DNA with and without Au_{55} clusters. Figure 12 shows the result of the molecular modeling calculations.

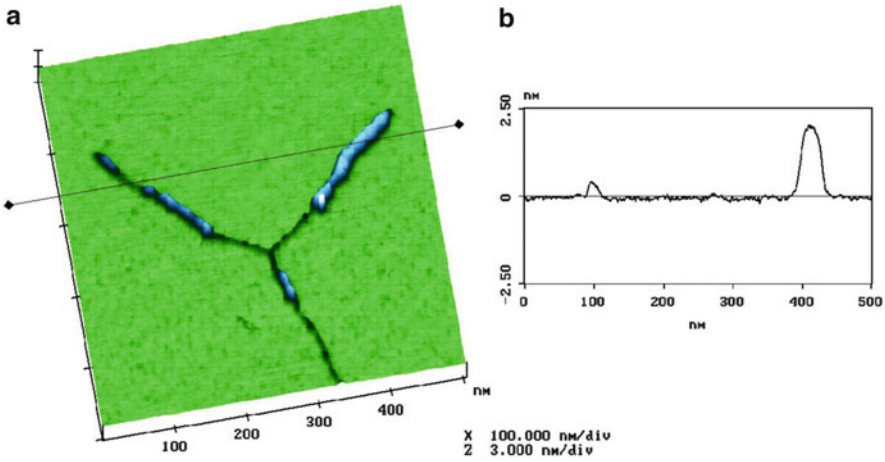

Fig. 11 (**a**) AFM image of DNA sections partially linked with Au_{55} clusters. (**b**) Height profile of unloaded and loaded parts, respectively. Figure reprinted with kind permission from [84]

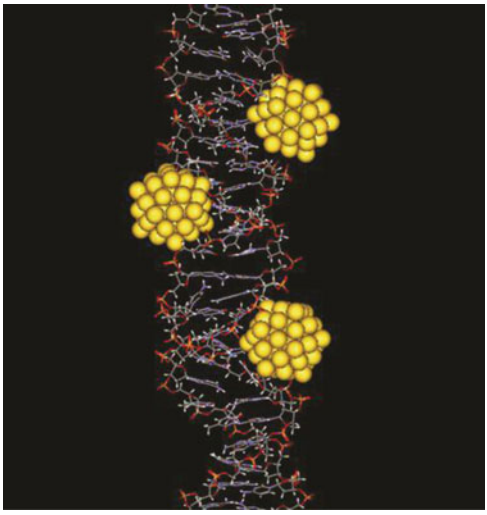

Fig. 12 Energy-minimized structure of B-DNA with Au_{55} clusters along the phosphate backbone of the major grooves. Figure reprinted with kind permission from [84]

The Au_{55} clusters are bound in a stable manner to the major grove of B-DNA as various investigations showed [85].These results clearly indicate that the original phosphine ligands can be removed by biological materials without any problem. An important consequence of this finding is that a DNA, damaged in this manner, can no longer be active in a cell, synonymous with cell death. In other words, 1.4 nm Au_{55} clusters must finally be toxic.

In a series of experiments the toxicity of Au_{55} has been investigated using 11 different types of human cancer cells in comparison with cisplatin, a commonly

Table 1 IC_{50} values of 11 human cancer cell lines treated with cisplatin (72 h) and Au_{55} (24 h). Table reprinted with kind permission from ref. [85]

Cell line		IC_{50} cisplatin 72 h (μM)	IC_{50} Au_{55} 24 h (μM)
MC3T3-E1	Normal bone cells	26.1 ± 1.27	1.65 ± 0.14
U2OS	Osteosarcoma	11.17 ± 2.02	0.64 ± 0.04
SK-ES-1	Osteosarcoma	0.79 ± 0.17	1.03 ± 0.18
MOR/P	Lung cancer cells	3.30 ± 0.3	2.10 ± 0.10
MOR/CPR	Lung cancer cells	7.10 ± 1.2	2.50 ± 0.10
CCD-919Sk	Fibroblast cells	0.45 ± 0.10	0.62 ± 0.07
BLM	Metastatic melanoma	54.70 ± 7.60	0.30 ± 0.10
MV3	Metastatic melanoma	>50	0.24 ± 0.02
SK-Mel-28	Melanoma	15.60 ± 2.26	1.12 ± 0.16
HeLa	Cervical cancer cells	7.93 ± 0.95	2.29 ± 0.10
Hek-12	Kidney cancer cells transfected with adenovirus	20.13 ± 6.0	0.63 ± 0.02

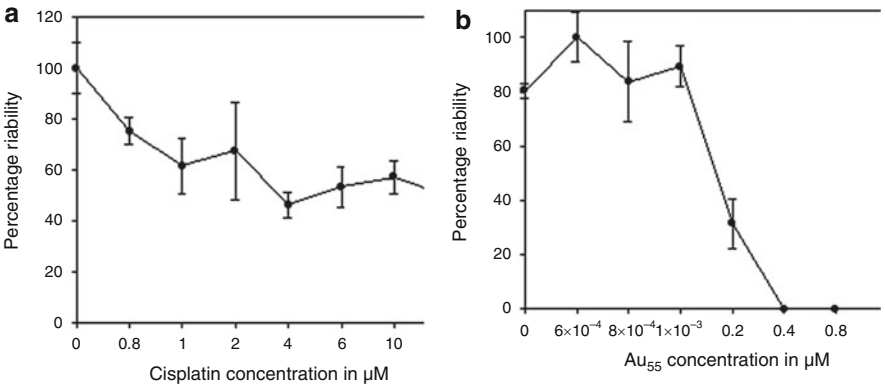

Fig. 13 Comparison of the viability of BLM cells treating them with cisplatin (**a**) and $Au_{55}(PPh_2C_6H_4SO_3Na)_{12}Cl_6$ (**b**). Figure reprinted with kind permission from [85]

used anticancer drug. Table 1 informs on the IC_{50} values of cisplatin and Au_{55}, i.e., the amount of material necessary to kill 50% of the cells. In each case, Au_{55} was more effective, especially considering the difference in time to reach IC_{50}, namely 24 h for Au_{55} and 72 h for cisplatin.

The difference between cisplatin and Au_{55} becomes also visible from Fig. 13a, b. BLM cells were treated with cisplatin and $Au_{55}(PPh_2C_6H_4SO_3Na)_{12}Cl_6$. Whereas the IC_{50} value for cisplatin is only reached with 50 μM, theAu_{55} cluster leads to the viability 0 with 0.4 μM [85].

In addition to the interaction with DNA, Au_{55} causes another reason for a fast cell death: oxidative stress. Necrosis and mitochondrial damage have been observed by incubation of HeLa cells, registered by flow cytometry [22, 86]. It is

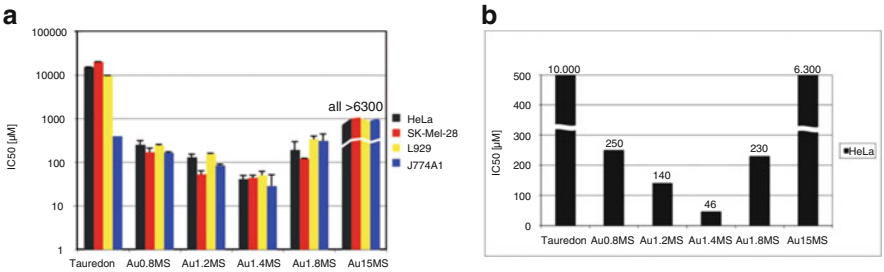

Fig. 14 (**a**) IC_{50} values (logarithmic scale) of four different types of cell lines in dependence of particle size. (**b**) Results for HeLa cells only in a linear scale (MS = monosulfonated triphenylphosphine, $PPh_2C_6H_4SO_3Na$). Figures reprinted with kind permission from [86]

known that larger AuNPs also cause oxidative stress. However, Au_{55} is, due to its structure and its special electronic properties, a much better source for oxidative stress. Its catalytic properties, based on the ability to excite O_2, but not to be oxidized itself (see Sect. 2, p. 9), contribute decisively to its toxicity. If the phosphine ligands are substituted by GSH, the toxicity is significantly reduced [22].

The question, if there is a size-dependent cytotoxicity of AuNPs, is still not answered by the experiments discussed above. A series of experiments with smaller and larger AuNPs, all equipped with $PPh_2C_6H_4SO_3Na$ molecules in the coating shell, give a clear answer. The cell lines HeLa, SK-Mel-28, L929, and J774A1 have been incubated with 0.8 (Au_9), 1.2, 1.4 (Au_{55}), 1.8, and 15 nm Au species [86]. Tauredon, a commercially available Au thiomalate complex, has been applied additionally. The result can be seen from Fig. 14.

As can be followed from Fig. 14a, b, the micromolar amounts for reaching the IC_{50} values for all four cell lines are a minimum for the 1.4 nm Au_{55} cluster. There is a lower toxicity for slightly smaller or larger particles, but without any doubt, Au_{55} is the most toxic one, as can better be seen from the linearly scaled Fig. 14b. The question, if such smaller or larger particles cause less toxicity for not ideally fitting into the major grooves or if reduced oxidative stress is responsible, cannot be answered yet. Some additional experiments concerning reactive oxygen species (ROS) shall be mentioned [22]. Oxidative stress in HeLa cells can be observed by using flow cytometry. However, 100 µM amounts of Au_{55} clusters cause heavy oxidative stress, increasing with increasing time (12–48 h). On the contrary, even 1,000 µM of 15 nm AuNPs do not cause any oxidative stress. As could be expected, 1.1 nm Au particles, coated with GSH, are also not able to generate oxidative stress, due to the much stronger bound thiol ligands that prevent formation of bare surfaces.

As already discussed, GSH-treated 1.4 nm Au_{55} clusters restored cell survival in contrast to the original phosphine-coated particles due to the existence of very strong Au–S bonds. Other sulfur-containing molecules such as *N*-acetylcysteine (NAC) on the cluster surface also reduce cytotoxicity. If the dissociation of TPPMS from the surface is hindered by excessive phosphine, cytotoxicity is also drastically

reduced, since the equilibrium of dissociation is shifted. However, GSH, NAC, and phosphines can also be considered as antioxidants. In order to exclude reducing properties of these compounds as reason for the restricted cytotoxicity, ascorbic acid as a strong reducer was tested. As could be expected, the cytotoxicity of $Au_{55}(Ph_2PC_6H_4SO_3Na)_{12}Cl_6$ was unchanged compared with experiments without ascorbic acid [22].These experiments clearly indicate the repeatedly mentioned condition that bare Au_{55} surfaces are necessary for the interaction with vital biological targets to observe cytotoxicity.

This finding is further corroborated by studies on the interaction of 1.4 nm Au clusters with ion channels [87]. The human ether-à-go-go-related potassium channel (hERG) is intensely studied and is known to interact with multiple molecular ligands. By patch clamp technique in hERG channel-transfected HEK293 cells, it was shown that 1.4 nm phosphine-stabilized AuNP irreversibly blocked hERG channels, whereas thiol-stabilized AuNP of similar size had no effect.

4 Properties In Vivo

4.1 Biodistribution

The toxicity phenomena discussed before have all been observed in cell cultures, i.e., in vitro. However, from experience we know that toxicity problems in a living being can be characteristically different depending on the kind of administration and distribution in the body. Radiolabeling by ^{198}Au isotopes allows very precise determination of the distribution in the different organs, though very low concentrations have to be used in order to avoid toxicity effects. In a series of experiments with 1.4, 5, 18, 80, and 200 nm AuNPs, all protected with the proven phosphine ligand $Ph_2PC_6H_4SO_3Na$, the influence of size on the biodistribution in healthy female Wistar–Kyoto rats in the course of 24 h has been studied [88–90]. γ-Spectroscopy has been applied to determine the gold content in the various organs. The administration was performed by intravenous injection (i.v., tail vein). As can be followed from Fig. 15, the 5, 18, 80, and 200 nm AuNPs are accumulated with 92–97% in the liver, in contrast to the 1.4 nm species which accumulates only with ca. 50% in this organ.

A detailed comparison of the biodistribution of 1.4 and 18 nm AuNPs is given in Fig. 16. A more or less quantitative accumulation of the 18 nm species in the liver can be registered, whereas 50% of the 1.4 nm clusters are distributed over the lung, spleen, kidney, blood, and urine [89, 90].

Considering the findings that traces of the 1.4 nm Au_{55} cluster could be found in the heart, brain, and uterus (not shown in Fig. 16), it clearly turns out that biodistribution of this species dominates, compared with larger AuNPs. Regarding its cell toxicity, Au_{55} particles must be considered as very dangerous if present in the blood stream.

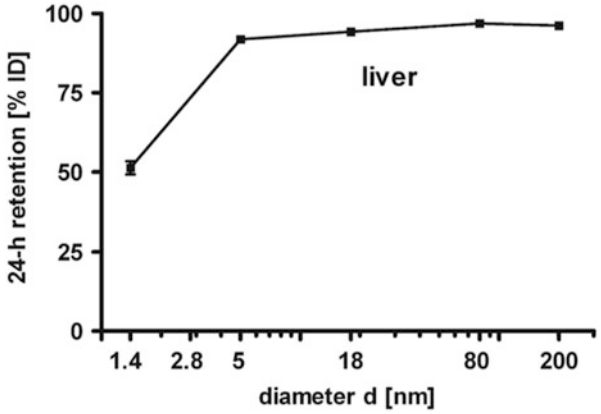

Fig. 15 Accumulation of 1.4, 5, 18, 80, and 200 nm AuNPs, all protected by $Ph_2PC_6H_4SO_3Na$, in the liver of rats after 24 h (i.v. injection). Figure reprinted with kind permission from [88]

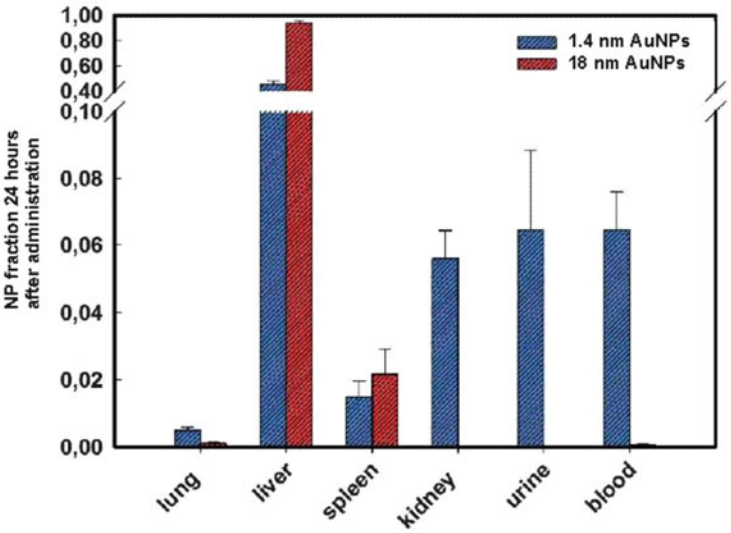

Fig. 16 Biodistribution of phosphine-coated 18 and 1.4 nm AuNPs after i.v. injection and 24 h retention. Figure adapted from [89]

There is still another question to be answered: which influence has the surface charge on biodistribution, if at all? Assuming a quantitative dissociation of the Na^+ ions, $Au_{55}(Ph_2PC_6H_{12}SO_3Na)_{12}Cl_6$ would be a 12-fold negatively charged particle; however, as we know, in a biological environment, substitution of the phosphines happens quickly. To study the influence of surface charge, strongly coordinated ligands have to be used, best guaranteed by Au–S bonds. Thioglycolic acid (TGA) is an ideal ligand system to investigate the influence of charge, because the carboxylic functions (COO^-) can be reacted with cysteamine (CA) in order to

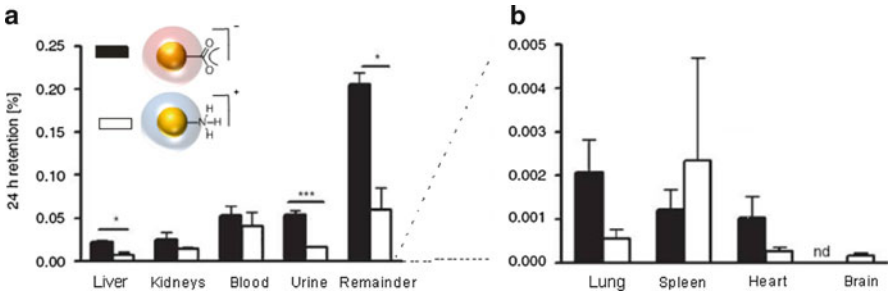

Fig. 17 Biodistribution of negatively and positively charged 2.8 nm AuNPs after intra-oesophageal application. Figure adapted from [91]

generate positive charges (NH_3^+). AuNPs (2.8 nm) coated with TGA and its positively charged derivative were used to find an answer [88]. As can already be followed from Fig. 15, phosphine-protected 2.8 nm particles accumulate less much in the liver compared with the larger particles by about 20%. The TGA-coated 2.8 nm particles accumulate with 81.6% in the liver, in good agreement with the also negatively charged phosphine-protected species. The positively charged CA-protected 2.8 nm particles assembled only with 72% in the liver with a higher concentration in other organs, for instance 11% in the spleen. As a conclusion it can be stated that biodistribution of positively charged AuNPs is slightly increased compared to negatively charged species.

An investigation, studying the absorption across intestinal barriers by intra-oesophageal instillation of phosphine-stabilized 1.4, 5, 18, 80, and 200 nm AuNPs as well as of TGA- and CA-covered 2.8 nm particles into healthy female rats showed again that biodistribution of the 1.4 nm clusters in secondary organs is maximum [91]. In contrast to the above-discussed situation, biodistribution of negatively charged TGA-coated 2.8 nm species was more expressed than that of the positively charged CA-protected particles of same size. Fig. 17 shows details.

4.2 Zebrafish: A New In Vivo Model

Due to the exponential growth of new nanomaterials and to the lack of screening assays and putative standards, there is a shortfall of correlative and predictive models to assess acute and chronic toxicities. This limits rapid preclinical development of new therapeutics and, therefore, it is of critical need to develop in vivo models which ideally maintain the biological representativeness. Small mammalian models are the most common method used to assess possible toxicities and biodistribution of nanomaterials in humans. Alternatively, *Danio rerio*, commonly known as zebrafish, has attracted much interest because of its unique features, manipulation accessibility, and short reproduction time [92–94]. Many fundamental

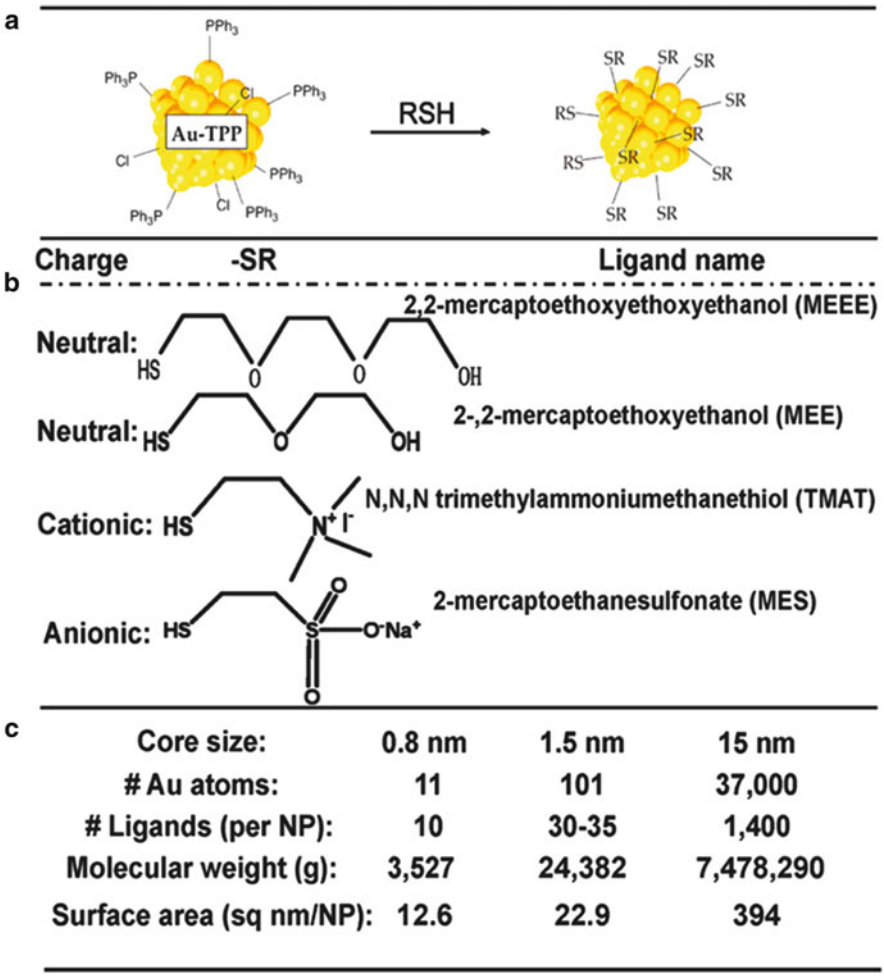

Fig. 18 (continued)

cellular and molecular pathways involved in the response to toxicants or stress are highly conserved between the zebrafish and mammals [95, 96].

Harper et al. tested AuNPs to determine the effect of core size, surface functionalization and charge on uptake rates, and the biological consequences of exposure [97]. AuNPs with core sizes of 0.8, 1.5, and 15 nm and positive, negative, and neutral surface charges were used (see Fig. 18). Chorions of fish embryos were chemically removed prior to the exposure of nanomaterials since the chorions may act as a physical barrier for AuNPs.

The 5-day exposure assay resulted in a clear surface charge-dependent toxicity. AuNPs with no charge do not adversely impact biological systems across a broad

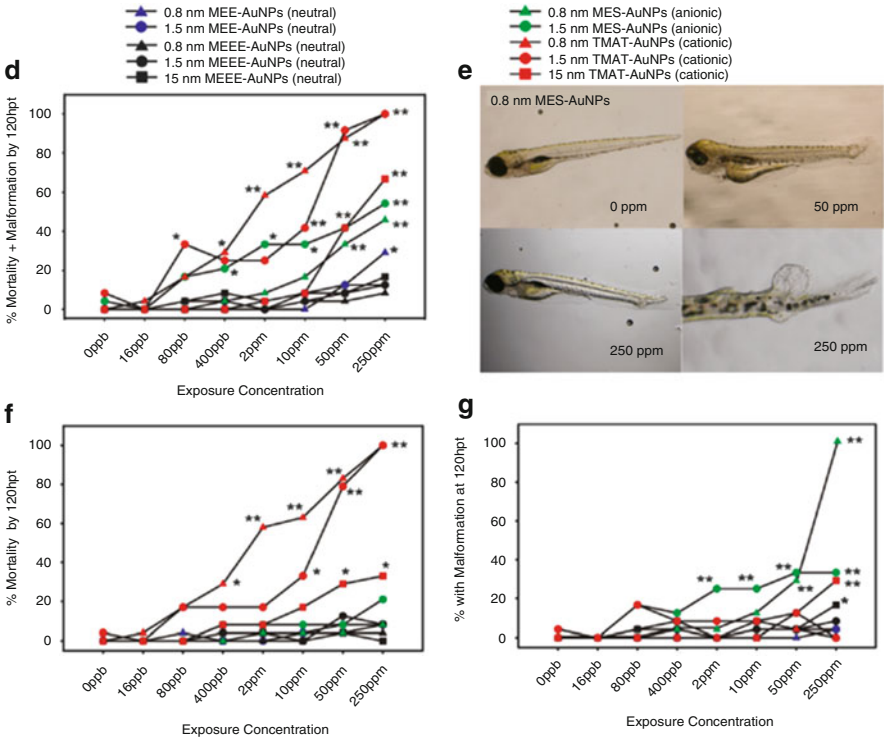

Fig. 18 AuNPs synthesis, structure, and properties. (**a**) Schematic scheme of the ligand exchange reaction starting from triphenylphosphine-stabilized AuNPs and leading to thiol-stabilized ones. (**b**) Charge, structure, and name for each ligand tested. (**c**) Chemical composition of the different AuNPs. Dose response results of embryonic zebrafish screen for tested AuNPs. (**d**) Percentage of zebrafish exhibiting either mortality or any malformation for each size and ligand tested across a spectrum of concentrations compared to control. (**e**) Examples of malformations seen upon exposure to 0.8 nm MES–AuNPs scored in the malformation category compared to control embryo. (**f**) Percentage of zebrafish dying after exposure to the AuNPs. (**g**) Percentage of zebrafish that survived but showing some malformation or abnormal behavior. Figure reprinted with kind permission from [97]

range of sizes. While positively charged TMAT–AuNPs primarily caused mortality, the negatively charged MES–AuNPs induced malformations (see Fig. 18). The uptake of the AuNPs was further investigated by instrumental neutron activation analysis (INAA), and it was shown that TMAT–AuNPs were not eliminated as rapidly as the other ones [97].

Pan et al. treated zebrafish embryos with TPPMS-capped 1.4 nm AuNPs (Au1.4MS), which were previously analyzed in HeLa cells [98]. In the cell test was shown that Au1.4MS was toxic while smaller and larger TPPMS-stabilized AuNPs were much less toxic [22, 86]. By the addition of GSH to Au1.4MS particles, the toxicity was inhibited due to replacement of the weak-binding TPPMS by the GSH hence resultant in a stronger gold thiolate bond [22].

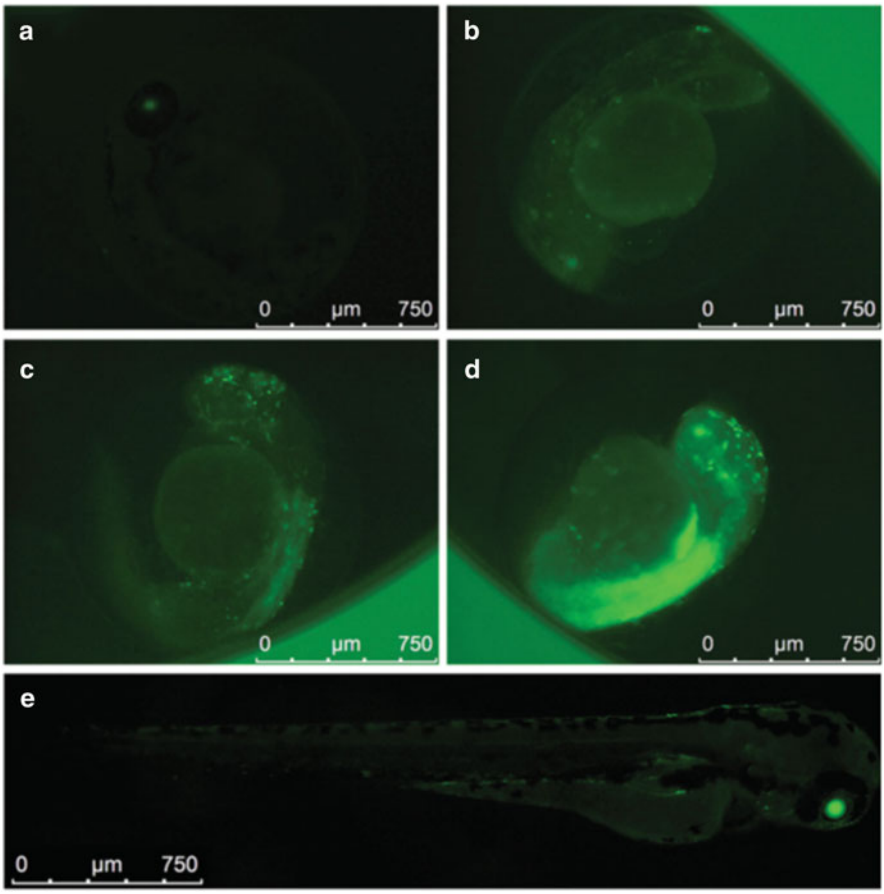

Fig. 19 Rapid induction of green fluorescent protein (GFP) expression in transgenic zebrafish triggered by toxic doses of Au1.4MS. Transgenic zebrafish embryos expressing GFP under the control of the heat shock protein were exposed to (**a**, **e**) embryo medium, (**b**, **d**) 200 µM Au1.4MS, and (**c**) 400 µM Au1.4MS. Spotty GFP signal was seen at 48 hpf in the presence of 200 µM Au1.4MS (**b**). The GFP signal increased with the toxic dose (**c**) and with time (**d**). In addition to the spotty GFP signal observed in the head region, strong GFP expression was present along the trunk at 48 hpf and was further enhanced at 72 hpf (**d**). Figure reprinted with kind permission from [98]

They showed that the toxicity in zebrafish model like in the cell culture depends on the size and ligand chemistry. At similar size AuNPs carrying ligands with high affinity to the gold atomic core were less toxic than AuNPs with more labile ligands. Along with the cytotoxicity of Au1.4MS-treated HeLa cells, the robust heat shock protein (HSP) stress response was observed. Therefore Pan et al. deemed transgenic heat shock reporter zebrafish ideal to test toxicity, teratogenicity, and upregulation of defense pathways. These transgenic zebrafish had similar responses to Au1.4MS-like wild-type zebrafish in terms of teratogenicity but were 20-fold more sensitive than wild type in reporting hepatotoxicity of Au1.4MS (Fig. 19).

Razansky et al. used PAI to image in vivo the expression of the fluorescence protein mCherry in the head of an adult transgenic zebrafish with a cross-sectional diameter of ~6 mm. The imaging results demonstrate the ability of the process to reveal many morphological features which matches well with the corresponding histology. Moreover, multispectral reconstructions accurately resolved fluorescence protein expression in the hindbrain of an intact living animal in high consistence with the corresponding epifluorescence image of the dissected brain [99].

5 Perspectives and Challenges

5.1 Cell Targeting

The examples given above illustrate some of the versatile applications of AuNPs in biological environments, addressing different fields in therapy and diagnosis and several recent reviews reflect that this is a rapidly evolving interdisciplinary research area [100]. However, any type of in vivo application should ideally follow the concepts of targeted delivery, which combines minimization of systemic exposure and, hence, decreased side effect with enhanced local concentration of the therapeutic or diagnostic agent for maximum efficacy. Cell targeting can be achieved along two conceptually different ways, i.e., passive and active targeting, respectively. While passive targeting utilizes, e.g., the enhanced permeability and retention (EPR) effect [101], by which small nanoparticles can accumulate in tumor tissue due to the disordered vasculature in tumors, active targeting relies on recognition molecules or molecular subunits, which can selectively bind to certain tumor cells and thus enhance the accumulation of the "targeting" compound at tumor sites. Although the passive targeting can lead to high uptake rates into the tumor tissue, the penetration into tumor interstitium is rather limited and varies the size or density of tumor tissue and is thus difficult to control. This may be enhanced by active targeting, as it was introduced for several types of "recognition molecules" bound to the surface of AuNPs, including small peptides [102, 103] and antibodies [104, 105]. One of the first promising examples was given in a study on targeted photothermal ablation of murine melanomas with targeted hollow gold nanospheres (HAuNs) of approx. 40 nm in diameter. It was found that the AuNPs were specifically taken up by melanoma cells associated with enhanced extravasation and dispersion into tumor matrix of targeted HAuNs compared to untargeted ones of the same size [105] (Fig. 20).

This control over biodistribution and localization of AuNPs gives rise to applications in nanomedicine, where AuNPs are utilized as efficient contrast agents for different imaging techniques, i.e., X-ray computed tomography (CT) and photoacoustic imaging (PAI). Furthermore therapeutic applications can be envisaged in the same manner, if an external stimulus such as light or X-ray

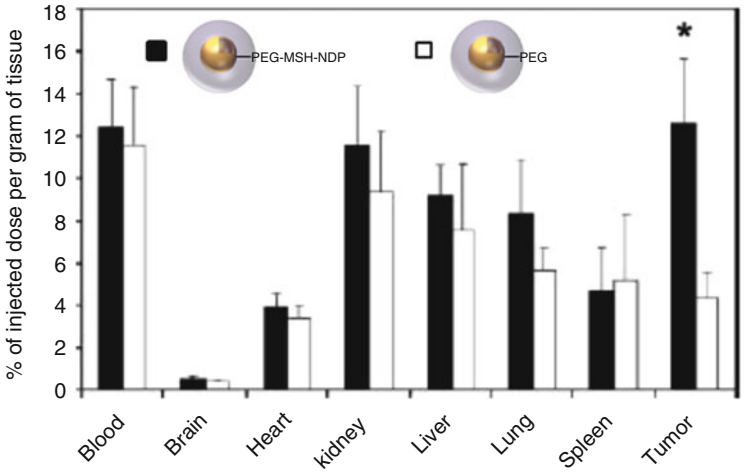

Fig. 20 Biodistribution of HAuNs targeted with NDP-MSH-PEG–HAuNs and untargeted, i.e., functionalized with PEG. Data are plotted as % of injected dose per gram of tissue. Mean FSD ($n = 5$). *, $P < 0.01$. Figure adapted from [105]

irradiation selectively addresses the AuNPs based on their size-dependent physical properties, such as SPR or X-ray radiosensitization. The potential applications that arise from these opportunities will be discussed in the following sections by means of selected examples.

5.2 *AuNPs as Contrast Agents in Molecular Imaging and as Therapeutic Agents*

Molecular imaging is an emerging field integrating molecular biology, chemistry, and radiology in order to gain understanding about biological processes and to identify diseases based on molecular markers, which appear earlier than the clinical symptoms [106]. The application of AuNPs in this area is increasing rapidly and offers excellent prospects for the development of new strategies for the diagnosis and treatment of cancer [107]. The reasons for this increasing attention to gold nanoconstructs are many: their size-dependent and shape-dependent plasmonic properties enable them to absorb and scatter light in the visible to NIR region, which may render them suitable for image-guided therapy and photothermal therapy (PTT). Significant synthetic advances now allow the design of AuNPs with highly controlled geometry, surface charge, physicochemical properties, and the decoration of their surfaces with polymers and bioactive molecules in order to improve biocompatibility and to achieve active targeting. This is stimulating the development of a diverse range of nanometer-sized objects that can recognize cancer tissue [107]. The use of the unique optical properties of AuNPs presents a

new opportunity for noninvasive imaging and therapy for a variety of diseases without exposing the rest of the body. Here, we introduce some imaging applications including X-ray computed tomography (CT) and photoacoustic imaging (PAI) and the opportunities of PTT as well as radiotherapy based on AuNP systems.

5.2.1 AuNPs for CT Imaging

X-ray computed tomography (CT) is clinically important because of its affordable price, high spatial resolution, unrestricted depth, and accurate anatomical information with reconstructed three-dimensional imaging [108]. The limitations of commercial iodine-based CT contrast agents such as rapid renal clearance, poor sensitivity, and toxicity have to be overcome, and AuNPs are interesting tools for that [109]. Their ability to absorb large amounts of X-ray radiation can be used to increase imaging contrast in diagnostic CT scans at lower radiation doses, which is based on the atomic weight of Au relative to atoms present in biological tissue. AuNPs have shown in vivo functionality as CT contrast agents for blood pool [110–116] and cancer imaging [117–124].

For passive targeting AuNPs are modified with PEG and its derivatives to enhance the circulation period in the blood. Kim et al. reinforced that by showing a 5.7 times higher attenuation of PEGylated AuNPs (~30 nm) than that of the current iodine-based CT contrast agent Ultravist [124]. Wang and his coworkers found that dendrimer-entrapped AuNPs can be detected through the attenuation of X-rays [117]. After either an intratumoral or an intraperitoneal administration of these particles, a xenograft tumor model could be imaged via CT.

The conjugation of antibodies or peptides onto the NP surface allows for active targeting. AuNPs with active tumor-targeting anti-HER2 antibodies enhance the visibility of millimeter-sized human breast tumors in mice in a 1.6-fold more efficient way than passive targeting AuNPs [123]. Chanda et al. reported enhanced CT attenuation of bombesin-functionalized AuNPs that selectively targeted cancer receptor sites that are overexpressed in the prostate, breast, and small-cell lung carcinoma [119]. Reuveni et al. demonstrated the in vivo feasibility of cancer diagnosis based on AuNPs as molecular markers using CT [118]. AuNPs with a diameter of 30 nm were functionalized with anti-epidermal growth factor receptor molecules and intravenously injected into nude mice implanted with human squamous cell carcinoma head and neck cancer. It is demonstrated that a small tumor, which is currently undetectable through anatomical CT, is enhanced and becomes clearly visible by the molecularly targeted AuNPs. As can be seen in Fig. 21, it is further shown that active tumor targeting is more efficient and specific than passive targeting with anti-rabbit IgG antibody-coated AuNPs with the same size.

Besides the imaging of cancer, Ghann et al. described a preparation of AuNPs with a core size of 10.7 nm that are stabilized with lisinopril via amine, disulfide, and thiol attachments to the AuNP surface to image the blood pool [115]. A stability study showed that the thiol lisinopril-coated AuNPs were the most stable ones and

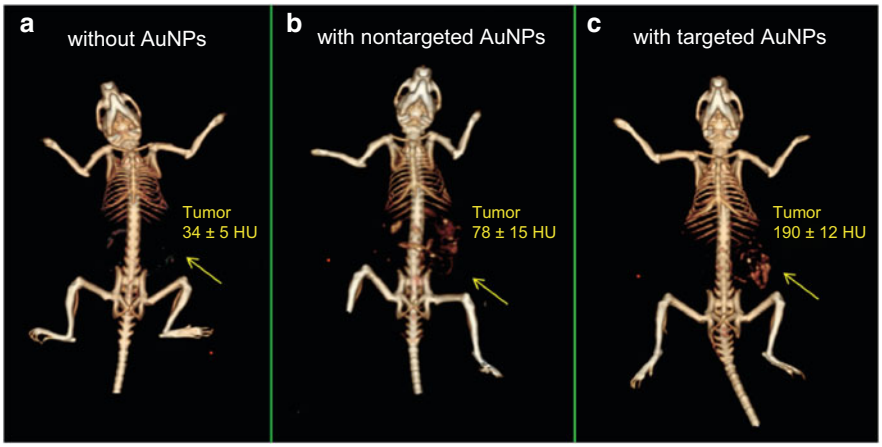

Fig. 21 In vivo X-ray CT volume-rendered images of mouse (**a**) before injection of AuNPs, (**b**) 6 h postinjection of nonspecific anti-rabbit IgG-coated AuNPs as a passive targeting experiment, and (**c**) 6 h postinjection of anti-epidermal growth factor receptor (EGFR)-coated AuNPs that specifically targeted the squamous cell carcinoma head and neck tumor. The anti-EGFR-targeted AuNPs show a clear contrast enhancement of the tumor (**c**, *yellow arrow*), which was undetectable without the AuNPs as contrast agents (**a**, *yellow arrow*). Figure adapted from [118]

therefore chosen for further studies to assess the targeting of angiotensin-converting enzyme (ACE) via X-ray CT. The resulting images displayed a high contrast in the region of the lungs and heart which indicates the targeting of ACE (see Fig. 22). The overexpression of ACE is associated with the development of cardiac and pulmonary fibrosis, and because of this the AuNPs could be a useful tool for the visualizing of cardiovascular pathophysiologies using CT imaging.

Cai and his coworkers injected PEG–GNPs with a size of 38 nm into adult mice via subcutaneous application [113]. Compared to the CT image contrast before PEG–GNP injection, the CT can produce clear images of the vascularity even 24 h after injection, indicating that the PEG–AuNPs have great potential as a blood-pool agent for CT imaging. In another study dendrimer-entrapped AuNPs with sizes in a range of 2–4 nm were injected subcutaneously into mice [110]. The vascular system could be imaged 5 and 20 min after injection and the urinary system could be imaged after 60 min. The feasibility for blood-pool CT imaging of PEGylated dendrimer-entrapped AuNPs after intravenous injection in rats and mice was explored as well resulting in an efficient blood-pool CT imaging of both rats and mice [116].

5.2.2 AuNPs for PAI Imaging

Photoacoustic imaging (PAI) is a technique which combines the advantages of optical and ultrasound imaging methods to visualize cancer tumor spreading and growth in vivo [125, 126] resulting in the ability to detect metal NPs with

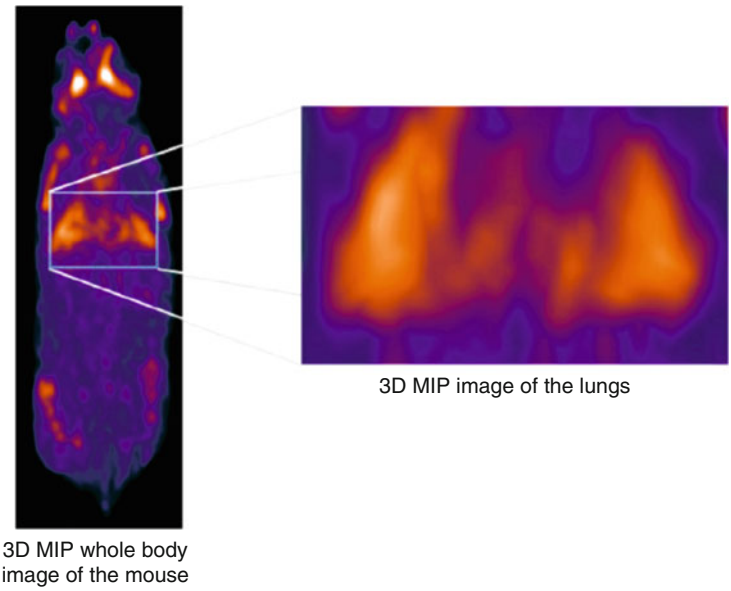

Fig. 22 3D subtraction CT image (measured at 80 and 140 kVp) of mice treated with thiol lisinopril-coated AuNPs resulting in a specific targeting of the lungs and heart (enlargement of the lungs and heart area on the right side). Figure reprinted with kind permission from [115]

nonionizing radiation relative deep in the tissue without the loss of high spatial resolution [126–128]. A temperature increase is induced by short pulses of electromagnetic irradiation in the range of strong absorbance. This causes a local increase in pressure via thermoelastic expansion leading to a generation of acoustic waves which can be detected with an ultrasound transducer [125–129].

AuNPs have gained immense interest for PAI since they combine size-dependent optical properties with a versatile surface chemistry [130–132]. As compared to the established group of organic dyes with its standard PAI contrast agent methylene blue (MB), recent research has demonstrated the superiority of AuNPs as they show high absorption cross sections combined with a resistance toward photobleaching. By controlling the particle size and geometry, the extinction characteristics of AuNPs can be tuned. Numerous groups have found that nanospheres [133–135], nanorods [136–143], nanoshells [132], hollow nanospheres [127], and nanocages [144–146] are eminently suitable.

The first studies with gold nanomaterials were done by Sokolov et al. who showed that 12 nm AuNPs conjugated with anti-epidermal growth factor receptor (anti-EGFR) antibodies specifically bound to EGFR proteins that are overexpressed on the surfaces of cervical cancer cells [147]. The receptor-mediated aggregation of AuNPs causes plasmon coupling of the clustered NPs, leading to an optical redshift of the plasmon resonances. Based on these results, the group of Emelianov demonstrated in ex vivo mouse tissue that multiwavelength photoacoustic imaging can detect cancer with high selectivity and sensitivity based on the plasmon

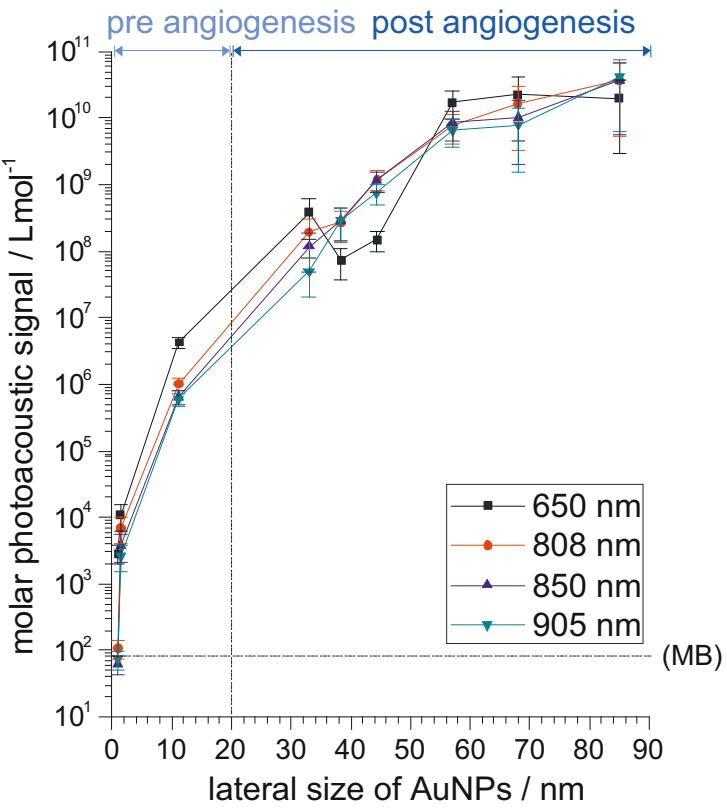

Fig. 23 Molar PA signal intensities as a function of the lateral particle size for the four laser excitation wavelengths. Error bars indicate the standard deviations evaluated with error propagation calculations resulting from statistical analysis of STEM micrographs. Lines are drawn to guide the eyes. Figure adapted from [150]

resonance coupling effect of the EGFR-targeted AuNPs [148, 149]. In addition to that plasmon resonance coupling AuNPs have been suggested for imaging of macrophages in atherosclerotic plaques for an early detection of cancer [133].

In a recent study, Gutrath et al. showed that the molar extinction of spherical AuNPs with core diameters of 1.0, 1.4, and 11.2 nm, gold nanorods (AuNRs) with longitudinal/transversal elongation of 38/9 and 44/12 nm, and HAuNs' with outer/inner diameters of 33/19, 57/30, 68/45, and 85/56 nm can be correlated with the molar PA signal intensity of the respective AuNPs [150]. For increasing lateral particle size, increasing molar photoacoustic signal intensity is observed, which is shown in Fig. 23. The studied AuNPs exhibit significantly larger molar PA intensities as compared to the commonly used dye MB, except for spherical Au1.0NPs, which exhibited results comparable to the values of MB. The particle-size-dependent evaluation of the PA signal intensities is of great interest because larger particles are useful to obtain molecular imaging of post-angiogenesis

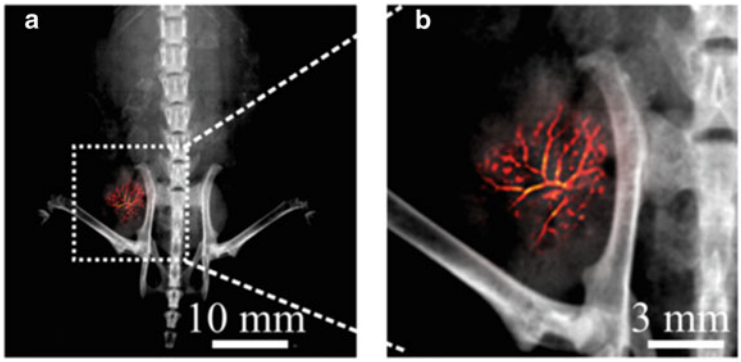

Fig. 24 Combined X-ray and PA images of a mouse tumor in vivo, which clearly show the location and the blood vessels of the tumor. (**a**) Overlay of X-ray image and PA image. (**b**) Enlargement of the corresponding image area highlighted by an inset in panel **a**. Figure reprinted with kind permission from [156]

processes, whereas only small NPs are able to infiltrate the nonvasculated parts of tumors for efficient targeting. These results were confirmed by Popović et al. who observed that particles within the 10–150 nm-size range show a particle-size-dependent uptake mechanism after injection into a mouse bearing a Mu89 human melanoma xenograft [151]. When a mixture of 12, 60, and 125 nm particles is injected in vivo the 12 nm particles extravasated easily and diffused from the vessels with minimal hindrance, the 60 nm particles extravasated but do not leave the immediate perivascular space, while the 125 nm particles did not appreciably extravasate.

By using anti-HER2-conjugated AuNRs, Agarwal et al. detected prostate cancer with PAI [139]. This method can also be used to detect and localize AuNRs with an approximate size of 50 × 15 nm at a very low concentration deep within tissue [152]. AuNRs of varying aspect ratios (3.7 and 5.9) and functionalized with different molecules to target MBT2 and HepG2 cells were used by Li et al. [153]. Jokerst et al. varied the aspect ratios of AuNRs in the range of 2.4–3.5, and those with an aspect ratio of 3.5 showed the highest ex vivo and in vivo PA signal [154]. Therefore these particles were used to image subcutaneous xenografts of the 2008, HEY and SKOV3 ovarian cancer cell lines in living mice. A linear relationship between the PA signal and the concentration of the injected AuNRs was observed. Another study demonstrated multiple selective targeting on oral cancer cells with HER2-antibody-(aspect ratio of 3.7) and EGFR-antibody-conjugated AuNRs (aspect ratio of 5.9) [155]. Huang et al. demonstrated a combined cancer imaging method using X-ray and PAI with PEG–AuNRs as contrast agents [156]. Figure 24 shows that the combination of X-ray and PAI can provide more comprehensive details of the tumor such as position, size, and vascular network. This is of great interest because vasculature regulates the metabolic and hemodynamic states of biological tissues wherefore the visualizing of blood vessels enables the tracking of cancer metastasis and monitoring of tumor angiogenesis.

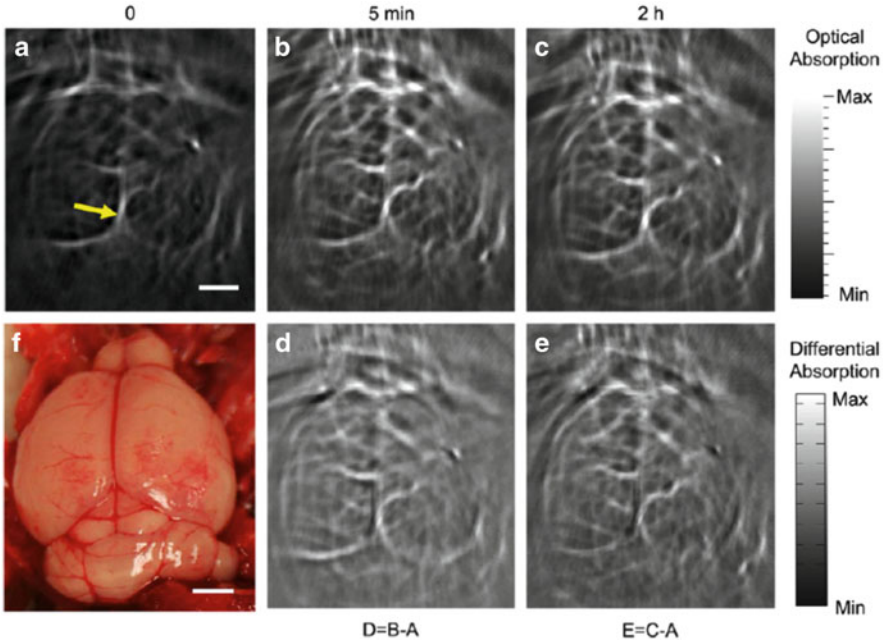

Fig. 25 Noninvasive PA images of a mouse brain in vivo employing PEG–HAuNs and NIR light at a wavelength of 800 nm. PA images received (**a**) before (the arrow pointed on the middle cerebral artery), (**b**) 5 min after, and (**c**) 2 h after the intravenous injection of PEG–HAuNs. (**d**, **e**) Differential images obtained by subtracting the preinjection image from the postinjection images (Image **d** = Image **b** − Image **a**; Image **e** = Image **c** − Image **a**). (**f**) Open-skull photograph of the mouse brain cortex obtained after the data acquisition for PAT. Scale bar = 2 mm. Figure reprinted with kind permission from [127]

The application of PEGylated hollow gold nanospheres (HAuNs) with a diameter of ~40 nm in nude mice showed the brain vasculature with great clarity and more detail structures. The images shown in Fig. 25 depicted blood vessels as small as ~100 mm in diameter which could be clearly seen with PEG–HAuNs as PAI system [127].

Beneath AuNPs, AuNRs, and HAuNs, also gold nanocages (AuNCs) have shown great promise in PAI. In one report, 50 nm AuNCs were intradermally injected on the left forepaw pads of Sprague–Dawley rats to image sentinel lymph nodes (SLN) noninvasively [157]. With the passing of time, the contrast at the SLN gradually and the PA signal within the SLN were increased. It was also demonstrated that the total image depth below the skin surface of 33 mm could be reached with good contrast which is substantial because this depth is greater than the mean depth of SLNs in human beings [157]. PEGylated AuNCs were used by Yang et al. to confirm the contrast enhancement for PA imaging in vivo [146]. The particles were injected into Sprague–Dawley rats via the tail vein and better resolved images of the cerebral cortex after administration were recorded. For the

visualizing of this layer in the brain of Sprague–Dawley rats, also PEGylated gold nanoshells were used by injection via the tail vein as well [132]. The nanoshells were administrated three times successively, and after the final injection the rat brain was imaged sequentially 10 times for more than about 6 h. The PA signal enhancement after the injection as a function of time was quantified with a maximal signal increase of about 63%.

In a recent report Bao et al. used PEGylated gold nanoprisms (AuNRs) with a uniform thickness of ca. 10 nm, with three congruent edge lengths of ca. 120 nm in in vivo settings [158]. The mice were treated with this AuNRs in order to visualize tumor angiogenesis in gastrointestinal cancer cells. It is shown that the AuNRs have the capacity to penetrate tumors and provide a high-resolution signal amplifier for PAI.

5.2.3 AuNPs as Agents for Photothermal Therapy

As compared to the diagnostic approach followed by PAI during photothermal experiments, a therapy approach is proposed by photothermia. Due to their SPR properties AuNPs are able to absorb light from incident radiation with high efficiency (extinction coefficient ~10^9 M^{-1} cm^{-1}) [159] in the near-infrared (NIR) region of the electromagnetic spectrum and convert it into heat [83, 160, 161]. The generated heat is subsequently delivered to the immediate surroundings of the AuNPs and allows a highly specific thermal ablation of diseased or infected tissue [162–165]. The advantage of the use of light in the NIR region is that the tissue damage and attenuation by biological fluids and tissues are minimal.

In 2003 Pitsillides et al. were the first who demonstrated that AuNPs can be used for PTT [166]. Since that time, several other studies have examined the use of AuNPs in PTT. Nam and coworkers designed AuNPs with a size of 10 nm with a pH-dependent agglomeration behavior [167]. The incubation of HeLa and B16 F10 mouse melanoma cells with these AuNPs shows an aggregation of the AuNPs in a typical tumor intercellular pH, leading to a shift of their absorption to the far- and near-IR spectral regions and thus to a utilization in PTT.

Nevertheless, AuNRs [168], HAuNs [105], AuNCs [104, 144, 169–171], and gold/silica nanoshells [172] with SPR frequencies in the NIR range are more promising agents for PTT because the absorption of the NPs can be tuned by synthetically varying the aspect ratio and shell thickness : core radius. The latter were some of the first applied in PTT by Halas and West [172–175]. Based on efficiently destroying breast carcinoma cells with PEGylated silica/gold nanoshells, the particles were injected into the tumor interstitium of SCID mice bearing sarcoma xenografts. A subsequent NIR light exposure demonstrated a 4–6 mm depth of thermal damage [172]. Later on NIR PTT was demonstrated using systemically administered PEGylated nanoshells in a colon cancer mouse model. All tumors in nanoshell-treated mice were completely ablated after a single PTT treatment and the animals appeared healthy and tumor free for more than 90 days posttreatment. In contrast the tumors of the control animals and the additional

sham-treated animals (laser treatment without nanoshell injection) continued to grow, with nearly 50% mortality at day 10 [174].

For vascular-targeted PTT of glioma nanoshells were conjugated to VEGF and/or PEG to thermally ablate VEGF receptor-2-positive endothelial cells upon NIR laser irradiation [176]. It was observed that VEGF-coated but not PEG-coated nanoshells bound to VEGF receptor-2-positive cells in vitro to enable targeted photothermal ablation. Subsequent in vivo studies in mice-bearing intracerebralglioma tumors showed that VEGF targeting could double the proportion of nanoshells bound to tumor vessels and vasculature was disrupted following laser exposure.

AuNPs with an interior composition of gold sulfide, or gold/gold sulfide composite structures, were first produced by self-assembly by Zhou et al. and were shown to have strong NIR-absorbing properties [177]. Gobin et al. compared gold/gold sulfide AuNPs with an overall diameter of 35–55 nm that provides higher absorption as well as potentially better tumor penetration, with gold/silica nanoshells with an overall diameter of 120–160 nm [178]. At relatively low concentrations and laser powers, the heating profiles of gold/gold sulfide AuNPs showed temperatures high enough to effect tumor ablation by hyperthermia. The smaller size of the gold/gold sulfide NPs yields a particle with higher absorbing cross-sectional area ratio than the gold/silica nanoshell.

Hu et al. noted that AuNRs and AuNCs have much larger absorption and scattering cross sections than nanoshells wherefore these are better candidates for PTT [179]. The use of AuNRs, which can more efficiently absorb photons to generate heat, as PTT agent is based on the pioneering work of Catherine Murphy's group [180]. These particles have been extensively studied for PTT applications in vitro [168, 181, 182] and in vivo [183, 184]. Fundamental work by El-Sayed and coworkers has provided insights into how to optimize metallic NP-based PTT, including how shape influences heat generation efficiency [185] and the critical temperatures associated with therapy (typically 70–80°C) [186]. They also found that AuNRs labeled with an EGFR-targeting ligand were effective for PTT under NIR illumination in vitro [168]. The feasibility of in vivo PTT treatment of squamous cell carcinoma xenografts with PEGylated AuNRs was demonstrated by the inhibition of average tumor growth for direct and intravenous delivery methods [183].

Von Maltzahn et al. described an approach to improve plasmonic therapy by using computational simulations to understand the effect of NP concentration on heating in vivo. Therefore an X-ray CT scan was utilized to characterize the distribution of intratumorally and intravenously administered PEGylated AuNRs in human tumor xenograft bearing mice. The high absorption efficiency of the AuNRs in both the X-ray and NIR regions enabled real-time visualization and therapy [187]. To assess the utility of the high X-ray absorption of PEG–NRs for detection of in vivo, PEG–AuNRs were directly injected into the tumors of mice bearing bilateral human MDA-MB-435 tumors, implanted either in the mammary fat pad or the rear flank. It was found that X-ray CT rapidly detailed

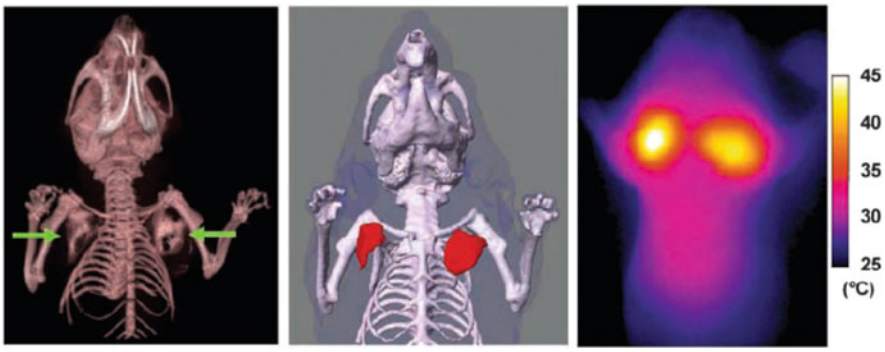

Fig. 26 Photothermal heating of passively targeted AuNRs in tumors. PEG–AuNRs or saline was given i.v. to mice bearing MDA-MB-435 tumors on opposing flanks. After AuNRs had cleared from circulation (72 h after injection), the right flank was irradiated (beam size indicated by *dotted circle*). Figure reprinted with kind permission from [187]

the three-dimensional distribution of PEG–NRs in tumors, showing clear distinction between AuNRs and soft tissues, as seen in Fig. 26.

To prolong the circulation time, optimize the tumor targeting, and decrease the liver uptake, Choi et al. prepared AuNR-loaded, chitosan-conjugated, pluronic-based nanocarriers which could serve as imaging agents for cancer cells and as a very effective hyperthermia agent for PTT [184]. By delivering the nanocarriers via an intravenous injection followed by NIR laser irradiation to the tumor site resulted in a very efficient thermolysis in vivo, achieving a complete tumor resorption without damage to the surrounding tissue.

Xia and coworkers studied AuNCs as photothermal transducers for therapeutic applications [104, 144, 169–171]. They utilized PEGylated AuNCs with an edge length of 45 nm for selective destruction of neoplastic tissue using a bilateral tumor model. The particles accumulated in tumors with a relatively high efficiency leading to a slightly higher amount of AuNCs in the tumor periphery than in the inner core. With an infrared camera the temperature increase during photothermal treatment was monitored which is shown in Fig. 27.

The effect of PTT on cells by larger, more rapid temperature increases, often referred to as “ablative” treatments, is considered to be necrosis with the corresponding melting of cell membranes and organelles [188]. In contrast to that mild temperature increases (known as hyperthermia), mostly proceed via apoptotic pathways, and are known to perturb a variety of normal cellular functions [183]. Huang et al. designed AuNR elastin-like polypeptide matrices loaded with the heat shock protein (HSP) inhibitor 17-(allylamino)-17-demethoxygeldanamycin (17-AAG) to give insights into the release of heat shock proteins (HSPs), which help to restore normal processes to the cell, and their relation to PTT [181]. They demonstrated that AuNRs in combination with 17-AAG improve significantly (>90%) death of cancer cells, while “single treatments” (i.e., hyperthermia alone and 17-AAG alone) demonstrated minimal loss of cancer cell

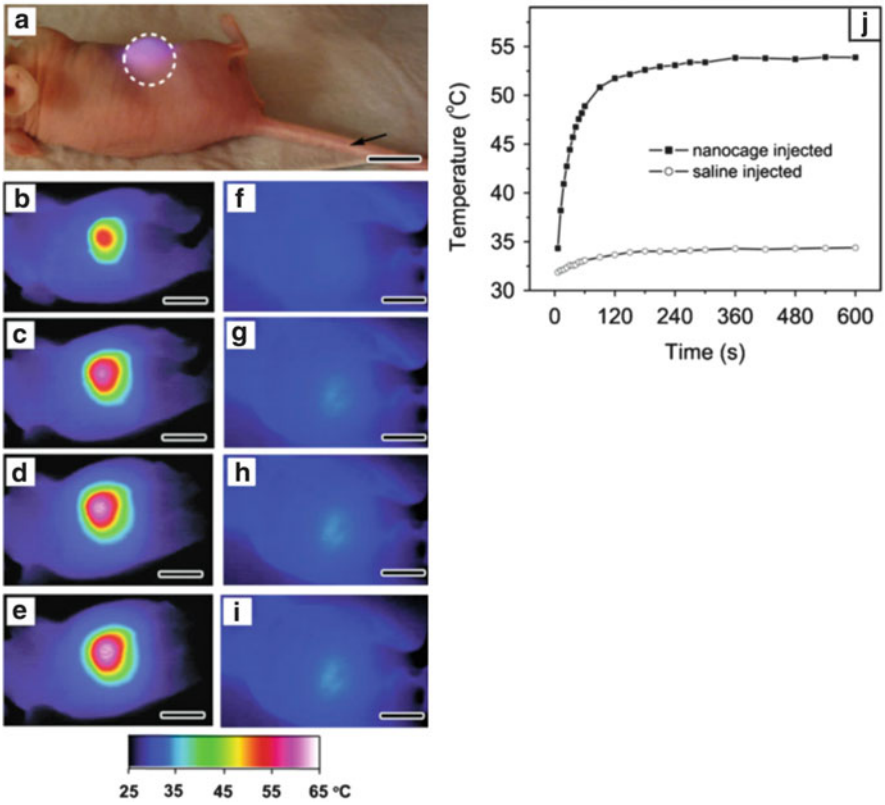

Fig. 27 (**a**) Photograph of a tumor-bearing mouse under photothermal treatment. PEGylated nanocages or saline was administrated intravenously through the tail vein as indicated by an *arrow*. After the NCs had been cleared from the circulation (72 h after injection), the tumor on the right flank was irradiated with a beam size indicated by the dashed circle. (**b**–**g**) Thermographic images of nanocage-injected (**b**–**e**) and saline-injected (**f**–**i**) tumor-bearing mice at different time points: (**b**, **e**) 1 min, (**c**, **f**) 3 min, (**d**, **g**) 5 min, and (**e**, **i**) 10 min. (**j**) Plots of average temperature within the tumors (*dashed circle*) as a function of irradiation time. All scale bars are 1 cm. Figure reprinted with kind permission from [170]

viability (<10%). This result seems to imply that in addition to the local thermal effects, significant improvements in NP-mediated PTT can also take advantage of limiting cellular responses.

5.2.4 AuNPs in Radiotherapy

Another method which is widely used to help reduce tumor size is through radiofrequency. Since the early 1990s, it has been utilized as a treatment for destroying liver tumors [189]. However, this method does have its drawbacks,

such as accuracy, invasive needle placement, and toxic effects, on the tissue surrounding the tumor and also on internal organs [190, 191]. These side effects have a drastic limitation on the amount of radiation used during treatment.

Several studies have focused on the use of AuNPs as novel high-Z radiosensitizing agent to increase the sensitivity of tumors irradiated with clinical X-ray beams [192, 193]. Numerous experimental [194–196] and theoretical studies [197–199] have shown that clinically significant enhancements are achievable with AuNPs-treated tumors in combination with X-ray therapy.

In vitro studies showed AuNP radiosensitization by irradiation of cells and plasmid DNA [200–204]. Irradiating plasmid DNA in the presence of 5 nm AuNPs leads to single-strand and double-strand break enhancement [202]. Rahman et al. observed a biological dose enhancement factor of up to 24.6 when irradiating bovine aortic endothelial cells in the presence of 1.9 nm AuNPs [203]. Roa et al. were the first who reported that 10.8 nm glucose-capped AuNPs trigger the activation of CDK kinases leading to cell cycle accumulation in the G2/M phase and acceleration in the G0/G1 phase [205]. This leads to the suggestion that p53 and the CDK kinases are targets for AuNPs. A striking sensitization to ionizing radiation is achieved as well. In another study AuNPs with an approximate size of 45 nm showed an increase of the effectiveness of proton radiotherapy for the killing of prostate tumor cells of about 15–20% [206].

Despite the rapid increase of in vivo studies investigating the uptake and distribution of AuNPs, there remains a lack of studies of in vivo radiosensitization with these particles. In 2004, the suitability of AuNPs for radiotherapy was examined by Hainfeld et al. in vivo [192]. Nontargeted 1.9 nm AuNPs (AuroVist) in combination with 250 kV radiation were shown to prolong survival in Balb/C mice bearing EMT-6 murine breast cancer tumors. One month after the treatment, a dramatic reduction in tumor growth was observed. Based on these results, a second experiment with a longer follow-up study in mice which received a slightly lower radiation dose alone or with AuNPs was pursued. A remarkable tumor regression in mammary tumors and long-term survival without any significant toxicity were demonstrated thus indicating the utility of these particles for radiotherapy. In a recent study by Hainfeld et al., a highly radioresistant murine squamous cell carcinoma was used in mice [207]. A significant tumor growth delay and a long-term tumor control were observed by combining AuNPs with irradiation. Chang et al. used 13 nm citrate-stabilized AuNPs in a mouse model with B16F10 murine melanoma cells. A significant in vivo tumor growth delay and increased survival were noted when AuNPs were injected 24 h before irradiation [195]. The median survival of the mice with 65 days was shorter than in the Hainfeld study but the AuNP concentration used is much lower.

While demonstrating the potential efficacy of AuNP radiosensitization, the large variations in these studies revealed AuNP radiosensitization to be highly sensitive to a number of physics and pharmacological parameters such as irradiation energy, AuNP size and concentration, and intracellular localization [192, 202, 203]. Toward understanding and predicting the effects of these parameters, there have been a number of Monte Carlo simulation studies exploring AuNP dose enhancement [197, 198, 208–213].

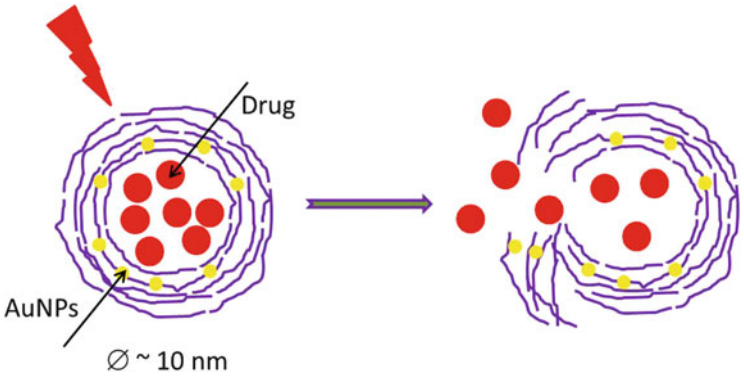

Fig. 28 Sketch of the opening process of a polymer container filled with the drug and additionally containing AuNPs for photoinduced heating process. Figure adapted from [90]

5.3 Drug Delivery

If AuNPs shall be used as therapeutic agents based on their cytotoxicity in the future, a fundamental challenge has to be faced. One of the most common drawbacks of the present treatment of tumors is the small specificity of the respective drugs that means that the number of damaged tumor cells compared with the number of damaged healthy cells is far too small. Therefore, worldwide efforts are being made to improve the situation, among others by using the so-called drug delivery (drug release) systems. The goal is to transport a drug specifically into a tumor in order to avoid damage of healthy cells as far as possible. One promising attempt is the use of micro- or nano-sized hollow containers which are filled with chemotherapeutics or cytotoxins. The advantage of this technique is the possibility to modify the surface of the capsules by tumor-specific antibodies without the need to modify the drug itself. Accumulated in the tumor, the containers open themselves or by stimuli from outside, for instance, by photoinduced heating of AuNPs, also present in the containers [163, 166, 214–216]. The capsules usually consist of polymers which can easily be modified by tumor-specific antibodies. Poly (alkylcyanoacrylate) even degrades rapidly in vivo without any photoinduction of AuNPs [217]. Figure 28 elucidates the artificial opening process using AuNPs.

The use of AuNPs for photoinduced heating is only of importance for the opening of the polymer containers. Another chance is the direct use of AuNPs as a drug. The cell toxicity of Au_{55} with its ultrasmall 1.4 nm diameter has already been discussed in Sect. 3. Experiments to transport 1.4 nm Au particles in polymer spheres are presently under investigation (Simon U, Mayer C, private communication).

Though not yet tested for the use of AuNPs, mesoporous silica nanoparticles are a promising alternative to hollow nanospheres. They are intensively under investigation, especially to study single particle tracking to living cells by fluorescence microscopy allowing the discrimination between active transport and random motion [218–220].

Also still under investigation for use as drug delivery systems are the so-called polymersomes. Polymersomes consist of a double layer of polymers with a hydrophilic and a hydrophobic function, cross-linked by various polymers. The combinations form a hollow sphere, comparable with the structure of liposomes from which the name polymersome derives. Their size can be varied between 100 nm and 100 μm [221]. They are able to transport bioactive molecules to the relevant cells and to release them there [222].

6 Summary

This review has summarized relevant aspects on the properties and the bioresponse of AuNPs in the context of a rapidly growing field of applications, i.e., the application in vivo and in vitro for medical purposes. It has been shown by a number of selected examples that most of the AuNPs synthesized so far are considered nontoxic, making them suited for in vivo applications, e.g., for imaging and therapy. Special focus is laid on AuNPs in the sub-2 nm range, which under certain conditions can become toxic. This sheds light on how adverse effects of AuNPs in biological systems may occur and, at the same time, suggests how such toxic effect may be used in therapy as well. The present state of knowledge is summarized on the mechanism how such small AuNPs may interact with biomolecules and cells, addressing the effect of shape complementarity in the sense that AuNPs approach the size of biological molecules and subcellular structures and thus may even behave as molecular ligands.

It becomes evident that the high degree of control over particle size and ligand chemistry opens up an avenue of novel applications in a biological environment.

References

1. Teo BK, Shi X, Zhang H (1992) Pure gold cluster of 1:9:9:1:9:9:1 layered structure: a novel 39-metal-atom cluster $[(Ph_3P)_{14}Au_{39}Cl_6]Cl_2$ with an interstitial gold atom in a hexagonal antiprismatic cage. J Am Chem Soc 114:2743
2. Gutrath BS, Oppel IM, Presly O, Beljakov I, Meded V, Wenzel W, Simon U (2013) $[Au_{14}(PPh_3)_8(NO_3)_4]$: an example of a new class of $Au(NO_3)$-ligated superatom complexes. Angew Chem Int Ed 52:3529
3. Briant CE, Theobald BRC, White JW, Bell LK, Mingos DMP, Welch AJ (1981) Synthesis and X-ray structural characterization of the centred icosahedral gold cluster compound $[Au_{13}(PMe_2Ph)_{10}Cl_2](PF_6)_3$; the realization of a theoretical prediction. J Chem Soc Chem Commun 201
4. Mingos DMP (1976) Molecular-orbital calculations on cluster compounds of gold. J Chem Soc Dalton Trans 1163
5. Mingos DMP (1996) Gold – a flexible friend in cluster chemistry. J Chem Soc Dalton Trans 561

6. Gutrath BS, Englert U, Wang Y, Simon U (2013) A missing link in undecagold cluster chemistry: single-crystal X-ray analysis of $[Au_{11}(PPh_3)_7Cl_3]$. Eur J Inorg Chem 2013 (12):2002–2006
7. Schwerdtfeger P (ed) (2002) Relativistic electronic structure theory, part 1: fundamentals. Elsevier, Amsterdam
8. Schwerdtfeger P (ed) (2005) Relativistic electronic structure theory, part 2: applications. Elsevier, Amsterdam
9. Hess BA (ed) (2002) Relativistic effects in heavy-element chemistry and physics. Wiley-VCH, New York
10. Mie G (1908) Beiträge zur Optik trüber Medien, speziell kolloidaler Metallösungen. Ann Phys 330:377
11. Schmid G, Brune H, Ernst H, Grunwald A, Grünwald W, Hofmann H, Krug H, Janich P, Mayor M, Rathgeber W, Simon U, Vogel V, Wyrwa D (2006) Nanotechnology: assessment and perspectives. In: Wissenschaftsethik und Technikfolgenabschätzung, vol. 27. Springer, Berlin
12. The Royal Society and The Royal Academy of Engineering, Science Policy Section (2004) Nanoscience and nanotechnologies: opportunities and uncertainties. The Royal Society and The Royal Academy of Engineering, Science Policy Section, London
13. Bezryadin A, Dekker C, Schmid G (1997) Electrostatic trapping of single conducting nanoparticles between nanoelectrodes. Appl Phys Lett 71:1273
14. Schmid G, Pfeil R, Boese R, Bandermann F, Meyer S, Calis GHM, van der Velden JWA (1981) $Au_{55}[P(C_6H_5)_3]_{12}CI_6$ — ein Goldcluster ungewöhnlicher Größe. Chem Ber 114:3634
15. Chi LF, Hartig M, Drechsler T, Schwaack T, Seidel C, Fuchs H, Schmid G (1998) Single-electron tunneling in Au_{55} cluster monolayers. Appl Phys A 66:187
16. van der Velden JWA, Vollenbroek FA, Bour JJ, Beurskens PI, Smits JMM, Bosman WP (1981) Recueil J Roy Netherlands Chem Soc 100:148
17. Schmid G, Morun B, Malm J-O (1989) $Pt_{309}Phen^*_{36}O_{30 \pm 10}$, a four-shell platinum cluster. Angew Chem Int Ed 28:778
18. Schmid G, Klein N, Morun B, Lehnert A (1990) Two, four, five-shell clusters and colloids. Pure Appl Chem 62:1175
19. Boyen HG, Ethirajan A, Kästle G, Weigl F, Ziemann P, Schmid G, Garnier MG, Büttner M, Oelhafen P (2005) Alloy formation of supported gold nanoparticles at their transition from clusters to solids: does size matter? Phys Rev Lett 94:016804
20. Pei Y, Shao N, Gao Y, Zeng XC (2010) Investigating active site of gold nanoparticle $Au_{55}(PPh_3)_{12}Cl_6$ in selective oxidation. ACS Nano 4:2009
21. Turner M, Golovko VB, Vaughan OPH, Abdulkin P, Berenguer-Murcia A, Tikhov MS, Johnson BFG, Lambert RM (2008) Selective oxidation with dioxygen by gold nanoparticle catalysts derived from 55-atom clusters. Nature 454:981
22. Pan Y, Leifert A, Ruau D, Neuss S, Bornemann J, Schmid G, Brandau W, Simon U, Jahnen-Dechent W (2009) Gold nanoparticles of diameter 1.4 nm trigger necrosis by oxidative stress and mitochondrial damage. Small 5:2067
23. Smith BA, Zhang JZ, Giebel U, Schmid G (1997) Direct probe of size-dependent electronic relaxation in single-sized Au and nearly monodisperse Pt colloidal nano-particles. Chem Phys Lett 270:139
24. Schmid G, Klein N, Korste L, Kreibig U, Schönauer D (1988) Large transition metal clusters—VI. Ligand exchange reactions on $Au_{55}(PPh_3)_{12}Cl_6$—the formation of a water soluble Au_{55} cluster. Polyhedron 7:605
25. Saha K, Bajaj A, Duncan B, Rotello VM (2011) Beauty is skin deep: a surface monolayer perspective on nanoparticle interactions with cells and bio-macromolecules. Small 7:1903
26. Schmid G (1985) Developments in transition metal cluster chemistry — the way to large clusters. Struct Bond 62:51

27. Cho W-S, Cho M, Jeong J, Choi M, Cho H-Y, Han BS, Kim SH, Kim HO, Lim YT, Chung BH, Jeong J (2009) Acute toxicity and pharmacokinetics of 13 nm-sized PEG-coated gold nanoparticles. Toxicol Appl Pharmacol 236:16
28. Li JJ, Hartono D, Ong C-N, Bay B-H, Yung L-YL (2010) Autophagy and oxidative stress associated with gold nanoparticles. Biomaterials 31:5996
29. Johnston HJ, Hutchison G, Christensen FM, Peters S, Hankin S, Stone V (2010) A review of the in vivo and in vitro toxicity of silver and gold particulates: particle attributes and biological mechanisms responsible for the observed toxicity. Crit Rev Toxicol 40:328
30. Shang L, Brandholt S, Stockmar F, Trouillet V, Bruns M, Nienhaus GU (2012) Effect of protein adsorption on the fluorescence of ultrasmall gold nanoclusters. Small 8:661
31. De Paoli Lacerda SH, Park JJ, Meuse C, Pristinski D, Becker ML, Karim A, Douglas JF (2010) Interaction of gold nanoparticles with common human blood proteins. ACS Nano 4:365
32. Treuel L, Nienhaus GU (2012) Toward a molecular understanding of nanoparticle–protein interactions. Biophys Rev 4:137
33. Dhar S, Daniel WL, Giljohann DA, Mirkin CA, Lippard SJ (2009) Polyvalent oligonucleotide gold nanoparticle conjugates as delivery vehicles for Platinum(IV) warheads. J Am Chem Soc 131:14652
34. Rosi NL, Mirkin CA (2005) Nanostructures in biodiagnostics. Chem Rev 105:1547
35. Elghanian R, Storhoff JJ, Mucic RC, Letsinger RL, Mirkin CA (1997) Selective colorimetric detection of polynucleotides based on the distance-dependent optical properties of gold nanoparticles. Science 277:1078
36. Storhoff JJ, Elghanian R, Mucic RC, Mirkin CA, Letsinger RL (1998) One-pot colorimetric differentiation of polynucleotides with single base imperfections using gold nanoparticle probes. J Am Chem Soc 120:1959
37. Storhoff JJ, Lazarides AA, Mucic RC, Mirkin CA, Letsinger RL, Schatz GC (2000) What controls the optical properties of DNA-linked gold nanoparticle assemblies? J Am Chem Soc 122:4640
38. Mucic RC, Storhoff JJ, Mirkin CA, Letsinger RL (1998) DNA-directed synthesis of binary nanoparticle network materials. J Am Chem Soc 120:12674
39. Taton TA, Lu G, Mirkin CA (2001) Two-color labeling of oligonucleotide arrays via size-selective scattering of nanoparticle probes. J Am Chem Soc 123:5164
40. Rosi NL, Giljohann DA, Thaxton CS, Lytton-Jean AKR, Han MS, Mirkin CA (2006) Oligonucleotide-modified gold nanoparticles for intracellular gene regulation. Science 312:1027
41. Seferos DS, Giljohann DA, Hill HD, Prigodich AE, Mirkin CA (2007) Nano-flares: probes for transfection and mRNA detection in living cells. J Am Chem Soc 129:15477
42. Demers LM, Mirkin CA, Mucic RC, Reynolds RA, Letsinger RL, Elghanian R, Viswanadham G (2000) A fluorescence-based method for determining the surface coverage and hybridization efficiency of thiol-capped oligonucleotides bound to gold thin films and nanoparticles. Anal Chem 72:5535
43. Jin R, Wu G, Li Z, Mirkin CA, Schatz GC (2003) What controls the melting properties of DNA-linked gold nanoparticle assemblies? J Am Chem Soc 125:1643
44. Giljohann DA, Seferos DS, Prigodich AE, Patel PC, Mirkin CA (2009) Gene regulation with polyvalent siRNA-nanoparticle conjugates. J Am Chem Soc 131:2072
45. Mirkin CA, Letsinger RL, Mucic RC, Storhoff JJ (1996) A DNA-based method for rationally assembling nanoparticles into macroscopic materials. Nature 382:607
46. Nam J-M, Park S-J, Mirkin CA (2002) Bio-barcodes based on oligonucleotide-modified nanoparticles. J Am Chem Soc 124:3820
47. Park S-J, Lazarides AA, Mirkin CA, Brazis PW, Kannewurf CR, Letsinger RL (2000) The electrical properties of gold nanoparticle assemblies linked by DNA. Angew Chem Int Ed 39:3845

48. Taton TA, Mucic RC, Mirkin CA, Letsinger RL (2000) The DNA-mediated formation of supramolecular mono- and multilayered nanoparticle structures. J Am Chem Soc 122:6305
49. Cutler JI, Auyeung E, Mirkin CA (2012) Spherical nucleic acids. J Am Chem Soc 134:1376
50. Lee J-S, Han MS, Mirkin CA (2007) Colorimetric detection of mercuric ion (Hg^{2+}) in aqueous media using DNA-functionalized gold nanoparticles. Angew Chem Int Ed 46:4093
51. Zheng G, Daniel WL, Mirkin CA (2008) A new approach to amplified telomerase detection with polyvalent oligonucleotide nanoparticle conjugates. J Am Chem Soc 130:9644
52. Han MS, Lytton-Jean AKR, Oh B-K, Heo J, Mirkin CA (2006) Colorimetric screening of DNA-binding molecules with gold nanoparticle probes. Angew Chem Int Ed 45:1807
53. Xu X, Daniel WL, Wei W, Mirkin CA (2010) Colorimetric Cu^{2+} detection using DNA-modified gold-nanoparticle aggregates as probes and click chemistry. Small 6:623
54. Lytton-Jean AKR, Mirkin CA (2005) A thermodynamic investigation into the binding properties of DNA functionalized gold nanoparticle probes and molecular fluorophore probes. J Am Chem Soc 127:12754
55. Seferos DS, Prigodich AE, Giljohann DA, Patel PC, Mirkin CA (2009) Polyvalent DNA nanoparticle conjugates stabilize nucleic acids. Nano Lett 9:308
56. Giljohann DA, Seferos DS, Patel PC, Millstone JE, Rosi NL, Mirkin CA (2007) Oligonucleotide loading determines cellular uptake of DNA-modified gold nanoparticles. Nano Lett 7:3818
57. Cutler JI, Zhang K, Zheng D, Auyeung E, Prigodich AE, Mirkin CA (2011) Polyvalent nucleic acid nanostructures. J Am Chem Soc 133:9254
58. Patel PC, Giljohann DA, Daniel WL, Zheng D, Prigodich AE, Mirkin CA (2010) Scavenger receptors mediate cellular uptake of polyvalent oligonucleotide-functionalized gold nanoparticles. Bioconjugate Chem 21:2250
59. Cutler JI, Zheng D, Xu X, Giljohann DA, Mirkin CA (2010) Polyvalent oligonucleotide iron oxide nanoparticle "click" conjugates. Nano Lett 10:1477
60. Witten KG, Rech C, Eckert T, Charrak S, Richtering W, Elling L, Simon U (2011) Glyco-DNA–gold nanoparticles: lectin-mediated assembly and dual-stimuli response. Small 7:1954
61. van Kasteren SI, Campbell SJ, Serres S, Anthony DC, Sibson NR, Davis BG (2009) Glyconanoparticles allow pre-symptomatic in vivo imaging of brain disease. Proc Natl Acad Sci USA 106:18
62. Ebisu S, Shankar Iyer PN, Goldstein IJ (1978) Equilibrium dialysis and carbohydrate-binding studies on the 2-acetamido-2-deoxy-d-glucopyranosyl-binding lectin from *Bandeiraea simplicifolia* seeds. Carbohydr Res 61:129
63. Zook JM, Long SE, Cleveland D, Geronimo CLA, MacCuspie RI (2011) Measuring silver nanoparticle dissolution in complex biological and environmental matrices using UV–visible absorbance. Anal Bioanal Chem 401:1993
64. Kittler S, Greulich C, Diendorf J, Köller M, Epple M (2010) Toxicity of silver nanoparticles increases during storage because of slow dissolution under release of silver ions. Chem Mater 22:4548
65. Ho C-M, Yau SK-W, Lok C-N, So M-H, Che C-M (2010) Oxidative dissolution of silver nanoparticles by biologically relevant oxidants: a kinetic and mechanistic study. Chem Asian J 5:285
66. Liu J, Hurt RH (2010) Ion release kinetics and particle persistence in aqueous nano-silver colloids. Environ Sci Technol 44:2169
67. Liu J, Sonshine DA, Shervani S, Hurt RH (2010) Controlled release of biologically active silver from nanosilver surfaces. ACS Nano 4:6903
68. Zhang W, Yao Y, Sullivan N, Chen Y (2011) Modeling the primary size effects of citrate-coated silver nanoparticles on their ion release kinetics. Environ Sci Technol 45:4422
69. Braydich-Stolle L, Hussain S, Schlager JJ, Hofmann M-C (2005) In vitro cytotoxicity of nanoparticles in mammalian germline stem cells. Toxicol Sci 88:412

70. Soto K, Carrasco A, Powell TG, Garza KM, Murr L (2005) Comparative in vitro cytotoxicity assessment of some manufactured nanoparticulate materials characterized by transmission-electron microscopy. J Nanopart Res 7:145
71. Foldbjerg R, Dang DA, Autrup H (2011) Cytotoxicity and genotoxicity of silver nanoparticles in the human lung cancer cell line, A549. Arch Toxicol 85:743
72. Benn TM, Westerhoff P (2008) Nanoparticle silver released into water from commercially available sock fabrics. Environ Sci Technol 42:4133
73. Geranio L, Heuberger M, Nowack B (2009) The behavior of silver nanotextiles during washing. Environ Sci Technol 43:8113
74. Navarro E, Piccapietra F, Wagner B, Marconi F, Kaegi R, Odzak N, Sigg L, Behra R (2008) Toxicity of silver nanoparticles to *Chlamydomonas reinhardtii*. Environ Sci Technol 42:8959
75. Kaegi R, Sinnet B, Zuleeg S, Hagendorfer H, Mueller E, Vonbank R, Boller M, Burkhardt M (2010) Release of silver nanoparticles from outdoor facades. Environ Pollut 158:2900
76. Nowack B, Krug HF, Height M (2011) 120 Years of nanosilver history: implications for policy makers. Environ Sci Technol 45:1177
77. Lea MC (1889) Am J Sci 37:476
78. Gottschalk F, Scholz RW, Nowack B (2010) Probabilistic material flow modeling for assessing the environmental exposure to compounds: methodology and an application to engineered nano-TiO_2 particles. Environ Model Softw 25:320
79. Asharani PV, Lianwu Y, Gong Z, Valiyaveettil S (2011) Comparison of the toxicity of silver, gold and platinum nanoparticles in developing zebrafish embryos. Nanotoxicology 5:43
80. Asharani PV, Xinyi N, Hande MP, Valiyaveettil S (2010) DNA damage and p53-mediated growth arrest in human cells treated with platinum nanoparticles. Nanomedicine 5:51
81. Mahl D, Diendorf J, Ristig S, Greulich C, Li Z-A, Farle M, Köller M, Epple M (2012) Silver, gold, and alloyed silver–gold nanoparticles: characterization and comparative cell-biologic action. J Nanopart Res 14:1153
82. Connor EE, Mwamuka J, Gole A, Murphy CJ, Wyatt MD (2005) Gold nanoparticles are taken up by human cells but do not cause acute cytotoxicity. Small 1:325
83. Murphy CJ, Gole AM, Stone JW, Sisco PN, Alkilany AM, Goldsmith EC, Baxter SC (2008) Gold nanoparticles in biology: beyond toxicity to cellular imaging. Acc Chem Res 41:1721
84. Liu Y, Meyer-Zaika W, Franzka S, Schmid G, Tsoli M, Kuhn H (2003) Gold-cluster degradation by the transition of B-DNA into A-DNA and the formation of nanowires. Angew Chem Int Ed 42:2853
85. Tsoli M, Kuhn H, Brandau W, Esche H, Schmid G (2005) Cellular uptake and toxicity of Au_{55} clusters. Small 1:841
86. Pan Y, Neuss S, Leifert A, Fischler M, Wen F, Simon U, Schmid G, Brandau W, Jahnen-Dechent W (2007) Size dependent cytotoxicity of gold nanoparticles. Small 3:1941
87. Leifert A, Pan Y, Kinkeldey A, Schiefer F, Setzler J, Scheel O, Lichtenbeld H, Schmid G, Wenzel W, Jahnen-Dechent W, Simon U (2013) Differential hERG ion channel activity of ultrasmall gold nanoparticles. Proc Natl Acad Sci USA 110:8004
88. Hirn S, Semmler-Behnke M, Schleh C, Wenk A, Lipka J, Schäffler M, Takenaka S, Möller W, Schmid G, Simon U, Kreyling WG (2011) Particle size-dependent and surface charge-dependent biodistribution of gold nanoparticles after intravenous administration. Eur J Pharm Biopharm 77:407
89. Semmler-Behnke M, Kreyling WG, Lipka J, Fertsch S, Wenk A, Takenaka S, Schmid G, Brandau W (2008) Biodistribution of 1.4- and 18-nm gold particles in rats. Small 4:2108
90. Schmid G (2012) Metal nanoparticles: electronic properties, bioresponse, and synthesis. In: Scott RA (ed) Encyclopedia of inorganic and bioinorganic chemistry. Wiley VCH, doi:10.1002/9781119951438.eibc0284.pub2
91. Schleh C, Semmler-Behnke M, Lipka J, Wenk A, Hirn S, Schäffler M, Schmid G, Simon U, Kreyling WG (2012) Size and surface charge of gold nanoparticles determine absorption across intestinal barriers and accumulation in secondary target organs after oral administration. Nanotoxicology 6:36

92. Lin S, Zhao Y, Nel AE, Lin S (2012) Zebrafish: an in vivo model for nano EHS studies. Small. doi:10.1002/smll.201202115
93. George S, Xia T, Rallo R, Zhao Y, Ji Z, Lin S, Wang X, Zhang H, France B, Schoenfeld D, Damoiseaux R, Liu R, Lin S, Bradley KA, Cohen Y, Nel AE (2011) Use of a high-throughput screening approach coupled with in vivo zebrafish embryo screening to develop hazard ranking for engineered nanomaterials. ACS Nano 5:1805
94. Fako VE, Furgeson DY (2009) Zebrafish as a correlative and predictive model for assessing biomaterial nanotoxicity. Adv Drug Deliv Rev 61:478
95. Simmons SO, Fan C-Y, Ramabhadran R (2009) Cellular stress response pathway system as a sentinel ensemble in toxicological screening. Toxicol Sci 111:202
96. Yang L, Kemadjou J, Zinsmeister C, Bauer M, Legradi J, Muller F, Pankratz M, Jakel J, Strahle U (2007) Transcriptional profiling reveals barcode-like toxicogenomic responses in the Zebrafish embryo. Genome Biol 8:R227
97. Harper SL, Carriere JL, Miller JM, Hutchison JE, Maddux BLS, Tanguay RL (2011) Systematic evaluation of nanomaterial toxicity: utility of standardized materials and rapid assays. ACS Nano 5:4688
98. Pan Y, Leifert A, Graf M, Schiefer F, Thoröe-Boveleth S, Broda J, Halloran MC, Hollert H, Laaf D, Simon U, Jahnen-Dechent W (2013) High-sensitivity real-time analysis of nanoparticle toxicity in green fluorescent protein-expressing zebrafish. Small 863
99. Razansky D, Distel M, Vinegoni C, Ma R, Perrimon N, Koster RW, Ntziachristos V (2009) Multispectral opto-acoustic tomography of deep-seated fluorescent proteins in vivo. Nat Photonics 3:412
100. Dreaden EC, Alkilany AM, Huang X, Murphy CJ, El-Sayed MA (2012) The golden age: gold nanoparticles for biomedicine. Chem Soc Rev 41:2740
101. Matsumura Y, Maeda H (1986) A new concept for macromolecular therapeutics in cancer chemotherapy: mechanism of tumoritropic accumulation of proteins and the antitumor agent Smancs. Cancer Res 46:6387
102. Tkachenko AG, Xie H, Coleman D, Glomm W, Ryan J, Anderson MF, Franzen S, Feldheim DL (2003) Multifunctional gold nanoparticle-peptide complexes for nuclear targeting. J Am Chem Soc 125:4700
103. de la Fuente JM, Berry CC (2005) Tat peptide as an efficient molecule to translocate gold nanoparticles into the cell nucleus. Bioconjug Chem 16:1176
104. Chen J, Wang D, Xi J, Au L, Siekkinen A, Warsen A, Li Z-Y, Zhang H, Xia Y, Li X (2007) Immuno gold nanocages with tailored optical properties for targeted photothermal destruction of cancer cells. Nano Lett 7:1318
105. Lu W, Xiong C, Zhang G, Huang Q, Zhang R, Zhang JZ, Li C (2009) Targeted photothermal ablation of murine melanomas with melanocyte-stimulating hormone analog-conjugated hollow gold nanospheres. Clin Cancer Res 15:876
106. Shilo M, Reuveni T, Motiei M, Popovtzer R (2012) Nanoparticles as computed tomography contrast agents: current status and future perspectives. Nanomedicine 7:257
107. Barreto JA, O'Malley W, Kubeil M, Graham B, Stephan H, Spiccia L (2011) Nanomaterials: applications in cancer imaging and therapy. Adv Mater 23:H18
108. Willmann JK, van Bruggen N, Dinkelborg LM, Gambhir SS (2008) Molecular imaging in drug development. Nat Rev Drug Discov 7:591
109. Krause W (2002) Liver specific X-ray contrast agents. Top Curr Chem 222:173
110. Wang H, Zheng L, Guo R, Peng C, Shen M, Shi X, Zhang G (2012) Dendrimer-entrapped gold nanoparticles as potential CT contrast agents for blood pool imaging. Nanoscale Res Lett 7:190
111. Hainfeld JF, Slatkin DN, Focella TM, Smilowitz HM (2006) Gold nanoparticles: a new X-ray contrast agent. Br J Radiol 79:248
112. Kojima C, Umeda Y, Ogawa M, Harada A, Magata Y, Kono K (2010) X-ray computed tomography contrast agents prepared by seeded growth of gold nanoparticles in PEGylated dendrimer. Nanotechnology 21:245104

113. Cai Q-Y, Kim SH, Choi KS, Kim SY, Byun SJ, Kim KW, Park SH, Juhng SK, Yoon K-H (2007) Colloidal gold nanoparticles as a blood-pool contrast agent for X-ray computed tomography in mice. Invest Radiol 42:797
114. Peng C, Wang H, Guo R, Shen M, Cao X, Zhu M, Zhang G, Shi X (2011) Acetylation of dendrimer-entrapped gold nanoparticles: synthesis, stability, and X-ray attenuation properties. J Appl Polym Sci 119:1673
115. Ghann WE, Aras O, Fleiter T, Daniel M-C (2012) Syntheses and characterization of lisinopril-coated gold nanoparticles as highly stable targeted CT contrast agents in cardiovascular diseases. Langmuir 28:10398
116. Peng C, Zheng L, Chen Q, Shen M, Guo R, Wang H, Cao X, Zhang G, Shi X (2012) PEGylated dendrimer-entrapped gold nanoparticles for in vivo blood pool and tumor imaging by computed tomography. Biomaterials 33:1107
117. Wang H, Zheng L, Peng C, Guo R, Shen M, Shi X, Zhang G (2011) Computed tomography imaging of cancer cells using acetylated dendrimer-entrapped gold nanoparticles. Biomaterials 32:2979
118. Reuveni T, Motiei M, Romman Z, Popovtzer A, Popovtzer R (2011) Targeted gold nanoparticles enable molecular CT imaging of cancer: an in vivo study. Int J Nanomedicine 6:2859
119. Chanda N, Kattumuri V, Shukla R, Zambre A, Katti K, Upendran A, Kulkarni RR, Kan P, Fent GM, Casteel SW, Smith CJ, Boote E, Robertson JD, Cutler C, Lever JR, Katti KV, Kannan R (2010) Bombesin functionalized gold nanoparticles show in vitro and in vivo cancer receptor specificity. Proc Natl Acad Sci USA 107:8760
120. Popovtzer R, Agrawal A, Kotov NA, Popovtzer A, Balter J, Carey TE, Kopelman R (2008) Targeted gold nanoparticles enable molecular CT imaging of cancer. Nano Lett 8:4593
121. Aydogan B, Li J, Rajh T, Chaudhary A, Chmura S, Pelizzari C, Wietholt C, Kurtoglu M, Redmond P (2010) AuNP-DG: deoxyglucose-labeled gold nanoparticles as X-ray computed tomography contrast agents for cancer imaging. Mol Imaging Biol 12:463
122. Lijowski M, Caruthers S, Hu G, Zhang H, Scott MJ, Williams T, Erpelding T, Schmieder AH, Kiefer G, Gulyas G, Athey PS, Gaffney PJ, Wickline SA, Lanza GM (2009) High sensitivity: high-resolution SPECT-CT/MR molecular imaging of angiogenesis in the Vx2 model. Invest Radiol 44:15
123. Hainfeld JF, O'Connor MJ, Dilmanian FA, Slatkin DN, Adams DJ, Smilowitz HM (2011) Micro-CT enables microlocalisation and quantification of Her2-targeted gold nanoparticles within tumour regions. Br J Radiol 84:526
124. Kim D, Park S, Lee JH, Jeong YY, Jon S (2007) Antibiofouling polymer-coated gold nanoparticles as a contrast agent for in vivo X-ray computed tomography imaging. J Am Chem Soc 129:7661
125. Xu M, Wang LV (2006) Photoacoustic imaging in biomedicine. Rev Sci Instrum 77:041101
126. Homan K, Mallidi S, Cooley E, Emelianov S (eds) (2011) Combined photoacoustic and ultrasound imaging of metal nanoparticles in vivo. Pan Stanford Publishing Pte. Ltd., Austin
127. Lu W, Huang Q, Ku G, Wen X, Zhou M, Guzatov D, Brecht P, Su R, Oraevsky A, Wang LV, Li C (2010) Photoacoustic imaging of living mouse brain vasculature using hollow gold nanospheres. Biomaterials 31:2617
128. Emelianov SY, Li P-C, O'Donnell M (2009) Photoacoustics for molecular imaging and therapy. Phys Today 62:34
129. Oraevsky AA (2009) Gold and silver nanoparticles as contrast agents for optoacoustic imaging. In: Wang LV (ed) Photoacoustic imaging and spectroscopy. Taylor and Francis, New York
130. Cobley CM, Chen J, Cho EC, Wang LV, Xia Y (2011) Gold nanostructures: a class of multifunctional materials for biomedical applications. Chem Soc Rev 40:44
131. Homberger M, Simon U (2010) On the application potential of gold nanoparticles in nanoelectronics and biomedicine. Phil Trans R Soc A 368:1405

132. Wang Y, Xie X, Wang X, Ku G, Gill KL, O'Neal DP, Stoica G, Wang LV (2004) Photoacoustic tomography of a nanoshell contrast agent in the in vivo rat brain. Nano Lett 4:1689
133. Wang B, Yantsen E, Larson T, Karpiouk AB, Sethuraman S, Su JL, Sokolov K, Emelianov SY (2009) Plasmonic intravascular photoacoustic imaging for detection of macrophages in atherosclerotic plaques. Nano Lett 9:2212
134. Zhang Q, Iwakuma N, Sharma P, Moudgil BM, Wu C, McNeill J, Jiang H, Grobmyer SR (2009) Gold nanoparticles as a contrast agent for in vivo tumor imaging with photoacoustic tomography. Nanotechnology 20:395102
135. Yoon SJ, Mallidi S, Tam JM, Tam JO, Murthy A, Johnston KP, Sokolov KV, Emelianov SY (2010) Utility of biodegradable plasmonic nanoclusters in photoacoustic imaging. Opt Lett 35:3751
136. Agarwal A, Shao X, Rajian JR, Zhang H, Chamberland DL, Kotov NA, Wang X (2011) Dual-mode imaging with radiolabeled gold nanorods. J Biomed Opt 16:051307
137. Olafsson R, Bauer DR, Montilla LG, Witte RS (2010) Real-time, contrast enhanced photoacoustic imaging of cancer in a mouse window chamber. Opt Express 18:18625
138. Chen L-C, Wei C-W, Souris JS, Cheng S-H, Chen C-T, Yang C-S, Li P-C, Lo L-W (2010) Enhanced photoacoustic stability of gold nanorods by silica matrix confinement. J Biomed Opt 15:016010
139. Agarwal A, Huang SW, O'Donnell M, Day KC, Day M, Kotov N, Ashkenazi S (2007) Targeted gold nanorod contrast agent for prostate cancer detection by photoacoustic imaging. J Appl Phys 102:064701
140. Chamberland DL, Agarwal A, Kotov N, Fowlkes JB, Carson PL, Wang X (2008) Photoacoustic tomography of joints aided by an Etanercept-conjugated gold nanoparticle contrast agent—an ex vivo preliminary rat study. Nanotechnology 19:095101
141. Chen Y-S, Frey W, Kim S, Kruizinga P, Homan K, Emelianov S (2011) Silica-coated gold nanorods as photoacoustic signal nanoamplifiers. Nano Lett 11:348
142. Taruttis A, Herzog E, Razansky D, Ntziachristos V (2010) Real-time imaging of cardiovascular dynamics and circulating gold nanorods with multispectral optoacoustic tomography. Opt Express 18:19592
143. Bayer CL, Chen Y-S, Kim S, Mallidi S, Sokolov K, Emelianov S (2011) Multiplex photoacoustic molecular imaging using targeted silica-coated gold nanorods. Biomed Opt Express 2:1828
144. Skrabalak SE, Chen J, Sun Y, Lu X, Au L, Cobley CM, Xia Y (2008) Gold nanocages: synthesis, properties, and applications. Acc Chem Res 41:1587
145. Moon GD, Choi S-W, Cai X, Li W, Cho EC, Jeong U, Wang LV, Xia Y (2011) A new theranostic system based on gold nanocages and phase-change materials with unique features for photoacoustic imaging and controlled release. J Am Chem Soc 133:4762
146. Yang X, Skrabalak SE, Li Z-Y, Xia Y, Wang LV (2007) Photoacoustic tomography of a rat cerebral cortex in vivo with Au nanocages as an optical contrast agent. Nano Lett 7:3798
147. Sokolov K, Follen M, Aaron J, Pavlova I, Malpica A, Lotan R, Richards-Kortum R (2003) Real-time vital optical imaging of precancer using anti-epidermal growth factor receptor antibodies conjugated to gold nanoparticles. Cancer Res 63:1999
148. Aaron J, Nitin N, Travis K, Kumar S, Collier T, Park SY, José-Yacamán M, Coghlan L, Follen M, Richards-Kortum R, Sokolov K (2007) Plasmon resonance coupling of metal nanoparticles for molecular imaging of carcinogenesis in vivo. J Biomed Opt 12:034007
149. Mallidi S, Larson T, Tam J, Joshi PP, Karpiouk A, Sokolov K, Emelianov S (2009) Multiwavelength photoacoustic imaging and plasmon resonance coupling of gold nanoparticles for selective detection of cancer. Nano Lett 9:2825
150. Gutrath BS, Beckmann MF, Buchkremer A, Eckert T, Timper J, Leifert A, Richtering W, Schmitz G, Simon U (2012) Size-dependent multispectral photoacoustic response of solid and hollow gold nanoparticles. Nanotechnology 23:225707

151. Popović Z, Liu W, Chauhan VP, Lee J, Wong C, Greytak AB, Insin N, Nocera DG, Fukumura D, Jain RK, Bawendi MG (2010) A nanoparticle size series for in vivo fluorescence imaging. Angew Chem Int Ed 122:8649
152. Eghtedari M, Oraevsky A, Copland JA, Kotov NA, Conjusteau A, Motamedi M (2007) High sensitivity of in vivo detection of gold nanorods using a laser optoacoustic imaging system. Nano Lett 7:1914
153. Li P-C, Wei C-W, Liao C-K, Chen C-D, Pao K-C, Wang C-RC, Wu Y-N, Shieh D-B (2007) Photoacoustic imaging of multiple targets using gold nanorods. IEEE Trans Ultrason Ferroelectr Freq Control 54:1642
154. Jokerst JV, Cole AJ, Van de Sompel D, Gambhir SS (2012) Gold nanorods for ovarian cancer detection with photoacoustic imaging and resection guidance via raman imaging in living mice. ACS Nano 6:10366
155. Li P-C, Wang C-RC, Shieh D-B, Wei C-W, Liao C-K, Poe C, Jhan S, Ding A-A, Wu Y-N (2008) In vivo photoacoustic molecular imaging with simultaneous multiple selective targeting using antibody-conjugated gold nanorods. Opt Express 16:18605
156. Huang G, Yang S, Yuan Y, Xing D (2011) Combining X-ray and photoacoustics for in vivo tumor imaging with gold nanorods. Appl Phys Lett 99:123701
157. Song KH, Kim C, Cobley CM, Xia Y, Wang LV (2008) Near-infrared gold nanocages as a new class of tracers for photoacoustic sentinel lymph node mapping on a rat model. Nano Lett 9:183
158. Bao C, Beziere N, del Pino P, Pelaz B, Estrada G, Tian F, Ntziachristos V, de la Fuente JM, Cui D (2013) Gold nanoprisms as optoacoustic signal nanoamplifiers for in vivo bioimaging of gastrointestinal cancers. Small 9:68
159. Orendorff CJ, Sau TK, Murphy CJ (2006) Shape-dependent plasmon-resonant gold nanoparticles. Small 2:636
160. El-Sayed MA (2001) Some interesting properties of metals confined in time and nanometer space of different shapes. Acc Chem Res 34:257
161. Alkilany AM, Thompson LB, Boulos SP, Sisco PN, Murphy CJ (2012) Gold nanorods: their potential for photothermal therapeutics and drug delivery, tempered by the complexity of their biological interactions. Adv Drug Deliv Rev 64:190
162. Kreibig U, Vollmer M (1995) Optical properties of metal clusters. Springer, Berlin
163. Skirtach AG, Dejugnat C, Braun D, Susha AS, Rogach AL, Parak WJ, Möhwald H, Sukhorukov GB (2005) The role of metal nanoparticles in remote release of encapsulated materials. Nano Lett 5:1371
164. Chou C-H, Chen C-D, Wang CRC (2005) Highly efficient, wavelength-tunable, gold nanoparticle based optothermal nanoconvertors. J Phys Chem B 109:11135
165. Pissuwan D, Valenzuela SM, Cortie MB (2006) Therapeutic possibilities of plasmonically heated gold nanoparticles. Trends Biotechnol 24:62
166. Pitsillides CM, Joe EK, Wei X, Anderson RR, Lin CP (2003) Selective cell targeting with light-absorbing microparticles and nanoparticles. Biophys J 84:4023
167. Nam J, Won N, Jin H, Chung H, Kim S (2009) pH-Induced aggregation of gold nanoparticles for photothermal cancer therapy. J Am Chem Soc 131:13639
168. Huang X, El-Sayed IH, Qian W, El-Sayed MA (2006) Cancer cell imaging and photothermal therapy in the near-infrared region by using gold nanorods. J Am Chem Soc 128:2115
169. Chen J, McLellan JM, Siekkinen A, Xiong Y, Li Z-Y, Xia Y (2006) Facile synthesis of gold–silver nanocages with controllable pores on the surface. J Am Chem Soc 128:14776
170. Chen J, Glaus C, Laforest R, Zhang Q, Yang M, Gidding M, Welch MJ, Xia Y (2010) Gold nanocages as photothermal transducers for cancer treatment. Small 6:811
171. Au L, Zheng D, Zhou F, Li Z-Y, Li X, Xia Y (2008) A quantitative study on the photothermal effect of immuno gold nanocages targeted to breast cancer cells. ACS Nano 2:1645
172. Hirsch LR, Stafford RJ, Bankson JA, Sershen SR, Rivera B, Price RE, Hazle JD, Halas NJ, West JL (2003) Nanoshell-mediated near-infrared thermal therapy of tumors under magnetic resonance guidance. Proc Natl Acad Sci USA 100:13549

173. Lal S, Clare SE, Halas NJ (2008) Nanoshell-enabled photothermal cancer therapy: impending clinical impact. Acc Chem Res 41:1842
174. O'Neal DP, Hirsch LR, Halas NJ, Payne JD, West JL (2004) Photo-thermal tumor ablation in mice using near infrared-absorbing nanoparticles. Cancer Lett 209:171
175. Loo C, Lowery A, Halas NJ, West J, Drezek R (2005) Immunotargeted nanoshells for integrated cancer imaging and therapy. Nano Lett 5:709
176. Day ES, Zhang L, Thompson PA, Zawaski JA, Kaffes CC, Gaber MW, Blaney SM, West JL (2012) Vascular-targeted photothermal therapy of an orthotopic murine glioma model. Nanomedicine 7:1133
177. Zhou HS, Honma I, Komiyama H, Haus JW (1994) Controlled synthesis and quantum-size effect in gold-coated nanoparticles. Phys Rev B 50:12052
178. Gobin AM, Watkins EM, Quevedo E, Colvin VL, West JL (2010) Near-infrared-resonant gold/gold sulfide nanoparticles as a photothermal cancer therapeutic agent. Small 6:745
179. Hu M, Chen J, Li Z-Y, Au L, Hartland GV, Li X, Marquez M, Xia Y (2006) Gold nanostructures: engineering their plasmonic properties for biomedical applications. Chem Soc Rev 35:1084
180. Murphy CJ, Sau TK, Gole AM, Orendorff CJ, Gao J, Gou L, Hunyadi SE, Li T (2005) Anisotropic metal nanoparticles: synthesis, assembly, and optical applications. J Phys Chem B 109:13857
181. Huang H-C, Yang Y, Nanda A, Koria P, Rege K (2011) Synergistic administration of photothermal therapy and chemotherapy to cancer cells using polypeptide-based degradable plasmonic matrices. Nanomedicine 6:459
182. Norman RS, Stone JW, Gole A, Murphy CJ, Sabo-Attwood TL (2007) Targeted photothermal lysis of the pathogenic bacteria, *Pseudomonas aeruginosa*, with gold nanorods. Nano Lett 8:302
183. Dickerson EB, Dreaden EC, Huang X, El-Sayed IH, Chu H, Pushpanketh S, McDonald JF, El-Sayed MA (2008) Gold nanorod assisted near-infrared plasmonic photothermal therapy (PPTT) of squamous cell carcinoma in mice. Cancer Lett 269:57
184. Choi WI, Kim J-Y, Kang C, Byeon CC, Kim YH, Tae G (2011) Tumor regression in vivo by photothermal therapy based on gold-nanorod-loaded. Functional Nanocarriers. ACS Nano 5:1995
185. Jain PK, Lee KS, El-Sayed IH, El-Sayed MA (2006) Calculated absorption and scattering properties of gold nanoparticles of different size, shape, and composition: applications in biological imaging and biomedicine. J Phys Chem B 110:7238
186. Huang X, Jain PK, El-Sayed IH, El-Sayed MA (2006) Determination of the minimum temperature required for selective photothermal destruction of cancer cells with the use of immunotargeted gold nanoparticles. Photochem Photobiol 82:412
187. von Maltzahn G, Park J-H, Agrawal A, Bandaru NK, Das SK, Sailor MJ, Bhatia SN (2009) Computationally guided photothermal tumor therapy using long-circulating gold nanorod antennas. Cancer Res 69:3892
188. Dreaden EC, Mackey MA, Huang X, Kang B, El-Sayed MA (2011) Beating cancer in multiple ways using nanogold. Chem Soc Rev 40:3391
189. Wood BJ, Ramkaransingh JR, Fojo T, Walther MM, Libutti SK (2002) Percutaneous tumor ablation with radiofrequency. Cancer 94:443
190. Minelli C, Lowe SB, Stevens MM (2010) Engineering nanocomposite materials for cancer therapy. Small 6:2336
191. Arvizo R, Bhattacharya R, Mukherjee P (2010) Gold nanoparticles: opportunities and challenges in nanomedicine. Expert Opin Drug Deliv 7:753
192. Hainfeld JF, Slatkin DN, Smilowitz HM (2004) The use of gold nanoparticles to enhance radiotherapy in mice. Phys Med Biol 49:N309
193. Pradhan AK, Nahar SN, Montenegro M, Yu Y, Zhang HL, Sur C, Mrozik M, Pitzer RM (2009) Resonant X-ray enhancement of the auger effect in high-Z atoms, molecules, and nanoparticles: potential biomedical applications. J Phys Chem A 113:12356

194. Kong T, Zeng J, Wang X, Yang X, Yang J, McQuarrie S, McEwan A, Roa W, Chen J, Xing JZ (2008) Enhancement of radiation cytotoxicity in breast-cancer cells by localized attachment of gold nanoparticles. Small 4:1537
195. Chang M-Y, Shiau A-L, Chen Y-H, Chang C-J, Chen HHW, Wu C-L (2008) Increased apoptotic potential and dose-enhancing effect of gold nanoparticles in combination with single-dose clinical electron beams on tumor-bearing mice. Cancer Sci 99:1479
196. Zhang X, Xing JZ, Chen J, Ko L, Amanie J, Gulavita S, Pervez N, Yee D, Moore R, Roa W (2008) Enhanced radiation sensitivity in prostate cancer by gold-nanoparticles. Clin Invest Med 31:E160
197. Cho SH (2005) Estimation of tumour dose enhancement due to gold nanoparticles during typical radiation treatments: a preliminary Monte Carlo study. Phys Med Biol 50:N163
198. Cho SH, Jones BL, Krishnan S (2009) The dosimetric feasibility of gold nanoparticle-aided radiation therapy (GNRT) via brachytherapy using low-energy gamma-/X-ray sources. Phys Med Biol 54:4889
199. Roeske JC, Nuñez L, Hoggarth M, Labay E, Weichselbaum RR (2007) Characterization of the theorectical radiation dose enhancement from nanoparticles. Technol Cancer Res Treat 6:395
200. Brun E, Sanche L, Sicard-Roselli C (2009) Parameters governing gold nanoparticle X-ray radiosensitization of DNA in solution. Colloids Surf B Biointerfaces 72:128
201. Foley EA, Carter JD, Shan F, Guo T (2005) Enhanced relaxation of nanoparticle-bound supercoiled DNA in X-ray radiation. Chem Commun 3192
202. Butterworth KT, Wyer JA, Brennan-Fournet M, Latimer CJ, Shah MB, Currell FJ, Hirst DG (2008) Variation of strand break yield for plasmid DNA irradiated with high-Z metal nanoparticles. Radiat Res 170:381
203. Rahman WN, Bishara N, Ackerly T, He CF, Jackson P, Wong C, Davidson R, Geso M (2009) Enhancement of radiation effects by gold nanoparticles for superficial radiation therapy. Nanomed Nanotechnol Biol Med 5:136
204. Liu C-J, Wang C-H, Chen S-T, Chen H-H, Leng W-H, Chien C-C, Wang C-L, Kempson IM, Hwu Y, Lai T-C, Hsiao M, Yang C-S, Chen Y-J, Margaritondo G (2010) Enhancement of cell radiation sensitivity by pegylated gold nanoparticles. Phys Med Biol 55:931
205. Roa W, Zhang X, Guo L, Shaw A, Hu X, Xiong Y, Gulavita S, Patel S, Sun X, Chen J, Moore R, Xing JZ (2009) Gold nanoparticle sensitize radiotherapy of prostate cancer cells by regulation of the cell cycle. Nanotechnology 20:375101
206. Polf JC, Bronk LF, Driessen WHP, Arap W, Pasqualini R, Gillin M (2011) Enhanced relative biological effectiveness of proton radiotherapy in tumor cells with internalized gold nanoparticles. Appl Phys Lett 98:193702
207. Hainfeld JF, Dilmanian FA, Zhong Z, Slatkin DN, Kalef-Ezra JA, Smilowitz HM (2010) Gold nanoparticles enhance the radiation therapy of a murine squamous cell carcinoma. Phys Med Biol 55:3045
208. Zheng Y, Sanche L (2009) Gold nanoparticles enhance DNA damage induced by anti-cancer drugs and radiation. Radiat Res 172:114
209. Leung MKK, Chow JCL, Chithrani BD, Lee MJG, Oms B, Jaffray DA (2011) Irradiation of gold nanoparticles by X-rays: Monte Carlo simulation of dose enhancements and the spatial properties of the secondary electrons production. Med Phys 38:624
210. Carter JD, Cheng NN, Qu Y, Suarez GD, Guo T (2007) Nanoscale energy deposition by X-ray absorbing nanostructures. J Phys Chem B 111:11622
211. Zhang S, Gao J, Buchholz T, Wang Z, Salehpour M, Drezek R, Yu T-K (2009) Quantifying tumor-selective radiation dose enhancements using gold nanoparticles: a Monte Carlo simulation study. Biomed Microdevices 11:925
212. Montenegro M, Nahar SN, Pradhan AK, Huang K, Yu Y (2009) Monte Carlo simulations and atomic calculations for Auger processes in biomedical nanotheranostics. J Phys Chem A 113:12364

213. Jones BL, Krishnan S, Cho SH (2010) Estimation of microscopic dose enhancement factor around gold nanoparticles by Monte Carlo calculations. Med Phys 37:3809
214. Sperling RA, Rivera Gil P, Zhang F, Zanella M, Parak WJ (2008) Biological applications of gold nanoparticles. Chem Soc Rev 37:1896
215. Angelatos AS, Radt B, Caruso F (2005) Light-responsive polyelectrolyte/gold nanoparticle microcapsules. J Phys Chem B 109:3071
216. Skirtach AG, Muñoz Javier A, Kreft O, Köhler K, Piera Alberola A, Möhwald H, Parak WJ, Sukhorukov GB (2006) Laser-induced release of encapsulated materials inside living cells. Angew Chem Int Ed 45:4612
217. Vauthier C, Labarre D, Ponchel G (2007) Design aspects of poly(alkylcyanoacrylate) nanoparticles for drug delivery. J Drug Target 15:641
218. Sauer AM, Schlossbauer A, Ruthardt N, Cauda V, Bein T, Bräuchle C (2010) Role of endosomal escape for disulfide-based drug delivery from colloidal mesoporous silica evaluated by live-cell imaging. Nano Lett 10:3684
219. Schloßbauer A, Sauer AM, Cauda V, Schmidt A, Engelke H, Rothbauer U, Zolghadr K, Leonhardt H, Bräuchle C, Bein T (2012) Cascaded photoinduced drug delivery to cells from multifunctional core–shell mesoporous silica. Adv Healthcare Mater 1:316
220. Ruthardt N, Lamb DC, Bräuchle C (2011) Single-particle tracking as a quantitative microscopy-based approach to unravel cell entry mechanisms of viruses and pharmaceutical nanoparticles. Mol Ther 19:1199
221. Gaitzsch J, Appelhans D, Voit B (2012) Responsive polymersome. Nachr Chem 60:1176
222. Brinkhuis RP, Rutjes FPJT, van Hest JCM (2011) Polymeric vesicles in biomedical applications. Polym Chem 2:1449

Struct Bond (2014) 161: 243–278
DOI: 10.1007/430_2013_136

Published online: 7 December 2014

Gold Clusters in the Gas Phase

Alex P. Woodham and André Fielicke

Abstract Gold clusters exhibit strong size and charge state dependent variations in their properties. This is demonstrated by significant changes in their geometric structures and also in their chemical properties. Here we focus on clusters containing up to about 20 gold atoms and briefly review their structural evolution emphasising the role of isomerism and structural fluxionality. The discussion of chemical properties is limited to the interaction of gold clusters with molecular oxygen and carbon monoxide, separately, and their interaction in CO/O_2 co-adsorbates on gold clusters eventually leading to CO oxidation. Whilst highlighting results obtained using different experimental approaches, special attention is given to the insights obtained using infrared multiple photon dissociation (IR-MPD) spectroscopy.

Keywords Carbon monoxide · Catalysis · Gold clusters · Oxygen · Reactions · Structure · Vibrational spectroscopy

Contents

A.P. Woodham and A. Fielicke (✉)
Institut für Optik und Atomare Physik, Technische Universität Berlin, Hardenbergstr 36, D-10623 Berlin, Germany

Fritz-Haber-Institut der Max-Planck-Gesellschaft, Faradayweg 4-6, D-14195 Berlin, Germany
e-mail: fielicke@physik.tu-berlin.de

1 Introduction

When investigating supported gold clusters, either on a perfectly crystalline surface or a more "real" sample, the presence of the substrate represents a significant obstacle to accurate characterisation. Whilst techniques do exist to overcome these difficulties, as have been detailed elsewhere in this review series, it is often advantageous to remove the clusters from the support and instead investigate them as free species in the gas phase.

Such a transition into the gas phase has several key advantages; firstly size selectivity is comparatively trivial and so property changes of the clusters can be investigated on an atom-by-atom basis. Similarly, due to the isolation afforded by working in the gas phase, ionic species can be interrogated allowing for the effects of the charge state of the cluster to be directly probed. The insights into charge state effects can be related to known charging phenomena of clusters adsorbed to surfaces [1–3]. It also provides an additional tool to probe the interplay of the electronic and geometric structures and their effects on the reactivity of the clusters, something which is known to be critically important for gold. Lastly, the transition to the gas phase opens up a multitude of experimental characterisation techniques which are well established and understood.

Gas-phase studies have already had a marked impact on the understanding of the structures of the gold clusters. For example, it has been found that small anionic gold clusters adopt a fascinating array of structural motifs, from planar structures which persist until much larger than expected cluster sizes [4–7] through to hollow cage motifs [8] and finally tetrahedral structures – like the Au_{20} pyramid [9, 10]. Such structural assignments are only possible by comparison of the experimental data with theoretical predictions and here again clusters in the gas phase serve an important role: They are simplified model systems against which quantum chemical approaches can be tested for their suitability before application to more complex systems, for example, particles interacting with a substrate.

In addition to these fundamental investigations of the bare cluster structures, the complexes with ligands at well-defined, variable coverage, achieved through sequential addition, can also be studied. This allows for insights into reactive intermediates [11–15] and even entire catalytic reaction cycles to be mapped out [16, 17].

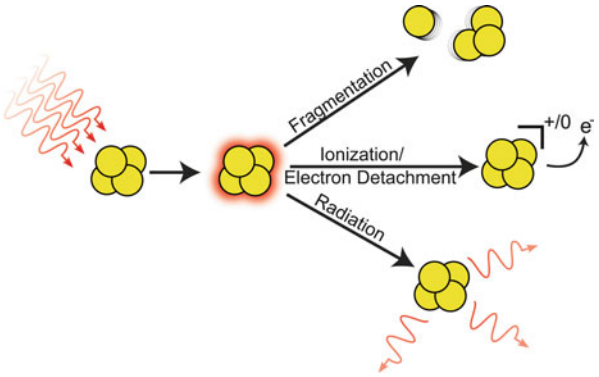

Fig. 1 Schematic for energy loss pathways for an optically excited cluster

These advantages, however, are not without their cost. Gas-phase clusters are usually not produced size-selectively, but the aggregation process instead leads to a broad distribution of sizes. Thus, in most cases, experimental characterisation needs to be coupled with mass spectrometric size determination or selection in order to assign properties, e.g. spectral characteristics, to a single species or cluster size. Additionally, in the case of spectroscopy, the number densities typically achievable are too low for Beer–Lambert-type absorption measurements. These issues can be addressed in a variety of ways, for example, applying non-optical techniques, such as electron diffraction or ion mobility, which are more direct measures of a cluster's geometric structure and sensitive to smaller quantities of substrate. Alternatively, action spectroscopy can be employed where, rather than looking for the effects of matter upon light, one looks for the effects of the light upon the matter. In this way it is possible to observe processes which are free from the background signal of the probing laser pulse. Optical spectroscopy has the advantage over the more direct methods that whilst it can provide structural information (e.g. through vibrational spectroscopy) it also gives access to information concerning the electronic structure of the clusters as well (via UV–vis spectroscopies). Figure 1 shows the energy loss mechanisms available to an isolated cluster which has been excited by photon absorption and which can be exploited as markers for action spectroscopy. Of these three decay paths, only the fragmentation and ionisation or electron detachment are regularly employed in gold cluster spectroscopy.

In this review we provide an overview of some of the key developments in the gas-phase studies of gold clusters, starting with a brief outline of experimental techniques; we then highlight the structural properties of gold clusters in different charge states before finally discussing the interaction of gold clusters with O_2 and CO as prototypical reactants in the oxidation reactions which gold nanoparticles are famous for. The structural information on charged gold clusters as obtained from trapped ion electron diffraction (TIED) and ion mobility experiments have recently been reviewed [18] as have the developments from anion photo electron spectroscopy (PES) [19, 20]. Finally, the chemistry of ionic gold clusters (and their binary silver–gold and pure silver analogues) has also been discussed elsewhere [21].

These reviews focus on the charged gold clusters and surprisingly large differences in, for example, their geometric shapes and the size for the 2D–3D transition have been found between the charge states. Such a dramatic influence of charge state raises intriguing questions concerning the intermediate case, that of the neutral clusters, which shall be discussed in more detail here.

2 Experimental Methods

2.1 Mass Spectrometry

Conceptually one of the simplest experimental techniques applied to clusters, and indeed the basis of most gas-phase studies, is mass spectrometry. Very different techniques for mass analysis have been applied to separate and/or trap charged clusters, for example, classical electric or magnetic sector-field instruments, time-of-flight measurements, quadrupole mass filters, and Paul or Penning traps. Mass spectrometry is indispensable in the analysis and control of cluster formation in cluster sources where typically a supersaturated atomic vapour aggregates into a distribution of cluster sizes. By now, this field of mass spectrometric characterisation of clusters is very well established and so we shall refrain from discussing further technical details here. It should be noted that mass spectrometry requires the presence of charged clusters; however, by employing suitable ionisation techniques prior to mass analysis, information on the neutral clusters may also be obtained. Despite its conceptual simplicity, a great deal of information can be extracted from the mass analysis of a cluster distribution, concerning relative stabilities of different clusters (cf. “magic” sizes) and the reactivity of the clusters.

In addition to this, kinetic reaction studies can also be performed, i.e. analysing the products formed with changing reaction times or reactant partial pressure. Knowledge of the kinetics allows for the individual steps in the reaction paths to be modelled and ultimately can lead to the elucidation of complete reaction mechanisms [16, 17].

2.2 Trapped Ion Electron Diffraction

One approach to investigating cluster structures is trapped ion electron diffraction (TIED) [22, 23]. In TIED, an electron beam of several tens of keV is directed at a sample of size-selected clusters held in an ion trap. The electrons are diffracted by the atoms and the resulting diffraction pattern is recorded, typically with a CCD camera. The radial variance in the electron intensity pattern is then compared with simulated curves, and structural assignment is made based upon the best agreement between theory and experiment. Experimentally the cluster sizes which can be

investigated are limited at the lower end by the atomic scattering intensity and at the high end by the mass resolution of the experiment. In practice, this leads to a size range of $n = 10$–200 for Au_n being experimentally tractable [18] and, owing to the trap requirements, is limited to charged clusters. Further, as the high energy electron beam can induce ionisation and fragmentation, often anionic species are preferred as they result in neutral products, which are then lost from the trap and so do not complicate the recorded radial distribution function.

2.3 Ion Mobility

Another non-optical approach to structural determination of clusters is the measurement of their collisional cross sections via ion mobility [24]. Charged clusters are injected into a drift cell filled with a pressure of inert gas (typically He) and an electrostatic potential gradient applied across it. The ionic clusters are then guided towards the far end of the drift cell by this potential and their arrival times are measured. Those clusters with a larger cross section experience more collisions with the buffer gas and thus a greater resistance to their motion, resulting in a longer drift time. Again candidate structures obtained from quantum chemical calculations can be used to generate theoretical collisional cross sections which are compared with experiment, resulting in structural assignment. Unlike TIED, ion mobility measurements are not limited at a smaller size but differences in collisional cross sections for structural isomers become increasingly marginal as clusters become larger, effectively limiting the upper size which can be investigated. Obviously as the clusters are accelerated with an electrostatic interaction, this also can only be applied to charged species.

2.4 Action Spectroscopy

Optical spectra can be recorded by using action spectroscopy to overcome the limitations of transient absorption (Beer–Lambert type) spectroscopy. As has been mentioned, action spectroscopy reverses the traditional paradigm of looking at the effects of matter on light by looking for changes in the clusters themselves as the marker for optical absorption. By performing these spectroscopies in the UV–IR frequency range, one is able to directly probe both the geometric (IR) and electronic (UV–vis) structures of the clusters.

2.4.1 Anion Photoelectron Spectroscopy

For metal clusters, one of the most commonly applied action spectroscopies is anion PES. In this variant of photoemission spectroscopy [25], the anionic clusters

are mass selected, allowing for insights into the evolution of the internal electronic structure as the clusters grow atom-by-atom [26]. Typically, UV–vis photons are used to detach electrons from the anionic clusters, and the resulting kinetic energy distribution of the detached electrons is recorded. The observed distribution is governed by the energy balance equation:

$$KE_{e-} = h\nu - BE + E_{\mathrm{int,I}} - E_{\mathrm{int,F}} \quad (1)$$

where $KE_{\mathrm{e}-}$ is the electron kinetic energy, $h\nu$ the photon energy, BE the binding energy of the electron (=−Electron Affinity (EA)) and E_{int} is the combined internal electronic, vibrational and rotational energy of the initial (I) and final (F) states, respectively. When starting with an anionic cluster in its ground state, i.e. $E_{int,\mathrm{I}}$ equals 0, the resulting distribution for the kinetic energy of the electrons reflects the internal energy contained within the final structure, with the fastest electrons corresponding to the EA of the cluster. Alternatively electron detachment may occur from electronically or vibrationally excited states of the anion giving even more detailed information on the electronic and geometric structures of the observed clusters. For example, the observation of vibrational hot bands provides access to the vibrational constants of the anionic state. It should be noted that, as with all spectroscopies, there are selection rules which govern the observable transitions and in the case of anion photoelectron spectroscopy, the observed transitions are governed by the Franck–Condon factor [27].

Typically photon energies far in excess of the EA (UV photons) are used and the resulting spectra are compared to the calculated EAs, excitation energies, and/or electronic density of states from trial structures, allowing for structural assignment of the anionic structure. In such a regime, the effects of the vibrational energy can mostly be ignored as $E_{\mathrm{elec}} \gg E_{\mathrm{vib}}$. An alternative scheme, utilising the principles of ZEKE and SEVI [27] where photons much closer to threshold detachment are used, allows for greater absolute energy resolution and thus vibrational progressions are more regularly recorded and lower frequency vibrational progressions are theoretically accessible. Such vibrational information may also then be compared with theoretical modelling allowing for structural assignment [28].

There are, however, some considerations which must be borne in mind when using anion PES. Firstly, whilst the technique is in principle sensitive to both the anionic and neutral states of the cluster, because the photodetachment is considered to be a prompt process, that is, fast on the timescale of nuclear motion, it actually gives information on the neutral cluster in the geometry of the anion. This can have consequences when concluding about neutral cluster properties based on PES results, particularly because the structures of gold clusters can vary significantly with the charge state [18, 29]. Secondly, the vibrational selection rules for anion PES are such that generally only the transitions between totally symmetric vibrations are allowed and this somewhat limits the utility of vibrationally resolved anion PES.

2.4.2 UV–vis Dissociation

An alternative method using ultraviolet/visible (UV–vis) photons is to induce fragmentation, typically of complexes formed between the cluster of interest and a rare-gas "tag". Through monitoring of the mass spectrometric intensities, changes induced by the UV–vis photons allow for the electronic excitation spectrum of the clusters to be recorded, which again may be compared to theory and leads to a structural assignment. For a truly accurate understanding, one needs knowledge of both the ground-state and the excited-state properties, which are often computationally very demanding to calculate [30–32]. Perhaps owing to the additional computational difficulties associated with electronic spectroscopies, the number of investigations utilising this technique for gold clusters is somewhat limited [31–35]. These investigations reveal the strong relativistic effects in gold clusters, borne out in strong *s-d* hybridisation, and are given as the cause for both the relatively complicated optical spectra observed and the failure of the plasmon model, as extended from bulk properties, in predicting the observed spectra. An alternative approach to such spectra is the investigation of mass-selected neutralised clusters in rare-gas matrices [36].

A further modification to this dissociation spectroscopy is to record the resultant kinetic energy distributions of the fragments using the VMI technique. This allows for more detailed information concerning the excited states of the clusters and the energy partitioning between the different fragments to be elucidated. Currently, however, this technique has been limited in its application to the gold–rare-gas heterodimers [37, 38].

2.4.3 Infrared Multiple Photon Dissociation (IR-MPD)

Whilst UV–vis excitation probes electronic transitions, vibrational transitions can similarly be excited by using infrared light. The vibrational spectrum of a cluster is a sensitive fingerprint of its geometric structure. As the energy of an individual photon in the mid and far IR is significantly reduced compared to that in the UV–vis range, inducing ionisation, electron detachment or fragmentation usually requires absorption of very many IR photons by a single cluster [39–41]. One way of reducing the number of photons needed to induce a mass spectrometrically detectable action is the application of the "messenger tagging" method. In this variant, an atom or molecule is weakly bound to the surface of the cluster, introducing a readily fragmentable bond into the system. Thus when sufficient energy is deposited into the cluster via IR absorption, this bond breaks resulting in a change in mass, serving as a "messenger" for the absorption. Depending on the messenger and the frequency of the probed vibrational mode, the binding energy may be sufficiently low to be sensitive to the absorption of single IR photons.

For many metal clusters, the vibrational fundamentals lie below 400 cm^{-1} (~50 meV). Despite the weak bonding in the cluster system, fragmentation of

messenger complexes still usually requires absorption of multiple photons. This, coupled with the low IR absorption cross sections of metal clusters, necessitates the use of an intense, widely tunable IR source. At present, the only method for generating sufficiently intense IR pulses at these wavelengths is to use IR Free Electron Lasers (FELs), and so far all these experiments on gas-phase clusters have been performed at the Free Electron Laser for Infrared eXperiments facility (FELIX) in the Netherlands [42]. To date, FEL-based IR-MPD has been applied to investigate the structures of a wide range of transition metal clusters; more explicit details of the experiment can be found elsewhere [43, 44].

In addition to using rare-gas atoms as messengers for the IR absorption, it is possible to instead rely on the dissociation of a complex with a ligand of chemical relevance, e.g. CO or O_2 as will be discussed later on. This has the further advantage of introducing a stronger (typically several orders of magnitude) chromophore into the cluster, facilitating the IR-MPD process.

3 Structure and Isomerism

3.1 Ionic Species

Initial experimental investigations into the structures of free, bare gold clusters focused on the ionic species and a summary of the structures identified based on ion mobility and electron diffraction studies [18] is reproduced in Fig. 2. The small gold clusters remain two-dimensional until, at a certain critical size, they begin to form double-layered or three-dimensional structures (as opposed to polyhedral motifs). This structural pattern has been attributed to the relativistic effect leading to a strong *s-d* hybridisation (as was also observed from UV–vis spectroscopy, see earlier) [45–47]. It is interesting to note the substantial differences between the structures of the anions and cations – the anions remaining 2D until much larger cluster sizes than their cationic counterparts. Whilst this is the most prominent structural deviation, other significant differences can also be observed between the larger clusters. Figure 2 also clearly demonstrates the existence of structural isomers for some of the cluster sizes. Recently more cases of structural isomerism or fluxionality have been found and the implications of this for the observed reactivities have been noted.

The first direct evidence for structural isomerism in gold clusters came from the ion drift studies of both the cations and anions [4, 48, 49]. For the anions, a bimodal distribution was observed in the arrival time of Au_{12}^- which was interpreted as due to two isomers being present, one 2D and one 3D, indicating Au_{12}^- as the critical size for this transition. The presence of both a 2D and a 3D isomer for Au_{12}^- has been confirmed from multiple experiments [4, 7, 50]. The critical size for the 2D to 3D transitions, however, remains a contentious issue because of discrepancies with the corresponding theoretical calculations [51–55]. The presence of isomers and

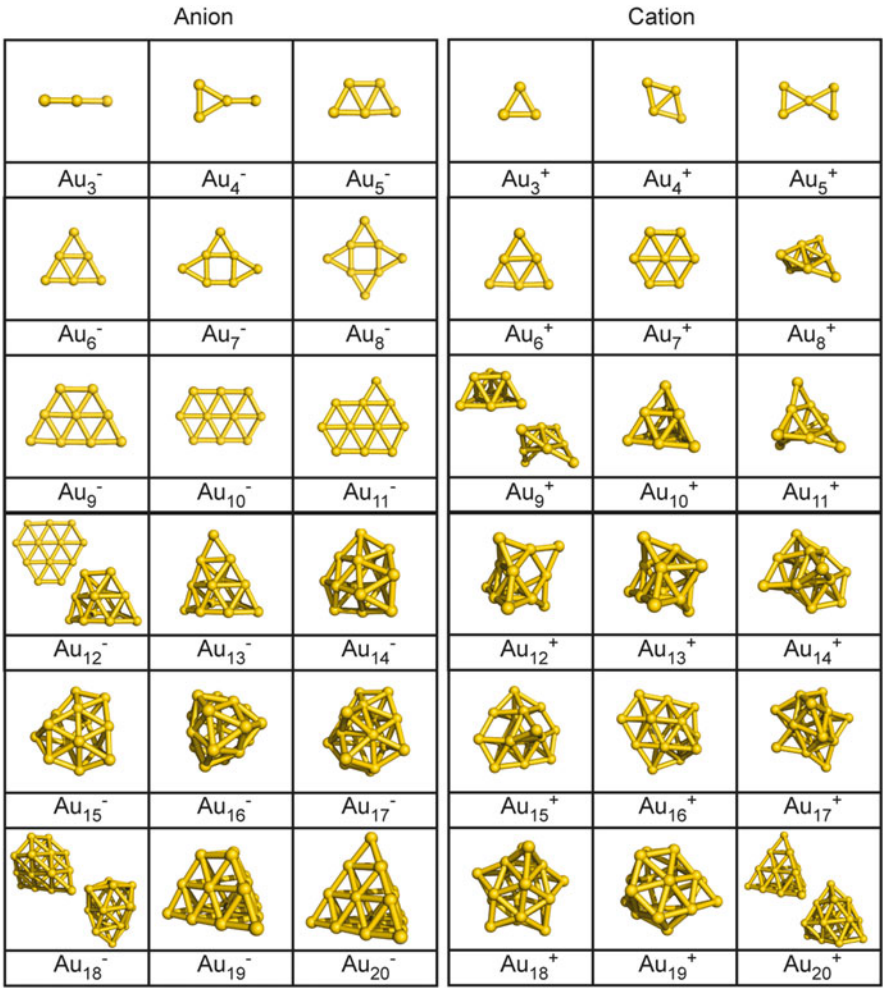

Fig. 2 Structures of anionic and cationic gold clusters, structures are taken from [18]

their interconversion was also observed for Au_9^+ [48]. When the ion drift experiment was performed at reduced temperatures, what had initially been a single feature in the arrival time distribution resolved into two separate peaks, as shown in Fig. 3. Such behaviour indicates that the cluster is undergoing rapid isomerisation between two structural forms at elevated temperatures, and upon cooling the barrier to inter-conversion becomes insurmountable and so the isomers become trapped.

Further insights into the importance of isomerism have been obtained from anion PES. For example, in the photoelectron spectrum of Au_{10}^-, several weaker features at low electron-binding energy (BE) were observed and ultimately assigned to three additional isomers [56]. In this particular case, the separation was achieved by exploiting the cluster's varying reactivity towards molecular oxygen allowing for

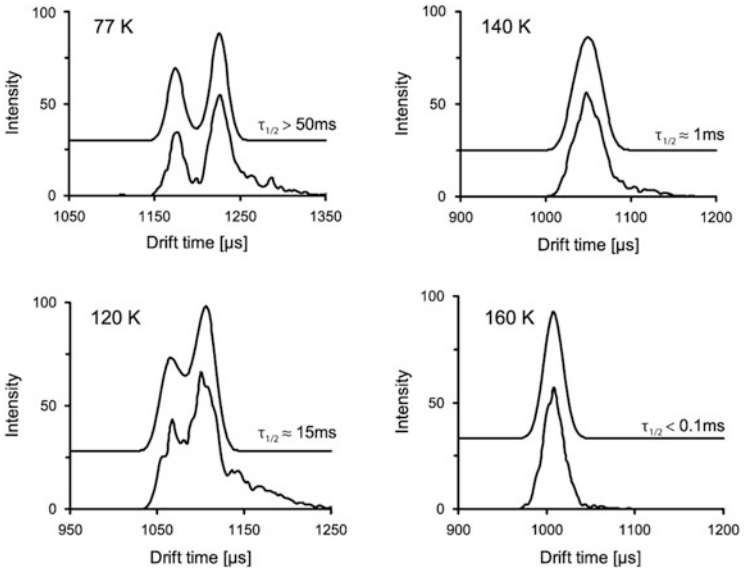

Fig. 3 Arrival time distribution for Au_9^+ as a function of drift cell temperature. At low temperature, two isomers are detected, whilst at elevated temperature their rapid inter-conversion leads to only a single peak in the drift-time distribution. See Fig. 2 for the structures of the two isomers. Reprinted with permission from Weis et al. [48]. Copyright 2002, AIP publishing LLC

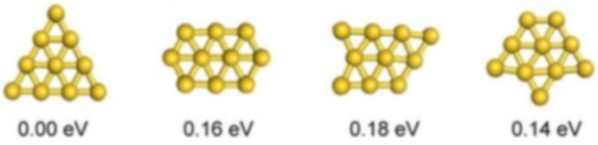

Fig. 4 The four isomers of Au_{10}^- detected using anion PES and their relative energies to the ground-state D_{3h} structure

the isomers to be removed from the molecular beam to leave only the ground-state species (which is unreactive towards O_2). The four isomeric structures and their relative energies are given in Fig. 4.

Similar investigations for the gold clusters Au_7^-–Au_{18}^- have also led to several isomers being identified, either by exploiting their different reactivity with O_2 and Ar or through isoelectronic substitution. Ar binding is stronger to planar surfaces (see later), and thus Ar tagging is particularly sensitive when there is a significant change in the geometrical structure between the two competing isomers, e.g. 2D vs. 3D or cage vs. non-cage (cf. the planar faces of the pyramidal structures) [10, 57]. Similarly the use of O_2 as a reactive tag is limited because the odd-numbered clusters are completely unreactive with O_2 (see later). This led to the slightly more elaborate technique of isoelectronic substitution, i.e. exchanging a gold atom with a silver or copper atom. For example, with Au_7^- and Au_8^-, such a

substitution does not greatly affect the geometric structure, but does alter the relative energies, and thus populations, of the different isomers allowing for the observed PES to be deconvoluted into the contributions arising from the different isomeric forms [57–59].

This wealth of information concerning the isomers of the anionic clusters is not matched for the cationic species. The apparent lack of structural isomerism for most cationic gold clusters may be an artefact of the methodology used to probe their structures. Specifically, because the second ionisation energies of gold clusters are prohibitively high for tabletop laser systems, a direct analogue to anion PES is not possible, and instead the majority of the structural information comes from TIED and ion drift measurements. The latter is not very sensitive to small structural changes which do not alter the collision cross section significantly, whilst TIED requires the presence of a considerable fraction of the isomer in order to resolve the different structures. Furthermore, these techniques occur on a timescale much longer than anion PES (which is almost always assumed to be a prompt photoemission process), and so if the structural isomerism is connected with rapid inter-conversion (fluxionality), it may be averaged over in the experiments.

3.2 Neutrals

Through the efforts of the above research relying on TIED, ion mobility measurements and anion PES, a comprehensive understanding about the structures of the charged gold clusters has been achieved. Comparatively little experimental work, however, has been done on the neutral clusters. The origin of this discrepancy is eminently clear: Experimentally the above techniques do not work, nor are they easily adapted to work for neutral systems. All of them require the interaction of the charge on the particles with external fields to allow for the clusters from the nascent distribution to be resolved by size, either in time or space. Once separated in this way, they can then be spectroscopically addressed on a species by species basis.

Dissociation spectroscopy, as described above, can be performed on a non-mass-selected molecular beam containing charged *and* neutral species. As the irradiation of the cluster beam is done *prior* to mass analysis, it is possible to add an ionisation step after the spectroscopic probe, allowing for the recording of mass-specific spectra for the neutral species. Figures 5 and 6 show far-infrared spectra of Au_7, Au_{19} and Au_{20} measured with krypton as a messenger [29]. Au_nKr complexes are formed at 100 K by seeding the He gas with a few per cent of Kr and they are then interrogated using the IR-MPD technique as outlined in the methods section. Ionisation is performed using 7.9 eV photons (F_2 laser). Structural assignments

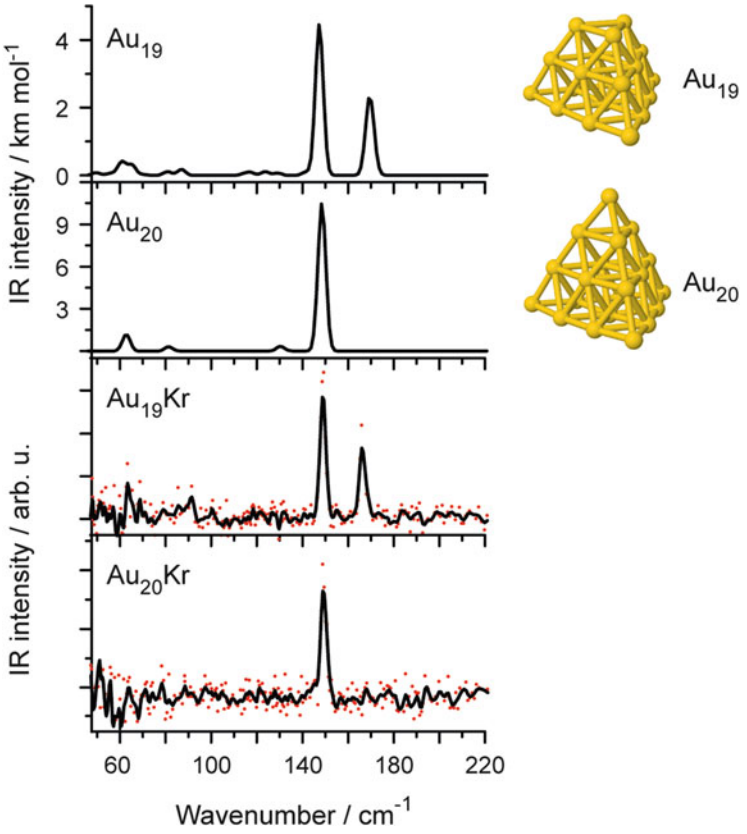

Fig. 5 Experimental IR-MPD spectra of $Au_{19}Kr$ and $Au_{20}Kr$ and calculated far-IR spectra for Au_{19} and Au_{20}. For details, see [29]

become possible only by comparison with IR spectra predicted from quantum chemical calculations.

For Au_{19} and Au_{20}, the harmonic vibrational spectra calculated using density functional theory within the gradient-corrected approximation allow for unequivocal assignment to pyramidal structures [29]. Neutral Au_{20} has the same tetrahedral structure, comprising fcc-like packing with four (111) faces of Au, as found for the corresponding anion [9] and observed for one isomer of the cationic species [61]. Similarly, Au_{19} is isostructural to its anion [10]. The infrared spectra rather elegantly demonstrate the loss of symmetry upon removing a single gold atom from the T_d Au_{20} to the C_{3v} Au_{19} cluster leading to a splitting of the single intense peak in Au_{20} into two signals.

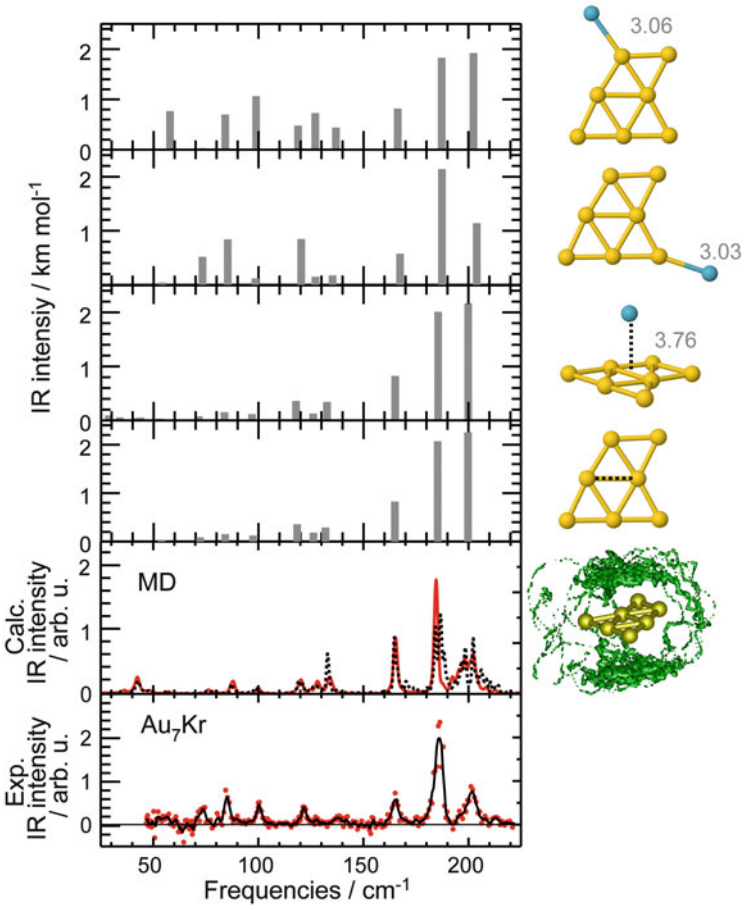

Fig. 6 IR-MPD spectrum for Au_7Kr (*bottom panel*), finite temperature IR spectra from molecular dynamics simulations at 100 K (2nd from *bottom*; *red trace*, Au_7Kr; *dashed black*, Au_7) and harmonic IR spectra for the given limiting structures (*remaining panels*). At 100 K the Kr is not bound to a specific Au atom, but preferentially localised above and below the Au_7 plane (*green*: 80 % isosurface). From [60]

The good agreement between the experimental IR-MPD spectra of $Au_{19}Kr$ and $Au_{20}Kr$ and the harmonic vibrational spectra of the bare clusters allows for the conclusion that in these cases (i) the messenger is not significantly perturbing the vibrational properties of the gold clusters and (ii) the vibrations are largely harmonic. This may not be generally true and, particularly for small clusters, larger deviations between the spectra and the predictions can be found.

The influence of Kr binding on the predicted harmonic IR spectra of Au_7 is illustrated in the upper panels of Fig. 6. Upon binding Kr, the relative intensities of

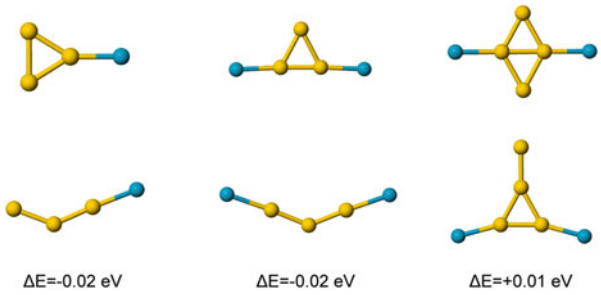

Fig. 7 Structures of small Au_nKr_m clusters. The upper isomers are assigned by comparing IR-MPD spectra with calculated finite temperature IR spectra whilst the *lower row* shows isomers close in energy (the difference is given relative to the *upper row structure*). The structures in the *lower row* may weekly contribute to the observed spectra or have an ionisation energy too high to be detected [60]

the vibrational modes change in a manner dependent on the location of the binding. Using dispersion-corrected DFT, one finds similar binding energies for all the binding sites shown ($\Delta E_B \approx 0.1$ eV). Nevertheless, at 100 K the binding to the plane is (for entropic reasons) significantly favoured as illustrated by the 80 % isosurface for the presence of Kr as obtained from a molecular dynamics simulation (MD). The finite temperature IR spectrum of Au_7Kr obtained from the autocorrelation function of the dipole moment in the MD simulations gives a good match to the experimental spectrum, but the comparison with a spectrum for the bare Au_7 obtained in the same manner reveals only a minor influence of the Kr ligand. A closer analysis of the nuclear dynamics shows that this deviation from the linear absorption spectrum, and in particular the broadening of the highest frequency peak, is due to anharmonic behaviour. MD simulations at higher temperature illustrate that the comparably weak bond in the inner rhombus of Au_7 (Fig. 6, dashed line in the Au_7 structure) can break resulting in an isomerisation between two equivalent forms of this cluster making it rather fluxional [60]. Such dynamical behaviour appears to not be special for this size but important also for larger sizes, e.g. Au_{13} [62].

For still smaller clusters, a similar treatment predicts a localised bonding of the Kr atoms in the cluster plane as illustrated in Fig. 7. The Kr atoms are (at 100 K) no longer mobile owing to two effects: Firstly the strength of the van der Waals interaction scales with the number of Au atoms the Kr can interact with and thus the non-localised van der Waals bonding becomes weaker whilst the (localised) chemisorption in the plane becomes stronger. Further, due to the reduced size of the cluster, the entropic favourability of the van der Waals-bound Kr is reduced as there are fewer sites the Kr atom may sit. In these small Au_nKr_m complexes, the Kr is relatively strongly bound by 0.15–0.20 eV per Kr atom, and thus the rare-gas atoms

need to be explicitly considered in order to explain the observed far-IR-MPD spectra. For all the sizes shown, theory predicts the presence of isomers within about 0.02 eV; however in all cases, only a single isomer (top row in Fig. 7) is needed to satisfactorily explain the observed spectra [60].

3.3 Doped Species

In addition to studies on pure Au clusters, there has been a wealth of investigations, both experimental and theoretical, on gold clusters containing impurity atoms. By introducing such dopants, new physical properties may emerge, e.g. related to modifications of the geometric and/or electronic structure. Depending on the dopant element, it may act as an electron donor or acceptor in essence changing the number of valence electrons in the cluster [63–71]. Clearly such a topic has the potential to be massive in scope and here we focus on the remarkable case of Au_{16} as being exemplary [72–75].

Au_{16} is found to form a stable cage as an anion. For the transition metal elements (including the isoelectronic Cu and Ag), these dopant atoms can be incorporated inside this hollow Au_{16}^- cage with the s electrons of the metal being donated to the valence orbitals of the gold cluster. For 1 e^- donor species (Cu, Ni and Ag), this results in a stable *anionic* 18 e^- valence electron system with the slight further complication in the case of Ni arising due to the additional d-electrons [73]. For the other d-metals, they instead donate 2 electrons into the valence electron system, i.e. the 18 valence electron system is realised in the *neutral* species, with the anionic clusters showing the opening of a new electronic shell. Notably, and of great interest for the development of future nanomaterials, the resultant transition metal centres do not experience a quenching of the latent spin moments arising from the d-electrons in such an interaction. This provides the tantalising possibility that the atomic-like magnetism can be preserved and protected by encapsulation into a golden cage [73].

Lastly, Au_{16}^- has been doped with the main group elements Si, Ge and Sn. With these elements, an altogether different binding motif is observed. Instead of endohedral doping, they displace a Au atom from the cage structure; in the latter two cases, this atom is relocated to a capping site elsewhere on the gold cage, whilst for Si this displaced atom becomes a “dangling” atom bound to the Si itself. This is in line with the recently observed strong Au–Si bonds and observation of gold-based silane analogues [65–67, 75].

Comparable experimental information for the neutral species is scarce. To the best of our knowledge, the only such data relates to the small yttrium-doped gold clusters [76, 77] and a sample of the recorded IR-MPD spectra (measured by monitoring depletion of the parent xenon complexes) as well as comparisons to predicted harmonic spectra are presented in Fig. 8. The agreement between theory

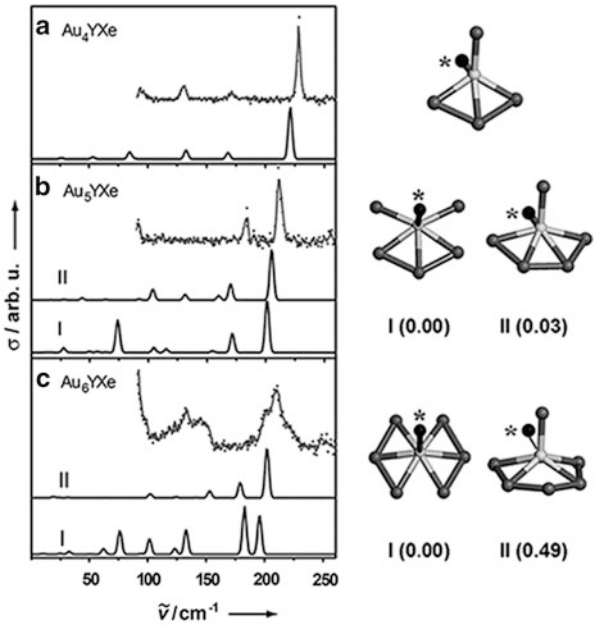

Fig. 8 IR-MPD spectra and predictions of harmonic IR spectra for isomers of Au_4Y–Au_6Y (*light sphere*, Y; *dark spheres*, Au; *black sphere*, Xe). Relative energies are given in eV. From [76]

and experiment for the Au_4Y and Au_5Y clusters is excellent and the well-resolved and narrow (bandwidth limited) lines are accurately reproduced by the harmonic calculations. This is not so for Au_6Y where the experimental spectrum consists of broad features which are not adequately reproduced in the harmonic prediction. This, it transpires, arises from an isomerisation occurring on the timescale of the experiment between limiting forms of structure I passing through an intermediate of D_{6h} symmetry. Interestingly, this intermediate structure is predicted to be a delocalised σ-aromatic system in the anionic cluster as it possesses 10 e^- (cf. Hückel's $4n + 2$ electron rule). Further calculations reveal that such a cluster should possess an appreciable ring current as determined by calculating nucleus-independent chemical shifts, a hallmark of aromaticity [76].

All of the low-energy isomers calculated for the Au_nY clusters are given in Fig. 9 with the structures favoured on the basis of experiment and theory highlighted. In general, the clusters are seen to adopt structures in which the number of Au–Y bonds is maximised with the centred 7-member ring structure, which forms at Au_7Y, being a favoured motif for the larger clusters. This motif is not observed for pure gold clusters, but is stabilised by the incorporated Y due to it being a 10 e^- system (as a neutral subunit).

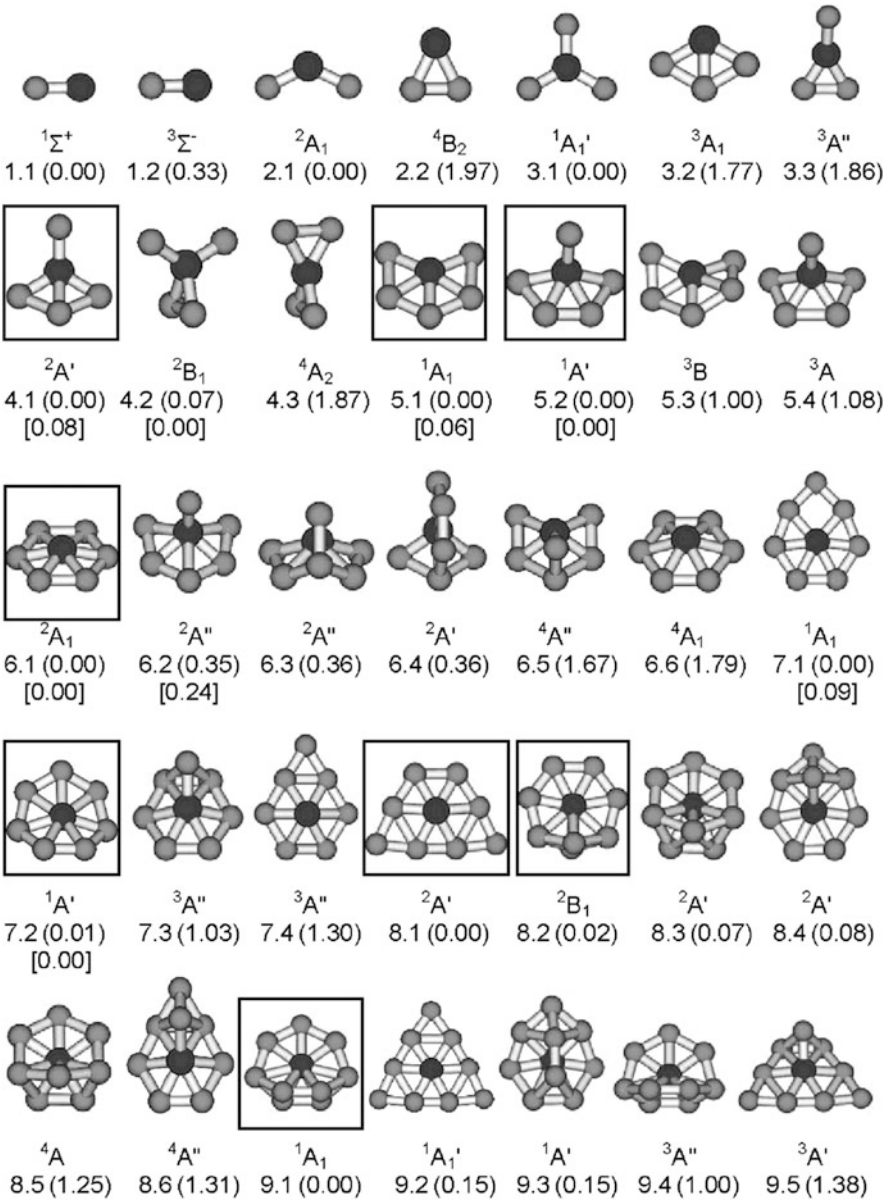

Fig. 9 Predicted structures of $AuY\text{-}Au_9Y$. The structures identified by comparison to experiment are framed. Relative energies are given for the BP86/cc-pVDZ-PP level of theory in eV (*square brackets* give values at the CCSD(T)/cc-pVTZ-PP level of theory). From [77]

4 Gold Cluster Complexes

Knowledge of the bare gold cluster structures is a vital first step towards understanding the origins of their chemistry at the nanoscale. More direct insights into the function of the clusters in a reactive environment, however, can be obtained by studying complexes of these clusters with small ligands of catalytic relevance. From an experimental point of view, the focus is often either on investigating the kinetics of complex formation (or transformation) or on structural (spectroscopic) characterisation. To date complexes of gold clusters with a variety of ligands have been investigated but, in the interests of space, we limit the present discussion to two of the most studied: O_2 and CO. Additionally, the reaction kinetics have been the subject of two comparatively recent reviews [21, 78], which highlight the roles of gold and binary silver–gold clusters and their reactions with small molecules. As such in the present work, we shall place the emphasis on the spectroscopic characterisation of gold cluster complexes.

4.1 Molecular Oxygen

Perhaps the most famous property of gold nanoparticles is their ability to catalyse low-temperature oxidations using molecular oxygen as a feedstock [79–83]. These reactions are fascinating given that the typical mechanism for metal-catalysed oxidation reactions, the Mars–van Krevelen mechanism [84], relies on the formation of oxide ions, O^{2-}, a process which is known to be unfavourable for gold surfaces. Clearly, nanoscale materials may show a different chemistry, and indeed small gold oxide clusters, i.e. species containing dissociated O_2, can be produced [85–89]. Their formation, however, relies on the activation of molecular oxygen in the plasma plume formed during laser ablation, a highly energetic process quite unlike that found in a real catalyst. Nevertheless, the question still remains: How does nanoscale gold react with and activate molecular oxygen?

4.1.1 Anions

The majority of the experimental investigations into gold cluster complexes with molecular oxygen have focused on the anions. Charged systems are experimentally easier to study, as previously mentioned, and the cations are less reactive towards oxygen, with the exception of the decamer (Au_{10}^+) [13].

For the anions, only the even-sized clusters, Au_{2n}^-, show appreciable reactivity with O_2 [13, 90, 91]. This has been attributed to the alternating open/closed shell of the gold clusters arising from the $5d^{10}6s^1$ electron configuration of the Au atom [90]. This alternating shell structure means the even-sized anions (which have open shells) typically show lower electron-binding energies (BE) than their neighbouring clusters. This oscillation in the BE of the clusters has been correlated with the energy for the association reaction $Au_n^- + O_2 \rightarrow Au_nO_2^-$ as shown in Fig. 10. The only significant deviation from this correlation occurs at Au_{16}^-, which shows an anomalously high BE

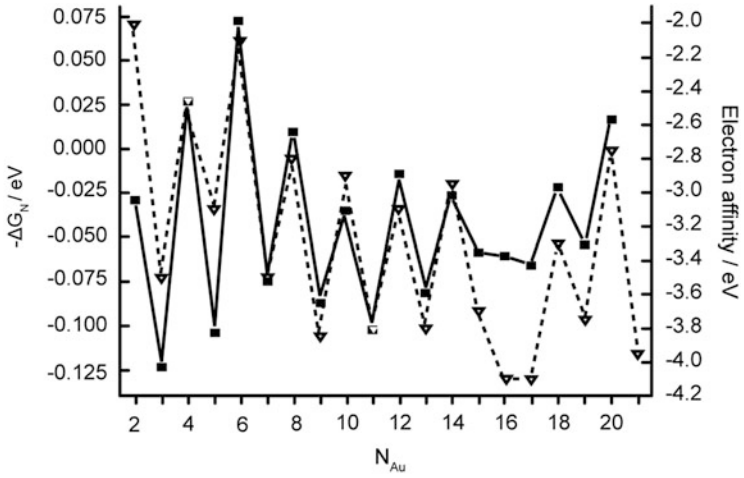

Fig. 10 Free energy for the complex formation reaction $Au_n^- + O_2 \rightarrow Au_nO_2^-$ (closed squares, left axis) and the negative of the electron affinity of the corresponding neutral cluster (which is equal to the electron-binding energy, BE, in the anion; *open triangles*, *right axis*). Reprinted from Salisbury et al. [90]. Copyright (2000) with permission from Elsevier

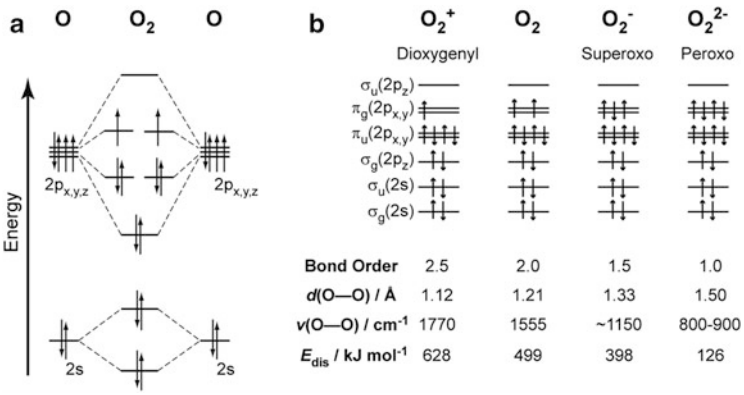

Fig. 11 MO Scheme for O_2 and the corresponding orbital occupancies for the different oxidation states of O_2. Additionally the formal bond order, O–O bond distance, vibrational frequency and bond dissociation energy are given for all the oxidation states. Numerical values from [93]

and no reaction with O_2. This has been attributed to the cage structure of Au_{16}^- benefiting from spherical aromaticity, stabilising the anion [92].

This preferential reactivity of the even-sized anions leads to a simple binding model for the complexes: The unpaired electron of the gold cluster is donated into the partially occupied HOMO of O_2 (the MO diagram for which is shown in Fig. 11). Since this π^* orbital is of O–O anti-bonding character, this weakens the oxygen bond to form a superoxo (O_2^-) moiety (bond dissociation energy 398 vs. 499 kJ mol^{-1}; see Fig. 11). In this way, the O_2 becomes activated upon complexation with the gold cluster leaving it open to further attack.

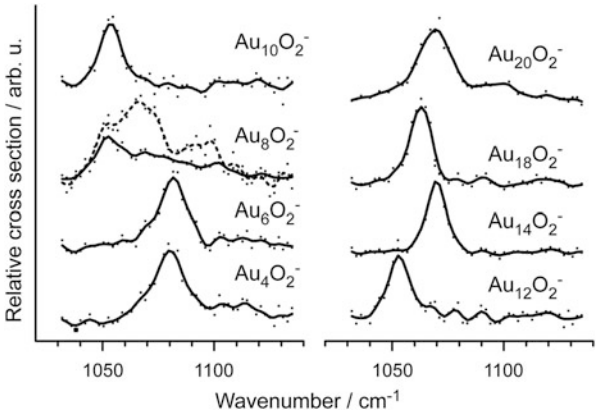

Fig. 12 IR-MPD spectra for the even-sized gold cluster complexes $Au_nO_2^-$. All show an absorption in the energy range which corresponds to a superoxo stretch. Two traces are given for $Au_8O_2^-$ demonstrating the limiting cases of the spectra observed by varying the source conditions. From [11]

Evidence for this binding mechanism comes from multiple sources. Several anion PES spectra have been recorded for these clusters and provide two crucial observations: Firstly, a vibrational progression is seen in the spectra of $Au_2O_2^-$, $Au_4O_2^-$ and $Au_6O_2^-$ with stretching frequencies ranging between 1226 and 1443 cm^{-1} [14, 15, 94]. Such a vibrational frequency corresponds to a partially activated O_2, somewhere between physisorbed oxygen and a superoxo species. Secondly, when the experiment is performed at cryogenic temperatures, it is possible to form the oxygen complexes with the odd-sized clusters. The resulting spectra, however, are almost identical to that of the parent bare gold anion, indicating that no electronic structure changes have occurred in the complexation, i.e. a purely van der Waals interaction [15].

Another PES study [95], which focused on the larger anions (Au_6^-–Au_{20}^-), found a transition in the binding geometry of the superoxo moiety from being bound to a single Au atom (μ^1) to two Au atoms (μ^2) with a critical size for the change at Au_8^-. This conclusion, however, is based on the supporting DFT calculations as no vibrational progressions were observed in the PES.

Direct evidence for the presence of superoxo species comes from IR-MPD spectroscopy. The IR-MPD spectra for the dioxygen complexes of the anionic species Au_4^-–Au_{20}^- clearly show absorption between 1,050 and 1,100 cm^{-1} (Fig. 12) [11]. This unambiguously demonstrates the presence of a superoxo moiety bound to the gold cluster as no other vibrational fundamentals are expected at these frequencies. The observed frequencies, however, disagree with the vibrational progressions recorded from anion PES. This is most likely due to the nature of PES which is sensitive to both the anionic and the neutral states. The vibrational progressions in the anion PES are now thought to instead arise from photodetachment to an electronically excited state of the neutral cluster which corresponds to the reaction of the gold cluster with singlet oxygen, rather than being representative of the superoxo state [15].

Two very different experiments, anion PES [95] and IR-MPD [11], permit an experimental cross validation for the special behaviour observed for the $Au_8O_2^-$ complex. Both studies find that the observed experimental spectra are very sensitive on the exact source conditions employed. In the reproduced

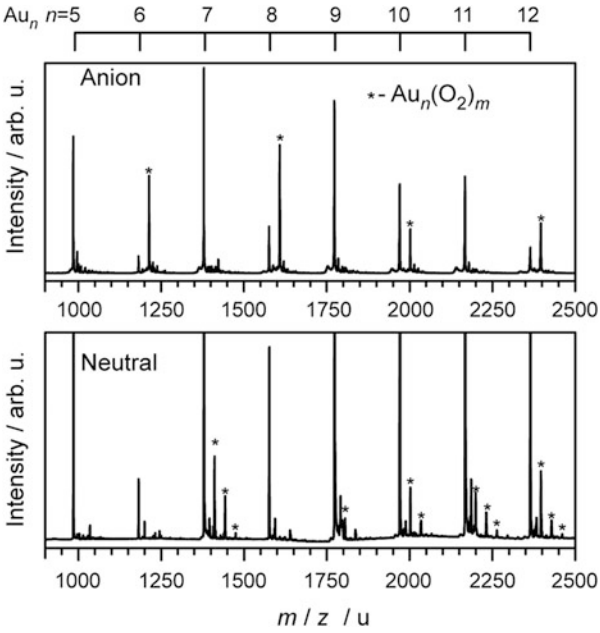

Fig. 13 Mass spectra in the range of Au_5 to Au_{12} when reacted with O_2. The *upper panel* shows the anionic species (reacted at −100 °C), the lower the neutral (reacted at −177 °C). All $Au_n(O_2)_m^{-/0}$ species are labelled with an asterisk. Other peaks in the mass spectrum relate to water and other impurities. Neutral clusters are ionised by 7.9 eV photons from an F_2 laser

IR-MPD spectra these are given as two different traces for $Au_8O_2^-$. Accompanying DFT calculations reveal that this is due to an adsorbate driven isomerisation between two forms of the $Au_8O_2^-$ cluster complex. Depending on the residence time in the reaction channel, either the cluster complex corresponding to the ground-state Au_8^- structure (a 4-pointed star) or the excited-state structure (an -edge-capped centred hexagon) prevails. It transpires that the complex of the edge-capped centred hexagon structure is lower in energy than the 4-pointed star complex but a significant barrier to the rearrangement exists (0.43 eV) hence the possibility for kinetic trapping [95]. Further, both investigations find that this structural change is accompanied with a transition from a μ^1 bound complex for the 4-pointed star to a μ^2 complex in the edge-capped centred hexagon.

4.1.2 Neutrals

One of the suggested mechanisms for the catalytic activity of nano-dispersed gold particles builds upon the observation that gold clusters are found to become negatively charged when deposited over defect sites in oxide supports and, indeed, such systems have been shown to be catalytically active [1, 2]. This, in part, drove the experimental and theoretical interest in the anionic gold cluster complexes with oxygen. Neutral clusters, however, are much more likely to be present in a real catalyst and thus it is interesting to investigate if and how neutral gold clusters interact with molecular oxygen.

Figure 13 compares the mass spectra of the anionic gold cluster complexes and the neutral cluster complexes when using 7.9 eV photons for ionisation. As was

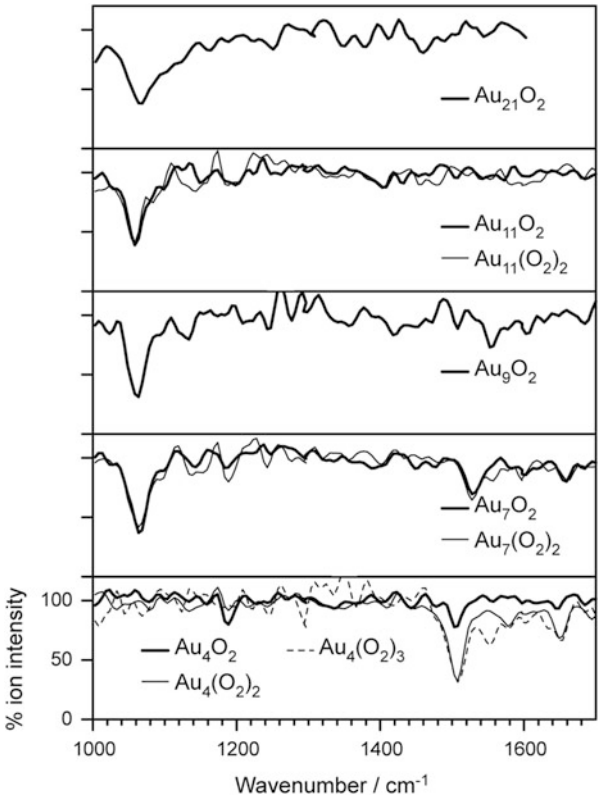

Fig. 14 IR-MPD spectra for oxygen complexes of neutral gold clusters. The observed absorptions correspond to superoxo moieties (O_2^-; ~1050 cm^{-1}) and physisorbed O_2 (O_2^0; ~1550 cm^{-1}). Reprinted with permission from Woodham et al. [12]. Copyright 2013 American Chemical Society

mentioned earlier, the reactivity for the anions is dominated by the even-sized clusters whereas mass peaks corresponding to both even and odd-sized cluster complexes are observed in the neutral mass spectrum. The ionisation energies (IEs) of gold clusters tend to be high, and therefore the 7.9 eV photons do not efficiently ionise all the clusters with a single photon. As such the ionisation cross sections have a marked effect on the observed distribution. Unfortunately these cross sections are not known for the different species and so no definitive conclusions concerning the reactivity can be drawn from these mass spectra. Those species which can be ionised, however, can have spectroscopic probes applied to them. Figure 14 shows the IR-MPD spectra for such complexes of neutral gold clusters [12].

For $Au_{10}(O_2)_{1–2}$ and $Au_{12}(O_2)_{1–3}$, no bands are observable in the range of 1,000–1,700 cm^{-1}. This indicates that either the oxygen dissociates upon binding to the gold clusters, resulting in the formation of a gold oxide which is not expected to possess a vibrational fundamental at these frequencies, or the oxygen is sufficiently weakly adsorbed to the cluster that the formally IR-inactive O–O stretch is not sufficiently perturbed to become IR-active. As yet no evidence exists to distinguish the two scenarios.

The other complexes show vibration fundamentals in two ranges, one corresponding to a superoxo moiety between 1,000 and 1,100 cm^{-1} and is seen

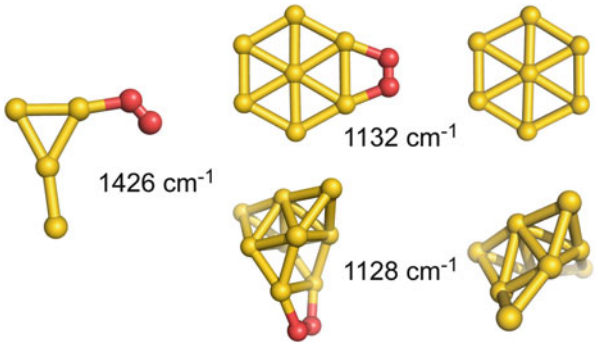

Fig. 15 Structures of Au_4O_2, Au_7O_2 and Au_9O_2. The theoretically predicted vibrational frequency for the O–O stretch is given for the complexes. For comparison, the bare cationic cluster structures of Au_7^+ and Au_9^+ are also presented. There is a clear similarity between the neutral cluster complex and the cationic bare cluster

for all the odd-sized clusters. The second is due to a slightly activated O_2 moiety, essentially physisorbed, at around 1,500–1,520 cm^{-1} and is observed for $Au_7(O_2)_{1-2}$ as a minor additional peak and as the only feature in $Au_4(O_2)_{1-3}$. The extreme similarity between the spectra with a single O_2 and those with multiple O_2 units suggests that these additional oxygen molecules are purely spectators and only bound by a weak van der Waals type interaction. The presence of superoxo vibrations for the odd-sized clusters is in line with the binding model derived from the anionic clusters, where a single unpaired electron is required for donation into the π^* HOMO of the oxygen molecule. The smaller band indicating unactivated O_2 in Au_7O_2 is most likely due to an isomeric structure, either in the binding position of the O_2 or of the gold cluster core structure itself.

As with the anionic clusters, interpretation of the data is aided by supporting quantum chemical calculations. The suggested structures (Fig. 15) are not the putative global minima, which are always found to be dissociated species [96–100], but the lowest energy structures which contain a molecular O_2. Of these structures, the gold cluster cores for Au_7O_2 and Au_9O_2 do not have the known structures for the bare neutral clusters, but rather resemble the corresponding cationic clusters (also reproduced in Fig. 15). This demonstrates yet again the importance of structural flexibility in these systems. Upon binding O_2, the neutral gold cluster transfers an electron into the π^* HOMO, activating the O_2 and becoming formally positively charged. In response to this change in charge state, the cluster then undergoes a structural rearrangement to its preferred geometry for this charge state. For the tetramer, no such rearrangement is observed as the gold cluster core remains neutral upon binding the O_2.

Given that the reactivity is dependent upon the IE of the cluster, one can speculate as to the absence of the complexes $Au_{13}O_2$ to $Au_{19}O_2$. These clusters all possess an IE similar to, or less than, that of Au_7; however, given that these clusters are metallic, the resultant positive charge will become increasingly diluted throughout the cluster core as it increases in size. This charge dilution will result in a weaker ion–ion interaction with the formed superoxo moiety and thus the

complexation will become thermodynamically less favourable. At Au_{21}, the magic shell closing of a 20 e^- system dramatically lowers the IE, making the complex formation favourable once again.

Whilst the differences in the reactivity pattern of neutral and anionic gold clusters are essentially due to the cluster's charge, more subtle variations in charge density can be realised by electron-donating or electron-accepting ligands. One example of how the reactivity can be modified in this way is the activity of partially hydrogen-covered cationic gold clusters towards oxygen. As has been previously mentioned, the gold cations are thought to be unreactive towards molecular oxygen with the exception of Au_{10}^+ [13]. Upon binding H_2, however, all of the even-sized clusters (Au_2^+, Au_4^+ and Au_6^+) are found to now bind one O_2 molecule [101]. This cooperative effect is based on molecular hydrogen ligands effectively acting as electron donors, i.e. increasing electron density at the gold, and thereby enabling the activation of O_2 via single electron transfer as discussed above.

These combined investigations reveal that oxygen activation, at least in the gas phase, is dependent upon the ability of the gold cluster to transfer an electron into the π^* HOMO of the oxygen molecule. Thus only certain clusters are able to activate oxygen upon complexation. The extent of activation is comparable for all sizes and charge states, as the observed vibrational frequencies are similar for all the species presented. Lastly, the dynamic nature of the system is often very important for the observed reactivity, with the neutral clusters undergoing, sometimes dramatic, rearrangements in response to oxygen adsorption.

4.2 Carbon Monoxide

The prototypical reaction for modelling oxidative reactions with gold nanoparticles is the oxidation of carbon monoxide. Historically this reaction is of great significance as it was the first one observed to be catalysed by gold nanoparticles and spawned the entire research field [79, 80]. The reaction serves as a useful model for other oxidative reactions as well as being of industrial interest in its own right, for example, to selectively remove CO from process gases (e.g. CO from H_2 gas) or as a scrubbing agent in water-based fuel cells or car catalytic converters.

The binding of carbon monoxide to transition metals is a well-known phenomenon, typically described by the Blyholder model [102]. The Blyholder model assumes a two-component bonding interaction; one component is electron donation from the CO HOMO, which is of σ-bonding character, into an empty, correctly symmetry adapted orbital of the metal centre. This occurs concurrently with back-donation from filled metallic d-orbitals into the empty π* LUMO of the CO (the second component). From such a binding model, one can clearly see that metal–CO binding will be favoured for metallic centres which contain a partially filled set of d-orbitals. For gold clusters, this is not the case as the d-orbitals are completely filled and this is reflected in the weak binding of CO to gold surfaces [103] and indeed the rarity of gold-carbonyl complexes in both the solid and solution phases.

Similar to molecular oxygen, the binding to the metal centre involves orbitals which are of C–O anti-bonding character and so IR spectroscopy serves as an

excellent probe to the local coordination environment of the CO molecules, and changes in the C–O stretching frequency are routinely used to identify binding sites, motifs and strengths, and in particular the oxidation state of the metal, both on surfaces as well as in cluster carbonyls [104–106].

The properties of charged gas-phase clusters (both cations and anions) and their complexes with CO have been investigated in two regimes, a low-pressure one and a high-pressure one. In the high-pressure regime, the binding is best described by the Lindemann model for association reactions. Under such a model, an initially formed encounter complex (AB^*) is in equilibrium with the separated reagent species (A and B) and requires collision with a third body (M) to undergo collisional cooling to form the product species (AB) and an excited third body (M^*) as shown in Eq. (2). Conversely, conditions where such three-body collisions are effectively absent with other cooling processes dominating (i.e. radiative cooling or uni-molecular decay) are defined as the low-pressure regime.

$$A + B \Leftrightarrow AB^* + M \rightarrow AB + M^* \tag{2}$$

For cationic and anionic clusters, the behaviour in the low-pressure regime is similar [91, 107–109]. The interactions between the gold clusters and carbon monoxide are determined by simple electrostatic considerations and the ability of the resultant complexes to deposit the adsorption enthalpy into vibrational degrees of freedom. The first of these effects weakens the enthalpy of binding as the charge becomes diluted throughout the metallic droplet of the cluster with the binding enthalpy rapidly approaching that of the single crystal surface [109]. For Au_n^+ clusters, the binding energy has been experimentally determined to decrease for increasing cluster size from about 1 eV for $n = 5$ to below 0.65 eV for $n > 26$ and is calculated to be as high as 1.5 eV for the cationic dimer [109, 110]. As the binding energy is conserved in the complex, the smallest clusters are prone to fragmentation upon CO binding such that they are often difficult to characterise experimentally. For example, Au_3CO^+ has been seen to form from initially formed Au_4CO^+ and subsequent elimination of a neutral Au atom [109].

In the high-pressure regime, where collisional de-excitation dominates, the clusters can form multiply coordinated complexes, with saturation-limited compositions being observed. Example mass spectra for the ionic and neutral species are reproduced in Fig. 16. The saturation compositions appear not to be determined by simple electron counting rules [111, 112], from which one would predict the presence of many $Au_n(CO)_{m-1}^-$ compositions when comparing between the cationic and anionic species (the change from cation to anion involves the addition of 2 e^-, corresponding to one CO ligand). Instead it is found that for the cationic clusters and the smaller ($n < 6$) anionic clusters, the number of low coordination gold atoms (4 or fewer gold bonding partners) seems to provide a 1:1 correspondence with the CO saturation limit (for the gold cluster structures, see Fig. 2). In addition to this, several cluster sizes exhibit metastable compositions which convert to a higher saturation coverage number with increased CO concentrations; the data are summarised in Table 1. The metastable compositions are attributed to adsorption-driven structural rearrangements, again demonstrating the importance

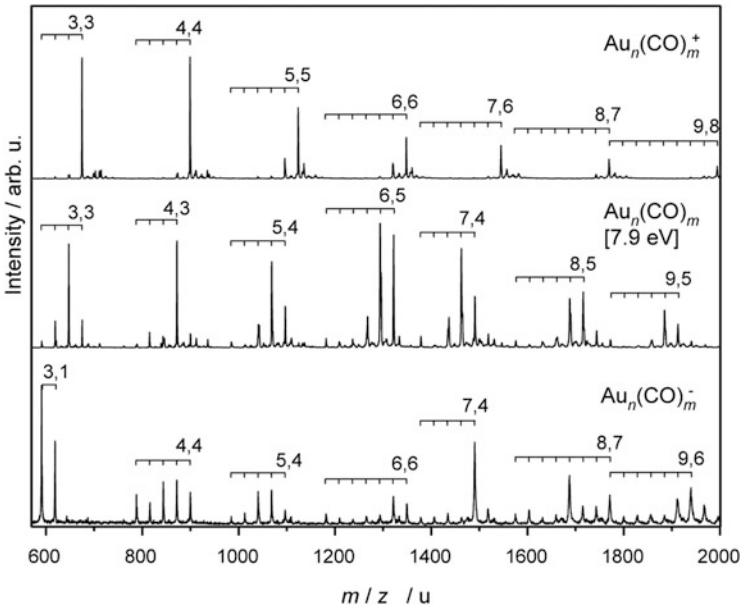

Fig. 16 Mass spectra for cationic (*top*), neutral (*middle*) and anionic (*bottom*) gold cluster carbonyl complexes. The compositions are given as (*n*,*m*) labels for the saturated species. The neutral mass spectrum was recorded after ionisation with 7.9 eV photons

Table 1 CO saturation number for different gold cluster sizes. Where two values are given this indicates evidence for a metastable intermediate saturation, which is observed until higher CO pressure. For neutral clusters saturation may not be fully reached for the mass spectrum shown in Fig. 16

Cluster size	Anion[a]	Neutral[b]	Cation
3	≥1	3 (3)	3
4	4	3 (3)	4
5	4 (4)	4 (5)	4,5
6	6 (4)	5	5,6
7	4,5 (4)	4 (6)	6
8	4,7 (5)	5 (7)	7
9	6 (6)	5 (7)	8

[a]Values in parentheses from [113]
[b]Values in parentheses from [114]

of structural flexibility in the chemistry of gold clusters [111, 115]. Similar adsorption-driven structural changes have also been observed with anion PES [116–119]. The structural rearrangements can be quite dramatic and attempt to maximise the number of low coordination number atoms to which the CO can bind (e.g. see Fig. 17). In some cases, these structural transformations are observed to occur even with the addition of a single CO molecule.

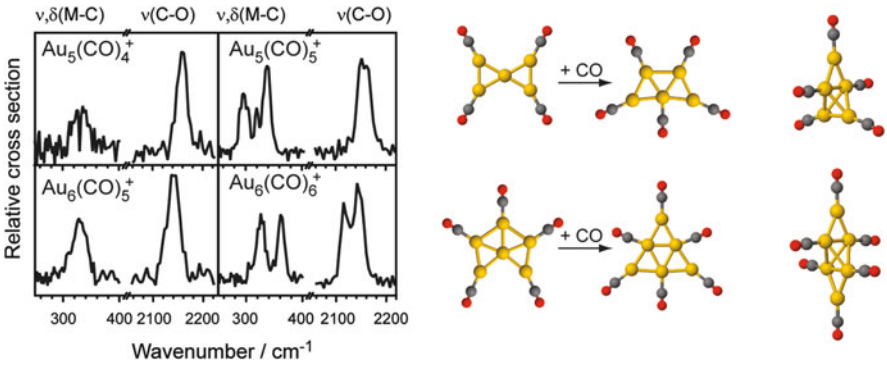

Fig. 17 IR spectra of $Au_5(CO)_{4,5}^+$ and $Au_6(CO)_{5,6}^+$. For the lower coverage intermediate saturation is observed, leading to the suggestion of a structural rearrangement upon addition of the next CO molecule. Initially a transformation between 2D isomeric structures has been suggested [111]. More recent DFT calculations predict the formation of 3D structures upon CO addition to the planar bare gold clusters (*right most structures*) [115]

Anion PES also provides further evidence for CO saturation effects for Au_2^-–Au_5^-. Here successive addition of CO is accompanied by a marked red-shift in the observed EA of the cluster, owing to the σ-donation from the CO which destabilises the HOMO of the gold cluster. After reaching saturation, however, each successive CO molecule induces a minor blue-shift due to the formation of a solvation shell, which again stabilises the charged species. In this way, saturation compositions of $Au_2(CO)_2^-$, $Au_3(CO)_2^-$, $Au_4(CO)_3^-$ and $Au_5(CO)_4^-$ were determined [118, 119].

A summary of the observed CO stretching frequencies as a function of cluster charge, size and coverage as determined via IR-MPD spectroscopy is presented in Fig. 18. For the smallest cationic clusters, the observed ν(CO) values are blue shifted relative to that of the free CO (2143 cm^{-1}). This shows that the binding of CO to gold clusters is non-classical as electrostatic effects dominate over the π-back-donation [120]. As the cluster size increases, however, the shift from the free CO value reduces. This can be interpreted as the clusters functioning as metallic droplets and the charge becoming increasingly diluted throughout the structure. The effect of such a dilution can be modelled [121] and the expected shift is 15 cm^{-1} over the range Au_3^+–Au_{10}^+. The actual, experimentally observed shift is on the order of 40 cm^{-1} indicating that some π-back-donation may play a role in the binding of CO, particularly for the larger clusters [111]. The anionic clusters behave in a manner which approximately mirrors that of the cations. The CO stretching frequencies are uniformly red shifted compared to the free CO value as the extra electron density of the anion makes π-back-donation more favourable, such that it dominates the electrostatic effect. As the clusters increase in size, this extra density again becomes diluted throughout all metal atoms, lessening the effect and giving rise to the observed increase in ν(CO) as the cluster size increases. As with the cations, the contribution to this shift from purely electrostatic

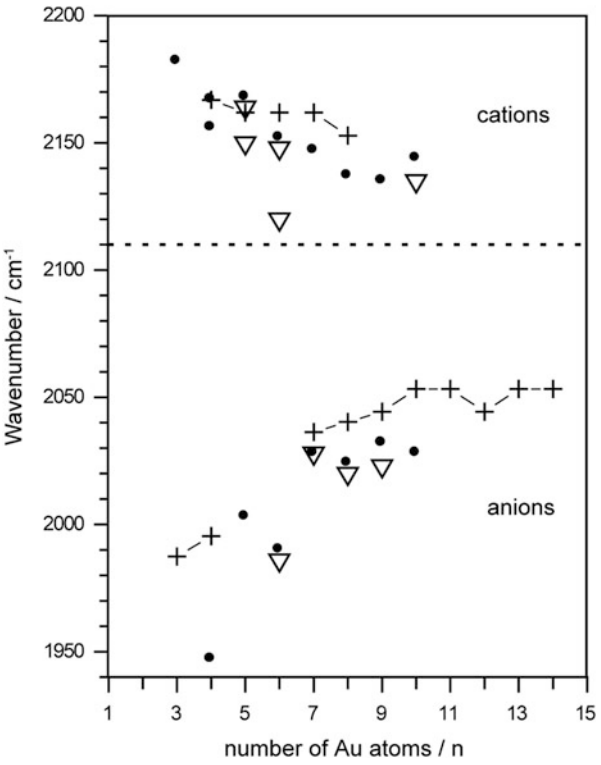

Fig. 18 Summary of the observed ν(CO) values for anionic and cationic gold cluster carbonyls. The values for the monocarbonyl complexes are marked by the *connected crosses* whilst the saturated ones by *closed circles*. In the cases where intermediate saturation complexes are formed, the high CO pressure compositions are represented by *open triangles*. The *dashed line* indicates the ν(CO) value for CO adsorbed on gold surfaces. Reprinted with permission from Fielicke et al. [112]. Copyright 2005 American Chemical Society

considerations should be 15 cm^{-1} over the series Au_3^-–Au_{10}^- whilst the observed shift is 80 cm^{-1} again likely due to the role of π-back-donation and other bonding effects [112]. With increasing CO coverage, there is also a blue-shift in the observed ν(CO) of ~4 cm^{-1} per CO molecule which arises due to increased competition for the electron density of the anionic cluster, reducing the share of this density each carbonyl receives. Perhaps expectedly, both the anions and cations tend towards a common value with increasing cluster size, which corresponds to ν(CO) found for neutral gold carbonyls (see below).

In terms of ν(CO), the binding of a single CO molecule is found to be largely insensitive to open/closed shell oscillations in the charged clusters, in contrast to O_2 (see before) or NO [122]. For the CO saturated charged clusters, some oscillatory behaviour becomes evident (Fig. 18), with the even-sized, i.e. open-shell, species exhibiting the lower ν(CO). It is not clear, however, if this slightly stronger activation of the CO ligands is entirely due to the electronic structure or if geometric effects and a change in CO coverage also contribute.

Lastly, saturation composition data for the neutral cluster complexes are also shown in Fig. 16. The observed compositions when ionising with 7.9 eV photons are almost identical when an ArF laser (6.4 eV) is used for photoionisation [114] indicating that binding of CO significantly lowers the IE, as the bare gold clusters

have IEs in the range of about 7–9 eV [123]. In general, the neutral complexes are observed to bind fewer carbonyl ligands compared with the anionic and cationic cluster complexes. This may be due to the lack of an ion–dipole interaction which plays a significant part in the energetics for the charged species as the σ-donation and π-back-donation are both relatively weak for these gold cluster carbonyls (as seen before). For the larger clusters (Au_9–Au_{68}) reactivity data in the low-pressure regime also exists [124]. These possess a behaviour similar to the charged species, in that the reactivity is dependent upon the ability of the cluster to stabilise the energy of adsorption within the molecular degrees of freedom. In addition to this, an approximate odd–even oscillation is observed, with the even clusters demonstrating enhanced reactivity. This has been explained by the 2 e^- donor nature of CO resulting in favourable binding to the (closed shell) even-sized clusters, presumably as the LUMO orbital is readily able to accommodate the two electrons of CO. The absence of a similar behaviour in the charged clusters would then be attributed to the ion–dipole interaction being the dominate term in the binding. Indeed, odd–even oscillations in ν(CO) are observed for partially CO saturated neutral gold clusters, with the open-shell systems showing lower ν(CO), as in the case of the charged clusters [125]. The absolute values are between 2,070 and 2,100 cm^{-1}, i.e. just halfway between the ν(CO) frequencies of the CO saturated cations and anions, as predicted by the charge dilution model [121].

This survey of the carbonyl complexes with gold in all three charge states reveals that their interaction is atypical when compared with other transition metals. The effect of π-back-bonding is minimal owing to the stability of the filled 5d orbitals and so the trends in the CO bond strength are instead dominated by electrostatic effects and the σ-donation from the carbonyl into the LUMO of the cluster. The saturation compositions of the gold clusters appear to be determined not by electron counting rules, as with other transition metal carbonyls, but rather from the interplay of electronic and structural considerations, with the availability of low-coordinate gold atoms being of paramount importance. This requirement for low-coordinate gold atoms is seen to be the driving force for large structural changes upon complexation with CO in order to maximise the number of available binding sites.

4.3 Carbon Monoxide and Oxygen

To gain further mechanistic insight into oxidation reactions on gold nanoparticles, co-adsorbate species, e.g. clusters containing both O_2 and CO, have been studied. Whilst studying the gold cluster complexes with a single kind of ligand allows for analysis of their individual binding mechanisms, it is their interaction which determines the chemistry in the co-adsorbate species. Under conditions where two different reactants are present, two scenarios are possible: The two species may compete with each other for binding sites and the resultant cluster distribution

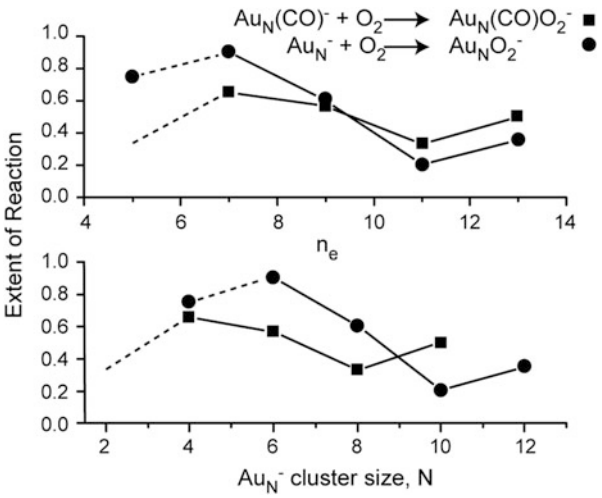

Fig. 19 Comparison of reaction extents for the association reactions of Au_nCO^- (*closed squares*) and Au_n^- (*closed circles*) with O_2. The *top panel* shows these as a function of valence electron count, whilst in the *bottom panel* as a function of cluster size. Reproduced with permission from Wallace and Whetten [126]. Copyright 2002 American Chemical Society

will reflect the ratio of the two sticking probabilities. Alternatively, the presence of one ligand may change the probability of the other ligand to bind, e.g. enhance it. One example for such cooperative binding of H_2 and O_2 on cationic gold clusters has been discussed before, and for other ligands, similar effects have been reported [101, 126–128].

Cooperative effects also determine the binding of CO and O_2 to the even-sized gold cluster anions. The preadsorption of either CO or O_2 can lead to massive enhancements of the reactivity for the next ligand with Au_4^- showing an enhancement of 18:1 [126]. Such behaviour again fits into the frontier orbital pictures which have been discussed before. In the case of initial O_2 binding, the resultant gold cluster core will be similar to the corresponding neutral cluster as it has transferred its excess electron density into the O_2 thus there is a vacant orbital which can accept two electrons from CO. Alternatively, if the CO complex forms first, then the donation of two electrons pushes the SOMO up in energy making its subsequent donation into an O_2 more favourable. Indeed a plot of the reaction probabilities as a function of the number of electrons in the cluster (Fig. 19) shows a remarkable similarity between the activity of the cluster carbonyl and the bare cluster with 2 additional gold atoms (i.e. 2 extra valence electrons).

With only one exception, this cooperative binding was not observed to change the rules for O_2 adsorption in that only a single O_2 was found to adsorb and only on the even-sized gold anions. The exception being Au_3^- which, when studied at cryogenic temperatures, is seen to form the species $Au_3COO_2^-$ and $Au_3CO(O_2)_2^-$ [128]. Unfortunately it is not clear if this is an electronic structure effect induced by the CO binding or a physisorption of the O_2 to the larger dipole of the Au_3CO^- complex.

In addition to the CO and O_2 co-adsorbates of these anionic clusters, mass peaks which correspond to ions containing an odd number of O atoms have been observed

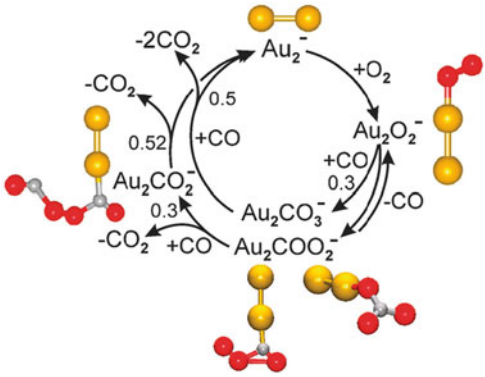

Fig. 20 Mechanism for the catalytic oxidation of CO by O_2 at Au_2^-. Reprinted from Bernhardt et al. [130]. Copyright 2005. With permission from Elsevier

[17, 126]. Such species may be formed upon transferring one of the O atoms supplied by O_2 to CO, i.e. resulting in its oxidation, and release of CO_2. For Au_2^- the reaction kinetics have been studied both experimentally and theoretically in great detail [17, 128, 129] providing the realisation of a catalytic cycle for CO oxidation (Fig. 20). The cycle begins with formation of the oxygen complex which then reacts with a single CO molecule. Two possible structures of this intermediate are discussed, either a carbonate or a peroxyformate species. For the carbonate species of Au_2^-, this then undergoes an Eley–Rideal reaction step with a second CO to evolve two CO_2 molecules and regenerate the starting Au_2^-. The alternative peroxyformate species also undergoes an Eley–Rideal reaction step to form a stabilised complex which then fragments to regenerate the bare gold cluster and evolve two CO_2 molecules. A similar mechanism has been suggested for neutral Au_2 but involving $Au_2(CO)_2$ as a catalytically active species [62].

The reactions between the neutral carbonyl clusters and O_2 have also been investigated under multiple collision conditions using a fast flow reactor [114]. The reaction is monitored by observing the loss of carbonyl-complex signal when oxygen is present in the reaction cell. In order to exclude the effects of losses from scattering, the observed depletion is compared with and normalised to the reduction in signal for a reaction cell filled with a partial pressure of N_2, which is assumed to be unreactive and have a scattering cross section similar to that of O_2. As with other studies of the neutral clusters, the data is hampered by the high IEs of the gold clusters and as such only the odd-sized clusters are measurable. For these species, all of the observed carbonyl complexes react with O_2 at 300 K with the cluster complexes $Au_3(CO)_2$ and $Au_5(CO)_4$ being local maxima in the reactivity which reduces at the largest cluster sizes investigated ($Au_9(CO)_6$). Unfortunately there is no clear electronic or structural argument to rationalise this observed variation in reactivity.

5 Conclusions

This chapter has presented a comprehensive review of the developments of gas-phase investigations into the structures of small gold clusters and their complexes with the prototypical reactants CO and O_2. The structural motifs adopted by the clusters are extremely unusual (when compared, e.g. to transition metal clusters) with extended two-dimensional flake structures, hollow cages and tetrahedra being observed. The potential energy surfaces for these clusters provide evidence for structural isomerism and fluxionality even at reduced temperatures.

The reactivity patterns of the gold clusters with O_2 can be largely rationalised by simple electron counting metrics, but structural aspects, i.e. the presence of low-coordinated Au atoms, are more relevant for the reactivity towards carbon monoxide. Whilst these metrics are not perfect, they do allow for an initial understanding of the underlying features of gold clusters which encourage the catalytic CO oxidation. Again, in the characterisation of the gold cluster complexes, evidence has been presented for the importance of structural isomerism and fluxionality, which may act as a driving force for reactivity in some cases.

Generally the systems investigated require computational support for assignment of the experimental findings. Thereby, these studies on gold clusters highlight the vital interplay between gas-phase experimental characterisation and accurate quantum chemical calculations. As more detailed experimental results, e.g. spectroscopic data, become available greater demands are placed on the supporting theory. For example, the 2D to 3D transition in anionic gold clusters that is experimentally found to occur at Au_{12} [4] had been a puzzle for theory [51] but can now be correctly described, thanks to more recent developments in density functional theory which are able to simulate dispersion interactions more accurately [5, 62, 131].

Acknowledgments We gratefully acknowledge the contributions from all authors of our original papers, the "Stichting voor Fundamental Onderzoek der Materie (FOM)" in providing beam time on FELIX and the skilful assistance of the FELIX staff, in particular A.F.G. van der Meer and B. Redlich. This work is supported by the Max Planck Society and the Cluster of Excellence "Unifying Concepts in Catalysis" coordinated by the Technical University Berlin and funded by the Deutsche Forschungsgemeinschaft (DFG) and through the DFG within the research unit FOR 1282 (FI 893/4). We thank G. Meijer for his continued support.

References

1. Yoon B, Häkkinen H, Landman U, Wörz AS, Antonietti J-M, Abbet S, Judai K, Heiz U (2005) Science 307:403
2. Molina LM, Hammer B (2005) J Catal 233:399
3. Lin X, Yang B, Benia H-M, Myrach P, Yulikov M, Aumer A, Brown MA, Sterrer M, Bondarchuk O, Kieseritzky E, Rocker J, Risse T, Gao H-J, Nilius N, Freund H-J (2010) J Am Chem Soc 132:7745

4. Furche F, Ahlrichs R, Weis P, Jacob C, Gilb S, Bierweiler T, Kappes MM (2002) J Chem Phys 117:6982
5. Johansson MP, Lechtken A, Schooss D, Kappes MM, Furche F (2008) Phys Rev A 77:053202
6. Huang W, Wang L-S (2009) Phys Rev Lett 102:153401
7. Häkkinen H, Yoon B, Landman U, Li X, Zhai H-J, Wang L-S (2003) J Phys Chem A 107:6168
8. Bulusu S, Li X, Wang LS, Zeng XC (2006) Proc Natl Acad Sci 103:8326
9. Li J, Li X, Zhai H-J, Wang L-S (2003) Science 299:864
10. Huang W, Bulusu S, Pal R, Zeng XC, Wang L-S (2009) ACS Nano 3:1225
11. Woodham AP, Meijer G, Fielicke A (2012) Angew Chem Int Ed 51:4444
12. Woodham AP, Meijer G, Fielicke A (2013) J Am Chem Soc 135:1727
13. Cox DM, Brickman R, Creegan K, Kaldor A (1991) Z Phys D—At, Mol Clusters 19:353
14. Kim YD, Ganteför G, Sun Q, Jena P (2004) Chem Phys Lett 396:69
15. Huang W, Zhai H-J, Wang L-S (2010) J Am Chem Soc 132:4344
16. Lang SM, Bernhardt TM, Barnett RN, Landman U (2011) J Phys Chem C 115:6788
17. Socaciu LD, Hagen J, Bernhardt TM, Wöste L, Heiz U, Häkkinen H, Landman U (2003) J Am Chem Soc 125:10437
18. Schooss D, Weis P, Hampe O, Kappes MM (2010) Philos Trans Roy Soc, A 368:1211
19. Wang L-S (2010) Phys Chem Chem Phys 12:8694
20. Wang L-M, Wang L-S (2012) Nanoscale 4:4038
21. Bernhardt TM (2005) Int J Mass Spectrom 243:1
22. Krückeberg S, Schooss D, Maier-Borst M, Parks JH (2000) Phys Rev Lett 85:4494
23. Maier-Borst M, Cameron DB, Rokni M, Parks JH (1999) Phys Rev A 59:R3162
24. von Helden G, Hsu M-T, Kemper PR, Bowers MT (1991) J Chem Phys 95:3835
25. Siegbahn K (1982) Rev Mod Phys 54:709
26. Leopold DG, Ho J, Lineberger WC (1987) J Chem Phys 86:1715
27. Neumark DM (2008) J Phys Chem A 112:13287
28. Yang Z, Leon I, Wang L-S (2013) J Chem Phys 139:021106
29. Gruene P, Rayner DM, Redlich B, van der Meer AFG, Lyon JT, Meijer G, Fielicke A (2008) Science 321:674
30. Onida G, Reining L, Rubio A (2002) Rev Mod Phys 74:601
31. Schweizer A, Weber JM, Gilb S, Schneider H, Schooss D, Kappes MM (2003) J Chem Phys 119:3699
32. Collings BA, Athanassenas K, Lacombe D, Rayner DM, Hackett PA (1994) J Chem Phys 101:3506
33. Gilb S, Jacobsen K, Schooss D, Furche F, Ahlrichs R, Kappes MM (2004) J Chem Phys 121:4619
34. Gloess AN, Schneider H, Weber JM, Kappes MM (2008) J Chem Phys 128:114312
35. Collings BA, Athanassenas K, Rayner DM, Hackett PA (1993) Z Phys D—At, Mol Clusters 26:36
36. Lecoultre S, Rydlo A, Felix C, Buttet J, Gilb S, Harbich W (2011) J Chem Phys 134:074302
37. Hopkins WS, Woodham AP, Plowright RJ, Wright TG, Mackenzie SR (2010) J Chem Phys 132:214303
38. Hopkins WS, Woodham AP, Plowright RJ, Wright TG, Mackenzie SR (2011) J Chem Phys 134:094311
39. Bekkerman A, Kolodney E, von Helden G, Sartakov B, van Heijnsbergen D, Meijer G (2006) J Chem Phys 124:184312
40. Haertelt M, Lapoutre VJF, Bakker JM, Redlich B, Harding DJ, Fielicke A, Meijer G (2011) J Phys Chem Lett 2:1720
41. Asmis KR, Fielicke A, von Helden G and Meijer G (2007) Vibrational spectroscopy of gas-phase clusters and complexes. In: Woodruff DP (ed) Atomic clusters: from gas phase to deposited. Elsevier, Amsterdam, the Netherlands, pp 327–371 (chap. 8)
42. Oepts D, van der Meer AFG, van Amersfoort PW (1995) Infrared Phys Technol 36:297

43. Fielicke A, Kirilyuk A, Ratsch C, Behler J, Scheffler M, von Helden G, Meijer G (2004) Phys Rev Lett 93:023401
44. Fielicke A, von Helden G, Meijer G (2005) Eur Phys J D 34:83
45. Pyykkö P (2004) Angew Chem Int Ed 43:4412
46. Pyykkö P (2005) Inorg Chim Acta 358:4113
47. Pyykkö P (2008) Chem Soc Rev 37:1967
48. Weis P, Bierweiler T, Vollmer E, Kappes MM (2002) J Chem Phys 117:9293
49. Gilb S, Weis P, Furche F, Ahlrichs R, Kappes MM (2002) J Chem Phys 116:4094
50. Xing X, Yoon B, Landman U, Parks JH (2006) Phys Rev B 74:165423
51. Koskinen P, Häkkinen H, Huber B, von Issendorff B, Moseler M (2007) Phys Rev Lett 98:015701
52. Assadollahzadeh B, Schwerdtfeger P (2009) J Chem Phys 131:064306
53. Häkkinen H (2008) Chem Soc Rev 37:1847
54. Li X-B, Wang H-Y, Yang X-D, Zhu Z-H, Tang Y-J (2007) J Chem Phys 126:084505
55. Olson RM, Varganov S, Gordon MS, Metiu H, Chretien S, Piecuch P, Kowalski K, Kucharski SA, Musial M (2005) J Am Chem Soc 127:1049
56. Huang W, Wang L-S (2009) Phys Chem Chem Phys 11:2663
57. Huang W, Pal R, Wang L-M, Zeng XC, Wang L-S (2010) J Chem Phys 132:054305
58. Pal R, Wang L-M, Huang W, Wang L-S, Zeng XC (2011) J Chem Phys 134:054306
59. Wang L-M, Pal R, Huang W, Zeng XC, Wang L-S (2010) J Chem Phys 132:114306
60. Ghiringhelli LM, Gruene P, Lyon JT, Rayner DM, Meijer G, Fielicke A, Scheffler M (2013) New J Phys 15:083003
61. Lechtken A, Neiss C, Stairs J, Schooss D (2008) J Chem Phys 129:154304
62. Beret EC, Ghiringhelli LM, Scheffler M (2011) Faraday Discuss 152:153
63. Pyykkö P, Runeberg N (2002) Angew Chem Int Ed 41:2174
64. Koyasu K, Naono Y, Akutsu M, Mitsui M, Nakajima A (2006) Chem Phys Lett 422:62
65. Kiran B, Li X, Zhai H-J, Wang L-S (2006) J Chem Phys 125:133204
66. Li X, Kiran B, Wang L-S (2005) J Phys Chem A 109:4366
67. Kiran B, Li X, Zhai H-J, Cui L-F, Wang L-S (2004) Angew Chem Int Ed 43:2125
68. Jena NK, Chandrakumar KRS, Ghosh SK (2011) J Phys Chem Lett 2:1476
69. Neukermans S, Janssens E, Tanaka H, Silverans RE, Lievens P (2003) Phys Rev Lett 90:033401
70. Janssens E, Tanaka H, Neukermans S, Silverans RE, Lievens P (2003) New J Phys 5:46.1
71. Tanaka H, Neukermans S, Janssens E, Silverans RE, Lievens P (2003) J Am Chem Soc 125:2862
72. Wang L-M, Pal R, Huang W, Zeng XC, Wang L-S (2009) J Chem Phys 130:051101
73. Wang L-M, Bai J, Lechtken A, Huang W, Schooss D, Kappes MM, Zeng XC, Wang L-S (2009) Phys Rev B 79:033413
74. Wang L-M, Bulusu S, Zhai H-J, Zeng X-C, Wang L-S (2007) Angew Chem Int Ed 46:2915
75. Wang L-M, Bulusu S, Huang W, Pal R, Wang L-S, Zeng XC (2007) J Am Chem Soc 129:15136
76. Lin L, Höltzl T, Gruene P, Claes P, Meijer G, Fielicke A, Lievens P, Nguyen MT (2008) ChemPhysChem 9:2471
77. Lin L, Claes P, Gruene P, Meijer G, Fielicke A, Nguyen MT, Lievens P (2010) ChemPhysChem 11:1932
78. Lang SM, Bernhardt TM (2012) Phys Chem Chem Phys 14:9255
79. Haruta M, Kobayashi T, Sano H, Yamada N (1987) Chem Lett 16:405
80. Haruta M, Yamada N, Kobayashi T, Iijima S (1989) J Catal 115:301
81. Bond GC, Thompson DT (1999) Cat Rev - Sci Eng 41:319
82. Mikami Y, Dhakshinamoorthy A, Alvaro M, García H (2013) Catal Sci Technol 3:58
83. Sanchez A, Abbet S, Heiz U, Schneider WD, Häkkinen H, Barnett RN, Landman U (1999) J Phys Chem A 103:9573
84. Mars P, van Krevelen DW (1954) Chem Eng Sci 1(3, Supplement):41

85. Kimble ML, Moore NA, Johnson GE, Castleman AW Jr, Burgel C, Mitric R, Bonacic-Koutecky V (2006) J Chem Phys 125:204311
86. Kimble ML, Castleman AW (2004) Int J Mass Spectrom 233:99
87. Kimble ML, Moore NA, Castleman AW, Bürgel C, Mitrić R, Bonačić-Koutecký V (2007) Eur Phys J D 43:205
88. Johnson GE, Reilly NM, Tyo EC, Castleman AW (2008) J Phys Chem C 112:9730
89. Kim YD, Fischer M, Ganteför G (2003) Chem Phys Lett 377:170
90. Salisbury BE, Wallace WT, Whetten RL (2000) Chem Phys 262:131
91. Lee TH, Ervin KM (1994) J Phys Chem 98:10023
92. Walter M, Hakkinen H (2006) Phys Chem Chem Phys 8:5407
93. Holleman AF, Wiberg E (1995) Lehrbuch der Anorganischen Chemie de Gruyter, Berlin, New York
94. Stolcic D, Fischer M, Ganteför G, Kim YD, Sun Q, Jena P (2003) J Am Chem Soc 125:2848
95. Pal R, Wang L-M, Pei Y, Wang L-S, Zeng XC (2012) J Am Chem Soc 134:9438
96. Mills G, Gordon MS, Metiu H (2002) Chem Phys Lett 359:493
97. Roldan A, Ricart JM, Illas F, Pacchioni G (2010) Phys Chem Chem Phys 12:10723
98. Franceschetti A, Pennycook SJ, Pantelides ST (2003) Chem Phys Lett 374:471
99. Fernández EM, Ordejón P, Balbás LC (2005) Chem Phys Lett 408:252
100. Boronat M, Corma A (2010) Dalton Trans 39:8538
101. Lang SM, Bernhardt TM, Barnett RN, Yoon B, Landman U (2009) J Am Chem Soc 131:8939
102. Blyholder G (1964) J Phys Chem 68:2772
103. Hammer B, Nørskov JK (1995) Nature 376:238
104. Hammer B, Morikawa Y, Nørskov JK (1996) Phys Rev Lett 76:2141
105. Fielicke A, Gruene P, Meijer G, Rayner DM (2009) Surf Sci 603:1427
106. Sterrer M, Yulikov M, Fischbach E, Heyde M, Rust H-P, Pacchioni G, Risse T, Freund H-J (2006) Angew Chem Int Ed 45:2630
107. Balteanu I, Balaj OP, Fox BS, Beyer MK, Bastl Z, Bondybey VE (2003) Phys Chem Chem Phys 5:1213
108. Hagen J, Socaciu LD, Heiz U, Bernhardt TM, Wöste L (2003) Eur Phys J D 24:327
109. Neumaier M, Weigend F, Hampe O, Kappes MM (2005) J Chem Phys 122:104702
110. Neumaier M, Weigend F, Hampe O, Kappes MM (2008) Faraday Discuss 138:393
111. Fielicke A, von Helden G, Meijer G, Pedersen DB, Simard B, Rayner DM (2005) J Am Chem Soc 127:8416
112. Fielicke A, von Helden G, Meijer G, Simard B, Rayner DM (2005) J Phys Chem B 109:23935
113. Wallace WT, Whetten RL (2000) J Phys Chem B 104:10964
114. Xie Y, Dong F, Bernstein ER (2011) Catal Today 177:64
115. Yang X-F, Wang Y-L, Zhao Y-F, Wang A-Q, Zhang T, Li J (2010) Phys Chem Chem Phys 12:3038
116. Pal R, Huang W, Wang Y-L, Hu H-S, Bulusu S, Xiong X-G, Li J, Wang L-S, Zeng XC (2011) J Phys Chem Lett 2:2288
117. Zhai H-J, Kiran B, Dai B, Li J, Wang L-S (2005) J Am Chem Soc 127:12098
118. Zhai H-J, Pan L-L, Dai B, Kiran B, Li J, Wang L-S (2008) J Phys Chem C 112:11920
119. Zhai H-J, Wang L-S (2005) J Chem Phys 122:051101
120. Lupinetti AJ, Fau S, Frenking G, Strauss SH (1997) J Phys Chem A 101:9551
121. Fielicke A, von Helden G, Meijer G, Pedersen DB, Simard B, Rayner DM (2006) J Chem Phys 124:194305
122. Fielicke A, von Helden G, Meijer G, Simard B, Rayner DM (2005) Phys Chem Chem Phys 7:3906
123. Jackschath C, Rabin I, Schulze W (1992) Ber Bunsen-Ges Phys Chem 96:1200
124. Veldeman N, Lievens P, Andersson M (2005) J Phys Chem A 109:11793
125. Fielicke A, Gruene P, Meijer G, Rayner DM (2008) Unpublished Data
126. Wallace WT, Whetten RL (2002) J Am Chem Soc 124:7499

127. Wallace WT, Wyrwas RB, Whetten RL, Mitrić R, Bonačić-Koutecký V (2003) J Am Chem Soc 125:8408
128. Hagen J, Socaciu LD, Elijazyfer M, Heiz U, Bernhardt TM, Wöste L (2002) Phys Chem Chem Phys 4:1707
129. Häkkinen H, Landman U (2001) J Am Chem Soc 123:9704
130. Bernhardt TM, Socaciu-Siebert LD, Hagen J, Wöste L, (2005) Appl Catal A 291:170
131. Mantina M, Valero R, Truhlar DG (2009) J Chem Phys 131:064706

Index